

Open Research Online

The Open University's repository of research publications and other research outputs

An investigation of fatigue crack growth acceleration

Thesis

How to cite:

Doré, Matthew James (2015). An investigation of fatigue crack growth acceleration. PhD thesis The Open University.

For guidance on citations see [FAQs](#).

© 2015 The Author

Version: Version of Record

Copyright and Moral Rights for the articles on this site are retained by the individual authors and/or other copyright owners. For more information on Open Research Online's [data policy](#) on reuse of materials please consult the policies page.

oro.open.ac.uk



**The Open
University**

**Faculty of Mathematics,
Computing & Technology**

Department of Engineering and Innovation

Materials Engineering Group

**AN INVESTIGATION OF FATIGUE
CRACK GROWTH ACCELERATION**

Matthew James Doré BEng(Hons)

September 2015

**A THESIS SUBMITTED TO THE DEPARTMENT OF ENGINEERING AND INNOVATION OF
THE OPEN UNIVERSITY FOR THE DEGREE OF DOCTOR OF PHILOSOPHY**

31 0350210 5



AN INVESTIGATION OF FATIGUE CRACK GROWTH ACCELERATION

By Matthew J Doré

This thesis is submitted for the degree of
Doctor of Philosophy.

[September, 2015]

© by Matthew J Doré (2015)

TWI Ltd
Granta Park
Great Abington
Cambridge
CB21 6AL
UK

The Open University
Faculty Mathematics, Computing & Technology
Walton Hall
Milton Keynes
MK7 6AA
UK

ACKNOWLEDGEMENT

This PhD research project was funded by the Industrial Members of TWI, as part of the Core Research Programme.

I would like to thank Dr Salih Gungor and Professor John Bouchard of the Open University and Professor Michael Fitzpatrick of Coventry University, for their supervision and guidance throughout this research project. I would also like to especially thank Dr Stephen Maddox formerly of TWI, for his supervision, guidance, patience and mentoring. Without his wealth of knowledge in this field, this work would not have been possible.

Thanks also to Mr Gordon Imlach for his training and assistance with the scanning electron microscope, Miss Jenny Crump for her assistance with the X-ray tomography, Dr Philippe Bastid for support with the FE modelling, Mr Philip Robinson for his assistance with the LabView software, and the TWI fatigue laboratory technicians, in particular Mr Daniel Bloom, for all his assistance over the last few years.

I would also like to thank Dr Yan-hui Zhang for many useful technical discussions, Dr Christophe Berre for his independent review, and Dr Martin Ogle for his encouragement and interest in my research.

A special thanks to my wife Katie for her understanding and patience, and my children Harrison and Tilly for allowing Daddy time to study. Thanks also to my mother Carol for all her support and encouragement over the years.

My final thanks are to my late father Anthony Doré who gave me my first appreciation of engineering and the drive to succeed and develop myself in this chosen field.

To live in the hearts and minds of others is not to die

Thomas Campbell, (1825)

ABSTRACT

The problem of fatigue crack growth acceleration was investigated in crack propagation studies and endurance testing. The study was driven by the needs of designers and researchers alike, to provide a better understanding of the mechanisms associated with accelerated growth, and recommendations on the use of Miner's rule to calculate fatigue life under variable amplitude loading.

The study was conducted on S355 structural steel and 6082 T6 aluminium alloy using centre-crack tension (CCT) specimens, with and without additional welding, and longitudinal fillet welded specimens. Crack growth rates under simple sequence loading and more complex variable amplitude (VA) loading, all cycling down from fixed tensile stress levels, were determined using optical or direct current potential drop methods and scanning electron microscope examination of fracture surface striations.

Under simple loading sequences, comprising two magnitudes of stress range, the presence of tensile underloads resulted in accelerated growth rates compared with those based on constant amplitude (CA) loading. Various possible mechanisms to explain crack growth acceleration and factors that might influence it, notably crack closure and welding residual stress, were evaluated. The most promising outcome came from finite element analysis (FEA) of the crack tip stress and strain. This showed that whereas under CA loading the material near the crack tip cycled about zero mean stress, the mean stress was tensile after the application of a tensile underload, thus resulting in a higher crack growth rate.

Fatigue endurance testing of welded joints performed under the same types of loading confirmed that Miner's rule overestimated the actual lives, consistent with the occurrence of acceleration. Thus, it was concluded that modification of the principle and application of Miner's rule is required

to allow for stress interactions that cause crack growth acceleration. Preliminary design recommendations were made.

PREFACE

This dissertation is submitted for the degree of Doctor of Philosophy at the Open University, Milton Keynes. The work was carried out under the supervision of Dr S Gungor and Professor J Bouchard of the Open University, Professor M E Fitzpatrick of Coventry University and Dr S J Maddox formerly of TWI, Cambridge, between the dates of October 2008 and September 2015.

Except where acknowledgement and reference to previous work is made, this work is, to the best of my knowledge, original and has been carried out without collaboration. Neither this, nor any substantially similar thesis has been, or is being, submitted for any other degree, diploma or qualification at any other university.

This thesis contains fewer than 100,000 words and is identical to that which was examined, except for corrections as required by the examiners.

The following papers were produced during the course of this study on work carried out in Chapters 5, 6 and 7.

Journal paper

Matthew J Doré and Stephen J Maddox, 2014: 'Investigation of Fatigue Crack Acceleration under Variable Amplitude Loading for a Structural Steel and Aluminium Alloy', *Advanced Materials Research Vols. 891-892 (2014) pp 581-587*, Trans Tech Publications, Switzerland.

Referred conference papers

Matthew J Doré and Stephen J Maddox, 2013: 'Accelerated Fatigue Crack Growth in 6082 T651 Aluminium Alloy Subjected to Periodic Underloads', *5th Fatigue Design Conference, Fatigue Design 2013, Procedia Engineering 66 (2013) pp 313-322*.

Matthew J Doré and Stephen J Maddox, 2014: 'Investigation of Fatigue Crack Acceleration under Variable Amplitude Loading for a Structural Steel and Aluminium Alloy', Proceedings of the 11th International Fatigue Congress, Melbourne, Australia.

The authors contribution to the research performed and that of others is given below.

Specimen manufacture: The manufacture of specimens was performed by TWI using standard specimen designs using dimensions as specified by the author.

Mechanical testing: Tensile testing, hardness measurements and chemical analysis was all performed at TWI as requested by the author. Low cycle fatigue testing was carried out by Westmoreland Mechanical Testing & Research with testing details specified by the author. All mechanical tests were performed in accordance with the relevant British Standards.

Fatigue crack growth rate, fatigue endurance, crack closure and residual stress relaxation testing was performed by the author at TWI. To aid completion of the extensive test programme, the author also trained laboratory staff in the preparation and setup of test specimens specific to the research performed.

Strain gauging and residual stress measurement: Strain gauging of specimens for the purpose of performing crack closure measurements was carried out by the author. Residual stress measurement using the centre hole air abrasive technique was initially carried out by the author and then by a laboratory technician under the direction of the author at TWI. Residual stress measurement by neutron diffraction was performed by the author at FRM2 Technische Universität München in Garching, Germany, under the supervision of Dr Michael Hofmann.

Finite element analysis: All work performed was by the Numerical Modelling Section at TWI. All model requirements, geometry, loading requirements, interpretation of data and model validation were specified/carried out by the author.

X-Ray computed tomography: This was conducted by Miss Jenny Crump at Southampton University on a specimen supplied and at a location specified by the author.

SYMBOLS AND DEFINITIONS

Symbol	Definition	Units
α	Non-dimensional crack length $\left(\frac{a}{b}\right)$ and Kinematic hardening	-
β, γ	Acceleration factor	-
γ	Rate at which c is reached during kinematic hardening	Strain
ΔK	Range of stress intensity factor	N/mm ^{3/2} , MPa.m ^{0.5}
ΔK_{eff}	Effective stress intensity factor range	N/mm ^{3/2} , MPa.m ^{0.5}
ΔK_{effth}	Effective stress intensity factor range at threshold	N/mm ^{3/2} , MPa.m ^{0.5}
ΔK_{eq}	Equivalent constant amplitude stress intensity factor range	N/mm ^{3/2} , MPa.m ^{0.5}
$\Delta K_{th}, \Delta K_0$	Threshold value of ΔK for crack propagation to occur	N/mm ^{3/2} , MPa.m ^{0.5}
$\Delta S_{eff}, \Delta \sigma_{eff}$	Effective stress range	N/mm ² , MPa
ΔS_{eq}	Equivalent constant amplitude stress range	N/mm ² , MPa
$\Delta \epsilon_p$	Plastic strain amplitude	-
ϵ	Strain	-
ϵ_e	Elastic strain	-
ϵ_p	Plastic strain	-
ϵ'_f	Fatigue ductility coefficient	-
ϵ_{xx}	Strain in X direction	-
ϵ_{yy}	Strain in Y direction	-
θ	Angle	degrees

λ	Distance between inner and outer supports	mm
μ	Linear attenuation coefficient	-
$\mu\varepsilon$	microstrain	-
π	Constant (3.14159...)	-
σ_c	Corrected stress	N/mm ² , MPa
σ_{ij}	Stress tensor	-
σ_{nom}	Nominal stress	N/mm ² , MPa
σ_{xx}	Stress in <i>X</i> direction	N/mm ² , MPa
σ_{yy}	Stress in <i>Y</i> direction	N/mm ² , MPa
σ_{yy}^{max}	Maximum residual stress in <i>Y</i> direction	N/mm ² , MPa
σ_{zz}	Stress in <i>Z</i> direction	N/mm ² , MPa
$\sum \frac{n}{N}$	Miner rule summation	-
ν	Poisson's ratio or Displacement (in the <i>y</i> direction)	- / mm
$\nu K_2/K_1$	Centre-hole biaxial interaction constant	-
a	Length of edge crack, depth of semi-elliptical surface crack or half length of through-thickness crack	mm
\bar{a}	Average crack length	mm
a_i	Initial crack length	mm
a_f	Final crack length	mm
$a/2c$	Elliptical crack front aspect ratio	-
A, C	Material constants for crack propagation equation	-
b	Rate at which Q is reached during isotropic hardening	Strain
B, T, t	Thickness	mm
c	Fatigue ductility exponent, or, Maximum hardening level -	

	above the initial elastic limit during kinematic hardening	-
d	Diffraction angle	degrees
d_0, θ_0	Material values in the unstressed condition	-
da/dN	Crack growth rate	mm/cycle ⁻¹
da/dN_{Minor}	Crack growth rate for minor cycles	mm/cycle ⁻¹
da/dN_{Major}	Crack growth rate for major cycles	mm/cycle ⁻¹
d_{hkl}	Lattice spacing	Angstroms
D	Damage sum from Miner's summation $\sum n/N$	-
D_{Lim}	Prescribed limit of the fatigue damage value	-
E	Young's modulus	MN/mm ² , GPa
F	Force	kN
F_{max}	Maximum force	kN
h	Planck constant	-
hkl	Crystallographic plane (Miller indices)	-
H	Isotropic hardening coefficient	-
I	X-ray beam intensity	Photons per unit time detected
I_0	X-ray beam energy	keV
K	Stress intensity factor	N/mm ^{3/2} , MPa.m ^{0.5}
K_I	Stress intensity factor under mode I loading	N/mm ^{3/2} , MPa.m ^{0.5}
K_C	Material fracture toughness	N/mm ^{3/2} , MPa.m ^{0.5}
K_{IC}	Plane strain fracture toughness	N/mm ^{3/2} , MPa.m ^{0.5}
K_{max}	Maximum stress intensity factor	N/mm ^{3/2} , MPa.m ^{0.5}
K_{op}	Crack opening stress intensity factor	N/mm ^{3/2} , MPa.m ^{0.5}
K_{peak}	Peak stress intensity factor	N/mm ^{3/2} , MPa.m ^{0.5}

K_t	Stress concentration factor	-
K_σ	Geometric mean of the stress concentration factor	-
K_ϵ	Geometric mean of the strain concentration factor	-
m	Exponent for crack propagation, or, Inverse slope to Log S_r – Log N curve	-
m_2	Value of m for $5 \times 10^6 < N \leq 10^8$ cycles	-
m_n	Neutron mass	meV
M_k	Magnification factor for weld toe crack	-
M_{ku}	Magnification factor at maximum depth of weld toe crack	-
M_{kc}	Magnification factor at the tips of semi-elliptical weld toe crack on plate surface	-
n	Number of cycles applied	-
N, N_c	Cycles to failure under CA or VA loading	Cycles
\bar{N}	Average endurance	Cycles
N_B	Blocks to failure	-
N_f	Load reversals to failure	-
N_{OC}	Constant amplitude endurance corresponding to S_{OC}	Cycles
P	Pressure	N/mm ² , MPa
p_i	Relative stress range used in VA loading spectra	-
q	Notch sensitivity index	-
Q	Maximum hardening level above the initial elastic limit - during isotropic hardening	-
r	distance from crack tip	mm
r_p	Plastic zone size or Plastic zone radius	mm
r_c	Cyclic plastic zone size or Cyclic plastic zone radius	mm

R	Stress ratio (S_{min}/S_{max})	-
R _{p0.2}	0.2% proof strength at test temperature	N/mm ² , MPa
S	Stress or Stress range	N/mm ² , MPa
S _{eq}	Equivalent stress	N/mm ² , MPa
S _{max} , σ _{max}	Maximum stress in cycle	N/mm ² , MPa
S _{mean} , S _m	Mean stress in cycle	N/mm ² , MPa
S _{OC}	Constant amplitude non-propagating stress range at 10 ⁷ cycles	N/mm ² , MPa
S _{OP}	Stress at which a crack opens	N/mm ² , MPa
S _r , ΔS	Stress range	N/mm ² , MPa
S _{r_{eff}}	Effective stress range	N/mm ² , MPa
S _{r_{max}}	Maximum stress range	N/mm ² , MPa
S _{ys} , YS, σ _{ys}	Yield stress (or 0.2% proof stress)	N/mm ² , MPa
t _{hkl}	Time of flight	Seconds
Tan, Cos, Sin	Trigonometric function	-
U	Fraction of load cycle for which a crack is open	-
V, Vr	Measured voltage	Volts
W	Specimen width	mm
x _{peak}	Offset used for un-symmetrical σ _{yy} ^{max} measurements	mm
Y	Geometric function of crack size and shape	-
Y ₀	Lead spacing used in direct potential drop	mm
ACPD	Alternating current potential drop	
AL	Aluminium plate specimen	
BC	Boundary condition	

BCAL	Block constant amplitude loading
BOP	Bead on plateCA Constant amplitude
CAFL	Constant amplitude fatigue limit
CAL	Constant amplitude loading
CAT	Computerized axial tomography
CCT	Centre crack tension
CEV	Carbon equivalent value
CL	Used to indicate a specimen used for crack closure measurement
COD	Crack opening displacement
CT	Compact tension
CTOD	Crack tip opening displacement
DCPD	Direct current potential drop
D-OES	Direct optical emission spectrometry
EDM	Electrical discharge machining
EPD	Electric potential difference
FCGR	Fatigue crack growth rate
FEA	Finite element analysis
FEGSEM	Field emission gun scanning electron microscope
FIL	Used to denote a plate specimen with fillet welded attachments
HAZ	Heat affected zone
HCF	High cycle fatigue
ICP-OES	Inductively coupled plasma optical emission spectrometry
LCF	Low cycle fatigue
LD	Longitudinal direction
LEFM	Linear elastic fracture mechanics

MMA	Manual metal arc
MT	Middle tension
ND	Normal direction
OLR	Overload ratio
PM	Parent material or parent metal
R	Indicates a CCT specimen with weld beads deposited (Residual stress)
RES	Indicates a specimen used for residual stress measurement
SBL	Single block loading
SCF	Stress concentration factor
SEM	Scanning electron microscope
SENB	Single edge notch bend
SIF	Stress intensity factor
ST	Steel plate specimen
TD	Transverse direction
TIG	Tungsten inert gas
ToF	Time of flight
UTS	Ultimate tensile strength
VA	Variable amplitude
VAL	Variable amplitude loading
WM	Weld metal
XCT	X-ray computed tomography
μ -CT	Micro-computed tomography

TABLE OF CONTENTS

Acknowledgements.....	i
Abstract.....	ii
Preface.....	iv
Symbols and Definitions.....	vii
Table of Contents.....	xiv
List of Tables.....	xxiii
List of Figures.....	xxviii
CHAPTER 1 INTRODUCTION.....	1-1
1.1 OVERVIEW.....	1-1
1.2 FATIGUE DESIGN	1-1
1.3 OBJECTIVES AND APPROACH.....	1-3
1.4 STRUCTURE OF THESIS	1-5
1.5 APPLICATION OF WORK PERFORMED	1-6
CHAPTER 2 BACKGROUND AND LITERATURE REVIEW.....	2-1
2.1 INTRODUCTION.....	2-1
2.2 CYCLIC STRESS-STRAIN RELATIONSHIPS	2-3
2.2.1 STRESS-LIFE (S-N).....	2-3
2.2.2 STRAIN-LIFE (ϵ -N).....	2-6
2.3 CRACK INITIATION.....	2-6
2.4 THEORY OF LINEAR ELASTIC FRACTURE MECHANICS	2-9
2.4.1 LOADING MODES.....	2-9
2.4.2 STRESS INTENSITY FACTOR.....	2-9
2.4.3 PLANE STRESS AND PLANE STRAIN.....	2-11
2.4.4 CRACK TIP PLASTICITY	2-12

2.5	FATIGUE CRACK PROPAGATION	2-16
2.6	INFLUENCING FACTORS ON FATIGUE CRACK GROWTH.....	2-21
2.7	THE EFFECT OF CRACK CLOSURE	2-23
2.8	RESIDUAL STRESSES	2-25
2.8.1	FORMATION OF RESIDUAL STRESSES THROUGH WELDING.....	2-25
2.8.2	RESIDUAL STRESS MEASUREMENT	2-27
2.8.3	RESIDUAL STRESS RELAXATION.....	2-28
2.9	CUMULATIVE DAMAGE.....	2-28
2.9.1	VARIABLE AMPLITUDE LOADING	2-28
2.9.2	CYCLE COUNTING METHODS	2-29
2.9.3	PALMGREN-MINER CUMULATIVE DAMAGE RULE.....	2-31
2.9.4	THE INFLUENCE OF NARROW AND WIDE BAND SERVICE LOADING.....	2-34
2.10	INTERACTION EFFECTS ON FATIGUE CRACK ACCELERATION	2-36
2.10.1	GENERALITIES	2-36
2.10.2	LOAD SEQUENCE EFFECTS AND OVERLOAD RATIO	2-36
2.10.3	INFLUENCE OF EFFECTIVE STRESS INTENSITY FACTOR ON ACCELERATION	2-40
2.11	SUMMARY OF THE BACKGROUND AND LITERATURE REVIEW AND IDENTIFICATION OF NOVELTY IN THE CURRENT WORK	2-41
CHAPTER 3 RESEARCH METHODOLOGY		3-1
3.1	INTRODUCTION	3-1
3.2	SPECIMEN IDENTIFICATION SYSTEM.....	3-1
3.3	MEASUREMENT OF FATIGUE CRACK GROWTH RATES	3-2
3.3.1	TEST SPECIMEN	3-2
3.3.2	FATIGUE CRACK GROWTH RATE TESTING	3-4
3.3.3	INTRODUCTION OF NOTCH	3-5
3.4	FATIGUE TESTS.....	3-6
3.4.1	TEST SPECIMENS.....	3-6

3.4.1.1	CENTRE CRACK TENSION SPECIMENS.....	3-6
3.4.1.2	FILLET WELDED SPECIMENS WITH LONGITUDINAL ATTACHMENTS.....	3-8
3.4.2	FATIGUE TESTING	3-11
3.4.3	TESTS UNDER SIMPLE LOAD SEQUENCES	3-11
3.4.4	TESTS UNDER VARIABLE AMPLITUDE SPECTRUM LOADING.....	3-13
3.5	MEASUREMENT AND MONITORING OF FATIGUE CRACK GROWTH.....	3-14
3.5.1	OPTICAL MEASUREMENT.....	3-14
3.5.2	POTENTIAL DROP METHODS	3-15
3.5.2.1	DIRECT CURRENT POTENTIAL DROP	3-15
3.5.2.2	ALTERNATING CURRENT POTENTIAL DROP	3-19
3.6	APPLICATION OF STRAIN GAUGES UNDER STATIC LOADING CONDITIONS TO ESTABLISH CRACK OPENING AND CLOSURE LEVELS.....	3-20
3.7	RESIDUAL STRESS MEASUREMENT	3-24
3.7.1	INTRODUCTION.....	3-24
3.7.2	CENTRE-HOLE METHOD	3-25
3.7.2.1	BACKGROUND.....	3-25
3.7.2.2	APPLICATION IN CURRENT RESEARCH PROJECT	3-28
3.7.3	NEUTRON DIFFRACTION	3-29
3.7.3.1	BACKGROUND.....	3-29
3.7.3.2	APPLICATION IN CURRENT RESEARCH PROJECT	3-32
3.8	FINITE ELEMENT ANALYSIS	3-34
3.8.1	MODEL DEVELOPMENT	3-34
3.9	FRACTOGRAPHIC EXAMINATION.....	3-47
3.9.1	METALLOGRAPHIC PREPARATION.....	3-47
3.9.2	SCANNING ELECTRON MICROSCOPE.....	3-47
3.9.3	X-RAY COMPUTED TOMOGRAPHY	3-48
3.10	SUMMARY	3-50
CHAPTER 4 MATERIAL SELECTION AND CHARACTERISATION		4-1

4.1	INTRODUCTION	4-1
4.2	SELECTED MATERIALS USE IN INDUSTRY	4-1
4.2.1	STRUCTURAL STEEL	4-1
4.2.2	ALUMINIUM ALLOY	4-2
4.3	MATERIAL CHARACTERISATION	4-3
4.3.1	GENERAL.....	4-3
4.3.2	TENSILE TESTING.....	4-3
4.3.2.1	STATIC PROPERTIES	4-3
4.3.2.2	CYCLIC PROPERTIES	4-4
4.3.3	HARDNESS TESTING.....	4-7
4.3.4	CHEMICAL ANALYSIS.....	4-8
4.4	FATIGUE CRACK GROWTH RATE TESTING	4-9
4.4.1	FATIGUE CRACK GROWTH RATE TESTING OF S355 STEEL SPECIMENS	4-9
4.4.2	FATIGUE CRACK GROWTH RATE TESTING OF 6082 T651 ALUMINIUM ALLOY SPECIMENS	4-18
4.5	X-RAY COMPUTED TOMOGRAPHY	4-26
4.6	SUMMARY.....	4-29

CHAPTER 5 THE EFFECT OF PERIODIC UNDERLOADS ON FATIGUE CRACK GROWTH RATE.....5-1

5.1	INTRODUCTION	5-1
5.2	FATIGUE CRACK GROWTH RATE TESTING	5-2
5.2.1	OUTLINE OF TESTS	5-2
5.2.2	CONSTANT AMPLITUDE LOADING	5-3
5.2.3	VARIABLE AMPLITUDE LOADING	5-4
5.3	EXPERIMENTAL RESULTS	5-6
5.3.1	FATIGUE TESTING UNDER CONSTANT AMPLITUDE LOADING.....	5-6
5.3.2	THE EFFECT OF UNDERLOAD MAGNITUDE ON CRACK GROWTH RATE FOR PLAIN SPECIMENS.....	5-9

5.3.2.1	SBL2 LOADING	5-9
5.3.2.2	SBL1.5 LOADING	5-12
5.3.3	THE EFFECT OF UNDERLOAD MAGNITUDE ON CRACK GROWTH RATE FOR WELDED SPECIMENS	5-15
5.3.3.1	SBL2 LOADING	5-15
5.3.3.2	SBL1.5 LOADING	5-18
5.3.4	SUMMARY OF THE EFFECT OF RESIDUAL STRESS ON APPLIED LOADING SEQUENCES.....	5-21
5.3.5	COMPARISON OF ACCELERATION FACTORS γ AND β	5-24
5.3.5.1	CALCULATION OF β	5-24
5.3.5.2	STEEL UNDER SBL2 LOADING.....	5-25
5.3.5.3	ALUMINIUM UNDER SBL2 LOADING.....	5-26
5.3.5.4	STEEL UNDER SBL1.5 LOADING.....	5-27
5.3.5.5	ALUMINIUM UNDER SBL1.5 LOADING.....	5-28
5.3.6	ESTIMATING CRACK GROWTH RATE BY EXAMINATION OF SPECIMEN FRACTURE SURFACES.....	5-29
5.4	SUMMARY OF FINDINGS	5-43
 CHAPTER 6 MECHANISMS INFLUENCING CRACK GROWTH ACCELERATION. 6-1		
6.1	INTRODUCTION.....	6-1
6.2	CRACK TIP PLASTICITY.....	6-2
6.2.1	THE ROLE OF CRACK CLOSURE IN FATIGUE CRACK GROWTH ACCELERATION	6-2
6.2.2	CRACK CLOSURE LEVEL MEASUREMENT	6-2
6.2.2.1	PLAIN S355 STEEL SPECIMENS	6-2
6.2.2.2	WELDED S355 STEEL SPECIMENS.....	6-4
6.2.2.3	PLAIN 6082 T651 ALUMINIUM ALLOY SPECIMENS	6-6
6.2.2.4	WELDED 6082 T651 ALUMINIUM ALLOY SPECIMENS	6-8
6.2.3	PLASTIC ZONE SIZE DETERMINATION.....	6-8

6.2.4	DISCUSSION ON THE EFFECTS.....	6-12
6.3	THE ROLE OF WELDING RESIDUAL STRESSES ON CRACK GROWTH ACCELERATION.....	6-14
6.3.1	INTRODUCTION.....	6-14
6.3.2	MEASURED RESIDUAL STRESS DISTRIBUTIONS.....	6-14
6.3.2.1	CCT SPECIMENS.....	6-14
6.3.2.2	FILLET WELDED SPECIMENS.....	6-19
6.3.3	RESIDUAL STRESS RELAXATION UNDER CYCLIC LOADING.....	6-22
6.3.3.1	CCT SPECIMENS.....	6-22
6.3.3.2	FILLET WELDED SPECIMENS.....	6-24
6.3.4	EFFECT ON RESIDUAL STRESS FOR A PROPAGATING CRACK.....	6-25
6.3.5	DISCUSSION ON THE EFFECTS.....	6-27
6.4	THE ROLE OF CRACK TIP MEAN STRESS ON CRACK GROWTH ACCELERATION	6-28
6.4.1	INTRODUCTION.....	6-28
6.4.2	MODELLING OF CRACK TIP STRESS STATE.....	6-31
6.4.2.1	PLAIN S355 STRUCTURAL STEEL.....	6-31
6.4.2.2	WELDED S355 STRUCTURAL STEEL.....	6-35
6.4.2.3	PLAIN 6082 T651 ALUMINIUM ALLOY.....	6-36
6.4.2.4	WELDED 6082 T651 ALUMINIUM ALLOY.....	6-39
6.4.3	DISCUSSION OF FINDINGS.....	6-41
6.5	METALLURGICAL MECHANISMS.....	6-45
6.5.1	CRACK TIP SHARPENING/BLUNTING.....	6-45
6.5.2	CRACK TIP BRANCHING.....	6-46
6.5.3	CYCLIC HARDENING/SOFTENING.....	6-47
6.6	DISCUSSION.....	6-47
6.6.1	THE EFFECT ON CRACK GROWTH RATE RESPONSE FOLLOWING PERIODIC UNDERLOADS.....	6-47

6.6.1.1	PLAIN SPECIMENS	6-47
6.6.1.2	WELDED SPECIMENS	6-52
6.6.2	THE ROLE OF RESIDUAL STRESS DURING PERIODIC TENSILE UNDERLOADING.....	6-55
6.6.3	ACCELERATED GROWTH OBSERVATIONS FROM STRIATION SPACINGS...	6-57
6.6.4	POSSIBLE MECHANISMS ASSOCIATED WITH CRACK GROWTH RATE ACCELERATION	6-58
6.7	CONCLUSIONS	6-61
CHAPTER 7 ENDURANCE TESTING OF WELDED JOINTS.....		7-1
7.1	INTRODUCTION.....	7-1
7.2	FATIGUE TESTING	7-2
7.2.1	OUTLINE OF TESTS.....	7-2
7.2.2	CONSTANT AMPLITUDE LOADING	7-2
7.2.2.1	CENTRE CRACK TENSION SPECIMENS.....	7-2
7.2.2.2	LONGITUDINAL FILLET WELDED SPECIMENS.....	7-2
7.2.3	VARIABLE AMPLITUDE LOADING	7-3
7.2.3.1	VARIABLE AMPLITUDE LOADING SPECTRUM	7-3
7.2.3.2	CENTRE CRACK TENSION SPECIMENS.....	7-3
7.2.3.3	LONGITUDINAL FILLET WELDED SPECIMENS.....	7-5
7.2.4	EQUIVALENT CONSTANT AMPLITUDE STRESS RANGE	7-8
7.2.5	METHODS OF FATIGUE CRACK DETECTION AND MEASUREMENT	7-9
7.3	RESIDUAL STRESS MEASUREMENT	7-10
7.4	CRACK CLOSURE MEASUREMENTS	7-12
7.5	EXPERIMENTAL RESULTS	7-14
7.5.1	CONSTANT AND VARIABLE AMPLITUDE TESTING OF PLAIN CCT SPECIMENS	7-14
7.5.2	THE EFFECT OF RESIDUAL STRESS ON CCT SPECIMENS TESTED UNDER CONSTANT AND VARIABLE AMPLITUDE LOADING.....	7-16

7.5.3	A FATIGUE CRACK GROWTH RATE ANALYSIS OF CCT SPECIMENS	7-19
7.5.4	THE EFFECT OF LOAD SEQUENCES ON FATIGUE CRACK GROWTH	7-22
7.5.5	VARIABLE AMPLITUDE TESTING OF FILLET WELDED SPECIMENS	7-25
7.5.6	FATIGUE CRACK GROWTH IN FILLET WELDED SPECIMENS	7-29
7.6	FRACTURE MECHANICS ANALYSIS OF FATIGUE CRACK GROWTH IN FILLET WELDED SPECIMENS	7-31
7.6.1	OUTLINE	7-31
7.6.2	CRACK GROWTH MEASUREMENTS.....	7-32
7.6.3	STRESS INTENSITY FACTORS	7-32
7.6.4	CRACK GROWTH CALCULATION.....	7-34
7.6.4.1	CRACK GROWTH UNDER CONSTANT AMPLITUDE LOADING FOR A FILLET WELDED SPECIMEN.....	7-34
7.6.4.2	CRACK GROWTH UNDER VARIABLE AMPLITUDE LOADING FOR A FILLET WELDED SPECIMEN.....	7-35
7.6.5	CALCULATION OF FATIGUE ENDURANCE	7-36
7.7	DISCUSSION	7-37
7.7.1	THE EFFECT OF VARIABLE AMPLITUDE LOADING ON CRACK GROWTH RATE FOR CCT SPECIMENS.....	7-37
7.7.2	LOAD SEQUENCE EFFECTS FOR RANDOMLY GENERATED SPECTRA.....	7-39
7.7.3	THE EFFECT OF VARIABLE AMPLITUDE LOADING ON THE FATIGUE PERFORMANCE OF THE FILLET WELDED SPECIMENS	7-39
7.7.4	CALCULATED RESPONSE UNDER SPECTRUM LOADING.....	7-41
7.7.5	VALIDITY OF MINERS RULE.....	7-42
7.8	CONCLUSIONS.....	7-44
CHAPTER 8 DISCUSSION		8-1
8.1	INTRODUCTION	8-1
8.2	CAUSE OF CRACK GROWTH ACCELERATION	8-2
8.3	IMPLICATIONS OF THE CURRENT WORK TO FATIGUE DESIGN	8-7

8.4	DESIGN GUIDANCE.....	8-9
CHAPTER 9 CONCLUSIONS AND RECOMMENDATIONS		9-1
9.1	RESEARCH AIM.....	9-1
9.2	CONCLUSIONS DRAWN	9-1
9.3	DESIGN RECOMMENDATIONS	9-4
9.4	RECOMMENDATIONS FOR FUTURE WORK.....	9-5
CHAPTER 10 REFERENCES.....		10-1
APPENDIX A SOFTWARE AND PROCESS FLOWCHARTS		
APPENDIX B FINITE ELEMENT ANALYSIS MODEL PLOTS AND VALIDATION		
APPENDIX C STRIATION MEASUREMENT - SCATTER IN ANALYSIS		
APPENDIX D FATIGUE CRACK GROWTH IN FILLET WELDED SPECIMENS		

LIST OF TABLES

Chapter 2

Table 2.10.1 Summary of experimental findings using simple loading spectra.....	2-38
--	------

Chapter 3

Table 3.7.1 Categories of residual stress measurement methods.....	3-24
---	------

Table 3.7.2 Residual stress measurement depths (Rossini et al., 2012).....	3-25
---	------

Table 3.8.1 FE models developed for steel and aluminium CCT specimens.....	3-40
---	------

Chapter 4

Table 4.3.1 Measured and certificate tensile properties of the S355 structural steel.....	4-4
--	-----

Table 4.3.2 Measured and certificate tensile properties of the 6082 T651 aluminium alloy....	4-4
---	-----

Table 4.3.3 Measured hardness (Vickers) for S355 structural steel and 6082 T651 aluminium alloy.....	4-7
---	-----

Table 4.3.4 S355 structural steel composition (in weight %)......	4-8
--	-----

Table 4.3.5 6082 T651 aluminium alloy composition (in weight %)......	4-9
--	-----

Table 4.4.1 Test parameters for fatigue crack growth rate tests in S355 steel.....	4-10
---	------

Table 4.4.2 Fatigue crack growth rate laws derived for S355.....	4-13
---	------

Table 4.4.3 Test parameters for fatigue crack growth rate tests in 6082 T651 aluminium alloy	4-19
Table 4.4.4 Fatigue crack growth rate laws derived for 6082 T651 aluminium alloy in air....	4-22
Table 4.5.1 HUTCH scan parameters for weld toe weld return location on a steel fillet welded specimen.....	4-27
 Chapter 5	
Table 5.2.1 Stresses used in periodic underload spectrum.....	5-5
Table 5.3.1 Summary of results from constant amplitude loading fatigue tests.....	5-6
Table 5.3.2 Paris law constants (C and m) derived for S355 structural steel and 6082 T651 aluminium alloy (Paris law constants given for da/dN in mm/cycle and ΔK in $N/mm^{3/2}$).....	5-8
Table 5.3.3 Summary of results from periodic underload fatigue tests of twice the magnitude (SBL2) of the minor stress range.....	5-9
Table 5.3.4 Paris law constants for plain materials used for derivation of the acceleration factors under SBL2 conditions. Constants m and C given for da/dN in mm/cycle and ΔK in $N/mm^{3/2}$.	5-11
Table 5.3.5 Summary of results from periodic underload fatigue tests of one and half times the magnitude of the minor stress range (SBL1.5).....	5-12
Table 5.3.6 Paris law constants m and C for plain materials used for derivation of the acceleration factor under SBL1.5 conditions.....	5-14
Table 5.3.7 Summary of results from periodic underload fatigue tests of twice (SBL2) the magnitude of the minor stress range for welded specimens.....	5-15
Table 5.3.8 Paris law constants for welded materials used for derivation of the acceleration factor under SBL2 conditions (Constants m and C given for da/dN in mm/cycle and ΔK in $N/mm^{3/2}$).	5-17

Table 5.3.9 Summary of results from welded periodic underload fatigue tests of one and half times (SBL1.5) the magnitude of the minor stress range.....	5-18
Table 5.3.10 Paris law constants for welded materials used for derivation of the acceleration factor under SBL1.5 conditions (constants m and C given for da/dN in mm/cycle and ΔK in $N/mm^{3/2}$).....	5-21
Table 5.3.11 Summary of total endurance and acceleration factors for tests performed under SBL2 sequence (ΔK in $N/mm^{3/2}$).....	5-22
Table 5.3.12 Summary of total endurance and acceleration factors for tests performed under SBL1.5 sequence (ΔK in $N/mm^{3/2}$).....	5-23
Table 5.3.13 Summary of acceleration factors, β	5-25
Table 5.3.14 Crack growth increment for CA specimens.....	5-31
Table 5.3.15 Summary of results from striation spacing measurements.....	5-36

Chapter 6

Table 6.2.1 Plastic zone radii for S355 steel under SBL2 and SBL1.5 underload sequences assuming plane stress conditions.....	6-9
Table 6.2.2 Plastic zone radii for 6082 T651 aluminium alloy under SBL2 and SBL1.5 underload sequences assuming plane stress conditions.....	6-10
Table 6.2.3 Plastic zone radii for S355 steel under SBL2 and SBL1.5 underload sequences assuming plane strain conditions.....	6-11
Table 6.2.4 Plastic zone radii for 6082 T651 aluminium alloy under SBL2 and SBL1.5 underload sequences assuming plane strain conditions.....	6-11

Chapter 7

Table 7.2.1 Details of loading spectrum used for VA loading tests of CCT specimens, Spectrum name VA-AL-70-0.25; VA-ST-210-0.25.....	7-4
Table 7.2.2 Details of the revised loading spectrum used for VA loading tests of CCT and fillet welded specimens, spectrums name VA-AL-90-0.25; VA-ST-210-0.25.....	7-4
Table 7.2.3 Details of loading spectrum used for VA loading tests of fillet welded specimens, spectrum name VA-AL-90-0.20; VA-ST-210-0.20.....	7-6
Table 7.2.4 Details of loading spectrum used for VA loading tests of fillet welded specimens, spectrum name VA-AL-90-0.40; VA-ST-210-0.40.....	7-7
Table 7.5.1 Summary of results obtained from plain CCT specimens tested under constant amplitude loading.....	7-14
Table 7.5.2 Summary of results obtained from plain CCT specimens tested under variable amplitude loading (spectrum name VA-AL-90-0.20 or VA-ST-210-0.25).....	7-15
Table 7.5.3 Summary of results obtained from welded CCT specimens tested under constant amplitude loading.....	7-16
Table 7.5.4 Comparison between endurance for plain and welded CCT specimens under CA loading based on CA S-N curves with slope of $m=3$	7-18
Table 7.5.5 Summary of results obtained from welded CCT specimens tested under variable amplitude loading (VA-AL-90-0.25; VA-ST-210-0.25).....	7-18
Table 7.5.6 Comparison between mean endurance for plain and welded CCT specimens under VAL at the equivalent CA stress range.....	7-19
Table 7.5.7 Details of the proportion of the VA loading spectrum used in relation to periodic underload sequence.....	7-24

Table 7.5.8 Summary of results obtained from fillet welded specimens tested under constant amplitude loading..... 7-26

Table 7.5.9 Summary of results obtained from fillet welded specimens tested under variable amplitude loading..... 7-28

LIST OF FIGURES

Chapter 2

Figure 2.2.1 Variable amplitude loading showing varying magnitude limits.	2-3
Figure 2.2.2 Sinusoidal waveform giving a constant cyclic stress range.....	2-4
Figure 2.2.3 Typical S-N relationship for welded joints.....	2-4
Figure 2.3.1 Schematic illustrating the formation of extrusion and intrusion slip bands during loading.....	2-7
Figure 2.4.1 Modes of crack surface displacement.....	2-9
Figure 2.4.2 Schematic illustration of crack tip region under mode I loading.....	2-11
Figure 2.4.3 Schematic showing plane stress and plane strain conditions.....	2-12
Figure 2.4.4 Irwin's illustration of plastic zone size (Meguid, 1989).....	2-13
Figure 2.4.5 Schematic of the monotonic and reversed plastic zone development at the crack tip during cyclic unloading.....	2-15
Figure 2.5.1 Fatigue specimen (manufactured from Q1N) tested under direct axial constant amplitude loading showing distinct beach marks, courtesy of TWI Ltd.....	2-17
Figure 2.5.2 Example of fatigue striations contained within loading blocks as seen through a scanning electron microscope on 6082 T651 aluminium alloy.....	2-17

Figure 2.5.3 Two stage simplified fatigue crack growth law ($R>0.5$) for steels in air (BSI, 2013).
Stage III also shown..... 2-19

Figure 2.6.1 Fracture surface of a through-thickness fatigue crack with transition from the tensile
mode to shear mode (Schijve et al., 2004)..... 2-22

Figure 2.7.1 A schematic illustration of some mechanisms associated with crack closure..... 2-24

Figure 2.8.1 Effect of residual stress on weld plates (Gurney, 2006)..... 2-25

Figure 2.8.2 Typical residual stress distributions due to a butt weld between two plates
(Gurney, 2006)..... 2-26

Figure 2.9.1 Illustrations of typical cycle counting methods with results included (Maddox, 1991),
a) Range pair, b) Rainflow, c) Reservoir..... 2-31

Figure 2.9.2 Typical example of a narrow band stress history..... 2-35

Figure 2.9.3 Typical example of a wide band stress history..... 2-34

Figure 2.10.1 Evolution of the hysteresis loop tail during fatigue crack propagation (Xiong et al.,
2006)..... 2-41

Chapter 3

Figure 3.3.1 Types of fatigue crack growth rate test specimen: a) Single edge notch bend specimen
(loaded in three point bending), b) Compact tension specimen, c) Centre crack tension specimen
(used in the present experimental work)..... 3-4

Figure 3.3.2 Detailed drawing of a centre crack tension specimen showing the notch dimensions
(weld beads also shown)..... 3-6

Figure 3.4.1 Steel CCT specimen with a 300mm long weld bead (EDM notch also shown)... 3-7

Figure 3.4.2 Detailed drawing of a centre crack tension specimen manufactured from 6mm thick 6082 T651 aluminium alloy (weld beads also shown)..... 3-8

Figure 3.4.3 Weld bead deposited on aluminium CCT specimen by weave technique to provide adequate width..... 3-8

Figure 3.4.4 Detailed drawing of a fillet welded specimen with longitudinal attachments manufactured from 8mm thick S355J2+N structural steel..... 3-9

Figure 3.4.5 Steel fillet welded specimen showing weld detail..... 3-9

Figure 3.4.6 Detailed drawing of a fillet welded specimen with longitudinal attachments manufactured from 6mm thick 6082 T651 aluminium alloy..... 3-10

Figure 3.4.7 Aluminium alloy fillet welded specimen showing weld detail..... 3-11

Figure 3.4.8 A CCT specimen with grit blasted ends and emery cloth applied..... 3-12

Figure 3.4.9 Simple load sequence with constant maximum stress and periodic underloads used in the present study; example shown is for aluminium alloy with an underload magnification of 2x minor stress range (SBL2)..... 3-12

Figure 3.4.10 Example of a VA loading spectrum used in this project. Spectrum shown is for a minimum p_i value of 0.25..... 3-14

Figure 3.5.1 Optical microscope system applied to a steel CCT specimen..... 3-15

Figure 3.5.2 CCT specimen connected to the DCPD system showing staggered PD wires (both specimen surfaces shown)..... 3-17

Figure 3.6.1 Typical positions of strain gauges for investigation of crack closure..... 3-21

Figure 3.6.2 Plots showing the straight line fit approach used to define crack closure: a) straight lines fitted to the upper and lower data points about the assumed closure stress based on the calculated error, b) Intercept points giving the maximum uncertainty of the assumed closure stress.....	3-23
Figure 3.7.1 Centre-hole residual stress system.....	3-26
Figure 3.7.2 Permanent stress measurement strain gauges used in this research project: a) Conventional strain gauge rosette, type FRS-2-11-120, b) Strain gauge rosette type CEA-13-062UM-120. Arrows indicate strain gauge elements.....	3-28
Figure 3.7.3 CCT (a) and Fillet welded (b) specimens showing trepanned holes after residual stress measurement.....	3-29
Figure 3.7.4 Bragg's law geometry in the plane of diffraction.....	3-30
Figure 3.7.5 CCT specimen incorporating a 300mm weld bead on the plate surface, measurement planes also shown.....	3-33
Figure 3.7.6 Fillet welded specimen incorporating longitudinal attachments, measurement plane also shown.....	3-33
Figure 3.7.7 Steel CCT specimen setup for residual stress measurement by neutron diffraction, using the Stress-Spec at FRM2.....	3-34
Figure 3.8.1 Illustration of a continuum mechanics problem (in black) resolved into a discrete problem (in blue) of geometrical elements.....	3-35
Figure 3.8.2 FE model with two planes of symmetry, plain steel CCT model shown.....	3-36
Figure 3.8.3 Illustration of the principles of isotropic and kinematic hardening.....	3-37
Figure 3.8.4 Comparison between model and LCF test data for a) S355 with a low initial elastic limit, b) S355 with a high initial elastic limit and c) 6082 aluminium alloy.....	3-39
Figure 3.8.5 Loading sequence applied to FE models.....	3-40

Figure 3.8.6 Crack tip meshing for S355 specimens. The meshing for Al6082 specimens was similar..... 3-42

Figure 3.8.7 Comparison between the initial input stress field, balanced stress fields, and the measured distribution for S355 steel for the direction longitudinal to the weld..... 3-44

Figure 3.8.8 Comparison between the initial input stress field, balanced stress fields, and the measured distribution for S355 steel for the direction transverse to the weld..... 3-45

Figure 3.8.9. Comparison between the initial input stress field, balanced stress fields, and the measured distribution for the 6082 aluminium alloy for the direction longitudinal to the weld. 3-46

Figure 3.8.10. Comparison between the initial input stress field, balanced stress fields, and the measured distribution for the 6082 aluminium alloy for the direction transverse to the weld... 3-46

Figure 3.9.1 Schematic illustration of the X-ray CT acquisition and reconstruction process (Landis and Keane, 2010)..... 3-49

Figure 3.9.2 Weld return location on a steel fillet welded specimen with longitudinal attachments..... 3-50

Figure 3.10.1 Overview of the research carried out and the analytical or test techniques employed 3-51

Chapter 4

Figure 4.2.1 Extent of HAZ softening in a fillet welded 6082 T651 aluminium alloy specimen with longitudinal attachments (BSI, 1991)..... 4-2

Figure 4.3.1 Cyclic properties for S355 structural steel, WMTR No. 100676; a) Maximum tensile and compressive stress, b) Cyclic stress-strain loops..... 4-6

Figure 4.3.2 Cyclic properties for 6082 aluminium alloy, WMTR No. 100679; a) Maximum tensile and compressive stress, b) Cyclic stress-strain loops..... 4-7

Figure 4.4.1 Summary of fatigue crack growth data for plain S355 steel specimens obtained at R=0.1.....	4-12
Figure 4.4.2 Summary of fatigue crack growth data for plain S355 steel specimens obtained at R=0.5.....	4-13
Figure 4.4.3 Summary of fatigue crack growth data for plain S355 steel specimens showing effect of stress ratio.....	4-14
Figure 4.4.4 Summary of fatigue crack growth data for S355 steel welded specimens obtained at R=0.1.....	4-15
Figure 4.4.5 Summary of fatigue crack growth data for S355 steel welded specimens obtained at R=0.5.....	4-16
Figure 4.4.6 Summary of fatigue crack growth data for S355 steel welded specimens showing effect of stress ratio.....	4-17
Figure 4.4.7 Summary of fatigue crack growth data for plain 6082 T651 aluminium alloy specimens obtained at R=0.1.....	4-20
Figure 4.4.8 Summary of fatigue crack growth data for plain 6082 T651 aluminium alloy specimens obtained under conditions of R=0.5.....	4-21
Figure 4.4.9 Summary of fatigue crack growth data for plain 6082 T651 aluminium alloy specimens showing effect of stress ratio.....	4-23
Figure 4.4.10 Summary of fatigue crack growth data for 6082 T651 aluminium alloy welded specimens obtained at R=0.1.....	4-24
Figure 4.4.11 Summary of fatigue crack growth data for 6082 T651 aluminium alloy welded specimens obtained at R=0.5.....	4-25
Figure 4.4.12 Summary of fatigue crack growth data for 6082 T651 aluminium alloy welded specimens showing effect of stress ratio.....	4-26

Figure 4.5.1 Weld return showing an approximate overview of the weld model, and location of weld toe undercut..... 4-27

Figure 4.5.2 Weld toe undercut observed at weld return location, a) defect viewed in 3D model, b) μ -CT slice of defect in x-y plane, c) defect dimensions in x-y plane..... 4-28

Figure 4.5.3 Location of plane in 3d volume, b) μ -CT slice in x-z plane, c) defect dimensions..... 4-28

Figure 4.5.4 Location of small notch-like defect (undercut) located adjacent to weld spatter at the end of the weld return..... 4-29

Chapter 5

Figure 5.2.2 Constant maximum stress waveform with periodic underloads used in the present study..... 5-5

Figure 5.3.1 Summary of fatigue crack growth rate data for tests under constant amplitude loading (SBL calculated response also shown) for a) S355 steel and b) 6082 aluminium alloy..... 5-7

Figure 5.3.2 Comparison of constant amplitude and periodic underload (SBL2) fatigue crack growth rate data for S355 steel and 6082 aluminium alloy..... 5-10

Figure 5.3.3 Comparison of constant amplitude and periodic underload (SBL1.5) fatigue crack growth rate data for S355 steel and 6082 aluminium alloy..... 5-13

Figure 5.3.4 Fracture surfaces of failed aluminium alloy specimens showing regions of flat to shear mode growth (highlighted in red) in; a) CCT-SBL1.5-AL-02 and b) CCT-SBL2-AL-01 5-14

Figure 5.3.5 Comparison of constant amplitude and periodic underload (SBL2) fatigue crack growth rate data for S355 steel in both the plain and welded (denoted by R) conditions..... 5-16

Figure 5.3.6 Comparison of constant amplitude and periodic underload (SBL2) fatigue crack growth rate data for 6082 Al alloy in both the plain and welded (denoted by R) conditions..... 5-17

Figure 5.3.7 Comparison of constant amplitude and periodic underload (SBL1.5) fatigue crack growth rate data for S355 steel in both the plain and welded (denoted by R) conditions..... 5-19

Figure 5.3.8 Comparison of constant amplitude and periodic underload (SBL1.5) fatigue crack growth rate data for 6082 aluminium alloy in both the plain and welded (denoted by R) conditions..... 5-20

Figure 5.3.9 Comparison of actual and calculated crack growth response for S355 steel in periodic underload (SBL2) tests. Plain and welded (denoted by R) conditions shown..... 5-26

Figure 5.3.10 Comparison of actual and calculated crack growth response for 6082 aluminium alloy in periodic underload (SBL2) tests. Plain and welded (denoted by R) conditions shown..... 5-27

Figure 5.3.11 Comparison of actual and calculated crack growth response for S355 steel in periodic underload (SBL1.5) tests. Plain and welded (denoted by R) conditions shown..... 5-28

Figure 5.3.12 Comparison of actual and calculated crack growth response for 6082 aluminium alloy in periodic underload (SBL1.5) tests. Plain and welded (denoted by R) conditions shown..... 5-29

Figure 5.3.13 Comparison of fatigue striations on fracture surfaces under loading spectrum with periodic underloads (SBL2); a) 6mm thick 6082 T651 aluminium alloy (CCT-SBL2-AL-01) at $a=23\text{mm}$, b) 8mm thick S355 structural steel (CCT-SBL2-ST-01) at $a=18\text{mm}$ 5-30

Figure 5.3.14 Comparison of CA crack growth rate data derived from striation spacing with test data..... 5-32

Figure 5.3.15 Examples of SEM images used in striation analysis (direction of crack propagation indicated): a) CCT-SBL2-AL-01 at 40mm, b) CCT-SBL2-AL-03R at 46mm, c) CCT-SBL1.5-AL-01 at 50mm and d) CCT-SBL1.5-AL-03R at 60mm..... 5-34

Figure 5.3.16 Comparison between crack growth increment from striations including associated error: a) Minor stress range with 40% error bars, b) Major stress range with 50% error bars.....	5-35
Figure 5.3.17 Comparison of acceleration factor (γ) obtained from striations and measured crack growth rates for plain material: a) SBL2 spectrum; b) SBL1.5 spectrum.....	5-38
Figure 5.3.18 Comparison of acceleration factor (γ) obtained from striations and measured crack growth rates for welded material: a) SBL2 spectrum; b) SBL1.5 spectrum.....	5-39
Figure 5.3.19 Macro photograph showing the fracture surface of specimen CCT-SBL1.5-AL-01. The tensile mode of growth is denoted by i, and the subsequent shear mode by ii.....	5-40
Figure 5.3.20 Diagram showing the four modes of growth associated with the 6082 6mm thick aluminium alloy subjected to SBL1.5 and SBL2 loading (actual test data also shown for comparison).....	5-40
Figure 5.3.21 Stage 2 growth observed on 6mm thick 6082 T651 aluminium alloy (CCT-SBL1.5-AL-03R); a) edge of specimen at a=22mm showing elongated regions (arrowed), b) middle of specimen at a=22mm showing uniform surface morphology.....	5-41
Figure 5.3.22 Macro photograph showing the fracture surface of specimen CCT-SBL1.5-AL-03R. The four stages of growth are highlighted.....	5-41
Figure 5.3.23 Fracture surface of CCT-SBL2-AL-02 showing a uniform surface morphology; a) edge of specimen at a=22mm, b) middle of specimen at a=22mm.....	5-42
Figure 5.3.24 Metallographic sections of 6mm thick 6082 T651 aluminium alloy (CCT-SBL1.5-AL-03R); a) edge of specimen, b) transverse section at a=22mm.....	5-43

Chapter 6

Figure 6.2.1 Recorded crack closure levels in plain S355 steel before, during and after an underload cycle from 156N/mm ² to 16N/mm ²	6-3
--	-----

Figure 6.2.2 Recorded crack closure levels in plain S355 steel during application of an underload stress from 156N/mm² to 16N/mm²..... 6-3

Figure 6.2.3 Recorded crack closure levels in welded S355 steel, during application of an underload stress from 156 N/mm² to 16N/mm²..... 6-5

Figure 6.2.4 Recorded crack closure levels in plain aluminium alloy before, during and after an underload cycle from 74N/mm² to 11N/mm²..... 6-6

Figure 6.2.5 Recorded crack closure levels in plain 6082 aluminium alloy during application of an underload stress from 74N/mm² to 11N/mm²..... 6-7

Figure 6.2.6 Recorded crack closure levels in welded 6082 aluminium alloy, upon application of an applied stress from 74N/mm² to 10.56N/mm²..... 6-8

Figure 6.2.7 Effect of thickness on crack tip plastic zone size..... 6-10

Figure 6.3.1 Residual stress distributions measured in S355 steel CCT specimens across the weld and extending out from the notch tips..... 6-15

Figure 6.3.2 Residual stress distributions measured in S355 steel CCT specimens extending out from the notch using neutron diffraction at 1.5mm depth..... 6-16

Figure 6.3.3 Through-thickness longitudinal stress variation measured in S355 steel CCT specimens extending out from the notch using neutron diffraction..... 6-16

Figure 6.3.4 Residual stress distribution in S355 steel CCT specimens across the weld using neutron diffraction..... 6-17

Figure 6.3.5 Residual stress distributions measured in 6082 aluminium alloy CCT specimens across the weld and extending out from the notch..... 6-18

Figure 6.3.6 Residual stress distributions measured in a 6082 aluminium alloy full penetration double sided butt weld..... 6-19

Figure 6.3.7 Residual stress distribution measured in S355 structural steel across the plate width 2mm from weld toe using centre hole..... 6-20

Figure 6.3.8 Residual stress distribution measured in S355 structural steel across the plate width 2mm from weld toe using neutron diffraction..... 6-21

Figure 6.3.9 Through-thickness longitudinal stress variation measured in S355 steel across the plate width 2mm from weld toe using neutron diffraction..... 6-21

Figure 6.3.10 Residual stress distribution measured in 6082 aluminium alloy across the plate width 2mm from weld toe using centre hole..... 6-22

Figure 6.3.11 Re-distribution of measured residual stresses following blocks of SBL2 periodic underloads in S355 steel..... 6-23

Figure 6.3.12 Re-distribution of measured residual stresses following blocks of SBL2 periodic underloads in 6082 aluminium alloy..... 6-24

Figure 6.3.13 Residual stress measured 2mm ahead of propagating crack in S355 steel using centre hole..... 6-26

Figure 6.3.14 Residual stress measured 2mm ahead of propagating crack in 6082 aluminium alloy using centre hole..... 6-26

Figure 6.4.1 Overview of the finite element analysis model processing routine 6-31

Figure 6.4.2 Variation of stress and strain 0.01mm from the crack tip in S355 structural steel, obtained at the maximum and minimum applied loads (minor cycles) under constant amplitude loading..... 6-32

Figure 6.4.3 Variation of stress 0.01mm from crack tip in S355 steel obtained at maximum and minimum applied loads for the first six blocks of cycles under SBL2 loading..... 6-33

Figure 6.4.4 Variation of strain 0.01mm from crack tip in S355 steel for different underload ratios. The SBL2.2 underload corresponds to zero minimum stress..... 6-34

Figure 6.4.5 Variation of stress 0.05mm from crack tip in welded S355 steel obtained at maximum and minimum applied loads for the first six blocks of cycles under SBL2 loading..... 6-35

Figure 6.4.6 Variation of stress 0.01mm from crack tip in 6082 Al alloy obtained at maximum and minimum applied loads (minor cycles) under constant amplitude loading..... 6-37

Figure 6.4.7 Variation of stress 0.01mm from crack tip in 6082 Al alloy obtained at maximum and minimum applied loads for the first six blocks of cycles under SBL2 loading..... 6-38

Figure 6.4.8 Variation of strain 0.01mm from crack tip in 6082 Al alloy for different underload ratios. The SBL2.3 underload corresponds to zero minimum stress..... 6-39

Figure 6.4.9 Variation of stress 0.01mm from crack tip in welded 6082 Al alloy obtained at maximum and minimum applied loads for the first six blocks of cycles under SBL2 loading... 6-40

Figure 6.4.10 Contour plot showing the deformed shape in the region of the crack tip for plain steel under SBL2 loading. The red line is the horizontal symmetry plane..... 6-43

Figure 6.4.11 Contour plot showing displacement in the crack tip wake following application of the underload for plain steel under SBL2 loading. The red line is the horizontal symmetry plane 6-44

Figure 6.5.1 Extent of crack tip bifurcation observed under SEM for: a) CCT-CAL-ST-16; b) CCT-SBL2-ST-01; c) CCT-CAL-AL-15; d) CCT-SBL2-AL-02..... 6-46

Figure 6.6.1 Accelerated growth based on the ratio of amplitudes, a) data taken from (Gurney, 1983), b) data taken from (Fleck, 1985)..... 6-49

Figure 6.6.2 Effect of underload magnitude on crack growth rate for S355 steel relative to the constant amplitude response..... 6-50

Figure 6.6.3 Effect of underload magnitude on crack growth rate for S355 steel relative to the constant amplitude response..... 6-50

Figure 6.6.4 Expanded view of Figure 5.3.9 showing difference in initial crack length for specimens CCT-SBL2-ST-03R and 05R..... 6-54

Figure 6.6.5 Assumed effect of tensile underloads on crack tip mean stress (Fleck, 1985)..... 6-60

Chapter 7

Figure 7.2.1 Variable amplitude loading spectrum cycling down from a constant maximum stress, Spectrum name VA-AL-90-0.25; VA-ST-210-0.25..... 7-5

Figure 7.2.2 Variable amplitude loading spectrum cycling down from a constant maximum stress, spectrum name VA-AL-90-0.20; VA-ST-210-0.20..... 7-6

Figure 7.2.3 Variable amplitude loading spectrum cycling down from a constant maximum stress, spectrum name VA-AL-90-0.40; VA-ST-210-0.40..... 7-7

Figure 7.2.4 CCT specimen fracture surface showing curved-front beachmarks. An 8mm thick steel specimen is shown..... 7-9

Figure 7.2.5 Fillet welded specimen fracture surface showing semi-elliptical beachmarks. An 8mm thick steel specimen is shown..... 7-9

Figure 7.3.1 Fillet welded specimen with centre hole measurements performed across the plate width close to the end of the welded attachment..... 7-11

Figure 7.3.2 Steel Fillet welded specimen setup for residual stress measurement using neutron diffraction at FRMII, Munich..... 7-11

Figure 7.4.1 Recorded crack closure levels in plain S355 steel, upon application of an applied stress from 280N/mm² to 70N/mm²..... 7-13

Figure 7.4.2 Recorded crack closure levels in plain 6082 aluminium alloy, upon application of an applied stress from 90N/mm² to 20N/mm²..... 7-13

Figure 7.5.1 Fatigue test results obtained from plain CCT specimens tested under constant maximum tensile stress conditions..... 7-15

Figure 7.5.2 Fatigue test results obtained from welded CCT specimens tested under constant maximum tensile stress conditions..... 7-17

Figure 7.5.3 Comparison of fatigue crack growth rates for plain CCT specimens tested under constant and variable amplitude loading..... 7-20

Figure 7.5.4 Comparison of fatigue crack growth rates for welded CCT specimens tested under constant and variable amplitude loading..... 7-22

Figure 7.5.5 Variable amplitude loading spectrum cycling down from a constant maximum stress, showing the proportion of the spectrum which relates to the periodic underload sequences for steel specimens..... 7-23

Figure 7.5.6 Variable amplitude loading spectrum cycling down from a constant maximum stress, showing the proportion of the spectrum which relates to the periodic underload sequences for aluminium alloy specimens..... 7-24

Figure 7.5.7 Constant amplitude fatigue test results obtained from fillet welded specimens tested under constant maximum tensile stress conditions..... 7-27

Figure 7.5.8 Variable amplitude fatigue test results obtained from fillet welded specimens tested under constant maximum tensile stress conditions..... 7-29

Figure 7.5.9 Comparison of fatigue crack growth rates for longitudinal fillet welded specimens tested under constant and variable amplitude loading..... 7-30

Figure 7.6.1 Steel specimen showing typical fatigue crack path at the end of the weld toe..... 7-32

Figure 7.6.2 Variable amplitude fatigue test results obtained from fillet welded specimens tested under constant maximum tensile stress conditions, compared with the calculated response using fracture mechanics..... 7-37

Chapter 9

Figure 9.4.1 A finite element SENB specimen model showing regular mesh used for crack propagation (courtesy of TWI)..... 9-6

Figure 9.4.2 Contour plots of a finite element SENB specimen model showing crack propagation (courtesy of TWI)..... 9-6

Chapter 1

INTRODUCTION

1.1 OVERVIEW

This research project was sponsored by the Integrity Management Group (IMG) at TWI Ltd, one of the world's foremost independent research and technology organisations for welding and joining. TWI is a membership-based not-for-profit organisation that provides a technical consultancy service across several industry sectors. The project was funded through TWI's Core Research Programme, which is one of the ways that TWI uses the fees paid by its members.

The project addresses a practical design problem associated with the calculation of the fatigue life of a welded structure or component subjected to variable amplitude (VA) loading. In particular, under some loading conditions the widely used simple linear damage accumulation method ('Miner's rule'), that assumes a stress cycle produces the same damage under VA loading as under constant amplitude (CA) loading, proves to be unsafe, in that the actual life is less than that estimated (Gurney, 2000; Berger *et al.*, 2002; Zhang and Maddox, 2009). This is thought to be due to some form of stress interaction that causes fatigue crack growth acceleration. The main aim of the project was to identify the mechanisms involved with a view to deriving improved design guidance that will enable more accurate fatigue life estimations to be made for spectrum loading conditions that produce crack growth acceleration.

1.2 FATIGUE DESIGN

The structural design of components or structures should allow for all relevant potential failure modes, such as fracture, buckling, creep or fatigue, by suitable choice of material, dimensions and

manufacturing method. Fatigue is relevant if the component or structure will be required to sustain varying applied loading. Mechanical fatigue has been found to be one of the most common failure mechanisms in engineering structures, accounting for 50 – 90% of all mechanical failures (Stephens *et al.*, 2001). Fatigue is of particular importance in welded structures because the fatigue strength of a welded joint can be considerably lower than that of the parent material (Gurney, 1978). This is because of the inevitable introduction of severe stress concentration features, notably at the weld toe, from which fatigue cracks readily propagate, with the result that the majority of the fatigue life is spent propagating a crack whereas most of the life of the un-welded material is spent initiating a fatigue crack (Maddox, 1974).

Fatigue design is most commonly based on the use of fatigue resistance data in the form of $S-N$ curves. These are curves fitted to the results of fatigue tests performed on relevant specimens under CA cyclic loading. This is loading that varies between fixed upper and lower limits, the difference between them being the stress range (twice the amplitude). These test results are plotted in terms of the applied stress range (S) versus the number of cycles of applied load to failure (N).

In reality, most structural components are required to sustain VA fatigue loading in service rather than the simple CA loading used to derive the $S-N$ curves. The most widely used method for using such $S-N$ curves to design components that will be required to sustain VA loading is the Palmgren-Miner linear cumulative damage rule, or Miner's rule as it is more often called (Miner, 1945). This is based on the assumption that the number of cycles (n) applied at a particular stress produces n/N ths of the damage required to cause failure, where N is the fatigue life obtained under CA loading at the same stress. Thus, the rule states that failure will occur when the sum of all ratios n/N equals unity, Eq. [1.1.1].

$$\frac{n_1}{N_1} + \frac{n_2}{N_2} + \frac{n_3}{N_3} + \dots + \frac{n_i}{N_i} = \sum_i \frac{n_i}{N_i} = 1 \quad [1.1.1]$$

where, N_i values are obtained from the relevant CA $S-N$ curve.

The above relationship can also be related to a fracture mechanics analysis of crack propagation under VA loading, over the life of a crack or until a pre-defined critical size is reached (Maddox, 1991) using Eq. [1.1.2]. This is further discussed in Chapter 2.

$$\int_{a_i}^{a_f} \frac{da}{(Y\sqrt{\pi a})^m} = CS_1^m n_1 + CS_2^m n_2 + \dots \quad [1.1.2]$$

where, a_i and a_f are the initial and final crack size, S_1, S_2, \dots and n_1, n_2, \dots are successive stress cycles at corresponding endurance, Y is a geometric factor and C and m are material constants.

In view of the scatter inherent in fatigue test data, Miner's rule can only be expected to provide estimates of fatigue life. However, in reality such estimates can be significantly different from the actual lives obtained under VA loading. In some instances the rule has been shown to be overly conservative, with actual lives considerably higher than estimated. However, of much greater concern are cases where it has been found to be unsafe, with actual lives significantly less than estimated (Tilly, 1985; Vormald and Seeger, 1991; Dahle, 1993; Tubby *et al.*, 1996; Gurney, 1985, 1992, 2000 and 2006; Berger *et al.*, 2002; Zhang and Maddox, 2009). These discrepancies are generally thought to arise from the assumption of linear damage accumulation when, in fact, there is some interaction between applied stresses that gives rise to either faster or slower crack growth than that obtained under CA loading, as assumed by the rule. Since the majority of the fatigue lives of welded joints are spent propagating cracks, such interactions are expected to be particularly significant in relation to their fatigue design.

1.3 OBJECTIVES AND APPROACH

The project aims to provide a better understanding of the factors that lead to unsafe life estimates and how they can be allowed for in fatigue design. To this end the following objectives and approach were adopted.

- a) Review existing published literature to ascertain the factors which lead to unsafe fatigue life estimates, with a view to providing necessary background information and an indication of the

current status of research which has addressed the same or similar problems to those being considered in the present project.

- b) Perform fatigue testing under simple loading conditions expected to produce crack growth acceleration.

In order to allow close examination of the effect of stress changes on crack growth, the tests were conducted on centre-cracked tension (CCT) plate specimens in which crack growth rate could be measured or deduced by subsequent examination of the fracture surfaces. Simple loading spectra with two magnitudes of stress were used.

- c) Investigate the mechanisms associated with crack growth acceleration with a view to determining the primary cause.

Finite element analysis was conducted to assist in the establishment of the primary mechanism involved in causing crack growth acceleration. As understanding of crack growth acceleration in welded joints and components was of prime concern, the effect of residual stress was also investigated along with the significance of crack closure under the form of loading used.

- d) Perform comparative endurance fatigue testing of CCT and fillet welded specimens under variable amplitude loading spectra.

Both Miner's rule damage summations and crack growth acceleration factors were used to establish the performance of specimens tested under the loading spectra used. The extent of crack closure as well as measured and calculated crack growth rates were also investigated.

- e) Discuss the implication of the results on current fatigue design and provide recommendations on design guidance to allow for fatigue crack growth acceleration under variable amplitude loading.

The test specimens were made from a medium strength structural steel and an aluminium alloy of the types widely used in welded structures. To this end, it was considered important to establish whether the objectives above (in particular b)-d)) result in similar findings for both materials. The

use of aluminium alloy also facilitated microscopic examination of fatigue striations on the fracture surfaces of test specimens. Necessary mechanical and chemical characterisation tests were performed on both materials.

1.4 STRUCTURE OF THESIS

Following Chapter 1 the remainder of the thesis is divided into eight main chapters, with References in Chapter 10.

Chapter 2 gives a comprehensive overview of the problems associated with fatigue of welded joints, in particular the use of Miner's rule, the role of residual stress and the influencing factors leading to accelerated crack growth under variable amplitude loading spectra.

Chapter 3 reviews the experimental methods used for studying the effect of crack growth acceleration, including techniques used for crack length and residual stress measurement and associated errors and uncertainties in their application.

Chapter 4 provides details of the materials used, the mechanical testing performed on them to establish properties relevant to the project and the results of those tests.

Chapter 5 presents the results of fatigue tests performed under cyclic loading with periodic underloads, conditions expected to produce crack growth acceleration. The effects of underload magnitude and the presence of welding residual stresses on the extent of acceleration were investigated. Different parameters for determining the levels of acceleration were also presented. Scanning electron microscopy was used to examine striations on fatigue fracture surfaces to study more closely the effect of load changes on crack growth rate.

Chapter 6 examines the mechanisms associated with the crack growth acceleration observed in Chapter 5. The significance of crack closure was investigated, along with the effect of residual stress. Finite element analysis was used for the analysis of stress/strain close to the crack tip. The results of the various studies, including the findings from the striation examination, are discussed with a view to identifying the main mechanisms involved in crack growth acceleration.

Chapter 7 provides a study of the performance of welded joints under variable amplitude loading using spectra designed to promote fatigue crack acceleration. Both crack growth calculations based on fracture mechanics and endurance fatigue testing were used to evaluate the performance.

Chapter 8 reviews the evidence gathered in the previous chapters with a view to identifying the main cause of crack growth acceleration and the practical implications on fatigue design. Guidance on how it might be allowed for in design was also considered.

Chapter 9 presents the conclusions drawn from the work performed in this research project and provides design recommendations as well as recommendations for future work to continue the research performed here.

1.5 APPLICATION OF WORK PERFORMED

It is expected that the results of the present project will be beneficial to all industries where fatigue endurance and fatigue crack propagation rates are fundamental to the design of welded structures and components subjected to variable amplitude loading.

On completion, the research performed will be made available to relevant British Standard committees to assist in the provision of better guidance on cumulative damage calculations under some of the circumstances where crack growth acceleration is likely to occur.

Chapter 2

BACKGROUND AND LITERATURE REVIEW

2.1 INTRODUCTION

The following review considers published and other work relevant to the factors which lead to unsafe fatigue life estimates, with a view to providing necessary background information and an indication of the current status of research which has addressed the same or similar problems to those being considered in the present research project.

Mechanical fatigue is one of the most common causes of structural failure and with it can bring severe consequences. It has long been accepted that components and structures subjected to repeated or fluctuating loads may fail in service, even if they would normally be able to sustain much higher loads in a static manner. Mechanical fatigue is defined as a mechanism of failure experienced by materials under the action of a fluctuating/repeated stress. It involves initiation and propagation of a crack under the action of repeated stresses well within the static capacity of the material (Forrest, 1962). With regard to fatigue properties, the magnitude of a repeatedly applied stress that causes failure after a specified number of applications is termed the fatigue strength, while the number of repetitions at an applied stress that leads to failure is termed the fatigue life. One of the dangers of this failure mechanism is that generally there is no prior indication of impending failure in the form of visible deformation in the region of fracture, even for ductile materials. Similarly, the progressive growth of a fatigue crack may be effectively undetectable until shortly before it reaches a critical size and failure occurs.

In addition to mechanical fatigue, other forms of fatigue include thermal, rolling contact, corrosion and fretting (Suresh, 1998). The focus of the current research is on mechanical fatigue and from hereafter is simply referred to as fatigue.

When considering metallic structures, welding is the most common joining method. Consequently, an understanding of fatigue of welded joints has been the subject of substantial research. Examples of industrial applications of welding where fluctuations of the working stress can arise are offshore structures for oil and gas recovery, bridges, cranes, handling equipment, masts, process equipment, vehicles and ship structures. A significant feature of welded joints is that they can have considerably lower fatigue strengths than that of the un-welded material (Gurney, 1978). In view of this, special attention must be paid to the avoidance of premature failure by fatigue in welded components and structures, typically using standards such as BS 7608 (BSI, 2014), DNV-RP-C203 (DNV, 2012), Eurocode 3 (BS EN, 2005), Eurocode 9 (BS EN, 2007) and BS 7910 (BSI, 2013).

There are two main approaches that are used for calculating the fatigue lives of components, based on cumulative damage (safe-life design) or crack propagation analysis (damage tolerant design) (Codrington, 2008; BSI, 2014). The former utilises the cyclic stress or strain range to characterise the total life to failure. Generally, the presence of any existing flaws is ignored. This means that the predicted fatigue life includes the number of cycles to initiate as well as propagate a crack. A particular disadvantage of this technique is the wide scatter in calculated fatigue lives. Such scatter can be attributed to the inconsistent nature of the crack initiation phase, which is highly dependent on the material microstructure and manufacturing procedures employed (Codrington, 2008). The latter, damage tolerant design, is based on the use of fracture mechanics principles to describe crack propagation from a known or assumed initial flaw or defect, providing knowledge of the fatigue crack growth in relation to the component/detail geometry, and applied cyclic loading. As such, the initiation phase is ignored, resulting in a reduction in the scatter in life predictions. Even so, the actual fatigue life may be very different from the calculated, depending on the accuracy of the initial flaw size measured.

2.2 CYCLIC STRESS-STRAIN RELATIONSHIPS

2.2.1 STRESS-LIFE ($S-N$)

During the 1850s and 1860s a German engineer carried out pioneering tests in an investigation into fatigue of railway axles by use of rotating bending specimens (Wohler, 1870). Plotting the results of these tests in terms of the applied cyclic stress and the number of applications to failure led to the establishment of the Wohler curve, or as it is more often known the stress/endurance curve ($S-N$ curve), one of the empirical laws of fatigue behaviour (Barnby, 1972). These are still used today as the main method for presenting fatigue test data obtained under any type of loading. Such test results are the main source of design data for avoiding fatigue. Testing is not limited to rotating bending and modern equipment allows tests to be performed under axial, bending or torsional loading. Such tests may be performed under what are termed constant amplitude (CA) or variable amplitude (VA) loading, the former being repeated loading between fixed limits and the latter loading between varying magnitude limits (see Figure 2.2.1); instances where loading such as that in Figure 2.2.1 occur are given later in Chapter 8 Section 8.3.

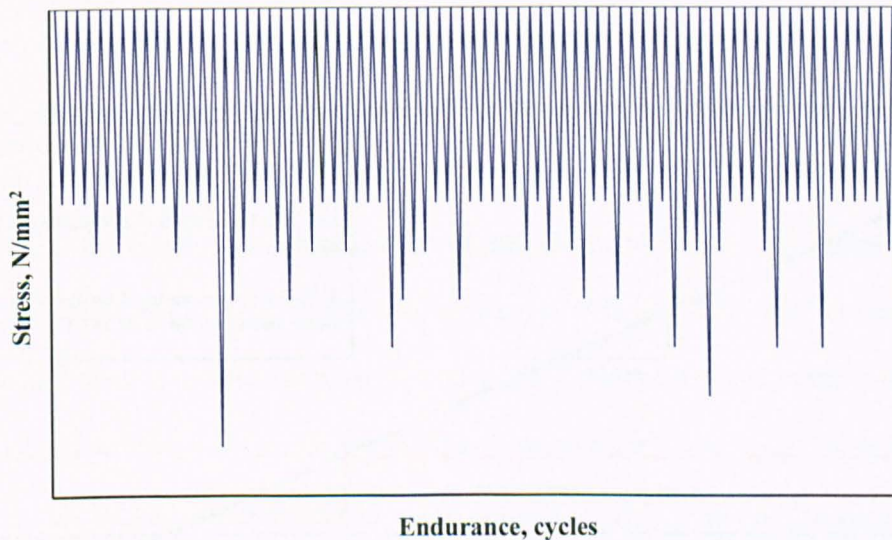


Figure 2.2.1 Variable amplitude loading showing varying magnitude limits.

However, basic reference data for use in fatigue design rules are obtained under CA loading. In such tests the applied load typically varies with time in a sinusoidal manner to give a constant cyclic stress range which is twice the amplitude (see Figure 2.2.2). When testing in air under CA

loading, steels have what is termed an ‘endurance limit’, or, a constant amplitude fatigue limit (CAFL).

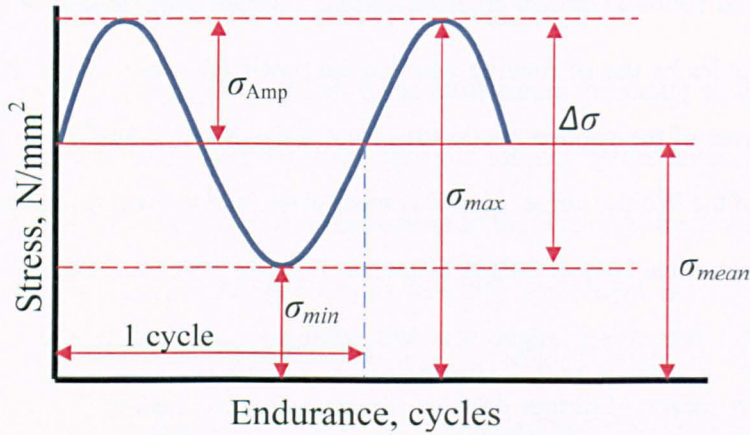


Figure 2.2.2 Sinusoidal waveform giving a constant cyclic stress range.

This is a point at which a structure can sustain repeated loading at a particular stress (sometimes termed the non-propagating stress range (S_{OC})) below which there will be no propagation. Various assumptions are made about the corresponding endurance (N_{OC}), typically ranging from 2×10^6 to 10^7 cycles, but 10^7 cycles is assumed in most modern design standards (BSI, 2014), see Figure 2.2.3.

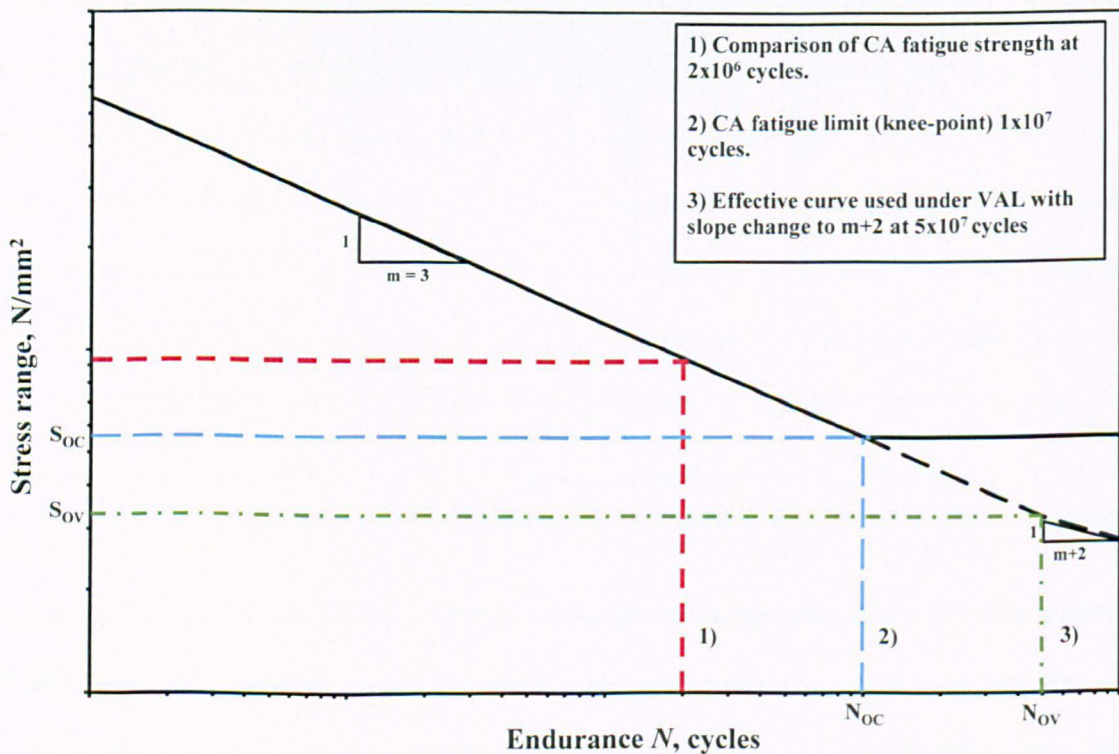


Figure 2.2.3 Typical S-N relationship for welded joints.

It should be noted that Figure 2.2.3 is typical for welded joints where life is dominated by crack growth propagation. In the case of $S-N$ curves for plain materials where crack initiation dominates, the slope of the curve, m , typically has a much shallower gradient with no identifiable knee-point (Suresh, 1998).

The $S-N$ curve is typically plotted on log-log scales, which generally produces a straight line relationship that can be expressed as:

$$\text{Log } N = \log A - m \log S \quad [2.2.1]$$

$$\text{or, } S^m N = A \quad [2.2.2]$$

where m and A are material constants. When considering welded structural steels it is usual to consider the slope of the curve (m) as 3.0, which is a reasonable average and normally used in fatigue design of welded joints (BSI, 2014). For design purposes use is made of $S-N$ curves that relate to the lower bound of the test data. The most widely used is set two standard deviations of $\log N$ below the mean.

Most fatigue design rules use a classification system that involves a series of $S-N$ curves to cover the range of potential fatigue strengths, each being relevant to one or more specific weld detail. The classification of the detail(s) is referred to by letters (e.g. BS 7608:2014) or a number corresponding to the fatigue strength at a specified fatigue life, usually 2×10^6 cycles (e.g. category 90 in the Eurocode scheme refers to a fatigue strength of 90N/mm^2 at 2×10^6 cycles). Under VA loading, the $S-N$ curve is usually extended beyond N_{OC} at a shallower slope. In BS 7608 the curve is first extrapolated without a slope change to what is termed the slope transition point endurance (N_{OV}) of 5×10^7 cycles corresponding to stress range S_{OV} . This is to take account of the stress ranges below S_{OC} , but exceeding 5N/mm^2 , which under VA loading can contribute towards fatigue damage (BSI, 2014).

The stress-life method is used extensively in applications where low amplitude cyclic stresses induce elastic deformation in a component designed for long life i.e. *High Cycle Fatigue* (HCF) (Suresh, 1998).

2.2.2 STRAIN-LIFE (ϵ - N)

In some applications, engineering components undergo plastic deformation as a result of the application of high amplitude cyclic stresses or their production at locations of high stress concentrations. For such instances it is more appropriate to consider strain-life (ϵ - N) as opposed to stress-life (S - N) (Suresh, 1998).

Realising the important role of plastic strains on fatigue life, Coffin (1954) and Manson (1954) independently proposed a plastic strain based continuum characterisation of *Low Cycle Fatigue* (LCF). They noted that a linear relationship for metallic materials was formed when the logarithm of the plastic strain amplitude, $\Delta\epsilon_p/2$, was plotted against the logarithm of the number of load reversals to failure, $2N_f$, i.e.

$$\frac{\Delta\epsilon_p}{2} = \epsilon_f' (2N_f)^c \quad [2.2.3]$$

where ϵ_f' is the fatigue ductility coefficient and c is the fatigue ductility exponent.

The strain-life approach is typically applied to plain or machined un-welded components with smooth surfaces, or notched components. Evaluation of notched members, in particular the deformation that occurs at the notch tip, commonly makes use of an estimate of the corresponding local strain. On this basis Neubers Rule (Neuber, 1961) approximates the elastic stress concentration factor, K_t , under conditions of plastic deformation and states:

$$K_t = \sqrt{K_\sigma K_\epsilon} \quad [2.2.4]$$

where K_σ and K_ϵ are the geometrical means of the stress and strain concentration factors.

2.3 CRACK INITIATION

Microscopic fatigue crack growth is strongly affected by the slip characteristic of the material, characteristic microstructural dimensions, applied stress and near-crack tip plasticity (Suresh, 1998).

In nominally defect free (un-notched) metals and alloys, repeated cyclic straining of the material leads to different amounts of net slip on different crystallographic glide planes. In practice, a limited number of crystallographic planes (due to their unfavourable orientation with respect to the maximum shear stress (Lassen and Recho, 2006)), are subject to plastic deformation, which in turn can result in the ‘roughening’ of the surface of the material (Wood, 1958). This slip induced surface roughening was first documented by Forsyth (1953) whilst working on solution treated Al-4 wt% Cu alloy. Due to a cyclic strain hardening effect during the reversed stage of a load cycle, the crystallographic planes do not slide back into their original position, resulting in yielding of the neighbouring planes as they slide in opposite directions. Intrusions and extrusions (valleys and hills) are then formed (Figure 2.3.1) following the to-and-fro motion of the slip bands (Forsyth and Stubbington, 1955; Cottrell and Hull, 1957); the intrusions then act as micro-cracks for further crack extension during the subsequent loading (Lassen and Recho, 2006).

In the case of engineering structures, the principal sites for the initiation of fatigue cracks are local areas of stress concentrations (Suresh, 1998). However, under fatigue loading the presence of a notch generally produces a lower stress concentrating effect than predicted by theoretical elastic analysis, particularly as the notch becomes sharper and the material becomes softer. This is predominantly a result of the notch geometry and material properties which determine the volume of material subjected to elevated stresses and the material sensitivity to the local strain gradient respectively.

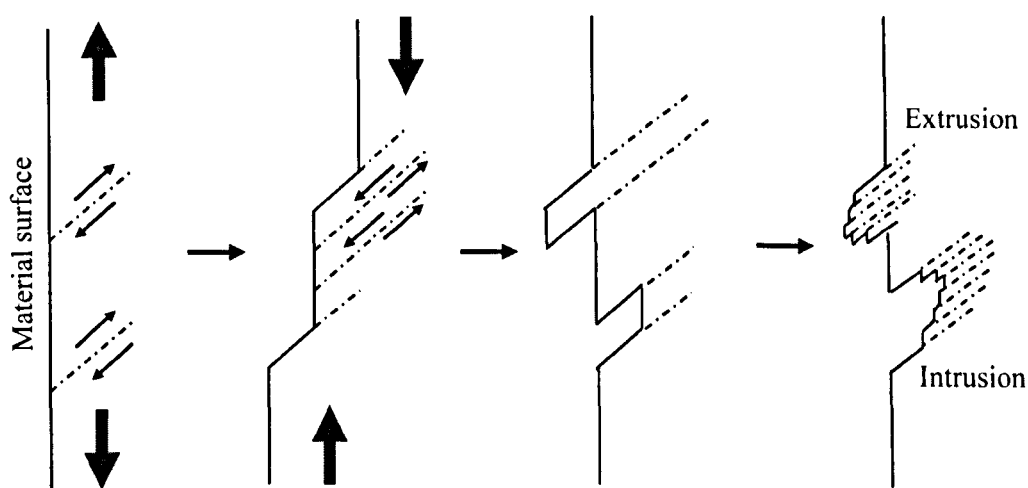


Figure 2.3.1 Schematic illustrating the formation of extrusion and intrusion slip bands during loading.

By use of the notch sensitivity index (Peterson, 1959) the degree of agreement between theoretical analysis and actual effects can be obtained. The index is defined as:

$$q = \frac{K_f - 1}{K_t - 1} \quad [2.3.1]$$

where q varies from zero to unity according to whether no notch is assumed or the full effect predicted by the elastic theory is assumed. K_t is a function of geometry and loading mode and K_f is determined empirically (Suresh, 1998).

Particular influences in fatigue cracking are areas of high stress concentration such as material discontinuities and manufacturing defects (inclusions). For welded joints stress concentrations arise as a result of the weld shape, particularly at the weld toe where it will be intensified as a result of undercut or a sharp re-entrant angle. In a stress analysis of welded joints Gurney (1976) found that weld toe stress concentrations ($K_t = \sigma_{max}/\sigma_{nom}$) in fillet welds ranged from 2 to 5. Other features are the weld root condition (caused by partial weld penetration) and residual stress, which is discussed later (see Section 2.8).

The crack initiation stage for welded joints occupies a much smaller proportion of life than that for a case such as a plain plate, where surface roughness induced by millscale produces K_t close to unity with the result that most of the fatigue life is spent initiating a crack. In fact, it can be said that in the case of welded joints the initiation stage is almost non-existent (Gurney, 2006). Fatigue cracks in welded joints usually initiate at the weld toe where there are very sharp defects which can really be regarded as small cracks. Work on fillet welded specimens manufactured from BS 15 mild steel and BS 968 medium strength steel (Signes *et al.*, 1967) found frequent occurrences of tiny (tenths of mm) sharp-tipped slag intrusions along the weld toes, trapped in the region between the weld and surrounding plate in partially-melted or pasty metal. Fatigue cracks were found to have propagated from such intrusions.

2.4 THEORY OF LINEAR ELASTIC FRACTURE MECHANICS

2.4.1 LOADING MODES

The reaction of a crack to applied loading is described in terms of the three possible crack face displacement modes (Figure 2.4.1).

Mode I represents an opening or tensile mode where the crack surfaces move directly apart. Mode II represents in-plane shear (sliding) whereby the crack surfaces slide over one another in a direction perpendicular to the leading edge of the crack. Mode III represents out-of-plane shear (tearing) whereby the crack surfaces move relative to one another and parallel to the leading edge of the crack. Where fatigue is concerned, traditional fracture mechanics methods have concentrated mainly on cracks growing under opening mode I (Lassen and Recho, 2006). This work is concerned only with mode I loading.

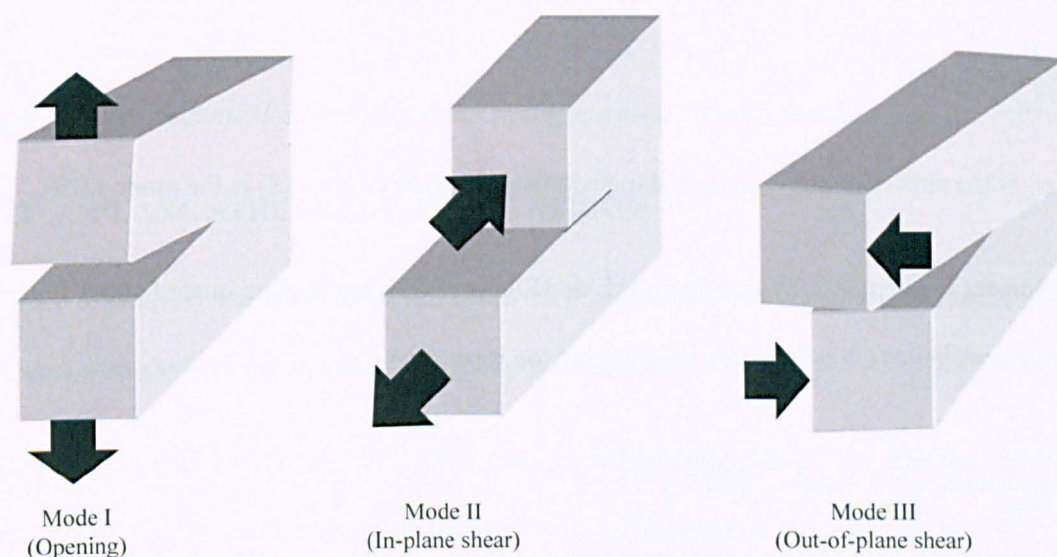


Figure 2.4.1 Modes of crack surface displacement.

2.4.2 STRESS INTENSITY FACTOR

It is well established that the presence of a crack in a stressed solid structure can cause it to fail at stresses much lower than the ultimate tensile strength of the material (Maddox, 1972). The fracture process itself takes place in a small region at the crack tip where the material yields and a plastic zone surrounds it. In theory, it is assumed that the stress concentration at the tip of a sharp crack is

infinite and therefore the stress at the crack tip must be infinite. This would suggest that the stresses and strains present within the plastic zone (see Section 2.4.4) will be controlled by the surrounding elastic stress and strain fields. Thus, provided the plastic zone is small it will not change the elastic stress field significantly (Maddox, 1972).

The modern methods of fracture mechanics started with the elastic stress analysis of cracked bodies by Irwin (Irwin, 1957), based on work performed by Westergaard on the stress field surrounding a crack in an infinite plate (Westergaard, 1939). Irwin quantified the near-tip fields for the linear elastic crack in terms of a stress intensity factor (SIF), K . The SIF incorporates the boundary conditions of the cracked body and is a function of loading, crack length and geometry. If the SIF is known, all the components of stress, strain and displacement can be determined as a function of distance from the crack tip, r , and angle, θ . Using the cylindrical co-ordinate system centred at the crack tip, this can be written as:

$$\sigma_{ij} = \frac{K_I}{\sqrt{2\pi r}} \cdot f_{ij}(\theta) \quad [2.4.1]$$

where σ_{ij} is the stress tensor, $f_{ij}(\theta)$ is a dimensionless function of θ and K_I is the mode I SIF.

For an element located at (r, θ) near the crack tip (Figure 2.4.2), the leading mode I stress fields for cartesian co-ordinates (Westergaard, 1939) are of the form:

$$\sigma_{xx} = \frac{K_I}{\sqrt{2\pi r}} \cos\left(\frac{\theta}{2}\right) \left[1 - \sin\left(\frac{\theta}{2}\right) \sin\left(\frac{3\theta}{2}\right) \right] \quad [2.4.2]$$

$$\sigma_{yy} = \frac{K_I}{\sqrt{2\pi r}} \cos\left(\frac{\theta}{2}\right) \left[1 + \sin\left(\frac{\theta}{2}\right) \sin\left(\frac{3\theta}{2}\right) \right] \quad [2.4.3]$$

$$\sigma_{xy} = \frac{K_I}{\sqrt{2\pi r}} \cos\left(\frac{\theta}{2}\right) \sin\left(\frac{\theta}{2}\right) \cos\left(\frac{3\theta}{2}\right) \quad [2.4.4]$$

$$\sigma_{zz} = \nu(\sigma_{xx} + \sigma_{yy}), \text{ in plane strain} \quad [2.4.5]$$

$$\sigma_{zz} = 0, \text{ in plane stress} \quad [2.4.6]$$

To characterise a linear elastic crack in the near tip region, it is therefore only necessary to know the SIF, K , which can be shown to be related to the applied stress and crack length by:

$$K = YS\sqrt{(\pi a)} \quad [2.4.7]$$

where Y is a dimensionless geometric factor which accounts for component geometry, including the crack shape, and a is the crack dimension.

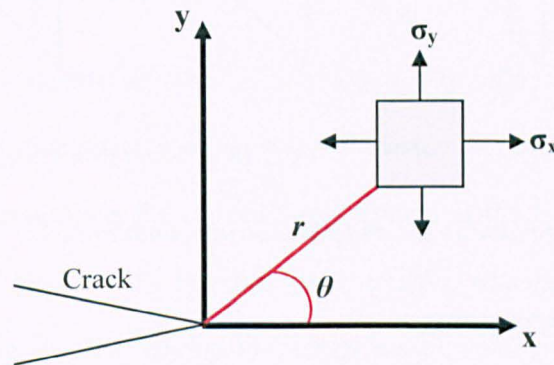
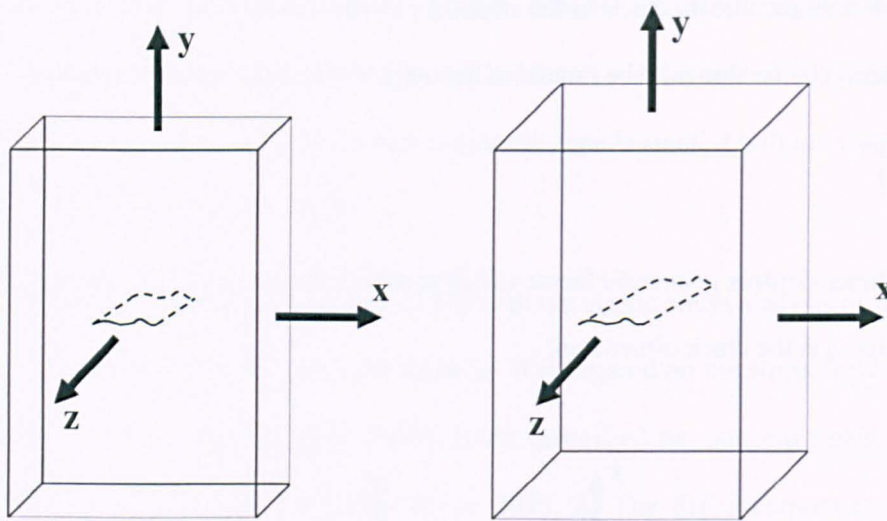


Figure 2.4.2 Schematic illustration of crack tip region under mode I loading.

2.4.3 PLANE STRESS AND PLANE STRAIN

In order to simplify the analysis of full three dimensional problems, plane stress and plane strain concepts were derived for thin and thick sections respectively.

Under *plane stress conditions*, for a thin plate loaded as in Figure 2.4.3a, the through-thickness stress cannot vary as there is no stress perpendicular to the plane of the plate (i.e. $\sigma_z = 0$, $\epsilon_z \neq 0$). In the case of a thick body (Figure 2.4.3b), due to the increase in cross-section resulting from the increase in thickness, the material is constrained in the z direction and ϵ_z is equal to zero (i.e. $\epsilon_z = 0$, $\sigma_z \neq 0$), resulting in a *plane strain condition*.



a) Plane stress (thin body)

b) Plane strain (thick body)

Figure 2.4.3 Schematic showing plane stress and plane strain conditions.

2.4.4 CRACK TIP PLASTICITY

The method of fracture mechanics depends largely on the stress at the crack tip being either elastic or elastic-plastic. Such that, the more plasticity there is the less useful is the elastic parameter K . For any brittle fracture or fatigue crack, plastic zones exist at the crack tip where the yield stress has been exceeded giving rise to crack tip yielding (Leaity, 1988). The crack tip stress state (i.e. plane stress or plane strain) depends on the size of the plastic zone in relation to the plate thickness and crack length.

Under cyclic loading there are two plastic zones of relevance. The first is the forward or monotonic zone which can be defined as the region of material experiencing plastic deformation when subjected to the maximum load in the cycle, corresponding to K_{max} . The second is the reversed or cyclic zone, which is a small region of material within the forward zone which undergoes reversed plasticity (reversed plastic flow) upon unloading to the minimum load (McClung, 1991; Rahgozar *et al.*, 2007). Here the plastic zone is influenced by ΔK , stress state and material behaviour.

An approximate estimate of the size of the plastic zone at the tip of a crack (see Figure 2.4.4) was obtained by Irwin from his elastic solution for the stress field around the crack tip (Irwin, 1958).

Based on his findings Irwin found that the zone extends a distance in front of the crack tip corresponding to:

$$r_p = \frac{1}{\beta\pi} \left(\frac{K_I}{\sigma_{ys}} \right)^2 \quad [2.4.8]$$

where σ_{ys} is the yield strength of the material and $\beta=2$ for plane stress or 6 for plane strain. r_p is generally defined as the plastic zone radius, therefore a plastic zone is typically twice that given here.

However, there are a number of other factors which may influence the size of the plastic zone. These include the strain hardening or softening characteristics of the material and the stress state. Under plane strain conditions the triaxial stress system at the crack tip would inhibit yielding, therefore increasing the effective material yield strength, whereas under plane stress conditions yielding would be easier, thus leading to a larger plastic zone size. This is because under plane stress conditions the material at the crack tip is under low restraint and is free to deform. Consequently the crack tip region can accommodate a high applied K before static fracture occurs.

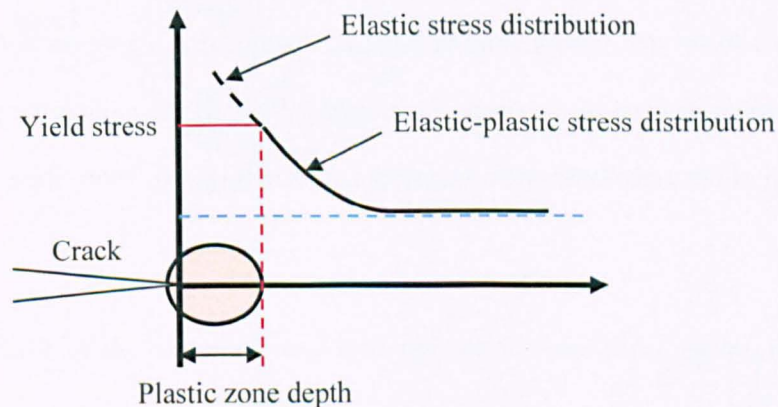


Figure 2.4.4 Irwin's illustration of plastic zone size (Meguid, 1989).

An alternative approach to Irwin's is Dugdale's strip yield model, which assumes that the plastic deformation is concentrated in front of the crack in a localised strip (Dugdale, 1960). This was further simplified (Rice, 1965) in an attempt to introduce some aspects of crack tip plasticity into an elastic analysis. The resulting plastic zone size for plane stress was close to that obtained

theoretically (Irwin, 1960), confirming Rice's solution. Rice investigated several different cracked body configurations and always found that small scale yielding could be represented by:

$$r_p = \left(\frac{K}{\sigma_{ys}} \right)^2 \quad [2.4.9]$$

Newman (1981) also further developed the Dugdale model and introduced the idea of a plastic constraint factor. This is often used to adjust the plane stress yield strength to account for plate thickness. In comparison to experimental results (Newman, 1995) reasonable success was achieved. However, there is much difficulty in discerning an appropriate value(s) for the constraint factor (Codrington and Kotousov, 2009).

Under cyclic loading, the first application of stress in a cyclic stress sequence produces a plastic zone which is the same as that produced by a static stress of the same magnitude (Maddox, 1971) and can be characterised by the stress intensity factor K_{max} . As the material yields ahead of the crack tip the monotonic plastic zone of dimensions given in Eq. [2.4.10] is produced. When the direction of loading reverses, the local stress is reduced to a level corresponding to a stress intensity factor K_{min} . Due to this reduction from K_{max} to K_{min} , the re-distribution of stresses in the near crack tip region leads to reverse plastic flow and the formation of a plastic zone (termed reversed or cyclic plastic zone) in front of the crack tip, embedded within the monotonic plastic zone, Figure 2.4.5. The radii of the monotonic and reversed plastic zones (Irwin, 1960; Rice, 1967) can be given as:

$$(r_p)_{monotonic} = \frac{1}{2\pi} \left(\frac{K_{max}}{\sigma_{ys}} \right)^2 \quad [2.4.10]$$

$$(r_p)_{cyclic} = \frac{1}{2\pi} \left(\frac{\Delta K}{2\sigma_{ys}} \right)^2 \quad [2.4.11]$$

where K_{max} is the maximum stress intensity in the loading cycle and $\Delta K = K_{max} - K_{min}$.

Consequently, a plastic zone equal to Eq. [2.4.11] alternates between compressive and tensile yield, whilst a larger zone based on the maximum value of K and σ_{ys} pulsates between zero and tensile yield. On this basis the plastic zone size for cyclic loading conditions would be one quarter the size of that used for monotonic (static) conditions.

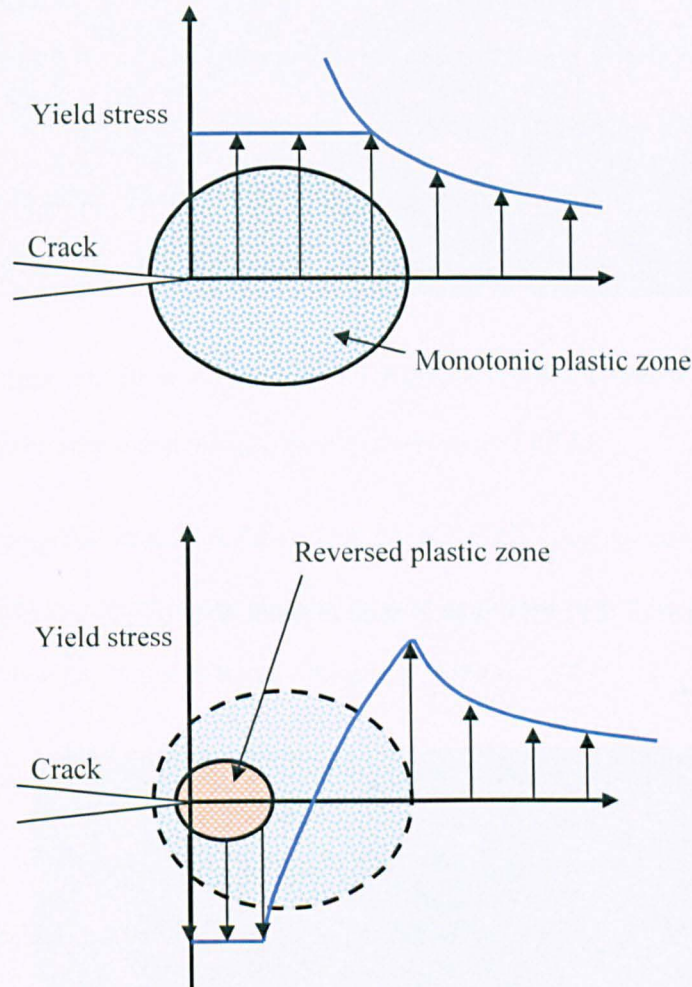


Figure 2.4.5 Schematic of the monotonic and reversed plastic zone development at the crack tip during cyclic unloading.

However, the approximation given in Eq. [2.4.10] underestimates the value of r_p because it ignores the redistribution of stress due to the plastic zone. Instead, Irwin found that by considering the von Mises yield criterion (1913), a better approximation of the plastic zone sizes under monotonic loading could be derived as given in Eq. [2.4.12] for plane stress or Eq. [2.4.13] for plane strain (Irwin, 1960).

$$r_p = \frac{1}{\pi} \left(\frac{K_{max}}{\sigma_{YS}} \right)^2 \quad [2.4.12]$$

$$r_p = \frac{1}{3\pi} \left(\frac{K_{max}}{\sigma_{YS}} \right)^2 \quad [2.4.13]$$

The stresses within the reverse plastic zone at the fatigue crack tip were estimated by Rice (1967) and are equal to the yield stress (σ_{ys}) in compression. Therefore, the smaller cyclic plastic zone (r_c), which as mentioned above alternates between compressive and tensile yield, can be determined by substituting for ΔK and $2\sigma_{YS}$ in Eq. [2.4.12] since the stresses move from tension to compression, giving:

$$r_c = \frac{1}{\pi} \left(\frac{\Delta K}{2\sigma_{YS}} \right)^2 \quad [2.4.14]$$

It was noted that the size of the cyclic plastic zone depends only on ΔK and is independent of the maximum value of K_{max} .

2.5 FATIGUE CRACK PROPAGATION

Whilst the crack initiation phase is governed by cyclic shear stress (see Section 2.3), the propagation phase is governed by the cyclic principal stress (Lassen and Recho, 2006). As noted previously, much of the fatigue life associated with welded joints, especially those with very low fatigue strength, is spent in fatigue crack propagation. This is because with many welded geometries, geometric stress concentrations, crack-like defects and tensile residual stresses, particularly at weld toe locations (Signes *et al.*, 1967; Maddox, 1970), cause fatigue cracks to initiate after relatively few cycles of applied stress (Maddox, 1974).

The fracture surface of a fatigue crack is typically smooth and usually exhibits concentric rings known as 'beach marks' spreading out from the initiation point, Figure 2.5.1. These markings are often associated with varying loads, dwell periods and differential corrosion.

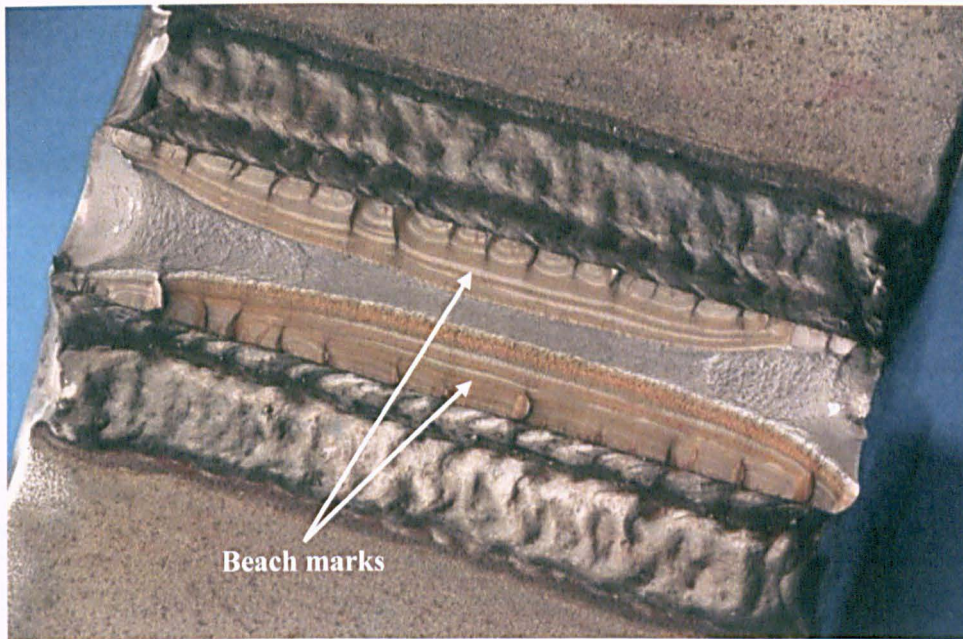


Figure 2.5.1 Fatigue specimen (manufactured from Q1N) tested under direct axial constant amplitude loading showing distinct beach marks, courtesy of TWI Ltd.

As the rate of propagation continues the surface progressively roughens until fracture occurs. It is possible to trace the crack front on the fracture surface by microscopy, and in doing so it is possible to view individual loading cycles between ‘striations’, Figure 2.5.2.

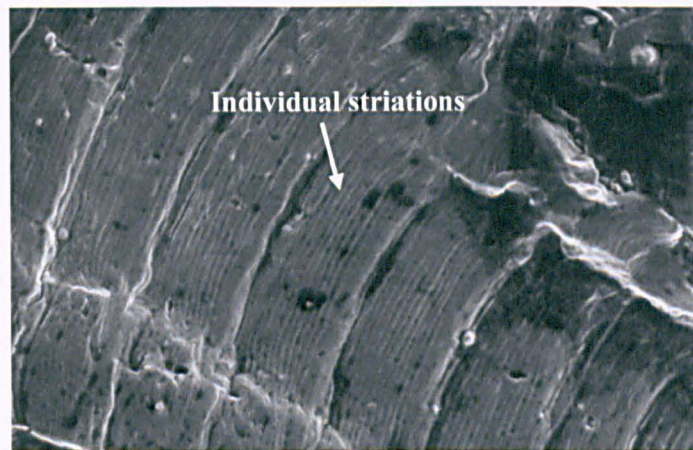


Figure 2.5.2 Example of fatigue striations contained within loading blocks as seen through a scanning electron microscope on 6082 T651 aluminium alloy.

Fatigue crack propagation can generally be defined in terms of three stages. *Stage I* is the transition to a finite crack growth rate from no propagation below a threshold value of ΔK . It concerns the initial extension of micro-cracks propagating within a slip band, which is on a plane of high shear

stress, and is generally considered to be encouraged by plasticity (see Section 2.4.4) surrounding the crack tip in the direction of primary slip resulting in a zig-zag crack path (Forsyth, 1962). *Stage II*, referred to as macro-cracking, concerns the propagation of a crack through the majority of the cross-section; this stage can be further sub-divided into 'crack growth in shear' and 'crack growth perpendicular to the applied tensile stress'. The final stage, *Stage III*, defines the final moments of crack propagation, whereupon the remaining cross-section is insufficient to sustain the applied load and brittle fracture or ductile collapse occurs.

To aid in evaluating crack growth rate, a number of empirical laws were proposed in the attempt to characterise the rate of crack propagation in *Stage II*, which usually takes up the majority of crack propagation stage. One such law is often used to characterise fatigue crack propagation rates in metallic materials (Paris *et al.*, 1962) and states that:

$$\frac{da}{dN} = C(\Delta K)^m \quad [2.5.1]$$

where da/dN is the increment of crack growth per cycle. C and m are material constants, referred to later as the Paris coefficient and exponent respectively. These are found experimentally by measuring the rate of crack growth under applied cyclic loading. Values for m are typically around 3 for a variety of metals.

When plotting fatigue crack propagation data (da/dN v ΔK), on log-log axes (Figure 2.5.3), the Paris law is associated with the linear region in the middle of the crack growth rate curve.

At lower values of ΔK , crack growth rates fall below values corresponding to the Paris law as a fatigue crack threshold ΔK_{th} (also denoted as ΔK_0) below which crack growth ceases, is approached (*Stage I* in Figure 2.5.3). This is typically below $da/dN = 10^{-7}$ mm/cycle, or in terms of ΔK , $63\text{N/mm}^{3/2}$ ($2\text{MPa}\cdot\text{m}^{1/2}$) for steel and $21\text{N/mm}^{3/2}$ ($0.7\text{MPa}\cdot\text{m}^{1/2}$) for aluminium alloys (in air, or other non-aggressive environments) (BSI, 2013), where crack growth rates are also much more sensitive to stress ratio, micro-structural variables and environmental conditions compared with the Paris regime (*Stage II* in Figure 2.5.3). Conversely, crack growth rates can be considerably higher than those corresponding to the Paris law at high values of ΔK , approaching the critical conditions

for fracture/failure, where rates are more sensitive to stress ratio ($R=K_{min}/K_{max}$) (Stage III in Figure 2.5.3). Growth rates in this regime are often associated with a change in fracture mechanism. In the Paris regime (Stage II), crack growth rate depends only on ΔK .

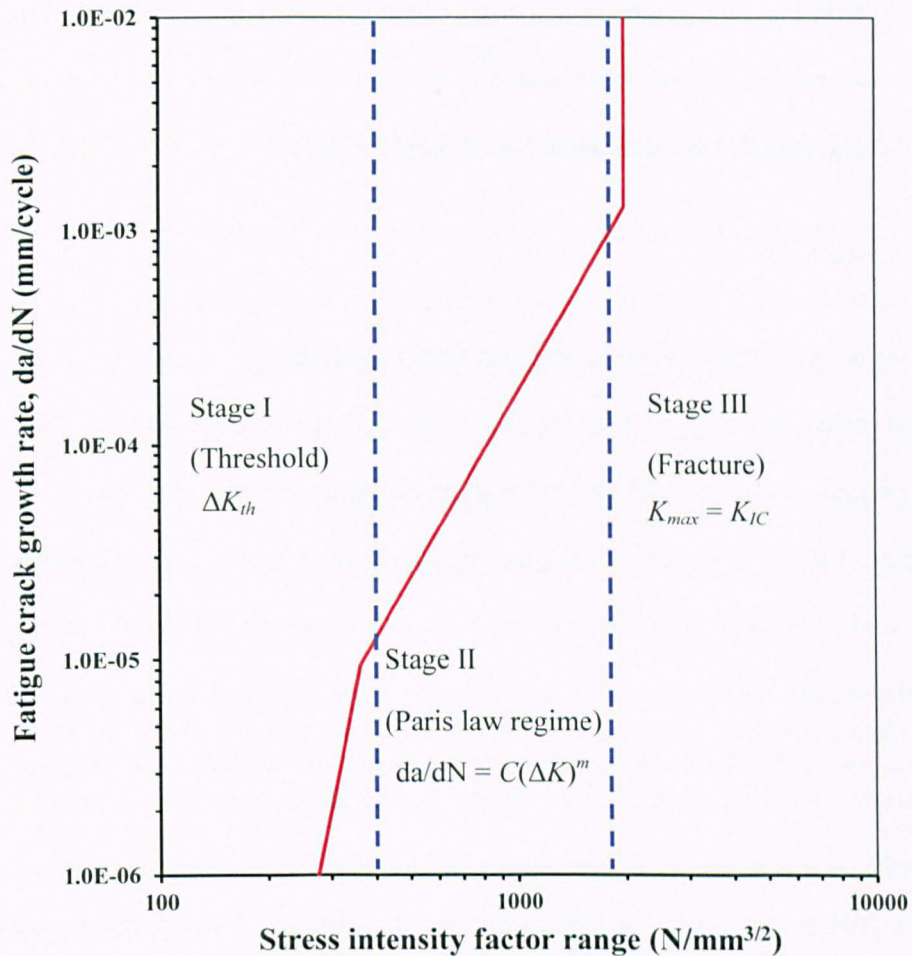


Figure 2.5.3 Two stage simplified fatigue crack growth law ($R>0.5$) for steels in air (BSI, 2013). Stage III also shown.

The Paris equation is a useful concept as it can be integrated to determine the number of cycles for a crack to propagate from its initial size (a_i) to a final size such as that corresponding to failure (a_f), by use of the procedure as detailed in BS 7910 (BSI, 2013), such that by combining Eq's. [2.4.7] and [2.5.1] and integrating between limits:

$$\int_{a_i}^{a_f} \frac{da}{(Y\sqrt{\pi a})^m} = C.S^m . N \quad [2.5.2]$$

Thus, an initial crack of size a_i is calculated to propagate to a size of a_f in N cycles under stress range S .

In the case of an as-welded joint where failure consists of growth from an inherent crack like flaw (e.g weld toe failure), if the geometry and size of inherent flaw remain the same from one weld to the next, as assumed for welded joints tested to generate $S-N$ data, and at failure the crack size is considerably larger than a_i , the integral in Eq. [2.5.2] is constant and the equation becomes:

$$S^m N = a \text{ constant} \quad [2.5.3]$$

This is the form of $S-N$ curve actually obtained from fatigue tests of welded joints (see Eq. [2.2.2]). Of course in reality variations in geometry and inherent flaw size exist such that the integral in Eq. [2.5.2] is not really constant. Such variations contribute towards the scatter observed in fatigue test data (Maddox, 1991). As well as predicting the correct form of the $S-N$ relationship, the fracture mechanics analysis also gives the slope of the $S-N$ curve, m , which is generally the same as that for the crack propagation data for the material, see Figure 2.5.3. As noted above, m , is usually around 3 which is the reason for the choice of $m=3$ for the slopes of the design curves given in BS 7608 (BSI, 2014).

Where crack propagation under VA loading is concerned, Eq. [2.5.2] is applied to successive stress cycles, such that if the spectrum comprises n_1 cycles at stress range S_1 and n_2 cycles at S_2 etc. then:

$$\int_{a_i}^{a_1} \frac{da}{(Y\sqrt{\pi a})^m} = CS_1^m n_1 \quad [2.5.4]$$

$$\int_{a_1}^{a_2} \frac{da}{(Y\sqrt{\pi a})^m} = CS_2^m n_2 \quad \text{etc.} \quad [2.5.5]$$

This continues over the life of the crack or until some pre-determined critical size (a_f) is reached, such that:

$$\int_{a_i}^{a_f} \frac{da}{(Y\sqrt{\pi a})^m} = CS_1^m n_1 + CS_2^m n_2 + \dots \quad [2.5.6]$$

The flexibility of the fracture mechanics approach is such that any of the four main variables a_i , a_f , ΔS and N can be calculated provided the other three are known.

2.6 INFLUENCING FACTORS ON FATIGUE CRACK GROWTH

There are a large number of factors which can affect the fatigue mechanism and thus the fatigue crack growth rate and fatigue life of a component or structure. In order to provide greater applicability of the results to practical engineering situations, it is vital that these parameters be considered in any fatigue analysis. In metallic materials fatigue crack propagation tends to be insensitive to material strength and also metallurgical factors (Pook, 2007). However, according to Codrington (2008) material effects including basic properties and grain structure can influence propagation rates.

Along with metallurgical factors, structural geometry effects including stress concentration factors (SCFs) and welding defects, applied loading (i.e. mean stress), and environmental conditions (i.e. temperature and the presence of any corrosive substances) are all parameters that influence crack propagation rates (Codrington, 2008).

The significance and effect of specimen thickness on fatigue crack growth rate is the subject of much debate within published literature (Codrington and Kotousov, 2009). This is particularly the case in CA loading tests which are generally used as the basis of estimations of crack growth under VA loading.

It is discussed (Codrington and Kotousov, 2009) that three conclusions drawn from experimental studies directly contradict one another (Park and Lee, 2000). The conclusions drawn were as follows:

- The effect of specimen thickness is negligible (Shahinian, 1972; Kim and Kim, 1998).

- Accelerated crack growth rates observed with increased thickness (Costa and Ferreira, 1998; Guo *et al.*, 1999; Park and Lee, 2000).
- Reduced growth rates observed with increased thickness (Jack and Price, 1972).

The mechanical argument behind the thickness effect on fatigue crack growth rate is that the stress and strain fields in the vicinity of the crack tip are strongly dependent upon the specimen thickness. As thickness increases the stress state will change from being largely plane stress to plane strain dominant (see Section 2.4.3). Where thin materials are considered (plane stress conditions), a transformation between square and slant fatigue crack propagation can occur. Whilst crack propagation rates (at high ΔK) increase as thickness increases, at the transition to slant fatigue crack propagation the rate decreases. At this transition stage 'shear lips' are formed (Figure 2.6.1) and increase in size during propagation (Schijve, 1974; Schijve *et al.*, 2004; Pook, 2007); as propagation continues the crack surface is inclined at 45° to the material surface, which upon reducing the level of load is reversible (Schijve, 1974).

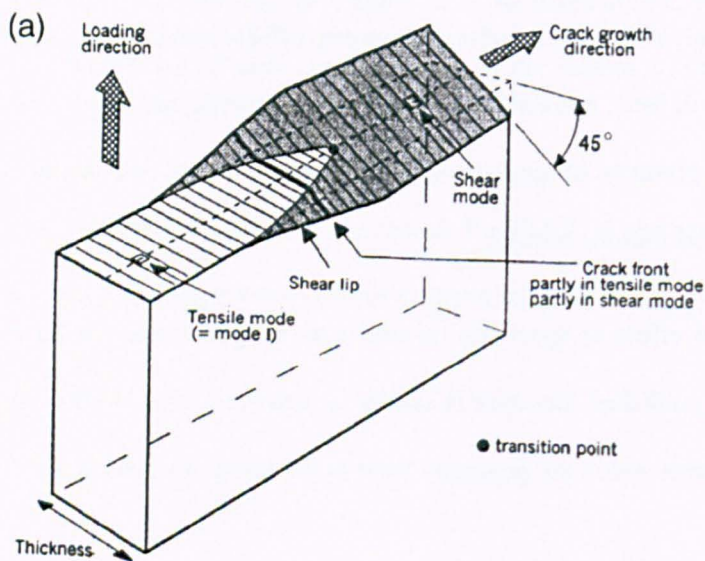


Figure 2.6.1 Fracture surface of a through-thickness fatigue crack with transition from the tensile mode to shear mode (Schijve *et al.*, 2004).

2.7 THE EFFECT OF CRACK CLOSURE

In consideration of the fatigue crack propagation process, particularly the influence of applied stress ratio (R), Elber postulated that only the portion of the cycle during which the crack tip is open is effective in propagating a crack (Elber, 1971). He went on to measure the point in the applied stress cycle at which crack closure occurred and found that this could be during the tensile part. Indeed, he found that cracks were in fact closed for a significant portion of tensile loading. He therefore defined the effective stress as:

$$\Delta S_{eff} = S_{max} - S_{op} \quad [2.7.1]$$

where S_{max} is the maximum stress in the cycle and S_{op} is the stress at which the crack opens.

Or in terms of stress intensity factors:

$$\Delta K_{eff} = K_{max} - K_{op} \quad [2.7.2]$$

From this the effective stress intensity range at the crack tip could be determined using:

$$\Delta K_{eff} = Y \cdot \Delta S_{eff} \sqrt{\pi a} \quad [2.7.3]$$

where Y is a geometry correction factor and a is the crack length.

By replacing ΔK in Eq. [2.7.3] for the effective stress intensity range, the growth rate can then be calculated using:

$$\frac{da}{dN} = Y (\Delta K_{eff})^m \quad [2.7.4]$$

Crack closure can be induced by several mechanisms (Suresh, 1998) including: crack tip plasticity and residual plastic deformation in the wake of the crack (Figure 2.7.1a)), the explanation proven by Elber (1971); oxide induced crack closure (Figure 2.7.1b)), due to corrosion products on the crack surface; roughness induced crack closure (Figure 2.7.1c)), which occurs when microscopic irregularities on opposite crack surfaces interfere with one another; transformation induced crack closure (Figure 2.7.1d)), which is when stress or strain induced phase transformations at the crack

tip zone lead to a net increase in the volume of transformed material; this is sometimes referred to as material ‘bulging’ (Makabe *et al.*, 2003, 2004 and 2005).

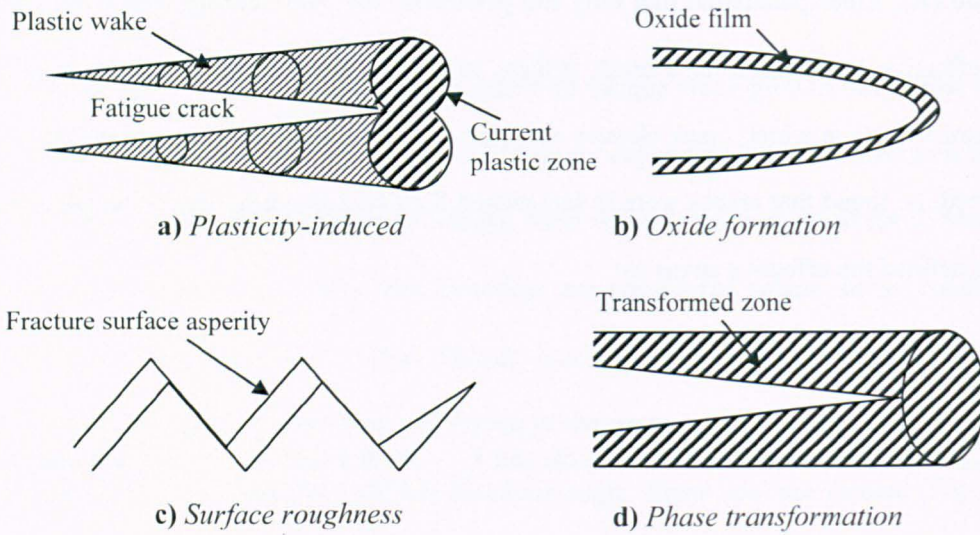


Figure 2.7.1 A schematic illustration of some mechanisms associated with crack closure.

However, in the context of the present study the first mechanism, related to crack tip plasticity, is of primary significance in that this is the only one that is likely to explain changes to fatigue crack growth rate due to the type of applied cyclic loading, CA or VA, in the materials considered. Indeed, Elber found indications that crack closure accounted for retardation and possibly acceleration in crack propagation rates under VA loading (Elber, 1971). In the case of the former, the explanation was that a particular loading event could increase the crack closure stress level such that the effective magnitude of the stress ranges following it would be reduced. In the latter, crack growth acceleration, the opposite could happen and the effective stress range of cycles following the loading event would be increased.

Under both CA and VA loading quantitative knowledge of the crack opening stress (S_{op}) is generally believed to be essential for crack growth estimations (Schijve, 1988), as it is required to define ΔK_{eff} , which in turn is considered to be the appropriate parameter for correlating crack growth rates under different cyclic loading conditions. From the practical viewpoint, it appears that the crack closing and opening stresses are indistinguishable (Fleck, 1982; Banerjee, 1984 and Mageed *et al.*, 1992) and so either can be used to determine ΔK_{eff} .

2.8 RESIDUAL STRESSES

2.8.1 FORMATION OF RESIDUAL STRESSES THROUGH WELDING

The formation of residual stresses can be the direct result of manufacturing processes whereby changes in shape or material properties are present. These manufacturing processes can be divided into three main categories:

- Mechanical processes – rolling of sheet metal, surface removal (machining) and component assembly.
- Chemical processes – surface hardening treatments (nitriding and carburizing).
- Thermal processes - quenching, casting and welding.

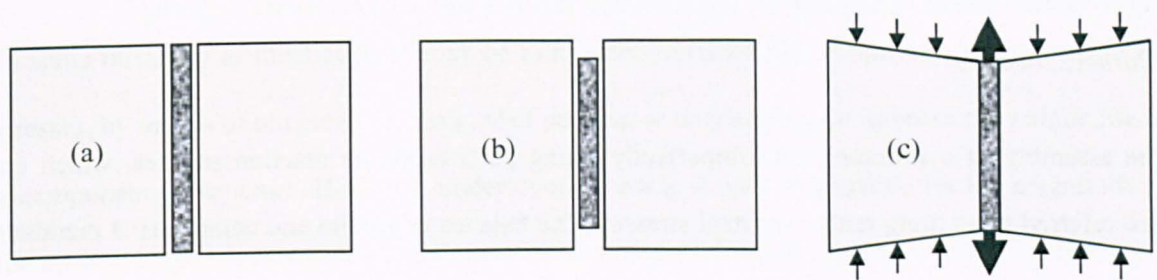


Figure 2.8.1 *Effect of residual stress on weld plates (Gurney, 2006).*

Welding is one of the most significant causes of residual stresses and typically produces tensile yield magnitude stresses in and close to the weld, balanced by compressive residual stresses elsewhere in the component. Figure 2.8.1 illustrates how residual stresses are formed. Immediately after welding (Figure 2.8.1a) the weld metal and adjacent parent material are hot. If the plates were unrestrained (Figure 2.8.1b), it is possible to see how the weld metal would shrink during cooling. However, as the plates are joined (Figure 2.8.1c), the subsequent cooling of the weld metal is restrained by the parent material, giving rise to a longitudinal tensile stress in the weld. This is balanced by the presence of compressive stresses in the adjacent material. The resulting longitudinal (parallel to the weld) and transverse (normal to the weld) residual stress distributions, assuming idealised conditions where a uniform through thickness stress distribution exists, are shown schematically in Figure 2.8.2 (a) and (b) respectively.

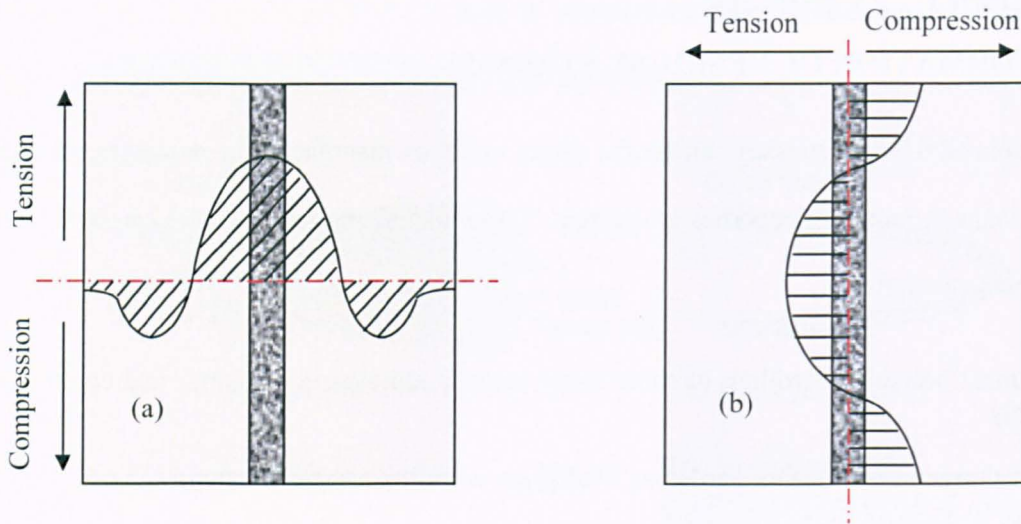


Figure 2.8.2 Typical residual stress distributions due to a butt weld between two plates (Gurney, 2006).

The assembly of a structure from imperfectly-fitting parts produces reaction stresses, which are also referred to as ‘long range’ residual stresses. The balance of tensile and compressive members in such a structure gives rise to a state of equilibrium.

This ‘long range’ residual stress is also referred to as ‘macro-stress’ or ‘type I stress’ and is one of three methods for categorising residual stresses based on length scales (Withers, 2008). Others include: micro-stresses or type II stresses, where stresses equilibrate over a number of grains, and type III stresses which exist and equilibrate over several atomic distances within a single grain. Only type I stresses are considered in the present work.

High tensile residual stresses have a significant effect on fatigue of welded joints. Fatigue loading is superimposed onto the residual stress, with the result that cycling is at a much higher mean stress than that applied. Typically the weld and adjacent material will experience stress cycling from yield stress tension downwards (Gurney, 2006)

It has been found that the magnitude of residual stresses is dependent on the tensile strengths of both the weld and parent material (Maddox, 1991). It is well established that in the presence of high tensile residual stress, loading that produces compressive stresses can still produce failure by fatigue (Gurney, 1977; Maddox, 1982). Consequently, most fatigue design rules assume that

applied tensile and compressive stresses are equally damaging, which is a marked contrast with design rules for un-welded parts.

Work performed by McClung (McClung, 2007) established that both the application of fatigue loading and the production of fatigue cracking can alter the residual stress field (see also Section 2.8.3) and should be taken into consideration in any estimates of the residual stresses in a structure.

Although there are many variables associated with fatigue of welded joints (weld defects, weld microstructure etc.) these are well characterised. However, there are few data on through-thickness distributions of residual stress especially after cyclic stressing.

In some instances residual stresses may be introduced intentionally, notably compressive residual stresses, by means of ultrasonic peening, shot peening or overloading, to improve the fatigue life of a component or structure. However, under cyclic loading it may be possible for the magnitude of the applied loads to reduce any beneficial effect by means of 'washing out' or redistribution of the compressive stresses.

2.8.2 RESIDUAL STRESS MEASUREMENT

Residual stress measurement methods can be either destructive or non-destructive. Destructive techniques generally involve the removal of material which generates partial relaxation of the residual stress field within a sample, allowing the resulting strain to be measured. This response in strain can then be used to calculate the residual stress generated under this deformation. Such techniques include: *centre hole drilling, deep hole drilling, the contour method and plate sectioning (layer removal)*.

In contrast to destructive techniques, non-destructive techniques allow residual stresses to be determined without changing or affecting the material properties, thus allowing the component / sample to remain re-useable. Typical methods include: *Diffraction based techniques (X-ray, Neutron and Synchrotron), ultrasonics and magnetic*.

Further information on residual stress measurement is given in Chapter 3.

2.8.3 RESIDUAL STRESS RELAXATION

Initial residual stress fields inherent or induced by the manufacturing process may not remain stable during service life and so can relax or redistribute due to a variety of mechanisms (McClung, 2007). McClung observed that relaxation/redistribution occurs when the summation of the residual stress and applied stress exceed the yield condition of the material. Both tensile and compressive residual stresses relax towards zero, although the changes are more pronounced for tensile stresses (McClung, 2007).

The application of cyclic loading of test specimens has demonstrated relaxation effects after a relatively small number of stress cycles (Frost *et al.*, 1974). Whether or not residual stresses are relaxed depends on the magnitude of the subsequent cyclic stressing in relation to the yield stress of the material (Frost *et al.*, 1974). Repeated loading can cause gradual changes in the residual stress over time, even if no single fatigue cycle induces local yielding (McClung, 2007).

Following an investigation where residual stresses were considerably relieved after one load cycle due to reversed stress cycling (Iida *et al.*, 1996), the effect was examined under the action of repeated loading (Iida and Takanashi, 1997). It was once again observed that on the application of one load cycle under $R=0$ and $R=-1$, both longitudinal and transverse residual stresses were significantly reduced, with additional reduction seen after further cyclic loading at the same stress range. The author noted that the extent of the residual stress relaxation increased with increase in applied stress range.

As mentioned in Section 2.8.1, the fact that fatigue failure of welded joints is still observed even under purely compressive loading (Gurney, 1977; Maddox, 1982), suggests that either locally, residual stresses do not relax or residual stresses do not need to be at yield to still produce the same tensile effective stress.

2.9 CUMULATIVE DAMAGE

2.9.1 VARIABLE AMPLITUDE LOADING

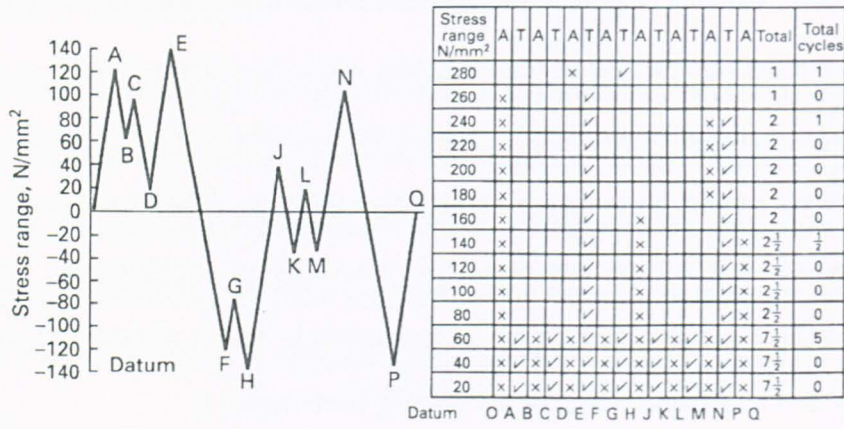
In service the great majority of structures and components at risk of fatigue failure are subjected to complex stress cycles which generally vary in a random manner and are known as variable

amplitude stresses. Variable amplitude stresses can arise due to varying loads, different forms of loading, or as a result of structural continuity (Note. where structural continuity is concerned this can give rise to complex influence lines of stress, such that stress interaction occurs between them i.e. adjacent wheels crossing an orthotropic bridge deck (Gurney, 2006)). It is important to establish the stress spectrum that will be experienced in service before estimating its effect in fatigue behaviour. The most common method for achieving this is by use of electrical resistance strain gauges to provide a reasonable picture of the working stress variation.

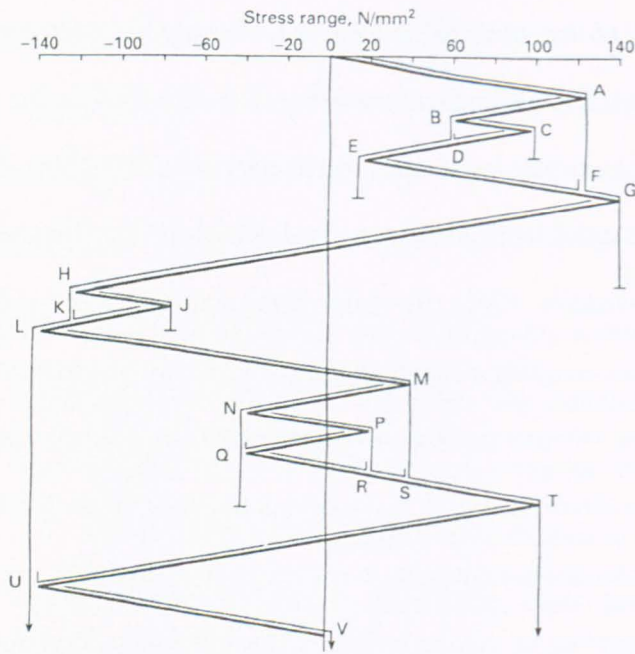
2.9.2 CYCLE COUNTING METHODS

Once the stress history of the structure/component is known, the complex waveform needs to be broken down into cycles. There are several counting methods which can be used, although there is very little evidence as to which is the most satisfactory (Gurney, 2006; Pook, 2007). The most relevant methods for loading applied to as-welded joints are the Range-Pair and Rainflow (or Reservoir) methods (Maddox, 1991), the latter being recommended in BS 7608 (BSI, 2014). Range-Pair and Rainflow counting methods (Figures 2.9.1a) and b)) respectively) combine positive and negative half cycles, whereas the Reservoir method (Figure 2.9.1c)) identifies complete cycles in terms of stress range (Maddox, 1991). It is worth noting that whilst Rainflow counting is one of the most common approaches to undertake, it was originally derived by considering the behaviour of metal under plastic cycling in relation to fatigue crack initiation. Therefore it may be premature to assume it is also appropriate for fatigue crack propagation.

When individual cycles cannot be distinguished there is a need for cycle counting to reduce the process to discrete cycles to permit the application of Miner's cumulative damage rule, which is discussed in the next section. Where life prediction methods are not sufficiently accurate to predict fatigue lives under VA service loadings, standard load histories are required.



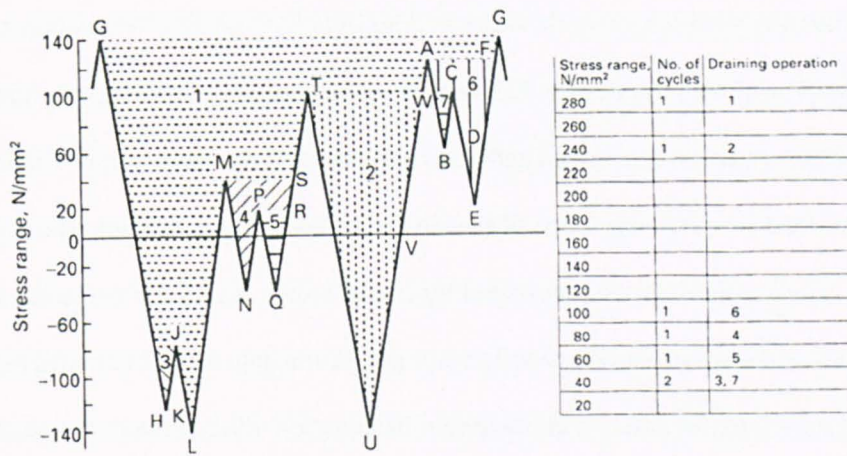
a)



Results:

Stress range, N/mm ²	Positive half-cycles	Negative half-cycles	Total cycles
20			
40	11	11	2
60	1	1	1
80	1	1	1
100	1	1	1
120			
140	11		11
160			
180			
200			
220			
240	1	1	1
260			
280		1	1

b)



c)

Figure 2.9.1 Illustrations of typical cycle counting methods with results included (Maddox, 1991), a) Range-pair, b) Rainflow, c) Reservoir.

The effect of different cycle counting methods on fatigue damage is something which for welded joints has not been fully investigated. One comparison by Gurney (1978) using rainflow, level crossing and range pair for several different loading spectra, found that rainflow consistently lead to values of $\sum n/N$ which were 33% greater than those values derived by range-pair. The level crossing method was higher still by 66% greater than range-pair. This equated to reductions in design stress of ~10% for rainflow and 16% for level crossing, as compared with the range-pair method. Clearly these differences are significant.

2.9.3 PALMGREN-MINER CUMULATIVE DAMAGE RULE

The most widely used method for estimating fatigue lives under VA loading is by use of the Palmgren-Miner linear cumulative damage rule, or Miner's Rule as it is commonly called (Miner, 1945). It states that fatigue damage from the application of n cycles of stress range S is directly proportional to n/N , where N is the CA life at S . On this basis, failure under VA loading consisting of n_i cycles at stress ranges S_i , where $i=1, 2, 3$, etc. can be expected when:

$$\frac{n_1}{N_1} + \frac{n_2}{N_2} + \frac{n_3}{N_3} + \dots + \frac{n_i}{N_i} = \sum_i \frac{n_i}{N_i} = 1 \quad [2.9.1]$$

where, N_i values are obtained from the relevant CA $S-N$ curve.

However, a limitation with Miner's rule is that it does not allow for any prior stress history that the structure or component may have seen. Relevant events include overloading, whereby any existing crack growth can be slowed or even halted due to blunting at the crack tip or the introduction of compressive residual stress. Some forms of tensile under-loading may result in the acceleration of a fatigue crack, giving a life less than predicted by Miner's rule. As Miner's rule does not take into account these effects, in practice failure as a result of VA loading does not always occur according to Eq. [2.9.1]. Therefore, for safety a damage sum in Equation 2.9.1, termed D , less than unity may be used to take account of such effects, giving:

$$\sum_i \frac{n_i}{N_i} = D \quad [2.9.2]$$

where D is typically in the range of 0.3 – 0.8 (Maddox, 1991).

Another problem associated with the application of Miner's summation is the treatment of low stresses in a spectrum. Under VA loading high stresses in a spectrum may propagate a crack to such an extent that stresses below the CAFL become damaging. Whilst it is accepted that such low stresses should be included, there is some debate over the best method to be employed. If, however, all the stress ranges are below that of the constant amplitude fatigue limit, which is usually assumed to correspond to 10^7 cycles, then the possibility of fatigue failure can be ignored. In the British fatigue design rules BS 7608 (BSI, 2014) it is assumed that for joints in air, the $S-N$ curve is bent at 5×10^7 cycles from a slope m to a shallower slope $(m+2)$, so that stresses below this point are assumed to be damaging but not as damaging as implied by the extrapolated $S-N$ curve (as discussed in Section 2.2.1). The existing European design standard, Eurocode 3 (BS EN, 2005), suggests a change of slope at 5×10^6 cycles with a final cut-off (where the curve is assumed to be horizontal) at 10^8 cycles. A more extreme recommendation is made by the US AASHTO bridge rules (AASHTO, 2010) which suggest that the $S-N$ curve to be extrapolated 'ad infinitum' with no slope change.

This problem was further investigated by Gurney (2000), whose findings suggest that for a convex upwards spectrum it makes little difference whether a straight or bent $S-N$ curve is used for design purposes; however for a concave upwards spectrum it can be unsafe to use a bent curve. He also

concluded that stresses down to a value of 10.1N/mm^2 under tensile loading, and $\pm 8.4\text{N/mm}^2$ under alternating loading were just as damaging as those implied by the extrapolated $S-N$ curve with a slope change. This was further confirmed more recently (Zhang and Maddox, 2009) also using a concave upwards spectrum, where it was found that for the two specimens considered conforming to a Class G and F joint detail (BSI, 2014) stresses down to $\leq 8.4\text{N/mm}^2$ and $\leq 31.5\text{N/mm}^2$, respectively, were found to be just as damaging as implied by the extrapolated $S-N$ curve. The key difference between the two spectra being that, in convex upwards spectra, the proportion of low stress cycles is low, hence they are not so significant in their contribution to fatigue damage, which is the opposite to that for concave upwards spectra.

Due to its simplistic nature, these problems have not deterred investigations into cumulative damage being assessed by the use of Miner's rule for both initiation and total life. On many occasions investigators have found instances where lives have been greatly safer than the lives predicted by Miner's rule. Of more concern, however, are occasions when lives are significantly lower than those predicted by the use of this method. There is extensive evidence to show that variable amplitude stress cycles could be more damaging than the same stress cycle under CA loading resulting in $\sum(n/N) < 1.0$ at failure (Tilly, 1985; Vormald and Seeger, 1991; Dahle, 1993; Tubby *et al.*, 1996; Gurney, 1985, 1992b, 2000 and 2006; Berger *et al.*, 2002).

One such investigation examined the effects of loading spectra with different mean stresses and the resulting validity of Miner's rule (Zhang and Maddox, 2009). The results showed that Miner's rule was substantially non-conservative for all tests performed cycling down from a constant maximum stress ('stalactitic' loading). Such loading is assumed to simulate the presence of high tensile residual stress for use in tests on welded specimens that cannot be relied upon to contain such high residual stresses. However, it may actually arise in some service loading conditions. The deficiency in Miner's rule was attributed primarily to the stress interaction effects resulting from the loading sequences used, whereby high stresses caused significant crack growth acceleration from subsequent lower stresses. It was concluded that, in the case for the constant maximum spectra, Miner's rule should be applied assuming $\sum(n/N) \leq 0.4$.

The Fraunhofer Institute in Germany (formally LBF) (Sonsino *et al.*, 2009) also suggests that under certain applications Miner's rule should be applied assuming $\Sigma(n/N) < 1$. Here they recommend that under constant mean stress conditions $\Sigma(n/N) \leq 0.5$, whilst for varying mean stress conditions such as under wide band loading $\Sigma(n/N) \leq 0.2$. This call for a reduction has also been echoed and applied by the International Institute of Welding (IIW) which recommends that Miner's rule should be applied assuming $\Sigma(n/N) \leq 0.5$ (Hobbacher, 1996).

A limited amount of research has gone into discovering the reasons why Miner's rule is substantially non-conservative; however, it is thought that the main factors relate to crack closure and load sequence effects. It is this problem that forms the basis of the present research project, which aims to investigate the factors that influence accelerated crack propagation under high mean stress spectra and how they can be allowed for in fatigue design.

2.9.4 THE INFLUENCE OF NARROW AND WIDE BAND SERVICE LOADING

Under narrow band loading, each positive $\frac{1}{2}$ cycle is followed by an equal and opposite $\frac{1}{2}$ cycle, returning to the same mean level, Figure 2.9.2. This form of loading does not include any sudden occurrences of overloads or small cycles and is generally performed with all cycles at a stress ratio, R , of 0. The ratio of upward going mean crossings to the number of peaks, termed 'irregularity', in narrow band loading is close to unity (Gurney, 2006).

With wide band loading, the mean stress of individual cycles within the spectrum varies widely (Figure 2.9.3) and generally involves a stress history with irregularity significantly less than 1.0 (Gurney, 2006).

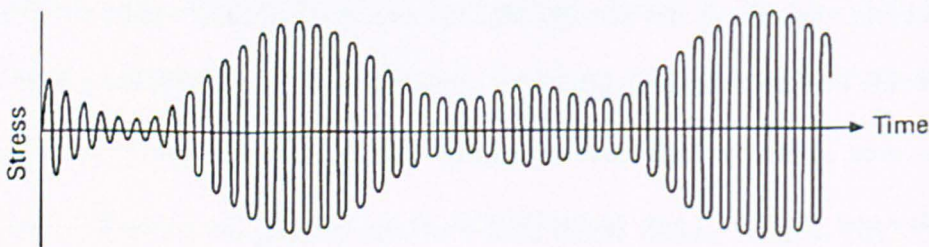


Figure 2.9.2 Typical example of a narrow band stress history.

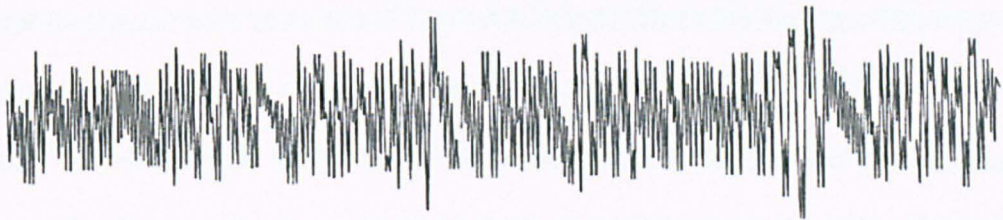


Figure 2.9.3 Typical example of a wide band stress history

In a series of comparative tests using the same spectrum of stress ranges applied in different forms, it was found that Miner's rule gave $\Sigma(n/N) = 0.5$ to 0.92 (Gurney, 1993). Gurney showed that higher mean stresses for smaller cycles can enable the propagation of a crack, even when the peak stress is at $R=0$. He also went on to state that other investigators (Haibach *et al.*, 1980; Pedersen and Agerstov, 1991; Sarkani, 1990) have also found low values of $\Sigma(n/N)$ under wide band loading, suggesting that one important feature of a loading spectrum is the variation of stress ratio for individual cycles. The current design rules BS 7608 (BSI, 2014) state that as far as welded joints are concerned, stress ratio is an irrelevant factor. However, findings discussed here would suggest otherwise. The findings of Gurney's work also show that another factor which affects the value of $\Sigma(n/N)$ under loading that consists of repeatedly applied blocks of a variable amplitude stress sequence is the block length, the shorter the block the lower $\Sigma(n/N)$ at failure. Under such conditions an alternative method known as the area rule was derived (Gurney, 1985). This states that:

$$Ln \left(\frac{N_B}{N_C} \right) = - (\text{area under curve } pi \text{ v. } Ln N_{Ei} \text{ exceedence diagram}) \quad [2.9.3]$$

where N_B is the number of blocks to failure (each block containing one excursion to the top limit stress), N_C is the life under CA loading for the top limit stress in the spectrum, pi is the proportion of the maximum stress in the spectrum, S_{max} (i.e. $S_i = pi \times S_{max}$) and N_{Ei} is the number of cycles per block equal to or exceeding pi times the top limit stress ($1.0 < p < 0$).

Whilst this technique was shown to be a satisfactory alternative to Miner's rule for the consideration of short block length spectra, due to the relatively low number of tests performed this can only be communicated as a tentative suggestion.

2.10 INTERACTION EFFECTS ON FATIGUE CRACK ACCELERATION

2.10.1 GENERALITIES

Investigations into the effects of crack growth retardation and acceleration are still being considered today. The actual mechanisms associated with them are still not well understood. The majority of work has concentrated on crack retardation effects (McEvily *et al.*, 1990; Makabe *et al.*, 2003 and Zhao *et al.*, 2008). However, as acknowledged in Section 2.9.3, life expectancy under service loading according to Miner's rule has identified occasions where VA stress cycles could be more damaging than the same stress cycle under CA loading, resulting in $\sum(n/N) < 1.0$ at failure. Such discrepancies in Miner's rule summations almost certainly arise from the assumption that damage accumulation is necessarily linear. It is, in fact, how individual cycles interact with one another which give rise to faster or slower crack growth than that predicted by the rule. Therefore, understanding the mechanisms behind crack acceleration which contribute to such fatigue damage is of extreme importance.

2.10.2 LOAD SEQUENCE EFFECTS AND OVERLOAD RATIO

Load sequence effects have been observed under various mean stress levels, not only stalactitic VA loading (Gurney, 1992 and 1993; Zhang and Maddox, 2009), but also through wide band loading (Gurney, 1993). It is thought that where compressive underloads follow tensile overloads, accelerated crack growth is generated by reverse plastic flow (Makabe *et al.*, 2003, 2004 and 2005), which is a phenomenon that occurs when residual stresses are changed from compressive to tensile due to material bulging in the thickness direction. If local compression is high enough, bulging behind the crack tip reduces the crack closure level and hence gives rise to a tensile residual stress in the overload zone as well as increasing the magnitude of the effective tensile stress range at the crack tip. Whilst the acceleration seems to be related to the magnitude of tensile overload (Makabe, 2004), study of the material bulging effect has been limited to through-thickness cracking in 4mm thick specimens and so further investigations should be considered to determine this effect for thicker specimens and for the more common surface crack.

Published attempts to understand stress interaction effects have utilised simple VA loading with two magnitudes of applied stress range, as summarised in Table 2.10.1. This provides an opportunity to understand how stresses interact and affect propagation rates.

By far the most common approach for investigating load sequence effects is by use of CA cycling with the periodic introduction of a *Single Peak Overload*. Such sequences involve three variables; overload ratio (OLR) ($K_{\text{peak}}/K_{\text{max}}$), stress ratio ($K_{\text{min}}/K_{\text{max}}$) and range of CA loading, ΔK . Under this form of loading, it has been found that there is a threshold level of OLR below which the application of an overload has no effect on crack propagation (Bernard *et al.*, 1976; Garwood, 1978; Voorwald *et al.*, 1991), ranging from 1.2 for Ti6Al4V to 1.5 for HT80 steel. High levels of OLR i.e. 2.5–3.0, generally result in crack arrest (Garwood, 1978; Blom, 1989), and intermediate values cause the number of delay cycles to increase (Bernard *et al.*, 1976; Kumar, 1991; Chand, 1992; Lu and Li, 1993).










Varying ΔK whilst maintaining an OLR of 2.0, results in a clear difference in behaviour, with low values generating immediate retardation and higher values giving initial acceleration followed by retardation (Matsuoka *et al.*, 1976; Ranganathan *et al.*, 1984; Dhar, 1989).

Tests on materials with two different yield strengths (690N/mm^2 and 350N/mm^2) at an OLR of 2.0 (Blom, 1989) showed that the higher strength material generates immediate retardation; however, initial acceleration followed by delayed retardation was evident in lower strength material. This can be related to plane strain conditions during overloading for the high strength material and plane stress for the lower strength (Gurney, 2006).

Of the simple loading types investigated, whilst acceleration effects may occur at some stage in the majority, only tests using a *step change of S_{mean} up* have really demonstrated appreciable increases in propagation rates over that of the standard CA rates (Jacoby *et al.*, 1976; Nowack *et al.*, 1979). Here crack growth acceleration in both 2024-T3 aluminium alloy and Ti-6AL-4V was attributed to strain hardening, whereby the high crack tip strain from the large increase in stress reduces the deformation capability in subsequent stress cycles (Jacoby *et al.*, 1976). Similar acceleration effects in a laboratory Al alloy were considered to be a result of strain hardening, reduced crack closure

levels and crack tip blunting, although none could be recognised as the main cause (Nowack *et al.*, 1979).

Table 2.10.1 Summary of experimental findings using simple loading spectra.

Form of loading	Sequence	Results	Source
Single peak overload		No effect for OLR 1.2 – 1.5. Intermediate values of OLR cause number of delay cycles to increase. At OLR of 2.0, plane strain or low ΔK gave immediate retardation. Plane stress or high ΔK gave acceleration then retardation.	Bernard <i>et al.</i> , 1976; Matsuoka <i>et al.</i> , 1976; Garwood, 1978; Ranganathan <i>et al.</i> , 1984; Blom, 1989; Dhar, 1989; Kumar, 1991; Voorwald <i>et al.</i> , 1991; Chand, 1992; Lu and Li, 1993; Schijve <i>et al.</i> , 2004; Lee, 2009
Multiple peak overload		Similar to that of single peak overload.	Matsuoka <i>et al.</i> , 1976; Dhar, 1989
Step change down		Immediate reduction in da/dN with no initial acceleration.	Chand and Garg, 1984; Chand, 1992
Step change up		Step increase in growth rate higher than standard CA, followed by gradual reduction to standard rate.	Chand and Garg, 1984; Ward-Close <i>et al.</i> , 1989
Low-High overload		Similar behaviour to a single peak overload, but with less retardation.	Garwood, 1978; Chand, 1992; Skorupa, 1998
High-low overload		Reduced overload effect compared with single peak overloads.	Jacoby <i>et al.</i> , 1976; Garwood, 1978; Chand, 1992; Skorupa, 1998; Schijve <i>et al.</i> , 2004, Lee, 2009
Step change of S_{mean} down		Abrupt decrease in da/dN , greater effect than that of a single peak overload.	Jacoby <i>et al.</i> , 1976; Nowack <i>et al.</i> , 1979; Chand and Garg, 1984; Chand, 1992
Step change of S_{mean} up		Immediate increase in da/dN to a higher than expected rate.	Jacoby <i>et al.</i> , 1976; Nowack <i>et al.</i> , 1979
Step change constant K_{max}		No transient effect. Immediate increase in da/dN . Greatest effect found with a ratio of 10:1 (minor to major cycles)	Druce <i>et al.</i> , 1979 Fleck, 1985; Schijve <i>et al.</i> , 2004; Zitounis and Irving, 2007

It is interesting to note that tests performed involving a *step change*, constant K_{max} found no transient effects i.e. crack growth rate was unaffected (Druce *et al.*, 1979). This is surprising since similar loading has been found to produce significantly shorter lives than predicted by Miner's rule in endurance tests of welded joints (Gurney, 1992 and 1993; Zhang and Maddox, 2009). Other crack growth tests, on both Al alloy (2014A-T4) and steel (BS 4360 50B), did show a strong stress interaction effect in that periodic underloads (one underload to every ten minor cycles) caused crack propagation rates typically 1.8 times faster than expected under CA loading (Fleck, 1985). Again various causes were considered (strain hardening and crack tip mean stress) but no single explanation was found. Further work is therefore required using simple loading spectra to ascertain if a stress interaction effect under this mode of loading does influence propagation rates and, if so, by what mechanism(s).

Stress interaction in BS 4360 Grade 50B structural steel tested at $R=0$ was also investigated by Gurney (Gurney, 1981) by restricting peaks of smaller cycles so that they were lower than the main constant amplitude cycle. It was assumed that stress interaction would consistently give an increase in life i.e. $n/N > 1$. Four loading spectra were investigated which consisted essentially of CA loading with one or more excursions applied on each stress cycle. Gurney found that the calculated Miner summation for these sequences actually lay in the range of 0.64 - 1.02. He also demonstrated that the magnitude of peak stress was irrelevant to the degree of stress interaction caused.

Further work considering the effect of R on tensile overloads (Zitounis and Irving, 2007) found accelerated crack growth for a two level spectrum, where near threshold load cycles at $R=0.9$ were interrupted with underloads to zero load. Not only was a reduction in the plasticity induced closure (crack tip) level found to be responsible, but also micro-structural induced closure caused by faceted crack growth, whereby faceted fracture may account for changes in K_{op} and consequent changes in growth rate. This effect of stress ratio, sequence loading, overloads and underloads was further investigated (Zhao *et al.*, 2008), where although it was agreed that compressive underloads tend to accelerate crack growth, reduced crack closure level, compressive residual stresses, crack tip blunting and strain hardening may also be responsible.

Accelerated crack propagation is not just confined to loading with $R \geq 0$, but can also arise in weld details under part-compressive loading. This is because the loading is superimposed onto the high tensile residual stresses due to welding, with the result that the loading is effectively tensile (see Section 2.8.1). Also, in high stress regimes, such as the growth of cracks from sharp notches, overloads cause yield magnitude notch root strains which accelerate growth (Topper and DuQuesnay, 2001). Yield magnitude compressive overloads crush asperities leaving a flatter material in the crack wake for propagation.

Crack growth under negative stress ratios considered by (Makabe *et al.*, 2005) showed that both retardation and acceleration effects were associated with crack tip opening displacement at the point of overload. Acceleration, however, was confined to $R = -1.5$. This was due to a change in the residual stress distribution following the applied minimum stress, whereby, if the local compression is high enough, reverse yielding occurs resulting in material bulging in the vicinity of the crack tip. Bulging subsequently reduces the closure levels behind the crack tip, which on return to zero load, brings about a state of residual tensile stress leading to accelerated crack growth. This investigation established that crack propagation behaviour is dependant of the baseline stress ratio, overload level and mechanical properties of the material.

2.10.3 INFLUENCE OF EFFECTIVE STRESS INTENSITY FACTOR ON ACCELERATION

As discussed in Section 2.7, the effective stress intensity factor (ΔK_{eff}) is the portion of the loading cycle during which the crack tip is open, and is therefore effective in propagating a crack. It was also noted that in predicting fatigue crack growth rates knowledge of this factor is believed to be essential (Schijve, 1988).

The work performed into material bulging (see Section 2.10.2) found that Eq. [2.10.1] originally proposed by McEvily *et al.*, (1990), satisfied various underload/overload scenarios, and that the rate of fatigue crack growth is a function of $\Delta K_{eff} - \Delta K_{effth}$, independent of the R value or overload level.

$$\frac{da}{dN} = A(\Delta K_{eff} - \Delta K_{effth})^2 \quad [2.10.1]$$

where A is a material constant and ΔK_{effth} is the effective threshold stress intensity factor range.

This effective stress intensity factor was also considered during compliance measurements on compact tension (CT) steel specimens under CA loading and block constant amplitude loading (BCAL) at applied loads of 2kN to 20kN. It was found that the expansion of the hysteresis loop and the extent of the hysteresis loop tail, Figure 2.10.1, made it possible to evaluate the fatigue crack propagation behaviour (Xiong *et al.*, 2006 and 2008). It was suggested that the expanding hysteresis loop and reducing hysteresis tail resulted in fatigue crack acceleration, with the effective stress intensity factor being the driving force, such that propagation will retard if there is insufficient compressive plasticity at the crack tip. Therefore, the residual stress distribution at the crack tip will govern acceleration (or retardation) effects based on tensile or compressive residual plastic zones (Xiong *et al.*, 2008). However, no mention of the assumed values of ΔK or ΔK_{eff} was given in either paper.

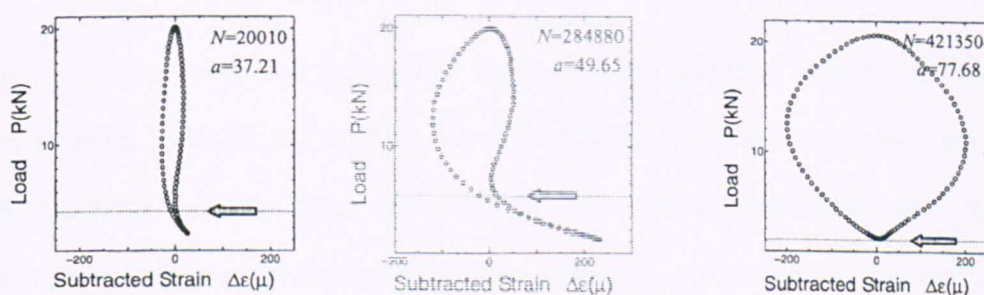


Figure 2.10.1 Evolution of the hysteresis loop tail during fatigue crack propagation (Xiong *et al.*, 2006).

2.11 SUMMARY OF THE BACKGROUND AND LITERATURE REVIEW AND IDENTIFICATION OF NOVELTY IN THE CURRENT WORK

The background study and literature review discussed in this chapter has identified the need for better understanding of the factors which lead to unsafe estimates on fatigue life. Whilst a substantial amount of work has investigated safe life estimates generated by fatigue crack retardation, limited work has explored the factors which are directly responsible for crack

acceleration. Much of the work which has been performed, to the authors knowledge, has identified three main contributing factors; metallurgical effects, load sequence effects and residual stresses, although none of these have provided definitive explanations for fatigue crack acceleration. The actual reasons behind fatigue crack acceleration may not lie with just one of these observed effects but some combination. It is this important problem that forms the basis of the present research project, which aims to provide better understanding of the factors which influence accelerated crack propagation under high mean stress spectra, and how they can be allowed for within the current design recommendations.

Other conclusions which have been drawn from this literature review have shown that, as discussed in Section 2.9.2, there are several cycle counting techniques currently being employed to break down complex stress histories (Range-pair, Rainflow, and Reservoir etc.). However, there is little evidence to suggest which of these techniques is the most appropriate when considering fatigue of welded joints (Gurney, 2006; Pook, 2007). The current tendency to adopt either Rainflow or Reservoir stems from the fact that they tend to produce the most severe counts with respect to fatigue, allowing a degree of conservatism.

The correct derivation of a loading spectrum in use with fatigue testing is therefore an important factor in the subsequent Miner's summation. Gurney explored the effect of different counting techniques under broadband loading (Gurney, 1978), the result of which produced differing damage summations by up to 66%, depending on those compared, or in terms of design stress, a reduction of up to ~16%. Whilst the tendency may be to adopt the most conservative method there is clearly a future need to further investigate and understand cycle counting techniques and their effects on fatigue life.

Whilst Miner's rule may be the simplest guidance on life estimates under spectrum loading it has been discussed (Section 2.9.3) that there are a number of limitations in its use; namely, how the influence of low stresses in the spectrum should be allowed for and how account could be taken of previous stress history. It has also been acknowledged that the CA fatigue curves which are used in

conjunction with Miner's rule contain a certain degree of scatter which in turn can produce different values of $\Sigma n/N$.

The overriding problem is that Miner's rule has been shown to significantly over estimate fatigue lives leading to unsafe life estimates. This is not just confined to circumstances which consider only propagation, but also for those which include initiation. Therefore, the consideration of two entities, initiation and propagation, for determining fatigue life estimates may be valid, or, alternatively, a single law which satisfies both these entities and produces a more reliable method for fatigue life estimates under spectrum loading.

As a result of the lack of understanding of the actual mechanism(s) responsible for accelerated fatigue crack propagation, how they interact and subsequently produce lives much shorter under VA loading than predicted using current cumulative damage methods, much of the data generated as part of this research project are novel. In order to provide such test data, existing analysis methods have been employed to understand stress interaction effects.

Chapter 3

RESEARCH METHODOLOGY

3.1 INTRODUCTION

This research project is predominantly empirical and, in addition to a thorough review of literature (Chapter 2), has generated an extensive data set through a variety of laboratory tests. Laboratory testing has focused on filling identified gaps in existing published data to improve the understanding of load sequence effects under simple loading with two magnitudes of stress range. In addition, VA loading has also been used to study the performance of welded joints using spectra designed to promote fatigue crack acceleration.

This Chapter describes the various experimental and analytical methods employed, including:

- a) the measurement of fatigue crack growth rates (FCGR) in notched specimens;
- b) load sequence and endurance fatigue testing, along with the application of strain gauges for static and cyclic responses and residual stress measurement;
- c) the application of finite element stress analysis (FEA) for modelling the effect of the applied underloads at the notch tip.
- d) fractographic examination of fatigue striations and sites of fatigue crack initiation at the weld toes of fillet welded specimens.

3.2 SPECIMEN IDENTIFICATION SYSTEM

Care was taken to use a clear specimen numbering system throughout to ensure that multiple references to the same specimen could always be tracked back to its manufacture and subsequent

treatment. Parent material samples used for characterisation purposes have been identified using the prefix 'PM' (for parent material) with two numbers following (e.g. PM1-01). The first digit refers to the batch number; the second refers to the individual specimen sequence number. For welded samples the same identification system has been used but with PM replaced by 'W' (e.g. W1-01).

FCGR test specimens were designated 'CCT' (centre crack tension) followed by the material, 'ST' for steel or 'AL' for aluminium alloy, the specimen sequence number and, where relevant, 'R' to denote a plate specimen with weld beads deposited to introduce residual stress (e.g. CCT-ST-03R).

In the case of periodic underload testing (see Section 3.4.3) of plain material, the prefix 'SBL1.5' or 'SBL2' for single block loading with underload range 1.5 or 2 times greater than the basic minor stress range respectively, as well as 'ST', or, 'AL' for the material, was also used (e.g. CCT-SBL2-ST-01). Where a CCT bead on plate specimen was used the specimen sequence number was followed by 'R'.

Fatigue endurance test specimens were first assigned the material type followed by 'CCT' or, in the case of fillet welded specimens, 'FIL'. After this came the loading type i.e. constant amplitude loading (CAL) or variable amplitude loading (VAL), then the sequence number as above (e.g. AL-FIL-VAL-02). Again for CCT bead on plate specimens 'R' is placed after the sequence number.

In the case of specimens used in periodic underload or endurance tests, the term 'CL' has also been included if a crack closure test was performed and 'R' again when using a bead on plate specimen (e.g. CCT-VAL-ST-CL-02R). The numbering of specimens used for residual stress measurement also included the term 'RES' (e.g. CCT-FIL-ST-RES-01).

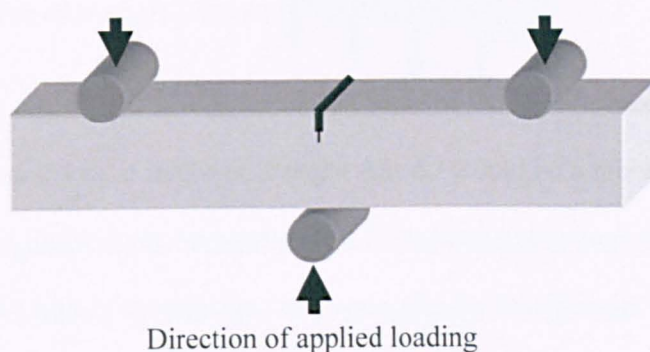
3.3 MEASUREMENT OF FATIGUE CRACK GROWTH RATES

3.3.1 TEST SPECIMEN

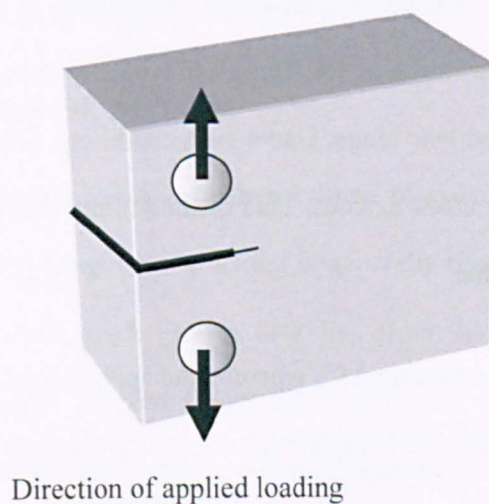
Fatigue crack growth rate (FCGR) tests are generally performed using either single edge notch bend (SENB), compact tension (CT), or centre crack tension (CCT) specimens, Figure 3.3.1a-c respectively. The two main standards covering FCGR testing are BS 12108:2012 (BSI, 2012) and

ASTM E647-13a (ASTM, 2013a); it should be noted that CCT specimens are referred to as middle tension (MT) in the ASTM standard but are referred to using the British designation CCT throughout this thesis.

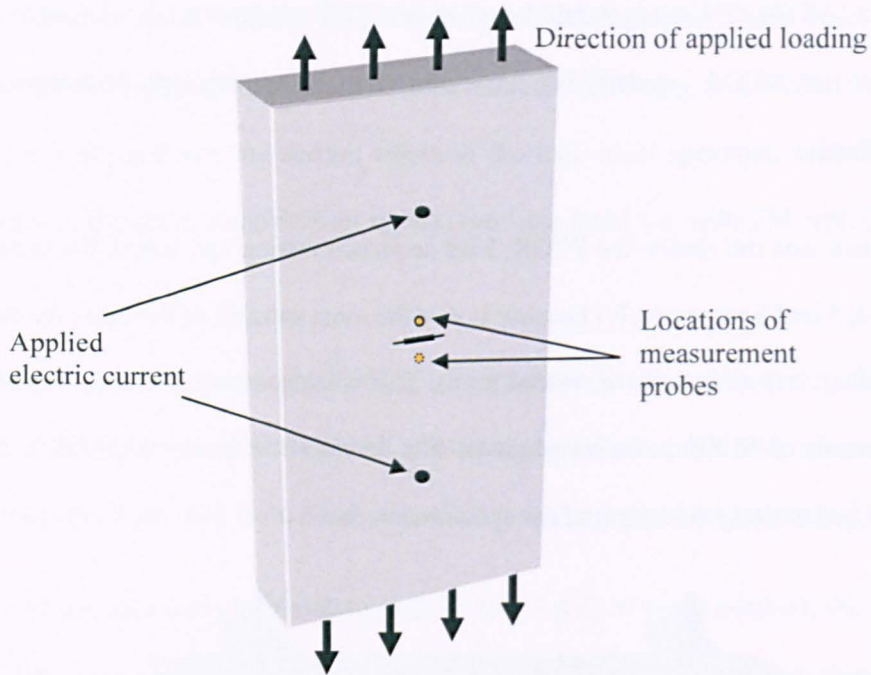
The CCT specimen was the choice for FCGR, load sequence testing and initial VA testing in this work (Chapters 4, 5 and 6 respectively) because it was the most suitable of the three for introducing high tensile residual stresses as arise in welded joints. This was necessary to enable the influence of such residual stresses on FCGR to be investigated. The residual stress was achieved by depositing continuous weld beads along the length of the specimen.



a)



b)



c)

Figure 3.3.1 Types of fatigue crack growth rate test specimen: a) Single edge notch bend specimen (loaded in three point bending), b) Compact tension specimen, c) Centre crack tension specimen (used in the present experimental work).

3.3.2 FATIGUE CRACK GROWTH RATE TESTING

A number of methods are available for determining FCGR data as a function of ΔK . The most common method for moderate values of ΔK (Stage II), typically above $350\text{N/mm}^{3/2}$ ($11\text{MPa}\cdot\text{m}^{1/2}$), is to test under constant applied load range. Under such conditions ΔK , and hence the crack growth rate (da/dN), increases as the crack extends. This method is referred to as ‘increasing ΔK ’ and is carried out using a fixed R value.

An alternative technique is ‘decreasing ΔK ’, whereby the applied load range is continually reduced at a specified rate. Such a technique is performed either at a constant R value or constant K_{max} by controlling the minimum and maximum loads accordingly. Use of constant R is the standard decreasing ΔK technique, as described in both BS 12108 and ASTM E 647. Whilst both decreasing ΔK techniques allow the determination of FCGR data approaching the fatigue crack growth threshold (the point below which no further crack propagation is achieved, defined as ΔK_0), the

constant K_{max} technique is particularly effective for minimising the extent of crack closure (portion during a tensile load cycle to which a crack remains closed, see also Chapter 2, Section 2.7) at low ΔK . Both the increasing and decreasing ΔK techniques were used in the present work to validate the basic CA performance against that given in BS 7910 (BSI, 2013).

A third method (although not used here) is to conduct tests under conditions of ‘constant ΔK ’ by continually shedding the applied load, as in the case for decreasing ΔK but by allowing the decrease in load range to counteract the increase in crack depth. This allows examination of factors other than ΔK on the crack growth rate, including cyclic loading frequency, crack depth and the weld metal or heat affected zone (HAZ) microstructure.

With reference to the use of ΔK , it is noted that in view of the significance of crack tip plasticity (see Chapter 2, Section 2.4.4), it might be thought that ΔJ would be a more appropriate parameter than ΔK for characterising the crack tip stress field. The J -integral is used as a means to determine the dissipated energy ahead of a crack tip and is typically used in fracture assessments, of ductile metals when LFM is no longer valid. This might also be the situation under fatigue loading, but only low cycle conditions where both generally and locally there is cyclic plasticity (Zhou and Cai, 1980). Under the high cycle fatigue conditions used in the present project, crack tip plasticity is highly localised (see Chapter 6) so that LFM is valid and ΔK is the appropriate parameter to use.

3.3.3 INTRODUCTION OF NOTCH

A notch is included in a fatigue crack growth specimen to provide the site for fatigue crack initiation. However, even then fatigue pre-cracking is generally required to initiate a sharp crack from the notch tip before valid crack growth data free from the influence of the notch (e.g. geometry, residual stress) can be captured. Generating a uniform pre-crack of the correct shape i.e. uniform across the specimen thickness, can be difficult. However, such a problem can be avoided by the use of electrical discharge machining (EDM).

This allows the introduction of a sharp notch and also lower residual stresses than other cutting or machining operations. The resulting correct geometry, allows valid crack growth data to be

obtained soon after fatigue crack initiation, typically neglecting just the data for the first 1mm of growth. For this reason, EDM was used to produce 16mm long notches in the present specimens, Figure 3.3.2. All notch dimensions were in line with recommendations given in BS 12108 (BSI, 2012).

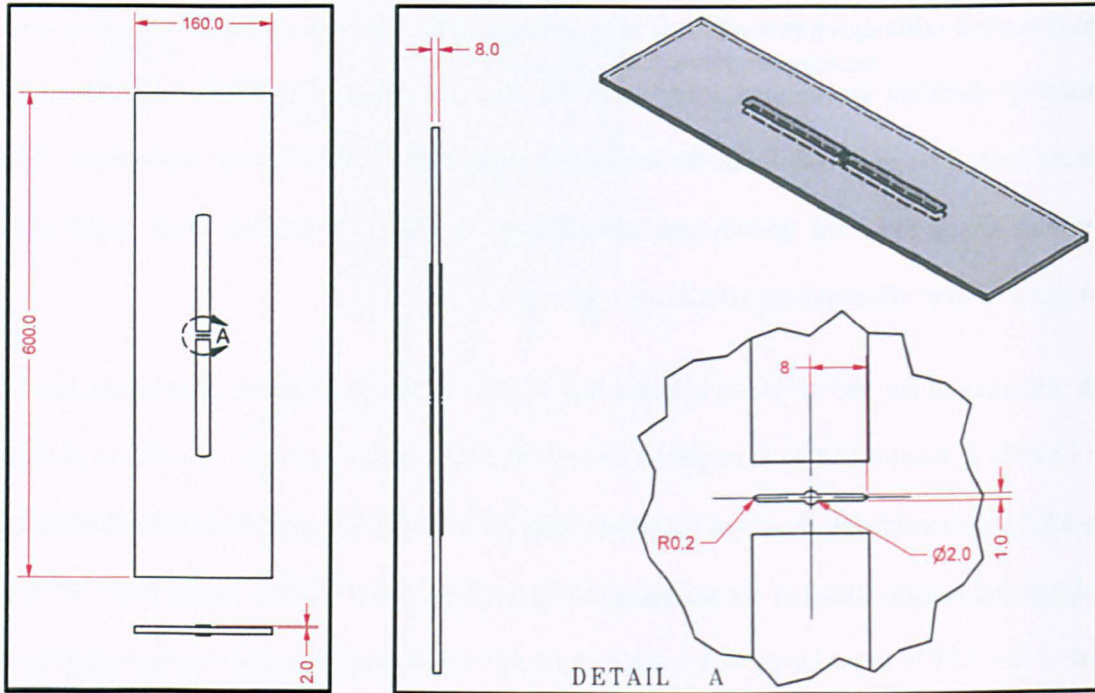


Figure 3.3.2 Detailed drawing of a centre crack tension specimen showing the notch dimensions (weld beads also shown).

3.4 FATIGUE TESTS

3.4.1 TEST SPECIMENS

3.4.1.1 CENTRE CRACK TENSION SPECIMENS

CCT specimens 600mm long and 160mm wide were cut from the 8mm thick S355J2+N steel plate parallel to the plate rolling direction, using a cold saw. In the cases when it was required for the specimen to contain high tensile residual stress acting transverse to the fatigue crack, manual metal arc (MMA) was used to apply a longitudinal weld bead 300mm long on both surfaces directly opposing one another, Figure 3.3.2 and 3.4.1.

Murex low carbon steel rutile electrodes (Fortrex 7018) 4mm in diameter with a heat input of between 1.7 and 1.9kJ/mm were used to produce a weld bead width similar to the notch length of

16mm. Previous work on similar specimens manufactured from mild and high-strength steels (Gurney, 1977) determined that using a heat input of 1.9kJ/mm, the tensile residual stress distribution extended 33mm from the weld centreline before being balanced by compressive residual stresses nearer the edge of the specimens. The extent of the tensile residual stress field was slightly less, 23mm, for a heat input of 1.2kJ/mm.

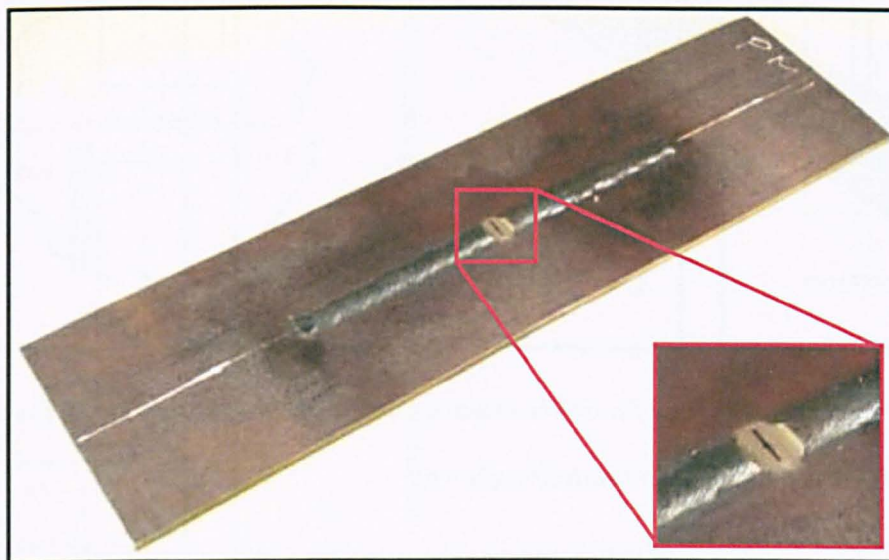


Figure 3.4.1 Steel CCT specimen with a 300mm long weld bead (EDM notch also shown).

CCT specimens 600mm long and 116mm wide were also produced from the 6mm thick 6082 T651 aluminium alloy, Figure 3.4.2. The method of cutting and direction of stressing was the same as that of the steel specimens discussed above.

Again weld beads were deposited on some specimens to induce tensile residual stresses. Tungsten inert gas (TIG) welding with a zirconiated tungsten electrode, 3.2mm diameter 4043 filler wire and a heat input of 1.26kJ/mm was used. The heat input was chosen on the basis of trials that showed it to be the most favourable condition to produce the required weld bead. Unlike the MMA process used on the steel specimens to produce a weld bead width similar to the notch length in one pass, the TIG process required the weld metal to be deposited using a weave technique to provide the same width of weld, Figure 3.4.3.

The central area of all specimens was subsequently machined flush using an end mill to allow notching by electro discharge machining (EDM), as seen in Figure 3.4.1.

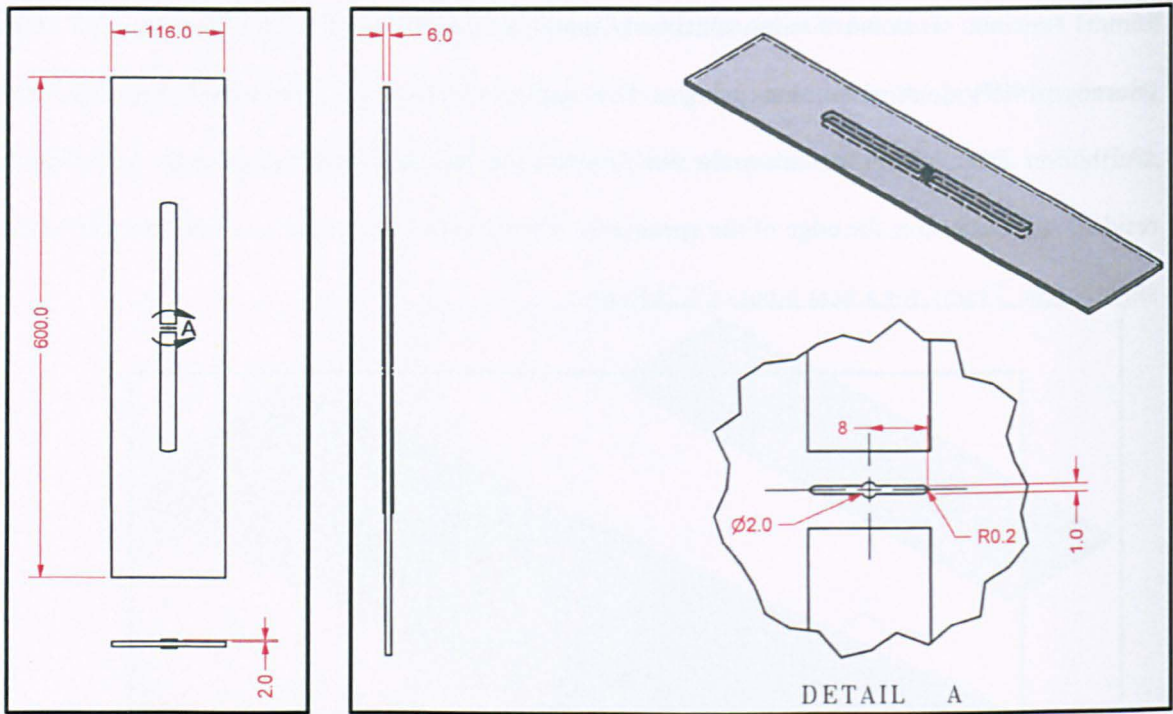


Figure 3.4.2 Detailed drawing of a centre crack tension specimen manufactured from 6mm thick 6082 T651 aluminium alloy (weld beads also shown).

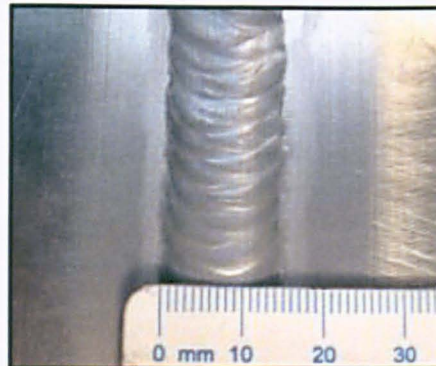


Figure 3.4.3 Weld bead deposited on aluminium CCT specimen by weave technique to provide adequate width.

3.4.1.2 FILLET WELDED SPECIMENS WITH LONGITUDINAL ATTACHMENTS

Fillet welded specimens 650mm long and 150mm wide were also manufactured from the 8mm thick S355J2+N steel plate, Figure 3.4.4. Longitudinal attachments 150mm long and 38mm high, in the same steel, were fillet welded centrally on each surface (i.e. directly opposing one another).

The fillet welds were made using the MMA process in the flat position in two runs with the specimens tilted to form a 'V'. Welding was carried out using 4mm diameter Murex Fortex 7018

electrodes with a heat input of 1.25kJ/mm and weld stop/start positions in the middle of the attachments so as to avoid, as far as possible, the effects of end craters. The fillet welds were carried around the ends of the attachments as shown in Figure 3.4.5. The resulting weld sizes were around 4.7mm throat thickness and 6mm leg length in all specimens.

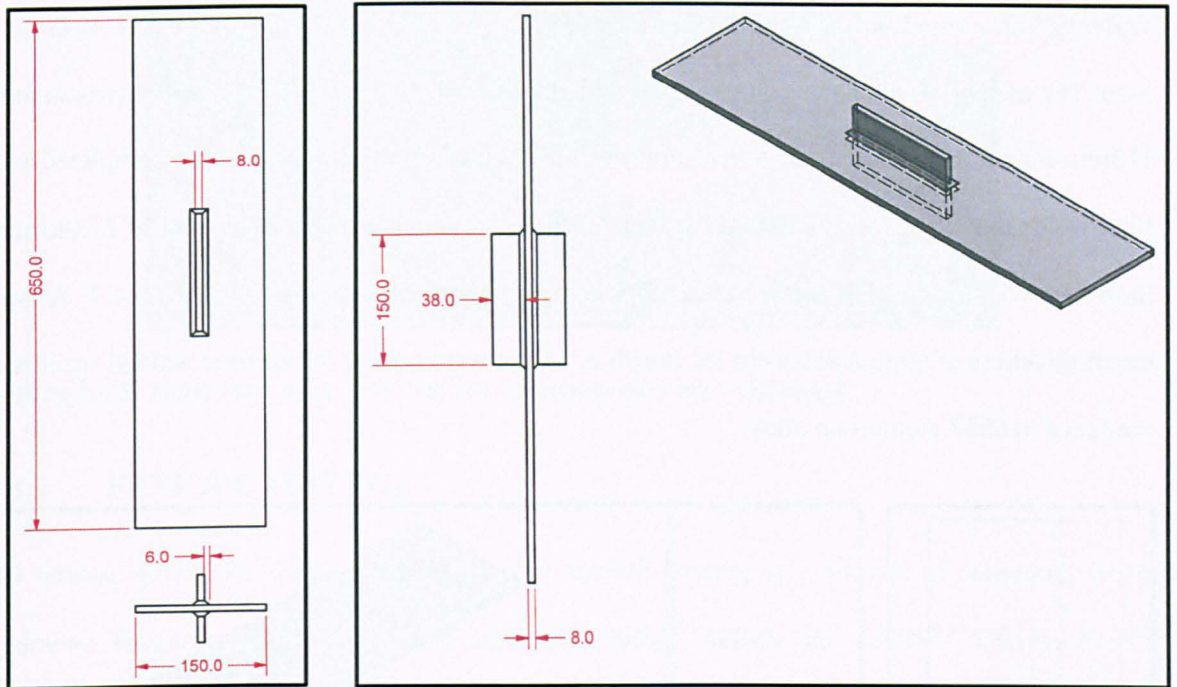


Figure 3.4.4 Detailed drawing of a fillet welded specimen with longitudinal attachments manufactured from 8mm thick S355J2+N structural steel.

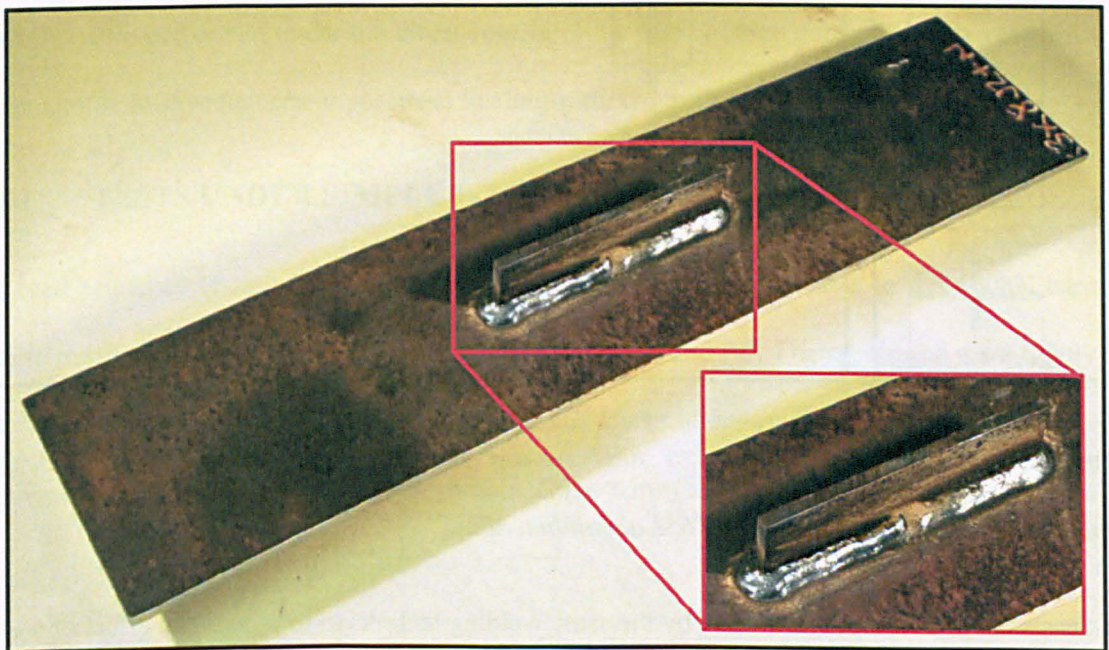


Figure 3.4.5 Steel fillet welded specimen showing weld detail.

Specimens of the same type and dimensions as shown in Figure 3.4.3 were also produced in the 6082 T651 aluminium alloy, the only difference being the base plate and attachment thicknesses which were 6mm, Figure 3.4.6. The fillet welds were made using the tungsten inert gas (TIG) process in the flat position in two runs with the specimens held in the horizontal position.

Welding was carried out using a zirconiated tungsten electrode with 3.2mm diameter 4043 filler wire. The method of manufacture was to join the attachments to the main plate with approximately 113mm long fillet welds using a heat input of 1.37kJ/mm. The joints were then completed with fillet welds that were carried around the ends of the attachments using a heat input of 2.20kJ/mm. Stop/start position were therefore some 30mm from the attachment ends, Figure 3.4.7. A weld throat thickness of 6mm and a weld leg length of 11mm were typical for all fillet welded specimens produced in 6082 aluminium alloy.

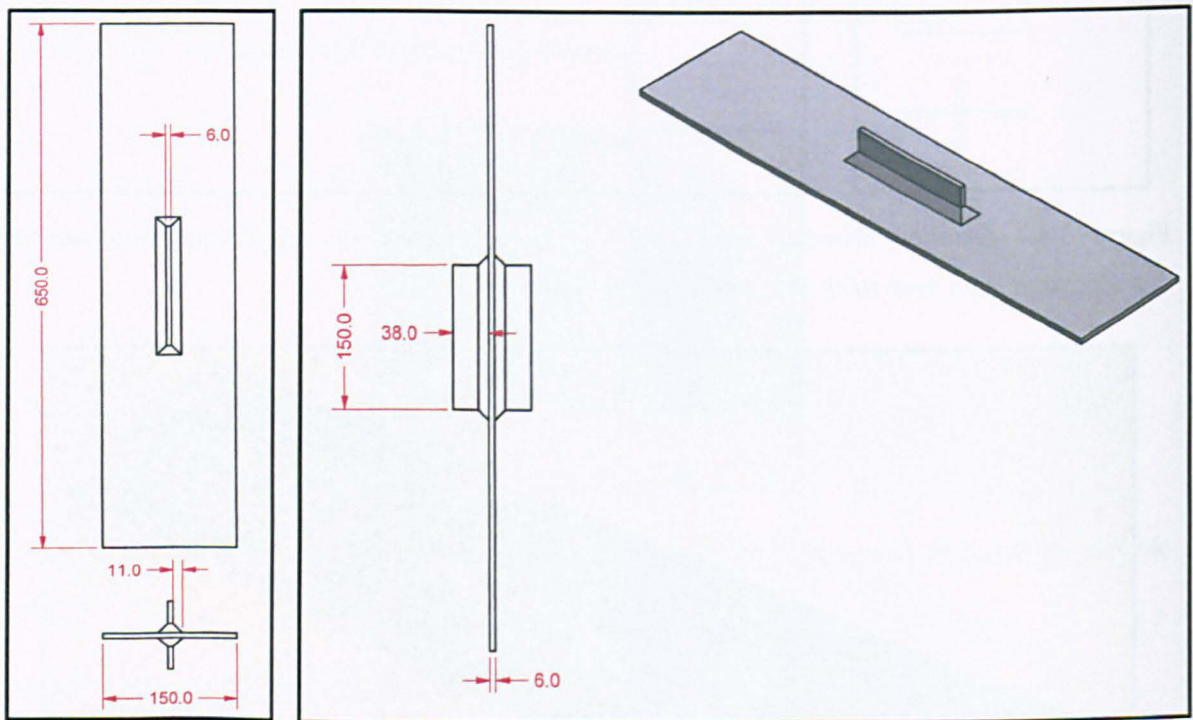


Figure 3.4.6 Detailed drawing of a fillet welded specimen with longitudinal attachments manufactured from 6mm thick 6082 T651 aluminium alloy.

For consistency, all welds were made by the same welding technician to reduce the effect of welder variation. Welder variation has been shown to produce a significant amount of scatter for nominally identical test specimens fabricated using the same procedure (Maddox, 1985).

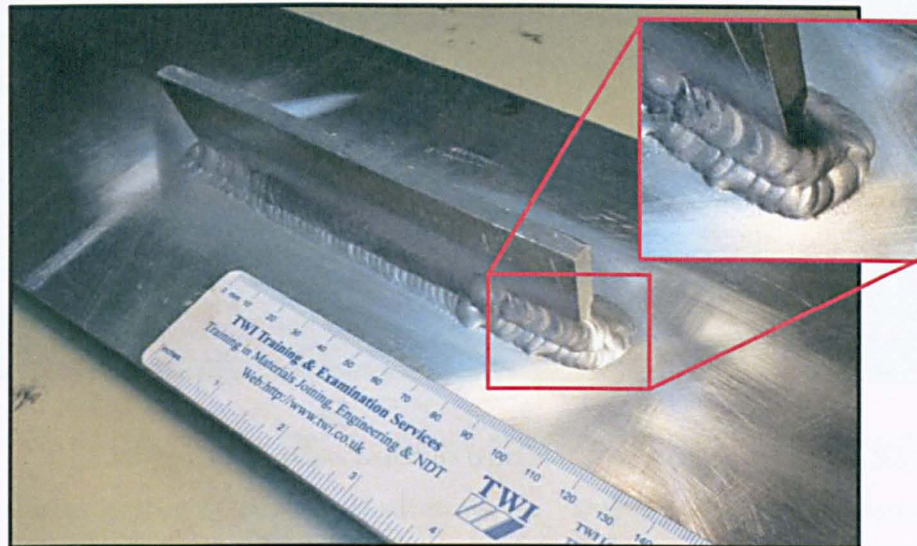


Figure 3.4.7 Aluminium alloy fillet welded specimen showing weld detail.

3.4.2 FATIGUE TESTING

All fatigue testing was carried out under axial applied loading in a number of calibrated servo-hydraulic fatigue testing machines of capacities 500kN, 600kN and 1000kN, interfaced with Instron 8400 controllers and personal computers (PC's). The tests were performed in air under ambient conditions and under load control.

CA tests were performed under the direct control of the 8500 Instron controllers, whereas VA tests under simple load sequences or spectrum loading were controlled through PC's.

3.4.3 TESTS UNDER SIMPLE LOAD SEQUENCES

All load sequence testing (Chapter 5) was performed on CCT specimens in the 600kN capacity testing machine interfaced with the Instron 8400 controller and PC. The specimens were lightly grit blasted over a region of 100mm from either end, and layers of emery cloth secured (Figure 3.4.8) to provide electrical insulation from the testing machine grips (see Section 3.5.2).

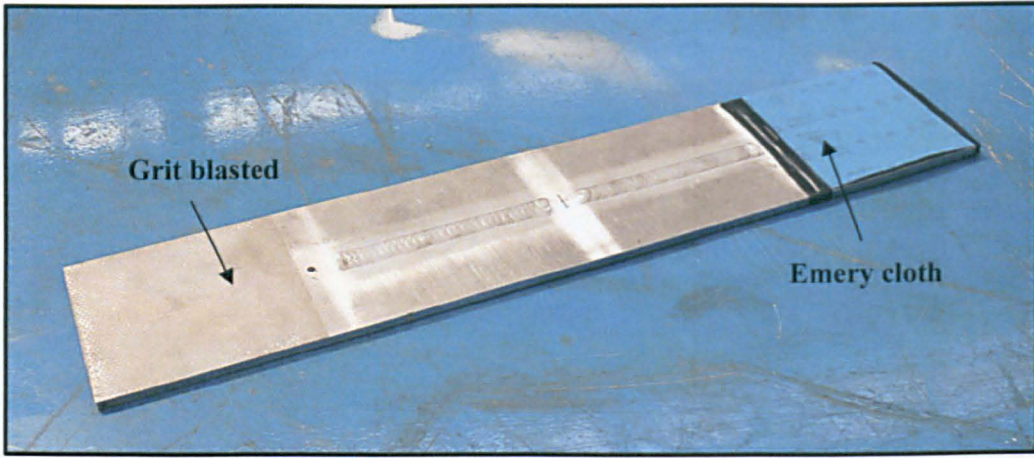


Figure 3.4.8 A CCT specimen with grit blasted ends and emery cloth applied.

The loading sequence spectra was created using National Instruments Labview version 2012 and comprised a block of stress cycles, all cycling down from a constant tensile stress of 156N/mm^2 for steel or 74N/mm^2 for aluminium alloy. Each block contained ten minor constant amplitude cycles, n , and one major (underload) cycle of either twice or 1.5 times the range of the ten minor cycles, Figure 3.4.9. The relationship between the number and magnitude of minor and major cycles used has been found experimentally to produce significant crack growth acceleration (Fleck, 1985).

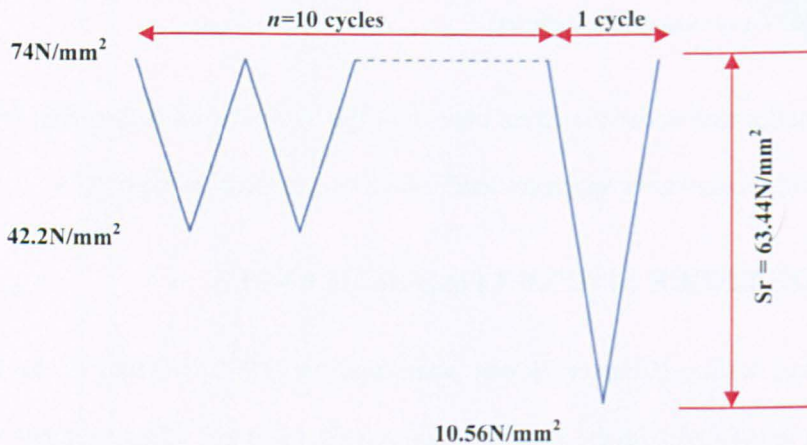


Figure 3.4.9 Simple load sequence with constant maximum stress and periodic underloads used in the present study; example shown is for aluminium alloy with an underload magnification of $2x$ minor stress range (SBL2).

Test frequency was controlled by entering the desired value into the Labview software. This frequency was then maintained automatically by running the CA cycles as fast as possible then

slowing down for the larger underload cycles. The achieved frequency on the software's control panel was displayed as the average and was typically within 2% of the desired value. Flowcharts of the basic software and testing process developed for this research are given in Appendix A.

Load spectra cycling down from a constant maximum stress were chosen, as previous experience indicates that cycling down from fixed tension produces acceleration (Gurney, 2000; Zhang and Maddox, 2009). It is also thought to reproduce the conditions that arise in welded joints containing high tensile residual stress (see Section 2.8). However, as the upper limit stress is not as high as yield, it was considered necessary for a thorough study also to carry out additional tests on specimens actually containing such residual stress. In industry, actual welded structures or components containing high tensile residual stress may still experience loading that cycles down from a constant tensile stress level in service, as discussed in Chapter 8.

3.4.4 TESTS UNDER VARIABLE AMPLITUDE SPECTRUM LOADING

Fatigue endurance tests (Chapter 7) were performed under spectrum loading on both CCT and fillet welded specimens. Unlike the load sequence tests described in Section 3.4.3, layers of emery cloth were not required, although in some instances specimen ends were again lightly grit blasted to aid gripping.

The VA loading spectra was again created using Labview (frequency being controlled in the same manner as discussed in Section 3.4.3) and comprised a block of stress cycles all cycling down from a constant maximum tensile stress in a random manner, with a fixed maximum stress range for each material (Figure 3.4.10). The subsequent blocks were repeated in the same order.

The block length in a given test depended on the minimum value of the relative stress range, p_i , where p_i is the ratio of the i th stress range to the maximum stress range in the spectrum. A p_i value of 0.25 was initially investigated as it had been shown, under this form of VA loading, to produce lives shorter than predicted by Miner's rule (Zhang and Maddox, 2009).

The value of p_i was subsequently varied in other tests ($p_i=0.20$ and $p_i=0.40$) to allow for differences in the number of smaller stress ranges to identify whether all those applied in the spectrum were damaging.

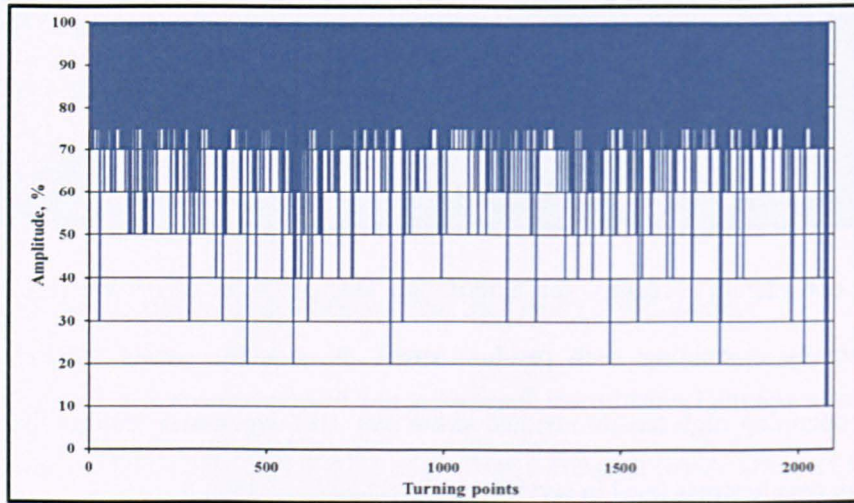


Figure 3.4.10 Example of a VA loading spectrum used in this project. Spectrum shown is for a minimum p_i value of 0.25.

3.5 MEASUREMENT AND MONITORING OF FATIGUE CRACK GROWTH

3.5.1 OPTICAL MEASUREMENT

By far the simplest method for monitoring crack growth is by optical measurement. This was performed in the present project on specimens with the surface lightly polished across the plate width on the fatigue crack path. A 2 megapixel resolution 20x to 200x magnification optical microscope was used to measure the crack length periodically during fatigue testing. Here a calibrated digital micrometre to an accuracy of within $\pm 0.02\text{mm}$ ($\pm 20\mu\text{m}$) and a resolution of 0.01mm ($10\mu\text{m}$) was employed. In order to capture the entire crack length, a bespoke jig was manufactured with movements in all three axis (x, y and z) to facilitate the optical microscope which was held to the testing machine by magnets, Figure 3.5.1.

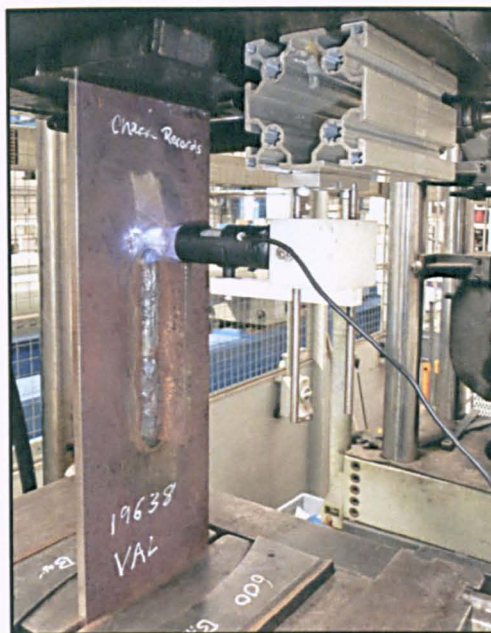


Figure 3.5.1 *Optical microscope system applied to a steel CCT specimen.*

3.5.2 POTENTIAL DROP METHODS

3.5.2.1 DIRECT CURRENT POTENTIAL DROP

Apart from the manual method of measuring the fatigue crack length optically, there are a variety of other methods which may be used to monitor the growth of fatigue cracks automatically during testing, as detailed in BS 12108 and ASTM E 647. One of these, the direct current potential drop (DCPD) technique, was used for most of the present fatigue crack growth tests. The method has been shown to provide accuracy to within 2% of measured crack length (ASTM, 2013a), which was considered to be adequate for the present project. The alternative alternating current potential drop (ACPD) method (see Section 3.5.2.2) is far more susceptible to electrical noise interference, and so was not deemed suitable for monitoring crack propagation in the CCT specimens.

The DCPD method itself requires that two wires be resistance welded to the plate surface on either side of the notch. In accordance with the ASTM standard (Annex A2 and A6) it is necessary for the wires to be attached diagonally opposing one another, so that the measured electrical resistance provides an estimate of the average crack length for non-uniform lengths. Due to the fragility of the wires when welded to the surface of a CCT specimen, in the present project a small (~1mm deep) interference fit hole was drilled at the desired locations and pins, onto which the electrical wires

could be soldered, pressed in. A specimen with the DCPD system connection wires attached is shown in Figure 3.5.2.

To ensure the optimum current was being drawn, a simple calibration exercise was performed on both material types to ensure that the natural noise of the system did not mask any measurements being recorded; this was particularly important for aluminium which has greater electrical conductivity than steel. For this, a current of 35-40amps (for steel) and 55-60amps (for aluminium) was passed through the specimen resulting in a two dimensional electrical field which was constant through the thickness at all points. The potential difference between the two sides of the crack was then measured.

One potential source of error that can arise when using DCPD is drift in the measurements of potential due to changes in temperature. One method to account for this error is to normalize the voltages measured at PD wires mounted to the specimen surface (Zitounis, 2003). However, this was not necessary because temperature measurements during the initial calibration exercise were found to be stable throughout.

It was of great importance to ensure that the specimen was electrically insulated from the test machine. In the present project this was achieved by introducing layers of emery cloth between the machine jaws and the plate surface (Figures 3.4.8 and 3.5.2). A further precaution taken to prevent the specimen heating up as the electric current flowed through it, thus avoiding any potential for temperature effects at the crack tip, was to switch the current on and off automatically at regular set intervals.

Through appropriate calibration (derived either experimentally, analytically or numerically) the potential drop measured on either side of the crack plane can be related to the crack length. As crack length increases the area of remaining ligament decreases resulting in an increase in electrical resistance and in potential difference. For CCT specimens a closed form analytical voltage versus crack size relationship for an infinitely long specimen, described in the ASTM standard, Eq. [3.5.1], was used (Johnson, 1965).

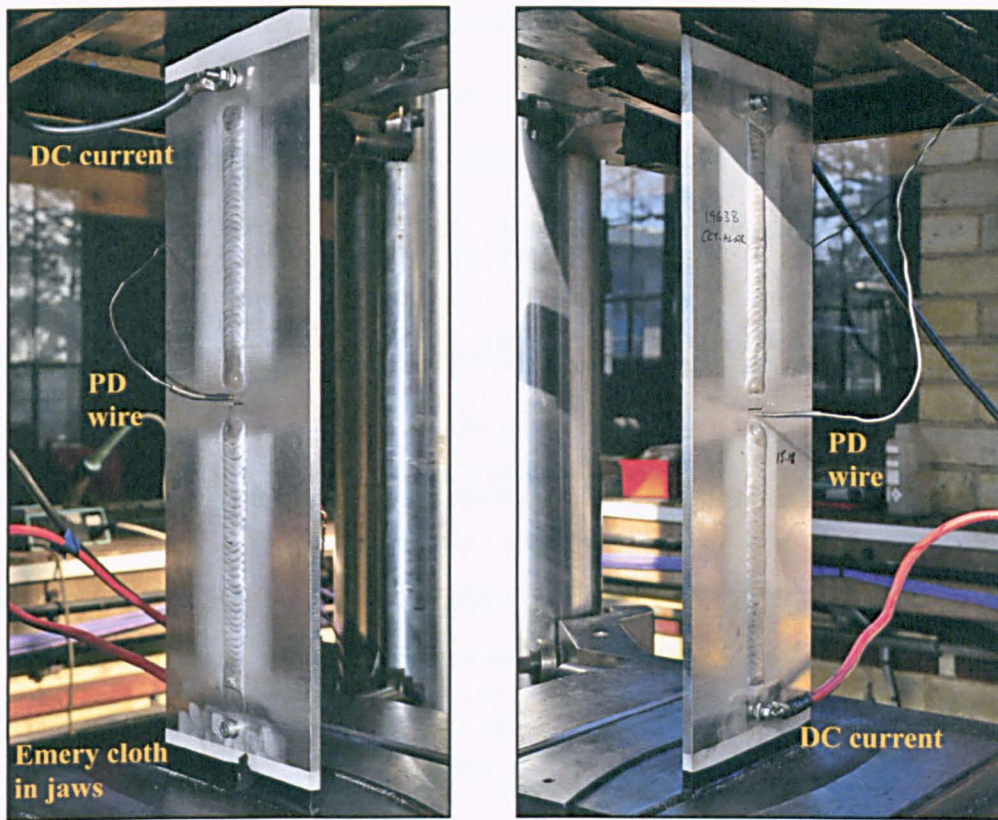


Figure 3.5.2 CCT specimen connected to the DCPD system showing staggered PD wires (both specimen surfaces shown).

$$a = \frac{W}{\pi} \cos^{-1} \left[\frac{\cosh\left(\frac{\pi}{W} * Y_0\right)}{\cosh\left[\frac{V}{V_r} * \cosh^{-1}\left[\frac{\cosh\left(\frac{\pi}{W} * Y_0\right)}{\cos\left(\frac{\pi}{W} * a_r\right)}\right]\right]} \right] \quad [3.5.1]$$

where a is the crack size (half-length in the case of a through-thickness crack in a CCT specimen), a_r is the reference crack size, W the specimen width, V is the measured electric potential difference (EPD) voltage, V_r is the measured voltage corresponding to a_r and Y_0 is the voltage measurement lead spacing from the crack plane.

Resolution depends on the specimen geometry and the material conductivity, but is typically 10-20 μm (Holtam, 2010) depending on the quality of the equipment used and the maximum systematic error in crack length. Following simple calibration under CA loading, comparing crack length from DCPD versus that observed optically from microscope (Section 3.5.1), the error

between the two techniques was found to be within 2.2% (0.02mm) for a 1mm surface crack length and 0.05% (0.01mm) for a 20mm crack length. This would result in a maximum error in crack growth rate of ~8% and ~5% for a 1mm and 20mm crack length respectively. Or in other words, 4.1×10^{-6} mm/cycle for a 1mm crack length and 1.7×10^{-5} mm/cycle for a 20mm crack length in the case of a 6082 aluminium alloy, and 1.2×10^{-6} mm/cycle for a 1mm crack length and 7×10^{-6} mm/cycle for a 20mm crack length in the case of S355 structural steel. However, the variation in crack growth rate error would depend on the number of cycles during the crack increment. The associated errors as described are therefore considered acceptable for the work performed.

Each time a voltage reading is taken, the corresponding load and number of cycles are also recorded. Crack growth rates (da/dN) can then be determined by use of the secant method which involves calculating the slope of the straight line connecting two adjacent data points on the a versus N curve Eq. [3.5.2], the average crack size can then be determined as in Eq. [3.5.3] using a measurement interval of 0.2mm (ASTM, 2013a). The corresponding ΔK was then calculated using the solution given in BS 7910 (BSI, 2013), see Eq. [3.5.4].

$$(da/dN)_{\bar{a}} = (a_{i+1} - a_i)/(N_{i+1} - N_i) \quad [3.5.2]$$

$$\bar{a} = \frac{1}{2}(a_{i+1} + a_i) \quad [3.5.3]$$

where a_i is the initial crack length, \bar{a} is the average crack size and N_i is the endurance for a given crack size.

$$\Delta K = \Delta S \sqrt{\pi a} \left(\text{Sec} \frac{\pi a}{2W} \right)^{\frac{1}{2}} \quad [3.5.4]$$

where a is crack length and W is plate width.

An alternative approach is to use the incremental polynomial method (ASTM, 2013a) which involves fitting a second order polynomial (parabola) to sets of $(2n+1)$ successive data points. This method is generally used in instances where poor data are collected and smoothing is required.

No correction for crack front shape was used but after each test the specimen was cut approaching the crack tip to reduce the size of the un-cracked ligament, and sprayed locally with liquid nitrogen

to embrittle the material and so allow the specimen be broken open with a minimum of distortion. The fracture surface could then be examined to determine the initial and final crack depths based on a weighted nine point average, as described in BS 7448-4 (BSI, 1997).

3.5.2.2 ALTERNATING CURRENT POTENTIAL DROP

The alternating current potential drop (ACPD) method is based on the 'skin effect', a characteristic of high frequency current flowing in a conductive material, whereby the majority of the current is confined to a thin skin at the surface of the material (Huang, 2004), resulting in a low current, typically 1 amp, requirement. The method can be applied using an automated system whereby a current is passed at set intervals during fatigue testing.

Compared to DCPD (Section 3.5.2.1), ACPD is a far more complex piece of equipment and is prone to suffer from inductive pick up (the effect of which can be minimized by reducing any cable loops). Also, measurement lead connections must be robust, as their movement during a test may affect the results.

As an alternative to a permanently installed monitoring system, ACPD can also be performed manually using hand held commercial systems to provide an estimate of crack depth, as used in the case of fillet welded specimens later (Chapter 7). Here, a spring loaded four pin probe (comprising both the current (500mA) and measurement poles)) is positioned such that the pins are placed across the crack (over the weld toe in this case) with the current flow perpendicular to the plane of the crack. The voltage drop (potential difference) across the crack is then measured and converted to crack depth via a micro-processor in the probe handle. This is achieved by comparing the measured voltages with those stored from calibration as well as the material characteristics.

Based on careful calibration on a reference block containing an artificial crack starting at a depth of zero up to 10mm, the claimed accuracy of the instrument¹ is ± 1 to $\pm 23\%$ for crack depths of 0-10mm and ± 1 to $\pm 25\%$ for crack depths of 10-100mm (without calibration), improving to ± 1 to

¹ http://www.karldeutsch.de/KD_RMG_EN_M1.html

$\pm 13\%$ for crack depths of 0-10mm and ± 1 to $\pm 15\%$ for crack depths of 10-100mm, following calibration.

3.6 APPLICATION OF STRAIN GAUGES UNDER STATIC LOADING CONDITIONS TO ESTABLISH CRACK OPENING AND CLOSURE LEVELS

The most commonly used technique for determining crack closure is the compliance technique (Fleck, 1984; Zitounis, 2003), whereby the crack opening displacement (COD) response of the specimen to the variation of the far field applied load is measured. The alternative is to use strain gauges to measure the change in strain adjacent to the crack tip during loading. In both the COD and strain gauge techniques a linear relationship between the applied stress and, in the case of the strain gauge method, microstrain, is assumed to represent a fully open crack. Crack closure is therefore assumed to coincide with the change to a non-linear relationship.

Both the COD and strain gauge methods were also used for the determination of crack closure in aluminium alloys (Lee *et al.*, 1996). The findings showed that the strain gauge method was more sensitive to local crack tip behaviour on a microscopic scale resulting in higher closure levels than observed by COD. However, whilst the strain gauge method precisely measured the local closure, its sensitivity varied depending on the relative distance between the point of measurement and the crack tip.

The use of strain gauges to detect closure levels has previously been used on a range of structural steels with a clearly defined change in linearity of the slope; hence crack closure being observed (Maddox *et al.*, 1978; Fleck, 1984; Fleck and Smith, 1984). This allowed the fraction of the load cycle for which the crack is open, U , to be derived using:

$$U = \frac{K_{\max} - K_{op}}{K_{\max} - K_{\min}} = \frac{\Delta K_{eff}}{\Delta K} \quad [3.6.1]$$

To establish crack opening/closure levels under applied sequence and VA loading, electrical resistance strain gauges, types FLA-2-11 for steel and FLA-2-23 for aluminium alloy, were

adhesively bonded to the surface of selected CCT specimens using cyanoacrylate cement. In the case of steel specimens, the regions of interests were polished (by pneumatic grinder) using successively finer grit bands (up to 240 grit) followed by a grinding flap wheel (320 grit). Each polishing operation was performed at 90 degrees to the previous one with the final pass being parallel to the specimen loading direction. The polished zones were then lightly abraded using Scotchbrite™ wire wool in a random manner to lightly key the surface. For the aluminium alloy specimens, the same methodology was applied only manually using successively finer grades of wet and dry paper (up to 800 grit) as opposed to bands or flap wheels.

After marking out the gauge locations, areas were cleaned using acetone and Mylar™ tape applied to hold the gauge in place whilst light pressure was applied to the strain gauge ensuring good contact through the cement. An acrylic solution (M-Coat A) was then applied to the gauges to provide light protection whilst handling. Strain gauges were wired in a triple twist configuration to a National Instruments SC2345 signal conditioning unit. The unit was wired in a half-bridge formation with a dummy gauge (or resistor) completing the circuit.

Measured microstrain values were recorded at set increments under static loading conditions to ascertain levels of crack opening/closure. Initially a calibration exercise was performed to determine the distance below and behind the crack tip to adhere the strain gauges in order to observe the effect of closure. This was found to be 4mm below the crack and 1.5mm behind the crack tip (half the width of the strain gauge). The applied strain gauges therefore detected the response in displacement of the material behind the crack to the variation of the far field applied stress. Figure 3.6.1 shows four gauges bonded to a steel specimen following measurement of crack closure at different crack lengths.

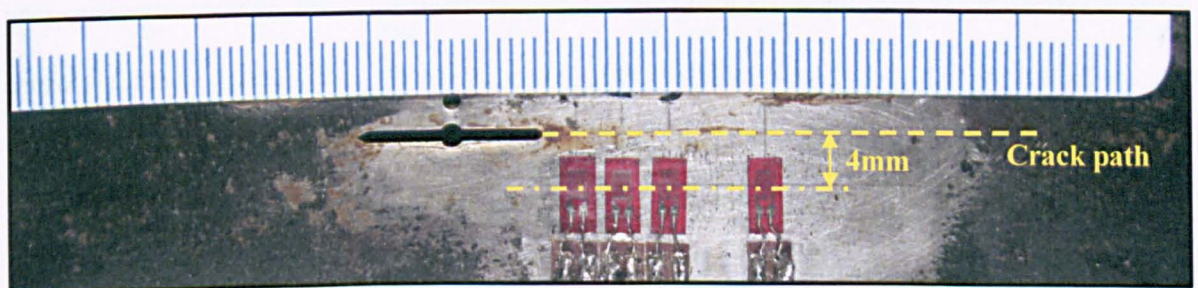
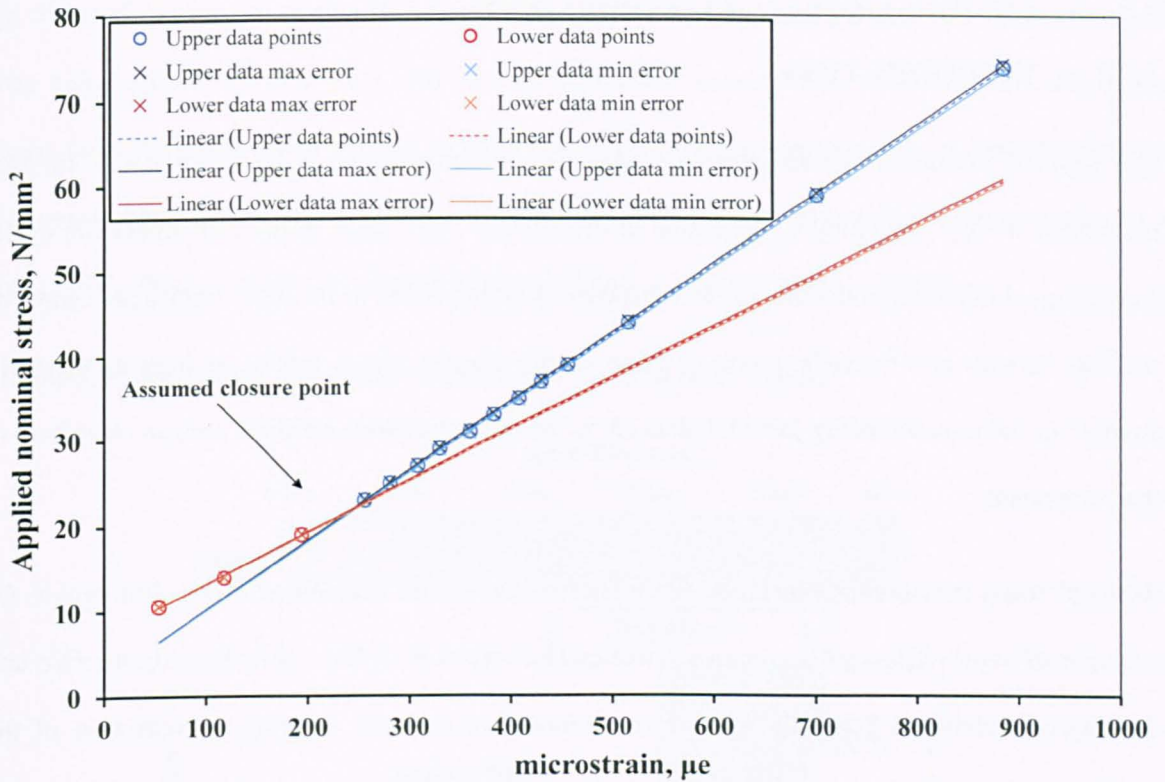


Figure 3.6.1 Typical positions of strain gauges for investigation of crack closure.

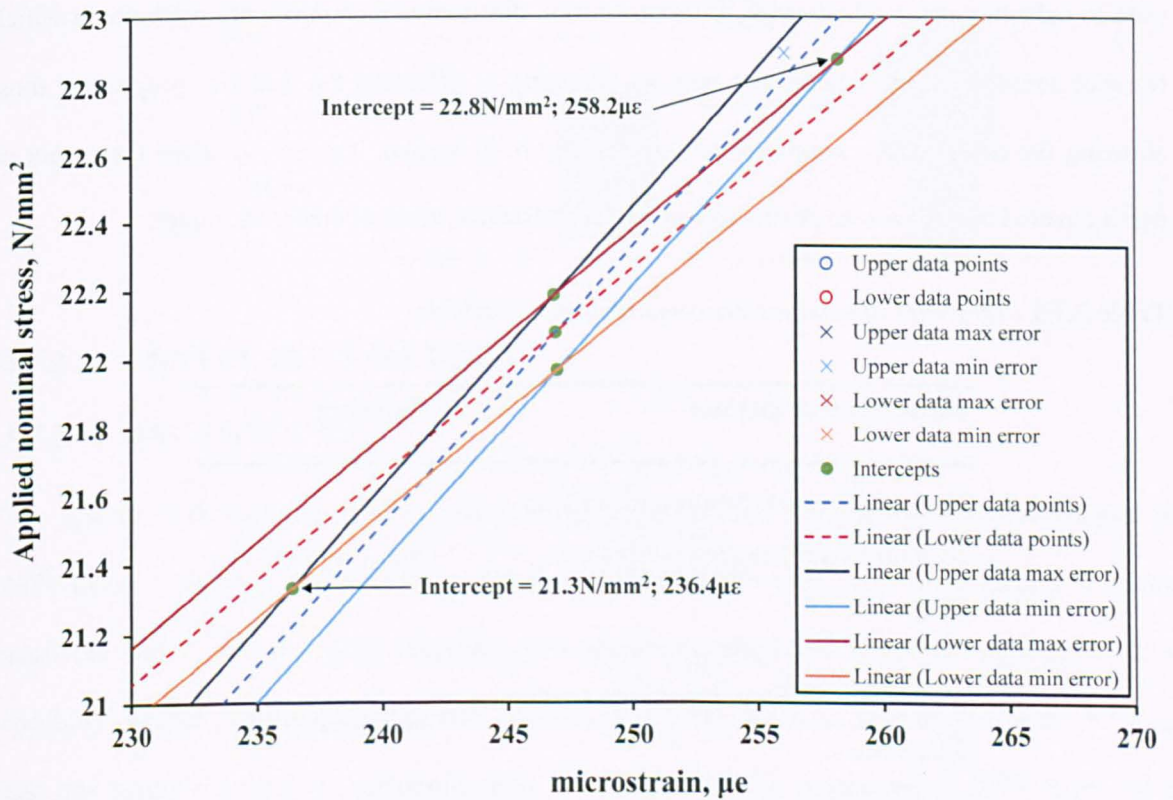
The measured response was compared with a straight line in order to identify whether there was any deviation from the linearity (Maddox *et al.*, 1978; Fleck, 1984; Fleck and Smith, 1984). Typically a curve fitting analysis is performed to detect the closure point, whereby the curve is split into two parts, with a straight line fit to the upper part and a second order polynomial to the lower part (Yieshieng and Schijve, 1995; Yigeng *et al.*, 2000; Zitounis, 2003). In the work performed here only the straight line fit was applied due to the technique employed giving microstrain values at defined loads, as opposed to the data generated by recording load versus displacement using the COD technique. For the purpose of the research performed, the levels of crack closure are therefore an approximation. The errors associated with curve fitting were found to be around 5% to 10% of the test measurement (Zitounis, 2003), this is therefore considered to be an appropriate degree of error for this study.

The uncertainties associated with using the straight line determination of crack closure in this study, was performed by first accounting for the errors in the system. These included $\pm 0.24\%$ for the 600kN load cell, $\pm 0.10\%$ for the strain logger, $\pm 0.01\text{mm}$ for the digital Vernier callipers (used for measuring the specimen width) and $\pm 0.06\text{mm}$ for the micrometre (used for measuring the specimen thickness). These expanded uncertainties (with the exception of the strain gauge logger) are based on standard uncertainties multiplied by a coverage factor of $k=2$ (providing a coverage probability of 95%). The combined standard uncertainty was then deduced based on either a normal or rectangular distribution. The resulting uncertainty in values of stress and microstrain were calculated as $\pm 0.49\%$ and $\pm 0.02\%$ respectively.

Applying this error to the individual data points, linear trendlines were then plotted to the mean, maximum and minimum values, Figure 3.6.2a-b. Trendline interception points produced a diamond shaped area of uncertainty, Figure 3.6.2b. The maximum extent of which (for conservatism) was used to define the maximum uncertainty in stress and microstrain at the assumed crack closure point. This was found to be $22.8 - 21.3 = 1.5\text{N/mm}^2$ and $258.2 - 236.4 = 21.8\mu\epsilon$. Therefore, it is considered that using this technique, the maximum uncertainty is $\pm 0.75\text{N/mm}^2$ on applied stress and ± 10.9 on measured microstrain.



a)



b)

Figure 3.6.2 Plots showing the straight line fit approach used to define crack closure: a) straight lines fitted to the upper and lower data points about the assumed closure stress based on the calculated error, b) Intercept points giving the maximum uncertainty of the assumed closure stress.

3.7 RESIDUAL STRESS MEASUREMENT

3.7.1 INTRODUCTION

The residual stresses in a component or structure are stresses caused by incompatible internal permanent strains. They may be generated or modified at every stage in the component life cycle, from original material production to final disposal. Welding is one of the most significant causes of residual stresses and typically produces large tensile stresses which can be as high as the yield strength of the material being joined, balanced by lower compressive residual stresses elsewhere in the component.

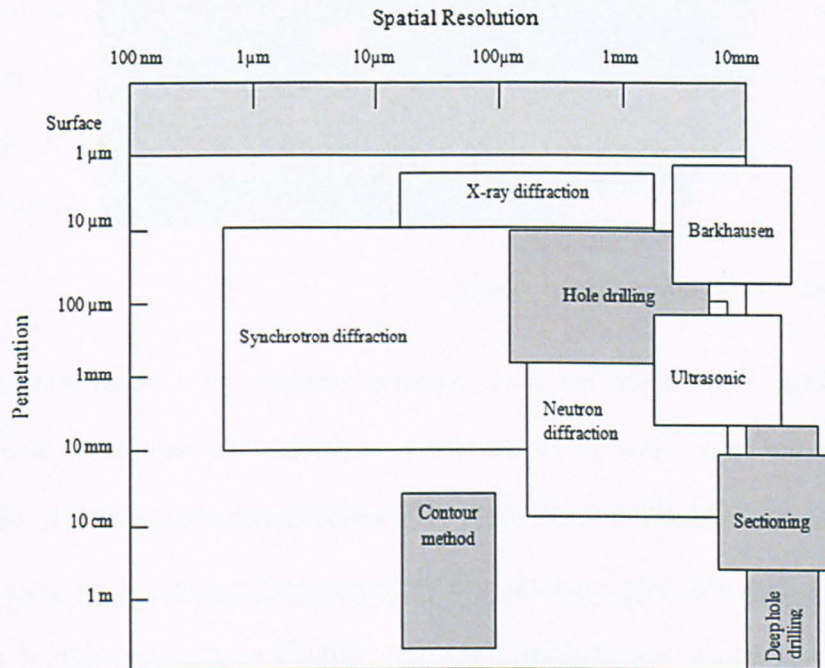
Residual stress measurement methods can be destructive, semi-destructive or non-destructive. An example of some of the most common techniques is given in Table 3.7.1. Semi-destructive and destructive techniques generally involve the removal of material to produce relaxation of the residual stress within a sample, and measurement of the resulting strain. This strain can then be used to calculate the residual stress. In contrast, non-destructive techniques are methods in which residual stresses can be determined without changing or affecting the material properties, thus, allowing the component / sample to remain useable if so wished. Table 3.7.2 gives the extent of depth covered by the various destructive and non-destructive measurement techniques.

Table 3.7.1 *Categories of residual stress measurement methods.*

Measurement method	Category
X-ray diffraction, Neutron diffraction, Synchrotron diffraction, Ultrasonic, Magnetic	Non-destructive
Centre hole drilling, Deep hole drilling, Ring core	Semi-destructive
Contour method, Slitting, Block removal, Sach's boring	Destructive

In the work performed in this research project two techniques were utilised, one destructive and one non-destructive (*centre-hole* and *neutron diffraction* respectively). As shown in Table 3.7.2, basic hole drilling is a near surface technique which resolves strains typically at around 0.010mm (10µm) to 1mm depth, whereas the use of neutrons allows residual stresses to be determined over a range of 0.10mm (100µm) to 100mm; both techniques are further discussed below.

Table 3.7.2 Residual stress measurement depths (Rossini et al., 2012).



3.7.2 CENTRE-HOLE METHOD

3.7.2.1 BACKGROUND

The system of determining residual stress using the centre-hole technique was first developed in 1934 using a two-step drilling method (Mathar, 1934). At this time centre-hole gauges were not available and it was not until 1966 that they were first employed under the application of a specially dressed end mill (Rendler and Vigness, 1966). The abrasive jet method (Figure 3.7.1) is just one centre-hole drilling technique used today and was first introduced in 1973 following a review of different techniques (Bush and Kromer, 1973). Three years later the technique was improved by use of an orbiting head (Beaney, 1976).

Other techniques encompassed by the term hole drilling in Table 3.7.2 include *ring core and incremental hole drilling*.

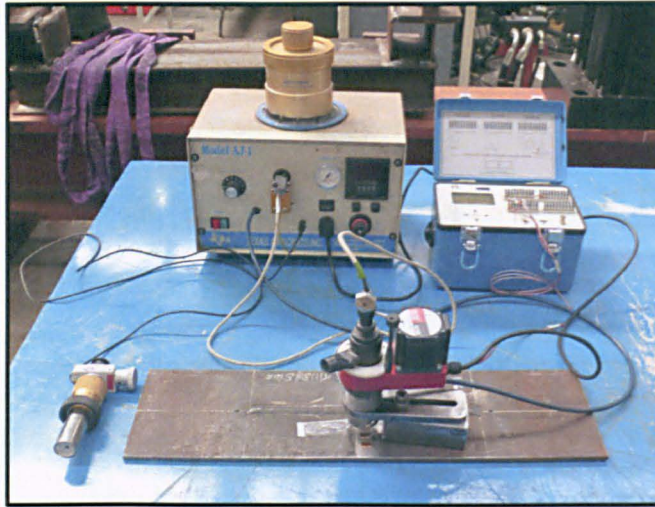


Figure 3.7.1 Centre-hole residual stress system.

Centre-hole drilling is probably the most common residual stress measurement method for situations where the stress close to the surface is required. This semi-destructive technique is usually calibrated in a uniform uniaxial stress field which can then be applied to uniform biaxial fields by superposition. However, conditions in the component may not be the same as that of the calibrated sample, in which case deviations may occur brought on from variation of the stress field over the depth of the hole and plasticity at the hole edge (Scaramangas *et al.*, 1982).

Once drilled, the relaxation of radial stresses at the edge of the hole cause a redistribution of stress which is detected by the strain gauges (Beaney, 1976). By use of Eq. [3.7.1] which was developed by Beaney and Proctor (1974), the strain can then be related to the residual stress in the material.

$$\sigma_{\max,\min} = \left(-\frac{1}{K_t} \right) \left(\frac{E}{2} \right) \left[\frac{\epsilon_1 + \epsilon_3}{1 - \nu K_2 / K_1} \pm \frac{1}{1 + \nu K_2 / K_1} \left\{ (\epsilon_1 - \epsilon_3)^2 + [2\epsilon_2 - (\epsilon_1 + \epsilon_3)]^2 \right\}^{1/2} \right] \quad [3.7.1]$$

where $1/K_t$ is a function of hole size, E is the Young's modulus of the material, ν is Poisson's ratio, $\epsilon_1, 2$ and 3 are the relaxed strains and K_1 and K_2 are constants

A three element rosette strain gauge is generally used in order to determine the principal stress directions. Thus for any given value of residual stress, the strain changes detected will vary with a

distance of 'x' from the edge of the hole to the strain gauge (Martin, 2000). Therefore, it is imperative that the hole drilled is not only round and of a known diameter, but that it is also in the centre of the gauge and equi-spaced from the strain gauge elements, to improve accuracy of the results.

If the residual stresses exceed approximately 50% of the yield stress, then errors can arise due to localised yielding (Withers and Bhadeshia, 2001). According to the original development work (Beaney, 1976) the error was found to be negligible for stresses less than 70% yield. Following a review of their data, (Scaramangas *et al.*, 1982) suggested that stresses above 65% of yield (or 0.2% proof stress) should be corrected for plasticity effects. Such that, measured stresses would be subject to correction using Eq. [3.7.2] :

$$\sigma_c = \frac{\sigma'_c}{\left[0.28 \left(\frac{\sigma'_c}{\sigma_o} \right) + 0.82 \right]} \quad [3.7.2]$$

where, σ_c is the corrected stress, σ'_c is the measured stress and σ_o is the yield strength.

A review on the accuracy of this method (Martin, 2000) found that errors in relaxed strain values are dependent on the alignment of the hole, strain measuring technique and the induced stresses from the hole forming process. They found that, if carried correctly, errors in strain measurement should not exceed $\pm 0.6\%$. Any errors in hole alignment would depend on the direction of misalignment with respect to the stress field and rosette direction and would be similar to that found for errors in hole diameter ($\pm 1.2\%$). Calibration tests by various researchers using Beaney and Proctor's method of analysis Eq. [3.7.1], found empirical values for stresses derived from three-element rectangular rosette gauges in the range of 0.3 ($\pm 1.2\%$), and showed that errors up to $\pm 5.2\%$ could exist in the derived stresses, with errors due to plasticity effects being $< 2\%$ for stresses up 65% of yield. Thus the total error using the air abrasive centre hole system is up to $\pm 10.2\%$.

3.7.2.2 APPLICATION IN CURRENT RESEARCH PROJECT

For the determination of permanent (residual) stresses (Chapter 6), electrical resistance strain gauges, both conventional strain gauge rosettes (Figure 3.7.2a) type FRS-2-11-120, and type CEA-13-062UM-120 (Figure 3.7.2b), were used. As opposed to conventional strain gauge rosettes, the latter make it possible to measure residual stresses closer to the area of interest, such as a weld toe. However, in all cases the governing factor behind the proximity to an obstruction i.e. a stiffener, is the drill head of the residual stress measurement equipment.

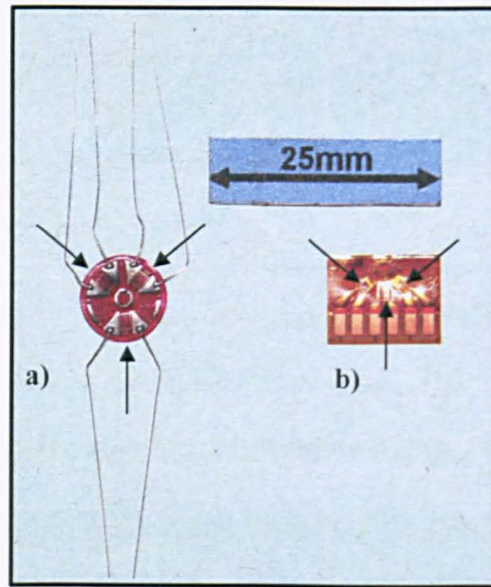


Figure 3.7.2 Permanent stress measurement strain gauges used in this research project: a) Conventional strain gauge rosette, type FRS-2-11-120, b) Strain gauge rosette type CEA-13-062UM-120. Arrows indicate strain gauge elements.

The same method of application of the gauges, as that described in Section 3.6 was used, except M-Coat A coatings were not applied.

Due to the availability of equipment and experience in its operation, the centre hole drilling method with an air abrasive system shown in Figure 3.7.1 was the primary residual stress measurement method used (Chapter 6). A series of calibration holes were first trepanned in identical spare material in order to set the correct operating pressure, orbiting speed and flow rate. 3 micron aluminium oxide was used as the cutting medium.

Measured strains ($\mu\epsilon$) were recorded using a Vishay P3 strain indicator. After each hole was cut the change in microstrain was again recorded and both the depth and diameter of the hole measured using a calibrated micrometer and x10 magnification ocular lens. The recorded strain was then converted to stress using Eq. [3.7.1] following the procedures given in ASTM E 837-13a (ASTM, 2013b).

Figure 3.7.3a-b shows both a CCT specimen, incorporating a weld bead on the plate surface and a fillet welded specimen instrumented with CEA-13-062UM-120 strain gauge rosettes following residual stress measurement.

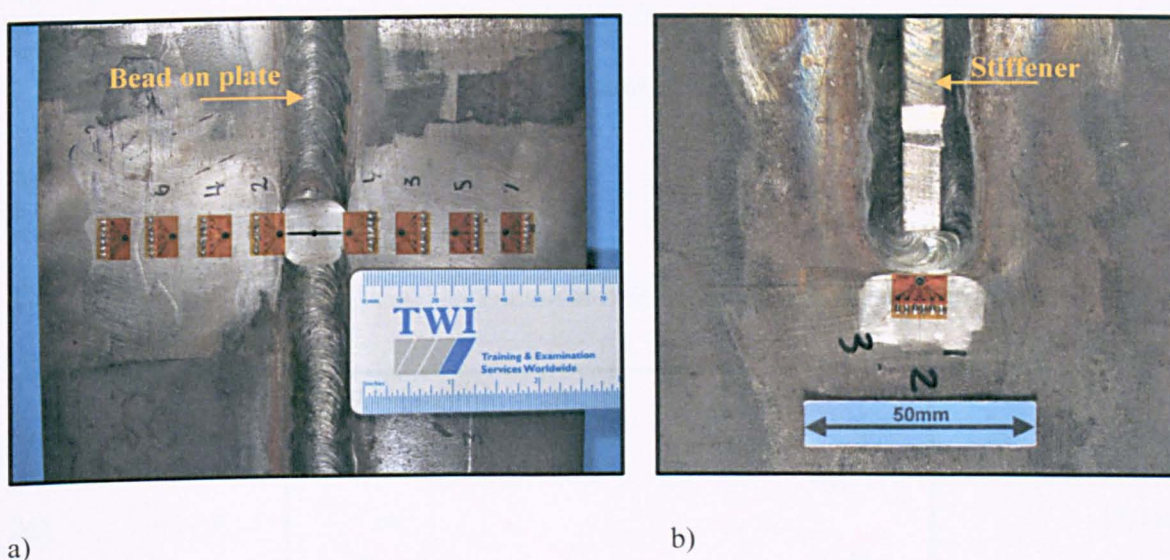


Figure 3.7.3 CCT (a) and Fillet welded (b) specimens showing trepanned holes after residual stress measurement.

3.7.3 NEUTRON DIFFRACTION

3.7.3.1 BACKGROUND

Diffraction techniques are well-established non-destructive tools for measuring strains (residual or applied) within polycrystalline materials. By changing the orientation of the sample, strain can be measured at a number of different angles allowing a stress component to be obtained.

The basic principle of residual strain scanning requires the determination of lattice spacing, d_{hkl} , (hkl denoting crystallographic plane (Hutchings *et al.*, 2005)), which cause changes in the spacing

of the lattice planes from their stress free condition (Kudryavtsev, 2008). The lattice spacing can be calculated using Bragg's diffraction law:

$$d_{hkl} = \frac{\lambda_{hkl}}{2 \sin \theta_{hkl}} = \frac{ht_{hkl}}{2m_n L \sin \theta_{hkl}} \quad [3.7.3]$$

where, λ_{hkl} is the wavelength, θ_{hkl} is the diffraction angle, h is Planck constant, m_n is the neutron mass, L is the neutron's travel down flight path and t_{hkl} is the time of flight (ToF).

Neutron strain scanning provides the average elastic strain within the gauge volume defined by the intersection of incident and diffracted beams (Hutchings *et al.*, 2005), Figure 3.7.4. After obtaining d_{hkl} , the elastic strain, ϵ_{xx} , along a direction 'x', is determined from the change in the lattice spacing, d_{xx} , of the crystalline material referred to the stress free value, d_0 , thus;

$$\epsilon_{xx} = \frac{d_{xx} - d_0}{d_0} \quad [3.7.4]$$

where d_0 is the material value in the unstressed condition.

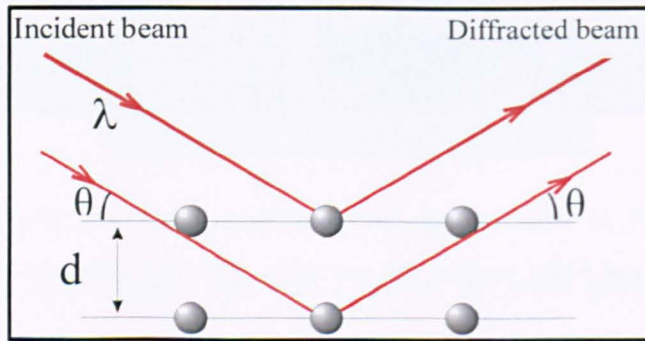


Figure 3.7.4 Bragg's law geometry in the plane of diffraction.

Stress calculations following the strain calculations are based on continuum mechanics, using Hooke's law. The stress is calculated from the elastic strains in the gauge volume measured along three mutually orthogonal directions as follows:

$$\sigma_{xx} = \frac{E}{(1+\nu)(1-2\nu)} [(1-\nu)\epsilon_{xx} + \nu(\epsilon_{yy} + \epsilon_{zz})] \quad [3.7.5]$$

$$\sigma_{yy} = \frac{E}{(1+\nu)(1-2\nu)} [(1-\nu)\epsilon_{yy} + \nu(\epsilon_{xx} + \epsilon_{zz})] \quad [3.7.6]$$

$$\sigma_{zz} = \frac{E}{(1+\nu)(1-2\nu)} [(1-\nu)\varepsilon_{zz} + \nu(\varepsilon_{xx} + \varepsilon_{yy})] \quad [3.7.7]$$

where E and ν are the crystallographic elastic constants for the hkl planes being measured.

The experimental uncertainties in the neutron diffraction results can be calculated using an error propagation method (Taylor, 1982). With this approach, the effect of the stressed and un-stressed lattice spacing, Δd (the error in the measurement of d) and Δd_0 (the error in the measurement of d_0), on the uncertainties in the strain and stress values is quantified.

The experimental uncertainties presented in this research report were derived using an error propagation method (Taylor, 1982) of the form:

$$\Delta z = \sqrt{\left(\frac{\partial z}{\partial x} \Delta x\right)^2 + \left(\frac{\partial z}{\partial y} \Delta y\right)^2} \quad [3.7.8]$$

where z is a function of x and y ; and Δx and Δy are the uncertainties in x and y . The uncertainty in a strain component ε_{xx} (say) is therefore:

$$\Delta \varepsilon_{xx} = \sqrt{\left(\frac{\partial \varepsilon_{xx}}{\partial d_{xx}} \Delta d_{xx}\right)^2 + \left(\frac{\partial \varepsilon_{xx}}{\partial d_0} \Delta d_0\right)^2} \quad [3.7.9]$$

if Eq. [3.7.4] is substituted in Eq. [3.7.9], Eq. [3.7.9] can be rewritten as:

$$\Delta \varepsilon_{xx} = \frac{d_{xx}}{d_0} \sqrt{\left(\frac{\Delta d_{xx}}{d_{xx}}\right)^2 + \left(\frac{\Delta d_0}{d_0}\right)^2} \quad [3.7.10]$$

The uncertainty in a stress component σ_{xx} (say) is similarly derived, ie

$$\Delta \sigma_{xx} = \sqrt{\left(\frac{\partial \sigma_{xx}}{\partial \varepsilon_{xx}} \Delta \varepsilon_{xx}\right)^2 + \left(\frac{\partial \sigma_{xx}}{\partial \varepsilon_{yy}} \Delta \varepsilon_{yy}\right)^2 + \left(\frac{\partial \sigma_{xx}}{\partial \varepsilon_{zz}} \Delta \varepsilon_{zz}\right)^2} \quad [3.7.11]$$

after the substitution of Eq's. [3.7.5] – [3.7.7] into Eq. [3.7.11], the following equation is obtained for the uncertainty in the stress component

$$\Delta\sigma_{xx} = C\sqrt{(1-\nu)^2\Delta^2\varepsilon_{xx} + \nu^2\Delta^2\varepsilon_{yy} + \nu^2\Delta^2\varepsilon_{zz}} \quad [3.7.12]$$

where the constant

$$C = \frac{E}{(1+\nu)(1-2\nu)} \quad [3.7.13]$$

Eq's. [3.7.9] to [3.7.12] relate the uncertainty in the strain and stress calculations to the uncertainty in the original stressed and un-stressed lattice parameter spacing's, Δd and Δd_0 , respectively.

3.7.3.2 APPLICATION IN CURRENT RESEARCH PROJECT

The use of neutron diffraction was employed on CCT and fillet welded specimens to determine the extent of the through-thickness residual stress distribution after welding and EDM notching (Chapter 6). The neutron diffraction measurements were carried out on the Stress-Spec monochromatic diffractometer at FRM2 in Garching, Germany. Ferritic steel is body centre cubic (bcc), and measurements were made using the $\{2\ 1\ 1\}$ plane, as it has been reported to correlate well with macroscopic elastic response (Lewis and Truman, 2010). The wavelength was set to 1.68Å (0.168nm) to achieve an almost cubic gauge volume by having a scattering angle (2θ) close to 90°.

The stress free lattice parameter can vary significantly in both the heat affected zone (HAZ) and the weld metal itself (Holden *et al.*, 2006). Thus, stress free reference cubes were machined using EDM from sections of the original welded plate. In some cases a stress free reference 'comb' is machined, however, it can be difficult to ensure the comb is fully stress relieved. In general retained stresses can be up to 20N/mm² (Ganguly, 2004). The dimensions of the cubes (3x3x3) were small enough to ensure they were virtually stress-free (Pearce *et al.*, 2008). The gauge volume used for the stress free sample was 2x2x2mm to ensure that the gauge volume was entirely within the cubes. As this material is relatively thin, plane stress rather than plane strain conditions were expected with no significant stress gradient through the thickness (Ganguly *et al.*, 2008).

Neutron diffraction was used to evaluate the full 3D strain tensor along the principal strain axes. Strain values were measured in the longitudinal (along the welding direction), transverse across the weld/notch) and normal (through-thickness) direction. These directions are further defined as LD, TD and ND as shown in Figures 3.7.5 and 3.7.6.

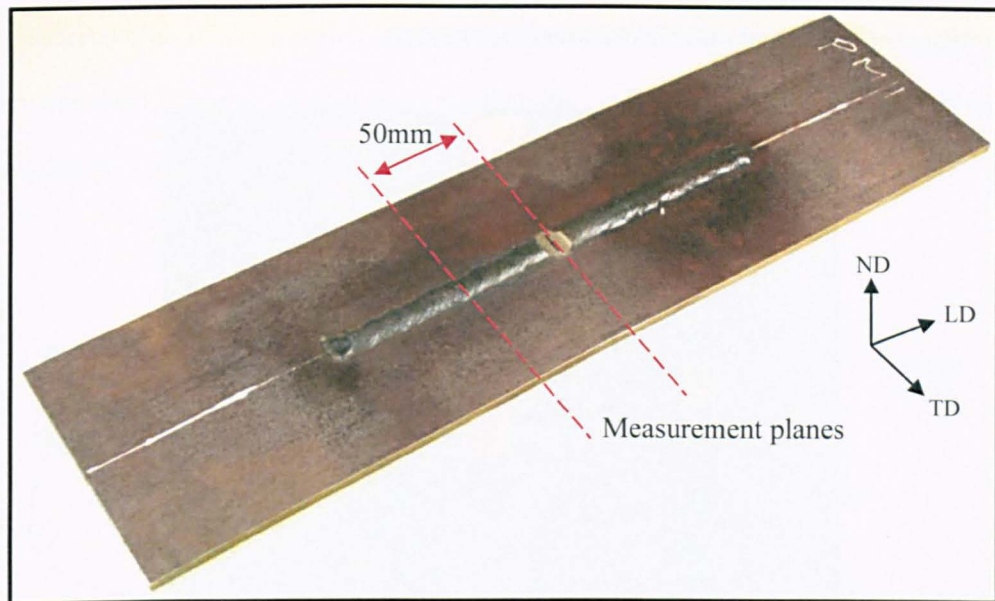


Figure 3.7.5 CCT specimen incorporating a 300mm weld bead on the plate surface, measurement planes also shown.

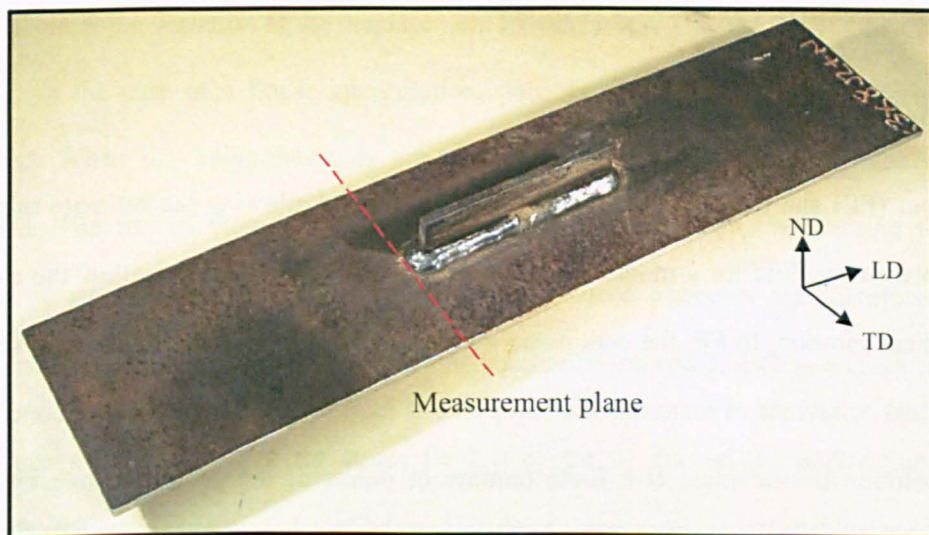


Figure 3.7.6 Fillet welded specimen incorporating longitudinal attachments, measurement plane also shown.

In both specimen types, measurements were made at 2mm intervals over the central region (weld, notch location or weld toe); this was increased to 5mm towards the edge of the plate. These locations were repeated through the specimen thickness at depths of 1.5, 2.75, 4.0, 5.25 and 6.5mm (where 4.0 denote mid-thickness). In the case of the CCT specimen, residual stress was also measured at a distance of 50mm from the reference plane (notch location), as indicated in Figure 3.7.5, to obtain the initial and un-cracked stress distribution.

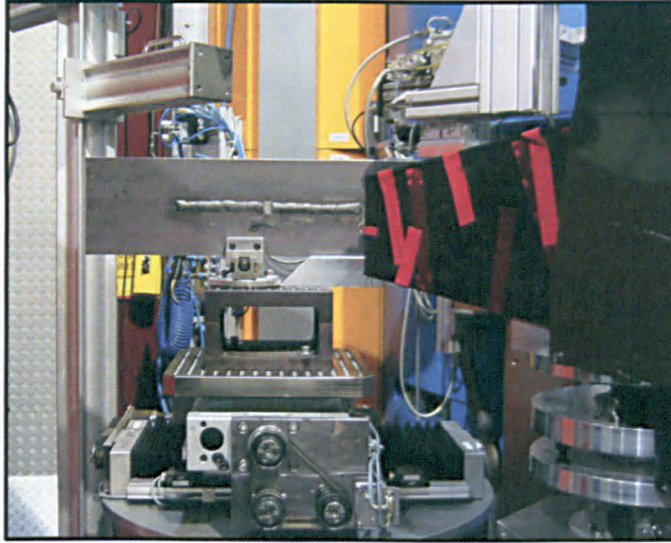


Figure 3.7.7 Steel CCT specimen setup for residual stress measurement by neutron diffraction, using the Stress-Spec at FRM2.

3.8 FINITE ELEMENT ANALYSIS

3.8.1 MODEL DEVELOPMENT

Finite element (FE) analysis is a numerical modelling method allowing the estimate of the stress field or displacement field for a model whose geometry or loading does not allow the calculation by an analytical solution. In FE, the continuum mechanics problem (i.e. the analysis of kinematics and mechanical behaviour of materials modelled as one mass) is transposed to a discrete problem, where the solution is calculated at a finite number of points of the geometry investigated. The interpolation of the variable values between each point where it is numerically calculated gives an estimate of the variable considered over the continuum geometry.

In a FE model, the geometry is partitioned into geometrical elements, defined by the nodes at the intersection of edges (corner-nodes), and eventually the nodes lying at the centre of edges (mid-nodes), Figure 3.8.1. Knowing the behaviour of the material, and assuming the displacement of each node, the software can calculate the strain and stress at particular points inside the elements, called Gauss points or integration points. Assuming initial displacements for all the nodes defined for the discretisation of the geometry, and using an iterative process, the software optimises the value of the displacements at each node so that the stresses calculated in the elements are in balance with the external loading applied.

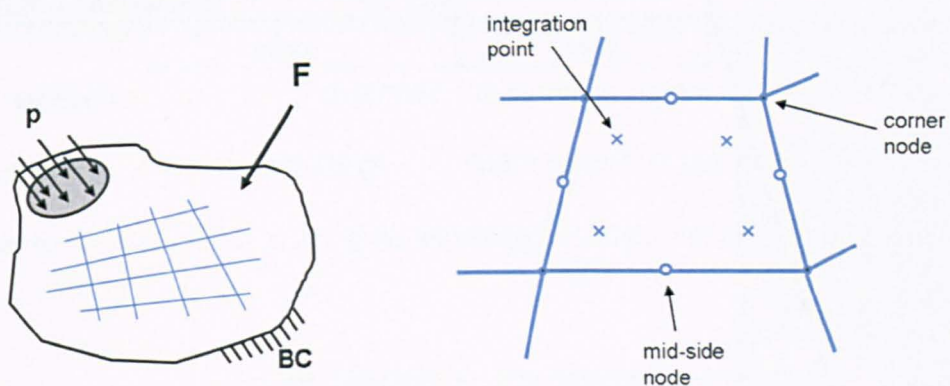


Figure 3.8.1 *Illustration of a continuum mechanics problem (in black) resolved into a discrete problem (in blue) of geometrical elements.*

In each element, the variation of the displacement between the nodes can be assumed to be linear or quadratic. In the case of a linear interpolation, only the displacements of the corner nodes are considered. When the interpolation is quadratic, the displacements of the mid-nodes are also considered. The use of elements with quadratic interpolation allows accounting for a sharper variation of strain, or stress, within each element. These elements are therefore particularly recommended in cases where a significant stress gradient is expected, such as a crack tip region.

For the analysis of the crack tip stress field (Chapter 6) due to the application of periodic underloads, the geometry was modelled as 2D plane stress, and was therefore meshed with 2D plane stress elements. The elements used assumed quadratic interpolation of the displacements. The mesh was significantly refined in the region of the crack path in order to capture the stress gradient near the crack tip.

The specimen geometry modelled was one quarter that of a CCT specimen such that two planes of symmetry (y-z and x-z) were included, Figure 3.8.2.

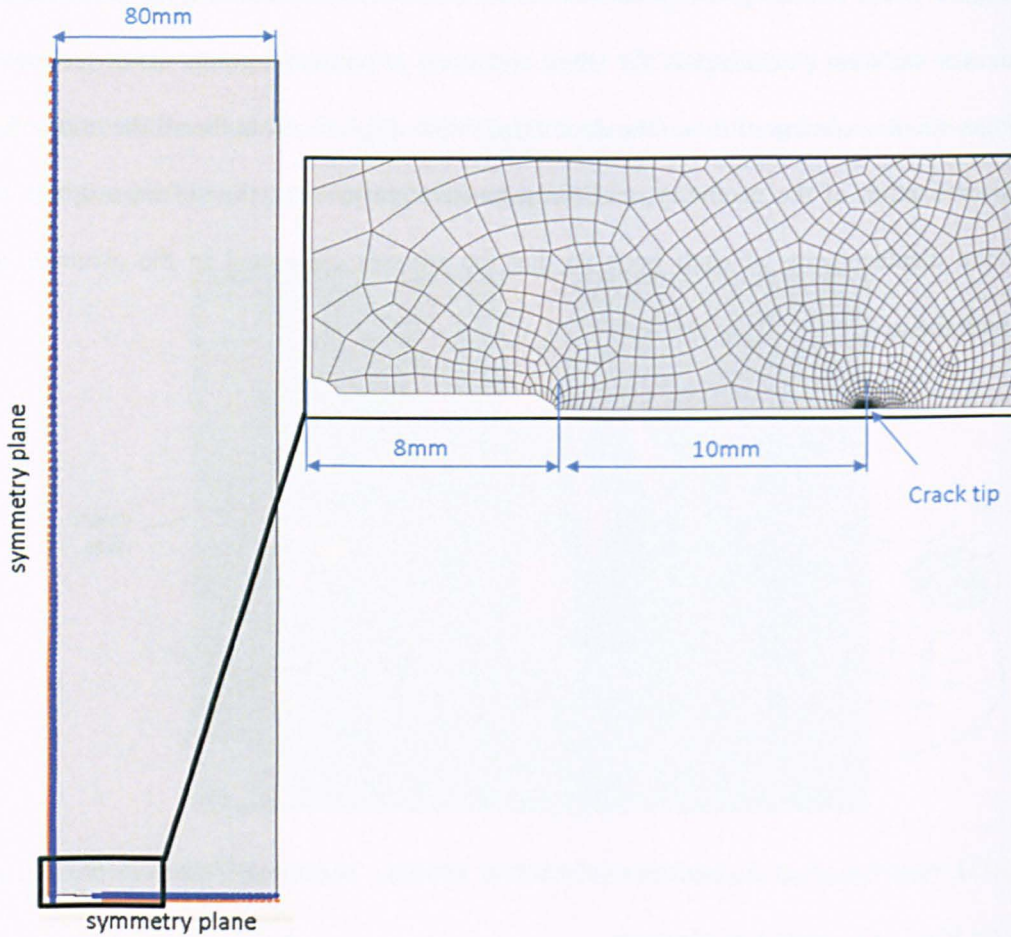


Figure 3.8.2 FE model with two planes of symmetry, plain steel CCT model shown.

The plastic behaviour of the material was assumed to follow the combined non-linear isotropic and kinematic hardening model. This model, described by Lemaître and Chaboche (1990), is available in the Abaqus database of models for metal plasticity (Abaqus, 2013). In this model, the total strain (ϵ) is divided into elastic strain (ϵ_e) and plastic strain (ϵ_p):

$$\epsilon = \epsilon_e + \epsilon_p \quad [3.8.1]$$

The flow stress varies with the cumulative plastic strain ϵ_p , either by increasing the yield stress for all directions of loading (Isotropic hardening), or by the elastic domain retaining a constant size, but moving about in the free space by translation (Kinematic hardening). Figure 3.8.3 illustrates the

principles of isotropic and kinematic hardening, and shows their respective effect on a low-cycle fatigue stress-strain curve.

Abaqus uses two variables, H and α , to implement this model. The equations describing the variation of the variables H for isotropic hardening and α for kinematic hardening are as follows:

$$H = Q[1 - \exp(-b\varepsilon_p)] \tag{3.8.2}$$

$$\alpha = \frac{C}{\gamma} [1 - \exp(1 - \gamma\varepsilon_p)] \tag{3.8.3}$$

where for isotropic hardening, Q is the maximum hardening level above the initial elastic limit and b is the rate (in strain) at which Q is reached. For kinematic hardening, the same is also true for C and γ respectively. The Parameters Q , b , C , and γ , as well as the Young's modulus and elastic limit, can be identified by comparing the experimental fatigue curves with data produced by the model.

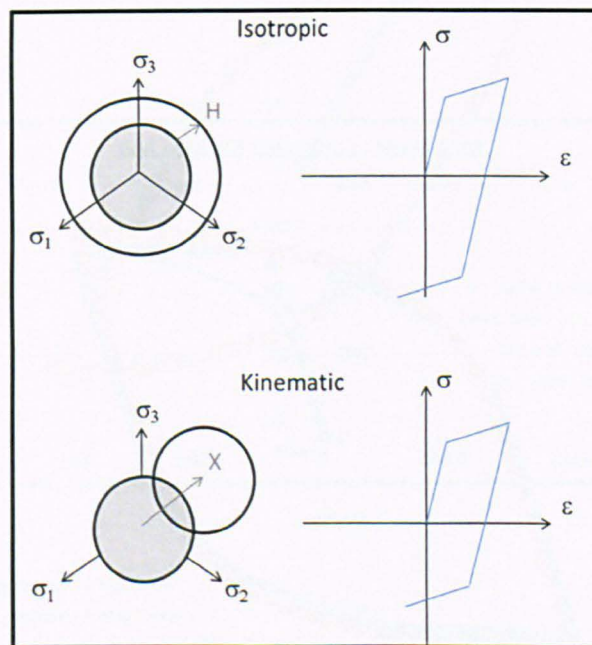
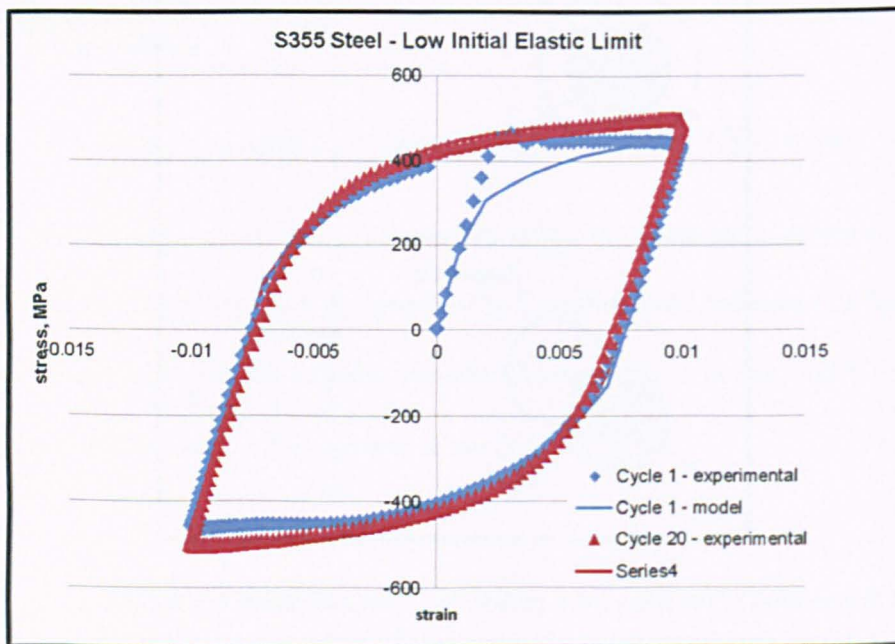


Figure 3.8.3 Illustration of the principles of isotropic and kinematic hardening.

A very simple model, made of one axisymmetric element with linear interpolation, was generated. The cyclic loading was defined by applying 20 series of tensile and compressive displacements. The magnitude of the applied displacements was determined from the strain range applied for each

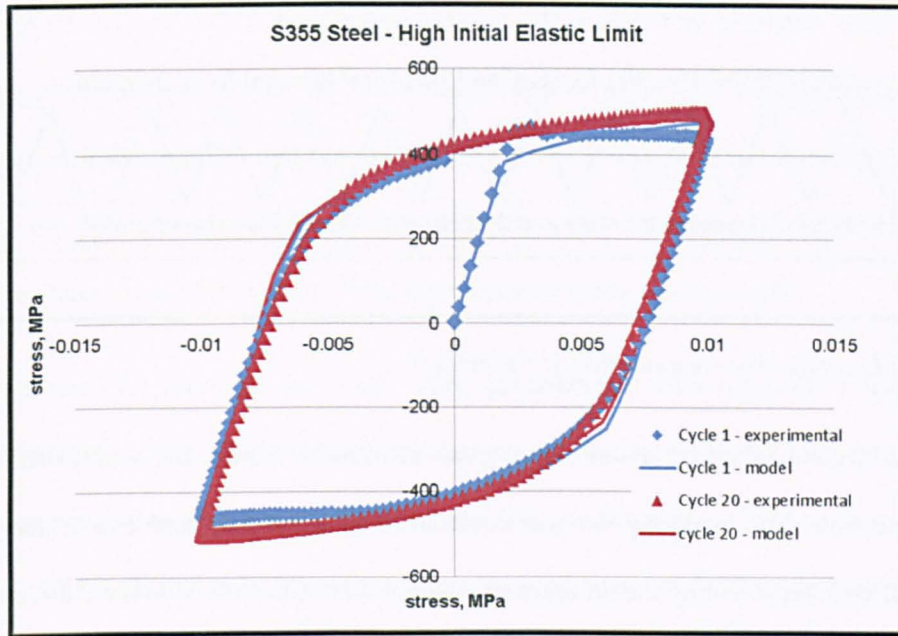
experimental test. The resulting cyclic stress history was recorded and compared with the experimental data, and the parameters were adjusted until good agreement was obtained between the experimental and simulated LCF curves.

Figures 3.8.4a-c show the comparison between the model and the LCF test data (Cycle 1 and Cycle 20, see also Chapter 4) for both materials investigated. It is worth noting that in the case of S355 steel, the first cycle is affected by the Luders plateau², which cannot be taken into account by the model. Two different sets of parameters were then identified: with the first set, the isotropic work hardening parameters were chosen in order to capture the variation of the stress when the applied strain was at its peak, however the initial elastic limit had to be adjusted to an artificially low value; in the second set, the elastic limit was more in agreement with the LCF curve observed in the first cycle, but using the identified parameters for the isotropic work hardening, the maximum stress in the first cycle was over-estimated. Because the aluminium alloy does not exhibit any singularity in the first cycle, a unique set of parameters was used to model its plastic behaviour described in Eq's. [3.8.2] and [3.8.3].

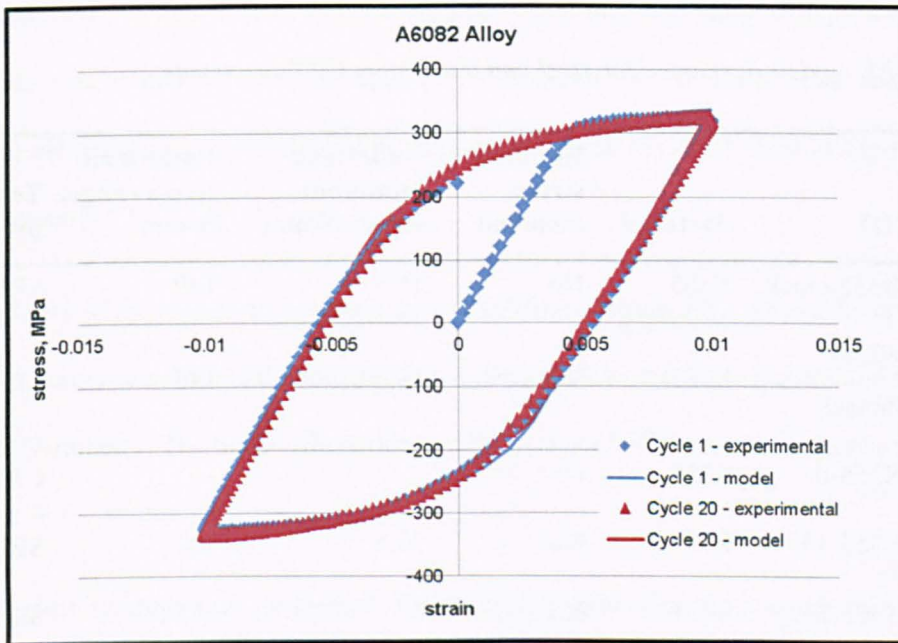


a)

² A region following the yield point in a tensile test, where localized bands of plastic deformation occur prior to strain hardening.



b)



c)

Figure 3.8.4 Comparison between model and LCF test data for a) S355 with a low initial elastic limit, b) S355 with a high initial elastic limit and c) 6082 aluminium alloy.

The magnitude of applied loading in each model was identical to that performed in the laboratory load sequence tests and comprised a number of CA (minor) cycles followed by a tensile underload then further minor cycles, Figure 3.8.5.

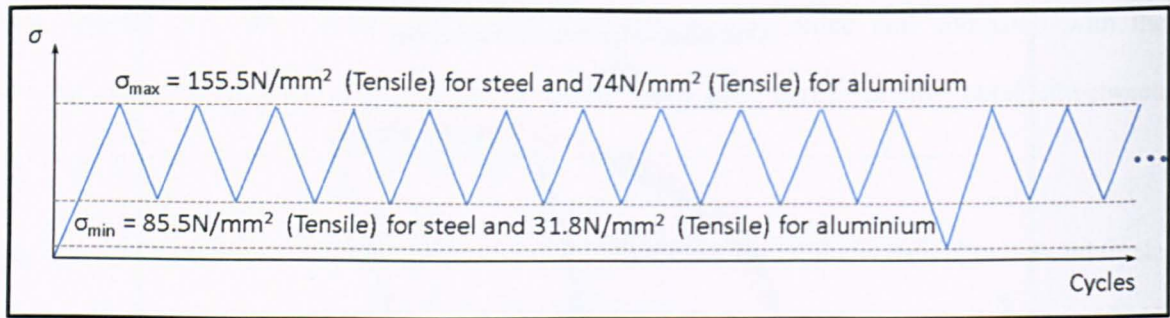


Figure 3.8.5 Loading sequence applied to FE models.

Loading was accomplished by assuming an even distribution across the width of the plate and applied to the ends. The loading point was constrained to allow displacements in the y direction. The nodes, at $x=0$, representing the un-cracked material were constrained in the y direction.

Ten models were created with different loading/boundary conditions. A summary of the models discussed in Chapter 6 is presented in Table 3.8.1.

Table 3.8.1 FE models developed for steel and aluminium CCT specimens.

Model ID	Material	Residual stress included	Underload minimum stress, N/mm ²	Underload stress range, N/mm ²	Test prefix
M-2D-S355-crack	S355	No	15.5	140	SBL2
M-2D-S355-RSnotchcrack	S355	Yes	15.5	140	SBL2
M-2D-S355-0	S355	No	-	-	CAL
M-2D-S355-15	S355	No	50.5	105	SBL1.5
M-2D-S355-22	S355	No	0	155.5	SBL2.2
M-2D-6082-crack	6082	No	10.6	63.4	SBL2
M-2D-6082-RSnotchcrack	6082	Yes	10.6	63.4	SBL2
M-2D-6082-0	6082	No	-	-	CAL
M-2D-6082-15	6082	No	26.3	47.7	SBL1.5
M-2D-6082-23	6082	No	0	74	SBL2.3

The models were defined as 2D plane strain. Initially, 2D plane stress elements were used as they were thought to be more appropriate in view of the thickness of the plate compared to its length and width. However, it was noticed that the use of plane stress elements resulted in the localisation of strain along the crack front, which was not observed in the experiments. The results obtained assuming the plane strain field were in better agreement with the observations.

The elements used for meshing the model were quadrilaterals with quadratic interpolation and reduced integration. Using quadratic interpolation allows the capturing of high stress gradients, such as those expected to be present at the crack tip. The crack tip stress field is also well captured when using collapsed elements (elements where two adjacent nodes are defined to lie at the location of the crack tip). In this case, it looks like the crack tip is meshed with triangular elements in the initial mesh. However, when plasticity is invoked the nodes can move independently when the load is applied. A comparative study of the stress field obtained using collapsed elements and quadrilaterals was conducted and is reported in Appendix B. It shows that the mesh with quadrilateral elements is sufficiently fine to capture the crack tip stress field in the same way as collapsed elements.

The element size in the region of the crack tip was 0.01mm. Figure 3.8.6 shows the crack tip mesh defined with normal quadrilateral elements and collapsed elements. Also highlighted in this figure is the line of symmetry. The nodes where this condition is not defined are in the crack wake and are free to move in the symmetry plane.

No mesh sensitivity study was performed. However, the mesh size at the crack tip was 0.01mm, which is of the order of the typical grain size of the structural materials considered (Lehto *et al.*, 2014; Bouquerel *et al.*, 2015), so that further refinement would be valid regarding the mathematical aspect of the analysis, but would be questionable regarding the relevance to the microstructure of the material. Also, all the analyses were carried out with the same model, so that a relatively quantitative comparison can be made between the results obtained with the different loading conditions.

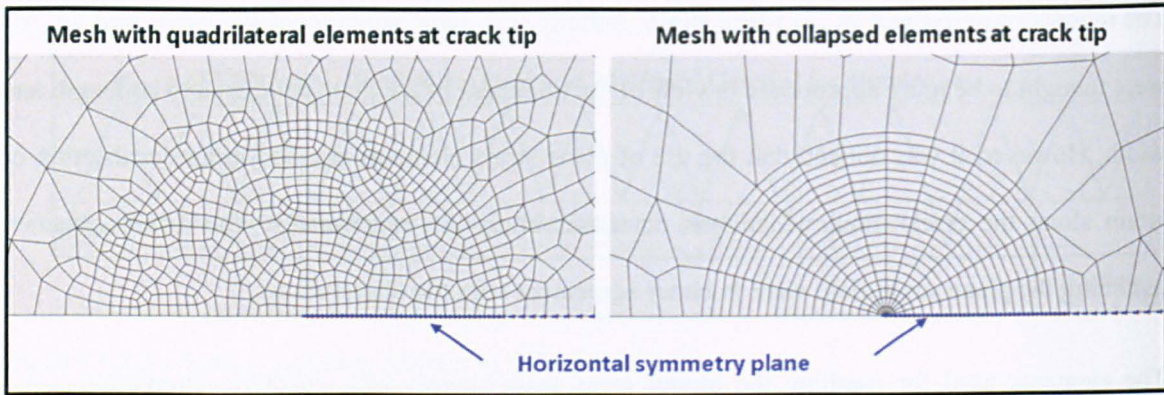


Figure 3.8.6 Crack tip meshing for S355 specimens. The meshing for Al6082 specimens was similar.

To characterise stress/strain in the maximum principal stress direction, set distances of 0.01mm, 0.05mm and 0.10mm from the crack tip were analysed. The examination of stress/strain at characteristic distances ahead of a crack tip is reminiscent of the Sigma-*d* method, typically used in the assessment of crack initiation in plain materials (Drubay *et al.*, 2003; Davies *et al.*, 2005).

Since the CCT specimens already contain a notch and for the purpose of the model analysis, a 10mm crack extending from the notch tip is already present (Figure 3.8.2), the sigma-*d* method would not be applicable in this instance.

To provide support for the FE model methodology and demonstrate its accuracy and robustness in representing the conditions at the crack tip under the applied loads, initial validation of the elastic response ahead of the crack tip was performed, Appendix B.

Here results of the FE model for the minor stress range were compared with the calculated response using LFM. The findings revealed that at a distance of >0.2mm from the crack tip, good agreement between the model and the calculated response was achieved, Figure B19. However, as one would expect, closer to the crack tip the LFM response failed to capture the large plastic deformation brought on from yielding, which had been allowed for in the FE model. Comparing the variation in crack tip response between the loading and unloading portions of the minor cycle (i.e. the elastic range), both the model and calculated response correlated well.

Following this, further validation was performed by considering Irwin's elastic-plastic offset from the LEM elastic curve (Lemaitre and Chaboche, 1990), Figure B21. The process involved calculating the corrected crack tip stress field allowing for the plastic zone ahead of the crack tip termed R_y . Assuming LEM and plane strain conditions, the stress at the crack tip (R_p) over the distance of $2 \times R_y$ was determined using the von Mises equivalent stress limited to the materials yield strength. By truncating the LEM curve at the value of R_p , the response agreed well with the minor cycle FEA results, Figures B22 and B23.

To establish the effect of residual stress during tensile unloading, the measured residual stress distribution extending across the plate from the notch width (Section 3.7) was used to define the residual stress profile extending from the notch (Bao *et al.*, 2010) using a closed form stress intensity factor (SIF) solution derived by a weight function method for a centre crack in an infinite plate width (Tada *et al.*, 2000), using:

$$\sigma_{YY}(x) = \sigma_{YY}^{\max} \cdot e^{\left(\frac{1}{2} \left(\frac{x - x_{peak}}{C} \right) \right)} \cdot \left[1 - \left(\frac{x - x_{peak}}{C} \right)^2 \right] \quad [3.8.4]$$

where σ_{YY}^{\max} is the maximum residual stress measured, x_{peak} is the offset used in un-symmetrical σ_{YY}^{\max} measurements and C is a constant derived experimentally for data fitting.

For the introduction of residual stresses into the FE model, the Abaqus subroutine SIGINI was used. In this, the first step of the analysis is the calculation of a balanced residual stress distribution. This is necessary because the residual stress field applied is often not at equilibrium. In this first step, when applying the stress distribution identified from the measurements to the model, achievement of a balanced residual stress distribution could not be obtained as the stress concentration and plastic strain at the notch tip were too high. The alternative solution was to apply the residual stress field before the notch was modelled, so that the balanced stress distribution was calculated in the un-notched condition, then to remove the elements corresponding to the notch to calculate the new stress distribution.

It is worth noting that this process does not strictly agree with the way the residual stress distribution was established, since Eq. [3.8.4] is for the residual stress distribution at a notch, but was applied to the model in the un-notched condition. However, the first measurement point is 2mm from the notch tip, where the stress distribution is hardly affected by the notch.

Figures 3.8.7 and 3.8.8 show the stress distribution before equilibrium, before notching, and after notching, compared with the actual measurements. Because of the symmetry of the model, the predicted FE residual stress is shown at only one side of the notch. These graphs show that, although the stress distribution was applied in the un-notched condition, the final predicted residual stress is very close to the measurements. Note that the balanced stress transverse to the weld is close to zero before notching. This is in agreement with the expected results after equilibrium. However, the notch³ causes the stress to rise to the measured values.

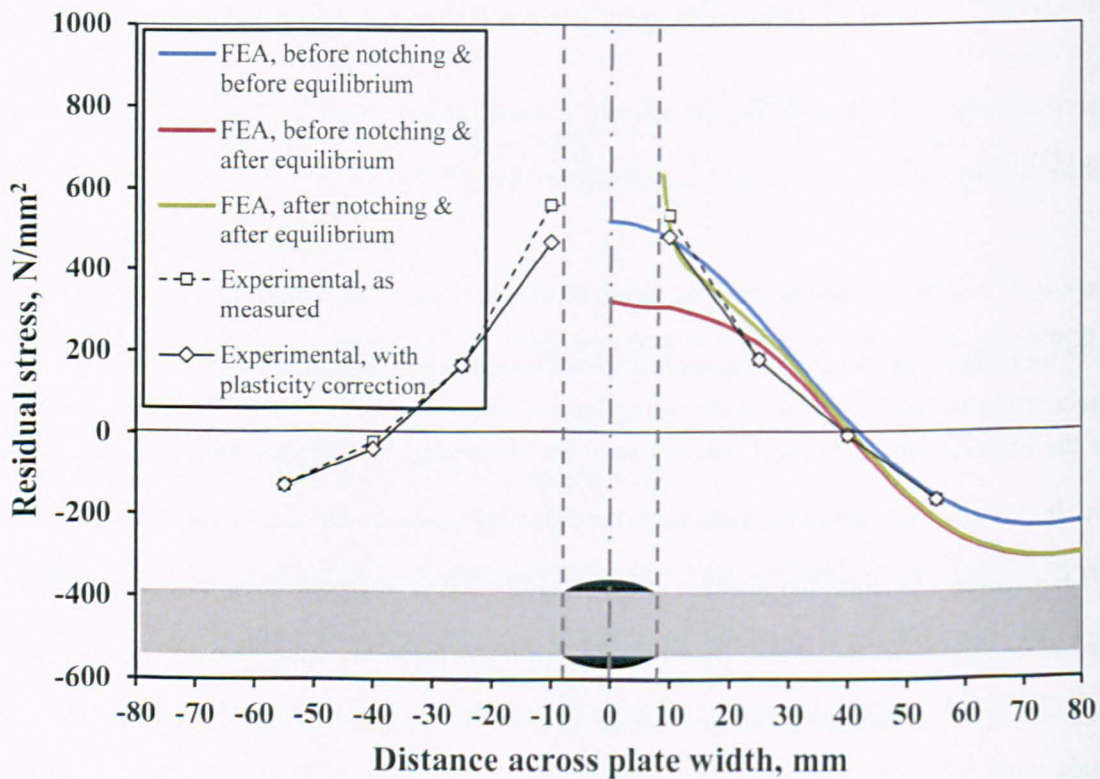


Figure 3.8.7 Comparison between the initial input stress field, balanced stress fields, and the measured distribution for S355 steel for the direction longitudinal to the weld.

³ The width of the weld bead, as indicated in the plots and the notch length in all cases and for both steel and aluminium alloy are equal.

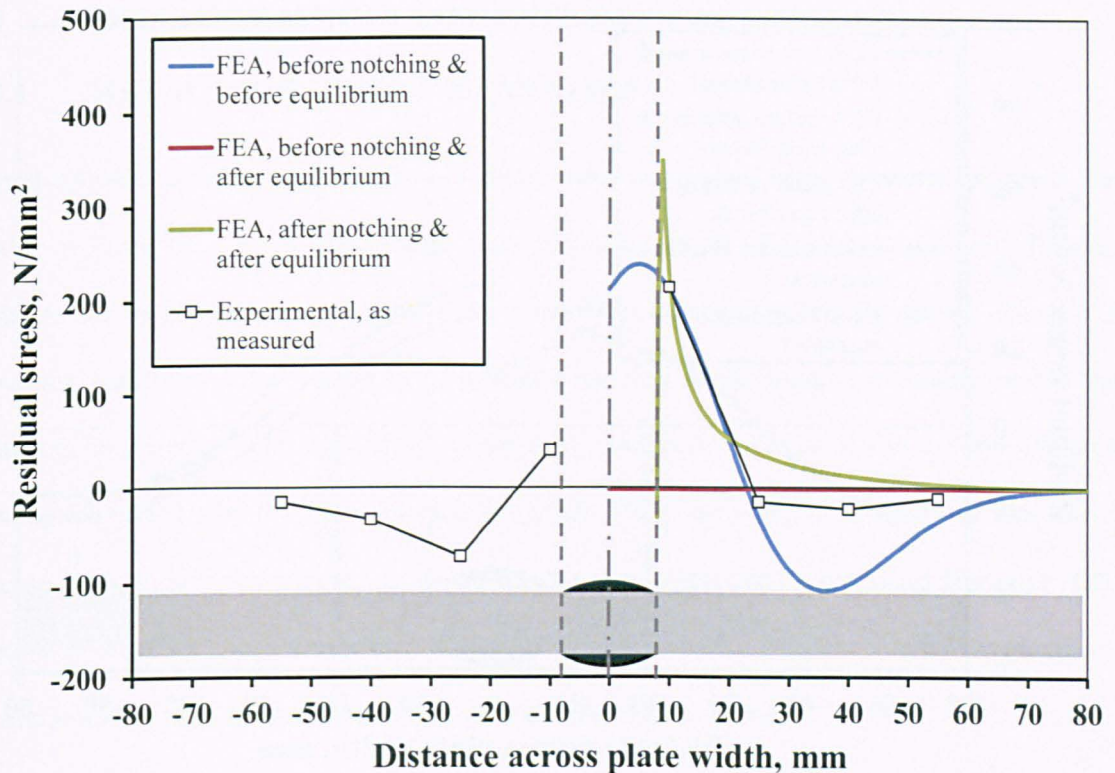


Figure 3.8.8 Comparison between the initial input stress field, balanced stress fields, and the measured distribution for S355 steel for the direction transverse to the weld.

The same methodology was applied in the case of the 6082 aluminium alloy and is shown in Figures 3.8.9 and 3.8.10. Also shown are the boundaries to the HAZ softened zone. This softened zone is a result of the welding process changing the original alloy constituents of 6082 in the T6 condition, due to over aging brought on by the high temperatures involved (Missori and Sili, 2000).

The FE model produced was validated using linear elastic fracture mechanics. The validation calculations are included in Appendix B.

All FEA was performed by the Numerical Modelling Section (NMO) at TWI, Cambridge. All model requirements, geometry, loading requirements, interpretation of data and model validation were specified/carried out by the author.

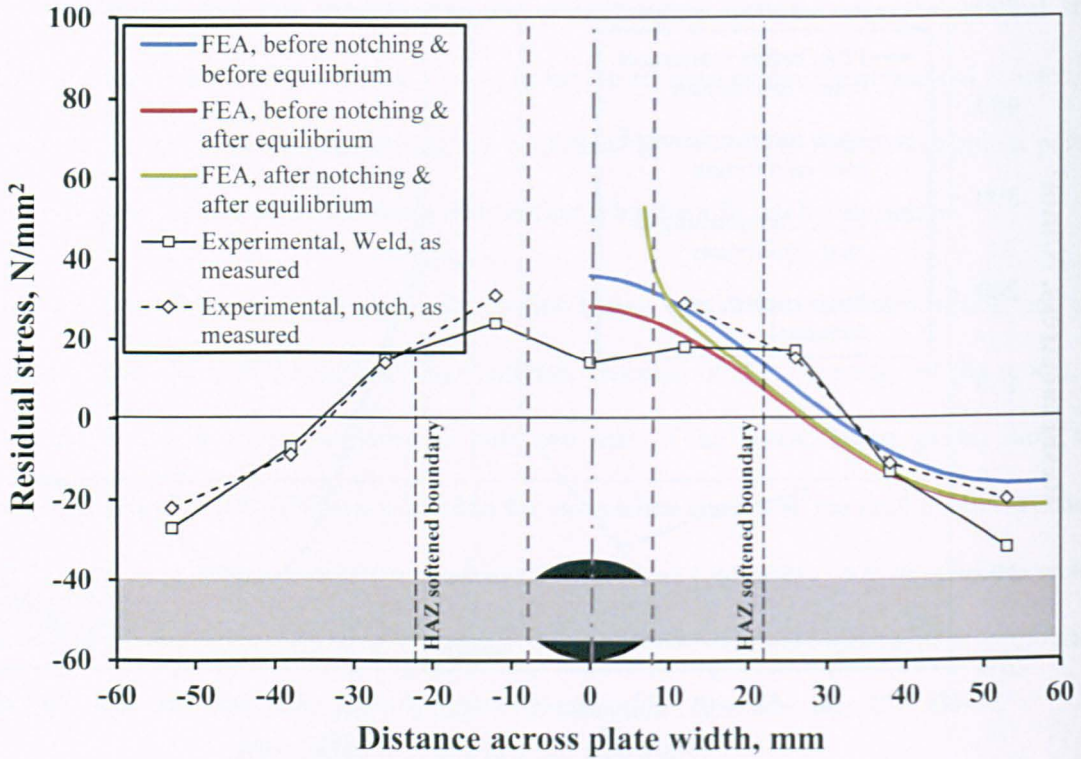


Figure 3.8.9. Comparison between the initial input stress field, balanced stress fields, and the measured distribution for the 6082 aluminium alloy for the direction longitudinal to the weld.

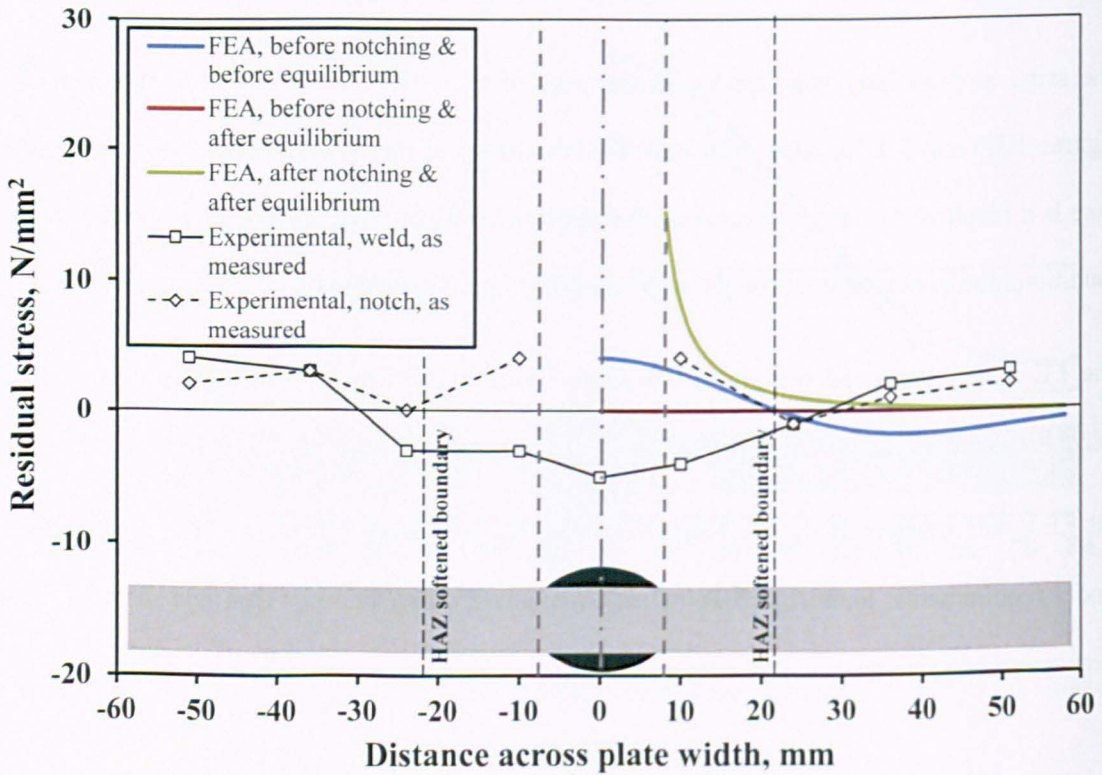


Figure 3.8.10. Comparison between the initial input stress field, balanced stress fields, and the measured distribution for the 6082 aluminium alloy for the direction transverse to the weld.

3.9 FRACTOGRAPHIC EXAMINATION

3.9.1 METALLOGRAPHIC PREPARATION

Metallographic samples were cut from fatigue tested specimens using a band-saw; these were further reduced to a more manageable size (where necessary) by means of a cut-off wheel. Samples for macro examination were then mounted in conductive Bakelite (20ml Phenolic hot mounting resin and 15ml Conductive Phenolic mounting resin) using a mounting press. Once mounted, they were ground back using successively finer abrasive discs of 180 to 1000 grit grade, rotating the samples by 90° between each grit grade. They were then polished again successively finer to 0.25µm. Samples were inspected for scratches, provided none were found they were etched using 2% Nital for steel, and either Kellers (with hydrofluoric acid) or sodium hydroxide for aluminium alloy, to allow the microstructure and weld to be examined.

Samples for examination in the scanning electron microscope (SEM) were again cut from specimens using a band-saw, but this time were cleaned in an ultrasonic bath of Acetone. In some instances Pyrene was used as the medium. This is a more aggressive remover of oxidising product but can easily destroy the fracture surface if the concentration is too high. Typically 2% Pyrene was used in the ultrasonic bath and increased to a maximum of 5% should it be required; five minutes was the maximum exposure time used for the steel samples (where necessary).

3.9.2 SCANNING ELECTRON MICROSCOPE

A scanning electron microscope (SEM) works by using electrons to form an image as opposed to light. A beam of electrons is produced at the top of the microscope and passes through an electromagnetic lens which focuses the beam on to the object. Once the electrons hit the object surface they are dispersed randomly and detectors capture a proportion of them and convert them into an image. In the work performed here, two detectors were used at varying stages of the analysis: the InLens detector which is mounted vertically within the objective lens captures a small proportion of the secondary electrons which travel vertically upwards. The side mounted secondary electron detector (SE2) drags electrons from the surface and therefore enhances the topographical nature of the system. Whilst the InLens detector loses the topographical effect, the detector can

perform better at high magnification particularly with a shorter working distance and hence greater proportion of captured secondary electrons.

For the experimental work performed within this research project, specimen fracture faces were examined using a Zeiss Supra 55VP field emission gun scanning electron microscope (FEGSEM) at the Open University, Milton Keynes and the Leo 1550 FEGSEM at TWI, Cambridge. All SEM microscopy performed in this thesis was carried out by the author.

For both FEGSEM systems the inlens secondary electron detector was used with an accelerating voltage of 3kV and 5kV for the Zeiss and Leo respectively. Steel specimens were examined at both 20k and 50k times magnification, and the aluminium alloy specimens were examined over a range of 10k to 50k times magnification. The purpose was to observe striations (Figure 2.5.2) on the fracture surface following periodic underloads and VA loading; striations define the position of the advancing crack front. Consequently, the space between them is the distance propagated by the crack under the relevant applied load cycle. In all cases, images were captured at set intervals extending out from the notch tip to examine any differences in striation spacing with respect to crack length.

3.9.3 X-RAY COMPUTED TOMOGRAPHY

X-ray computed tomography (XCT) is a non-destructive imaging technique which uses X-rays to produce three dimensional representations of a scanned object. Originally developed in the medical sector for computerized axial tomography (CAT) scans, the resolution was limited to around 0.5mm. Over the past two decades the technique has extended significantly with the availability of Industrial Micro-Computed Tomography (μ -CT) scanners capable of providing 3D and 4D micron-resolution, as well as synchrotron radiation sources that are capable of sub-micron resolutions (Wevers, 2012).

Its use in analysing welded joints is limited and to date no known work has investigated its ability to resolve the local weld toe geometry. Recent work has, however, seen its use in resolving surface features (i.e. corrosion pits), porosity, stress corrosion cracking, fatigue cracks and inclusions (Bettaieb *et al.*, 2011; Horner *et al.*, 2011; Gamboa *et al.*, 2014; Marrow *et al.*, 2014).

The system works by projecting an X-ray beam through a specimen at several increments about a 360° rotation of the specimen and taking a number of X-ray radiographs, Figure 3.9.1. These projections are then formed on a detector by the X-rays that attenuate energy as they traverse through the specimen (Kumar *et al.*, 2011). The amount of X-ray attenuation is a logarithmic function of the material absorptivity and thickness and is represented by:

$$I = I_0 \exp(-\mu t) \quad [3.9.1]$$

where I is the X-ray beam intensity, I_0 is the X-ray beam energy, t is specimen thickness in the beam direction and μ is the linear attenuation coefficient of the material.

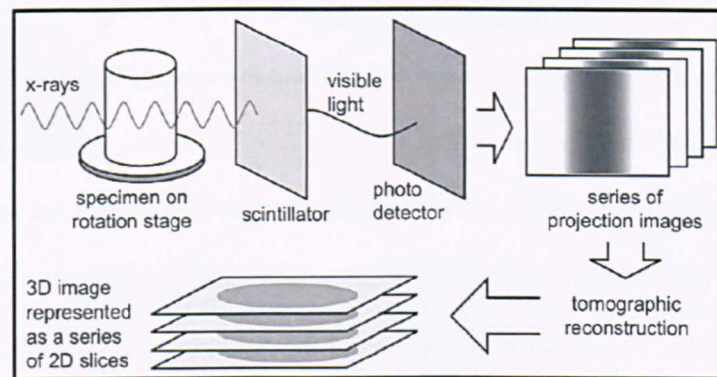


Figure 3.9.1 Schematic illustration of the X-ray CT acquisition and reconstruction process (Landis and Keane, 2010).

The radiographs are reconstructed into a 3D volume by finding the centre of rotation and using a back-filtered projection algorithm in CT3DPro software. The resulting 3D volumes are then analysed using 3D image processing software such as: VG Studios, AVIZO, CAD+, SCANIP and FIJI.

In the case of the steel fillet welded specimens with longitudinal attachments used in this project, two scans were carried out at the weld return location (Figure 3.9.2) using the 225kV HUTCH μ -CT machine at Southampton University by an Eng.Doc student, each scan taking 6.5 hours to complete. The two volumes were then aligned and stitched in VG Studios. Further details of the work performed are given in Chapter 4.

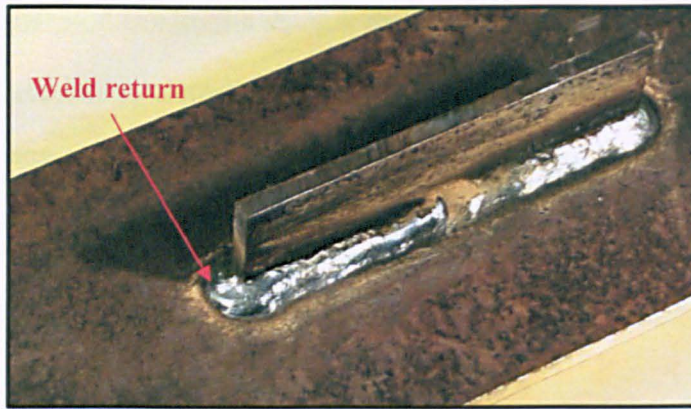


Figure 3.9.2 *Weld return location on a steel fillet welded specimen with longitudinal attachments.*

3.10 SUMMARY

This Chapter has identified a number of techniques employed to better understand fatigue crack acceleration under simple loading spectra and VA loading from a constant maximum stress. In each case the methods most relevant to this research project were identified. As shown and mentioned at various stages throughout this Chapter, the use of both steel and aluminium alloy specimens has been utilised in this research project. The materials selected and their characterisation is discussed in the following Chapter. The basic understanding of the selected materials was pivotal in applying the methodologies discussed herein. Chapters 5 to 7 present the research undertaken using the methodologies identified above. An overview of the research carried out is presented in Figure 3.10.1.

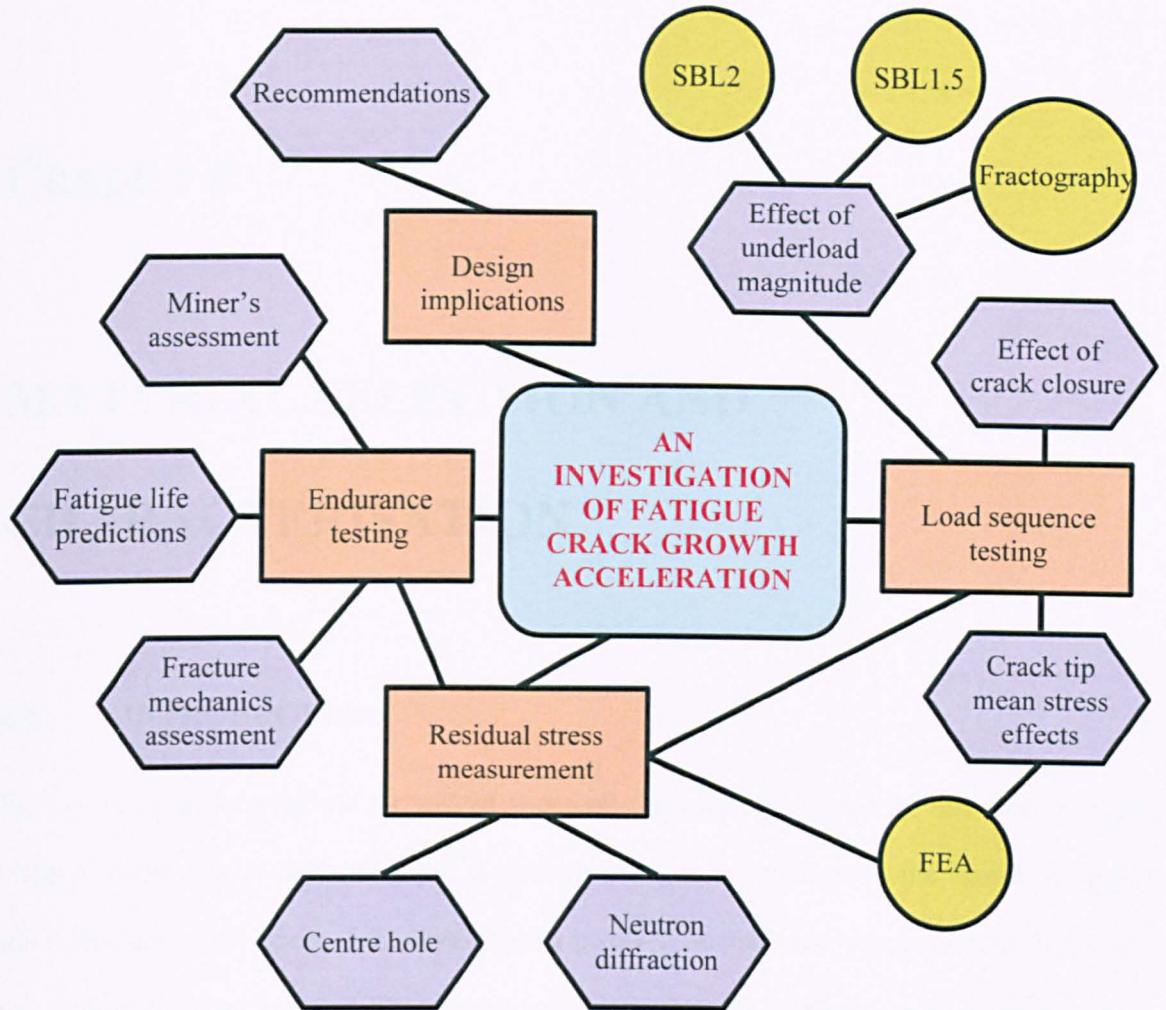


Figure 3.10.1 Overview of the research carried out and the analytical or test techniques employed.

Chapter 4

MATERIAL SELECTION AND CHARACTERISATION

4.1 INTRODUCTION

In view of its widespread use for welded structures the material selected for this study of fatigue under variable amplitude loading was a medium strength structural steel, the choice being S355 steel. However, one aspect of the investigation involved microscopic examination of striations on the fatigue fracture surfaces. This is generally very difficult in steels, even using a scanning electron microscope (SEM), whereas striations are more readily identifiable in aluminium alloys. Therefore, supplementary tests were included using a structural aluminium alloy, the choice being 6082-T651, another structural material widely used for welded structures. Details of the two materials and the material properties required for the present study are presented in this chapter.

4.2 SELECTED MATERIALS USE IN INDUSTRY

4.2.1 STRUCTURAL STEEL

Structural steel plate, type S355J2+N to BS EN 10025-2 (BS, 2004), produced by Corus UK Ltd., was used throughout this investigation in all aspects of experimental work performed. It was supplied in two batches (PM1 and PM2) in the normalised rolled 'N' condition, whereby the steel is cooled in air after the final rolling process from a temperature exceeding 900°C. The result is a refined grain size with improved mechanical properties, particularly fracture toughness (minimum impact requirement 27J at -20°C).

The steel is generally readily weldable but this was checked on the basis of its carbon equivalent value (CEV) (see Section 4.3.4).

4.2.2 ALUMINIUM ALLOY

The aluminium alloy used was grade 6082 T651 to BS EN 485 (BS, 2008), produced, again in two batches, by Constellium.

Alloy 6082 (Al Si Mg Mn) has reasonable weldability and corrosion resistance and also the highest strength of the 6000 series alloys. It is used extensively in engineering applications such as bridges, trusses, cranes, offshore and transport. The classification 'T651' refers to the heat treatment and normalisation processes, 'T6' being the solution heat treatment before quenching in cold water to give enhanced strength, and '51' denoting that the material was normalised by controlled stretching.

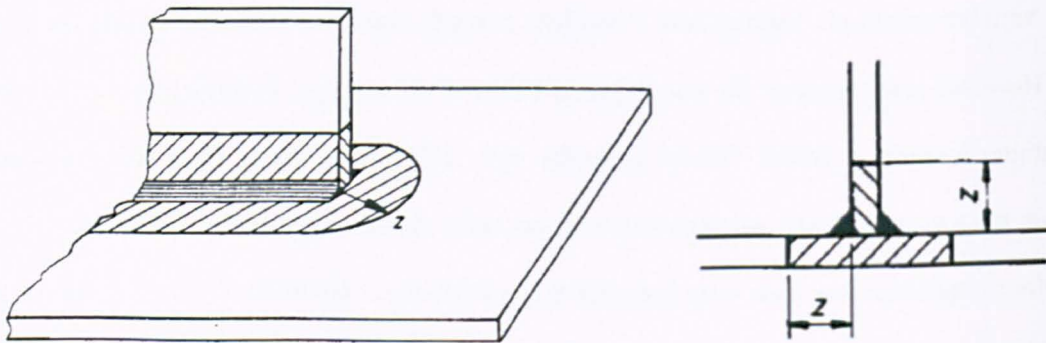


Figure 4.2.1 Extent of HAZ softening in a fillet welded 6082 T651 aluminium alloy specimen with longitudinal attachments (BSI, 1991).

A practical disadvantage of some structural aluminium alloys, including 6082, is that they are softened in the heat affect zone (HAZ) as a result of welding. In the type of fillet-welded joint used in the present investigation (Figure 4.2.1), according to (BSI, 1991) its strength reduction factor due to such softening is 0.50, and the softened zone extends to a radius, z , of 40mm (Figure 4.2.1). No guidance is given for the weld bead deposited on the CCT specimen used in the present work. Therefore, the actual extent of the softened zone was measured using Vickers micro hardness (Section 4.3.3). It was found to extend ~ 22 mm from the centre of the weld cap. For completeness, Vickers micro hardness measurements were also performed on the fillet welded specimen and the

softened zone was found to extend across the entire plate width of 110mm (55mm from each welded joint intersection (Figure 4.2.1)), perhaps due to the use of multiple weld passes and the limited number of heat paths.

4.3 MATERIAL CHARACTERISATION

4.3.1 GENERAL

The mechanical properties of the two materials were determined in accordance with the relevant British Standard tests, performed at TWI Ltd, TWI's subsidiary company The Test House (TTH) and Westmoreland Mechanical Testing & Research Ltd (WMTR).

4.3.2 TENSILE TESTING

4.3.2.1 STATIC PROPERTIES

Tensile testing was performed in accordance with BS EN 10002-1:2001 for the S355 steel and BS EN ISO 6892-1:2009 B for the 6082 aluminium alloy to determine the yield (0.2% proof), ultimate tensile strength (UTS), % elongation and the % reduction in area.

Tables 4.3.1 and 4.3.2 give the measured tensile properties for S355 structural steel and alloy 6082 respectively. In both cases the properties from the material data sheets 'certificate' values are also provided for comparison. All tensile tests were performed in UKAS accredited testing machines.

It can be seen in Table 4.3.1 that for both steel supplies, the measured yield stress (0.2% proof) is below the certificate values. However, the measured values are above the BS EN 10025 specified minimum of 355N/mm².

Referring to Table 4.3.2, it will be seen that the measured properties of the two batches of aluminium alloy were in reasonable agreement with the certificate values.

Table 4.3.1 Measured and certificate tensile properties of the S355 structural steel.

Property	S355J2+N Steel		S355, Certificate (PM1/PM2)	BSEN 10025 Grade S355J2+N
	PM1 (Heat no. 79876)	PM2 (Heat no. 69637)		
Yield stress (0.2% proof), N/mm ²	470	455	506/472	355 (min)
Tensile strength, N/mm ²	602	585	583/574	470-630
Elongation, %	26	31	28/26	(20 min)
Reduction Area, %	59	54	-/-	-

Table 4.3.2 Measured and certificate tensile properties of the 6082 T651 aluminium alloy.

Property	Aluminium alloy 6082 T651		6082 T651, Certificate ¹
	Batch 1	Batch 2	
Yield stress (0.2% proof), N/mm ²	322	325	310
Tensile strength, N/mm ²	339	345	340
Elongation, %	13.4	12.8	11
Reduction Area, %	46.7	40.9	-

4.3.2.2 CYCLIC PROPERTIES

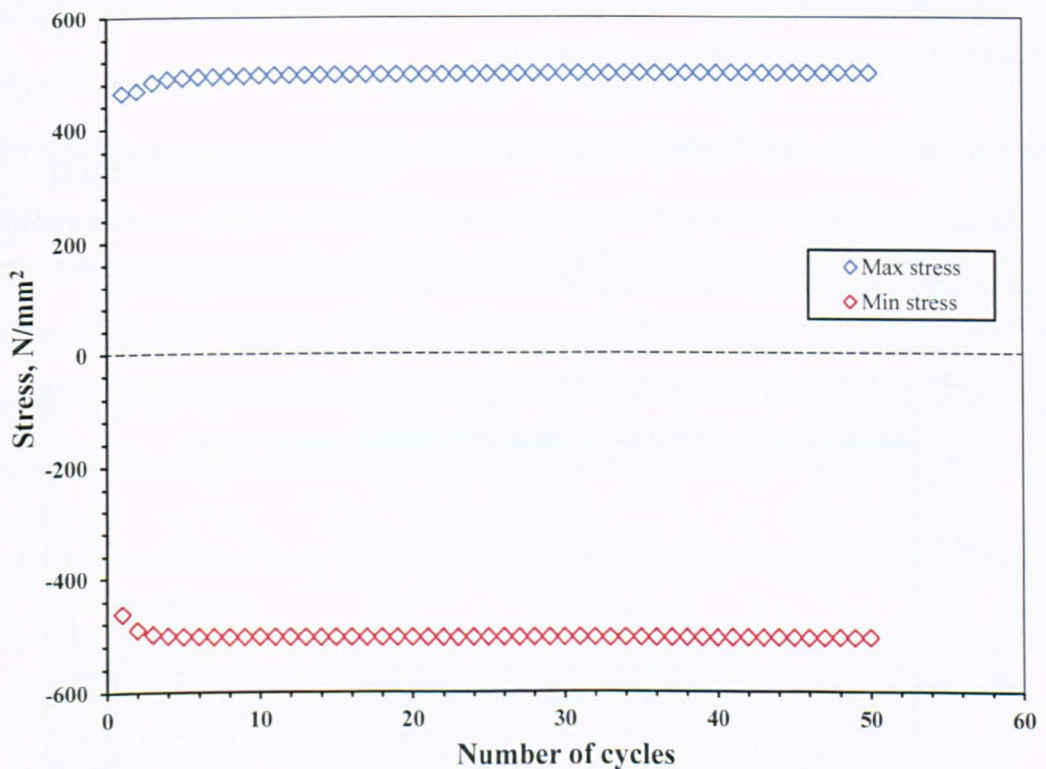
The cyclic stress-strain properties of the two materials were required to define their hardening characteristics (i.e. kinematic/isotropic) under fatigue loading, for finite element modelling (Chapter 6). They were obtained from strain-cycling low-cycle fatigue (LCF) tests, performed in accordance with BS 7270 (BSI, 2006) by WMTR. Small cylindrical specimens ~4mm diameter (two steel and two aluminium alloy) were prepared and longitudinally polished to produce a

¹ www.aalco.co.uk

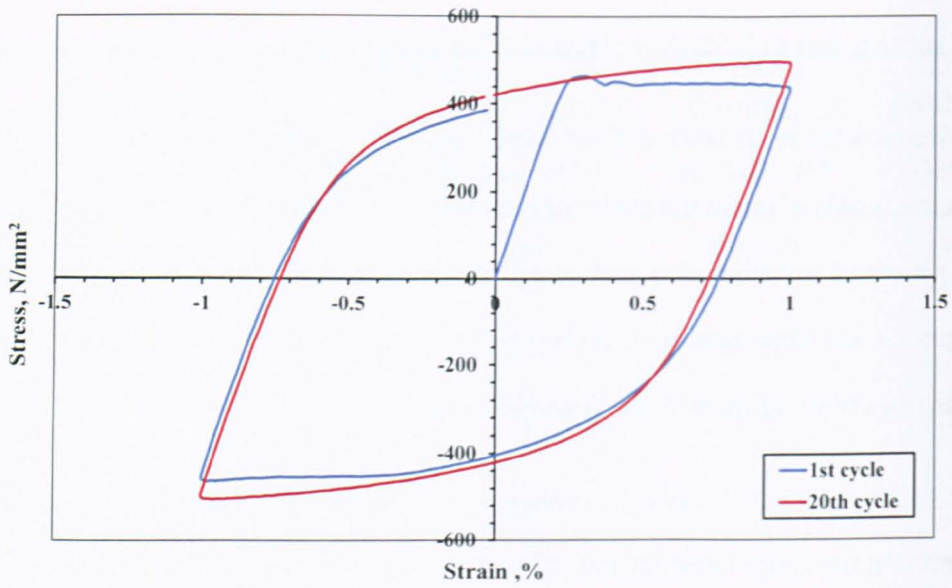
surface roughness $<3.2\mu\text{m Ra}$. Tests were performed using an Instron servo-hydraulic testing frame of 100kN capacity and an 8mm gauge length MTS extensometer.

Tests were conducted in air under ambient conditions (21°C) with an average humidity of 35-55% at a strain ratio (ratio of minimum strain/maximum strain in a cycle) R of -1 and a strain amplitude of 1%. A sinusoidal waveform was applied with a cycling frequency of 0.5Hz. Testing involved the application of a specified number of cycles (50 for steel, 100 for aluminium alloy) to adequately characterise the stabilised stress/strain hysteresis loop.

Figures 4.3.1a-b and 4.3.2a-b show the evolution of the maximum tensile and compressive stresses and the initial stress-strain loops for the S355 steel specimen (WMTR No. 100676) and the 6082 aluminium alloy specimen (WMTR No. 100679) respectively, with increasing number of cycles.



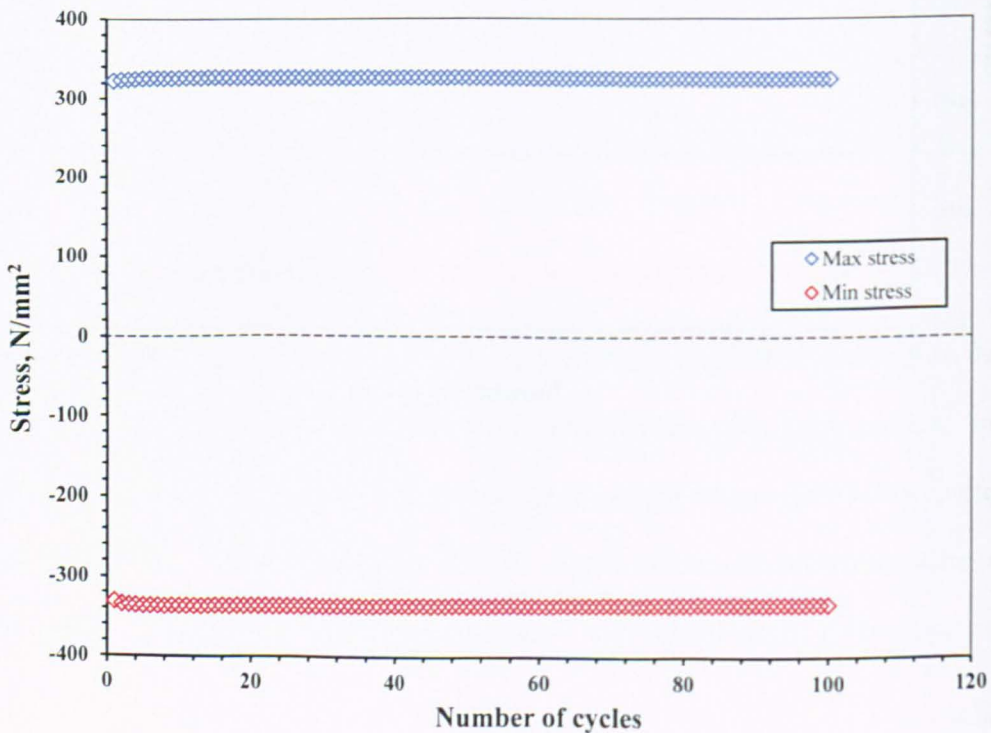
a)



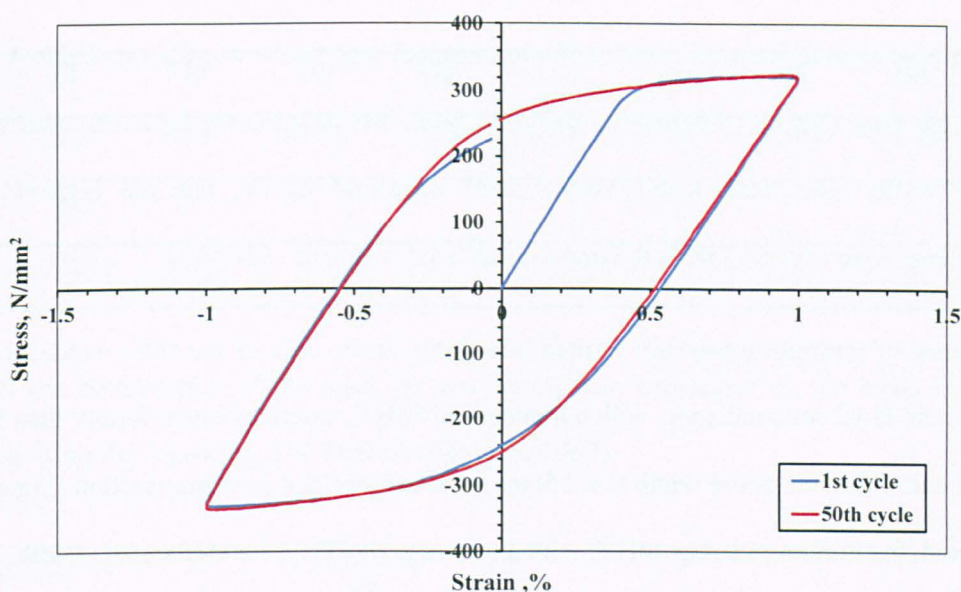
b)

Figure 4.3.1 Cyclic properties for S355 structural steel, WMTR No. 100676; a) Maximum tensile and compressive stress, b) Cyclic stress-strain loops.

For the steel specimen, cyclic hardening was evident from the increase in stress after the first few cycles. In the case of the aluminium alloy specimen, slight cyclic hardening was observed after the first two or three cycles, followed by marginal cyclic softening as the test progressed.



a)



b)

Figure 4.3.2 Cyclic properties for 6082 aluminium alloy, WMTR No. 100679; a) Maximum tensile and compressive stress, b) Cyclic stress-strain loops.

4.3.3 HARDNESS TESTING

Hardness testing was performed on a Vickers macro hardness testing machine using loads of 10Kg for steel and 5Kg for aluminium alloy. The Vickers machine was independently calibrated before use and the testing procedure was in accordance with BS EN ISO 6507-1:2005. Mid-thickness measurements were made in both materials. The results are given in Table 4.3.3.

Table 4.3.3 Measured hardness (Vickers) for S355 structural steel and 6082 T651 aluminium alloy.

	S355J2+N Steel	Aluminium alloy 6082 T651
Measured	181, 187, 185	100, 98.4, 102
Average	184HV ₁₀	100HV ₅

As mentioned in Section 4.2.2, the hardness variation in the region of the weld was measured in both the aluminium bead-on-plate and fillet-welded specimens. These were produced from a series of indentations made 2mm below the surface. In the case of the weld bead, the HAZ softened zone within ~22mm of the weld centreline had a much reduced hardness of 56HV, almost half that of the

un-welded parent material given in Table 4.3.3. It should however be noted that the hardness of the parent material remote from the weld (>50mm distance) was also lower than in Table 4.3.3, ~72-80HV, suggesting that the presence of the weld bead had reduced the hardness over the entire specimen width. The weld metal (WM) itself measured 62HV, but the highest hardness measurements were observed from the under-bead HAZ region at ~85HV.

The presence of multiple welds and limited heat paths in the case of the fillet welded specimens meant that the HAZ softened zone, with a hardness of 48HV, extended much further than found for the weld bead. Here, the entire width (i.e. 55mm from each welded joint intersection (Figure 4.2.1)) was affected, the minimum being 44HV, with an average of 55HV across the plate width. The WM hardness was found to be significantly lower, with an average value of 44HV.

4.3.4 CHEMICAL ANALYSIS

Direct optical emission spectrometry (D-OES) was used to measure the steel composition, while that of the aluminium alloy was determined by inductively coupled plasma optical emission spectrometry (ICP-OES). The results are given in Table 4.3.4 for steel and Table 4.3.5 for the aluminium alloy.

Table 4.3.4 S355 structural steel composition (in weight %).

Batch	C	Si	Mn	P	S	Cr	Mo	Ni	Al
PM1	0.16	0.42	1.40	0.015	0.008	0.016	<0.003	0.019	0.042
PM2	0.15	0.38	1.40	0.015	0.009	0.014	<0.003	0.019	0.041
	As	B	Co	Cu	Nb	Pb	Sn	Ti	V
PM1	<0.004	0.00004	<0.004	0.012	0.022	<0.005	<0.004	0.003	0.002
PM2	<0.004	0.00007	<0.004	0.013	0.018	<0.005	0.005	0.002	0.002
	W	Zr	Ca	Ce					
PM1	<0.01	<0.005	<0.0003	<0.002					
PM2	<0.01	<0.005	<0.0003	<0.002					

Table 4.3.5 6082 T651 aluminium alloy composition (in weight %).

Batch	Si	Mn	Ni	Mg	Cu	Zn	Pb	Sn	Fe
No. 1	0.91	0.45	<0.01	0.76	0.07	0.06	<0.01	<0.01	0.27
	Ti	Cr							
No. 1	0.01	0.02							

Based on the composition of the steel, its weldability can be judged on the basis of its CEV, calculated using the following IIW formula (Granjon, 1967):

$$CEV = C + \frac{Mn}{6} + \frac{Cr + Mo + V}{5} + \frac{Ni + Cu}{15} \quad [4.3.1]$$

Typically values <0.45 would indicate excellent weldability, 0.45 to 0.60 good (pre-heat required) and >0.60 poor (pre and post-heat required) (ASM, 1996).

In the case of the S355 steel used in this study, the CEV was calculated to be 0.40, indicating excellent weldability.

There is no measure such as the CEV available for judging the weldability of aluminium alloys. Welding of aluminium alloys may result in softened zones with material strength well below the yield strength of the base material. Appropriate choice of filler wire is required in order to avoid the onset of solidification cracking, which is common in aluminium alloys.

4.4 FATIGUE CRACK GROWTH RATE TESTING

4.4.1 FATIGUE CRACK GROWTH RATE TESTING OF S355 STEEL SPECIMENS

Fatigue crack growth rate (FCGR) testing was carried out in accordance with BS ISO 12108 (BSI, 2012) using a servo-hydraulic fatigue testing machine of 500kN capacity. Tests were performed under axial CA loading in air at a frequency of 4-12Hz and applied stress ratios of $R = 0.1$ and 0.5 . Two types of centre-cracked tension (CCT) specimen were tested, termed 'plain' and 'welded'. The former were plain steel plate specimens while the latter had weld beads deposited on the plate surfaces to introduce tensile residual stresses acting in the same direction as the applied loading, as

illustrated earlier in Figure 3.4.1. Crack length was measured by DCPD. The procedure was to propagate fatigue cracks from the central notch at the required initial ΔK for a distance of approximately 1 to 1.5mm. Crack growth data generated during this phase were neglected as being invalid. Precise details of the tests were as follows:

- Increasing ΔK tests were used to obtain Paris-law crack growth rate data over a ΔK range of approximately $350 - 2000 \text{ N/mm}^{3/2}$ ($11 - 63 \text{ MPa.m}^{0.5}$).
- Decreasing ΔK tests with a constant stress ratio were used to obtain Paris-law crack growth rate data from a ΔK of approximately 500 down to $100 \text{ N/mm}^{3/2}$ ($16 - 3 \text{ MPa.m}^{0.5}$).

A summary of the parameters used in each test is given in Table 4.4.1.

Table 4.4.1 Test parameters for fatigue crack growth rate tests in S355 steel.

Specimen no.	Test type	Test frequency, Hz	ΔK , $\text{N/mm}^{3/2}$	ΔK , $\text{MPa.m}^{1/2}$	Other test parameters
CCT PM1-01	Inc. ΔK	5	375 to 1350	12 to 43	R=0.5
CCT PM1-02	Inc. ΔK	5	850 to 1550	27 to 49	R=0.5
CCT PM1-03	Dec. ΔK , constant R	12	475 to 130	15 to 4	R=0.5
CCT PM1-04	Inc. ΔK	5	375 to 1750	12 to 55	R=0.1
CCT PM1-05	Dec. ΔK , constant R	12	550 to 200	17 to 6	R=0.1
CCT PM2-01 RES	Inc. ΔK	5	375 to 2000	12 to 63	R=0.1
CCT PM2-02 RES	Inc. ΔK	5	850 to 2800	27 to 88	R=0.1
CCT PM2-03 RES	Dec. ΔK , constant R	12	500 to 275	16 to 9	R=0.1
CCT PM2-04 RES	Inc. ΔK	5	375 to 1100	12 to 35	R=0.5
CCT PM2-05 RES	Inc. ΔK	5	850 to 1350	27 to 43	R=0.5
CCT PM1-06 RES	Dec. ΔK , constant R	12	475 to 100	15 to 3	R=0.5

In all tests it was necessary to ensure that the strict validity criterion of BS 12108 for the uncracked ligament ahead of the crack tip (Eq. [4.4.1]) was adhered to, thus further ensuring that the data produced were valid.

$$(W - 2a) \geq \frac{1.25\lambda F_{\max}}{BR_{p0.2}} \quad [4.4.1]$$

where W is the specimen width, $2a$ is the crack length, B is the specimen thickness, F_{\max} is the maximum force (kN), λ is the distance between external and internal supports and $R_{p0.2}$ is the 0.2% proof strength at test temperature.

Five tests were performed on the plain steel specimens, two at $R=0.1$ and three at 0.5 . The results are presented in Figures 4.4.1 and 4.4.2 respectively. Also shown for comparison are the mean and mean +2 standard deviations (sd) (recommended for design) two-stage curves for steels in air from BS 7910 (BSI, 2013).

Referring to Figure 4.4.1, the data show generally good correlation with the BS 7910 curves. Some scatter is observed during the decreasing ΔK tests, at approximately $200 - 300 \text{N/mm}^{3/2}$ ($6 - 10 \text{MPa.m}^{1/2}$).

The data in Figure 4.4.2, again correlate well with the curves given in BS 7910 and exhibit marginally less scatter than at $R = 0.1$.

The effect of stress ratio on FCGR for the plain material can be seen in Figure 4.4.3. As is generally found (Maddox *et al.*, 1978; Skorupa and Skorupa, 2005; Zhao *et al.*, 2008) the plain steel generally showed a slightly faster crack growth rate at $R=0.5$ than at $R=0.1$. Also as expected, there was a strong effect of R in the regime near the threshold (i.e. the threshold decreased with increase in R).

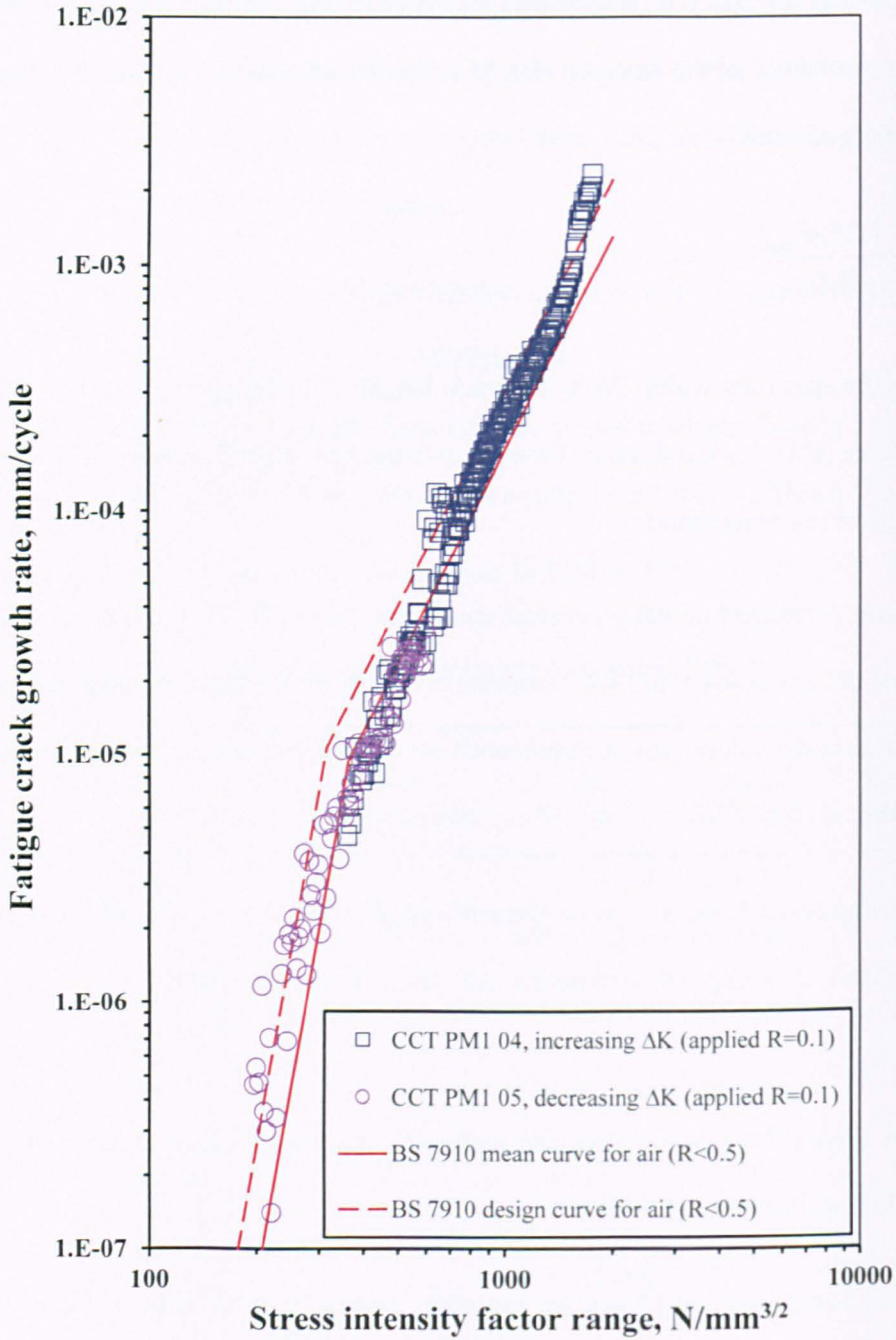


Figure 4.4.1 Summary of fatigue crack growth data for plain S355 steel specimens obtained at $R=0.1$.

Taking the data generated under each stress ratio and assuming that they follow a two-stage relationship, as in BS 7910, Paris law coefficients were determined by least squares linear regression treating $\log da/dN$ as the dependent variable. The two stage transition point given in BS 7910 was used for the data as visually they appeared to agree well. The resulting fatigue crack growth rate laws for da/dN in mm/cycle and ΔK in $N/mm^{3/2}$ are given in Table 4.4.2.

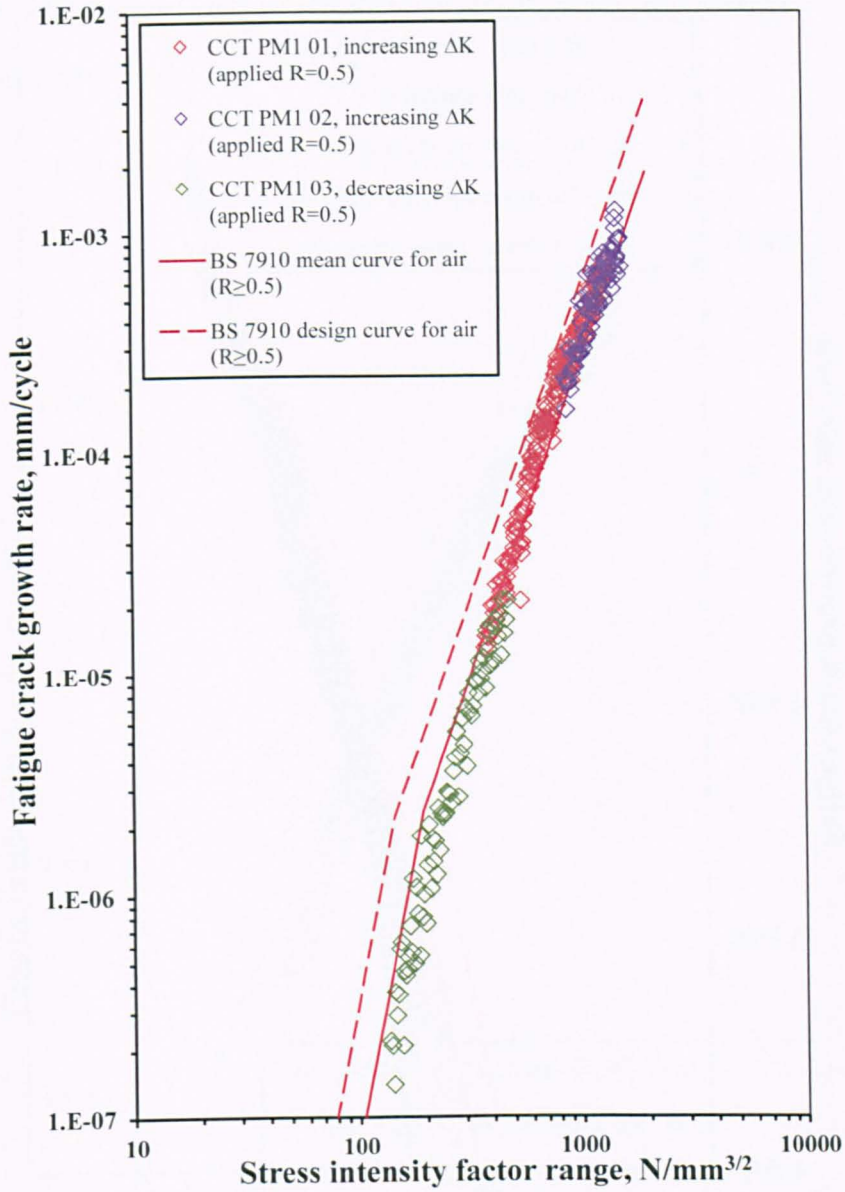


Figure 4.4.2 Summary of fatigue crack growth data for plain S355 steel specimens obtained at $R=0.5$.

Table 4.4.2 Fatigue crack growth rate laws derived for S355.

Stress ratio, R	S355 mean curve, plain				S355 mean curve, welded				Stage A/Stage B transition point ΔK $N/mm^{3/2}$
	Stage A		Stage B		Stage A		Stage B		
	C	m	C	m	C	m	C	m	
<0.5	9.42×10^{-19}	5.06	1.32×10^{-14}	3.41	1.11×10^{-18}	5.07	1.19×10^{-12}	2.78	363
≥ 0.5	1.37×10^{-17}	4.78	3.37×10^{-14}	3.33	2.76×10^{-13}	2.95	3.07×10^{-13}	3.01	196
Simplified curve for S355, welded				$m = 3, C = 2.78 \times 10^{-13}$					

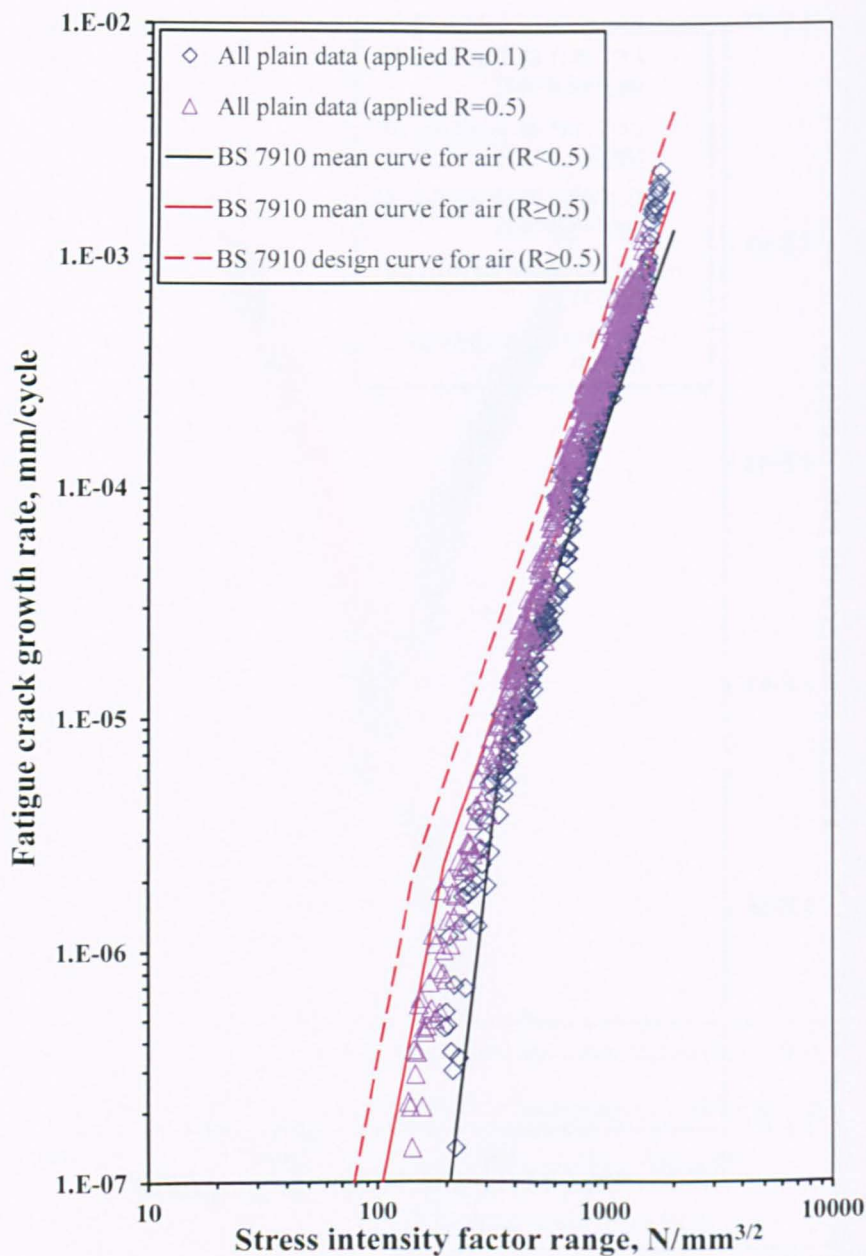


Figure 4.4.3 Summary of fatigue crack growth data for plain S355 steel specimens showing effect of stress ratio.

The increase in da/dN with R is one of the reasons why the presence of tensile residual stresses due to welding reduces fatigue life. In order to study the effect of high tensile residual stress directly, six tests were performed on CCT specimens with longitudinal weld beads on each surface. Tests were conducted with applied $R=0.1$ and 0.5 . The data obtained are presented in Figures 4.4.4 and 4.4.5 respectively, again in comparison with the BS 7910 mean and mean +2sd (design) curves. No account of the changing effective stress ratio at the crack tip as the crack grows through the weld

residual stress field has been included. Instead, the applied stress ratio as used in the PM tests is stated for comparison with BS 7910 (BSI, 2013).

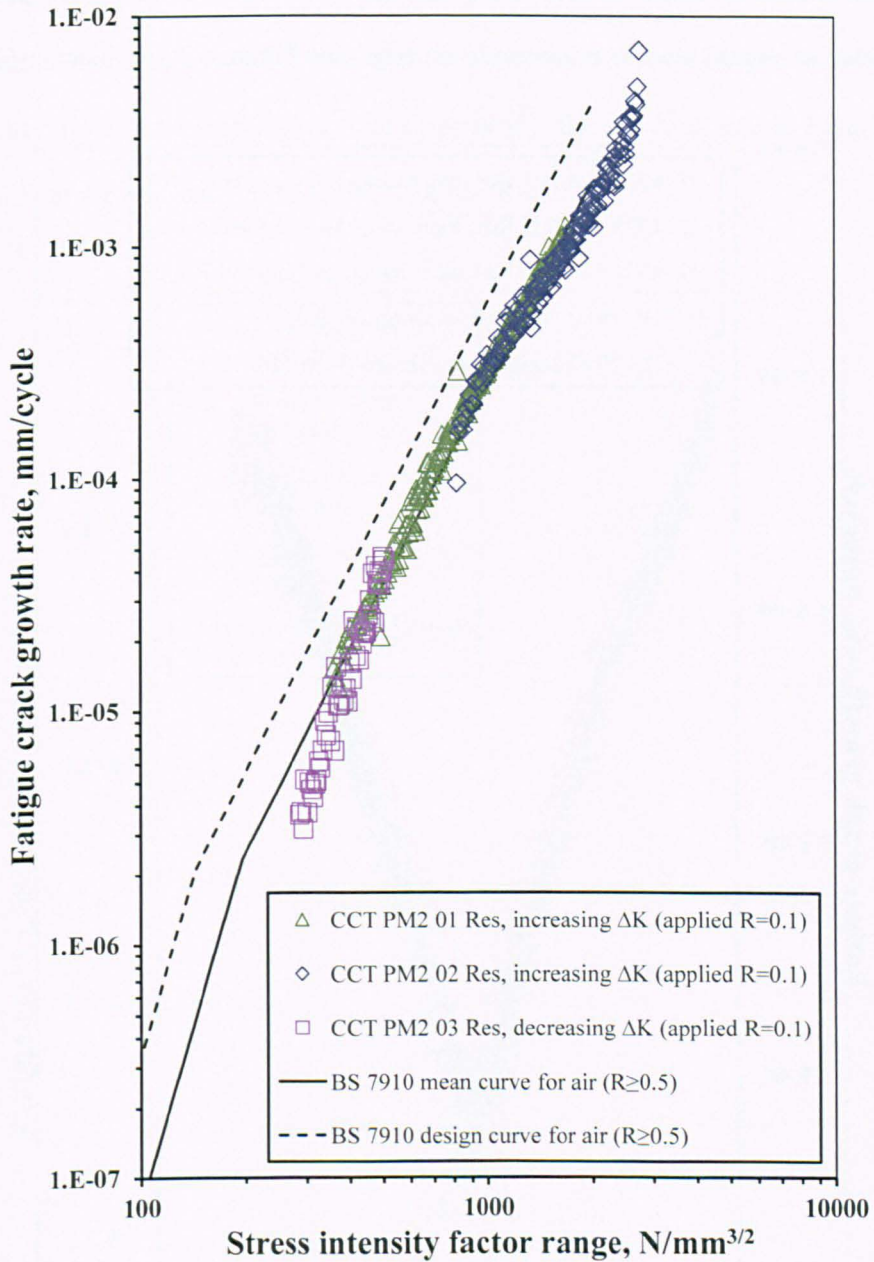


Figure 4.4.4 Summary of fatigue crack growth data for S355 steel welded specimens obtained at $R=0.1$.

The residual stress distribution in the CCT specimens with weld beads is discussed in detail in Chapter 6. The magnitude of residual stress found 2mm from the notch tip, using the centre hole technique, was 481N/mm², compared with the yield strength of 455-470N/mm² for this steel. This is reasonable since, as previously explained, the process of welding typically produces residual stresses of yield or proof strength magnitude in the region of the weld. The fact that the measured

residual stress is higher than yield/proof, results from the assumption in the residual stress measurement analysis, that a constant Young's modulus exists, in reality this is not the case. The residual stress is then expected to decrease away from the weld, becoming compressive before returning to zero or slightly tensile at the specimen edge (see Figure 6.3.1 in Chapter 6).

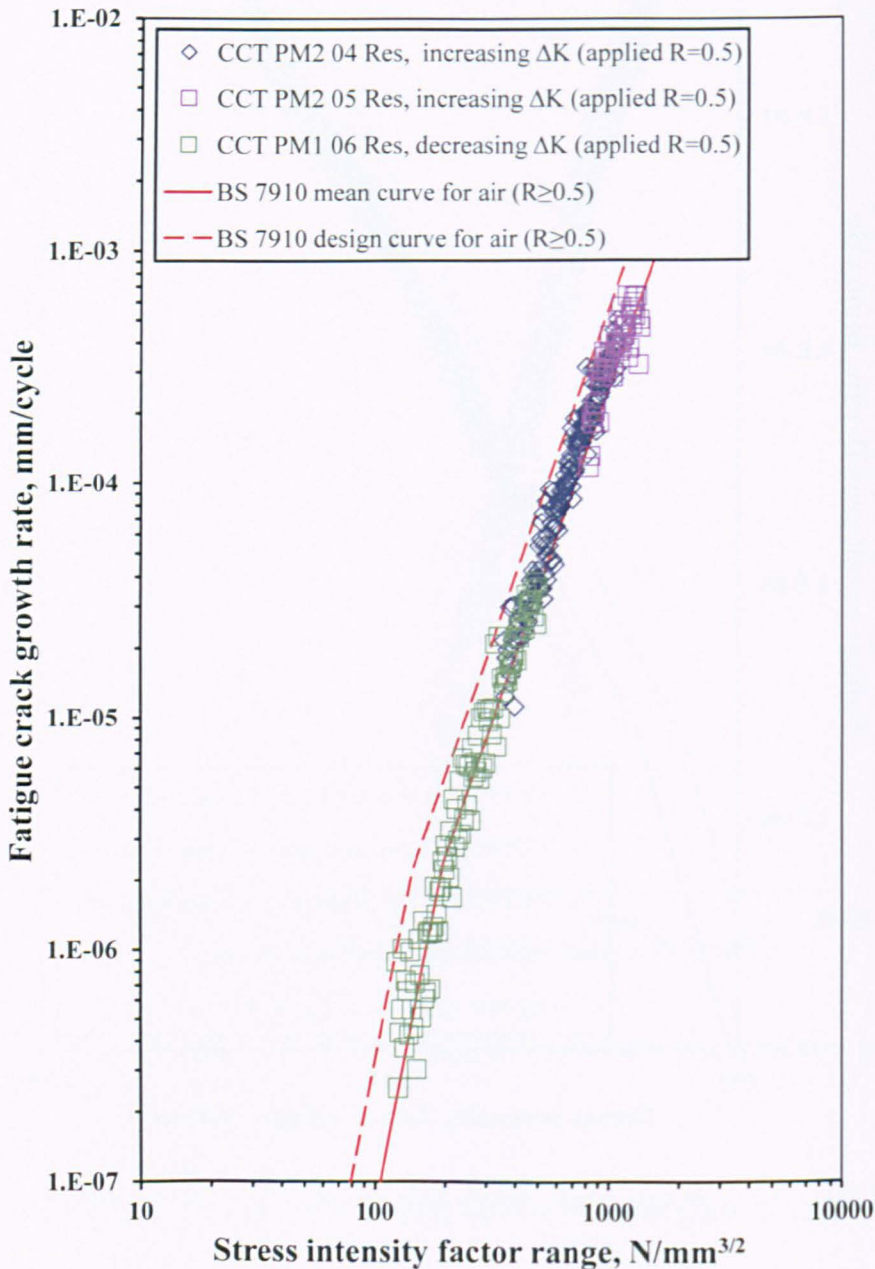


Figure 4.4.5 Summary of fatigue crack growth data for S355 steel welded specimens obtained at $R=0.5$.

In the case of the present CCT specimens, the residual stress distribution extending out from the central notch was measured. The residual stress was found to become compressive at a distance of 38mm from the centre of the notch.

With regard to fatigue crack growth, the data obtained at $R=0.1$ in Figure 4.4.4 show good agreement with the BS 7910 curve for $R \geq 0.5$. This is reasonable in view of the presence of tensile residual stresses, which have the effect of increasing the effective stress ratio. The results indicate that the effective stress ratio was 0.5 or higher. In the case of the specimens tested at $R=0.5$ the effective stress ratio will be even higher, Not surprisingly, the resulting data in Figure 4.4.5 again correlate well with the relevant curves in BS 7910, for $R \geq 0.5$.

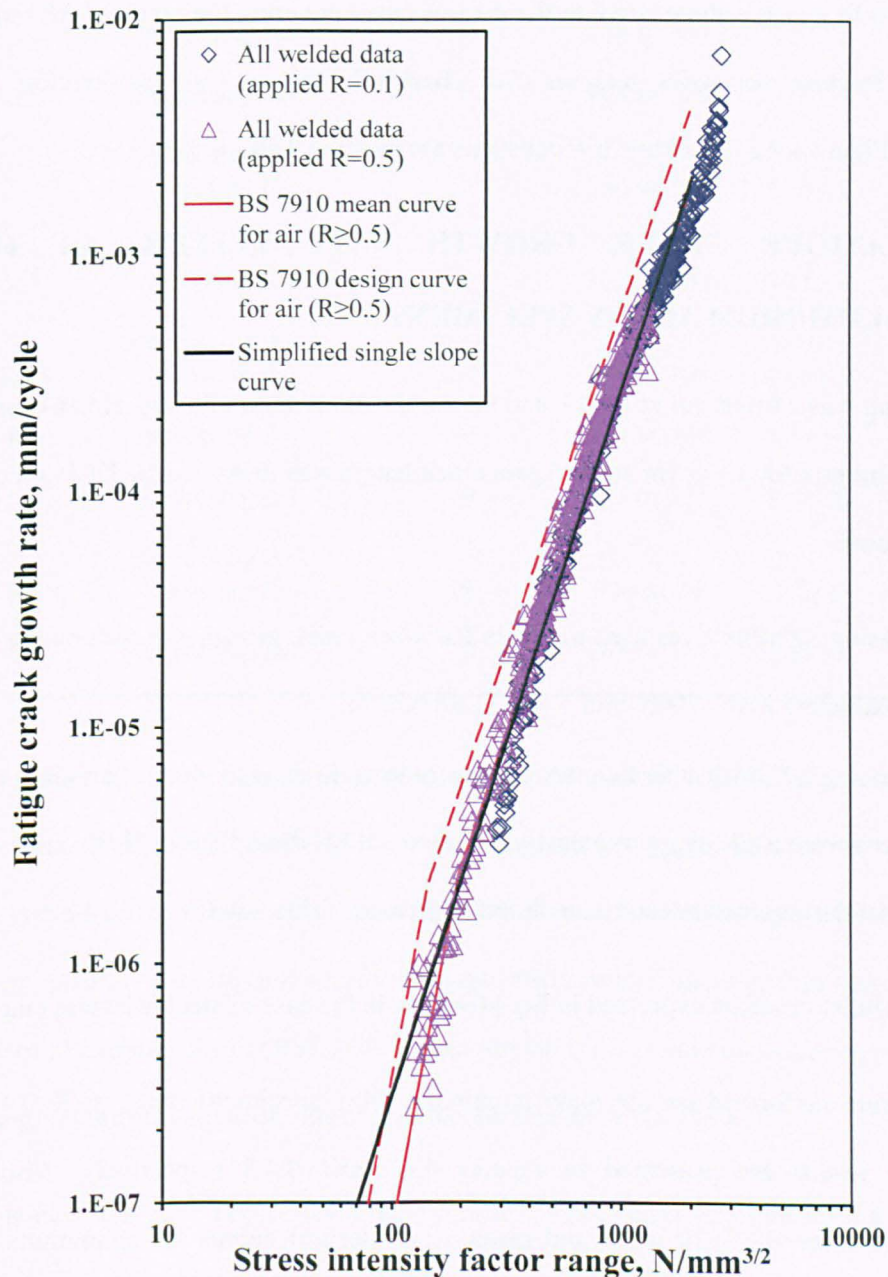


Figure 4.4.6 Summary of fatigue crack growth data for S355 steel welded specimens showing effect of stress ratio.

The Paris law coefficients for the weld bead specimens are given in Table 4.4.2. The results obtained at the two R values are compared in Figure 4.4.6. Where direct comparison is possible, above $\Delta K = 300\text{N/mm}^{3/2}$ ($9\text{MPa}\cdot\text{m}^{1/2}$), there is no significant difference. Thus, it seems that the presence of the high tensile residual stress has saturated the effect of R over the range considered.

In BS 7910 (BSI, 2013), a simplified single slope curve is given in addition to the standard two-stage curves in the recommended FCGR laws for steels. Looking at Figure 4.4.6, it looks equally reasonable to fit a single slope curve to the data. A curve covering the range of ΔK values relevant to the later fracture mechanics analyses (See Chapter 7, Section 7.6) was therefore fitted and is included in Figure 4.4.6. The Paris law constants are given in Table 4.4.2.

4.4.2 FATIGUE CRACK GROWTH RATE TESTING OF 6082 T651 ALUMINIUM ALLOY SPECIMENS

FCGR testing was carried out at R=0.1 and 0.5 on the aluminium alloy specimens using the same conditions and procedures as for steel. Again crack length was measured by DCPD. Further details were as follows:

- Increasing ΔK tests were used to obtain Paris-law crack growth rate data over a ΔK range of approximately $270 - 700\text{N/mm}^{3/2}$ ($8 - 22\text{MPa}\cdot\text{m}^{1/2}$).
- Decreasing ΔK tests with a constant stress ratio were used to obtain Paris-law crack growth rate data from a ΔK of approximately 330 down to $75\text{N/mm}^{3/2}$ ($10 - 2\text{MPa}\cdot\text{m}^{1/2}$).

A summary of the parameters used in each test is given in Table 4.4.3.

The same validity criterion expressed in Eq. [4.4.1] as in the case of steel tests was employed.

Five tests were performed on the plain aluminium alloy specimens, three at R=0.1 and two at R=0.5. The results are presented in Figures 4.4.7 and 4.4.8 respectively. Also shown for comparison are the BS 7910 mean and mean +2sd (design) curves for aluminium. These were derived on the basis of the difference in Young's Modulus between steel and aluminium using Eq. [4.4.2], as suggested in BS 7910 (2013).

$$C = \text{Stage A or } B_{\text{steel}} \left(\frac{E_{\text{steel}}}{E_{\text{al alloy}}} \right)^m \quad [4.4.2]$$

Table 4.4.3 Test parameters for fatigue crack growth rate tests in 6082 T651 aluminium alloy.

Specimen no.	Test type	Test frequency, Hz	ΔK , N/mm ^{3/2}	ΔK , MPa.m ^{1/2}	Other test parameters
CCT AL-01	Increasing ΔK	2	280 to 399	9 to 13	R=0.1
CCT AL-02	Increasing ΔK	2	268 to 469	8 to 15	R=0.5
CCT AL-03	Increasing ΔK	5	268 to 720	8 to 23	R=0.1
CCT AL-04	Decreasing ΔK , constant R	8	330 to 114	10 to 4	R=0.1
CCT AL-05	Decreasing ΔK , constant R	8	320 to 100	10 to 3	R=0.5
CCT AL-06 RES	Decreasing ΔK , constant R	10	334 to 108	11 to 3	R=0.1
CCT AL -08 RES	Increasing ΔK	10	275 to 504	9 to 16	R=0.1
CCT AL -09 RES	Increasing ΔK	10	275 to 513	9 to 16	R=0.5
CCT AL -10 RES	Decreasing ΔK , constant R	12	238 to 74	5 to 2	R=0.1
CCT AL -13 RES	Increasing ΔK	10	163 to 351	5 to 11	R=0.5

Referring to Figure 4.4.7, the data show generally good correlation with the mean curve given in BS 7910 for ΔK values $>200\text{N/mm}^{3/2}$ ($6\text{MPa.m}^{1/2}$), but much lower growth rates below this value. In addition, instead of the characteristic two stage crack growth relationship found for steel, the present aluminium alloy data suggest a multiple stage relationship. This effect has been observed in a wide range of aluminium alloys (BSI, 2007), even though it is not acknowledged in the 2-stage or simplified single stage crack growth rate curves recommended in BS 7910.

The data obtained at R=0.5, Figure 4.4.8, also hint at a multi-stage relationship but perhaps the most striking difference compared with the R=0.1 data in Figure 4.4.7 is the disagreement between the growth rates obtained under increasing and decreasing ΔK conditions above $250\text{N/mm}^{3/2}$ ($8\text{MPa.m}^{1/2}$).

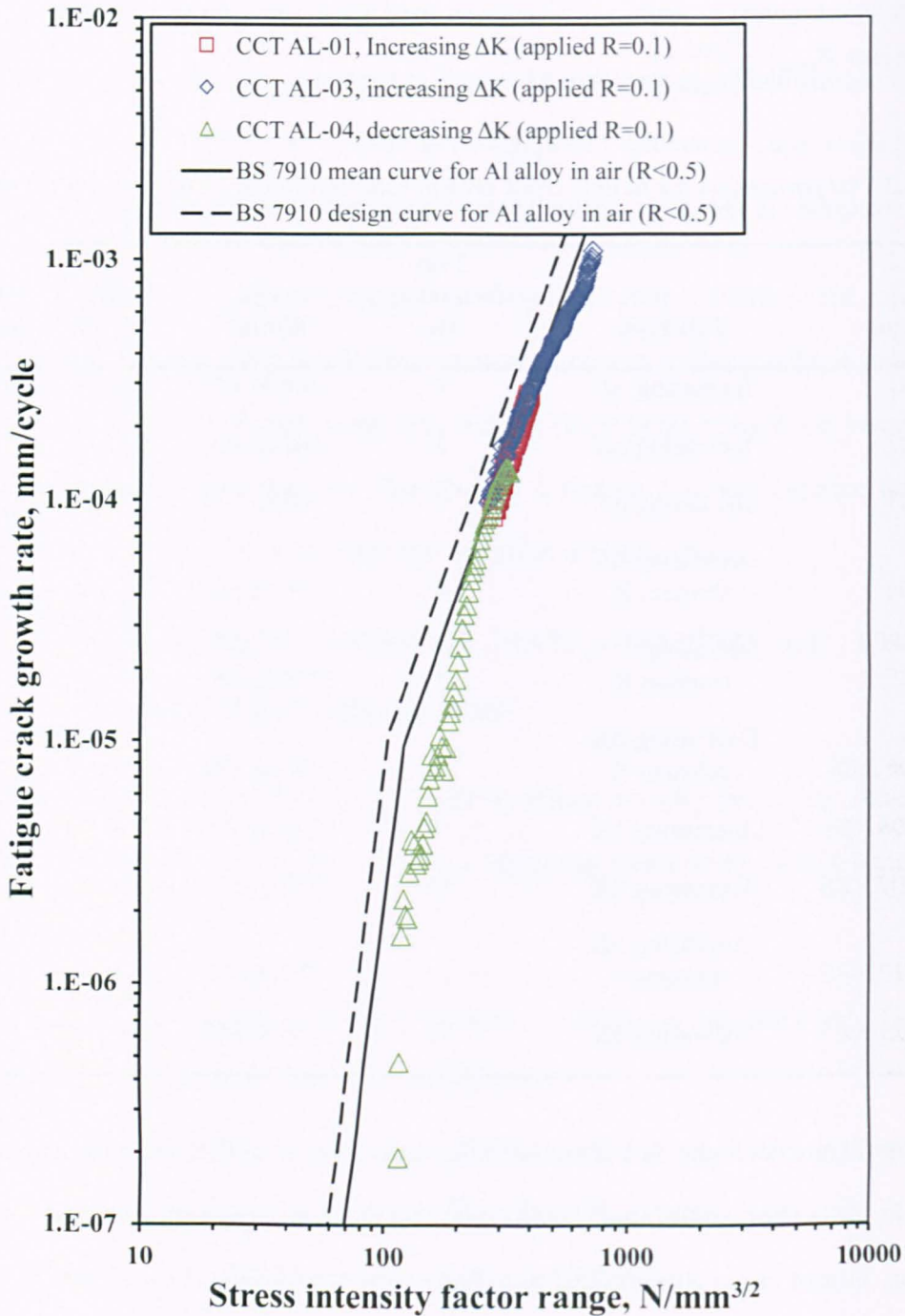


Figure 4.4.7 Summary of fatigue crack growth data for plain 6082 T651 aluminium alloy specimens obtained at $R=0.1$.

The consistency of the increasing ΔK data was thought to indicate that they were the more reliable and so the decreasing ΔK test was repeated (the green triangles). However, similar results were obtained. Therefore, the difference cannot be explained, although it could well simply be a reflection of the scatter inherent in fatigue test data.

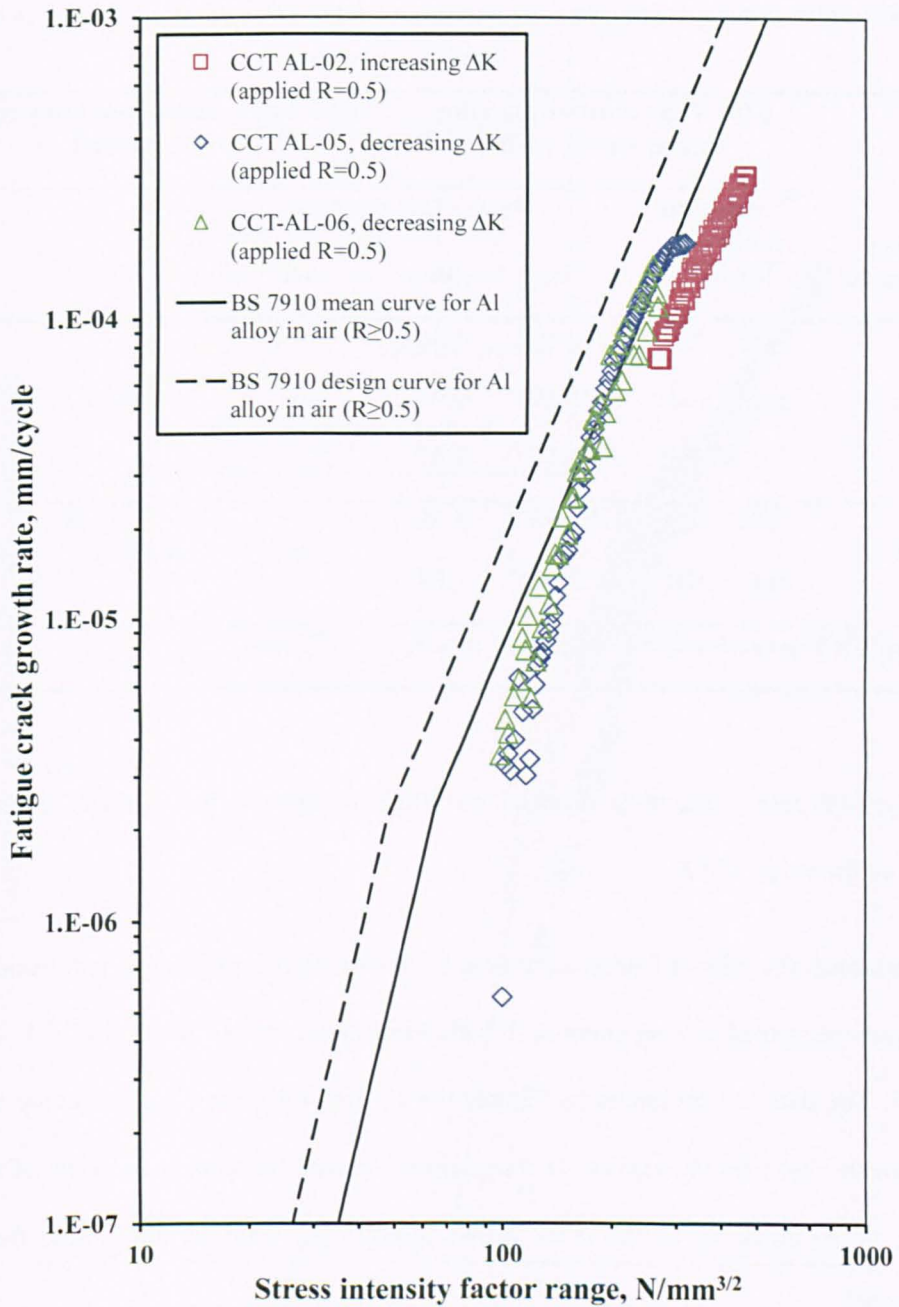


Figure 4.4.8 Summary of fatigue crack growth data for plain 6082 T651 aluminium alloy specimens obtained under conditions of $R=0.5$.

Paris law coefficients for multiple stage relationships fitted to each set of data were determined for da/dN in $mm/cycle$ and ΔK in $N/mm^{3/2}$ and are given in Table 4.4.4. The relevant stage transition points were selected visually from the natural slopes of the data. The effect of stress ratio on FCGR for the plain material is shown in Figure 4.4.9.

Table 4.4.4 Fatigue crack growth rate laws derived for 6082 T651 aluminium alloy in air.

Stress ratio, R	6082 T651 aluminium alloy mean curve, plain			6082 T651 aluminium alloy mean curve, welded		
	Transition point ΔK N/mm ^{3/2}	C	m	ΔK	C	m
<0.5	A/B = 120	1.61×10^{-15}	4.36	>63	6.29×10^{-12}	3.00
	B/C = 185	2.39×10^{-21}	6.91			
	C/D = 230	9.47×10^{-11}	2.47			
≥ 0.5	A/B = 120	1.12×10^{-17}	5.68	>63	8.56×10^{-12}	2.97
	B/C = 180	9.17×10^{-9}	1.68			
Simplified curve for 6082, welded			$m = 3, C = 6.87 \times 10^{-12}$			

The crack growth rate in the plain material was slightly higher at R=0.5 than 0.1, the difference depending on the value of ΔK .

Again, to establish the effect of stress ratio on a CCT specimen containing tensile residual stresses, five tests were performed on specimens with weld beads at an applied R=0.1 and 0.5, as detailed in Table 4.4.3. The data are presented in Figures 4.4.10 and 4.4.11 and again include the BS 7910 mean and mean +2sd (design) curves for comparison. As with the steel, no account of the changing stress ratio at the crack tip as the crack grows through the weld residual stress field has been included.

Referring to Figure 4.4.10, the data show good agreement with the BS 7910 curve for R \geq 0.5. As with the steel specimens, the magnitude of residual stress was determined 2mm from the notch tip (Chapter 6) and was found to be 77N/mm². This is clearly below the 0.2% proof strength given in Table 4.3.2, but this is to be expected in view of the lower strength of the material affected by HAZ softening. As noted previously, the effect of welding on 6082 aluminium alloy in the T6 condition is expected to reduce the proof strength, and hence residual stress, by a factor of two (BSI, 1991). However, the reduction here is much greater, suggesting that the low constraint on the cooling weld offered by the thin (6mm) further affected the magnitude of residual stress due to the weld beads.

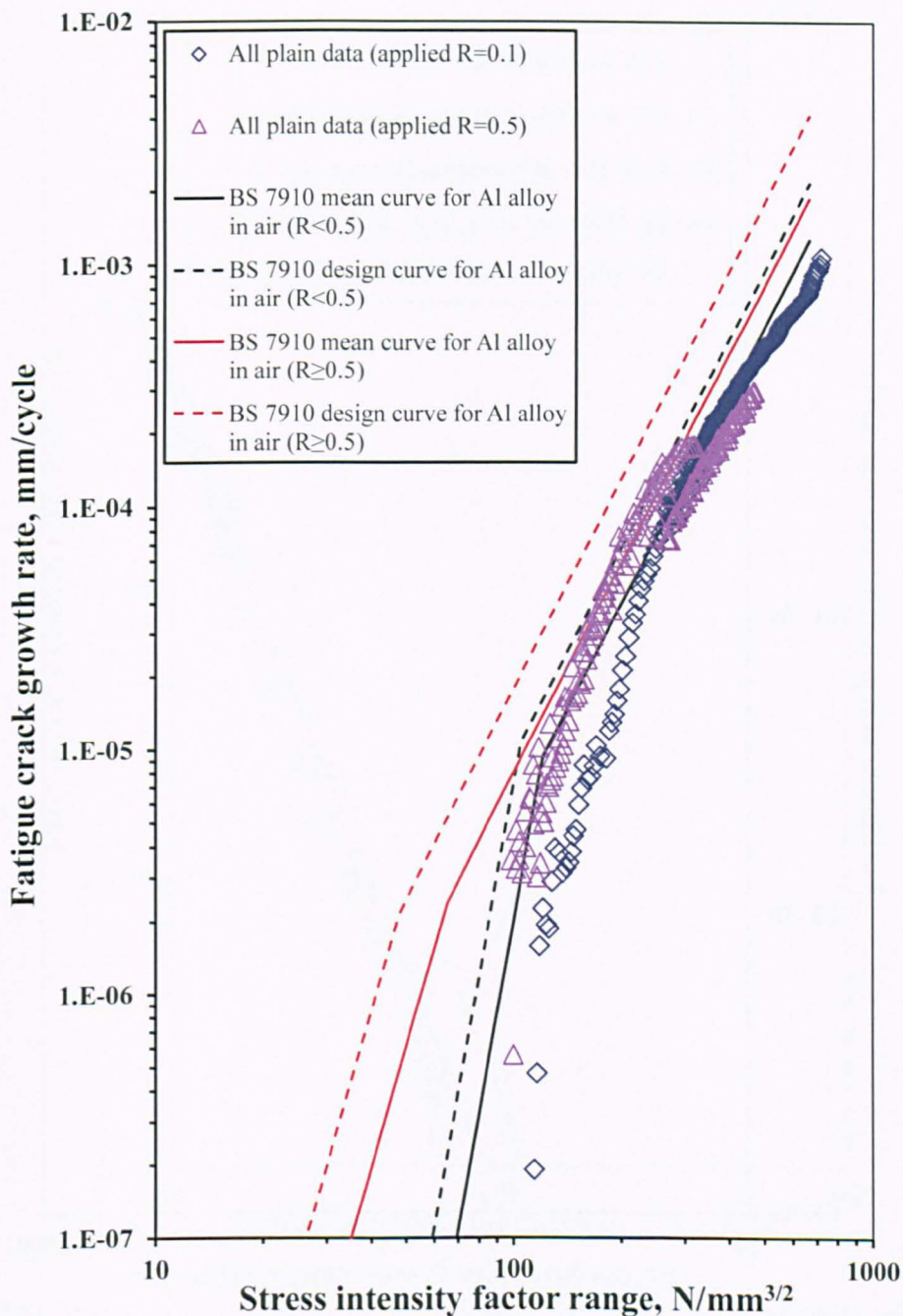


Figure 4.4.9 Summary of fatigue crack growth data for plain 6082 T651 aluminium alloy specimens showing effect of stress ratio.

Even though the residual stress was low, the effective stress ratio resulting from the application of cyclic loading at $R = 0.1$ is still relatively high. Based on the maximum measured residual stress of 77N/mm^2 , the effective stress ratio was calculated to be >0.50 (0.57). Thus, comparison with the BS 7910 $R \geq 0.5$ curves is reasonable, as reflected by their good agreement with the test data in Figure 4.4.10.

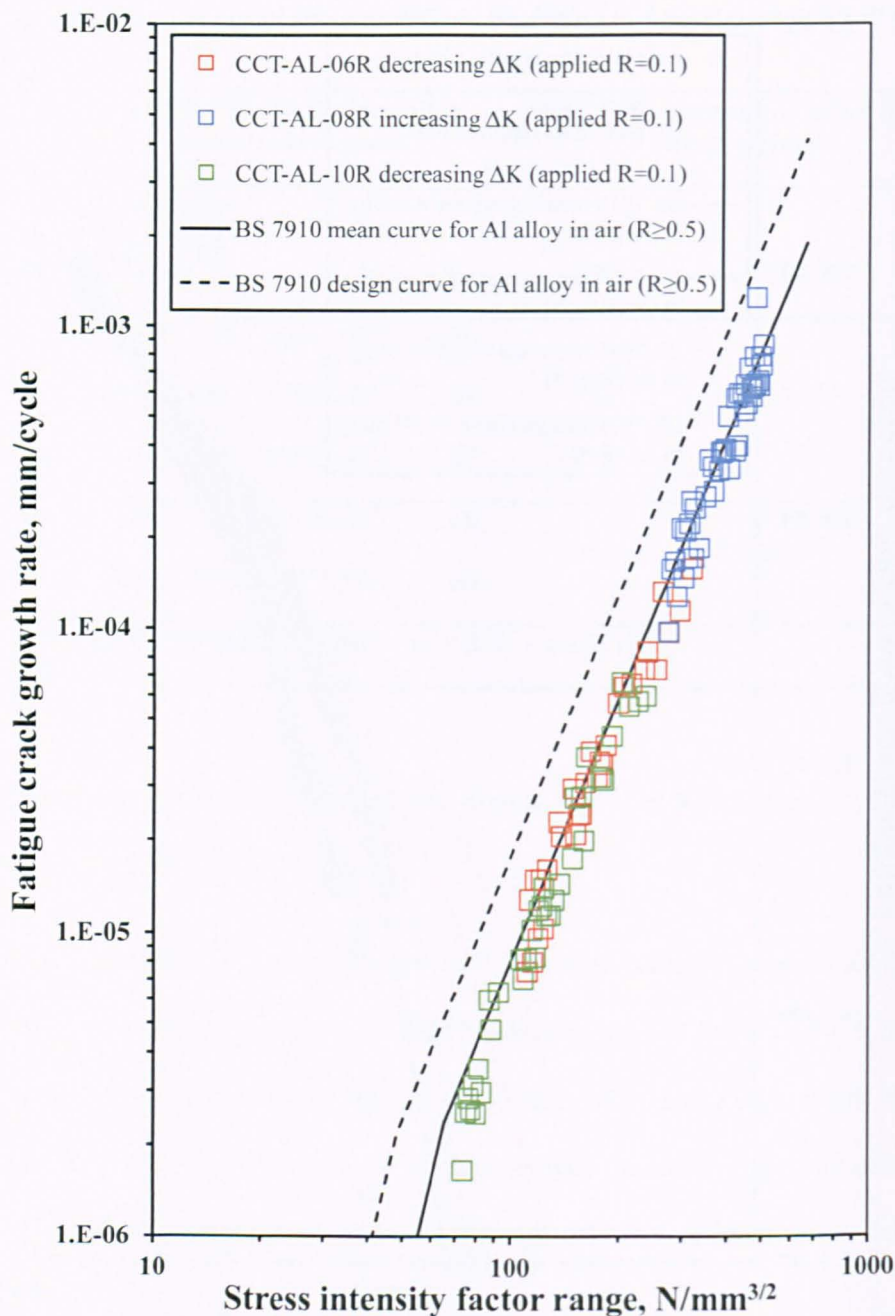


Figure 4.4.10 Summary of fatigue crack growth data for 6082 T651 aluminium alloy welded specimens obtained at $R=0.1$.

Turning to the results obtained with an applied stress ratio of 0.5 in Figure 4.4.11, the increasing ΔK data are in good agreement with the BS 7910 recommended mean curve. In contrast to the tests performed on plain aluminium specimens, there is good correlation between the ΔK -increasing and ΔK -decreasing test data.

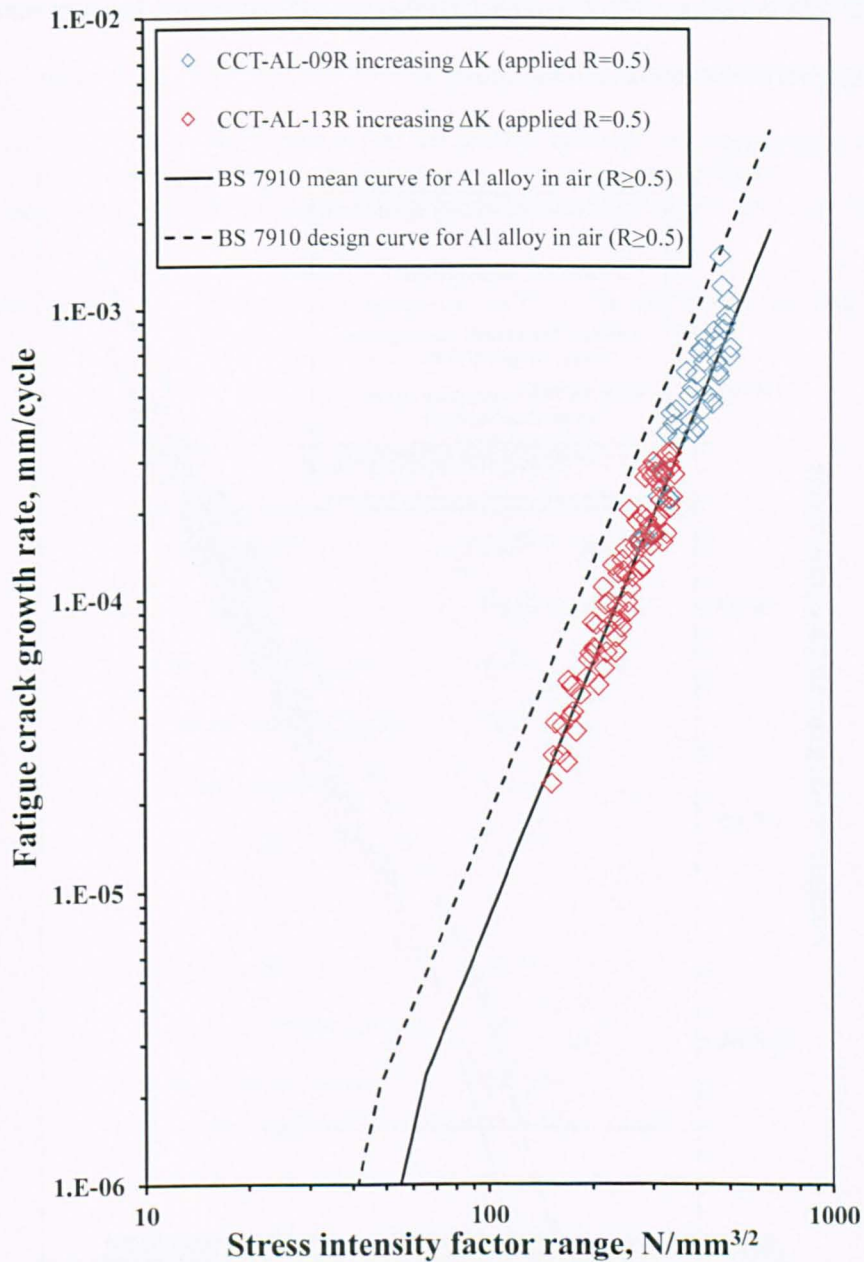


Figure 4.4.11 Summary of fatigue crack growth data for 6082 T651 aluminium alloy welded specimens obtained at $R=0.5$.

The Paris law coefficients for the welded specimens are given in Table 4.4.4. Over the available range and for both R values, the data do not support 2-stage crack growth laws and therefore single slope curves have been fitted to each. Indeed, as will be evident from the Paris law constants for the two R values and the comparison of the two sets of data in Figure 4.4.12, there was no significant effect of R and it would not be unreasonable to fit a single Paris law to the combined data. The resulting Paris law constants are included in Table 4.4.4. This situation is not surprising in view of the fact that the effective values of R in the presence of the tensile residual stress due to welding

were both high. As with the steel, it would seem that the influence of R has saturated, even in the presence of relatively low tensile residual stress.

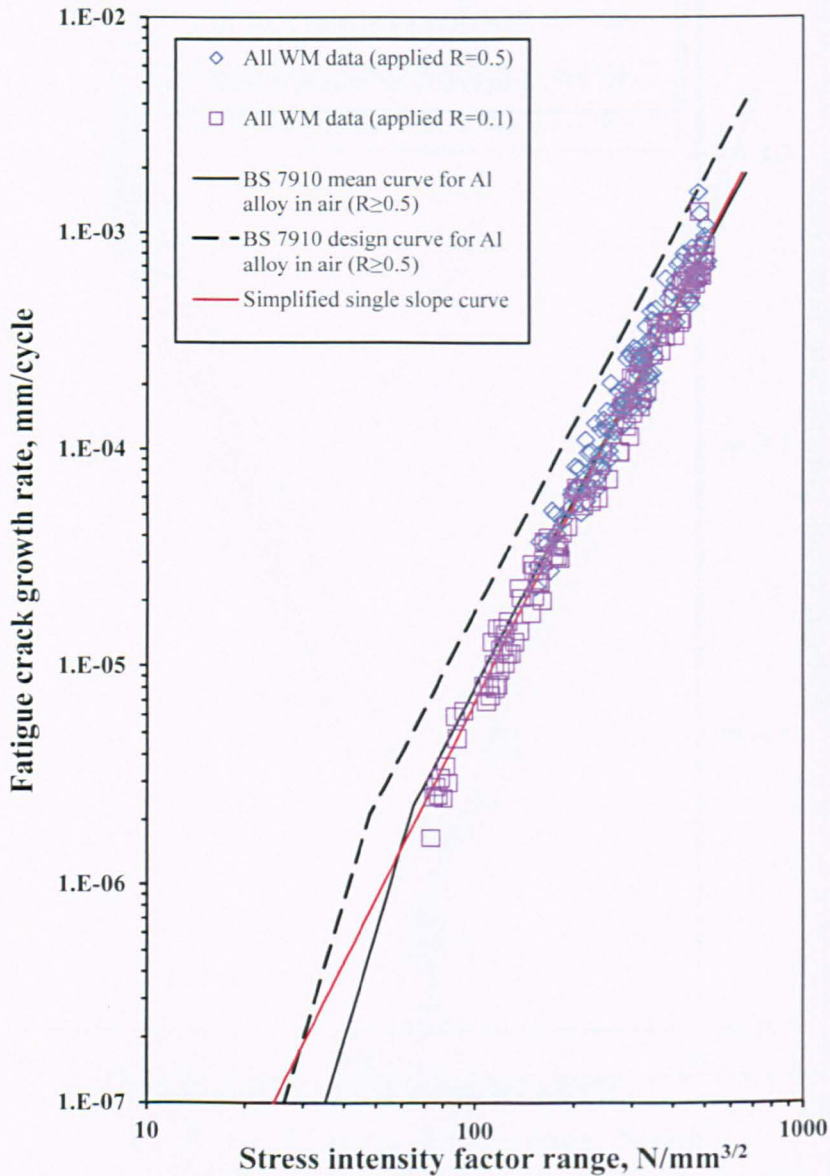


Figure 4.4.12 Summary of fatigue crack growth data for 6082 T651 aluminium alloy welded specimens showing effect of stress ratio.

4.5 X-RAY COMPUTED TOMOGRAPHY

As discussed in Chapter 3, x-ray computed tomography (X-CT) was used to provide an indication of the sizes of any flaws present at the toes of the welds in the S355 steel fillet-welded specimens. The area of interest was the weld return around the end of the attachment as this is the location where fatigue cracking occurs in this specimen. A 225kV HUTCH μ -CT machine at Southampton University was used to perform the measurements. The scan settings used are given in Table 4.5.1.

The most severe inherent flaw observed at the return weld toe in the fillet welded steel specimen was undercut, Figure 4.5.1. This was not located in the centre of the return weld, where fatigue cracking is most likely, but at one corner where the welder had tried to sweep around the end of the longitudinal attachment. However, it could still provide the site for fatigue crack initiation.

Table 4.5.1 HUTCH scan parameters for weld toe weld return location on a steel fillet welded specimen.

Scan parameter set 1	
μ -CT machine	225kV HUTCH
Target	Reflection
Beam energy (kV)	210
Beam intensity (μ A)	54
Filler material	Copper
Exposure (sec)	0.354
Gain	5
Projections	3,142
Frames per projections	16
Resolution (μ m)	13.69

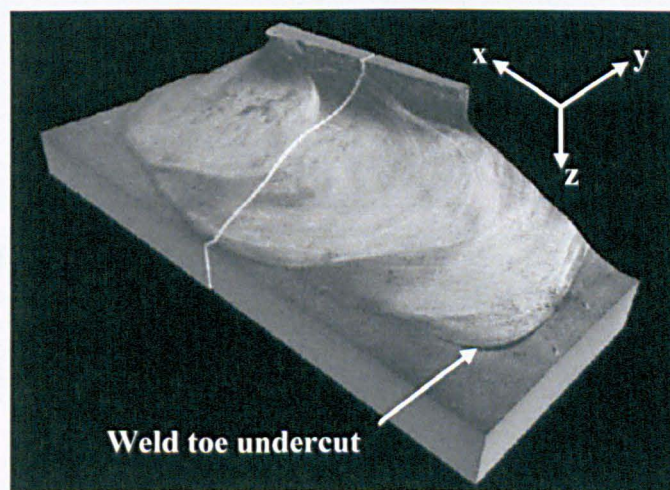


Figure 4.5.1 Weld return showing an approximate overview of the weld model, and location of weld toe undercut.

The secant length of the undercut was 4.55mm with an inner perimeter length of 4.66mm and an outer perimeter length of 5.25mm, the maximum width was found to be 0.77mm, Figure 4.5.2c).

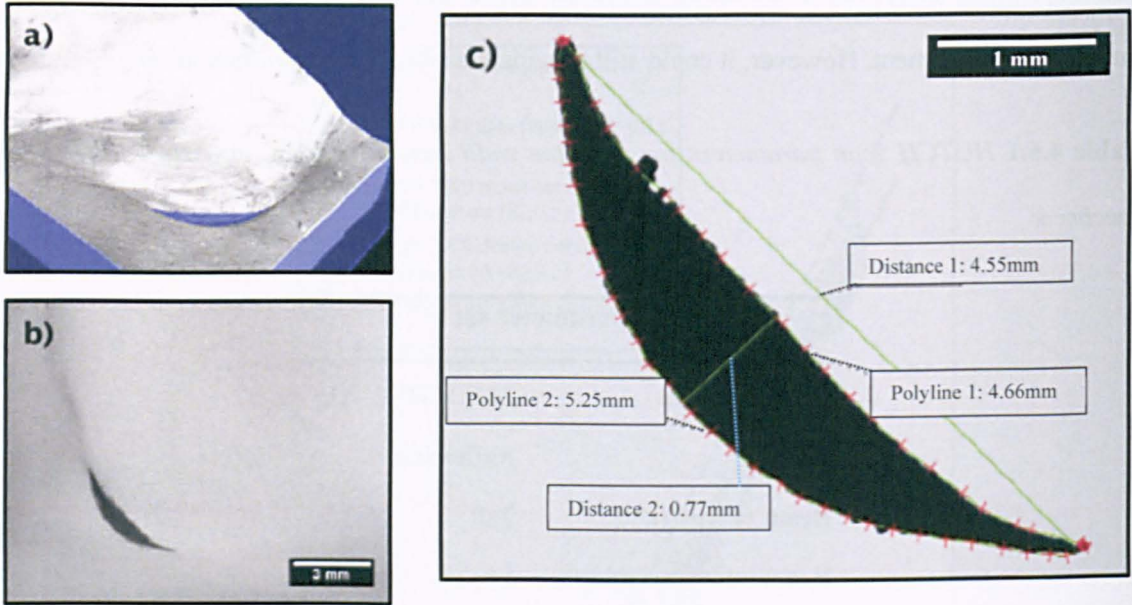


Figure 4.5.2 Weld toe undercut observed at weld return location, a) defect viewed in 3D model, b) μ -CT slice of defect in x-y plane, c) defect dimensions in x-y plane.

The 3D model was re-sectioned in the x-z plane to establish the maximum depth of the undercut, which was measured to be 0.29mm, Figure 4.5.3.

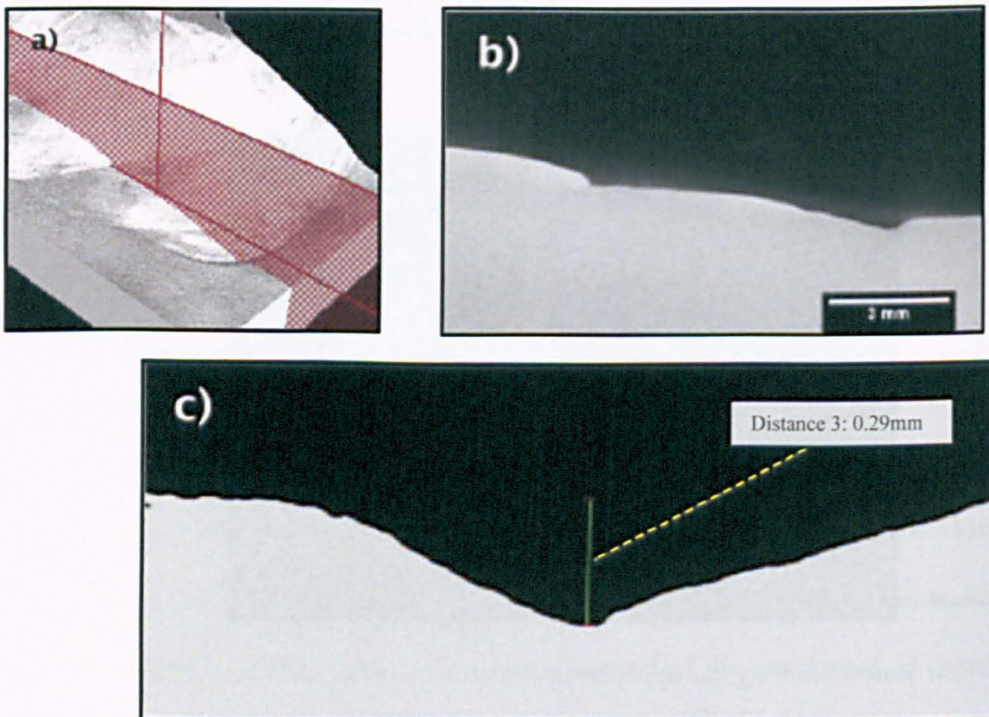


Figure 4.5.3 location of plane in 3d volume, b) μ -CT slice in x-z plane, c) defect dimensions.

Further examination along the weld toe found a small notch-like feature (undercut) associated with weld spatter (Figure 4.5.4) which measured 0.105mm in length and 0.030mm at its deepest point. This is comparable with measurements made on several fillet welded BS 968 high tensile steel specimens (Signes *et al.*, 1967), where it was reported that very slight undercut, up to 0.076mm in depth, was present in all specimens. It was concluded that a small degree of weld toe undercut must be expected even with good welding practice.

Defect sizes in fillet welded joints made from mild steel were also examined (Smith and Smith, 1982) by means of optical microscope, with average depths of 0.045mm being reported. Therefore, the undercut depicted in Figure 4.5.4 is likely to be a true reflection of typical values of undercut found in the S355 structural steel used in this research. The larger undercut shown in Figure 4.5.1 is likely to be due to poor positioning during welding and would not be representative for all specimens. It should, however, be noted that its depth (0.29mm) is not untypical and the BS 7608 design *S-N* curve for this weld detail is still considered to be applicable for undercut up to a depth of 1mm (BSI, 2013).

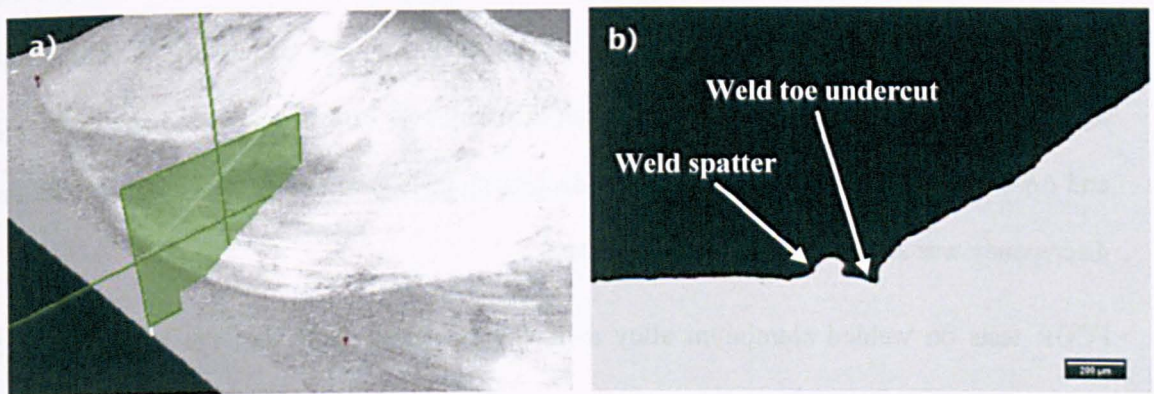


Figure 4.5.4 Location of small notch-like defect (undercut) located adjacent to weld spatter at the end of the weld return.

4.6 SUMMARY

The materials selection and characterisation work described in this Chapter has indicated the following:

- The two materials chosen for the project, namely S355J2+N structural steel and 6082 T651 aluminium alloy, both met the minimum specified tensile properties (0.2% proof and tensile strength) as denoted by material certificates.
- Low cycle fatigue testing revealed some cyclic hardening in the steel and marginal hardening followed by softening in the aluminium alloy.
- FCGR tests on plain steel at $R=0.1$ and $R=0.5$ showed good correlation with the recommended crack growth curves in BS 7910.
- FCGR tests on welded steel at $R=0.1$ showed good agreement with the BS 7910 $R \geq 0.5$ curves, indicating that the effective stress ratio due to the presence of tensile residual stress from welding was 0.5 or higher. The crack growth rate was no higher for an applied R of 0.5 indicating that the effect of R had saturated as a result of the presence of the high tensile residual stress.
- FCGR tests on plain aluminium alloy at $R=0.1$ showed good agreement with the mean curve in BS 7910 at $\Delta K > 200 \text{N/mm}^{3/2}$. Multiple stage crack growth was also observed with growth rates $< 200 \text{N/mm}^{3/2}$ being lower than the curve. At $R=0.5$, the data were in reasonable agreement with the BS 7910 curves, although disparity between the test type (ΔK -increasing and ΔK -decreasing) was found. Repeat ΔK -decreasing tests gave similar results; therefore the discrepancy was attributed to scatter in test data.
- FCGR tests on welded aluminium alloy at $R=0.1$ correlated well with the BS7910 $R \geq 0.5$ curves in spite of the relatively low level of residual stress due to welding. However, it was shown to be sufficient to increase the R value from the applied value of 0.1 to an effective value of 0.57. The crack growth rates at $R=0.5$ were in good agreement and it proved justifiable to combine the $R=0.1$ and 0.5 data to produce a Paris law. In contrast to the plain material tested at $R=0.5$, good agreement was obtained between the ΔK -increasing and ΔK -decreasing test results.
- X-ray tomography performed on steel fillet welded specimens found undercut at the weld return measuring $\sim 4.55 \text{mm}$ in length, 0.77mm in width and a depth of 0.29mm . However, this

was thought to be due to poor welder positioning and not a true reflection for all specimens. Further examination found more typical undercut resulting from weld spatter measuring 0.105mm in length by 0.030mm in depth, which agreed well with other findings in the literature.

Chapter 5

THE EFFECT OF PERIODIC UNDERLOADS ON FATIGUE CRACK GROWTH RATE

5.1 INTRODUCTION

This Chapter presents details of work performed, using methods described in Chapter 3, to establish the effect on fatigue crack growth rate of simple two-stress magnitude load sequences. These consisted of one large load cycle, termed an underload, followed by ten lower, termed minor, load cycles. Two forms of loading sequence were applied, with the same maximum stress but different magnitudes of underload, selected to encourage crack growth acceleration.

In addition to the effect of underload magnitude on crack growth rate, the effect of residual stress produced by bead-on-plate welds combined with the periodic underloads was investigated.

The Chapter also considers the calculated extent of crack growth under the two types of loading sequence, derived by linear summation of the CA loading growth rates on a cycle-by-cycle basis. These are compared with actual data, to estimate the crack growth acceleration factors. Fractographic examination was also used to estimate acceleration factors from striation spacings.

The effect of load interaction on crack propagation is assessed by the factors γ and β given in Eqs [5.1.1] and [5.1.2]:

$$\gamma = \frac{\text{Measured crack growth rate from VA loading test for specific sequence of } \Delta K \text{ values}}{\text{Calculated crack growth rate by linear summation of the CA crack growth response for the same range of } \Delta K \text{ values}} \quad [5.1.1]$$

$$\beta = \frac{\text{Number of cycles to reach a specific crack length based on a linear summation of CA response}}{\text{Actual number of cycles to reach the same crack length from periodic underload test}} \quad [5.1.2]$$

By definition, γ shows how much faster, or slower, the crack propagates compared with the growth expected on the basis of linear summation of CA crack growth rate. It is important to note that it refers to specific ΔK values since useful conclusions cannot be derived by comparing γ values at different values of ΔK .

The factor β shows how many times larger or smaller is the calculated number of cycles to reach a given crack length than the actual from the test. In the present study, β was determined at the final crack length and at crack lengths corresponding to the same ΔK s as those used to determine γ .

From the above definitions, if there are no significant load sequence effects from the periodic underload spectra, so that the calculated responses equal those in the tests, then γ and β will be unity. Anything greater than unity signifies crack growth acceleration, anything less suggests retardation.

By the same token, the widely adopted method for assessing damage under VA loading, provides similar information if the actual fatigue life under VA loading is compared with that calculated by Miner's rule. A ratio less than 1 indicates a shorter life than estimated (i.e. accelerated crack growth), with one greater than 1 suggesting a life longer than estimated (i.e. crack growth retardation). Therefore, establishing the typical acceleration factor from testing can provide an insight into the measures needed to adjust Miner's rule, to provide safe life estimates under spectrum loading.

5.2 FATIGUE CRACK GROWTH RATE TESTING

5.2.1 OUTLINE OF TESTS

Fatigue tests were performed at 10Hz for CA tests and an average of 3.5Hz for VA tests on 8mm thick by 160mm wide S355 structural steel and 6mm thick by 116mm wide 6082 aluminium alloy CCT specimens. To investigate the effect of tensile residual stress acting in the same direction as

the applied loads, identical specimens were also produced with the addition of back-to-back weld beads on the plate surfaces.

In all fatigue crack growth tests, the first 1 to 1.5mm of crack growth was neglected from the analysis because the cracks propagated from the notch tip and not a pre-fatigue crack. This is in accordance with both BS ISO 12108-12 (2012) and ASTM E647-13a (2013a).

Full details of the specimen geometry are given in Section 3.4, with material properties given in Section 4.3.

5.2.2 CONSTANT AMPLITUDE LOADING

A series of CA tests was performed on plain material to establish the number of cycles to failure, for comparison with tests performed under VA loading. In this respect, the applied loading was selected to produce the same stress ranges and stress ratios as those in the two-stress magnitude VA spectra (see Section 5.2.3).

In the case of tests performed under the minor stress range, those in steel were performed at a constant maximum tensile stress of 156N/mm², with stress range $\Delta\sigma$ of 70N/mm², giving a stress ratio (minimum stress/maximum stress in the cycle) $R=0.55$. A plot of recorded crack length versus number of cycles was used to determine the rate of crack growth, da/dN , at specific crack lengths. The corresponding values of ΔK ranged from ~ 350 to ~ 1100 N/mm^{3/2}. In the case of the aluminium alloy specimens, a constant maximum tensile stress of 74N/mm², with a stress range $\Delta\sigma$ of 31.8N/mm², was employed, giving a stress ratio $R=0.57$. Here crack growth over the ΔK range ~ 160 to ~ 400 N/mm^{3/2} was investigated.

The fatigue crack length, $2a$, ranged from the starter notch length of typically 16mm to a final crack length of ~ 94 mm for the steel or ~ 64 mm for the aluminium alloy specimens. Duplicate tests were performed on each material.

Tests were also performed on specimens with bead-on-plate welds at $R=0.10$ in order to demonstrate that the presence of the tensile residual stress due to welding increased the effective R to a value similar to those used in the above tests (e.g. >0.5), as shown in Chapter 4. The range of

ΔK values was chosen to overlap the data referred to above, and the additional test data (below) for the derivation of the acceleration factor. To this end, ΔK rose from $550\text{N/mm}^{3/2}$ to $1410\text{N/mm}^{3/2}$ for steel, and $170\text{N/mm}^{3/2}$ to $500\text{N/mm}^{3/2}$ for the aluminium alloy.

Both underload magnitudes were considered in the tests performed at the underload stress range. Under SBL2 loading (underload stress range of twice the minor stress range), stress ratios of $R=0.10$ (steel) and $R=0.14$ (aluminium alloy) were employed. For SBL1.5 loading (underload 50% higher than minor stress range), the ratios increased to $R=0.33$ (steel) and $R=0.35$ (aluminium alloy). In these sets of tests, ΔK rose from $747\text{N/mm}^{3/2}$ to $2203\text{N/mm}^{3/2}$ for steel, and $306\text{N/mm}^{3/2}$ to $994\text{N/mm}^{3/2}$ for the aluminium alloy. In both cases, the range of ΔK applied was selected to encompass the total crack length produced under the periodic underload spectra.

5.2.3 VARIABLE AMPLITUDE LOADING

The simple loading sequence employed (Figure 5.2.2) was designed to promote fatigue crack acceleration and comprised a block of stress cycles, all cycling down from a constant tensile stress, which was repeated until failure. Each block contained ten minor stress range cycles and one underload stress range cycle of one and a half times (SBL1.5) or twice (SBL2) the minor stress range (see Chapter 3 for more details).

Load spectra cycling down from a constant maximum stress were chosen, as previous experience indicates that cycling down from fixed tension produces acceleration (Gurney, 2000; Zhang and Maddox, 2009). The magnitude of the maximum stress was chosen based on tests performed by Fleck (1985). Due to the occurrence of acceleration in his tests, similar values of ΔK were chosen for the minor cycles and underload cycle. A stress ratio of $R>0.5$ was chosen for the minor cycles so that the situation was analogous to that assumed to exist in presence of tensile residual stress from welding, but it was not expected to be as significant because the upper limit stress level was not as high as yield. It was therefore considered necessary for a thorough study to also carry out tests on specimens with weld beads applied to the plate surfaces.

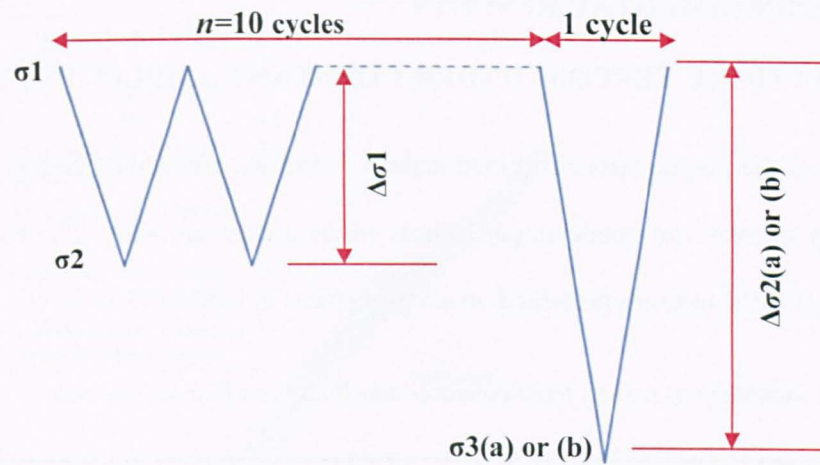


Figure 5.2.2 Constant maximum stress waveform with periodic underloads used in the present study.

The relationship between the number and magnitude of minor and major cycles used has been found experimentally to produce significant crack growth acceleration (Gurney, 1983; Fleck, 1985). Details of the stresses used in the spectrum for both the steel and aluminium alloy specimens are given in Table 5.2.1. Duplicate tests were performed in both materials and both conditions (plain and welded) to increase confidence in the results. The applied CA stress levels and underload ranges are shown in Table 5.2.1.

For all tests the fatigue life was defined as the number of cycles required to achieve a crack length approximately 60% of the specimen width. This ensured that direct comparisons could be made between the fatigue lives of the two materials, under the various loading conditions.

Table 5.2.1 Stresses used in periodic underload spectrum.

Stress identification	Applied stress, N/mm ²			
	S355 steel	R	6082 aluminium alloy	R
σ_1	156	-	74	-
σ_2	86	-	42	-
$\sigma_3(a)$	16	-	11	-
$\sigma_3(b)$	51	-	26	-
$\Delta\sigma_1$	70	0.55	32	0.57
$\Delta\sigma_2(a)$	140	0.10	63	0.14
$\Delta\sigma_2(b)$	105	0.33	48	0.35

Note. $\Delta\sigma_2(a)$ and (b) relate to the two different underload magnitudes investigated.

5.3 EXPERIMENTAL RESULTS

5.3.1 FATIGUE TESTING UNDER CONSTANT AMPLITUDE LOADING

The results of the fatigue tests performed under CA loading are summarised in Table 5.3.1. Good repeatability in lives was obtained, particularly in the aluminium alloy. The fatigue crack growth data obtained in the tests are presented on a log-log basis in Figure 5.3.1a-b.

Table 5.3.1 Summary of results from constant amplitude loading fatigue tests.

Specimen No.	Maximum stress, N/mm ²	Stress range, N/mm ²	Stress ratio, R	Initial ΔK , N/mm ^{3/2}	Final ΔK , N/mm ^{3/2}	Initial crack length, mm	Final crack length, mm	Cycles to failure
CCT-CAL-ST-16	156	70	0.55	375	1072	16.34	92.4	945,402
CCT-CAL-ST-17	156	70	0.55	380	1101	16.54	93.8	831,939
CCT-CAL-AL-12	74	32	0.57	163	370	15.8	61.8	267,448
CCT-CAL-AL-15	74	32	0.57	162	397	17.4	63.8	273,724

In Figure 5.3.1 it will be seen that similar results were obtained for steel regardless of R (Figure 5.3.1a), but that the aluminium alloy was sensitive to R (Figure 5.3.1b), da/dN increasing with increase in R. The addition of the results from the welded specimens showed that there was very little difference in FCGR between them and the tests performed at high stress ratio in the plain material for both steel and aluminium.

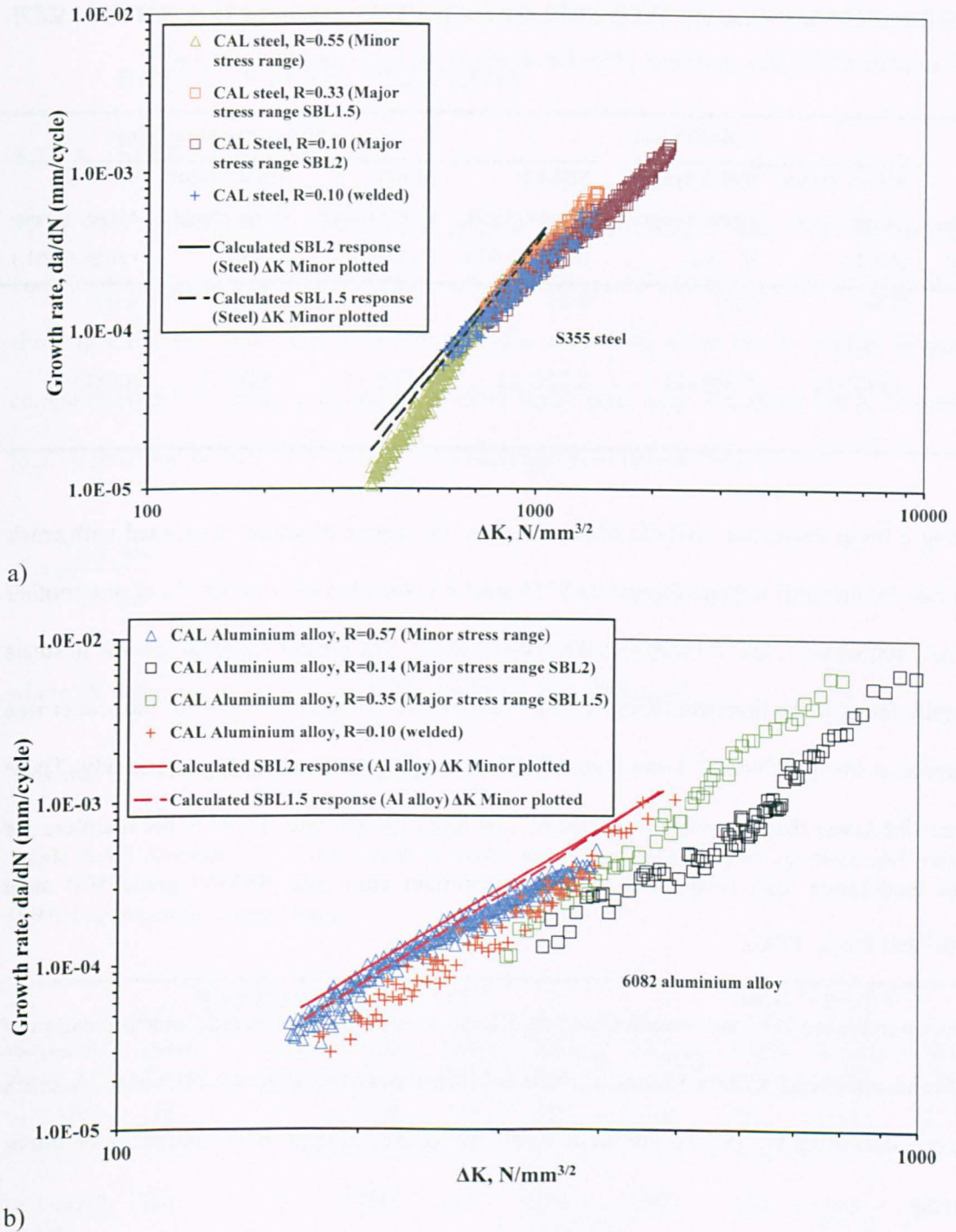


Figure 5.3.1 Summary of fatigue crack growth rate data for tests under constant amplitude loading (SBL calculated response also shown) for a) S355 steel and b) 6082 aluminium alloy.

Paris law coefficients (C and m (see Section 2.5)) were determined for each loading condition by least squares linear regression treating $\log da/dN$ as the dependent variable, Table 5.3.2.

Table 5.3.2 Paris law constants (*C* and *m*) derived for S355 structural steel and 6082 T651 aluminium alloy (Paris law constants given for *da/dN* in mm/cycle and ΔK in $N/mm^{3/2}$).

Paris law constant	S355 Steel			6082 Aluminium alloy		
	Minor stress range (CAL)	SBL2 Major stress range (CAL)	SBL1.5 Major stress range (CAL)	Minor stress range (CAL)	SBL2 Major stress range (CAL)	SBL1.5 Major stress range (CAL)
<i>m</i>	3.36	2.21	2.51	2.95	2.92	4.07
<i>C</i>	2.66E-14	5.34E-11	8.72E-12	1.17E-11	6.81E-12	8.98E-15

Following a linear regression analysis of the CA data, the degree of scatter associated with crack growth rate for identical tests performed on S355 steel was found to be within 8.7% of one another at low ΔK , $400N/mm^{3/2}$, and 2.7% at high ΔK , $1000N/mm^{3/2}$. The greater scatter at low ΔK in steels is generally found in the literature (King, 1998). For the 6082 aluminium alloy tests, the scatter was very similar at low ($175N/mm^{3/2}$) and high ΔK ($350N/mm^{3/2}$), 4.2% and 6.6% respectively. These are somewhat lower than the potential factor of 2 on crack growth rates stated in the literature for constant load range tests performed on 6082 aluminium alloy and BS4360 grade 50B steel (Shercliff and Fleck, 1990).

Also shown in Figure 5.3.1 are the calculated *da/dN* versus ΔK curves expected from application of the periodic underload spectra (SBL), derived by linear summation of the relevant CA crack growth rate data using Eq. [5.3.1]. For these, *da/dN* was plotted in terms of ΔK based on the minor stress range.

$$\frac{da}{dN}_{SBL} = \frac{\left(\left(\frac{da}{dN}_{minor} \times 10 \right) + \left(\frac{da}{dN}_{major} \times 1 \right) \right)}{11} \tag{5.3.1}$$

where da/dN_{major} was determined using the relevant major stress range crack growth law (SBL2 or SBL1.5) given in Table 5.3.2, and da/dN_{minor} was derived from the crack growth law for the minor stress range data. The numbers 1 and 10 are the numbers of major and minor cycles respectively in the relevant SBL block, and 11 is the total number of cycles for the SBL block.

5.3.2 THE EFFECT OF UNDERLOAD MAGNITUDE ON CRACK GROWTH RATE FOR PLAIN SPECIMENS

5.3.2.1 SBL2 LOADING

Table 5.3.3 summarises the results of the periodic underload fatigue tests where the magnitude of underload was twice that of the minor stress range. Compared with the results in Table 5.3.1, these show that the inclusion of periodic single cycle underloads gives rise to shorter fatigue lives compared with CA loading tests under the minor stress range only. The parameter β , defined in Eq. [5.3.2], provides an indication of the overall acceleration in fatigue crack growth:

$$\beta = \frac{\bar{N}_{CAL \text{ data}}}{\bar{N}_{SBL \text{ data}}} \tag{5.3.2}$$

where \bar{N} is the average endurance of the duplicate tests performed.

This was 1.99 for steel and 1.69 for aluminium alloy.

Table 5.3.3 Summary of results from periodic underload fatigue tests of twice the magnitude (SBL2) of the minor stress range.

Specimen No.	Minor stress cycles			UL ⁽¹⁾ stress range, N/mm ²	Initial ΔK_{minor} , N/mm ^{3/2}	Final ΔK_{minor} , N/mm ^{3/2}	Initial crack length, mm	Final crack length, mm	Cycles to failure	β
	Maximum stress, N/mm ²	Stress range, N/mm ²	Stress ratio, R							
CCT-SBL2-ST-01	156	70	0.55	140	348	1048	15.6	90.2	405,746	1.99
CCT-SBL2-ST-02	156	70	0.55	140	344	1042	15.2	89.8	487,536	
CCT-SBL2-AL-01	74	32	0.57	63	159	474	15.6	75.6	155,200	1.69
CCT-SBL2-AL-02	74	32	0.57	63	161	474	16	75.6	165,693	

Note. ⁽¹⁾ UL is defined as the underload or major stress cycle.

The measured crack growth rates due to the periodic underload sequence are compared with the calculated response in Figure 5.3.2 for both the steel and aluminium alloy.

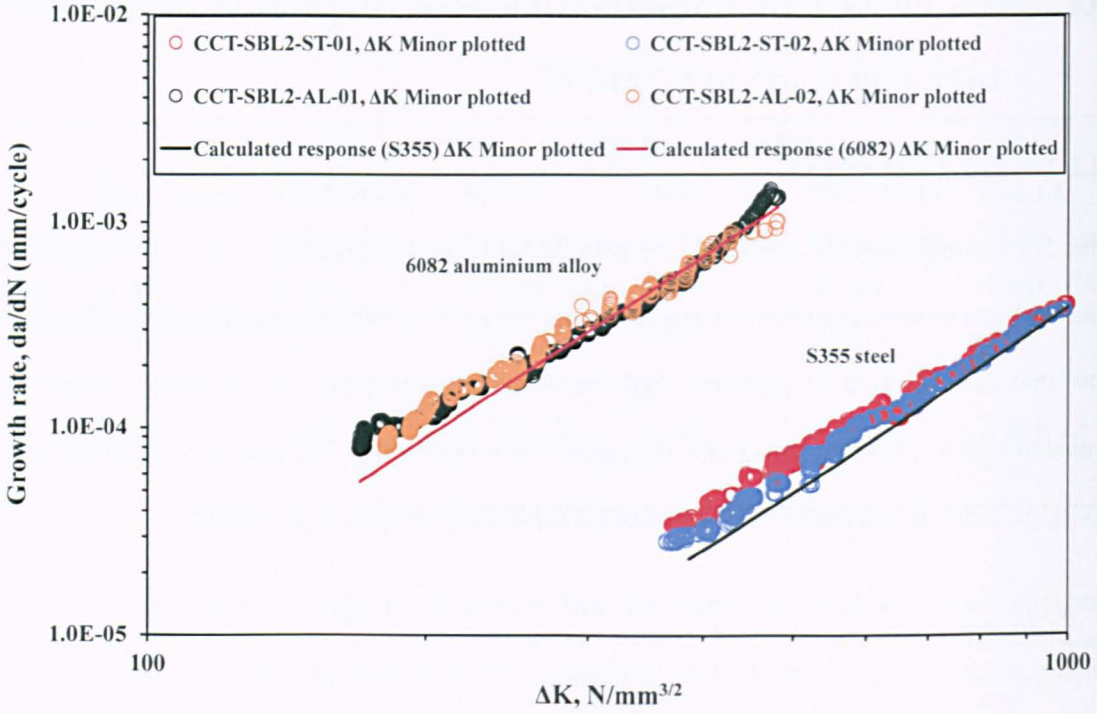


Figure 5.3.2 Comparison of constant amplitude and periodic underload (SBL2) fatigue crack growth rate data for S355 steel and 6082 aluminium alloy.

The periodic underload data are expressed in terms of ΔK_{minor} corresponding to the minor stress range. This choice was made on the basis that the main difference between crack growth under CA loading and SBL would be the increment of crack growth under the ten minor stress cycles. In other words, the crack growth increment due to the single underload cycle would be the same as that under CA loading. Then, comparison of the actual and calculated crack growth rate under SBL would indicate the change in crack growth rate under the minor stress due to the underload. An alternative approach, which is often used in the presentation of results obtained under VA loading, would be to use the equivalent CA value of ΔK , as given in Eq. [5.3.3], for comparison with the calculated response.

$$\Delta K_{Eqv} = \frac{\left((\Delta K \times 10)^m + (\Delta K \times 1)^m \right)^{1/m}}{11} \tag{5.3.3}$$

where m was assumed to be 3.

The effect was a 9% increase in ΔK . However, it is also necessary to express the calculated response in terms of ΔK_{Eqv} , which again results in a 9% increase in ΔK . Therefore, use of an

equivalent ΔK resulted in the same acceleration factor, and as the degree of acceleration was of prime concern, the choice of using ΔK_{minor} or ΔK_{Eqv} was irrelevant. Henceforth, for the periodic underload data presented, stress intensity factor range is given in terms of ΔK_{minor} .

It can be seen in Figure 5.3.2 that the FCGRs for the periodic underload tests generally lie above their respective calculated response, especially at low ΔK . The difference was less marked in the case of the aluminium alloy with the periodic underload data intersecting the calculated growth rate in the mid to high regime.

Paris law coefficients were determined by least squares linear regression analysis of each set of data and are presented in Table 5.3.4. In view of the good agreement between the duplicate sets of data, the results from each pair were combined in this analysis. These laws were used in conjunction with the relevant CA data to derive the crack growth acceleration factors, γ , included in Table 5.3.4.

Table 5.3.4 Paris law constants for plain materials used for derivation of the acceleration factors under SBL2 conditions. Constants m and C given for da/dN in mm/cycle and ΔK in $N/mm^{3/2}$.

Specimen No.	Data over ΔK range for γ		Acceleration factor, γ ,	
	m	C	$\Delta K_{minor}=400$	$\Delta K_{minor}=1000$
			($\Delta K_{minor}=200$)	($\Delta K_{minor}=400$)
CCT-SBL2-ST-01	2.47	1.53E-11	1.56	1.02
CCT-SBL2-ST-02	2.73	2.65E-12	1.28	1.07
ST -01 & 02 combined	2.58	7.38E-12	1.45	1.06
CCT-SBL2-AL-01	2.43	2.91E-10	1.28	0.90
CCT-SBL2-AL-02	2.41	3.39E-10	1.35	0.93
AL -01 & 02 combined	2.40	3.43E-10	1.29	0.89

Note. Bracketed ΔK values are for aluminium alloy.

The inclusion of the underloads has produced γ values of 1.45 and 1.06 at $400N/mm^{3/2}$ and $1000N/mm^{3/2}$ respectively in the steel, or 1.29 and 0.89 at $200N/mm^{3/2}$ and $400N/mm^{3/2}$ respectively

in the aluminium alloy. In other words, γ was greater at the lower ΔK values for both materials, as shown in Figure 5.3.2, and indeed crack growth acceleration only occurred then in the aluminium alloy, with an element of crack growth retardation at the higher ΔK value.

5.3.2.2 SBL1.5 LOADING

Considering next the results for a reduced magnitude of underload (1.5 times that of the minor stress range (SBL1.5)) in Table 5.3.5, the reduction in life is seen to be less than for the higher underload, by 16% for steel and 18% for aluminium alloy, which correspond to β values (Eq. [5.3.1]) of 1.66 for steel and 1.38 for aluminium alloy.

As before, the measured crack growth rates due to the periodic underload sequence are compared with the calculated response in Figure 5.3.3. In the case of the S355 steel, FCGRs for the periodic underload tests are again above the calculated. For the aluminium alloy, the periodic underload data are generally above the calculated response at low ΔK but rise as ΔK increases ($>300\text{N/mm}^{3/2}$) before returning to a similar crack growth rate response.

Table 5.3.5 Summary of results from periodic underload fatigue tests of one and half times the magnitude of the minor stress range (SBL1.5).

Specimen No.	Minor stress cycles			UL ⁽¹⁾ stress range, N/mm ²	Initial ΔK_{minor} , N/mm ^{3/2}	Final ΔK_{minor} , N/mm ^{3/2}	Initial crack length, mm	Final crack length, mm	Cycles to failure	β
	Maximum stress, N/mm ²	Stress range, N/mm ²	Stress ratio, R							
CCT-SBL1.5- ST-01	156	70	0.56	105	351	1044	15.8	89.9	534,400	1.66
CCT-SBL1.5- ST-02	156	70	0.56	105	354	1044	16.1	89.9	535,664	
CCT-SBL1.5- AL-01	74	32	0.57	48	162	481	16.1	75.7	192,400	1.38
CCT-SBL1.5- AL-02	74	32	0.57	48	162	481	16.1	75.7	199,555	

Note. ⁽¹⁾ UL is defined as the underload or major stress cycle.

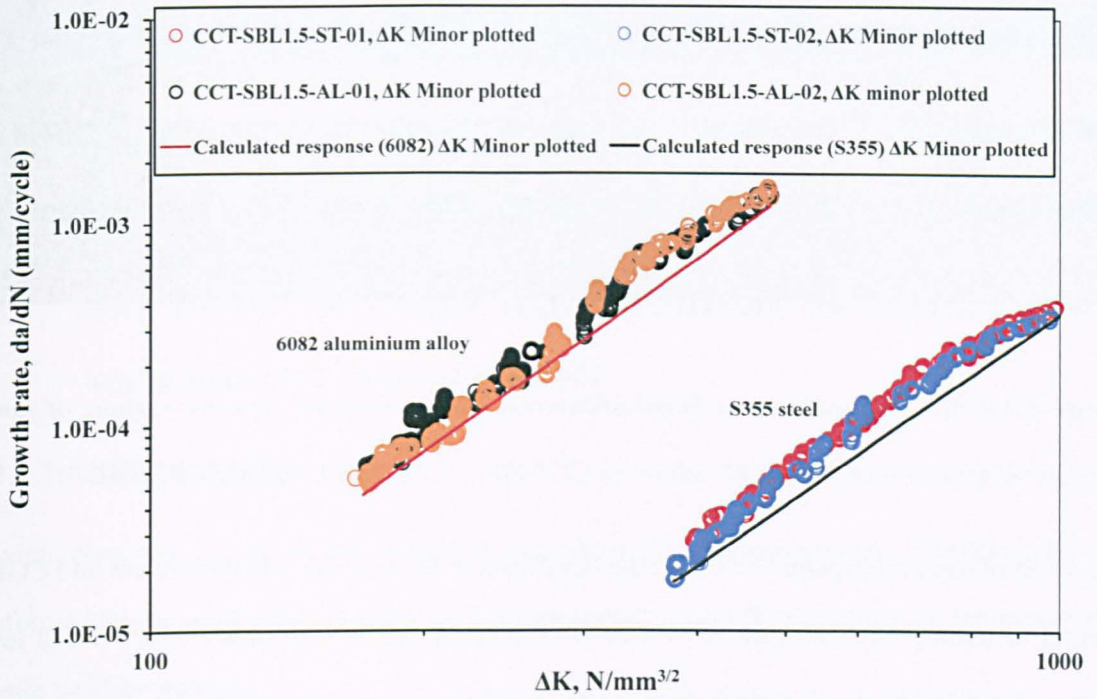
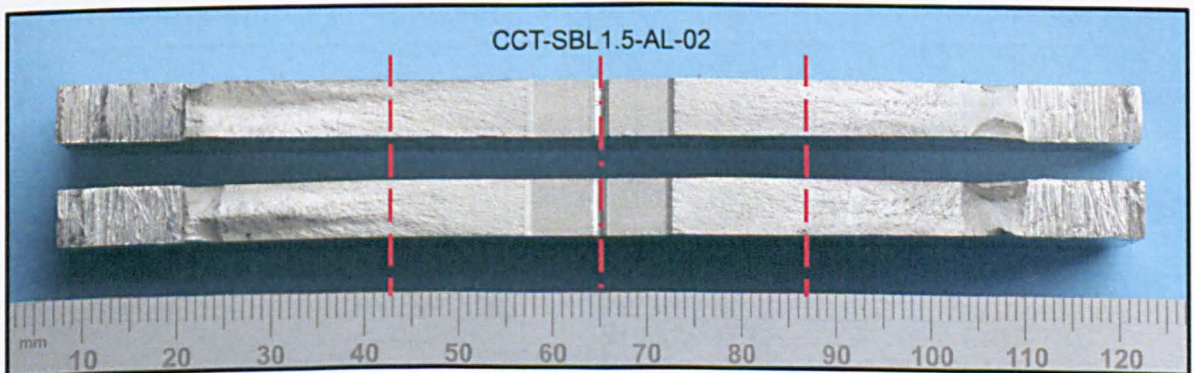
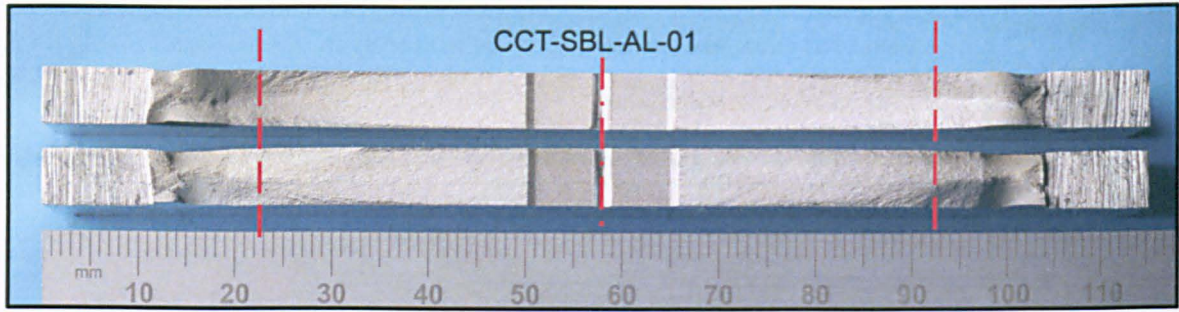


Figure 5.3.3 Comparison of constant amplitude and periodic underload (SBL1.5) fatigue crack growth rate data for S355 steel and 6082 aluminium alloy.

This increase in growth rate at around $300N/mm^{3/2}$ in the aluminium was not observed under SBL2, although in Figure 5.3.2 it can be seen that for CCT-SBL2-AL-01 an increase occurs but at a higher ΔK of around $420N/mm^{3/2}$. Examination of the specimen fracture surfaces (Figure 5.3.4a-b) showed that at $a = \sim 22mm$ the fatigue crack approaches the change from flat to shear mode growth for the SBL1.5 specimen. In contrast, growth in the full shear mode is achieved in the SBL2 specimen at $a = \sim 35mm$. These crack lengths correspond to ΔK values of $310N/mm^{3/2}$ and $450N/mm^{3/2}$ respectively, agreeing well with the increases in growth rate. This is further considered in Section 5.3.6.



a)



b)
Figure 5.3.4 Fracture surfaces of failed aluminium alloy specimens showing regions of flat to shear mode growth (highlighted in red) in; a) CCT-SBL1.5-AL-02 and b) CCT-SBL2-AL-01.

It is worth noting at this point that whilst the development of shear lips and their effect on FCGR is relevant to through-section crack growth across a plate, as in CCT specimens, for welded joints (such as those in Chapter 7) fatigue cracking from weld toes is predominantly flat. Therefore, it is the flat fracture region that is of most relevance to the behaviour of welded joints.

Once again, linear regression analysis was used to derive the Paris law constants (Table 5.3.6) and hence γ for the periodic underload data. The inclusion of the underloads produced increases in growth rate by factors of 1.39 and 1.35 at 400 and 1000N/mm^{3/2} respectively for steel, or 1.12 and 1.40 at 200 and 400N/mm^{3/2} respectively for aluminium alloy.

Table 5.3.6 Paris law constants m and C for plain materials used for derivation of the acceleration factor under SBL1.5 conditions.

Specimen No.	Data over ΔK range for γ		Acceleration factor, γ	
	m	C	$\frac{\Delta K_{minor}=400}{(\Delta K_{minor}=200)}$	$\frac{\Delta K_{minor}=1000}{(\Delta K_{minor}=400)}$
CCT-SBL1.5-ST-01	2.96	6.29E-13	1.56	1.36
CCT-SBL1.5-ST-02	3.17	1.52E-13	1.33	1.40
ST-01 & 02 combined	3.08	2.72E-13	1.39	1.35
CCT-SBL1.5-AL-01	3.17	4.95E-12	1.30	1.33
CCT-SBL1.5-AL-02	3.73	2.01E-12	1.03	1.55
AL-01 & 02 combined	3.46	9.14E-13	1.12	1.40

Comparing with SBL2 (Table 5.3.4), the use of the reduced underload resulted in a similar γ at low ΔK , but higher factors at high ΔK , by some 27% for the steel and 57% for the aluminium alloy. A difference in ΔK_{eff} is considered to be a plausible explanation for the observed higher γ factors within this regime, and will be discussed further in Chapter 6.

5.3.3 THE EFFECT OF UNDERLOAD MAGNITUDE ON CRACK GROWTH RATE FOR WELDED SPECIMENS

5.3.3.1 SBL2 LOADING

Having observed the effect of underload magnitude for plain specimens, further tests were performed using weld bead-on-plate CCT specimens to establish the effect of the presence of tensile residual stresses.

Table 5.3.7 summarises the results of the periodic underload fatigue tests where the magnitude of underload was twice that of the minor stress range. As is the case of the plain specimens, the fatigue lives are less than those obtained under CA loading, in this case by a factor of 2.87 for steel and 1.74 for aluminium alloy. However, these differences are higher than those for plain specimens, by 31% for steel and 3% for the aluminium alloy.

Table 5.3.7 Summary of results from periodic underload fatigue tests of twice (SBL2) the magnitude of the minor stress range for welded specimens.

Specimen No.	Minor stress cycles			UL ⁽¹⁾ stress range, N/mm ²	Initial ΔK_{minor} , N/mm ^{3/2}	Final ΔK_{minor} , N/mm ^{3/2}	Initial crack length, mm	Final crack length, mm	Cycles to failure	β
	Maximum stress, N/mm ²	Stress range, N/mm ²	Stress ratio, R							
CCT-SBL2-ST-03R	156	70	0.56	140	351	1042	15.8	1.66	307,190	2.87
CCT-SBL2-ST-05R	156	70	0.56	140	350	1045	15.7	90.0	311,365	
CCT-SBL2-AL-03R	74	32	0.57	63	157	474	15.2	1.38	158,360	1.74
CCT-SBL2-AL-04R	74	32	0.57	63	158	475	15.3	75.7	151,926	

Note. ⁽¹⁾ UL is defined as the underload or major stress cycle.

This greater difference between the plain and welded specimens is also evident in Figures 5.3.5 and 5.3.6, which show the FCGR data. The difference suggests that the presence of tensile residual stresses enhances the mechanism(s) responsible for fatigue crack growth acceleration due to an underload.

Turning to the Paris law coefficients in Table 5.3.8, the ‘combined’ welded specimen data show γ values of 1.86 and 1.36 at $400\text{N/mm}^{3/2}$ and $1000\text{N/mm}^{3/2}$ respectively for S355 steel, and 1.48 and 1.85 at $200\text{N/mm}^{3/2}$ and $400\text{N/mm}^{3/2}$ respectively for 6082 aluminium alloy.

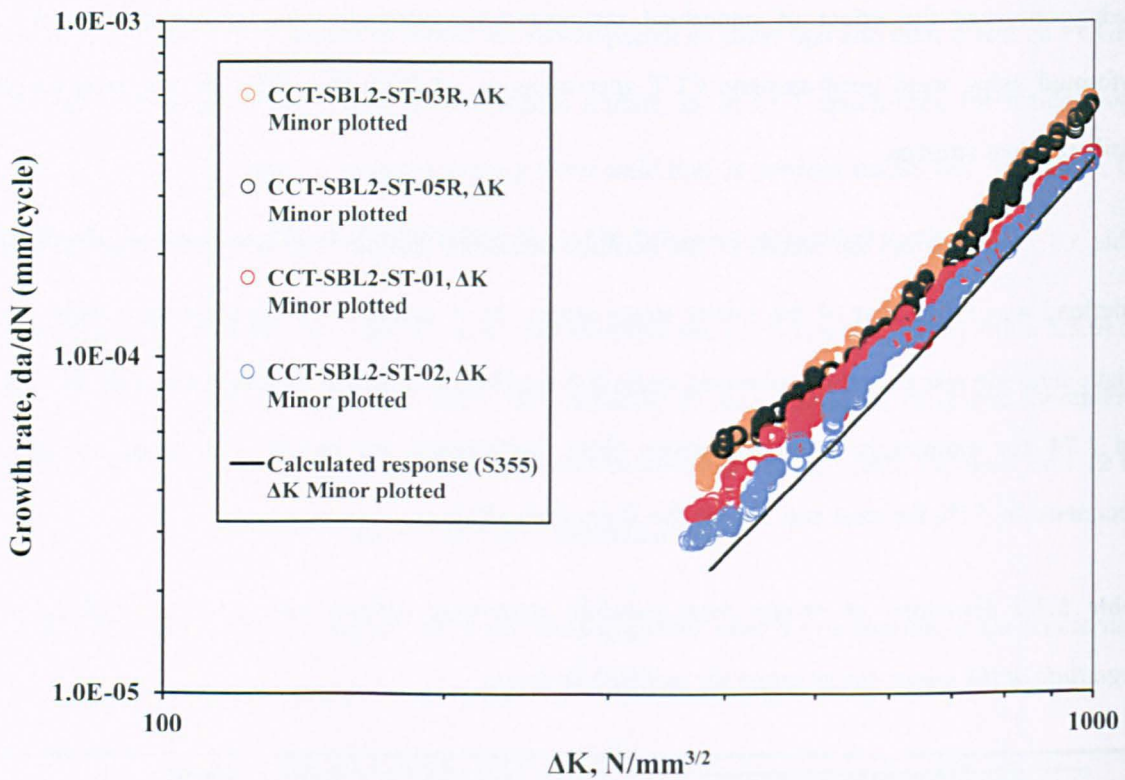


Figure 5.3.5 Comparison of constant amplitude and periodic underload (SBL2) fatigue crack growth rate data for S355 steel in both the plain and welded (denoted by R) conditions.

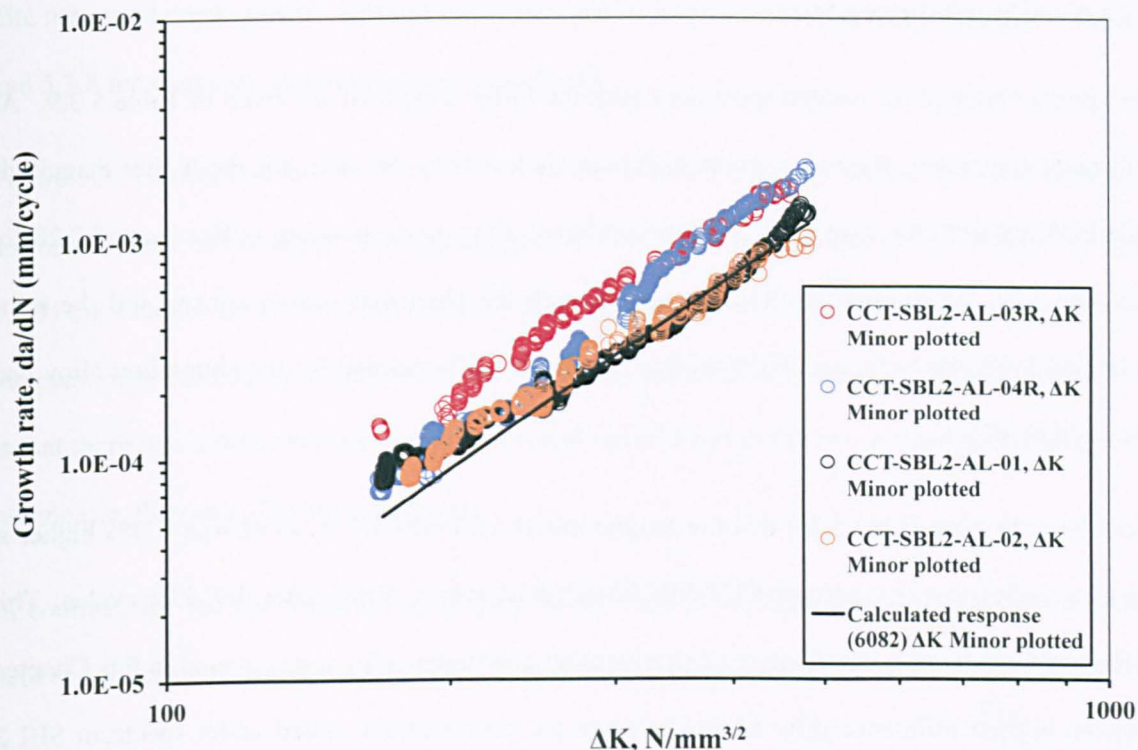


Figure 5.3.6 Comparison of constant amplitude and periodic underload (SBL2) fatigue crack growth rate data for 6082 Al alloy in both the plain and welded (denoted by R) conditions.

Table 5.3.8 Paris law constants for welded materials used for derivation of the acceleration factor under SBL2 conditions (Constants m and C given for da/dN in mm/cycle and ΔK in $N/mm^{3/2}$).

Specimen No.	Data over ΔK range for γ		Acceleration factor, γ	
	m	C	$\Delta K_{minor}=400$ ($\Delta K_{minor}=200$)	$\Delta K_{minor}=1000$ ($\Delta K_{minor}=400$)
CCT-SBL2-ST-03R	2.62	7.51E-12	1.88	1.42
CCT-SBL2-ST-05R	2.55	1.12E-11	1.84	1.30
ST-03R & 05R combined	2.59	8.88E-12	1.86	1.36
CCT-SBL2-AL-03R	2.77	7.93E-11	2.12	1.88
CCT-SBL2-AL-04R	3.71	2.93E-13	1.14	1.94
AL-03R & 04R combined	3.26	4.13E-12	1.48	1.85

5.3.3.2 SBL1.5 LOADING

The results obtained for welded specimens with the lower underload are given in Table 5.3.9. As with plain specimens, the reduction in endurance is less than that seen for the higher magnitude underload, by 21% for steel and 25% for aluminium alloy, corresponding to β values of 2.28 for steel and 1.31 for aluminium alloy. Compared with the plain material specimens and the same underload level, the endurance for steel was reduced by 27% but that for the aluminium alloy was increased by 6%.

It can be seen from Table 5.3.9 that the fatigue life of CCT-SBL1.5-AL-03R was ~21% higher at 226,615 cycles than its partner CCT-SBL1.5-AL-04R which failed after 187,230 cycles. This difference in endurance is well above those for other aluminium alloy tests covered in this Chapter, with the highest difference prior to this being in the plain material tested under spectrum SBL2, where the percentage difference between identical tests was only ~6%. Reviewing the test data it was found that CCT-SBL1.5-AL-03R took a significantly greater number of cycles (25,742) to propagate the fatigue crack from the notch to the desired 1.5mm than its partner. This may have been due to either a blunter notch tip or overloading of the specimen during setup. Had this not occurred then a reduction in endurance by ~5% (β of 1.39 as opposed to 1.31) may have been realised.

Table 5.3.9 Summary of results from welded periodic underload fatigue tests of one and half times (SBL1.5) the magnitude of the minor stress range.

Specimen No.	Minor stress cycles			UL ⁽¹⁾ stress range, N/mm ²	Initial ΔK_{minors} N/mm ^{3/2}	Final ΔK_{minors} N/mm ^{3/2}	Initial crack length , mm	Final crack length, mm	Cycles to failure	β
	Maximum stress, N/mm ²	Stress range, N/mm ²	Stress ratio, R							
CCT-SBL1.5- ST-03R	156	70	0.56	105	357	1051	16.3	90.5	394,478	2.28
CCT-SBL1.5- ST-04R	156	70	0.56	105	352	1002	15.9	86.5	385,859	
CCT-SBL1.5- AL-03R	74	31.8	0.57	47.7	158	481	15.4	75.7	226,615	1.31
CCT-SBL1.5- AL-04R	74	31.8	0.57	47.7	159	480	15.5	75.6	187,230	

Note. ⁽¹⁾ UL is defined as the underload or major stress cycle.

The measured crack growth rates due to the periodic underload sequence are given in Figures 5.3.7 and 5.3.8 for steel and aluminium alloy respectively.

Figure 5.3.7 shows that the FCGR data for periodic underload tests on the welded steel specimens are comfortably above those of the plain material. It is noted though that at $\sim 800 \text{ N/mm}^{3/2}$ (Figure 5.3.7) the data for the welded specimens separate with those for CCT-SBL1.5-03R tending towards the plain material data. A re-analysis of the results did not reveal any errors. A possible explanation is that there was a difference between the residual stress levels in the two welded specimens in this regime (i.e. the zone of residual tension).

In contrast, for the aluminium alloy (Figure 5.3.8) there is no significant difference between the periodic underload data for plain or welded specimens, both sets lying above the calculated curve.

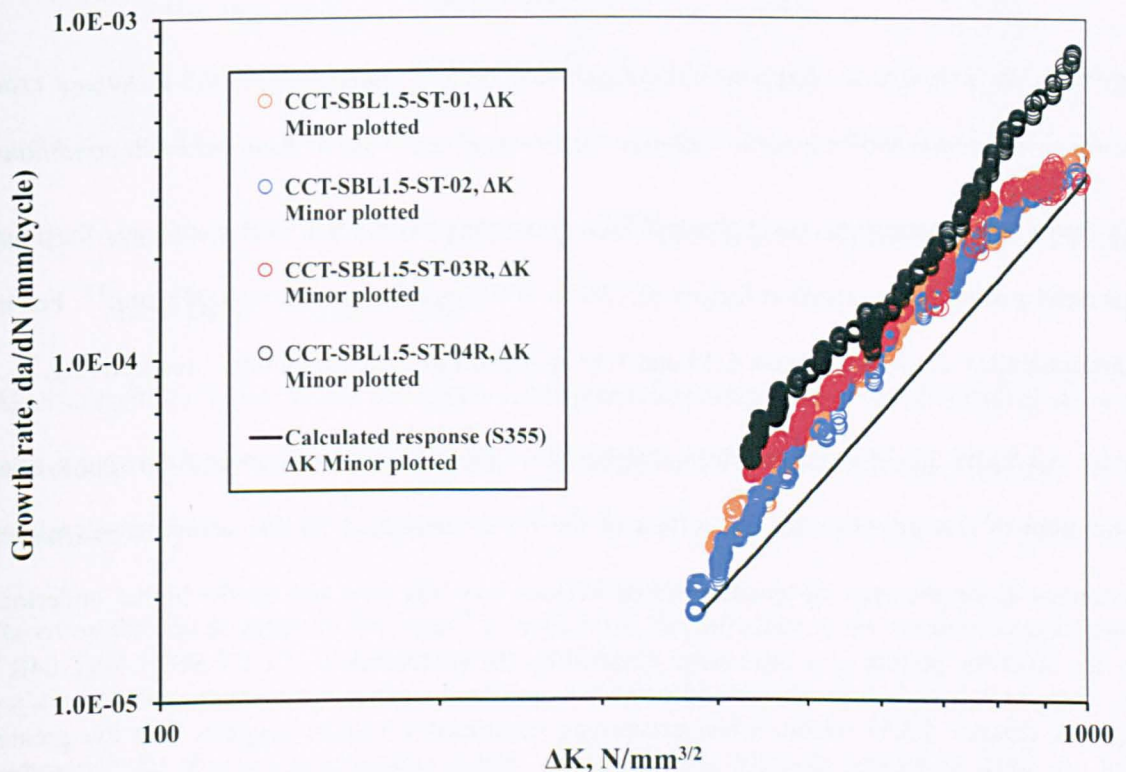


Figure 5.3.7 Comparison of constant amplitude and periodic underload (SBL1.5) fatigue crack growth rate data for S355 steel in both the plain and welded (denoted by R) conditions.

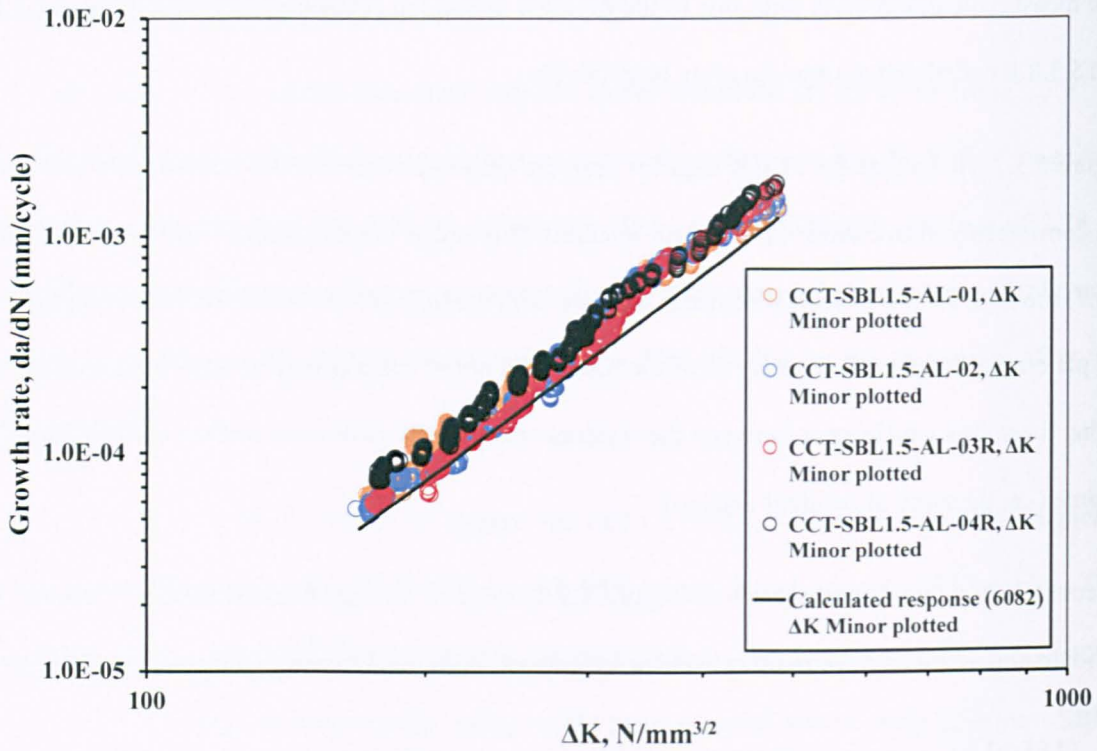


Figure 5.3.8 Comparison of constant amplitude and periodic underload (SBL1.5) fatigue crack growth rate data for 6082 aluminium alloy in both the plain and welded (denoted by R) conditions.

The Paris law constants given in Table 5.3.10 show that for welded steel specimens the lower underload results in acceleration factors of 1.92 at $400\text{N/mm}^{3/2}$ and 1.59 at $1000\text{N/mm}^{3/2}$. For the aluminium alloy the γ factors were 1.19 and 1.37 at $200\text{N/mm}^{3/2}$ and $400\text{N/mm}^{3/2}$ respectively.

Tables 5.3.8 and 5.3.10 therefore show that based on the calculated responses following a linear summation of CA growth rates, the effect of the lower underload for the combined aluminium specimens in the presence of tensile residual stresses was less than that for the higher underload. For the steel the picture is a little more clouded by the performance of CCT-SBL1.5-ST-04R at high ΔK (Figure 5.3.7) which, when comparing combined γ values, suggests that the greatest acceleration came from the SBL1.5 spectrum.

Table 5.3.10 Paris law constants for welded materials used for derivation of the acceleration factor under SBL1.5 conditions (constants m and C given for da/dN in mm/cycle and ΔK in $N/mm^{3/2}$).

Specimen No.	Data over ΔK range for γ		Acceleration factor, γ	
	m	C	$\Delta K_{\text{minor}}=400$ ($\Delta K_{\text{minor}}=200$)	$\Delta K_{\text{minor}}=1000$ ($\Delta K_{\text{minor}}=400$)
CCT-SBL1.5-ST-03R	2.82	1.70E-12	1.82	1.40
CCT-SBL1.5-ST-04R	3.07	4.44E-13	2.13	2.05
ST-03R & 04R combined	2.90	1.11E-12	1.92	1.59
CCT-SBL1.5-AL-03R	3.59	4.29E-13	1.05	1.43
CCT-SBL1.5-AL-04R	3.16	5.81E-12	1.45	1.47
AL-03R & 04R combined	3.34	1.84E-12	1.19	1.37

5.3.4 SUMMARY OF THE EFFECT OF RESIDUAL STRESS ON APPLIED LOADING SEQUENCES

As discussed in Chapter 4, and also given in Chapter 6, the magnitude of tensile residual stress due to welding adjacent to the central notch was $481N/mm^2$ for the steel and $31N/mm^2$ for the aluminium alloy.

Based on the results given in Sections 5.3.2 and 5.3.3, the influence of the residual stresses due to welding on the effect of the applied load sequences can be considered. Tables 5.3.11 and 5.3.12 summarise the observed acceleration factors and endurance for tests performed using the SBL2 and SBL1.5 sequences. It should be noted that acceleration factors for welded specimens were derived by comparing against CA data for plain material, in order to show the level of increase in acceleration due to welding. Had they be compared against welded CA data, the degree of acceleration may have been less.

In the case of the SBL2 sequence (Table 5.3.11) tests on the S355 steel, it can be seen clearly that the tensile residual stress introduced by the bead on plate welds led to a reduction in life resulting in an increase in acceleration factor as compared with the behaviour of plain specimens. However, for the aluminium alloy, the results are less clear.

The overall fatigue lives of the aluminium alloy specimens tested were reasonably similar. However, with regard to the acceleration factors, at low ΔK ($200\text{N/mm}^{3/2}$) the two welded specimens gave significantly different values, with CCT-SBL2-AL-03R showing a much higher acceleration factor (2.12) than CCT-SBL2-AL-04R (1.14) up to $\sim 300\text{N/mm}^{3/2}$ (See Figure 5.3.6), before returning to a similar response (1.88 to 1.94). The difference between the two is thought to be due to scatter or possibly a variation of the magnitude of residual stress between the specimens. At high ΔK the welded specimens exhibited significantly greater acceleration than the plain material, by a factor of 2.

Table 5.3.11 Summary of total endurance and acceleration factors for tests performed under SBL2 sequence (ΔK in $\text{N/mm}^{3/2}$)

Specimen No.	Endurance, cycles	Acceleration factor, γ	
		$\Delta K_{\text{minor}}=400$ ($\Delta K_{\text{minor}}=200$)	$\Delta K_{\text{minor}}=1000$ ($\Delta K_{\text{minor}}=400$)
CCT-SBL2-ST-01	405,746	1.56	1.02
CCT-SBL2-ST-02	487,536	1.28	1.07
CCT-SBL2-ST-03R	307,190	1.88	1.42
CCT-SBL2-ST-05R	311,365	1.84	1.30
ST-01 & 02 combined	-	1.45	1.06
ST-03R & 05R combined	-	1.86	1.36
CCT-SBL2-AL-01	155,200	1.28	0.90
CCT-SBL2- AL -02	165,693	1.35	0.93
CCT-SBL2- AL -03R	158,360	2.12	1.88
CCT-SBL2- AL -04R	151,926	1.14	1.94
AL-01 & 02 combined	-	1.29	0.89
AL-03R & 04R combined	-	1.48	1.85

When considering the SBL1.5 sequences (Table 5.3.12), tests performed on the S355 steel showed that whilst an appreciable degree of acceleration was present for the welded specimens at low ΔK (1.82 to 2.13), the high $\Delta K \gamma$ values for both plain and welded specimens were generally quite similar at around 1.40 (with the exception of CCT-SBL1.5-ST-04R). The total endurance were however considerably shorter for the welded specimens than the plain.

Table 5.3.12 *Summary of total endurance and acceleration factors for tests performed under SBL1.5 sequence (ΔK in $N/mm^{3/2}$)*

Specimen No.	Endurance, cycles	Acceleration factor, γ	
		$\Delta K_{\text{minor}}=400$ ($\Delta K_{\text{minor}}=200$)	$\Delta K_{\text{minor}}=1000$ ($\Delta K_{\text{minor}}=400$)
CCT-SBL1.5-ST-01	534,400	1.56	1.36
CCT-SBL1.5-ST-02	535,664	1.33	1.40
CCT-SBL1.5-ST-03R	394,478	1.82	1.40
CCT-SBL1.5-ST-04R	385,859	2.13	2.05
ST-01 & 02 combined	-	1.39	1.35
ST-03R & 04R combined	-	1.92	1.59
CCT-SBL1.5-AL-01	192,400	1.30	1.33
CCT-SBL1.5-AL-02	199,555	1.03	1.55
CCT-SBL1.5-AL-03R	226,615	1.05	1.43
CCT-SBL1.5-AL-04R	187,230	1.45	1.47
AL-01 & 02 combined	-	1.12	1.40
AL-03R & 04R combined	-	1.19	1.37

As with the SBL2 sequence, the effect of SBL1.5 on the 6082 aluminium alloy was different. Little or no effect of the residual stresses in the welded specimens was apparent; even the total fatigue lives of the plain and welded specimens were very similar. Again this is possibly a reflection of a low level of residual stress in the relevant parts of the specimens tested.

Overall it will be evident that the greatest observed effect of residual stress was during application of the SBL2 loading sequence for both materials.

5.3.5 COMPARISON OF ACCELERATION FACTORS γ AND β

5.3.5.1 CALCULATION OF β

The method used to calculate the crack growth rate under spectrum loading in the determination of γ was also used in the determination of β . In this case, the linear summation of the crack growth from the major and minor stress cycles was used to calculate the number of cycles (major and minor) needed to produce fatigue crack lengths approximately corresponding to the 'final crack lengths' indicated in Tables 5.3.3 and 5.3.5. Endurances for shorter crack lengths were also considered.

β values based on comparison of the calculated and actual numbers of cycles of the periodic underload sequence required to achieve the same crack length (92mm for steel, 76mm for aluminium) are also shown for both the SBL2 and SBL1.5 spectrum in Table 5.3.13. They are also shown in Figure 5.3.9 to 5.3.12 for S355 steel and 6082 aluminium alloy at the different underload magnitudes. In all cases both plain and welded data are compared with the calculated response. Also presented are β values at low and high ΔK corresponding to crack lengths of 10 and 43mm respectively for the steel, and 12 and 32mm respectively for the aluminium alloy.

Table 5.3.13 Summary of acceleration factors, β .

Material	Condition	Underload sequence	Final crack length	Acceleration factor, β	
				$\Delta K=400$ Steel $\Delta K=200$ Al alloy	$\Delta K=1000$ Steel $\Delta K=400$ Al alloy
S355	Plain	SBL2	1.11 to 1.30	1.34 to 1.47	1.11 to 1.30
S355	Welded	SBL2	1.60 to 1.63	1.45 to 5.43	1.60 to 1.63
6082 T651	Plain	SBL2	1.00 to 1.09	1.10 to 1.33	1.01 to 1.10
6082 T651	Welded	SBL2	1.06 to 1.14	0.99 to 1.15	1.04 to 1.13
S355	Plain	SBL1.5	1.19 to 1.23	0.95 to 1.17	1.19 to 1.23
S355	Welded	SBL1.5	1.50 to 1.68	1.81 to 1.82	1.49 to 1.68
6082 T651	Plain	SBL1.5	1.06 to 1.12	1.25 to 1.33	1.06 to 1.12
6082 T651	Welded	SBL1.5	1.00 to 1.12	1.02 to 1.33	1.00 to 1.12

5.3.5.2 STEEL UNDER SBL2 LOADING

Periodic underloads were found to reduce the number of cycles required to produce a given crack length in steel. The indicated β values at high ΔK (or at final crack length), as given in Table 5.3.13 for the plain (1.11 to 1.30) and welded (1.60 to 1.63) steel specimens under SBL2, are a little above the combined γ factors presented in Tables 5.3.4 and 5.3.8 (1.06 and 1.36 for plain and welded respectively). However, β and γ are similar at low ΔK .

It should however be noted that for the welded steel the β range at low ΔK in Table 5.3.13 is quite large, presumably due to differences in residual stress distribution resulting in differences in propagation rates. This is highlighted in Figure 5.3.9 where it is shown that specimen CCT-SBL2-ST-03R takes a little longer to propagate than CCT-SBL2-ST-05R, but towards final failure acceleration is very similar.

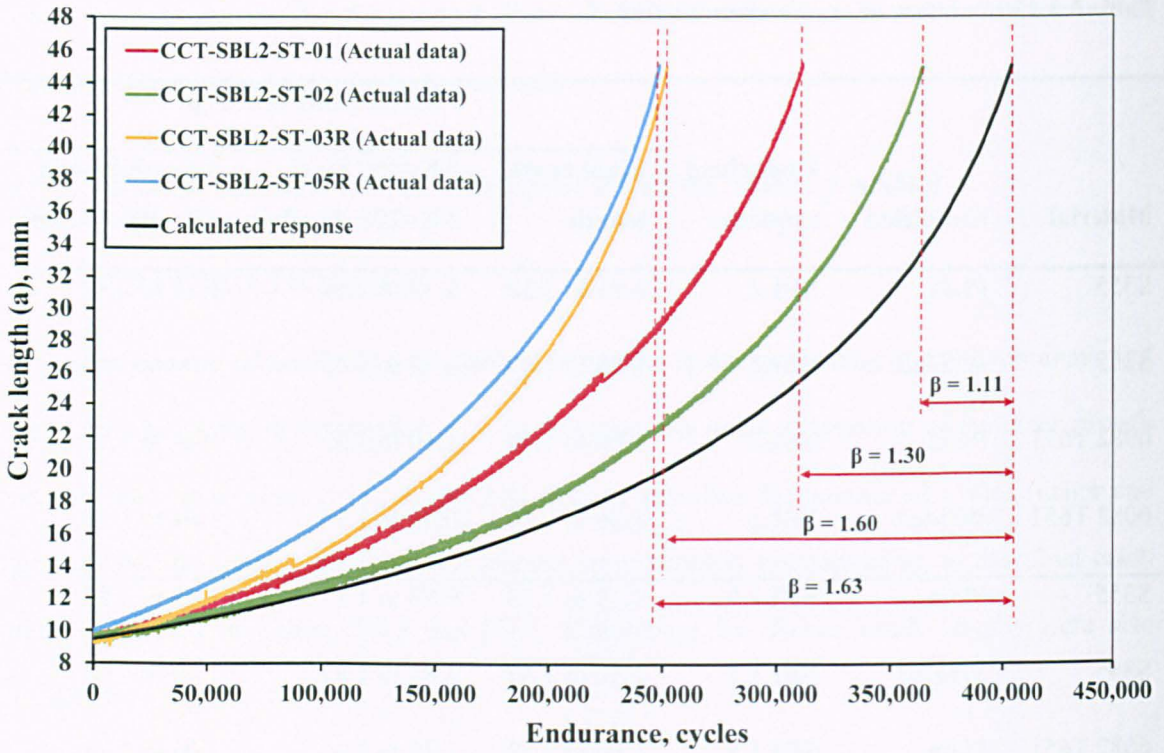


Figure 5.3.9 Comparison of actual and calculated crack growth response for S355 steel in periodic underload (SBL2) tests. Plain and welded (denoted by R) conditions shown.

5.3.5.3 ALUMINIUM UNDER SBL2 LOADING

In the case of aluminium alloy, β at failure or high ΔK was 1.01 to 1.10 for plain material and 1.04 to 1.13 for welded (Table 5.3.13 and Figure 5.3.10). The former range was very slightly above the combined γ for the plain material (0.89) but that for the welded material was significantly lower (1.85), see Tables 5.3.4 and 5.3.8. When comparing at low ΔK , the β and γ ranges are much closer for both the plain and welded material (with the exception of CCT-SBL2-AL-03R in Table 5.3.8).

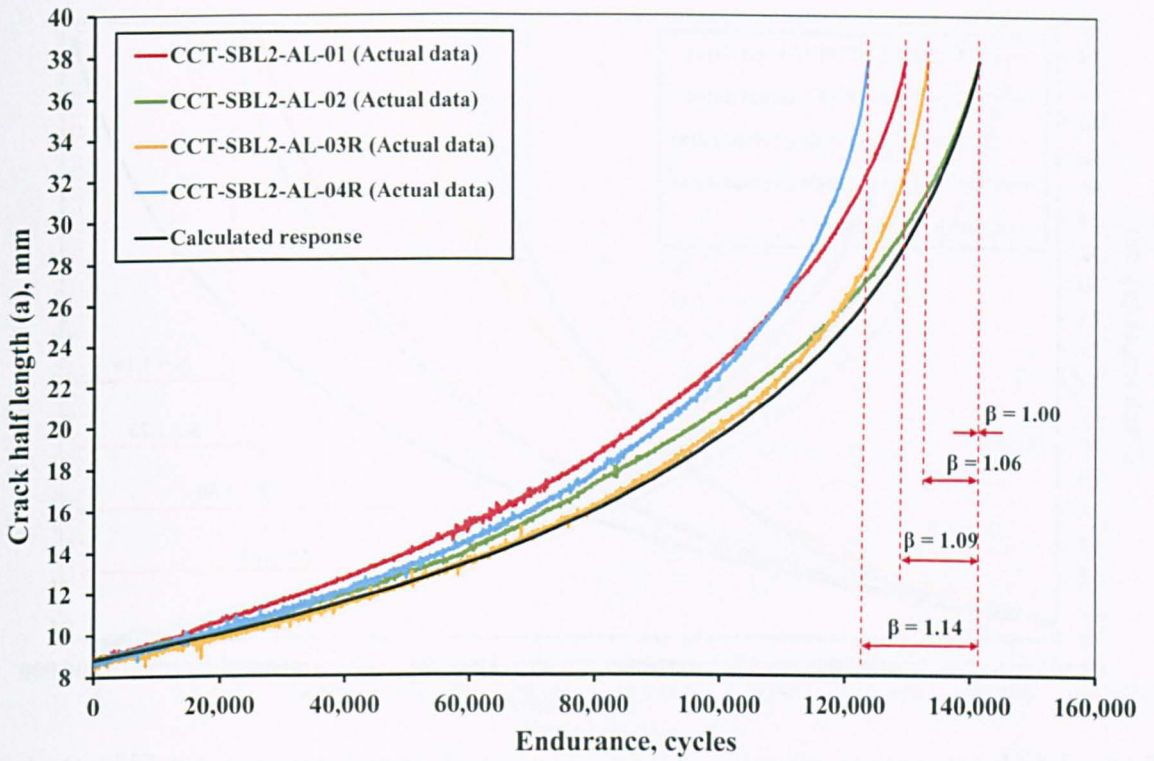


Figure 5.3.10 Comparison of actual and calculated crack growth response for 6082 aluminium alloy in periodic underload (SBL2) tests. Plain and welded (denoted by R) conditions shown.

5.3.5.4 STEEL UNDER SBL1.5 LOADING

Referring to the underload spectrum SBL1.5 for steel specimens, β corresponding to failure (Table 5.3.13 and Figure 5.3.11) was between 1.19 to 1.23 and 1.50 to 1.68 for plain and welded material respectively. In the case of the plain material these are slightly below the combined γ of 1.35 (see Table 5.3.6). However, β and γ are reasonably consistent for the welded material, where a γ value of 1.59 was derived (see Table 5.3.10).

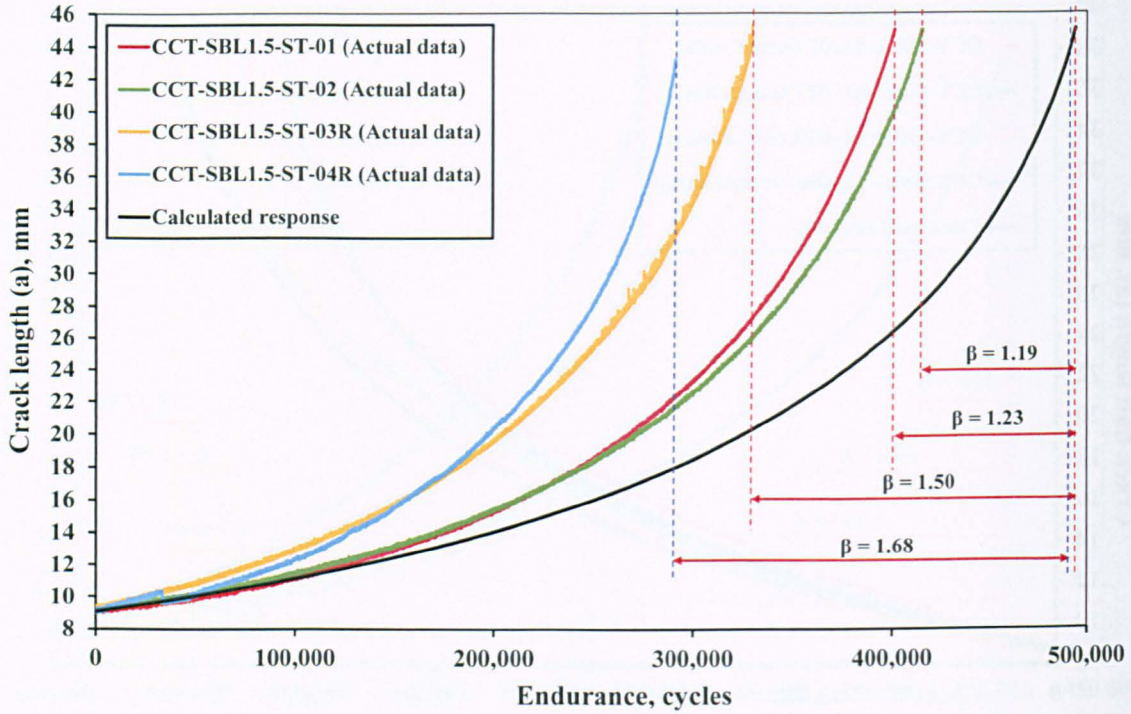


Figure 5.3.11 Comparison of actual and calculated crack growth response for S355 steel in periodic underload (SBL1.5) tests. Plain and welded (denoted by R) conditions shown.

As noted earlier, CCT-SBL1.5-ST-04R behaved differently at high ΔK (Figure 5.3.7) presumably due to differences in residual stress.

At low ΔK the β values in Table 5.3.13 for both plain (0.95 to 1.17) and welded steel (1.81 to 1.82) are a little below the combined γ factors in Table 5.3.6 for the plain material (1.39), but in reasonable agreement for the welded (1.92), Table 5.3.10.

5.3.5.5 ALUMINIUM UNDER SBL1.5 LOADING

For the 6082 aluminium alloy SBL1.5 data at high ΔK /final crack length (Figure 5.3.12), the β range (Table 5.5.13) for both plain (1.06 to 1.12) and welded (1.00 to 1.12) material is again below that found in terms of the combined γ . Here acceleration for the plain aluminium was 1.40 and 1.37 for the welded (Tables 5.3.6 and 5.3.10 respectively).

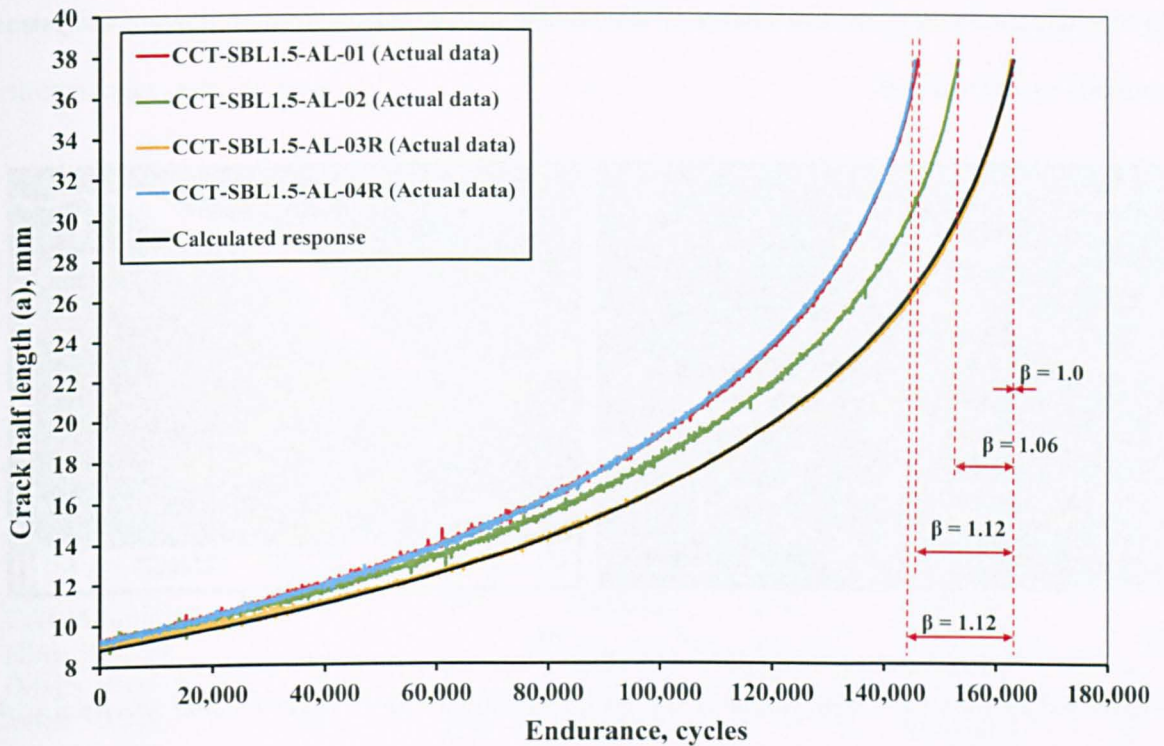


Figure 5.3.12 Comparison of actual and calculated crack growth response for 6082 aluminium alloy in periodic underload (SBL1.5) tests. Plain and welded (denoted by R) conditions shown.

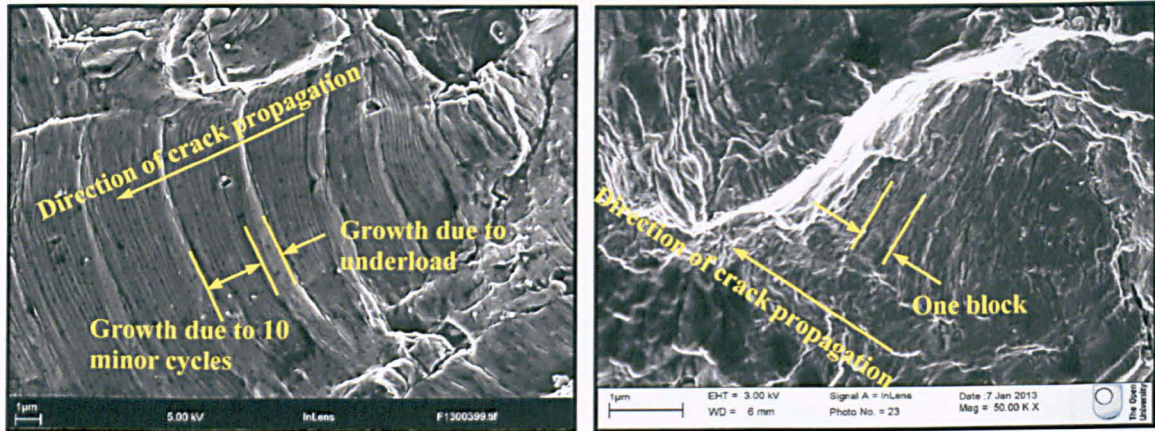
Considering this further, in Table 5.3.13 it can be seen that the effect of welding had very little effect on β for the low and high regimes, which was also found in Tables 5.3.6 and 5.3.10 for γ . However, the γ values did show a tendency to increase as ΔK increased.

5.3.6 ESTIMATING CRACK GROWTH RATE BY EXAMINATION OF SPECIMEN FRACTURE SURFACES

Failed specimens were broken open to allow examination of the fracture surfaces in a scanning electron microscope (SEM) to observe striations at various crack lengths and the crack front following each periodic underload. Striations define the position of the advancing crack front after each cycle. Consequently, the space between them is the distance propagated by the crack under the relevant applied load cycle. The main reason for examining striations was to observe the difference between effects of the two loading spectra at a local level.

As is generally found, the striations were well defined in the aluminium alloy but not in the steel, Figure 5.3.13a-b. Indeed, it only proved to be possible to distinguish between the crack growth due

to the major and minor stresses reliably in the aluminium. Consequently, the following analysis is confined to that material.



a) b)

Figure 5.3.13 Comparison of fatigue striations on fracture surfaces under loading spectrum with periodic underloads (SBL2); a) 6mm thick 6082 T651 aluminium alloy (CCT-SBL2-AL-01) at $a=23\text{mm}$, b) 8mm thick S355 structural steel (CCT-SBL2-ST-01) at $a=18\text{mm}$.

An initial step was to check that striation spacing at selected crack lengths corresponded to the measured crack growth increment per cycle at the same crack lengths in specimens tested under CA loading. The latter were represented by increments calculated using the mean crack growth laws for the aluminium alloy under the minor and major stress cycles in Table 5.3.2, for the ΔK values corresponding to the selected crack lengths. The resulting calculated crack growth increments are compared with those based on striation spacing in Table 5.3.14 and Figure 5.3.14. Since in practice the VA loading involves 10 cycles of the minor stress range, the increments for 10 minor stress cycles are given in Table 5.3.14.

It will be seen that there is reasonable agreement between the two but that the striation spacing values exhibit a wide degree of scatter. This probably reflects the many experimental errors that can arise in the identification and measurement of striations, such as uncertainty over the plane of the fracture surface with respect to the lens (i.e. parallax error), clear identification of striations corresponding to single cycles, thickness of graduation lines and scaling from photographs or the screen. All of these are difficult to quantify without a vast number of specimens. The impression from the results in Figure 5.3.14 is that, compared with the measured crack growth increments, the

error from striations for the minor stress range could be up to 40%, while that for the two major stress ranges could be around 50%.

Table 5.3.14 *Crack growth increment for CA specimens*

Specimen No.	2a, mm	ΔK	Fatigue crack growth increment, mm			
			From striations		From mean da/dN data	
			1 Major cycle	10 Minor cycles	1 Major cycle	10 Minor cycles
CAL Aluminium alloy, R=0.14 (Major stress range SBL2)	26	412	0.00042	-	0.00031	-
	30	448	0.00044	-	0.00039	-
	36	500	0.00043	-	0.00054	-
	40	536	0.00034	-	0.00066	-
	46	590	0.00065	-	0.00088	-
	50	627	0.00082	-	0.00106	-
	60	732	0.00133	-	0.00166	-
CAL Aluminium alloy, R=0.35 (Major stress range SBL1.5)	26	392	0.00028	-	0.00013	-
	30	425	0.00035	-	0.00018	-
	36	475	0.00039	-	0.00029	-
	40	506	0.00066	-	0.00038	-
	46	560	0.00108	-	0.00056	-
	50	594	0.00078	-	0.00073	-
	60	694	0.00137	-	0.00136	-
CCT-CAL-AL-12, R=0.57 (Minor stress range)	26	202	-	0.00118	-	0.00083
	30	220	-	0.00129	-	0.00104
	36	245	-	0.00120	-	0.00146
	40	263	-	0.00203	-	0.00178
	46	289	-	0.00154	-	0.00237
	50	308	-	0.00225	-	0.00287
	60	359	-	0.00432	-	0.00449

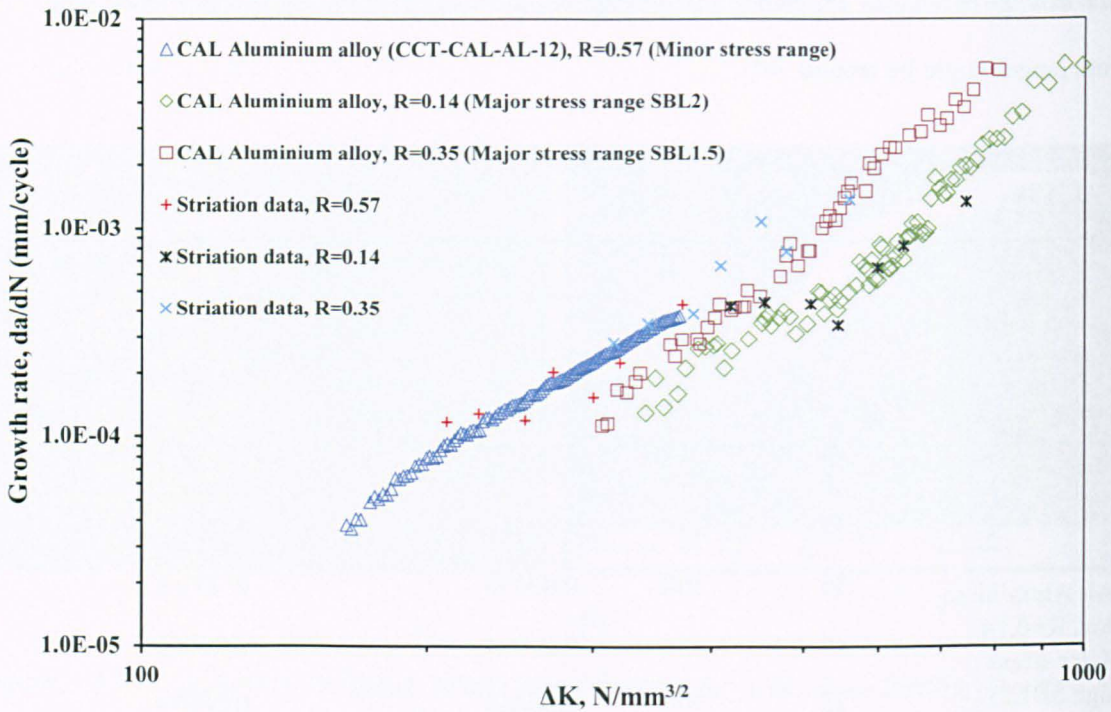


Figure 5.3.14 Comparison of CA crack growth rate data derived from striation spacing with test data.

An alternative approach would be to use linear regression analysis to fit Paris laws to the striation data and to derive confidence intervals (e.g. mean $\pm 2SD$, where SD = standard deviation of log da/dN based on striation spacings for 95% confidence intervals) for comparison with the plotted FCGR data for the same case. This would indicate whether the scatter in the measurement technique encompasses the measured data over the range of ΔK considered.

This approach was used for the data given in Figure 5.3.14 (see Appendix C), where it can be seen that for both CCT-CAL-AL-12 (R=0.57) and the major stress range data for SBL2 (R=0.14) the data do indeed fall within the confidence intervals. However, for the SBL1.5 major stress range data (R=0.35), lie below the lower bound curve (mean -2SD), particularly in the mid-low ΔK region ($2a = 26$ to 40 mm) where they are closer to mean -3SD. As mentioned above, this reflects the experimental errors associated with this technique.

Striation measurements were then made at the same crack lengths as those in Table 5.3.14 from examinations performed on four specimens tested under periodic underload spectra (two for each loading spectrum, plain and welded). Figure 5.3.15a-d shows examples of the images captured in

the SEM. The results are presented in Table 5.3.15. It will be seen that the striation spacing due to the minor stress range was generally greater than the crack growth increment obtained in the CA tests at the same stress range (Table 5.3.14) and that calculated using the CA fatigue crack growth law (Table 5.3.14), particularly under SBL2 loading. Even when considering the error associated with the measurement technique, provided the assumed error (40% or 50%) is applied to both data, a difference in growth rate can be reliably detected (Figure 5.3.16); with the SBL data exhibiting a greater crack growth increment than the CA data. Thus, both comparisons suggest that the crack growth rate accelerated after each underload cycle. With regard to the former, an alternative version of the acceleration factor γ has been introduced, defined as:

$$\gamma = \frac{\text{crack growth increment due to 10 minor cycles under spectrum loading from striations}}{\text{crack growth increment due to 10 minor cycles calculated using CA crack growth law}} \quad (5.3.4)$$

The fact that most values exceed unity provides further confirmation that the presence of a tensile underload increases the growth rate of subsequent minor stress cycles.

Recalling that it is generally assumed that an underload only affects crack growth under the applied stresses that follow, it will be seen from a comparison of Tables 5.3.14 and 5.3.15 that, according to the striation spacing, the growth rate has been increased for both the minor and major (underload) stress cycles. In this context, the resulting values of γ , which are included in Table 5.3.15, can be defined as:

$$\gamma = \frac{\text{crack growth increment due to 1 major cycle under spectrum loading from striations}}{\text{crack growth increment due to 1 major cycle calculated using CA crack growth law}} \quad (5.3.5)$$

The γ values tend to follow the same trend, with those corresponding to the major cycle (in the case of plain material) generally exceeding those for the minor cycles up to a crack length of 40mm after which the minor cycle values are the higher. For the welded material, the presence of tensile residual stresses has the effect of keeping the γ values for the major cycles above those for the minor. Thus, increased growth under both the minor and underload stresses contribute to the acceleration factors based on total growth under one VA loading block (i.e. one underload plus 10 minor stress cycles), which are included in Table 5.3.15. However, beyond 40mm the γ values from

the striations are generally less than or in the region of unity, indicating little or no interaction between the underloads and minor stress ranges. The same trend is found from the measured crack growth, but only for plain material under spectrum SBL2 loading. The relevant γ values at each of the crack lengths considered, based on the actual total crack growth, as measured in testing, and that calculated using the relevant CA crack growth law (from Table 5.3.14) are included in Table 5.3.15. Differences between these and the values based on striations can be expected since one set refers to striation measurements, with their attendant potential errors, on one specific specimen for each loading spectrum while the other refers to the average of results from duplicate tests.

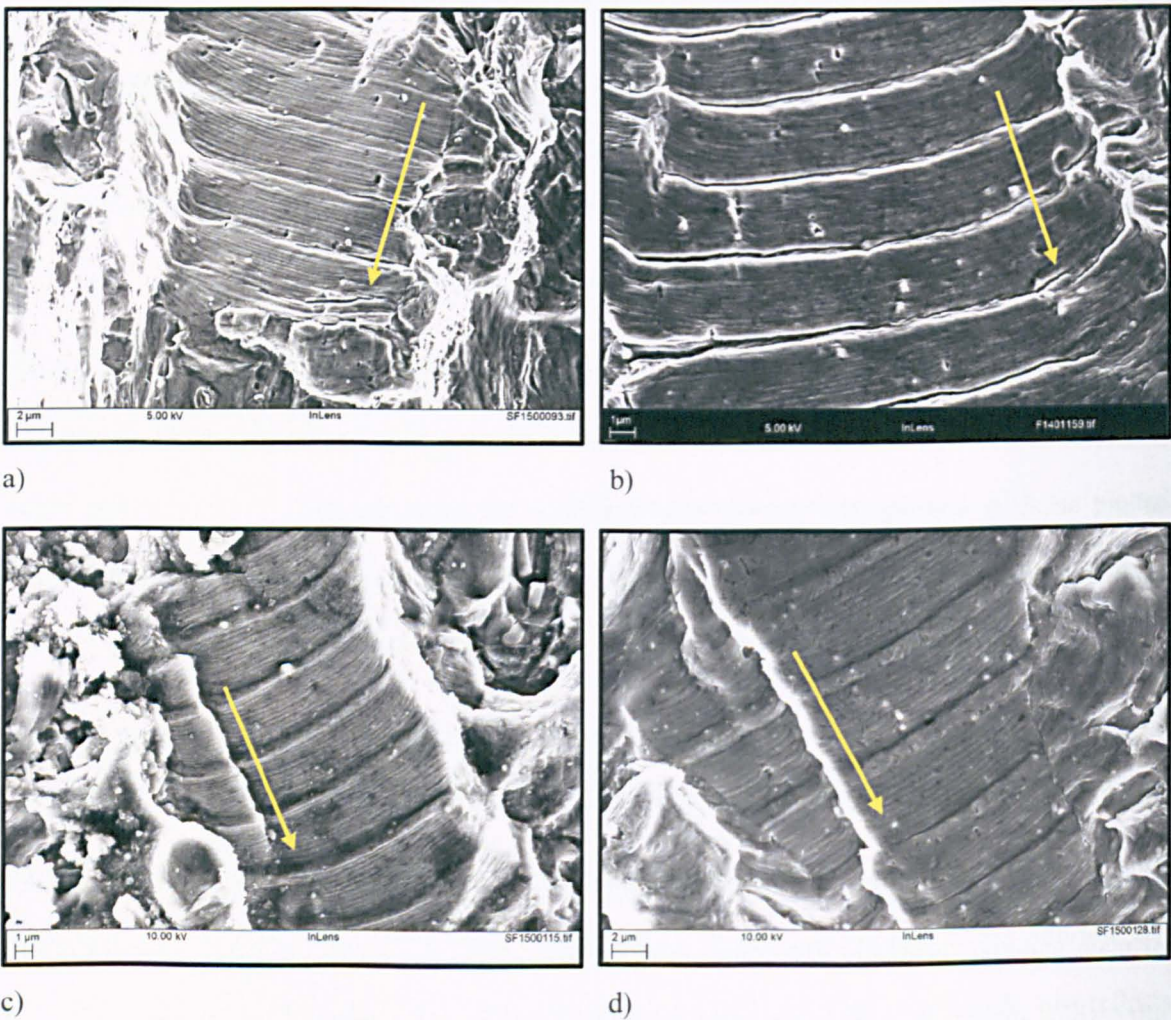
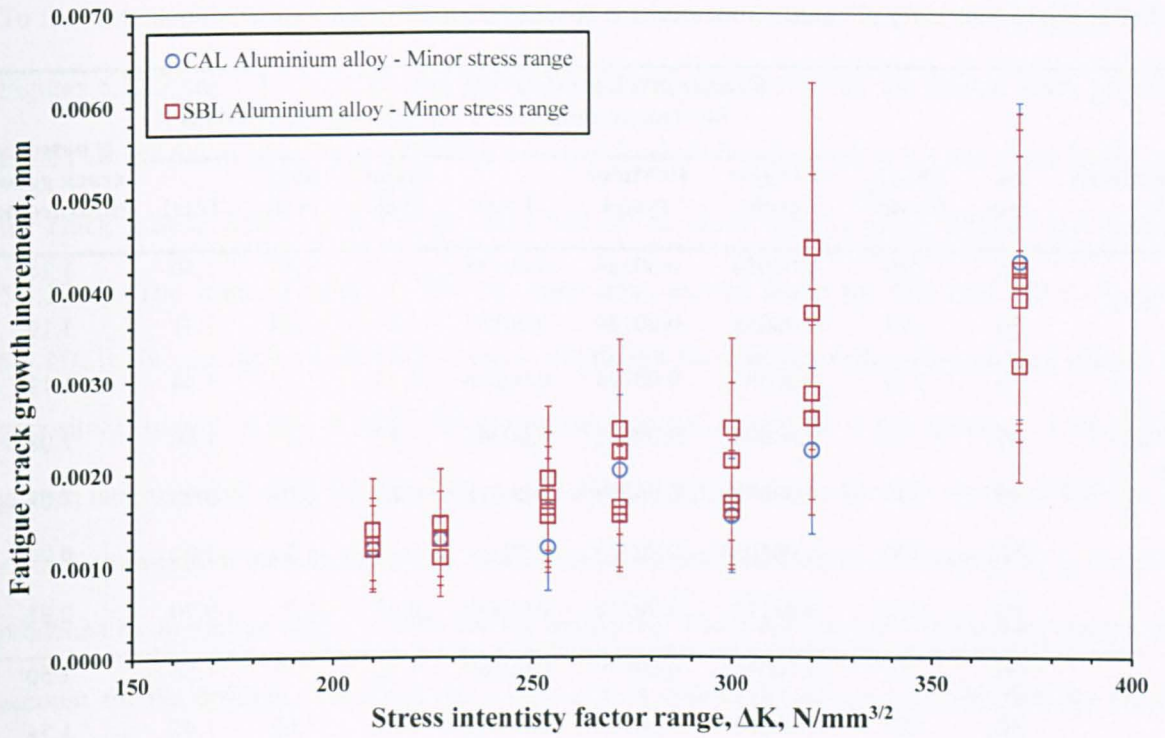
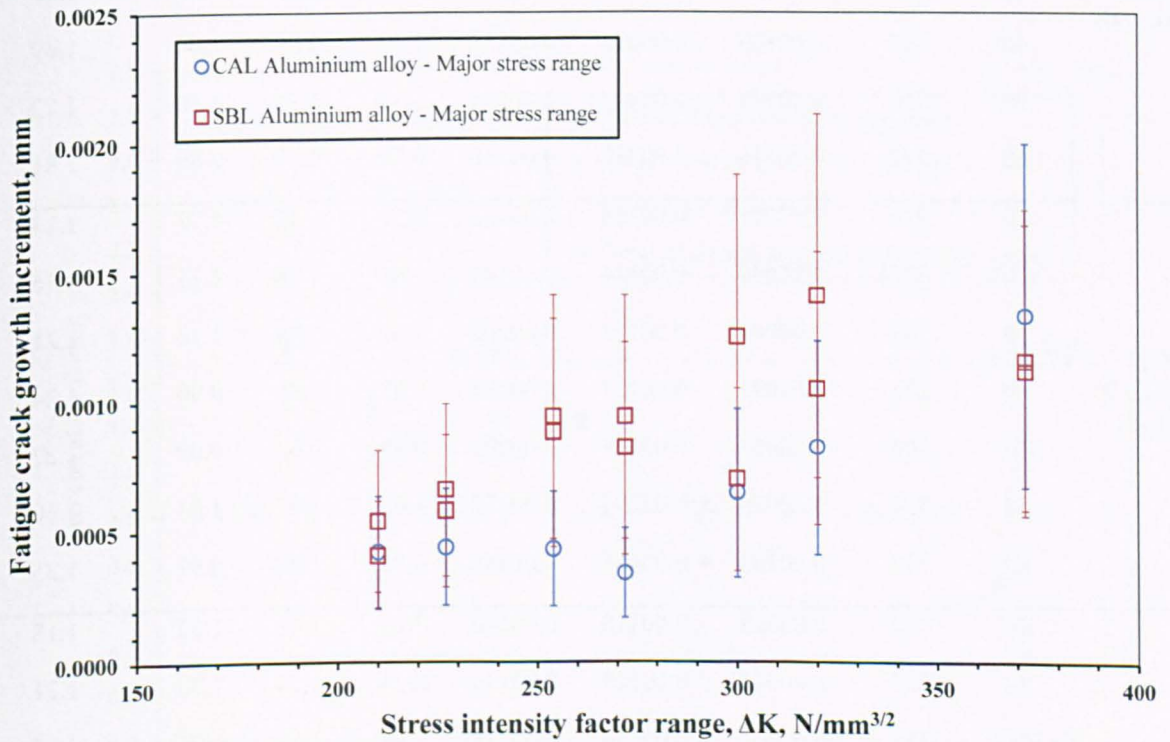


Figure 5.3.15 Examples of SEM images used in striation analysis (direction of crack propagation indicated): a) CCT-SBL2-AL-01 at 40mm, b) CCT-SBL2-AL-03R at 46mm, c) CCT-SBL1.5-AL-01 at 50mm and d) CCT-SBL1.5-AL-03R at 60mm.



a)



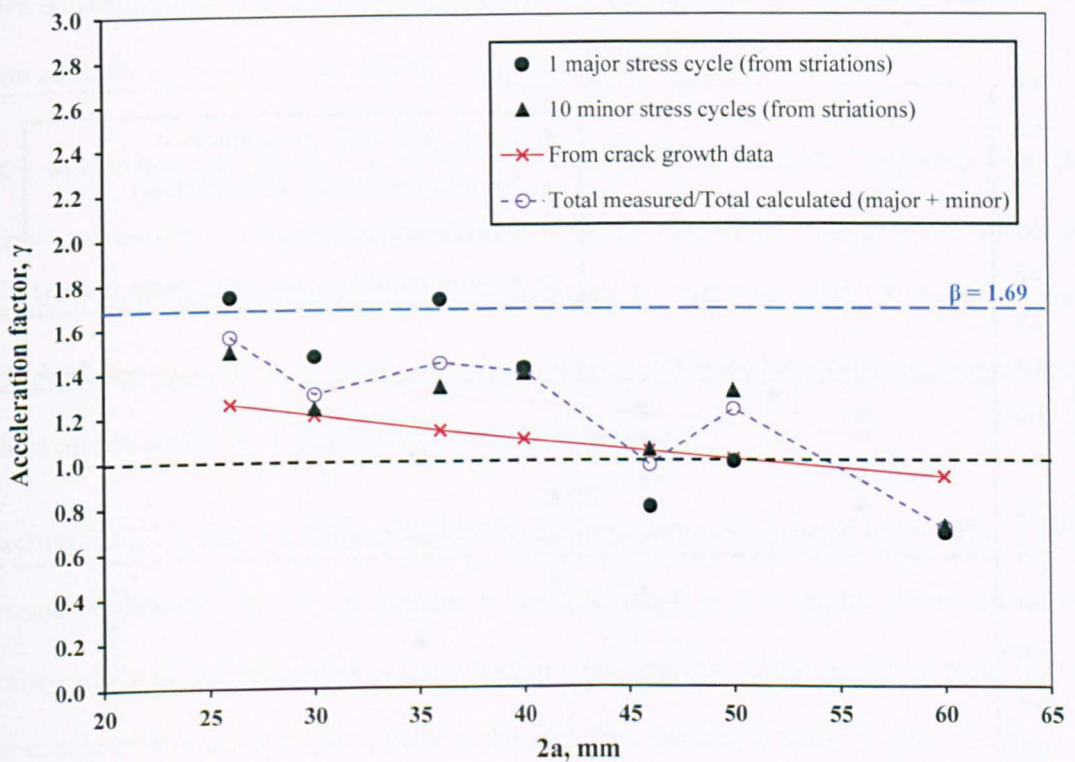
b)

Figure 5.3.16 Comparison between crack growth increment from striations including associated error: a) Minor stress range with 40% error bars, b) Major stress range with 50% error bars.

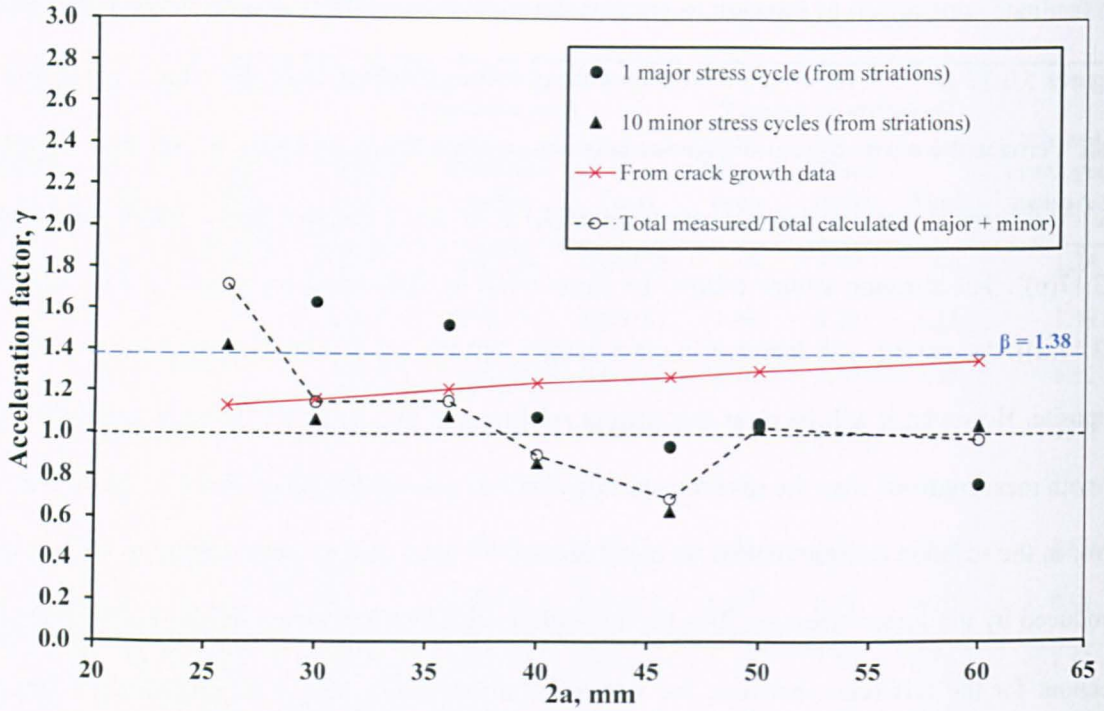
Table 5.3.15 Summary of results from striation spacing measurements.

Specimen No.	2a, mm	$\Delta K_{\text{Minor}, 3/2}$ N/mm ^{3/2}	Fatigue crack growth increment, mm			γ based on striations			γ based on crack growth measurement
			1 Major cycle	10 Minor cycles	Total	Major cycle	Minor cycle	Total	
CCT-SBL2-AL-01	26	210	0.00054	0.00124	0.00178	1.74	1.49	1.56	1.24
	30	227	0.00058	0.00129	0.00187	1.49	1.24	1.31	1.19
	36	254	0.00094	0.00194	0.00288	1.74	1.33	1.44	1.12
	40	272	0.00094	0.00247	0.00341	1.42	1.39	1.40	1.08
	46	300	0.00070	0.00248	0.00318	0.80	1.05	0.98	1.02
	50	320	0.00105	0.00376	0.00481	0.99	1.31	1.22	0.99
	60	372	0.00112	0.00318	0.00430	0.67	0.71	0.70	0.91
CCT-SBL2-AL-03R	26	210	0.00041	0.00139	0.00180	1.32	1.22	1.58	1.50
	30	227	0.00066	0.00146	0.00212	1.67	1.02	1.47	1.54
	36	254	0.00088	0.00174	0.00262	1.62	0.87	1.31	1.60
	40	272	0.00082	0.00223	0.00305	1.23	0.91	1.25	1.63
	46	300	0.00125	0.00213	0.00338	1.42	0.66	1.04	1.69
	50	320	0.00141	0.00447	0.00588	1.33	1.14	1.50	1.72
	60	372	0.00116	0.00412	0.00528	0.70	0.67	0.86	1.81
CCT-SBL1.5-AL-01	26	210	0.00047	0.00118	0.00165	3.57	1.42	1.72	1.13
	30	227	0.00030	0.00111	0.00141	1.63	1.06	1.15	1.16
	36	254	0.00044	0.00158	0.00202	1.52	1.08	1.16	1.21
	40	272	0.00041	0.00153	0.00194	1.08	0.86	0.90	1.24
	46	300	0.00053	0.00149	0.00202	0.94	0.63	0.69	1.27
	50	320	0.00076	0.00294	0.00370	1.05	1.02	1.03	1.30
	60	372	0.00103	0.00465	0.00568	0.76	1.04	0.97	1.35
CCT-SBL1.5-AL-03R	26	210	0.00028	0.00118	0.00146	2.13	1.42	1.52	1.18
	30	227	0.00041	0.00129	0.00170	2.23	1.24	1.38	1.21
	36	254	0.00057	0.00154	0.00211	1.97	1.05	1.21	1.27
	40	272	0.00059	0.00155	0.00214	1.55	0.87	0.99	1.30
	46	300	0.00051	0.00168	0.00219	0.90	0.71	0.75	1.35
	50	320	0.00082	0.00259	0.00341	1.13	0.90	0.95	1.39
	60	372	0.00117	0.00391	0.00508	0.86	0.87	0.87	1.47

To facilitate comparison of the various γ values for plain material they are presented graphically in Figures 5.3.17 and 5.3.18, which also shows the β values obtained from the fatigue crack growth tests. Perhaps the most striking difference between γ values based on striations and those based on the crack growth data is that for spectrum SBL1.5 at crack lengths above 40mm (see Figure 5.3.17(b)). The striation values follow the same trend as that found for spectrum SBL2 (Figure 5.3.17(a)), decreasing with increase in crack length, but the crack growth measurements show the opposite. However, it will be clear that greater reliance can be placed on the accuracy of the crack growth measurements than the striation spacing and thus a possible explanation for the difference is error in the striation measurements. As noted previously, such errors could amount to 40% in those produced by the minor stress or 50% for the underload. These are generally more than enough to account for the difference between the γ values from striations and crack growth data for crack lengths above 40mm in Figure 5.3.17(b), and indeed the exceptionally high value from the major stress cycle at $2a = 26\text{mm}$ (not plotted, see Table 5.3.15).

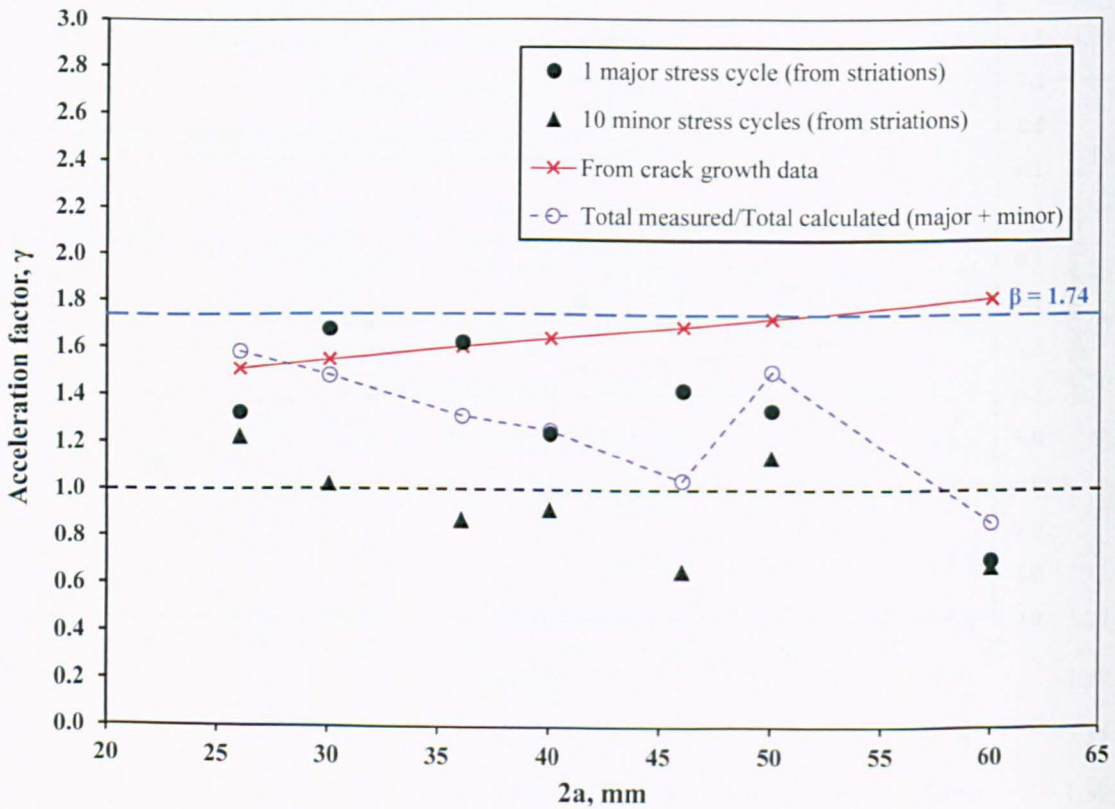


a)

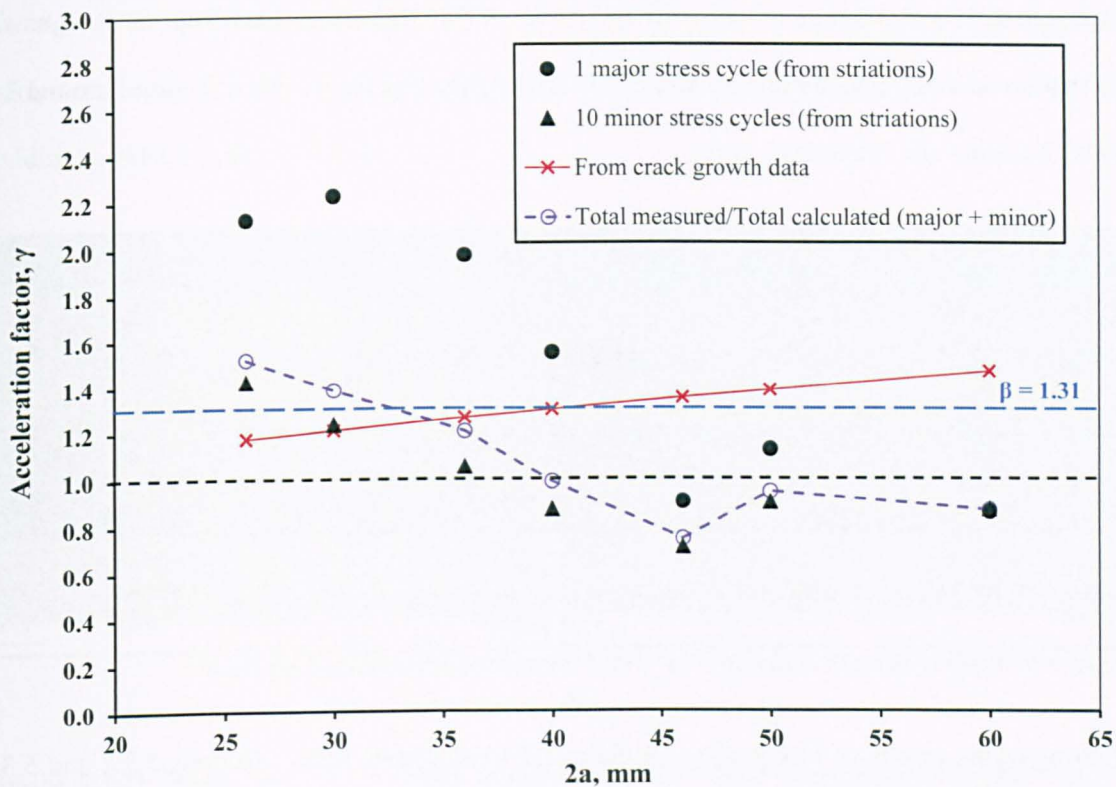


b)

Figure 5.3.17 Comparison of acceleration factor (γ) obtained from striations and measured crack growth rates for plain material: a) SBL2 spectrum; b) SBL1.5 spectrum.



a)



b)

Figure 5.3.18 Comparison of acceleration factor (γ) obtained from striations and measured crack growth rates for welded material: a) SBL2 spectrum; b) SBL1.5 spectrum.

For the welded material (Figure 5.3.18a-b) the γ values again show the same tendency as the plain material to decrease with increasing crack length. As in the case of the crack growth measurements in Figure 5.3.17b, both the crack growth measurements for SBL2 and SBL1.5 show the opposite effect. Again errors in striation measurements could account for the large differences in γ observed for the major stress cycle (Figure 5.3.18b) at $2a = 26$ to 36 mm.

In Section 5.3.2.2 it was noted that a slight increase in growth rate occurred under SBL1.5 loading at around $300\text{N/mm}^{3/2}$, which corresponds to a crack length of $a = 26$ mm. Observations on the fracture surface of the specimens suggest that this may be due to the transition from flat plane strain tensile growth to shear, particularly as the shear lips increase in width, Figure 5.3.19.

Based on tests performed under constant ΔK conditions (Edwards *et al.*, 1984), it was found that crack growth was much higher in the flat tensile mode than when shear lips had developed. The same finding following the analysis of striation spacings on flat and slanted growth in constant ΔK

tests resulted in a decrease in growth rate by a factor of 3 to 4 (Ling and Schjive, 1990). A similar observation was made on aluminium alloy 2024 where the decrease was by a factor of around 3 on da/dN (Zuidema and Mannesse, 1991).

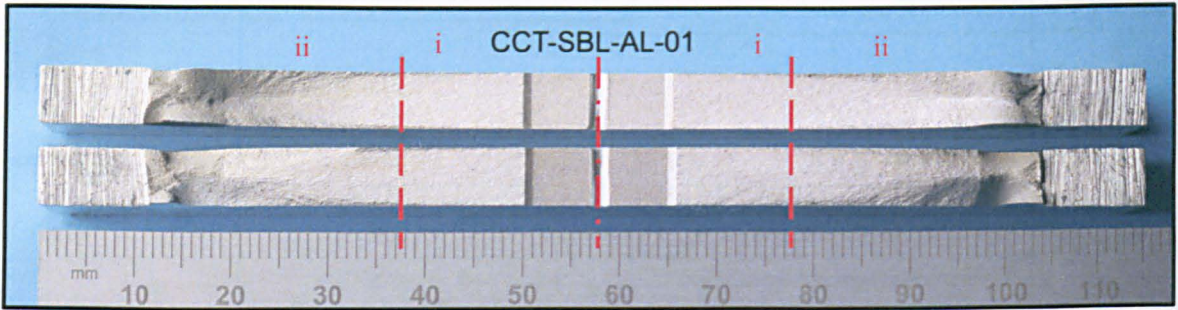


Figure 5.3.19 Macro photograph showing the fracture surface of specimen CCT-SBL1.5-AL-01. The tensile mode of growth is denoted by i, and the subsequent shear mode by ii.

Referring to the results of FCGR tests for plain and welded aluminium (Sections 5.3.2 and 5.3.3) specimens, increases in growth rates were observed close to the change from flat to shear modes. Further examination of specimen fracture surfaces and analysis of FCGR data revealed four stages of growth for these specimens, as shown in Figure 5.3.20.

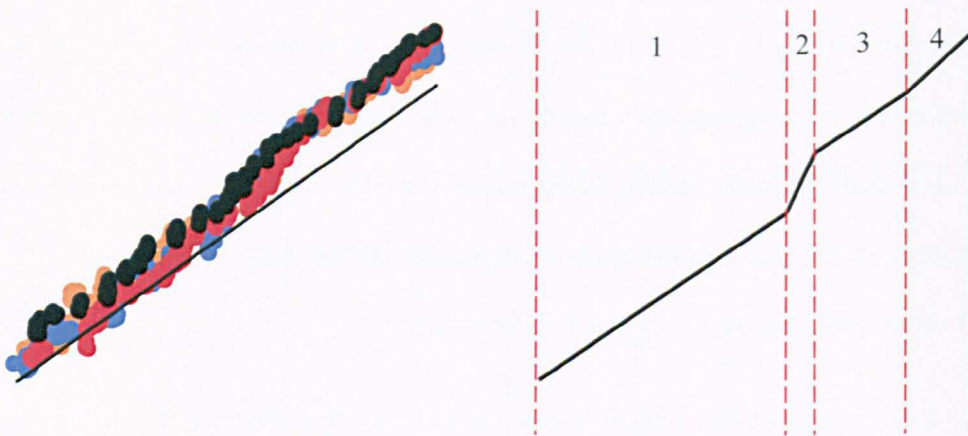


Figure 5.3.20 Diagram showing the four modes of growth associated with the 6082 6mm thick aluminium alloy subjected to SBL1.5 and SBL2 loading (actual test data also shown for comparison).

Stage 1 is the tensile mode growth which has been found to extend to $\sim 300N/mm^{3/2}$ ($\sim a=23mm$). Stage 2 concerns the slight increase in growth rate close to the transition from flat to shear growth and extends to $\sim 340N/mm^{3/2}$ ($\sim a=26mm$). Examination of this region under SEM showed that near

the edge of the specimen, where plane stress prevails, the surface morphology exhibited elongated featureless regions, which were not apparent at the centre of the specimen where plane strain conditions exist, Figure 5.3.21a-b.

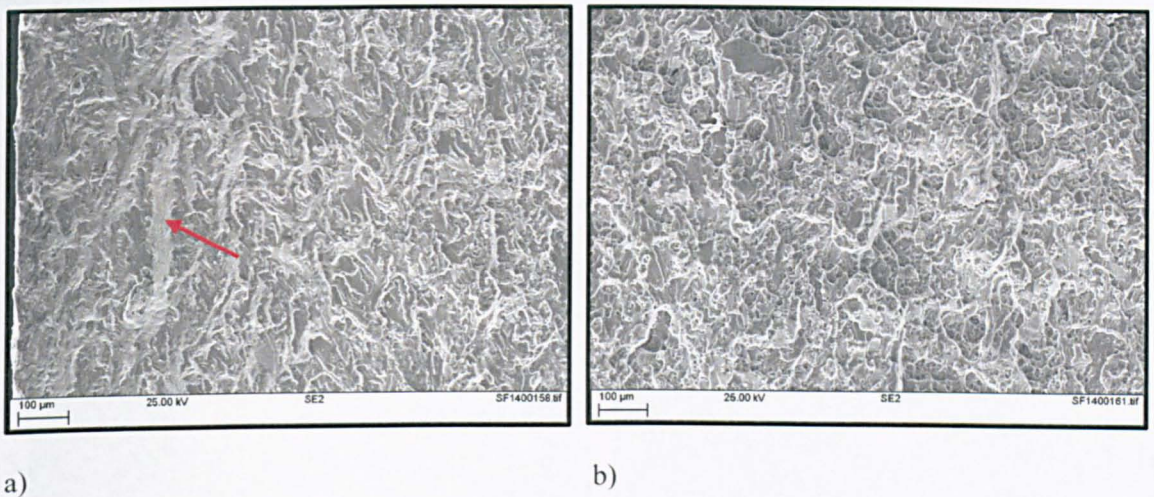


Figure 5.3.21 Stage 2 growth observed on 6mm thick 6082 T651 aluminium alloy (CCT-SBL1.5-AL-03R); a) edge of specimen at $a=22\text{mm}$ showing elongated regions (arrowed), b) middle of specimen at $a=22\text{mm}$ showing uniform surface morphology.

Stage 3 is the formation of shear lips and increasing lip width resulting in a slight decrease in growth rate, extending to $\sim 440\text{N}/\text{mm}^{3/2}$ ($\sim a=35\text{mm}$). The final stage is the full transition into double shear mode with increasing growth rate as the nett cross-section reduces. These four modes are also indicated in Figure 5.3.22.

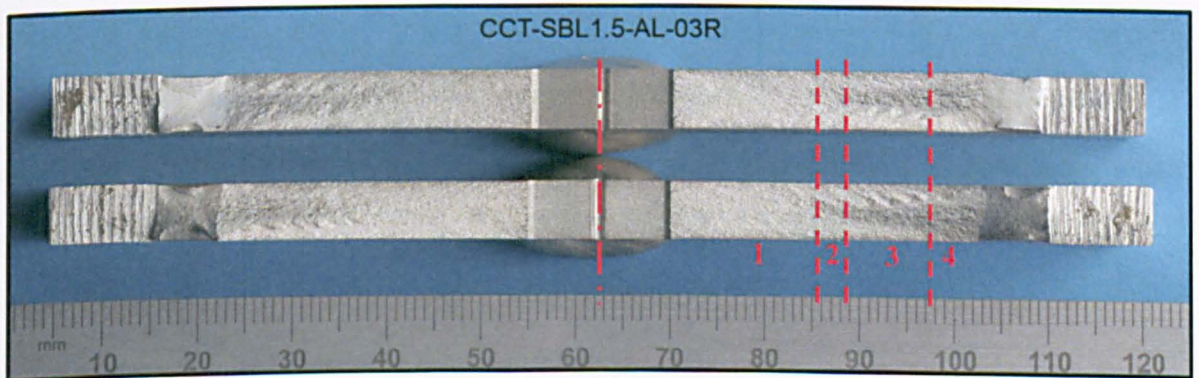
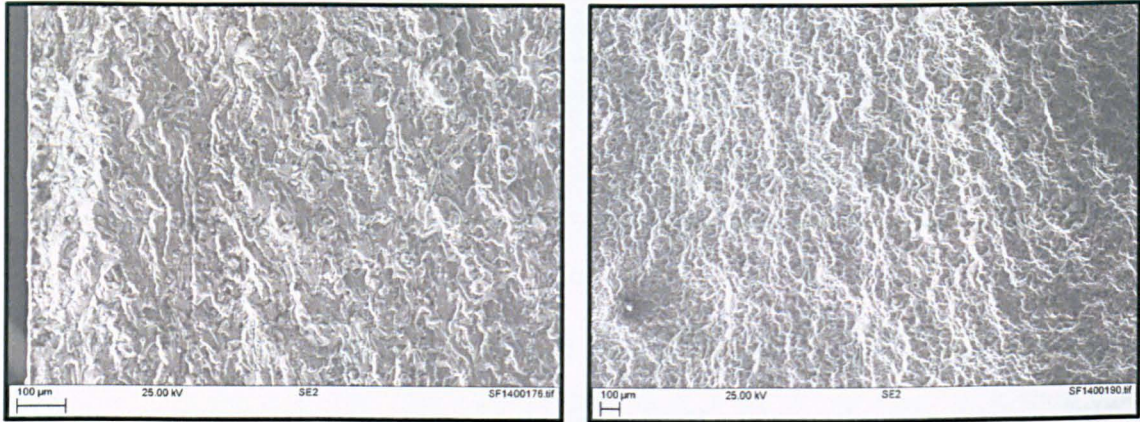


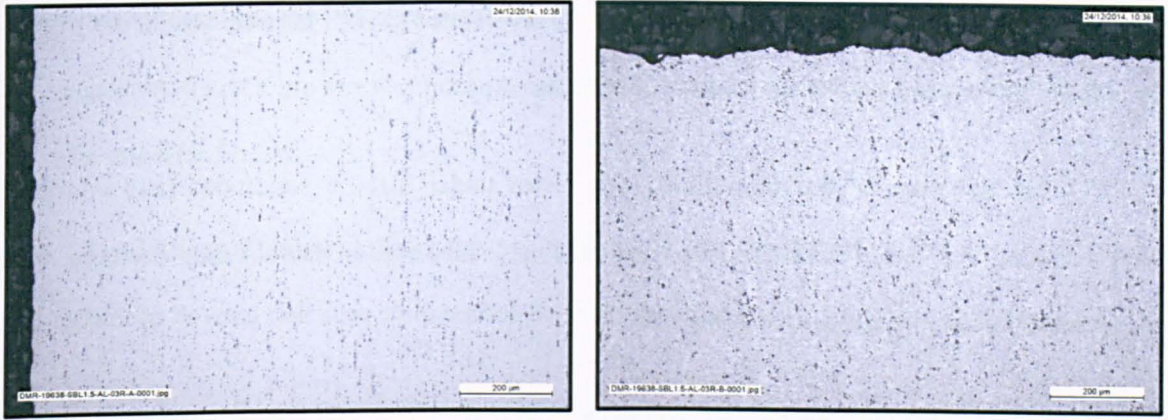
Figure 5.3.22 Macro photograph showing the fracture surface of specimen CCT-SBL1.5-AL-03R. The four stages of growth are highlighted.

For specimen CCT-SBL1.5-AL-03R (Figure 5.3.22), the elongated regions close to the specimen edge were also found at crack lengths of 11mm and 28mm and were therefore not the reason for the slight increase in observed growth rates. However, they were not apparent in specimen CCT-SBL2-AL-02, which did not display the same Stage 2 growth rate increase (Figure 5.3.6). Here the surface morphology at 11mm and 22mm was uniform across the specimen thickness, Figure 5.3.23a-b.



a) b)
Figure 5.3.23 Fracture surface of CCT-SBL2-AL-02 showing a uniform surface morphology; a) edge of specimen at $a=22\text{mm}$, b) middle of specimen at $a=22\text{mm}$.

Metallographic sections were taken from CCT-SBL1.5-AL-03R to identify possible explanations within the material microstructure for the slight increase in growth rate, Figure 5.3.24a-b. Nothing of any significance was observed. The presence of intermetallic particles is typical for 6xxx series aluminium alloys (Mrówka-Nowotnik, 2008). The intermetallic particle distribution in Figure 5.3.24a shows an expected effect of material thickness, with a random distribution near the surface and a more columnar distribution in the centre of the specimen; the opposite of what may have provided an explanation for the difference in crack growth.



a)

b)

Figure 5.3.24 Metallographic sections of 6mm thick 6082 T651 aluminium alloy (CCT-SBL1.5-AL-03R); a) edge of specimen, b) transverse section at $a=22\text{mm}$.

5.4 SUMMARY OF FINDINGS

Based on fatigue crack growth tests on CCT specimens made from S355 steel and 6082 T651 aluminium alloy, subjected to periodic underloads of two different magnitudes and the addition of welding residual stresses, the following conclusions were drawn:

- Tests under periodic underloading have resulted in lives shorter than observed under CA loading.
- Two different forms of acceleration factor, termed γ and β , were used to compare the data.
- The acceleration factor γ shows how many times larger is the crack growth rate for the periodic underload tests than the calculated crack growth rate determined by a linear summation of CA loading response.
- The acceleration factor β shows how much larger is the calculated number of cycles than that actually required in a periodic underload test to achieve the same crack length.
- For plain material tested using SBL2, accelerated growth was observed in the γ range of 1.02 to 1.56 for the steel and up to 1.35 for the aluminium alloy, although some retardation was apparent at high ΔK .

- For the reduced underload magnitude (SBL1.5), accelerated growth for steel was in the γ range of 1.35 to 1.56 and 1.03 to 1.55 for the aluminium alloy.
- With the exception of the aluminium alloy tested under SBL1.5 conditions (and one steel specimen, CCT-SBL1.5-ST-02), all tests exhibited acceleration factors that decrease with increase in crack length and/or at high ΔK .
- For the excluded, the greatest acceleration was at high ΔK , which was thought to be due to variations in the magnitude of residual stress between specimens, or differences in the zone of residual tension (for the steel), and potential differences in ΔK_{eff} for the aluminium.
- For the majority of the tests performed, it was found that the SBL1.5 spectrum resulted in higher acceleration factors than the SBL2 spectrum at high ΔK . It was considered that due to the difference in major cycle stress ratio, this was related to a higher ΔK_{eff} .
- Higher values of β were obtained from welded specimens due to the presence of tensile residual stresses particularly for steel. For the aluminium alloy, the same effect was true but far less pronounced.
- The ranges of γ acceleration factors for the SBL2 sequence also increased, to 1.30 to 1.88 for steel and 1.14 to 2.12 for the aluminium alloy.
- Under SBL1.5, the γ acceleration factor for steel increased, ranging from 1.40 to 2.13, but for the aluminium no real increase was apparent with values in the range 1.05 to 1.47.
- As with the plain material, the greatest level of acceleration in the welded specimens was at low ΔK , with the exception of the SBL1.5 aluminium alloy tests (and CCT-SBL2-AL-04R) which again behaved in the opposite manner.
- Examination of the effect of periodic underloads on fatigue crack growth based on striation spacings was confined to the aluminium alloy. Two alternative forms of acceleration factor γ were identified, in each case considering either the crack growth increment due to the minor or major cycles from striations versus those calculated using CA crack growth laws.

- Observations on the fracture surfaces of the aluminium alloy specimens confirmed that accelerated crack growth was not just confined to the period following the underload but also the underload itself.
- The addition of tensile residual stresses by welding had a negligible effect on γ from striation spacings beyond that already observed for plain material.
- The findings of load sequence tests for two magnitudes of stress range and two magnitudes of underload (major stress cycle), have been presented. The factors thought to be contributing towards fatigue crack growth acceleration are evaluated in Chapter 6.

Chapter 6

MECHANISMS INFLUENCING CRACK GROWTH ACCELERATION

6.1 INTRODUCTION

Following a review of literature on applied loading interaction effects that can cause fatigue crack acceleration, in Chapter 2, and evidence of accelerated growth during periodic underload fatigue testing, as highlighted in Chapter 5, this Chapter presents both theoretical and experimental investigations into the mechanisms influencing crack growth acceleration.

The main areas investigated include:

- a) the measurement of crack closure and the influence of plastic zones and their estimated sizes on its occurrence.
- b) the measurement of weld residual stresses, their redistribution and their effect on crack growth.
- c) the application of finite element stress analysis (FEA) for modelling the effect of the applied underloads at the crack tip.

The findings from load sequence testing in Chapter 5 and the role of influencing mechanisms considered in this Chapter are then discussed and the main mechanism(s) influencing crack growth acceleration under this form of loading are identified.

6.2 CRACK TIP PLASTICITY

6.2.1 THE ROLE OF CRACK CLOSURE IN FATIGUE CRACK GROWTH ACCELERATION

As noted in the previous chapter, both the underload stress and the minor stress cycles following it produced higher crack growth rates than expected from the behaviour under CA. A possible explanation for this is that the crack closure stress levels were lower than those obtained for the same applied stresses and crack lengths under CA loading, so that the effective stress ranges were higher under VA than CA loading. This was investigated on the basis of crack closure measurements in both plain and welded specimens.

6.2.2 CRACK CLOSURE LEVEL MEASUREMENT

As discussed in Section 3.6, crack closure was detected using uniaxial strain gauges bonded to the surface of CCT specimens 1.5mm behind the crack tip. The crack closure stress for a given fatigue crack was found by measuring the load at which the crack surfaces came into contact, indicated on the applied stress versus measured strain curve as the point of non-linearity. Hence, the proportion of stress range for which the crack was open, U , was found. In order to consider the effect of prior loading on both the underload and minor stresses, crack closure measurements were made before the application of the underload, during the underload and immediately after its application, all at various crack lengths.

6.2.2.1 PLAIN S355 STEEL SPECIMENS

It was found that the crack closure stress level for the minor stress range, both before and after an underload and for all crack lengths considered, was constant, as illustrated for a crack length of 12mm in Figure 6.2.1. However, the crack closure stress level for the underload varied with crack length, as shown in Figure 6.2.2. These results were obtained during the application of the SBL2 spectrum underload but the minimum stress levels for both SBL2 and SBL1.5 are indicated.

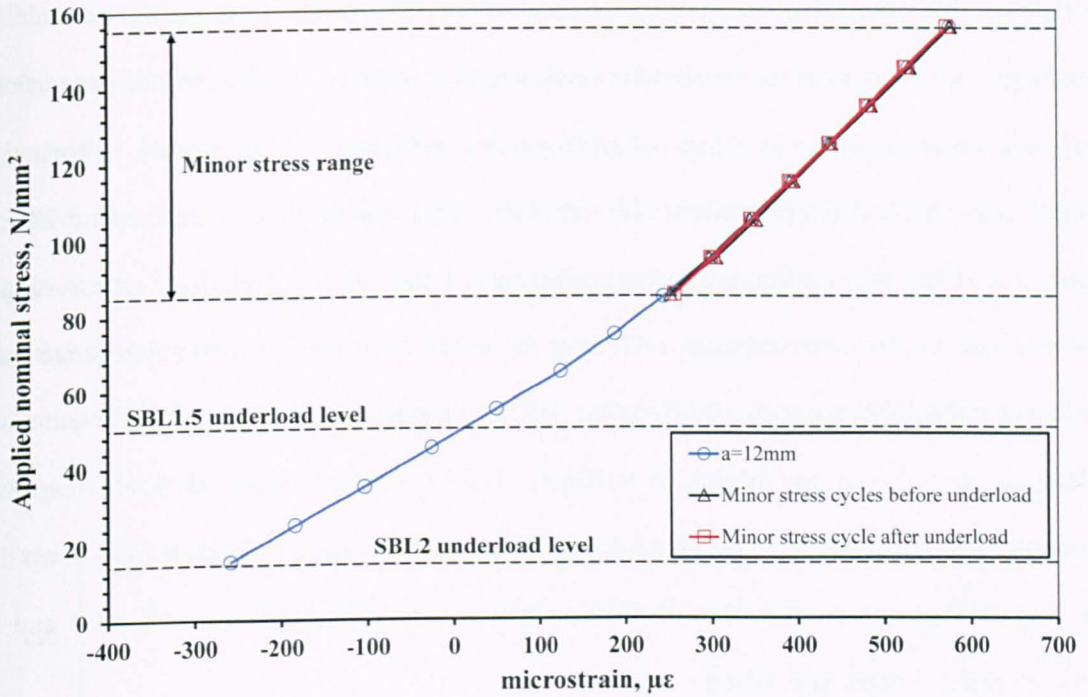


Figure 6.2.1 Recorded crack closure levels in plain S355 steel before, during and after an underload cycle from 156N/mm^2 to 16N/mm^2 .

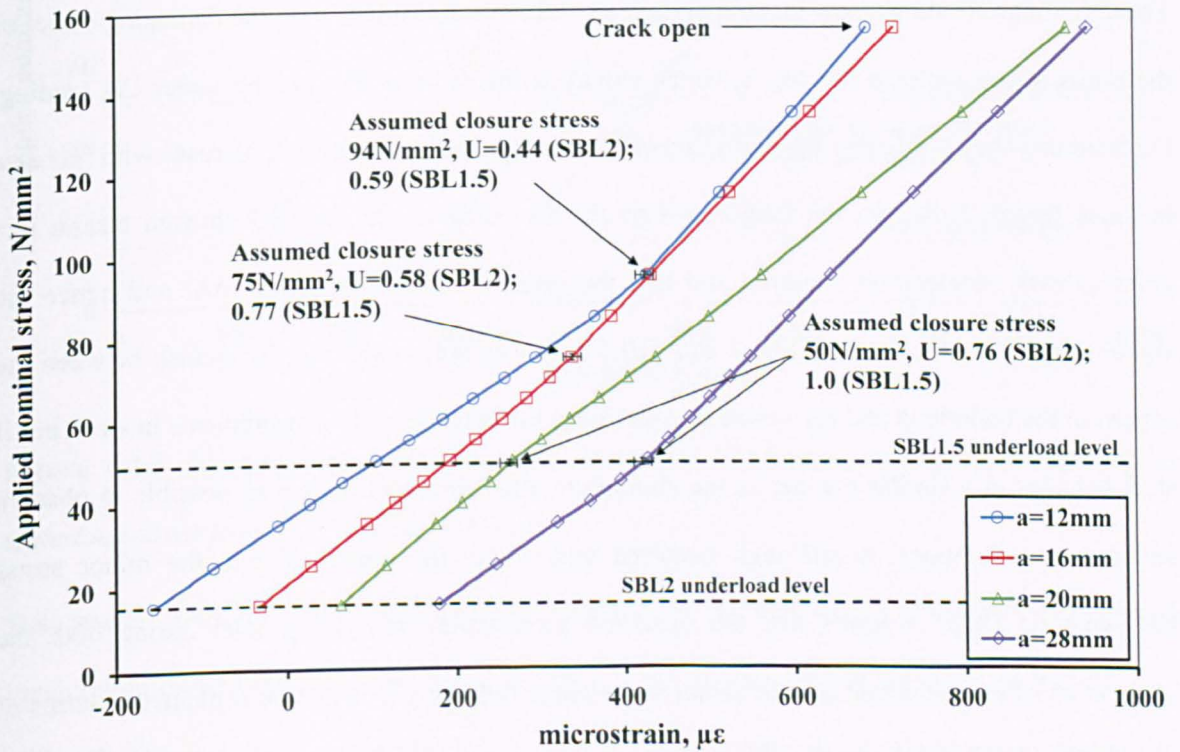


Figure 6.2.2 Recorded crack closure levels in plain S355 steel during application of an underload stress from 156N/mm^2 to 16N/mm^2 .

The findings in Figure 6.2.2 therefore suggest that under SBL2 loading, for which the underload stress range was 140N/mm^2 , at the shortest crack length considered, $a = 12\text{mm}$, the proportion of the applied stress range that is effective in propagating the crack, while the crack is open, U , is $(156-94)/140 = 0.44$. U then increases with increase in crack length until at and beyond 20mm it stabilizes at 0.76 . When considering the application of the SBL1.5 underload (stress range = 105N/mm^2), it will be evident that at $a = 12\text{mm}$ the proportion of the applied stress range that is effective $(156-94)/105$ gives $U = 0.59$. As for SBL2, this then increases with crack length until it stabilizes at $U = 1.0$ at and beyond $a = 20\text{mm}$. These stabilized values of U are reasonably comparable with those obtained by Maddox and Booth (1986) under CA loading from 8mm thick mild steel CCT specimens of 0.70 to 0.85 for the SBL2 underload stress ratio of $R = 0.1$ and $U = 1.0$ for the SBL1.5 stress ratio of 0.6 .

In summary, the above measurements indicate that the crack never closes under the minor stress range and that the effective magnitude of the underload increases with increase in crack length. These findings would suggest that the underload will have no influence on the damaging effect of the minor stress cycles following it, which would be the same as that arising under CA loading. Furthermore, they imply that the damaging effect of the underload itself will increase with increase in crack length. However, the fatigue test results presented in section 5.3.2 showed that in fact crack growth acceleration occurred and that the greatest effect was at low ΔK , and hence the shorter crack lengths, for both SBL2 and SBL1.5. It was not possible to distinguish between the effects of the underload and minor stress cycles from the crack growth measurements in steel, but if steel behaves in a similar manner to the aluminium alloy, in which it proved possible to observe and measure striations, acceleration occurred under both the underload and the minor stress following it. Thus, it seems that the observed acceleration in crack growth during both the application of the underload and the minor stress range following it cannot be explained in terms of a crack closure mechanism.

6.2.2.2 WELDED S355 STEEL SPECIMENS

As in the case of the plain steel, the crack remained fully open throughout the application of the minor stress cycles. However, in contrast to plain steel the same was found for the underload stress

cycle, at least until the crack was relatively long, as seen in Figure 6.2.3. For the SBL2 sequence $U = 1.0$ over the first 16mm of crack growth. Above 20mm the slight evidence of non-linearity suggests that closure occurred at 35N/mm^2 , equating to $U = 0.86$. In the case of the SBL1.5 sequence, the closure results suggest that 100% ($U = 1.0$) of the applied stress range is always effective. Thus, overall it seems that the residual stress due to welding has the effect of holding open the fatigue crack and thus preventing closure. The fact that there was evidence of some closure at long crack lengths could well reflect the decrease in residual stress level due to the cyclic loading, as discussed later (see Figure 6.3.11).

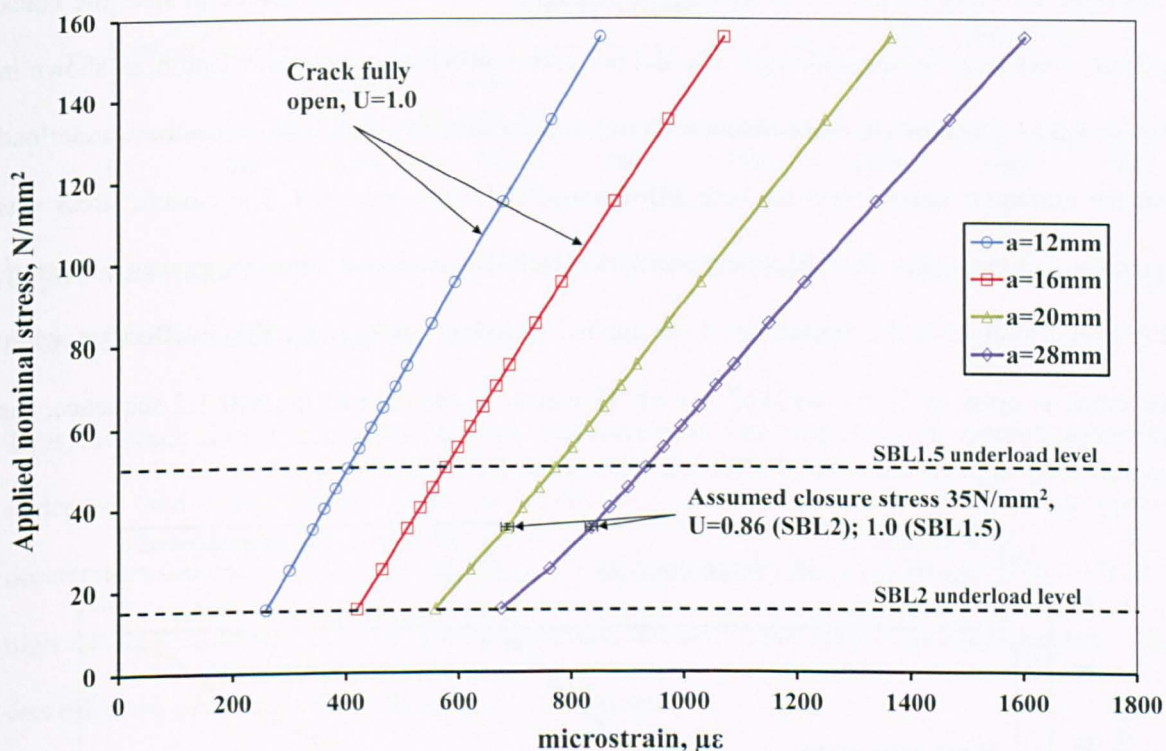


Figure 6.2.3 Recorded crack closure levels in welded S355 steel, during application of an underload stress from 156N/mm^2 to 16N/mm^2 .

The results from the load sequence tests (Section 5.3.3) indicated significant crack growth acceleration under both SBL2 and SBL1.5, giving $\gamma = 1.86$ and 1.92 respectively, at low ΔK ($a \sim 10\text{mm}$). The fact that γ under SBL2 decreased at crack lengths above 20mm when closure was also observed, might suggest a link to crack closure effects; although some acceleration still exists suggesting there is no closure. However, in order to get this link this would mean that the closure stresses were different for CA loading, such that to get acceleration from both the underload and

minor stress following it, the value of U would need to have been <1.0 under CA loading; but as explained above, the crack remained fully open throughout the minor stress cycles. Overall, since $U = 1.0$ for both minor and underload cycles, no interaction would be expected. So, the fact that there was acceleration indicates that closure is not the explanation.

6.2.2.3 PLAIN 6082 T651 ALUMINIUM ALLOY SPECIMENS

As in the case of the plain steel, it was found that the crack closure stress level for the minor stress range, both before and after an underload and for all crack lengths considered, was constant, as illustrated for crack lengths of 12 and 20mm in Figure 6.2.4. However, unlike in steel the crack closure stress level for the underload also did not vary significantly with crack length, as shown in Figure 6.2.5. These results were obtained during the application of the SBL2 spectrum underload but the minimum stress levels for both SBL2 and SBL1.5 are indicated. The closure stress was typically 23N/mm^2 . For the SBL2 sequence, for which the underload stress range was 63N/mm^2 , this would imply that the proportion of the applied underload stress range that is effective, while the crack is open, is $U = (74-23)/63 = 0.81$. However, in the case of the SBL1.5 sequence, the proportion of applied stress that is effective increases to $U = 1.0$.

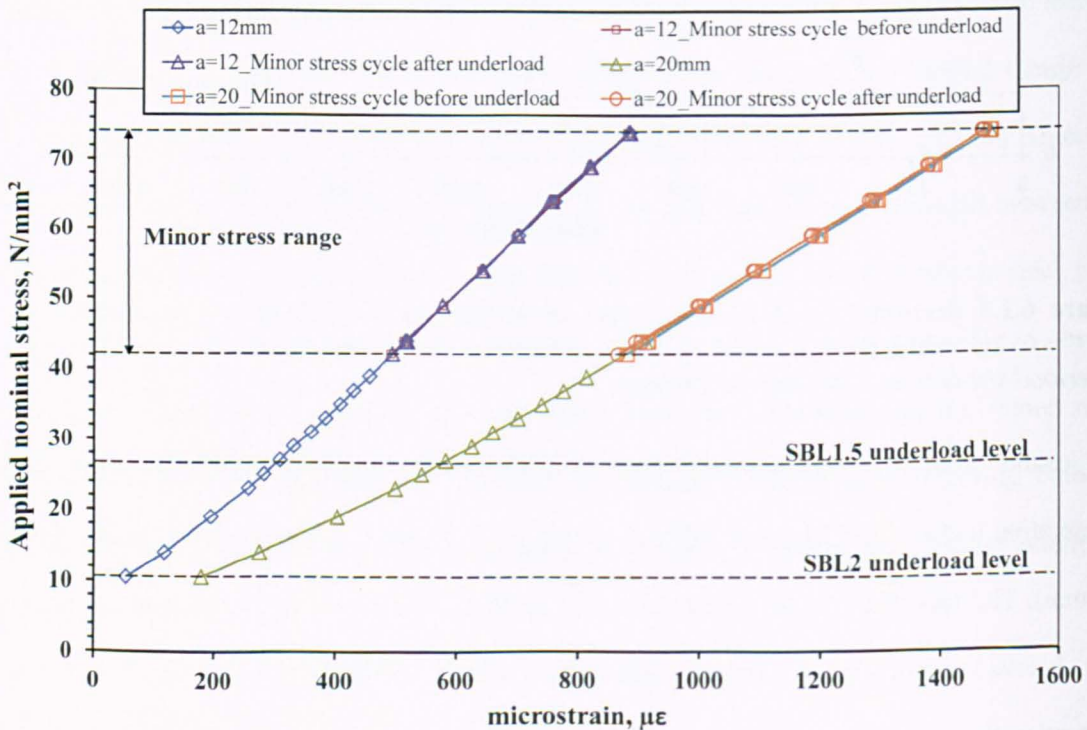


Figure 6.2.4 Recorded crack closure levels in plain aluminium alloy before, during and after an underload cycle from 74N/mm^2 to 11N/mm^2 .

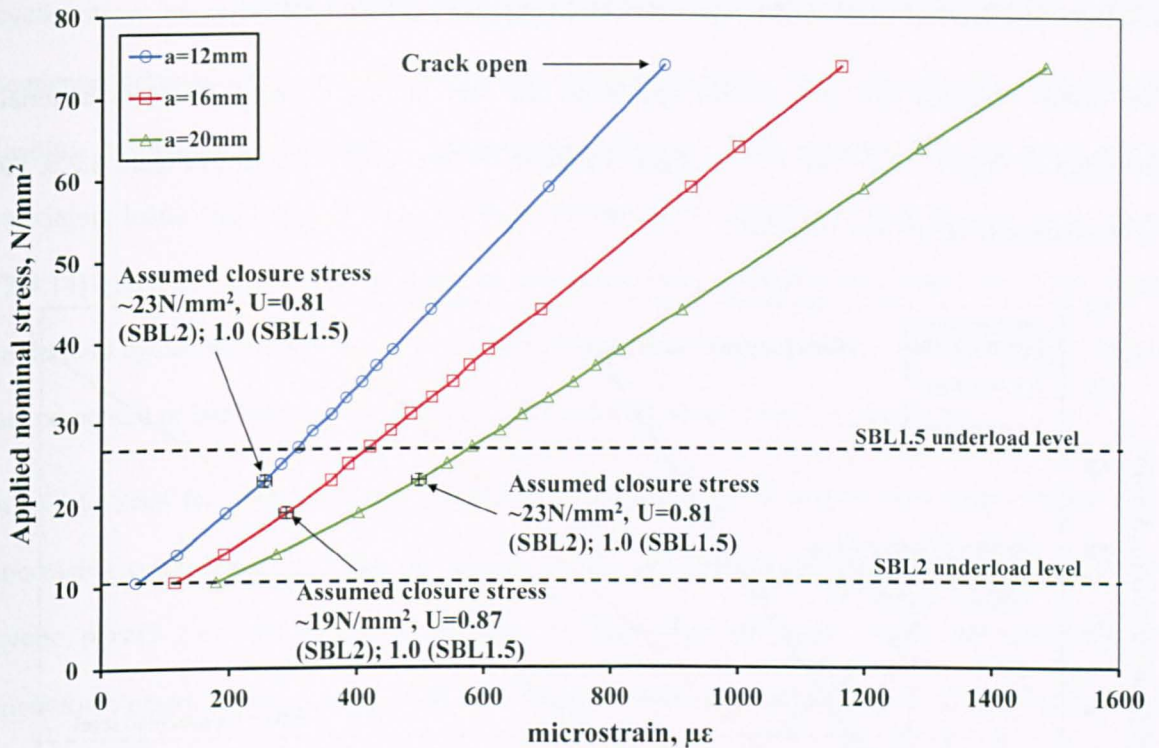


Figure 6.2.5 Recorded crack closure levels in plain 6082 aluminium alloy during application of an underload stress from 74N/mm^2 to 11N/mm^2 .

Thus, the crack closure measurements imply that there should be little or no interaction between the underload and minor stress cycles. However, as indicated in Section 5.3.2, crack growth acceleration did occur. In the case of SBL2, γ was again greater at low ΔK ($a = \sim 12\text{mm}$) than at high ΔK ($a = \sim 32\text{mm}$), 1.29 and 0.89 respectively, but the proportion of applied stress range that was effective whilst the crack was open, U , was the same.

Under SBL1.5, γ was greater at high ΔK ($a = \sim 32\text{mm}$) than low, 1.40 and 1.12 respectively. Closure measurements did not extend to this crack length, but the results in Figure 6.2.5 suggest that the crack was fully open under these loading spectra. Thus, as in the case of SBL2, the proportion of applied stress range that was effective was the same, therefore suggesting that the observed acceleration was not governed by levels of closure or effective stress range.

6.2.2.4 WELDED 6082 T651 ALUMINIUM ALLOY SPECIMENS

The results obtained from the welded specimens are very similar to those for plain material, presented in Figure 6.2.5, with only a slight change in closure level. As seen in Figure 6.2.6, the assumed closure stress was 19N/mm^2 .

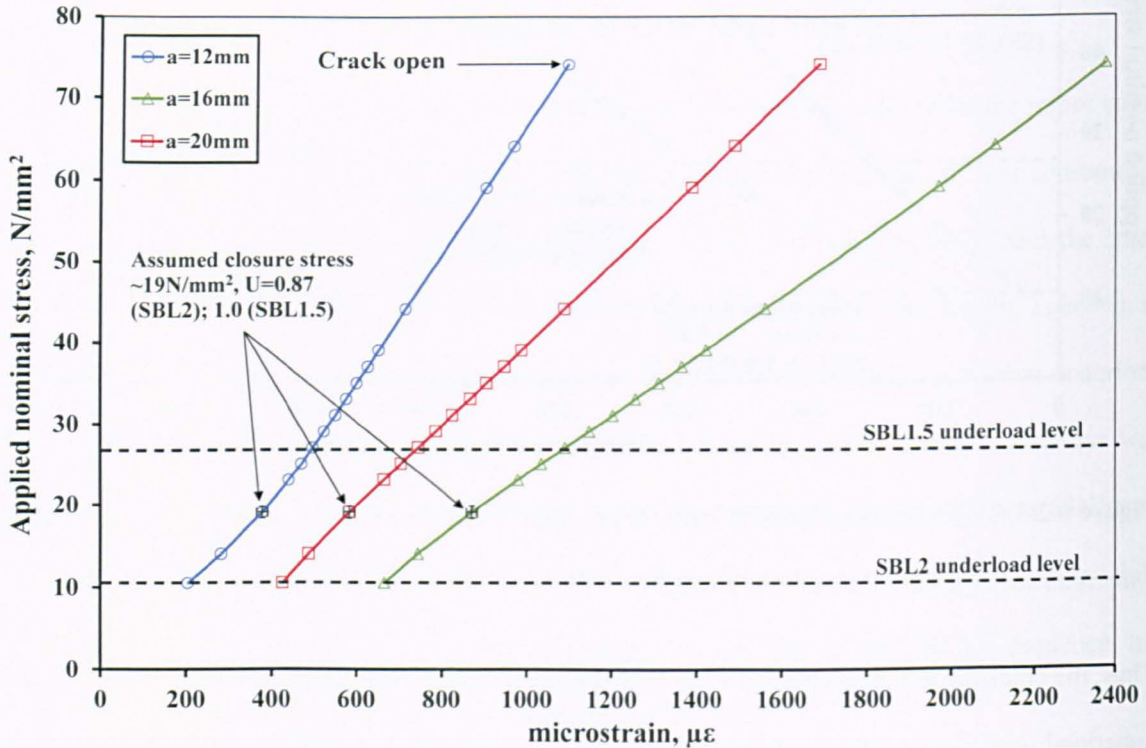


Figure 6.2.6 Recorded crack closure levels in welded 6082 aluminium alloy, upon application of an applied stress from 74N/mm^2 to 10.56N/mm^2 .

Thus, as with the plain material, $U = 1.0$ for SBL1.5. However, with the same closure stress level for SBL2, compared with plain material the proportion of applied stress range that is effective has increased slightly, to 0.87, presumably due to the presence of tensile residual stresses from welding. However, again in comparison with the plain material, the same conclusion regarding the significance of crack closure can be drawn, namely that it was not linked with the observed crack growth acceleration (Section 5.3.3).

6.2.3 PLASTIC ZONE SIZE DETERMINATION

As discussed in Section 2.4.4, under cyclic loading the yielding of material ahead of the crack tip results in the formation of (i) a monotonic plastic zone, due to the application of the maximum applied stress in the cycle, and (ii) a smaller reversed or cyclic plastic zone due to the applied

cyclic stress range within it (see Figure 2.4.5). This can, depending on the applied loading sequence, bring about a zone of local increase in stress (Suresh, 1998), but typically under tensile loading, results in a small zone of compression due to tensile yielding near the crack tip at maximum load (Zhao *et al.*, 2003). The sizes of these plastic zones are given by Eqs. [2.4.12] and [2.4.14] given in Chapter 2. The resulting monotonic and reversed plastic zones sizes due to the underload cycles in the SBL2 and SBL1.5 load sequences for a number of different crack lengths are presented in Tables 6.2.1 and 6.2.2 for steel and aluminium alloy, respectively.

It will be seen for both sequences that the monotonic and cyclic plastic zone sizes increase with increasing crack length and that the greater tensile underload range in SBL2 results in a larger cyclic plastic zone than that due to SBL1.5. Regardless of crack length, the proportion of monotonic plastic zone occupied by the cyclic plastic zone embedded within it is 20% for steel and 18% for aluminium alloy under the SBL2 spectrum, and 11% for steel and 10% for aluminium alloy under the SBL1.5 spectrum. Therefore, as the size of the cyclic plastic zone is around $\frac{1}{5}$ of the monotonic zone under SBL2 and $\frac{1}{9}$ under SBL1.5, the area of the plastic zone that is constantly under tension is reasonably large.

Table 6.2.1 Plastic zone radii for S355 steel under SBL2 and SBL1.5 underload sequences assuming plane stress conditions.

Sequence	SBL2						SBL1.5					
	8	12	16	20	24	28	8	12	16	20	24	28
a, mm	8	12	16	20	24	28	8	12	16	20	24	28
K_{max}, N/mm^{3/2}	349	388	419	447	472	496	349	388	419	447	472	496
Monotonic zone size, μm	188	231	270	307	342	378	188	231	270	307	342	378
ΔK, N/mm^{3/2}	314	349	377	402	425	446	236	262	283	301	318	335
Cyclic zone size, μm	38	47	55	62	69	77	21	26	31	35	39	43

Table 6.2.2 Plastic zone radii for 6082 T651 aluminium alloy under SBL2 and SBL1.5 underload sequences assuming plane stress conditions.

Sequence	SBL2						SBL1.5					
	8	12	16	20	24	28	8	12	16	20	24	28
a, mm	8	12	16	20	24	28	8	12	16	20	24	28
K_{max} , N/mm ^{3/2}	167	186	202	217	231	245	167	186	202	217	231	245
Monotonic zone size, μm	85	106	125	144	164	185	85	106	125	144	164	185
ΔK , N/mm ^{3/2}	143	159	173	186	198	210	107	120	130	140	149	158
Cyclic zone size, μm	16	19	23	26	30	34	9	11	13	15	17	19

Of course, as mentioned in Chapter 5, due to the lack of material constraint near the free surface of the specimen, plane stress conditions will prevail. This results in a large plastic zone at the surface which gradually reduces in size towards mid-thickness, where plane strain conditions exist, Figure 6.2.7.

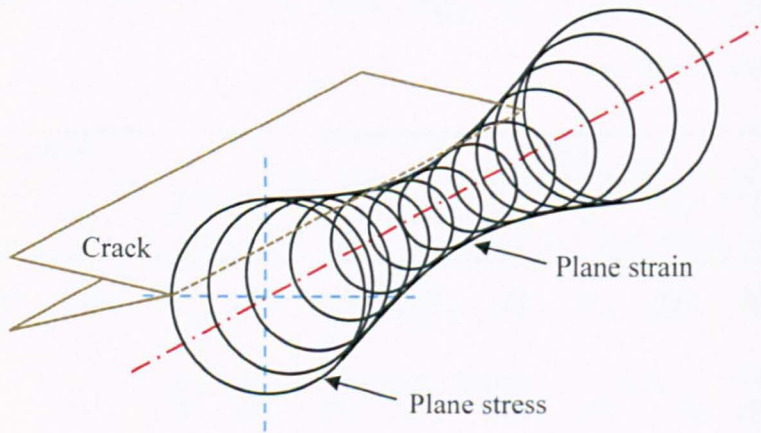


Figure 6.2.7 Effect of thickness on crack tip plastic zone size.

Therefore, allowing for plane strain conditions at the centre of the specimen, the theoretical monotonic and reversed plastic zone sizes for a range of crack lengths were derived using Eq. [2.4.13] and are presented in Tables 6.2.3 and 6.2.4. Although the resulting plastic zones are significantly smaller than for plane stress, the ratio between the monotonic and reversed plastic zones is still the same as determined for plane stress conditions.

This therefore suggests that under SBL1.5, the area ahead of the crack tip constantly under tension is larger than under SBL2. Therefore, based purely on plastic zone sizes, as a greater proportion of the crack tip region beyond the cyclic zone is under tension, more opportunity for an accelerating effect using the SBL1.5 spectra might be expected.

Table 6.2.3 Plastic zone radii for S355 steel under SBL2 and SBL1.5 underload sequences assuming plane strain conditions.

Sequence	SBL2						SBL1.5					
	8	12	16	20	24	28	8	12	16	20	24	28
a, mm												
K_{max} , N/mm ^{3/2}	349	388	419	447	472	496	349	388	419	447	472	496
Monotonic zone size, µm	63	77	90	102	114	126	63	77	90	102	114	126
ΔK , N/mm ^{3/2}	314	349	377	402	425	446	236	262	283	301	318	335
Cyclic zone size, µm	13	16	18	21	23	26	7	9	10	12	13	14

Table 6.2.4 Plastic zone radii for 6082 T651 aluminium alloy under SBL2 and SBL1.5 underload sequences assuming plane strain conditions.

Sequence	SBL2						SBL1.5					
	8	12	16	20	24	28	8	12	16	20	24	28
a, mm												
K_{max} , N/mm ^{3/2}	167	186	202	217	231	245	167	186	202	217	231	245
Monotonic zone size, µm	28	35	42	48	55	62	28	35	42	48	55	62
ΔK , N/mm ^{3/2}	143	159	173	186	198	210	107	120	130	140	149	158
Cyclic zone size, µm	5	6	8	9	10	11	3	4	4	5	6	6

This suggestion that SBL1.5 produces a larger tensile area ahead of the crack tip than SBL2 underload would support findings in Chapter 5 for tests performed on plain material, where it was observed for both steel and aluminium alloy that SBL1.5 resulted in higher acceleration factors than SBL2 (in both cases at high ΔK , $a = \sim 43\text{mm}$ for steel and $\sim 32\text{mm}$ for aluminium alloy). However, for tests on welded specimens, it was found for the steel that acceleration factors were reasonably similar for the different spectra, whilst for the aluminium alloy acceleration was greatest using the SBL2 spectra.

It should be borne in mind that the estimated tensile plastic zones ahead of the crack tip for the SBL2 and SBL1.5 spectra were both large, and therefore both in theory may contribute towards the possible onset of accelerated growth beyond the reversed plastic zone where tensile stresses exist due to the monotonic zone.

6.2.4 DISCUSSION ON THE EFFECTS

As discussed in Chapter 2, crack closure is the premature contact between the surfaces of the crack and is attributed to crack wake plasticity (plasticity induced crack closure). A number of approaches have investigated both the measurement technique and closure point determination, but the compliance curve technique, as used in the present study, is considered to be one of the most powerful and important (Fleck, 1984; Schijve, 1986; Zitounis, 2003).

Crack closure is relevant to fatigue in that it influences the proportion of applied stress range or stress intensity factor range that is actually effective in propagating a crack, defined as $\Delta\sigma_{eff}$ or ΔK_{eff} respectively. It has been shown to provide an explanation for the influence of applied mean stress or stress ratio on CA fatigue life or crack growth rate. In theory, it should also be possible to explain applied load interaction effects under VA loading, such as crack growth retardation due to tensile overloads or crack growth acceleration due to underloads. With regard to the latter, it was anticipated that acceleration would occur during the application of the minor stress cycles following an underload, because it would reduce the crack closure stress and so increase $\Delta\sigma_{eff}$ or ΔK_{eff} . In fact, what has been demonstrated is that crack closure does not reflect the changes in

acceleration found in simple load sequence testing with two magnitudes of stress range, as presented here.

Work performed on Al8090 (Zitounis and Irving, 2002) using a similar spectrum shape, with high R ratio minor cycles interspersed with single underloads to zero load, indicated that over a range of crack lengths and different ratios of the number of small high R cycles to underload cycles, the crack closure stress was reduced in the presence of the high R cycles, thus increasing ΔK_{eff} and hence causing the crack to propagate faster. However, an explanation for how such small near-threshold high R cycles decrease the crack opening stress of larger low R ratio cycles, was not given. It was postulated that residual stress fields ahead of the crack tip may be responsible.

A feature of the present test results (see Figure 6.2.2) that has been observed elsewhere, in a study on Ti-17 (Russ *et al.*, 2001), was that FCGR acceleration occurred for load cycles where closure was not detected. This indicated that the effective crack driving force must be influenced by something other than closure and applied ΔK . Russ *et al.* therefore considered that load interaction effects were influenced more by conditions in the highly stressed zone immediately ahead of the crack tip. The suggestion that crack advance is controlled by the damage process occurring within the highly localized fracture zone immediately ahead of the crack tip has also been noted elsewhere (Korsunky *et al.*, 2009).

For loading sequences with minor cycles at $R=0.7$ and underloads at $R=0.1$, Russ *et al.*, (2001) found that the underload cycle disturbed the material ahead of the crack tip in such a way that resistance to propagation was reduced and crack growth under the subsequent high R minor stress cycles accelerated. Further work considering this using FEA (Russ and Johnson, 2002) showed that when comparing before and after the $R=0.1$ underload, the underload increased the y -displacements both in front of and behind the crack tip. Zitounis (2003) suggested that as a result of this, the plastic zone just behind the crack tip (Figure 2.4.5) is stretched towards the inner part of the material (i.e. towards the direction of loading) by the tensile stresses in the monotonic plastic zone, leading to a separation of the crack faces. Therefore, any closure associated with load cycles at low R is delayed, with surfaces coming into contact later than expected under simple CA loading.

As surmised in (Section 6.2.1), the crack closure stress level for the minor stress range, both before and after an underload and for all crack lengths considered, was constant. Thus, the underload will have no influence on the damaging effect of the minor stress cycles following it. Therefore, a crack closure argument does not support differences in observed acceleration factors.

With respect to the conditions ahead of the crack tip due to the applied underload, as a tensile underload produces a tensile monotonic plastic zone (Suresh, 1998), which is significantly greater than the cyclic plastic zone, as determined in Section 6.2.3, it is conceivable that having this region ahead of the crack tip and extending slightly behind it separating the crack faces (Zitounis, 2003), may contribute towards the level of crack growth acceleration observed. However, it is not considered to be the mechanism responsible for generating acceleration.

6.3 THE ROLE OF WELDING RESIDUAL STRESSES ON CRACK GROWTH ACCELERATION

6.3.1 INTRODUCTION

In Chapter 5 it was shown that the introduction of tensile residual stresses through welding further accelerated crack growth under periodic underload cyclic loading. The observed increase was, however, more pronounced in steel than aluminium alloy.

To understand the role of welding residual stresses in crack growth acceleration, it was first necessary to measure their distribution, determine how they redistribute ahead of an advancing crack and finally, to establish the effect they have on the highly stressed material at the crack tip.

6.3.2 MEASURED RESIDUAL STRESS DISTRIBUTIONS

6.3.2.1 CCT SPECIMENS

Residual stress measurement was performed on S355 steel and 6082 T651 aluminium alloy CCT specimens. Figure 6.3.1 presents the residual stress distributions across the weld and extending out from the notch tips¹ for steel, obtained using the centre hole technique.

¹ The width of the weld bead, as indicated in the plots and the notch length in all cases and for both steel and aluminium alloy are equal.

In Figure 6.3.1 it will be seen that tensile residual stresses exceeding yield (470N/mm^2) were measured at both the weld and notch locations (518N/mm^2 and 481N/mm^2 , respectively), with compressive longitudinal stresses balancing them beyond $\sim 35\text{mm}$ from the weld toe and $\sim 40\text{mm}$ from the notch tip. Measurements in the notch region were therefore in good agreement with the residual stress distribution across the weld. The fact that the measured residual stress is higher than yield/proof, results from the assumption in the residual stress measurement analysis, that a constant Young's modulus still applies above yield, in reality due to plasticity this is not the case.

Measurements were also performed on steel CCT specimens using the neutron diffraction technique, for comparison with the centre-hole measurements and to establish the through-thickness distribution, Figure 6.3.2. It will be seen that tensile residual stresses exceeding yield, in the region of 407N/mm^2 , were detected close to the notch. This is a little lower than that measured by centre-hole. However, when the through-thickness distribution is considered (Figure 6.3.3) it will be seen that at 6.5mm depth (equivalent to 1.5mm from the opposite surface), the maximum stress measured was 455N/mm^2 , closer to that observed by centre-hole. The residual stress level at mid-thickness was similar to that at 6.5mm depth, suggesting minimal through-thickness variation.

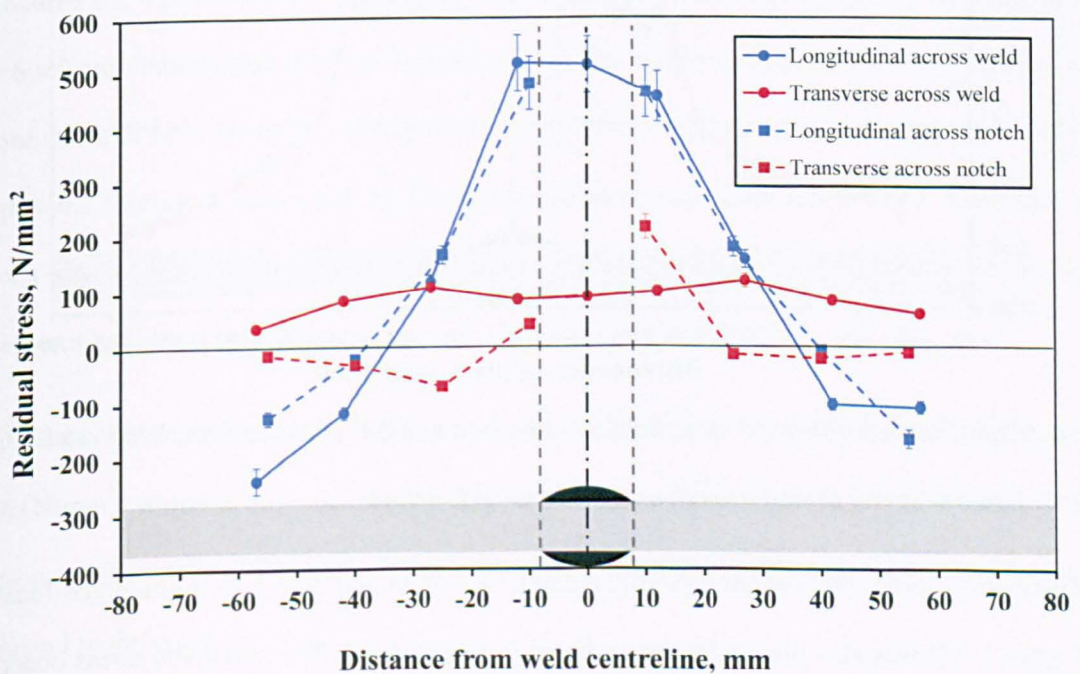


Figure 6.3.1 Residual stress distributions measured in S355 steel CCT specimens across the weld and extending out from the notch tips.

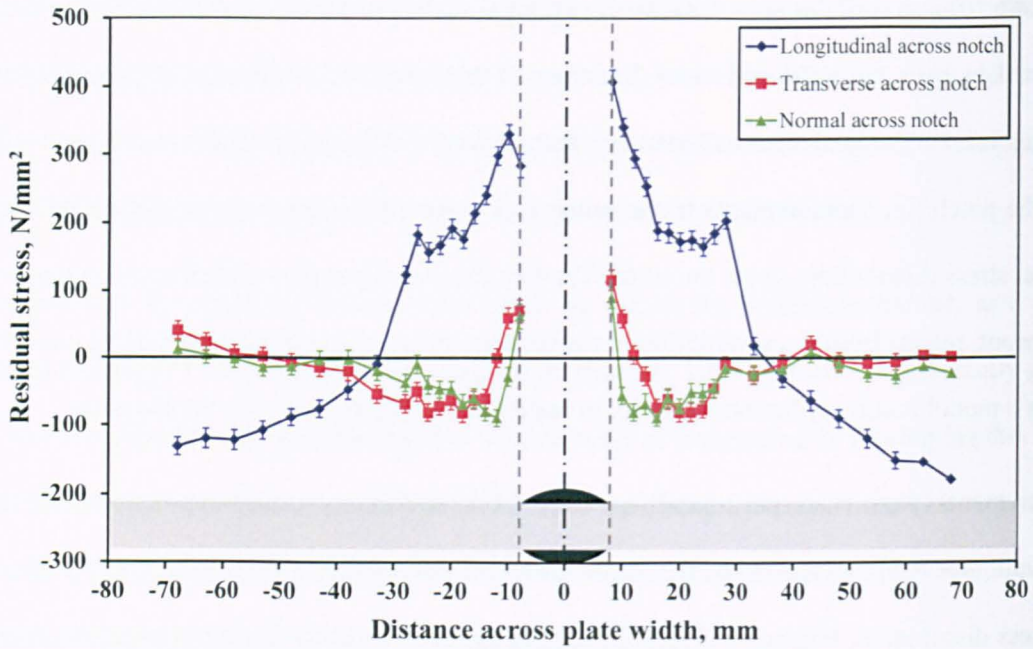


Figure 6.3.2 Residual stress distributions measured in S355 steel CCT specimens extending out from the notch using neutron diffraction at 1.5mm depth.

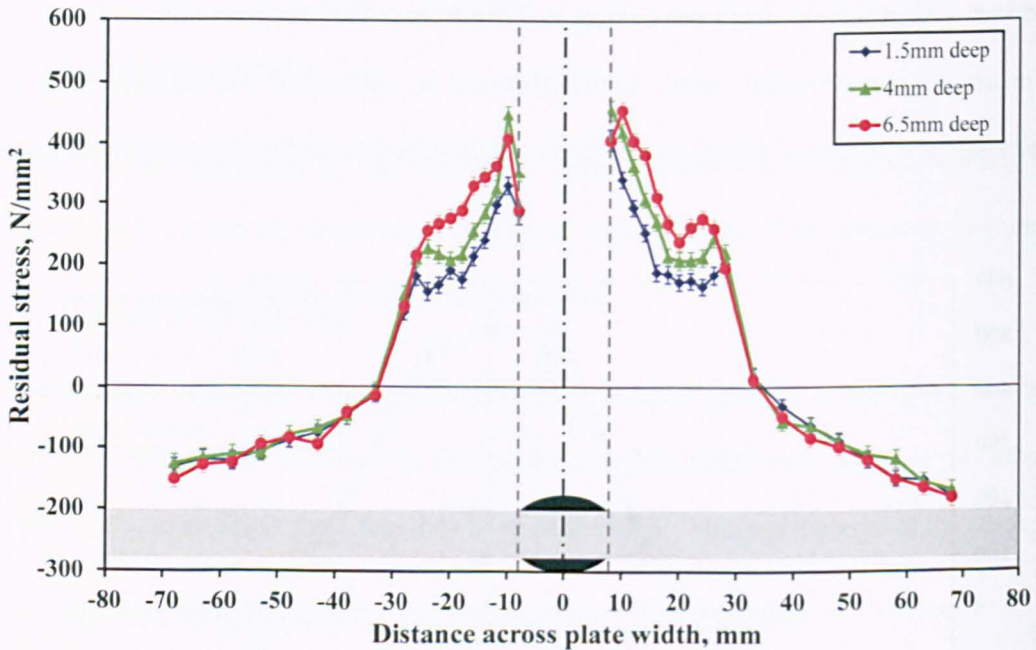


Figure 6.3.3 Through-thickness longitudinal stress variation measured in S355 steel CCT specimens extending out from the notch using neutron diffraction.

The distribution across the welded region at a depth of 1.5mm and 50mm from the notch location (see Figure 3.7.5) was also measured and is shown in Figure 6.3.4. The maximum stress observed at a distance of 2mm from weld toe was 481N/mm^2 , agreeing with the centre hole findings (Figure 6.3.1) following plasticity correction (see Section 3.7.2). The distance from the weld toe at which

the residual stress becomes compressive was 32mm, again agreeing well with the centre-hole findings.

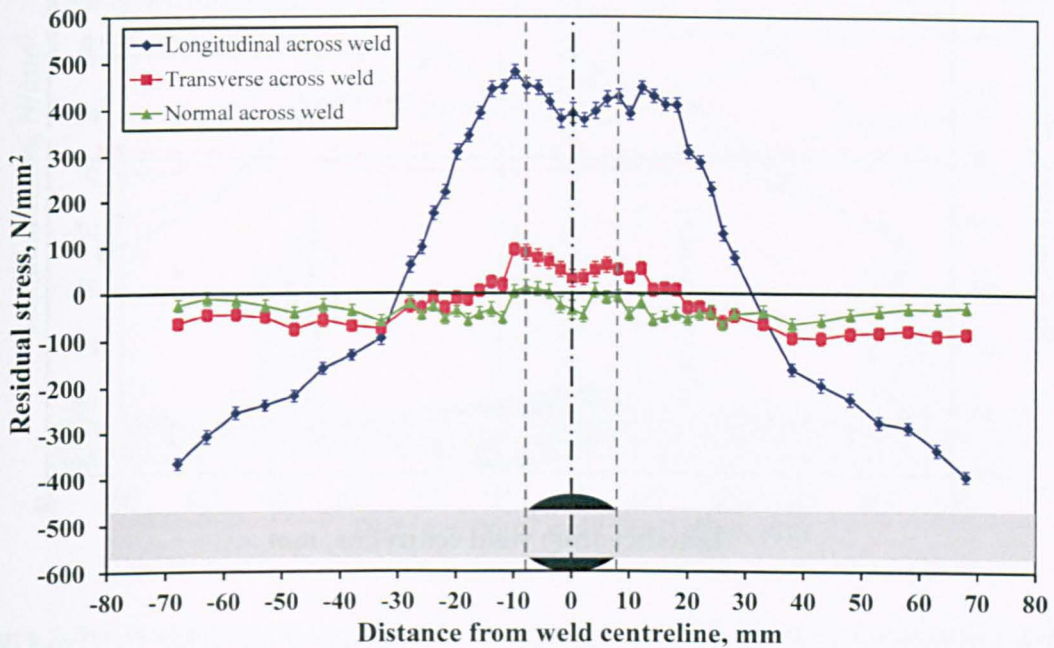


Figure 6.3.4 Residual stress distribution in S355 steel CCT specimens across the weld using neutron diffraction.

For the aluminium alloy (Figure 6.3.5) the magnitude of residual stress is below that of the measured 0.2% proof stress (Table 4.3.2). This is due to HAZ softening adjacent to the weld which, for 6082 aluminium alloy in the T6 condition, typically results in a reduction of the material's 0.2% proof strength by a factor of 2 (BSI, 1991). The ~22mm zone of HAZ softening is also shown in Figure 6.3.5 and was determined by Vickers hardness measurement (see Chapter 4, Section 4.3.3). It can also be seen that the tensile longitudinal stresses are balanced by compressive longitudinal stresses after 34mm from the weld toe and 32mm from the notch tip.

With the softening effect of the HAZ considered, the 0.2% proof strength of the material reduces to $\sim 161\text{N/mm}^2$, which is still considerably higher than the maximum residual stress measured in the region of the weld (24N/mm^2). It was, however, slightly higher at 31N/mm^2 , in the material adjacent to the notch.

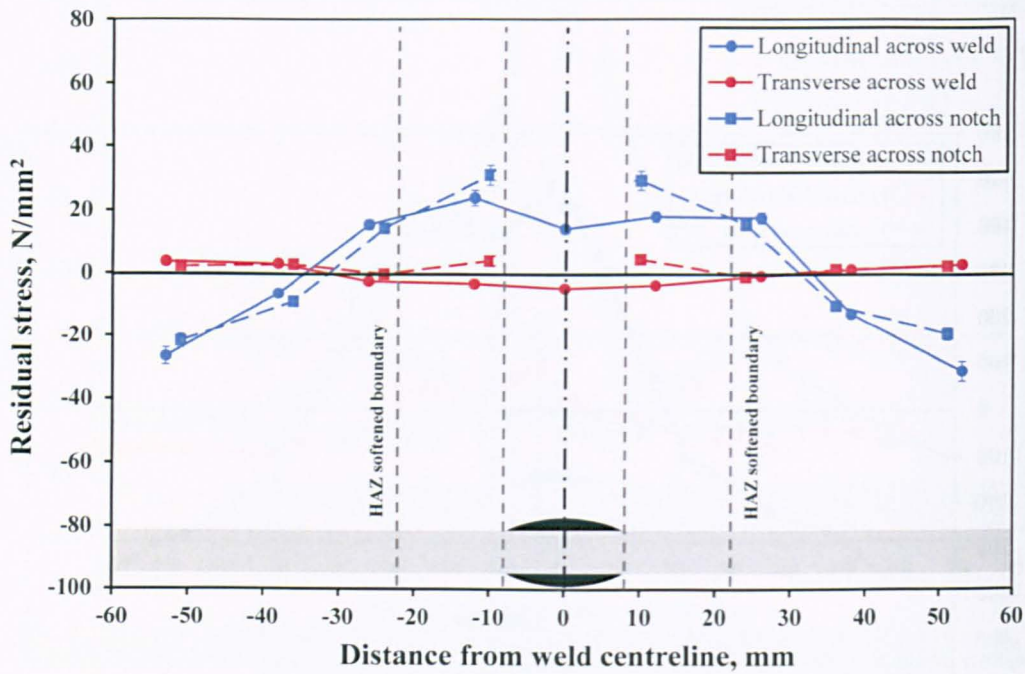


Figure 6.3.5 Residual stress distributions measured in 6082 aluminium alloy CCT specimens across the weld and extending out from the notch.

To check if a larger volume of weld metal, and hence a higher heat input, results in higher residual stresses, a full penetration double sided butt weld was produced in the same 6082 T651 aluminium alloy plate. The maximum residual stress measured here was 55N/mm^2 ; more than double that for the bead-on-plate (BOP). However, this was 26mm from the weld toe as opposed to 12mm for the BOP weld, Figure 6.3.6. The HAZ softened boundary for the full penetration butt weld was determined as $\pm 40\text{mm}$ from the weld centreline (see Chapter 4, Section 4.2.2) following the guidance given in the British Standard (BSI, 1991), and is shown in Figure 6.3.6. It can be seen that the residual stress distribution 12mm from the toe for both the butt and BOP welds agree very well. The difference between the BOP and butt weld is that the stresses in the butt weld remain tensile over a greater width of the CCT specimen.

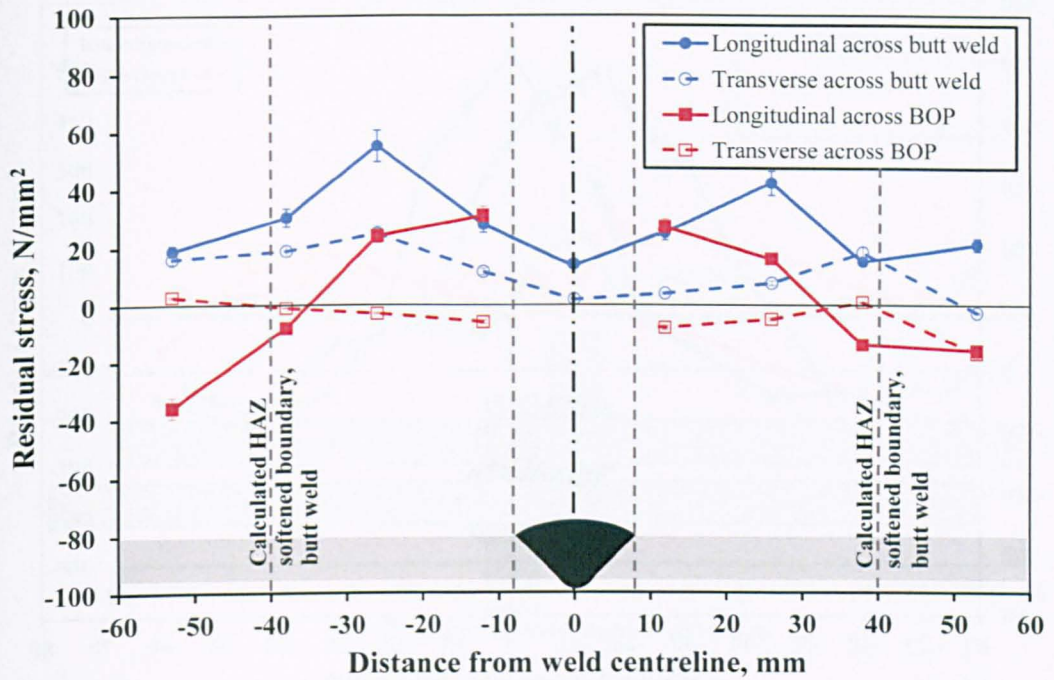


Figure 6.3.6 Residual stress distributions measured in a 6082 aluminium alloy full penetration double sided butt weld.

Whilst Figure 6.3.6 shows that the increased weld volume has increased the level of measured stress and the residual tension zone width, the magnitude of residual stress is still rather low. It is thought that the material thickness of only 6mm is a contributing factor, due to the low level of restraint it offers to the forces generated during contraction of the weld. A thicker specimen would try to resist this force generating higher tensile residual stress.

6.3.2.2 FILLET WELDED SPECIMENS

The residual stress distribution determined using the centre-hole technique for S355 steel specimens incorporating a fillet welded longitudinal attachment is shown in Figure 6.3.7. At a distance of 2mm from the weld toe and extending across the plate width, the maximum longitudinal stress found (following plasticity correction) was 515N/mm². As can be seen, the level of stress fell away quickly with increasing distance from the end of the attachment, becoming compressive around 35mm either side of the attachment centre-line.

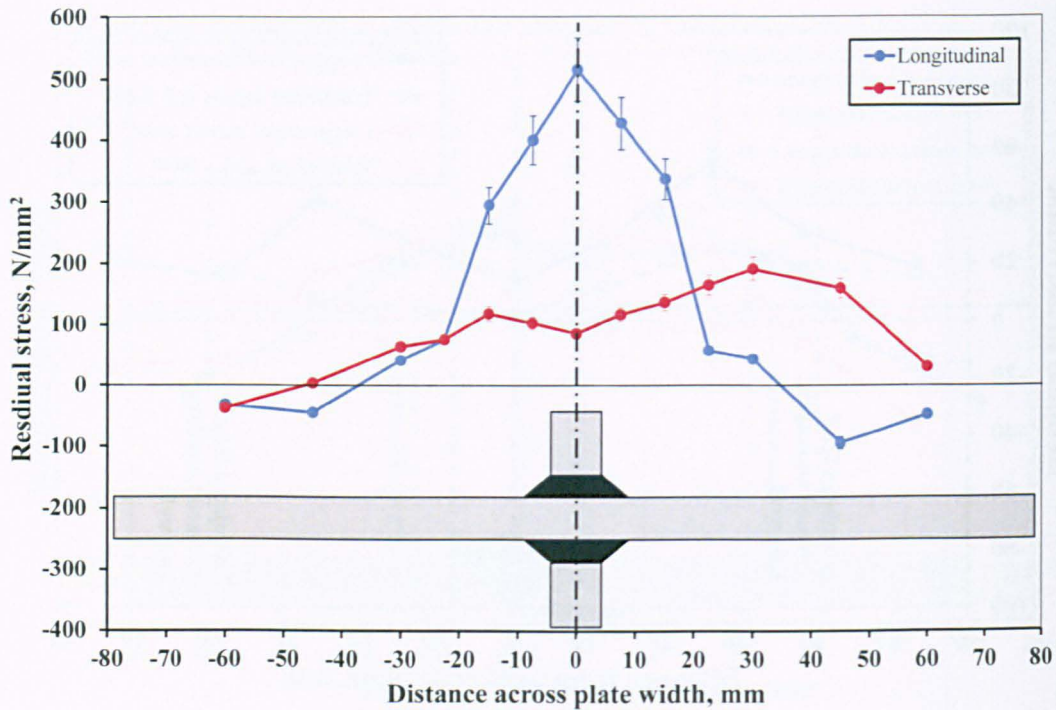


Figure 6.3.7 Residual stress distribution measured in S355 structural steel across the plate width 2mm from weld toe using centre hole.

Again for comparison, measurements were also made using neutron diffraction, Figure 6.3.8. Here it is shown that the maximum residual stress at a depth of 1.5mm from the plate surface was 487N/mm^2 , slightly lower than that measured by centre-hole but still above yield. When considering the through-thickness variation (Figure 6.3.9) it is shown that unlike in the welded CCT specimens, there is some variation of peak stress through the thickness, with the greatest measurement of 572N/mm^2 at mid-thickness (4mm). At a depth of 6.5mm (1.5mm from the opposite surface) a value of 530N/mm^2 was recorded. In all cases the observed stress distribution changed from tensile to compressive at approx. 30-36mm, reasonably consistent with that found by centre-hole.

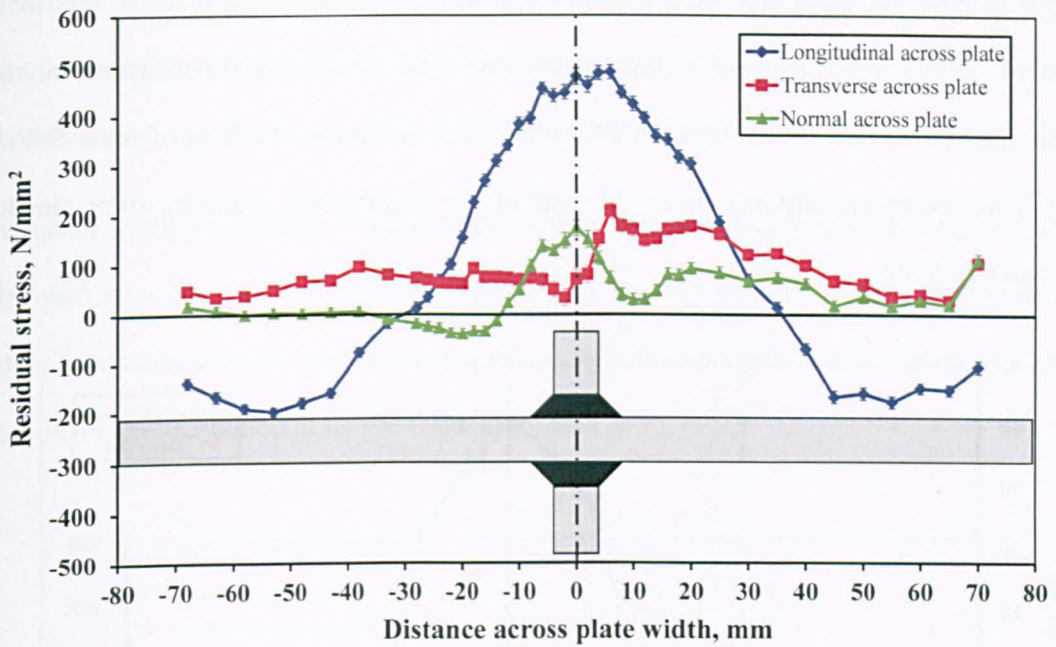


Figure 6.3.8 Residual stress distribution measured in S355 structural steel across the plate width 2mm from weld toe using neutron diffraction.

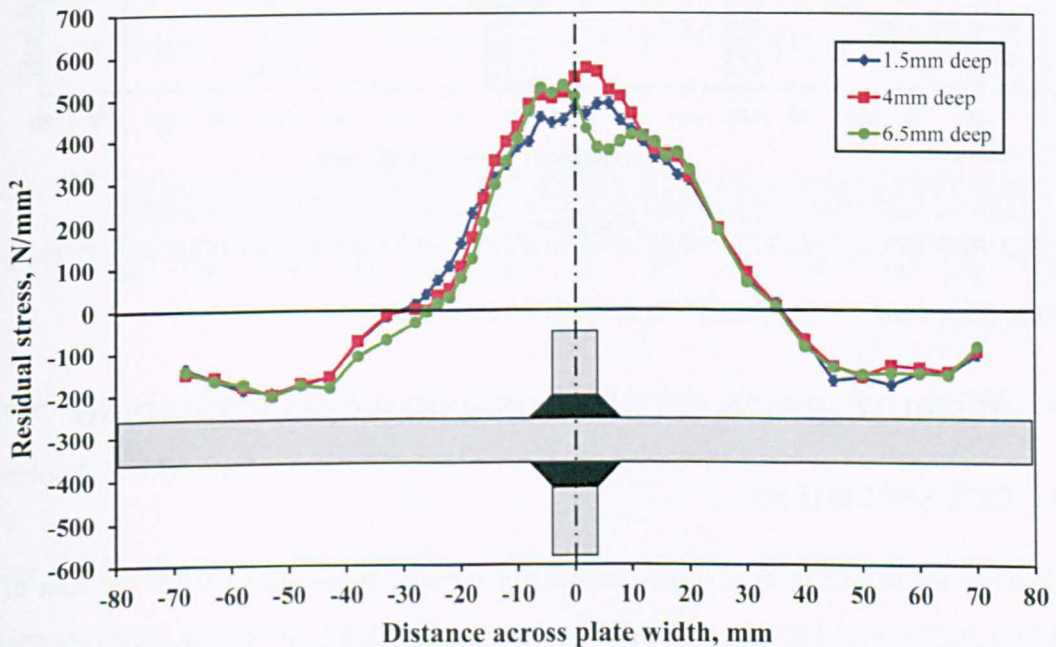


Figure 6.3.9 Through-thickness longitudinal stress variation measured in S355 steel across the plate width 2mm from weld toe using neutron diffraction.

Turning to the same type of specimen in the aluminium alloy (Figure 6.3.10), the maximum stress measured was 41N/mm^2 , still well below the material's 0.2% proof stress even when allowing for

the effect of HAZ softening (see Section 6.3.2.1). As discussed for CCT specimens, it is thought that the low level of residual stress is partly attributable to the low material thickness of only 6mm (Section 6.3.2.1). As was found for the fillet welded steel specimens, the level of stress fell away quickly with increasing distance from the end of the attachment, changing from tensile to compressive at 24mm.

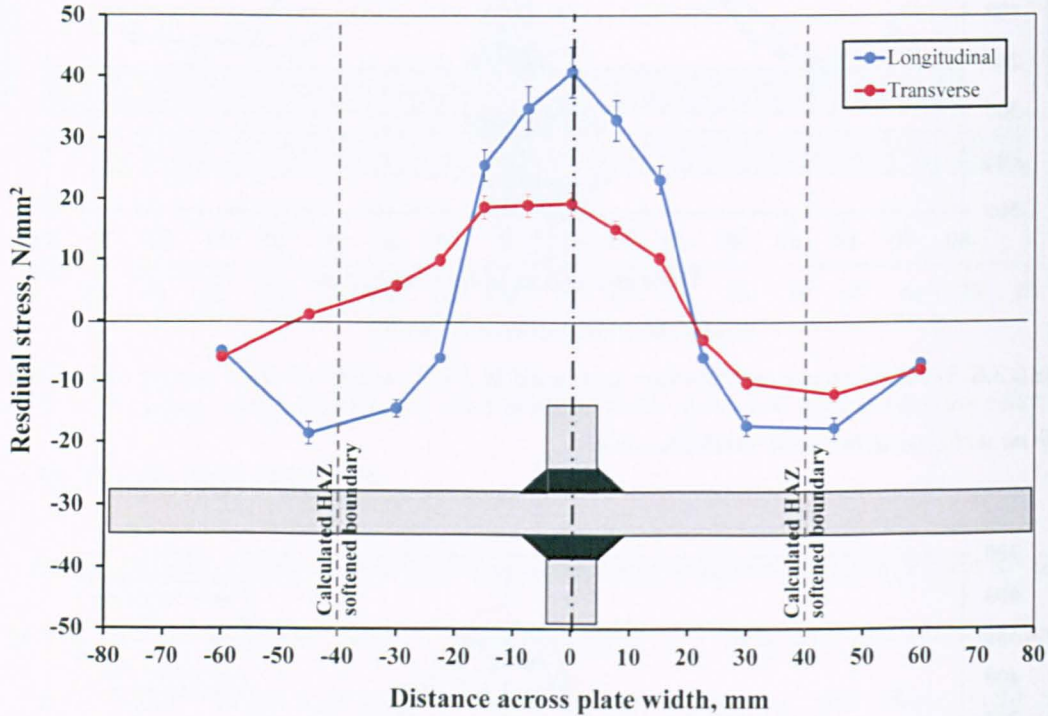


Figure 6.3.10 Residual stress distribution measured in 6082 aluminium alloy across the plate width 2mm from weld toe using centre hole.

6.3.3 RESIDUAL STRESS RELAXATION UNDER CYCLIC LOADING

6.3.3.1 CCT SPECIMENS

Relaxation (or redistribution as it is also termed) of residual stress occurs when the sum of the applied and residual stress exceeds the yield condition of the material. The relaxation of residual stresses in welded CCT specimens was observed following periodic underloading using the SBL2 sequence.

The maximum plasticity-corrected residual stress established in the S355 steel specimens in the region of the notch was 481N/mm^2 . Following the application of one loading block (i.e. ten minor and one underload cycle) the stress relaxed to 77N/mm^2 (84% reduction), Figure 6.3.11.

Subsequent loading in blocks of 10 and 100 slightly increased this value resulting in a stress of 168N/mm^2 after 100 blocks. It can therefore be seen that the majority of relaxation under cyclic loading is contained within the first loading block, with further cyclic loading having a significant effect on the re-distribution of tensile residual stresses.

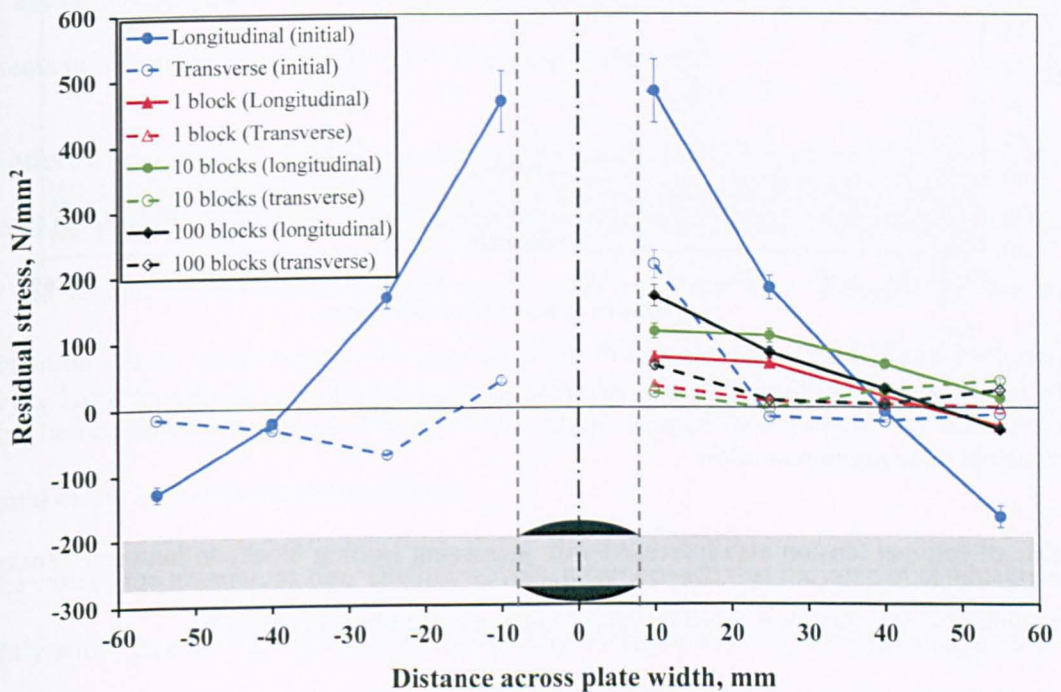


Figure 6.3.11 Re-distribution of measured residual stresses following blocks of SBL2 periodic underloads in S355 steel.

Figure 6.3.11 also shows that whilst the tensile residual stress decreased, the zone of residual tension increased to between 46mm and 58mm, although this may just be a result of scatter in the measurements performed.

For the 6082 aluminium alloy the maximum measured residual stress in the region of the notch was 31N/mm^2 , Figure 6.3.12. After one loading block this was reduced by 39% to 19N/mm^2 . Subsequent loading of 10 blocks reduced this further to 12N/mm^2 (61% of the original); beyond

this no significant difference was observed. Therefore, as in the case of the steel, the majority of the observed relaxation was during the first loading block.

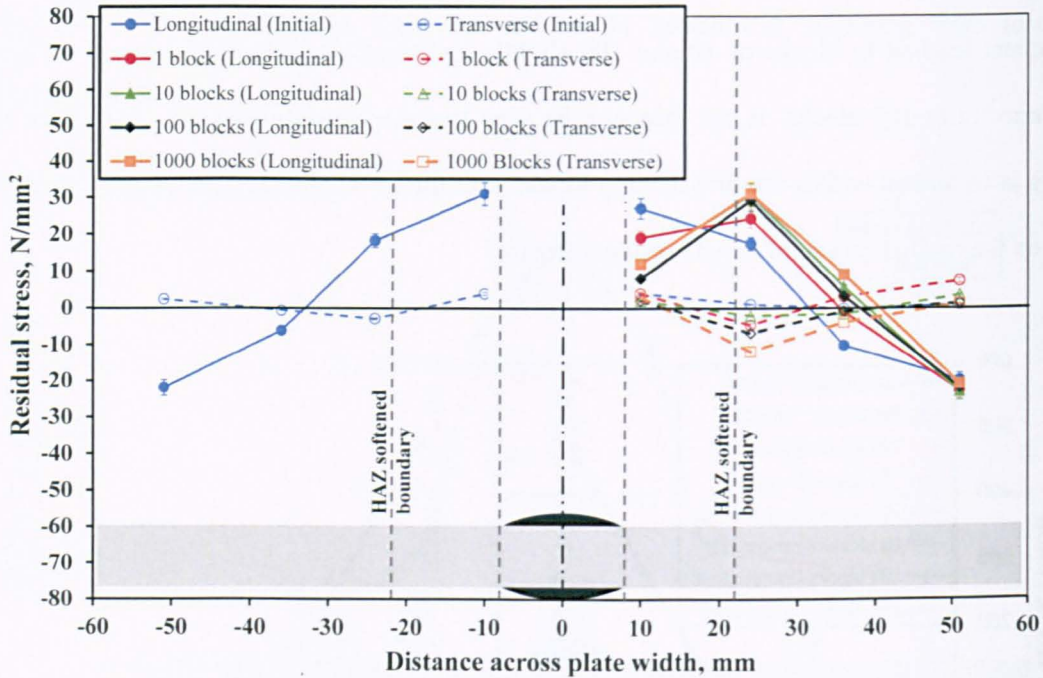


Figure 6.3.12 Re-distribution of measured residual stresses following blocks of SBL2 periodic underloads in 6082 aluminium alloy.

The zone of residual tension also increased with increasing loading blocks to between 32mm and 41mm; again this may just be a result of scatter in the measurements performed.

6.3.3.2 FILLET WELDED SPECIMENS

Following determination of the initial residual stress distribution, the steel fillet welded specimen (FIL-ST-RES-01) was cycled from zero to 200N/mm^2 ($\sim 40\%$ yield) to determine the degree of relaxation after a pre-defined number of cycles (one and ten).

On application of one cycle, a 72% reduction in residual stress from 515N/mm^2 to 142N/mm^2 was observed adjacent to the weld toe at the centre of the weld return. Following ten cycles, the stress increased slightly giving a total reduction of 67% (172N/mm^2) lower than the original. Therefore, the majority of relaxation under cyclic loading is contained within the first cycle; subsequent cycles (up to ten) gave no further reduction.

For the aluminium alloy specimen (FIL-AL-RES-01), once the residual stress distribution had been obtained the specimen was cycled from zero to 120N/mm^2 (~75% of softened 0.2% proof stress). After the first cycle the maximum stress reduced by 197% from 41N/mm^2 to -40N/mm^2 . Ten cycles only slightly increased the level of reduction to 204% giving a stress of -43N/mm^2 . Again measurements were performed close to the weld toe at the centre of the weld return as in the original location of maximum stress (see Section 6.3.2.2).

6.3.4 EFFECT ON RESIDUAL STRESS FOR A PROPAGATING CRACK

The above Sections have established the residual stress distribution following welding and its subsequent relaxation (redistribution) following cyclic loading.

The effect on the residual stress of crack propagation across a CCT specimen was considered next. As will be seen in Figure 6.3.13, the residual stresses measured 2mm ahead of the crack tip show that the extent of the tensile residual stress zone is shorter than indicated by the original distribution. Here it is shown that the residual stress falls to zero at around 22mm from the notch centre before becoming compressive at around 32mm, a zone 20-45% narrower than that of the original extent of residual tension (40mm).

In the case of the aluminium alloy (Figure 6.3.14), it can be seen that the zone of residual tension is slightly wider than the 32mm originally depicted by the residual stress distribution at around 39mm (an increase of 22%). However, what is most noticeable is the increase in stress immediately after the HAZ softened boundary, where the residual stress 2mm ahead of the propagating crack reaches 114N/mm^2 , which is significantly closer to the 161N/mm^2 0.2% proof stress of the material derived when allowing for the effect of the weld.

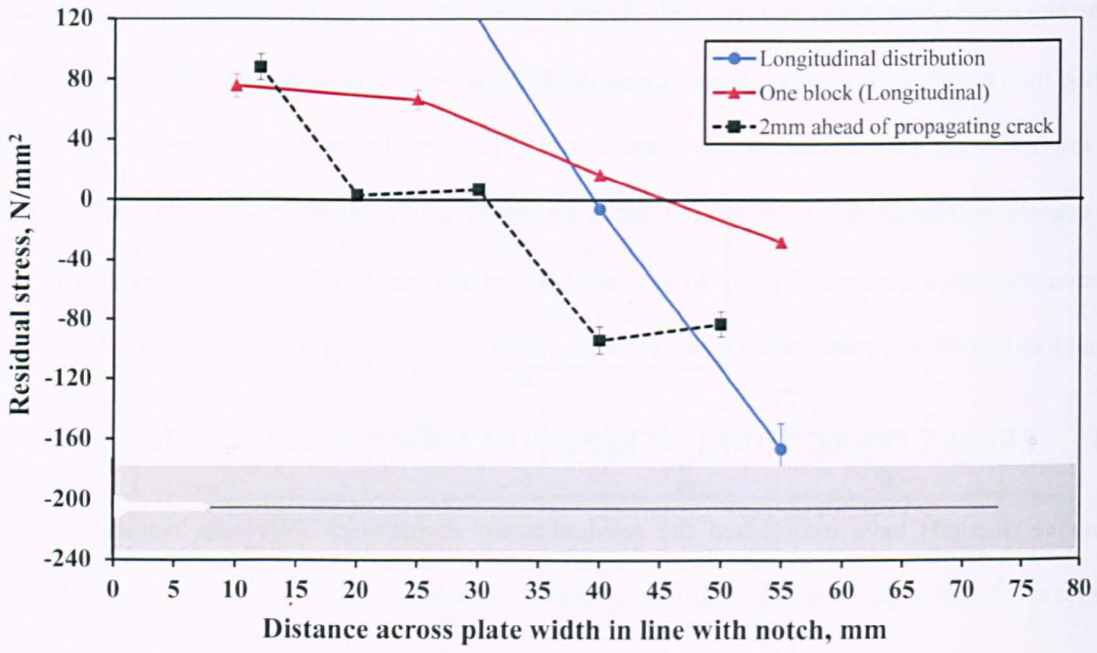


Figure 6.3.13 Residual stress measured 2mm ahead of propagating crack in S355 steel using centre hole.

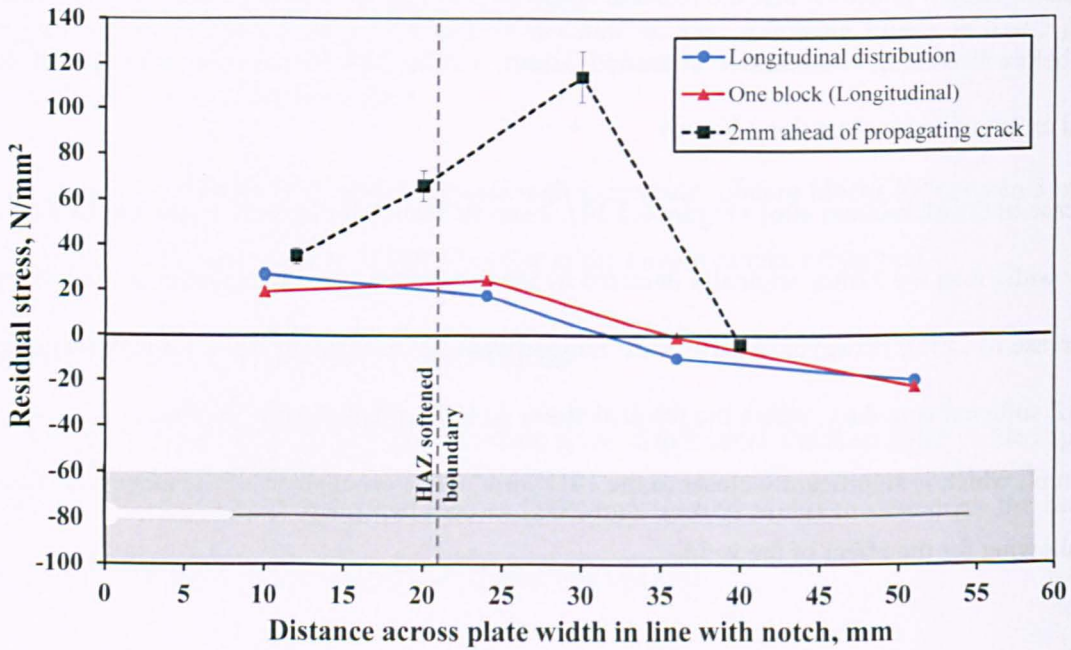


Figure 6.3.14 Residual stress measured 2mm ahead of propagating crack in 6082 aluminium alloy using centre hole.

6.3.5 DISCUSSION ON THE EFFECTS

As discussed in Chapter 2, the presence of a weld can introduce yield magnitude tensile residual stresses, depending on the level of constraint imposed on the cooling weld by the part being welded. It was shown in Chapter 5 that the presence of a tensile residual stress distribution from welds in the vicinity of a crack generally gave rise to greater crack growth acceleration under a periodic underloading sequence than in plain material. It was surmised that the tensile residual stress assisted the already present tensile stress at the crack tip (within the monotonic plastic zone, Figure 2.4.5) in maintaining greater crack opening, with the result that a greater proportion of the loading cycle contributed to crack propagation.

Measured crack closure levels (Section 6.2) indicated that a crack closure argument, or at least that based on the possibility of an increased $\Delta\sigma_{eff}$ following an underload, does not support differences in observed acceleration factor. This was due to the closure stress level of the minor stress cycles being the same both before and after the underload (i.e. closure was not detected at the high R ratio minor cycles), such that the underload has no influence on the damaging effect of the minor stress cycles following it.

The effect of residual stress relaxation under cyclic loading has been investigated by a number of researchers (Iida *et al*, 1996; Iida and Takanashi, 1997; Holzapfel *et al*, 1998; Zhuang and Halford, 2001). Significant relief of residual stresses due to welding and to surface treatments (e.g. peening) has been reported, by as much as 132% (Iida and Takanashi, 1997), on application of the first loading cycle. Further gradual relief has been observed with increasing numbers of repetitions of the same applied cyclic loading. In extreme cases, residual stresses have been shown to relax entirely in the first few cycles (Wallace and Frankel, 1949).

The maximum residual stress measured in the welded CCT specimens was 481N/mm² in steel and 31N/mm² in the aluminium alloy. The greatest relaxation under periodic underloading sequence loading (SBL2) occurred following the first loading block, with a reduction of 84% for the steel and 39% for the aluminium alloy. For fillet welded specimens, under CA cycling, a single cycle of ~40% of the material's yield strength for steel and ~75% of the materials softened 0.2% proof

stress resulted in a 72% relaxation in residual stress for the steel and 197% for the aluminium alloy from the initial measured values of 515N/mm² and 41N/mm² for the steel and aluminium respectively. Following ten cycles, no further reduction was observed for the steel and only a slight increase in reduction for the aluminium alloy.

The findings for steel agreed well with those by Blom, who observed relaxation in fillet welded specimens incorporating longitudinal attachments manufactured from Domex 350XP, of 50 to 80% of the initial value in the first cycle (Blom, 1995).

The results of the residual stress measurements 2mm ahead of the propagating crack (Figures 6.3.13 and 6.3.14) would suggest that with reference to the load sequence tests described in Chapter 5, any crack growth accelerating effects affected by welding residual stresses close to the tip of the crack would, for the steel specimens, be in the shorter crack length or lower ΔK region. For the aluminium alloy specimens, due to the presence of the HAZ softened zone, any acceleration resulting from the addition of welding residual stresses would be greatest at longer crack lengths or higher values of ΔK . Both of these findings agree well with the acceleration factors given in Table 5.3.11.

This therefore supports the hypothesis that the introduction of tensile residual stresses through welding plays an important role in further assisting the tensile stress at the tip, caused by the tensile underload, in accelerating crack growth.

6.4 THE ROLE OF CRACK TIP MEAN STRESS ON CRACK GROWTH ACCELERATION

6.4.1 INTRODUCTION

In Chapter 5 it was considered that a plausible mechanism for crack growth rate acceleration was related to the local mean stress at the crack tip. The effect of mean stress under CA and VA loading (Russ *et al.*, 2001; Arcari and Dowling, 2012) as well as that postulated by Fleck after observing crack advance in the minor cycles of his loading spectra (Fleck, 1985), would suggest that periodic tensile under-loads assist in maintaining a higher tensile mean stress for the subsequent minor

stress cycles. The results of load sequence testing in the present work agreed with Fleck's findings, with accelerated growth accompanying the minor cycles. A new finding in this study was that it also accompanied the major cycle (underload).

To provide a better understanding of the effect of underloads on fatigue crack growth, finite element stress analysis (see Section 3.8) was used to calculate the changes in stress and strain that take place in the crack tip stress field in CCT specimens as a result of the application of the periodic underload sequences. In addition to the SBL1.5 and SBL2 loading performed in Chapter 5, a tensile underload of magnitude greater than 2 was also investigated to determine its effect in the region of the crack tip. To this end, SBL2.2 for steel and SBL2.3 for aluminium alloy were introduced; in both cases resulting in a minimum stress of zero for the underload. Particular attention was paid to the number of cycles required to achieve stable strain cycling, the extent of any strain accumulation (e.g. the change in distance for minor and underload cycles) and the possible changes to the local mean stress at the crack tip that might affect crack growth acceleration. Table 3.8.1 gives a full list of the models developed for both the steel and aluminium cases. From these, the stress and strain at the crack tip due to the minimum and maximum loads in the applied loading cycles were extracted, and their evolution was plotted on graphs in order to determine the effects of the underloads, at various underload ratios, and the presence of tensile residual stress, as would be produced by welding.

The stresses and strains reported here are those acting in the direction of loading of the CCT specimens, that is perpendicular to the symmetry plane where the crack propagates (S22). In all the models analysed, the crack was assumed to have propagated by 10mm from the initial notch tip. The change in crack length due to propagation was not taken into account, because it was not compatible with the chosen crack tip mesh (see Section 3.8.1). The loading cycle was therefore applied with no initial stress, except in the cases modelling specimens containing residual stresses from welding. This assumed that the stress pattern resulting from the combination of the earlier loading cycles and crack growth was "overwritten" by the newly applied maximum load, and that the work hardening in the elements of interest was significantly higher than immediately before the crack tip had reached the position investigated.

The data analysed and discussed are mainly those obtained 0.01mm from the crack tip, but data 0.05mm and 0.10mm from the tip were also extracted. Data 0.01mm from the tip were assumed to be those most relevant to the fatigue crack growth mechanism, although some damage could exist from strain cycling further ahead of the crack tip. The data at the crack tip node and at the mid-side node of the first element were not considered because they may have been affected by the close proximity of the crack tip singularity.

The data reported were obtained for six series of loading cycles. Each series consisted of ten minor CA cycles, followed by one major (underload) cycle. The loading sequence applied is shown schematically in Figure 3.8.5. The stresses used in the periodic underload spectra are presented in Table 5.2.1. Only a selected number of data are discussed in this section, but all the data are reported in Appendix B.

An overview of the FEA model processing routine is presented in Figure 6.4.1. Here it is shown that such parameters as materials data, meshing and loading history, are the input for the analysis performed. Post-processing of the results then generates stress and/or strain contour plots, the nodes of which at particular distances of interest from the crack tip (0.01mm, 0.05mm and 0.10mm), are used to generate stress and strain history plots; in this case, highlighting the effect of underloads on crack tip mean stress. The materials data and meshing input parameters (specific to steel and aluminium alloy) remained unchanged for the respective models, but the cyclic loading spectrum was modified to suit the SBL1.5 or SBL2 conditions. Post-processing was then repeated and different stress/strain histories generated, as presented in Appendix B and in Figures 6.4.2 to 6.4.9.

The data analysed and discussed are mainly those obtained 0.01mm from the crack tip, but data 0.05mm and 0.10mm from the tip were also extracted. Data 0.01mm from the tip were assumed to be those most relevant to the fatigue crack growth mechanism, although some damage could exist from strain cycling further ahead of the crack tip. The data at the crack tip node and at the mid-side node of the first element were not considered because they may have been affected by the close proximity of the crack tip singularity.

The data reported were obtained for six series of loading cycles. Each series consisted of ten minor CA cycles, followed by one major (underload) cycle. The loading sequence applied is shown schematically in Figure 3.8.5. The stresses used in the periodic underload spectra are presented in Table 5.2.1. Only a selected number of data are discussed in this section, but all the data are reported in Appendix B.

An overview of the FEA model processing routine is presented in Figure 6.4.1. Here it is shown that such parameters as materials data, meshing and loading history, are the input for the analysis performed. Post-processing of the results then generates stress and/or strain contour plots, the nodes of which at particular distances of interest from the crack tip (0.01mm, 0.05mm and 0.10mm), are used to generate stress and strain history plots; in this case, highlighting the effect of underloads on crack tip mean stress. The materials data and meshing input parameters (specific to steel and aluminium alloy) remained unchanged for the respective models, but the cyclic loading spectrum was modified to suit the SBL1.5 or SBL2 conditions. Post-processing was then repeated and different stress/strain histories generated, as presented in Appendix B and in Figures 6.4.2 to 6.4.9.

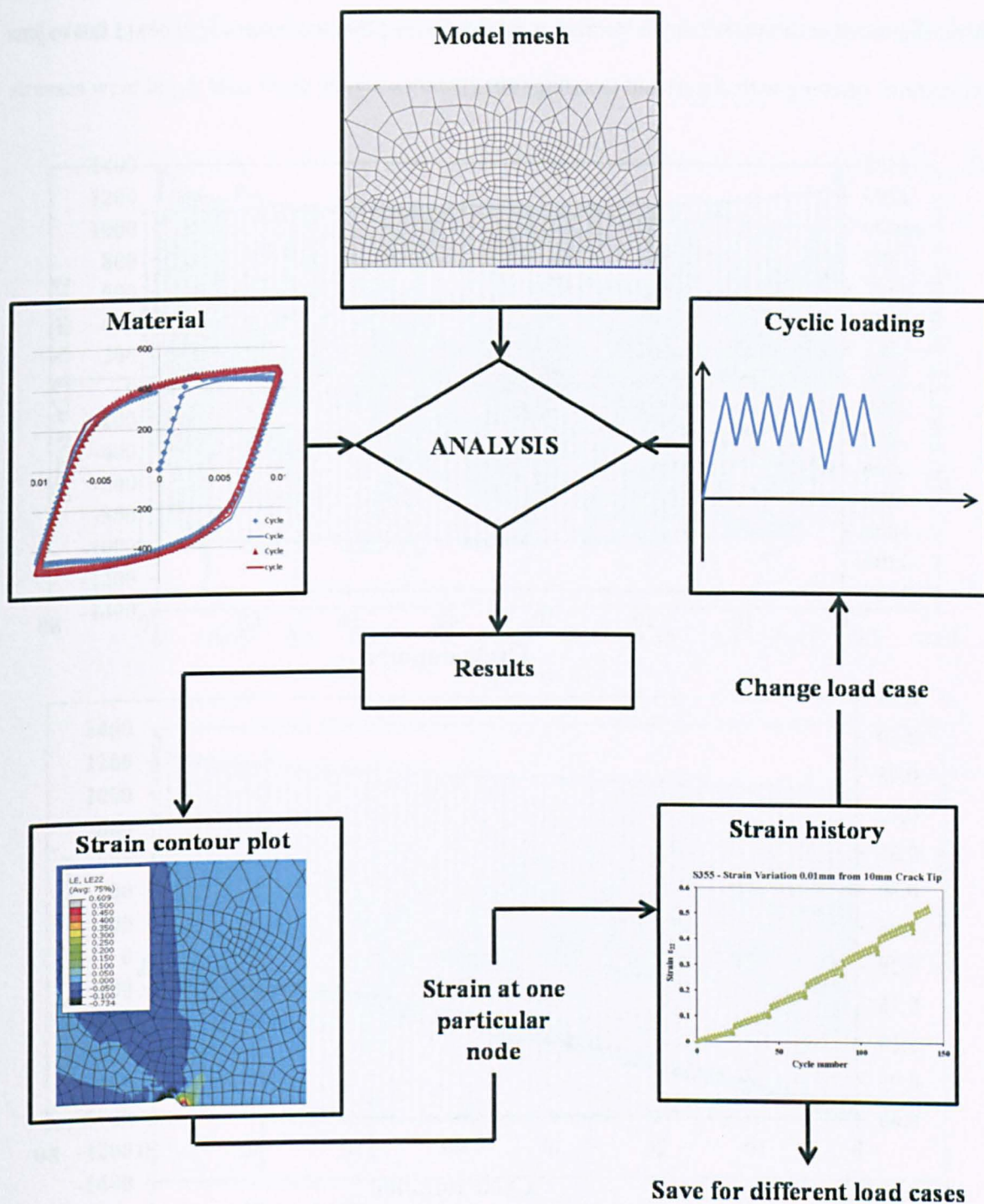


Figure 6.4.1 Overview of the finite element analysis model processing routine.

6.4.2 MODELLING OF CRACK TIP STRESS STATE

6.4.2.1 PLAIN S355 STRUCTURAL STEEL

Figure 6.4.2 shows the CA response of material 0.01mm from the crack tip to the application of the minor stress cycles. It can be seen that after 71 cycles, the mean stress has relaxed to zero, although it also shows that full stability has not yet been achieved, as seen by the increase in strain with

increasing number of cycles not yet ‘turning over’, suggesting that the mean stress could fall to just below zero, agreeing with Arcari and Dowling (2012).

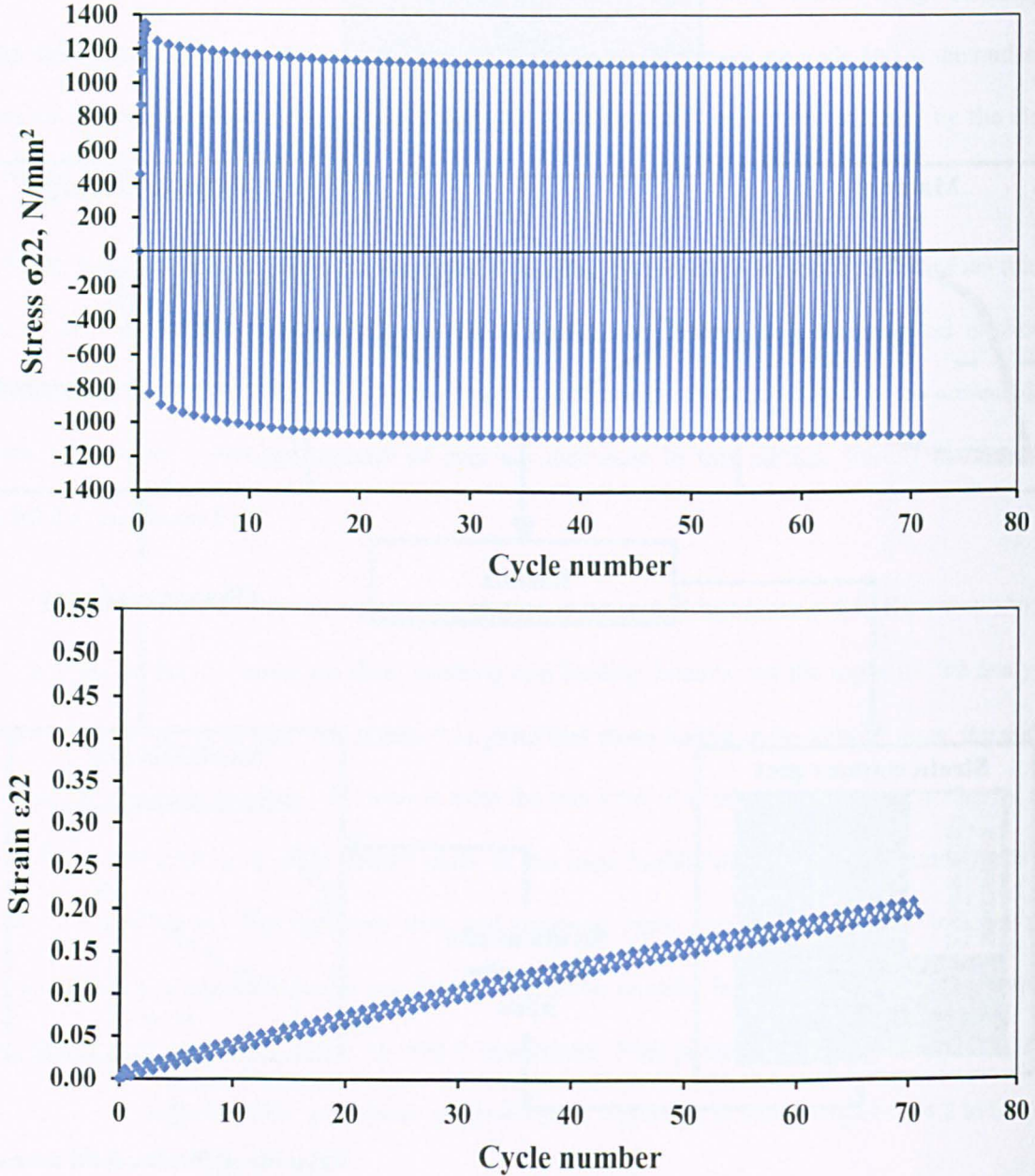


Figure 6.4.2 Variation of stress and strain 0.01mm from the crack tip in S355 structural steel, obtained at the maximum and minimum applied loads (minor cycles) under constant amplitude loading.

Under SBL2 loading and at the same location, Figure 6.4.3, the results show that the stability of the stress-strain cycle cannot be achieved due to the slight increase in stress after application of the underload. They also show that strain accumulates between each underload and during each

underload cycle itself, consistent with the observation in Section 5.3 that striation spacing for both stresses were larger than those obtained under CA loading.

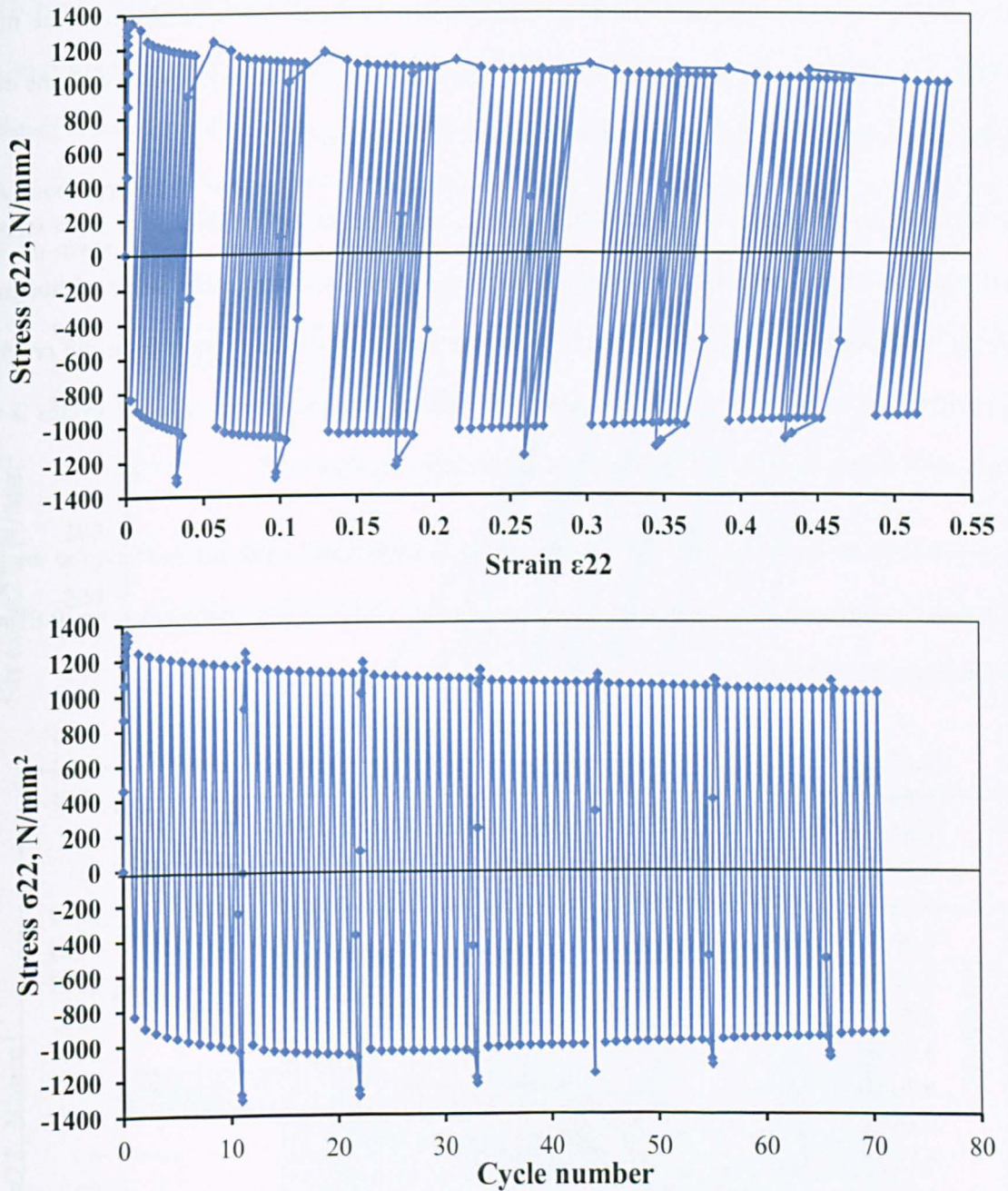


Figure 6.4.3 Variation of stress 0.01mm from crack tip in S355 steel obtained at maximum and minimum applied loads for the first six blocks of cycles under SBL2 loading.

The same can be seen for SBL1.5 loading, although strain accumulation for the underload itself is slightly reduced at 0.016 strain (Figure B2) versus 0.030 under SBL2 loading (Figure 6.4.3). For SBL2.2 loading (Figure B6), the slight increase in the magnitude of the underload stress, shows no

real increase in tensile mean stress above SBL2. However, strain accumulation is slightly greater (0.040).

In each of these underload cases, the stress-strain hysteresis shows that shakedown of the minor cycles to a mean of around zero would occur very gradually over a number of cycles with the effect of the underload reducing as the number of blocks of cycles increase.

At 0.05mm from the crack tip under SBL2 loading, the effect of the underload on mean stress is very pronounced (Figure B4) with no relaxation of minor cycles to zero mean stress, although the attempt to shakedown happens at a much faster rate than at 0.01mm. Further from the crack tip (0.1mm) the effect of the underload has dissipated, although the mean stress after 71 cycles is well above zero, slowly relaxing as the number of cycles increase, Figure B5.

A comparison of the strain for each loading cycle is shown in Figure 6.4.4. Here the analysis indicates that there will be a regular increase in strain at the node closest to the crack tip (0.01mm); this increase was proportional to the underload applied.

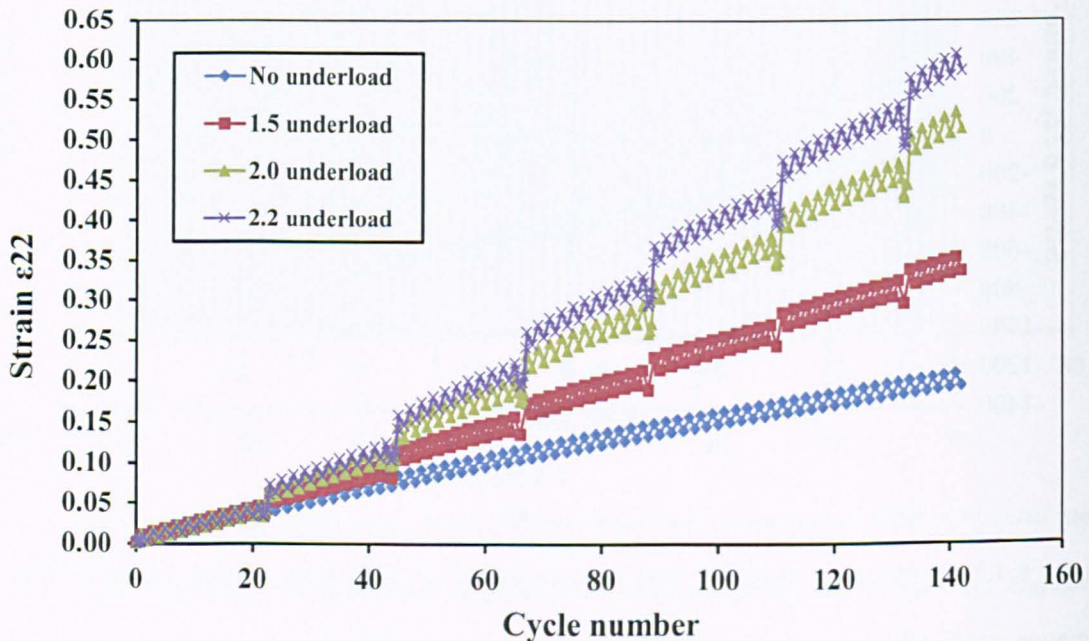


Figure 6.4.4 Variation of strain 0.01mm from crack tip in S355 steel for different underload ratios.

The SBL2.2 underload corresponds to zero minimum stress.

6.4.2.2 WELDED S355 STRUCTURAL STEEL

Figure B7 shows the effect of the inclusion of welding residual stresses of a specified magnitude of 481N/mm^2 , following plasticity correction (Figure 3.8.7), on the variation in stress and strain 0.01mm from the crack tip under SBL2 loading. The crack tip stress field is added to the existing constant welding residual stress, thus generating extensive plastic strain. However, as a result of this, there appears to be no effect of the underload on the minor stress cycles, with stable cycling at a mean stress of zero.

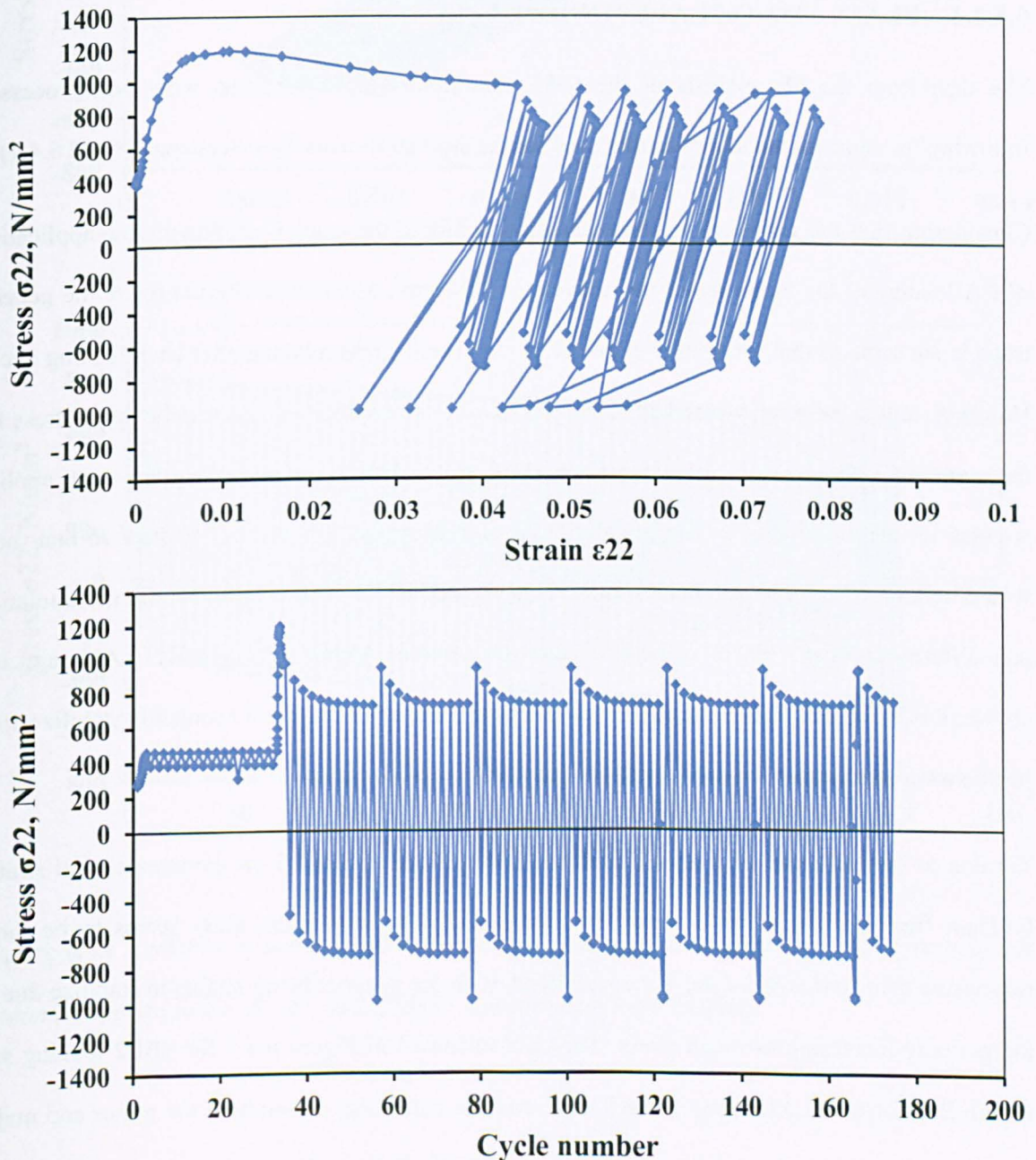


Figure 6.4.5 Variation of stress 0.05mm from crack tip in welded S355 steel obtained at maximum and minimum applied loads for the first six blocks of cycles under SBL2 loading.

Further from the crack tip, at 0.05mm, the plastic strain is less extensive so that the effect of the underloads can be seen more clearly, Figure 6.4.5. Here the underload increases the mean stress of the minor cycles above that of the minor cycles preceding the underload, increasing the mean stress at the crack tip. Beyond this location, the presence of the underload had only a slight effect on the succeeding minor cycles, whilst the welding residual stresses tends to delay the relaxation effect, keeping the tip in a region of tension for a longer period and over a greater distance, as seen 0.1mm from the crack tip in Figure B9.

6.4.2.3 PLAIN 6082 T651 ALUMINIUM ALLOY

The data from the FE analysis of the 6082 aluminium alloy specimens were post-processed following the same methodology as that used for the steel specimens, (see Sections 3.8 and 6.4.1).

Considering first the variations in stress and strain close to the crack tip following the application of CA loading of the minor stress range cycle of 32N/mm^2 , as shown in Figure 6.4.6, the general trend is the same as that for steel (Figure 6.4.2) with mean stress relaxing after each loading cycle. However, unlike the steel, which had reached zero mean stress after ~ 71 cycles, the mean stress for the aluminium alloy is still in tension after ~ 140 cycles. This is not surprising since the applied stresses for the aluminium were a smaller proportion of proof strength than in steel so that there would be less crack tip plastic deformation. This can be seen by a reduction in strain accumulation and differences in the rate of accommodation (relaxation), Figures B1 and B11. Although not shown, it is assumed that the aluminium alloy would continue to relax and eventually stabilize at or just below a mean stress of zero (similar to the steel).

Turning to the influence of a tensile underload, the effect of SBL1.5 on the stresses and strains 0.01mm from the crack tip is shown in Figure B12. The aluminium alloy seems to be more responsive than steel was for the same underload, with the material being unable to stabilize due to the periodic increasing of mean stress. This is also shown in Figure 6.4.7 for SBL2 loading and Figure B15 for SBL2.3 loading. In each case, strain accumulates during both the minor and major cycles giving rise to a change in displacement with that of the major cycle being just as pronounced, if not more so, than the minor cycles increasing in both cases as the underload ratio is

increased. The same effect was evident from striation spacings, with increases in growth from both the major and minor cycles (Section 5.3.6).

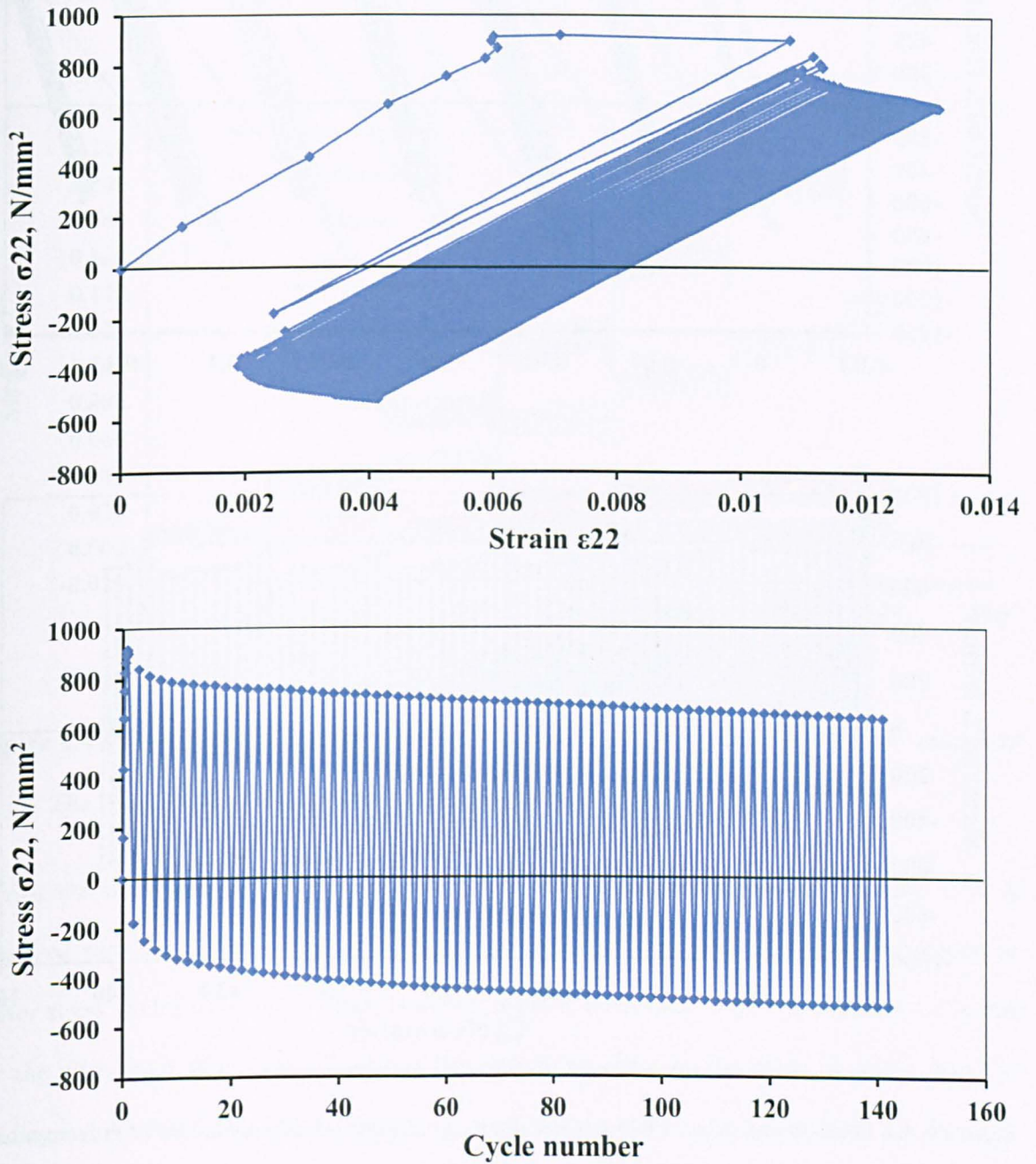


Figure 6.4.6 Variation of stress 0.01mm from crack tip in 6082 Al alloy obtained at maximum and minimum applied loads (minor cycles) under constant amplitude loading.

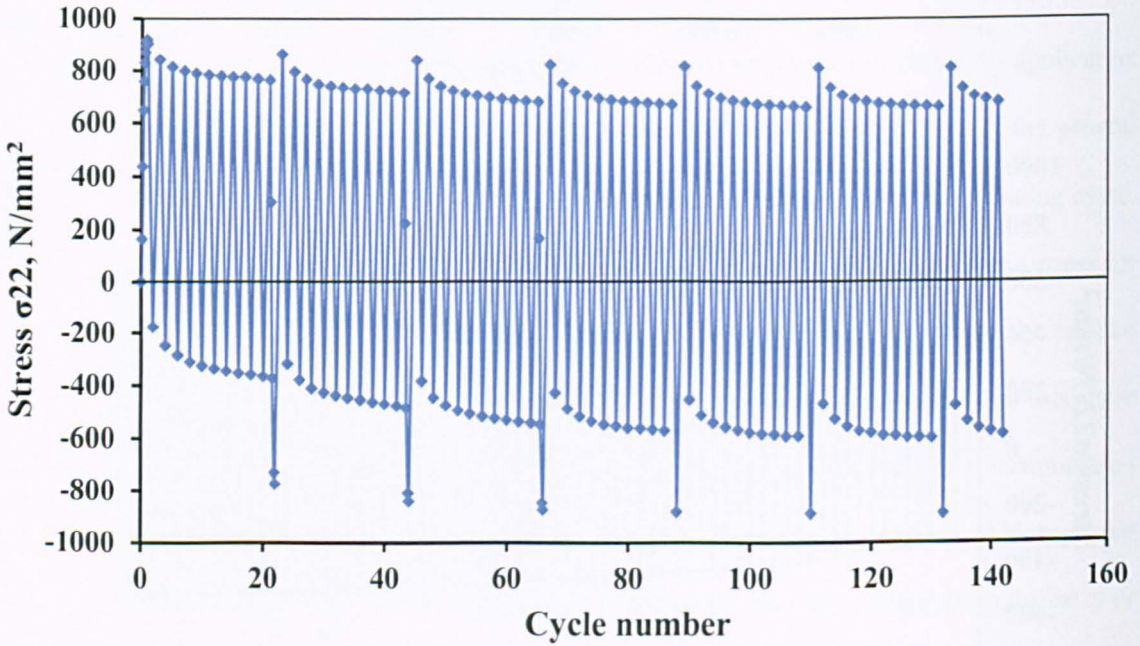
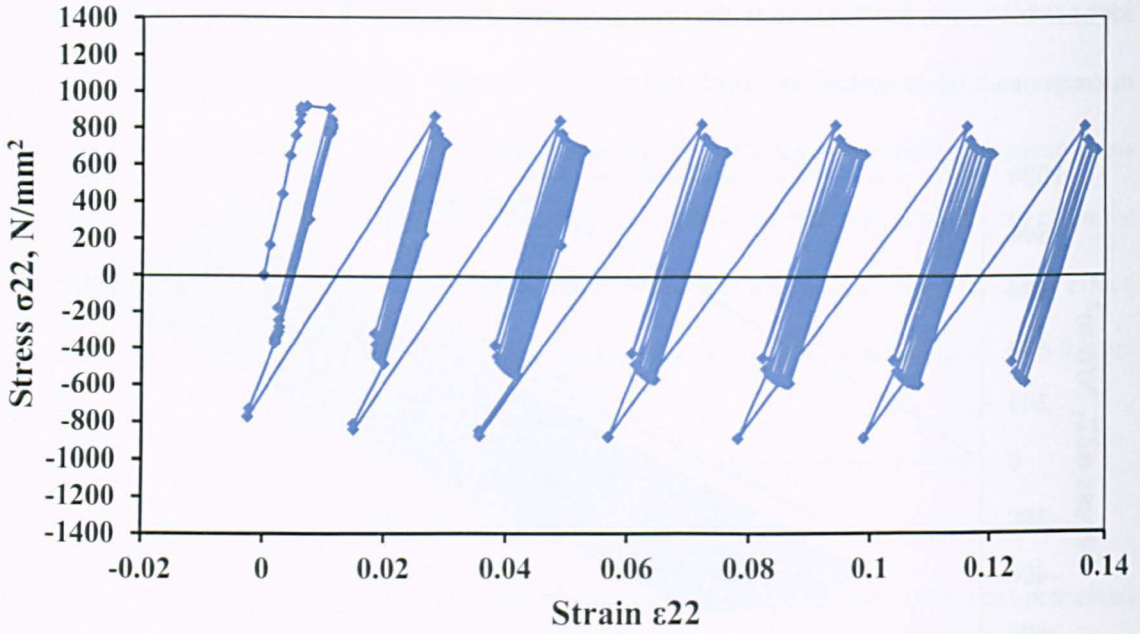


Figure 6.4.7 Variation of stress 0.01mm from crack tip in 6082 Al alloy obtained at maximum and minimum applied loads for the first six blocks of cycles under SBL2 loading.

As the distance from the crack tip is increased to 0.05mm (Figure B14), the effect of the underload during SBL2 loading diminishes and whilst the mean stress is still tensile, it reduces following each block of loading cycles.

The change in strain for each loading cycle is shown in Figure 6.4.8. As in the case of the steel (Figure 6.4.4) a regular increase in strain at the node closest to the crack tip (0.01mm) is observed; this increase was proportional to the underload applied.

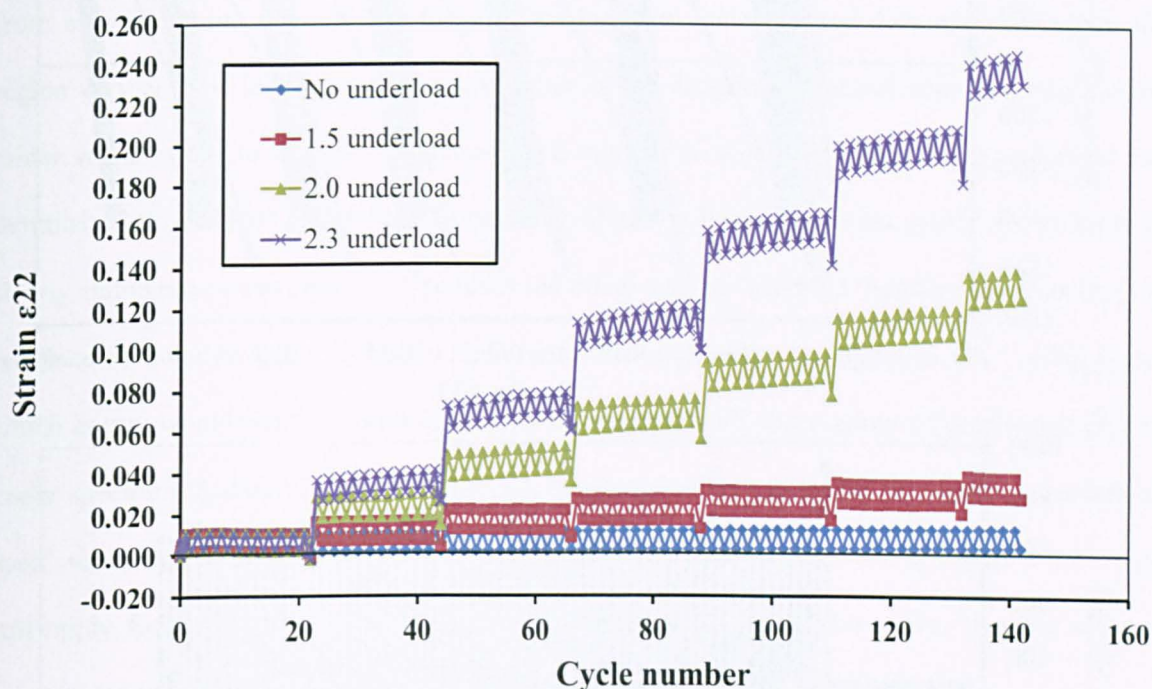


Figure 6.4.8 Variation of strain 0.01mm from crack tip in 6082 Al alloy for different underload ratios. The SBL2.3 underload corresponds to zero minimum stress.

Whilst the strain data for the steel (Figure 6.4.4) were of higher magnitude, the same trend is observed with the highest underload ratio generating the greatest strain and lowest relaxation of minor stress cycles for the underload. However, what is interesting to note in Figure 6.4.8 is that for the aluminium alloy, SBL1.5 loading has little more effect on the crack tip strain than CA loading, whilst SBL2 and SBL2.3 produce a much greater increase in mean strain. For the steel (Figure 6.4.4), the CA loading had not fully stabilized and so the crack tip strain continued to increase.

6.4.2.4 WELDED 6082 T651 ALUMINIUM ALLOY

As for the steel, the effect of load cycling onto an existing tensile residual stress field from welding on the cumulative strain and local mean stress was investigated under SBL2 loading, initially 0.01mm from the crack tip, Figure 6.4.9.

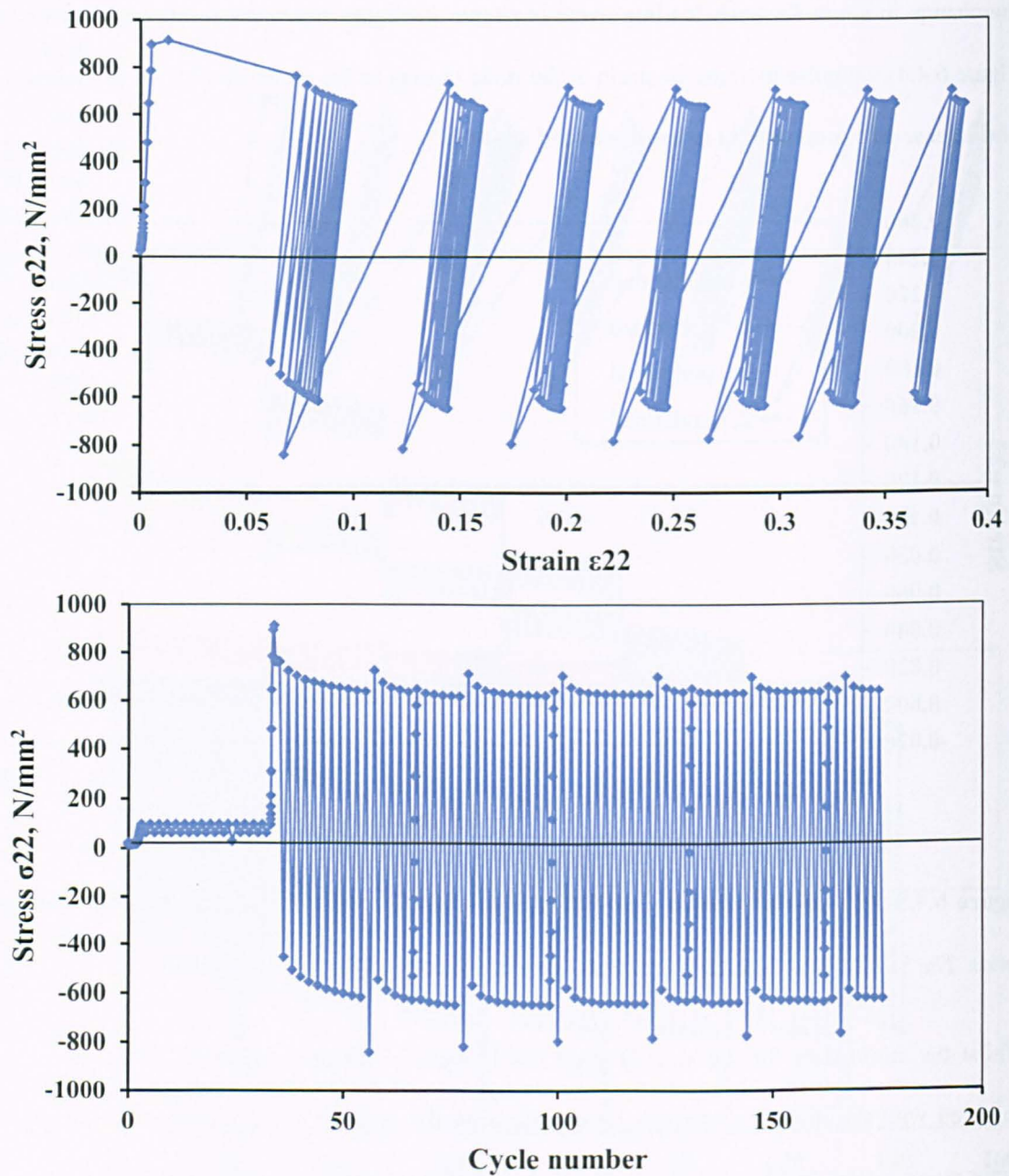


Figure 6.4.9 Variation of stress 0.01mm from crack tip in welded 6082 Al alloy obtained at maximum and minimum applied loads for the first six blocks of cycles under SBL2 loading.

These data suggest that the cumulative strain and crack tip mean stress increase when residual stresses are taken into account, which was not observed for the steel at the same distance from the crack tip. However, unlike in steel, at 0.05mm (Figure B17) the underload had no effect so the mean stress change was the same as if there had been no underload, resulting in a steady decrease in mean stress with increasing number of cycles, much the same as for plain aluminium alloy at the same location (Figure B14). Based on this result, the data at a distance of 0.1mm were not plotted.

6.4.3 DISCUSSION OF FINDINGS

Under CA loading, the application of minor stress cycles produce local cyclic stress close to the crack tip that cycles from tension to compression, with the local mean stress gradually reducing from a tensile value to zero. The FE analyses for plain material have demonstrated that in the region very close to the crack tip, the application of the underload does not allow the local tensile minor stress cycles to reduce to a compressive state. Even when the effect of the underload has diminished (Figures B5 and B14), the resulting effect on the minor stress cycles shows them to slowly stabilize at a tensile stress. The observed effect near the crack tip therefore suggests that the presence of the underload maintains a higher mean stress than that arising under CA loading alone, which in turn would result in faster crack growth, agreeing with observations of accelerated growth under spectrum loading in Chapter 5. Indeed, the same is likely to be the case with the underload itself, since the progressive decrease in local mean stress towards zero seen in Figure 6.4.2 would still apply for CA loading. If so, this again is consistent with the observation that the striation spacing due to the periodic underload was greater than that seen under CA loading.

The above can be seen to varying degrees for each underload ratio and for both materials at a distance of 0.01mm from the crack tip. Beyond this the material behaviour changes slightly. The steel continues to display the same effect of the underload 0.05mm from the crack tip, but the effect has diminished in the aluminium alloy. The effect has also diminished for the steel 0.1mm from the crack. However, as mentioned above, no significant shakedown of the minor cycles is observed, therefore indicating that the crack tip stabilizes in high tension (at least for this distance ahead of the crack tip), as shown in Figures B5 and B14 and observed under VA loading of 7xxx series aluminium alloys (Arcari and Dowling, 2012).

The reason for the diminishing effect of the underload is likely to be associated with the decreasing levels of plasticity further from the crack tip. Considering Figure 4.3.1a and 4.3.2a, it can be seen that during the first few cycles of the LCF curve, the material begins to harden (accommodation is taking place with plasticity tending to make the stress cycle symmetrical). It is during this region of plasticity that the effect of the underloads can be seen. Once the material reaches a steady state, the effect of plasticity is reduced and the effect of the underload diminishes.

The load sequence tests performed in Chapter 5 showed that in the case of plain material, crack growth acceleration was highest under SBL2 loading at low ΔK but highest at high ΔK under SBL1.5 loading. The results of the FE strain calculations above suggest that the local increase in strain is proportional to the applied underload. It is reasonable to assume that the same would apply to changes in da/dN . Obviously the analysis in terms of the number of cycles investigated in the FE analysis was limited; also crack propagation was not modelled, so that only one value of ΔK was assumed. Thus, any changes to the local strain pattern during crack growth are not included. The anticipated effect on the results would be expected to remain unchanged for the crack length currently considered, but may result in a larger area affected by the region of tensile stress ahead of the crack tip for increasing crack lengths (see Section 9.4).

Interestingly, for welded steel no increase in mean stress was observed under SBL2 loading 0.01mm from the crack tip (with mean stress also stabilizing at approximately zero), but at 0.05mm it was. For the welded aluminium, the opposite was true but instead of stabilizing at a mean of zero, a tensile mean stress was observed. It may therefore be inferred that welded aluminium would show greater signs of accelerated crack growth as the crack tip mean stress was in tension for both distances from the crack tip. However, comparing results from Chapter 5 under SBL2 loading, similar levels of acceleration were observed, albeit at opposite values of ΔK (or crack lengths).

Whilst the test data in Chapter 5 showed that the introduction of welding residual stresses increased the levels of accelerated crack growth, the FE analysis indicates that their introduction does not produce an increase in mean stress in the vicinity of the crack tip, as compared with that for the plain material. This suggests that even though the presence of a tensile residual stress field serves to enhance any accelerating effect (presumably by means of pre-damage to the material ahead of a propagating crack), it is the presence of a tensile mean stress at the crack tip which generates acceleration in the first instance.

Evidence from the FE models that the presence of a tensile underload serves to increase the stress in the vicinity of the crack tip for subsequent minor stress cycles supports observations on the fracture surfaces of specimens tested under periodic underloading. From these it was found that

accelerated crack growth occurred after and during the application of each underload cycle (Section 5.3.6). Whilst these observations were on aluminium alloy, accelerated growth at a reasonably similar level also occurred in the steel. Therefore, it is reasonable to assume that the underload has the same effect here.

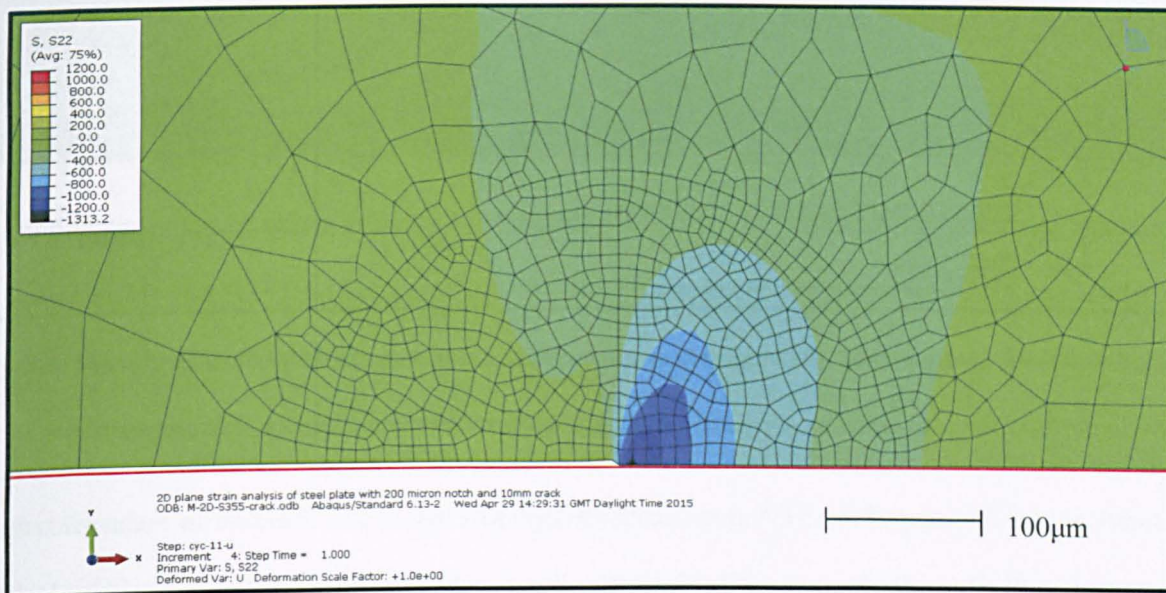


Figure 6.4.10 Contour plot showing the deformed shape in the region of the crack tip for plain steel under SBL2 loading. The red line is the horizontal symmetry plane.

With regard to crack closure, it can be seen in Figure 6.4.10 that on application of the minimum stress for the underload (15.5N/mm^2) the crack on the left hand half of the figure does not cross the horizontal symmetry plane (indicated by the red line). This shows that there is no crack closure taking place in the model. This can also be shown clearly in Figure 6.4.11, by the vertical displacement in the wake of the crack tip. Here a displacement of 0.002mm to 0.004mm (2 to $4\mu\text{m}$) is observed, indicating that the crack did not close. Whilst there was some limited crack closure detected in some of the tests described in Section 6.2, their levels were generally very low with the majority of the applied stress range being effective (i.e. crack open). Therefore, the fact that the FE models do not implicitly demonstrate the slight degree of closure observed (in some cases) experimentally, it is not considered that they invalidate the results. As it is the general effect of mean stress at the crack tip being considered, the FE models are deemed to be representative.

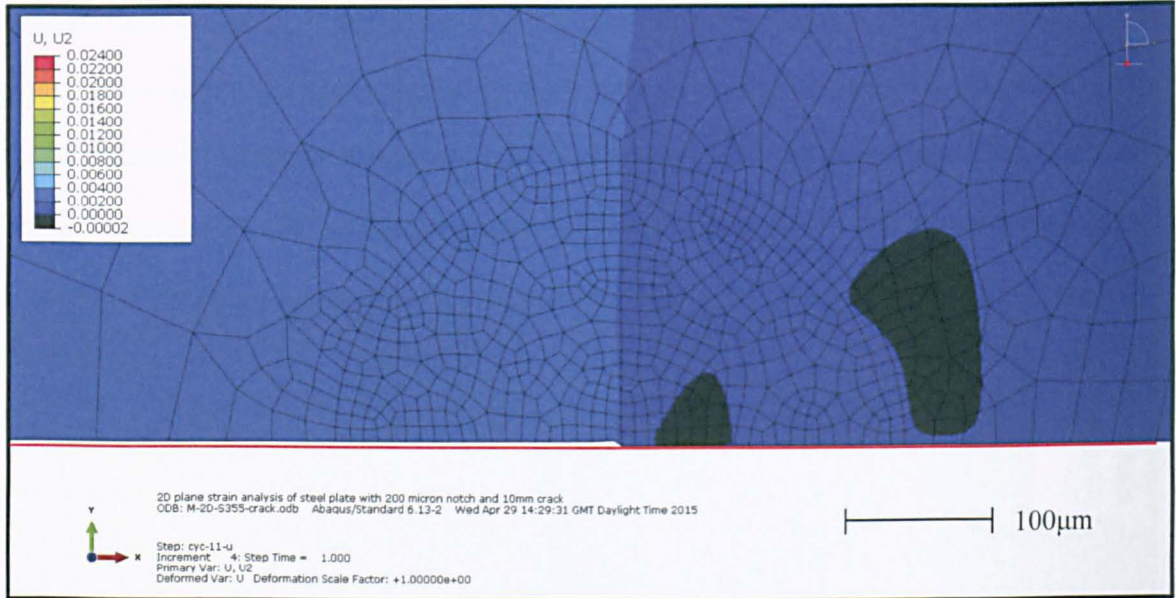


Figure 6.4.11 Contour plot showing displacement in the crack tip wake following application of the underload for plain steel under SBL2 loading. The red line is the horizontal symmetry plane.

Based on the findings of the FEA that accelerated growth through an increase in mean stress is occurring 0.01mm to 0.05mm from the crack tip, it is considered that the estimated cyclic plastic zones sizes are in fact smaller than given in Tables 6.2.1 to 6.2.4, resulting in a much larger proportion of the monotonic tensile zone, thus, increasing the area ahead of the crack tip which is always under tension.

Referring to the stress-strain plots in Appendix B, the data exhibit a ‘progressive shift’ in the direction of increasing strain, a phenomenon known as cyclic creep or ratchetting (Zhao *et al.*, 2003). For the steel, the level that this is observed was more prominent at 0.01mm from the crack tip for plain material and is seen to increase as the underload magnitude increases. The effect was not so apparent in the welded material. The same was also true for the aluminium alloy, although it was also observed in the welded models at the same distance from the crack tip (0.01mm).

Ratchetting strain was also observed from FEA of nickel alloys (Tong *et al.*, 2013), where it was suggested that through progressive accumulation of strains at the crack tip, at a critical level material separation would occur resulting in crack propagation. This was also suggested in an earlier investigation on thin wall copper tubular specimens (Kapoor, 1994). Further, FEA of crack propagation (Zheng *et al.*, 2014), examining the elasto-plastic fields in the vicinity of the crack tip,

also agree with this accumulation of strain, the build-up of which occurs at a 'critical distance' ahead of the crack tip. Once a critical strain value is reached, plastic energy is dissipated resulting in the propagation of the crack.

This effect of ratchetting and its increase with increasing underload magnitude can be clearly seen in Figures 6.4.4 and 6.4.8, by the significant increase in strain during each block of load cycles and following the underload. The same effect was observed in 7mm thick stainless steel (Grade 316L) compact tension (CT) specimens by means of stereo-DIC (3D digital image correlation), SEM-DIC (application of gold micro-grids by lithographic process in the region of the crack tip, examined under SEM) and 3D FEA (Tong *et al.*, 2015). Here a stationary crack was loaded incrementally in tension, at $R=0.1$, and the measured strain captured at a distance of 0.0285mm and 0.057mm ahead of the crack tip; this was subsequently reduced to a range of 0.006 to 0.014mm.

It is therefore considered, that whilst the effect of mean stress at the crack tip due to the presence of the underload results in accelerated growth above that of CA loading, the actual fracture process at the crack tip is due to ratchetting strain, the effect of which increases with increasing underload magnitude.

6.5 METALLURGICAL MECHANISMS

6.5.1 CRACK TIP SHARPENING/BLUNTING

Although not considered in this research, Fleck (1985) hypothesized that if the crack tip was able to re-sharpen during periodic unloading, crack growth acceleration would occur under subsequent load cycles. Using similar SBL2 loading to that in the present study, and specimens of an equivalent steel grade, plastic replication of the crack tip was examined under SEM. No evidence of crack sharpening was found, but instead the underload had slightly blunted the crack tip, suggesting that this would cause crack growth retardation rather than acceleration.

Espinosa *et al.* (2013) suggest that an underload produces crack tip sharpening as a result of the compressive stress between the crack flanks, which reshapes the crack tip and lowers the crack opening stress. The resulting higher effective stress range would then cause increased crack growth. In other words, accelerated crack growth is really due to the change in crack closure

conditions. However, as shown in Section 6.2.1 crack closure was not detected for the minor stress cycles in the present tests, indicating that this mechanism is not responsible for the observed crack growth acceleration.

Thus, it seems to be very unlikely that crack growth acceleration following an underload can be explained on the basis of crack tip sharpening.

6.5.2 CRACK TIP BRANCHING

It is considered that crack tip branching would result in lower stress intensity at the crack tip, than if a single crack was generated. Thus, under VA loading, such branching would result in crack growth retardation (Fleck, 1985).

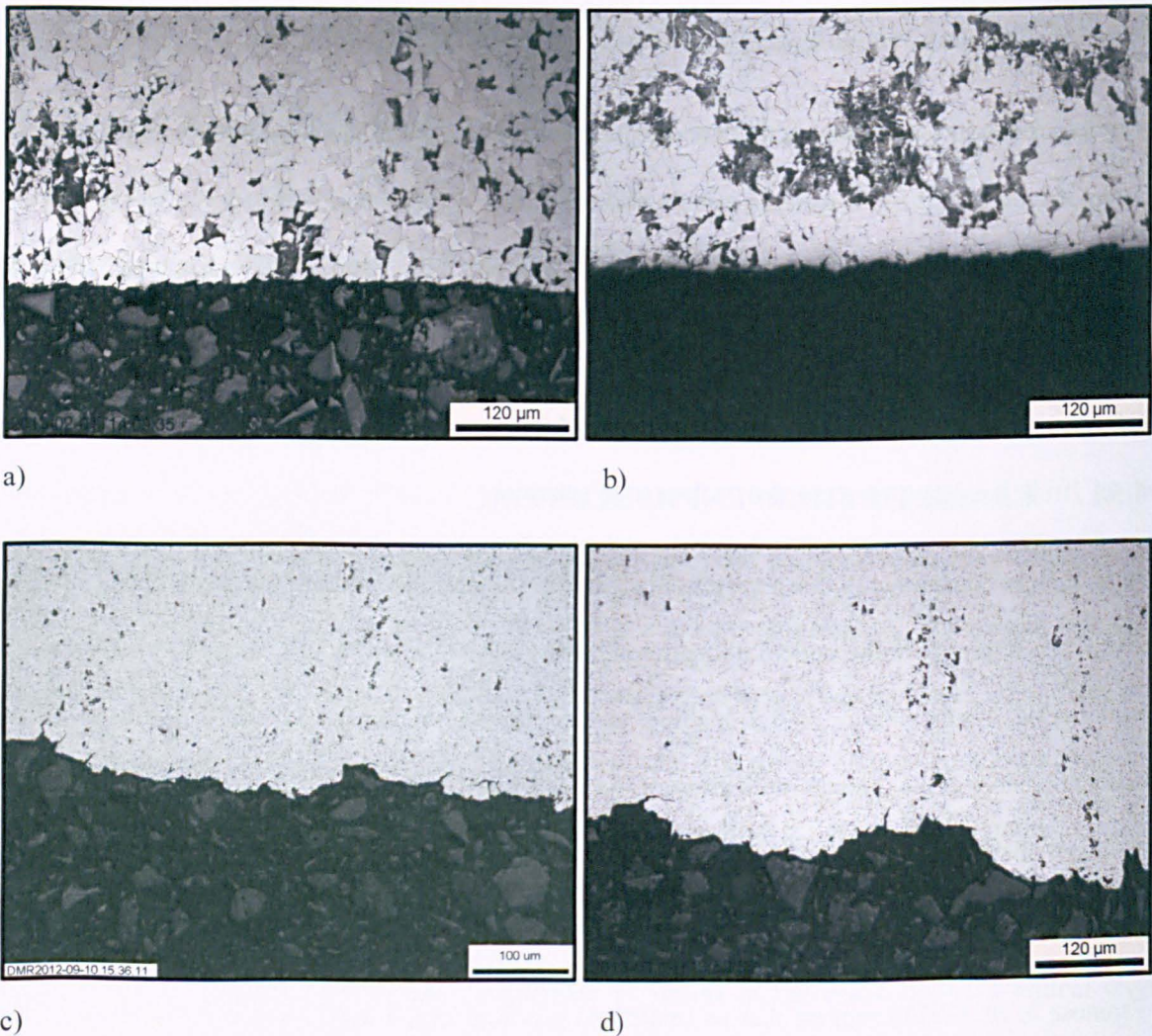


Figure 6.5.1 Extent of crack tip bifurcation observed under SEM for: a) CCT-CAL-ST-16; b) CCT-SBL2-ST-01; c) CCT-CAL-AL-15; d) CCT-SBL2-AL-02.

The fracture surfaces of steel and aluminium alloy specimens tested under the minor CA cycles and SBL2 loading were examined under SEM, Figure 6.5.1a-d. It can be seen that under SBL2 loading (Figures 6.5.1b (steel) and Figure 6.5.1d (aluminium alloy)), the degree of branching was comparable with that under CA loading (Figures 6.5.1a (steel) and Figure 6.5.1c (aluminium alloy)), suggesting that accelerated growth is not caused by a reduction in the amount of branching.

6.5.3 CYCLIC HARDENING/SOFTENING

Where single peak overloads are concerned, the associated crack growth delay increases with the rate at which a material cyclically hardens (Knott and Pickard, 1977). It is considered therefore that the converse of this argument would be true, that crack growth acceleration increases with the rate at which a material cyclically softens.

Cyclic stress-strain tests described in Chapter 4 showed that after the first few cycles both the present materials were reasonably cyclically stable, that is their monotonic and cyclic strengths were comparable. Therefore, cyclic hardening or softening does not explain the presence of accelerated growth within this study.

6.6 DISCUSSION

6.6.1 THE EFFECT ON CRACK GROWTH RATE RESPONSE FOLLOWING PERIODIC UNDERLOADS

6.6.1.1 PLAIN SPECIMENS

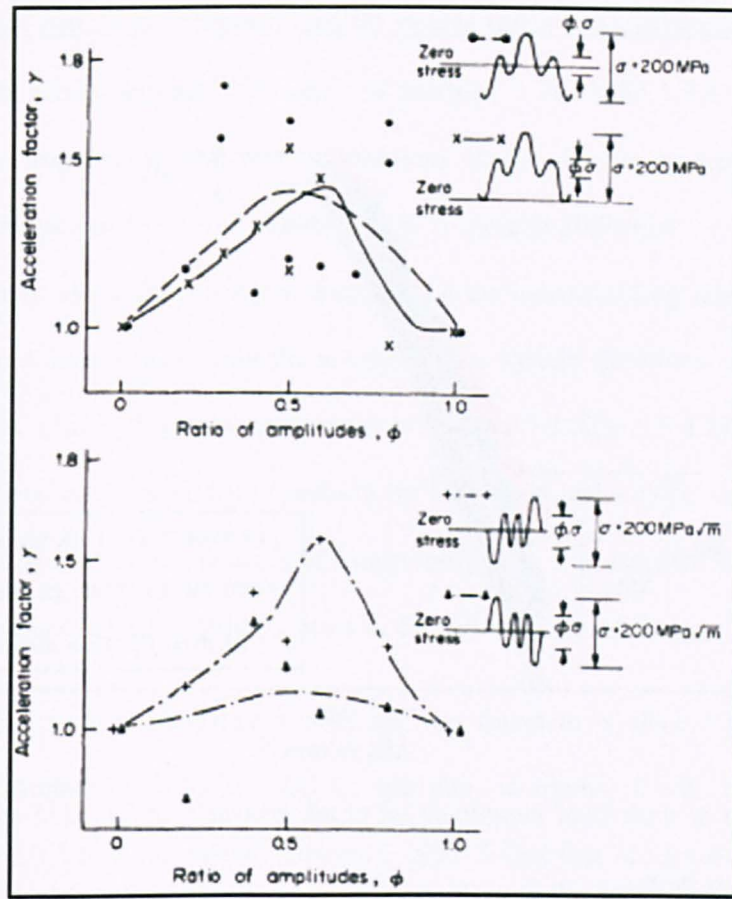
Accelerated fatigue crack growth was observed in S355 structural steel and 6082 T651 aluminium alloy subjected to periodic underloads. The range of acceleration factors observed in this study was in line with those found by other investigators (Gurney, 1983 and Fleck, 1985). These studies showed γ values in the range of 1.10 to 1.80 for structural steel (BS4360 Grade 50B) and around 1.50 for an aluminium alloy (2014A T4). In the present project under SBL2 loading, γ values for individual plain material tests were in the range of 1.02 to 1.56 (1.06 to 1.45 for the combined duplicate test results) for structural steel and 0.90 to 1.35 (0.89 to 1.29 combined) for aluminium alloy.

A similar investigation with periodic underloads on 8090 T852 and 7010 T76351 aluminium alloys (Zitounis and Irving, 2007) recorded higher acceleration factors (termed α in their analysis) than those obtained here, from 1.0 to ~14. The 7010 aluminium values were similar to the present ones at 1.0 to 1.5, but the 8090 alloy values ranged from 3.5 to 14, increasing as the level of K_{max} increased. These high values were attributed to a distinct change in crack growth mechanism associated with the particular microstructure of the alloy. The origin of this change were considered to be environmental (water vapour at the crack tip), as well as high levels of microstructurally induced crack closure during the minor (CA) cycles, both of which are irrelevant in the present case. For both of these materials acceleration was also subject to a significant amount of scatter. Further acceleration factors by Zitounis for Ti 1023 (Zitounis, 2003) were in the range of 1.0 to 2.59 and were therefore in the region of those observed here.

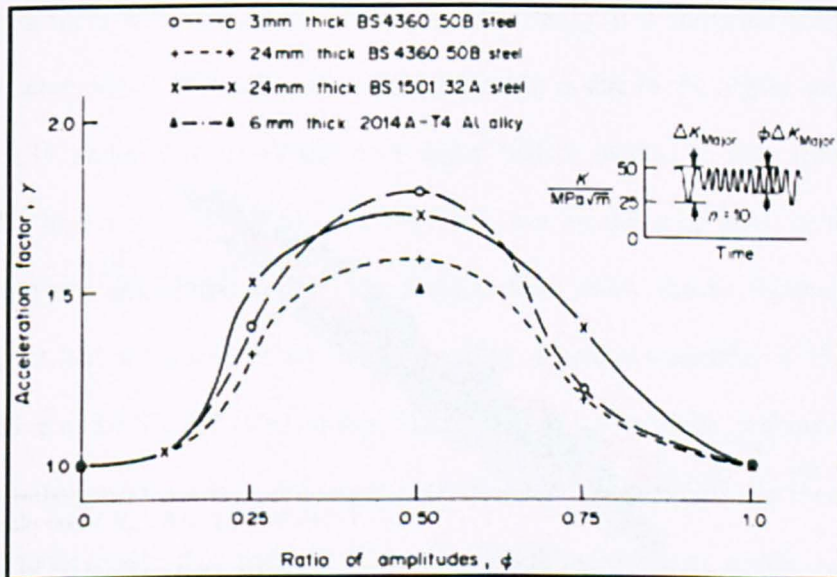
Based on published literature (Gurney, 1983 and Fleck, 1985), it was assumed for the present study that reducing the underload magnitude would also reduce γ . Both the studies mentioned showed that the maximum γ occurred for an underload magnitude of twice the minor stress and that lower or higher values resulted in a decrease in γ , as shown in Figure 6.6.1.

This was not found to be the case in the present study, the acceleration factors being rather similar for underloads of 1.5 and 2 times the minor stress range. This is because the acceleration relative to a calculated load sequence response derived from the CA data was considered here. The same magnitudes of stress range for minor and major cycles were used to generate the life estimates for the SBL2 and SBL1.5 sequences. Had the load sequence results been compared directly with the CA data for the minor stress range, then an effect of load sequence magnitude would have been observed with SBL2 resulting in a higher γ than SBL1.5, Figure 6.6.2.

It will be seen in Figure 6.6.2 that the greatest acceleration was typically at low ΔK . This is not surprising when considering the fact that fatigue crack growth in general is more sensitive in this regime to material and loading variations, especially applied stress ratio or residual stress at the crack tip, than at high ΔK . The same observation is true for the 6082 aluminium alloy under SBL2 but not for SBL1.5, where the reverse was found, Figure 6.6.3.



a)



b)

Figure 6.6.1 Accelerated growth based on the ratio of amplitudes, a) data taken from (Gurney, 1983), b) data taken from (Fleck, 1985).

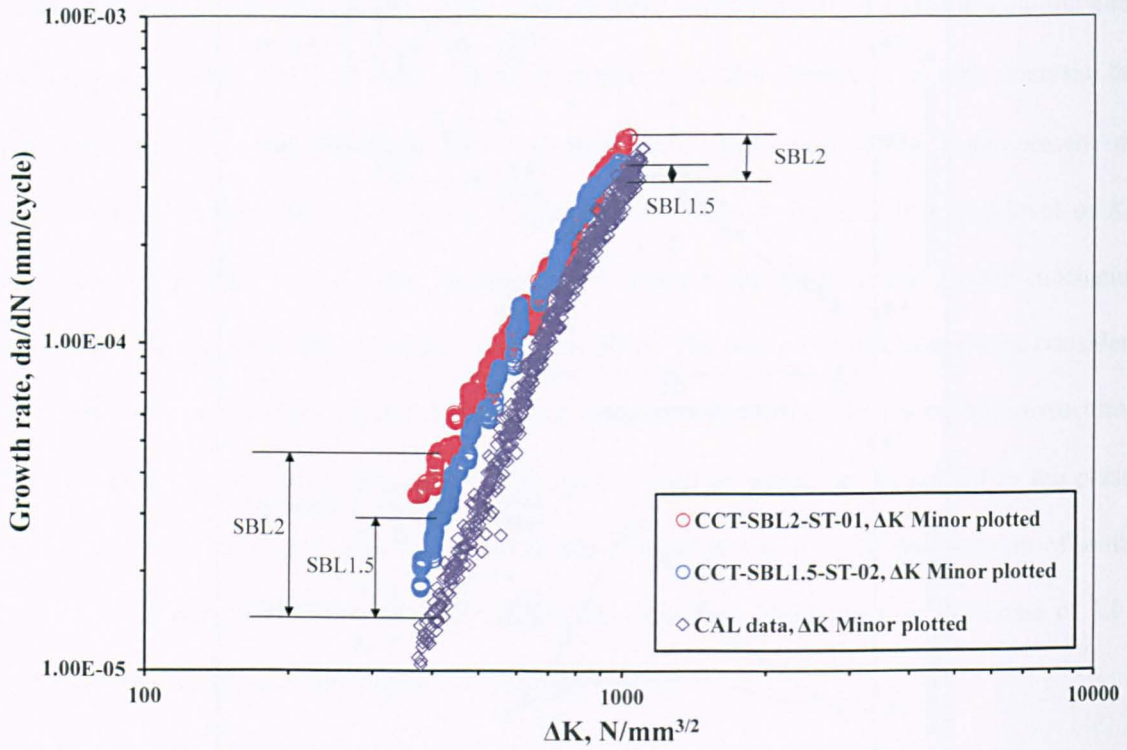


Figure 6.6.2 Effect of underload magnitude on crack growth rate for S355 steel relative to the constant amplitude response.

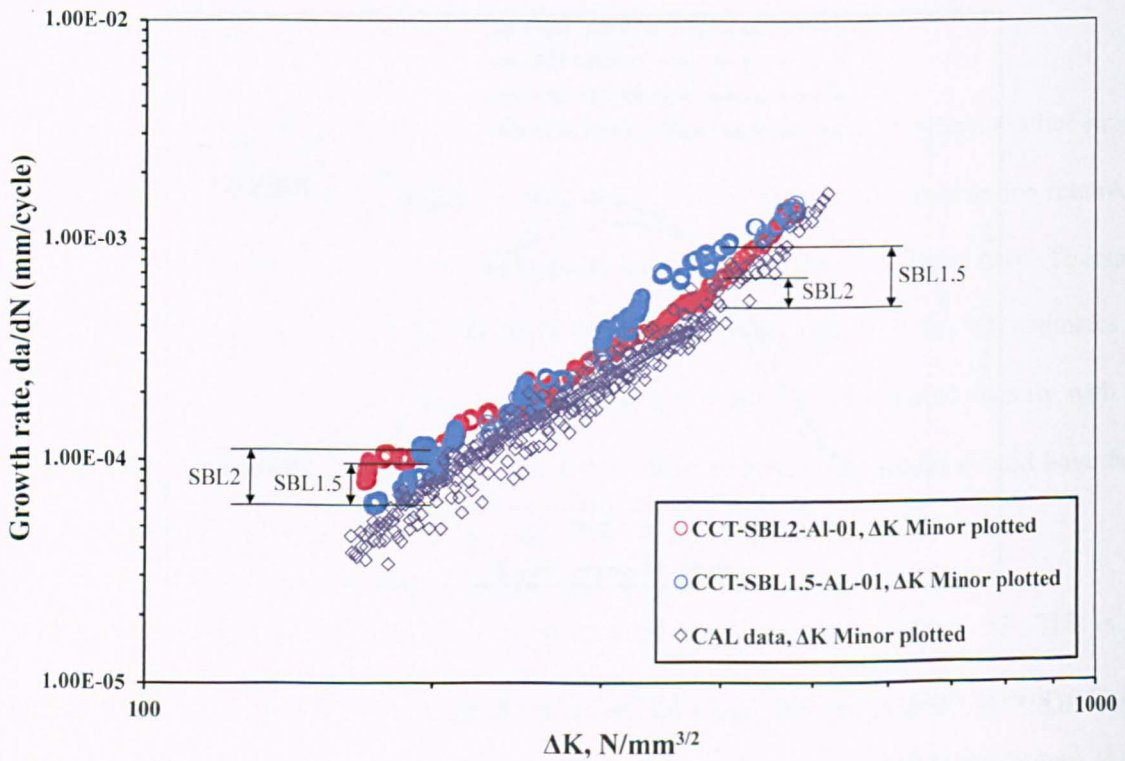


Figure 6.6.3 Effect of underload magnitude on crack growth rate for 6082 aluminium alloy relative to the constant amplitude response.

This was evident in both tests performed (and for welded specimens) and could be seen as a slight increase in growth rate at around $300\text{N/mm}^{3/2}$ ($9.5\text{MPa}\cdot\text{m}^{0.5}$) in Figure 5.3.8. The increase in the plain specimens corresponded well with observations on the fracture surfaces just prior to and following the formation of shear lips, Figure 5.3.18. At around $300\text{N/mm}^{3/2}$ ($\sim a = 23\text{mm}$) an area extending for $\sim 3\text{mm}$ along the crack was found to be the corresponding region for the increase observed. However, no explanation for the increase in the welded specimens could be found from either fractographic or metallographic examinations (Figures 5.3.22 and 5.3.23 respectively). As it was found to be related to the SBL1.5 spectrum for both plain and welded aluminium specimens but only the SBL2 spectrum for welded aluminium specimens, it is assumed that the phenomenon is related to differences in tensile residual stress in the region of the crack tip.

The region of double shear occurring at high ΔK was found to produce γ factors significantly greater in the aluminium alloy for the SBL1.5 spectrum as compared with the SBL2 spectrum, Section 5.3.2.2. FCGR tests on Al8090 (Zitounis, 2003) found that acceleration effects increased with increasing K_{max} . However, as S_{max} for the minor stress cycles in the present case was the same for both spectra there will be no difference in values of K_{max} . It is therefore considered that the increase in acceleration at high ΔK under SBL1.5 loading is due to the higher stress ratio in this regime (i.e. 0.35 under SBL1.5 versus 0.15 under SBL2), which in turn would lead to the possibility of a higher ΔK_{eff} under SBL1.5, resulting in a greater proportion of the major cycle contributing towards crack propagation. The findings from crack closure measurements (Figure 6.2.3) do suggest that in the case of the aluminium alloy, a greater proportion of the applied stress range is effective under SBL1.5 ($U=1.0$) than SBL2 ($U=0.81$), which may account for the increase in acceleration observed here. It is also worth reiterating that the cyclic plastic zone under SBL1.5 was estimated to be smaller than under SBL2 loading, resulting in a larger tensile zone ahead of the crack tip, see Section 6.2.2.

Considering that γ and β acceleration factors are derived from different equations and are used to examine different aspects of accelerated growth, i.e. acceleration in crack growth response (γ) and change in number of cycles to reach a given endurance (β), the β acceleration factors given in Table 5.3.13 for plain material were found to be in reasonable agreement with the values of γ for the

SBL2 spectrum (Table 5.3.11) but a little below those for the SBL1.5 spectrum (Table 5.3.12). Further determination of β acceleration factors corresponding to the low ΔK s used to determine the γ values showed them to be much closer, with the exception of the plain steel specimens under SBL1.5, which were slightly lower.

The factors from both methods give value to the analysis by clearly indicating the presence of crack growth acceleration, with anything greater than unity signifying accelerated growth and anything less, retardation. Also, as Miner's rule uses a similar approach in determining fatigue damage between actual numbers of cycles for a particular stress range with those calculated, determination of acceleration factors can provide an indication into the measures needed to adjust Miner's rule and provide safer life estimates under spectrum loading.

6.6.1.2 WELDED SPECIMENS

The introduction of tensile residual stress by the addition of weld beads in Section 5.3.3, further increased the extent of acceleration, with maximum γ values reaching 1.88 and 2.13 (1.86 and 1.92 combined) for the SBL2 and SBL1.5 spectra (respectively) for S355 steel at low ΔK (Tables 5.3.8 and 5.3.10). This is a little below that observed during VA testing of BS 4360 grade 50 structural steel cycling down from a constant maximum stress (Zhang and Maddox, 2009), where the maximum γ found was 2.60. The same was also evident for the 6082 aluminium alloy, with maximum values of 2.12 (1.85 combined) for SBL2 and 1.47 (1.37 combined) for SBL1.5 being derived at low and high ΔK respectively (Tables 5.3.8 and 5.3.10).

The high value at low ΔK in CCT-SBL2-AL-03R is in direct contrast to the other welded aluminium results under SBL2 and SBL1.5 spectra which tended to produce greater acceleration at high ΔK . The reason for this is not known, but is expected to be related to the distribution of residual stress in that particular specimen.

For the remaining specimens with the highest γ values at the higher ΔK end (Table 5.3.12), the slight increase in growth rate can be seen in Figure 5.3.8, and was also present to some degree for CCT-SBL2-AL-04R in Figure 5.3.6. A possible reason for this is that the crack is propagating outside the HAZ softened zone but still within the influence of the tensile residual stress due to

welding, resulting in the crack tip being exposed to an increase in stress. However, the increase occurs at the same ΔK values as for the plain material under SBL1.5 (Figure 5.3.3). Measurements on the fracture surface again agreed with observations of changes in flat tensile mode growth to the formation of shear lips at around $a = \sim 23\text{mm}$. As discussed in Section 6.6.1.1, the fact this slight increase was not apparent in the plain SBL2 specimens, suggests that it is related to the crack tip tensile stress due to the underload and presence of welding residual stresses.

With the magnitude of residual stress for the aluminium specimens found to be low (31N/mm^2) the observed effect in Figure 5.3.8 shows that there was very little difference in growth rate between plain and welded. However, this slight increase in welding tensile residual stress in addition to that produced locally at the crack tip by differences between the cyclic and monotonic zones (Section 6.2.3), may be the reason for the same sudden increase in growth rate as found under SBL1.5.

For the steel specimens tested under either sequence the acceleration was greatest at low ΔK (Tables 5.3.8 and 5.3.10) which, as discussed previously, is expected to be due to the increased sensitivity of crack growth rate to loading variables in this regime.

In Figure 5.3.7, specimen CCT-SBL1.5-ST-04R appeared to show a much greater degree of acceleration over both the plain material and the other welded specimen (CCT-SBL1.5-ST-03R). This is also shown in Table 5.3.10 with γ values of 2.05 versus 1.40 being measured at high ΔK . It was first thought that perhaps CCT-SBL1.5-ST-04R had a shorter crack length than CCT-SBL1.5-ST-03R which is why the same behaviour had not been observed, but in fact its crack length was longer by approximately 4mm. The exact reason for this is therefore not known, but it is assumed that either a variation in the magnitude of residual stresses between the specimens or a difference between the tensile stress zones in the residual stress distributions are plausible factors.

The β acceleration factors at failure given in Table 5.3.13 are predominantly below the γ acceleration factors (Tables 5.3.8 and 5.3.10). In the case of the steel specimens, when comparing the β values for the welded material with the plain, it can again be seen that the presence of the weld, and therefore the tensile residual stresses, further accelerated growth. For the aluminium alloy specimens, there is little effect of welding on β acceleration factors.

Considering the β acceleration factors at low ΔK , for the steel specimens under the SBL2 spectra, greater acceleration was detected at low ΔK although a significant amount of scatter between values for CCT-SBL2-ST-03R (1.45) and CCT-SBL2-ST-05R (5.43) was observed. This was thought to be due to variations in residual stress distribution resulting in differences in propagation rates. Whilst this could be seen in Figure 5.3.9, there was very little difference in terms of growth rate between the two specimens in Figure 5.3.5. As the β factor at low ΔK is for a crack length of 10.2mm for steel, it is therefore plausible that whilst efforts had been made to ensure sufficient crack growth data from near the notch tip were removed, it may be that for CCT-SBL2-ST-03R slightly greater crack growth, and hence number of cycles, was required which is highlighted by β . Indeed the very first few data points in Figure 5.3.5 do suggest this and so too does Figure 5.3.9, when expanding the Y-axis (Figure 6.6.4).

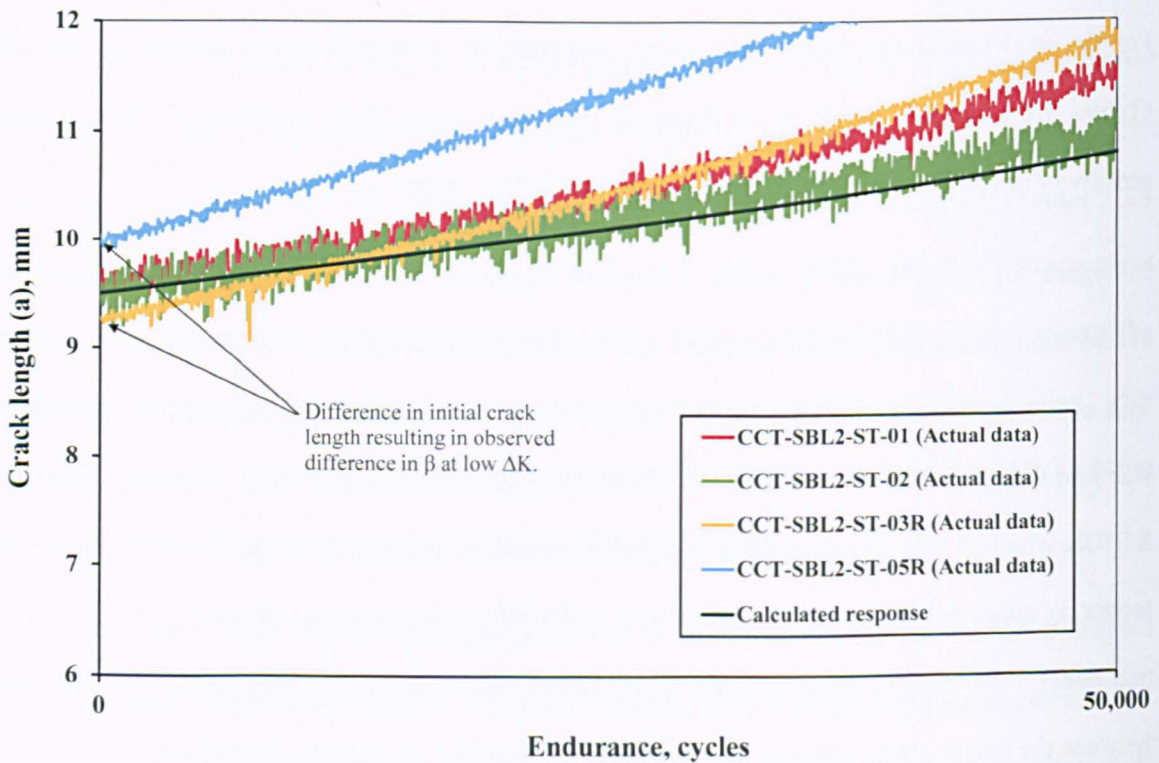


Figure 6.6.4 Expanded view of Figure 5.3.9 showing difference in initial crack length for specimens CCT-SBL2-ST-03R and 05R.

In general, the β acceleration factors at low and high ΔK were typically a little lower than γ . The inconsistencies are in agreement with those observed for plain specimens. On the whole, β does not provide such an accurate indication of the effect of load changes as γ , as it combines all the local

effects due to underloads with other effects that cause scatter in crack growth data while γ considers them individually

In view of the observed levels of γ acceleration for welded joints, which are typically around 2.0, it should be brought to attention that, of great concern, particularly for designers, is that under this form of VA loading, fatigue life has been found to be significantly shorter than predicted by Miner's rule, typically by half i.e. $\Sigma n/N = 0.5$ (Gurney, 2000; Maddox, 2005; Zhang and Maddox, 2009). Therefore, the level of γ acceleration found in these tests is comparable with the reduction in life found.

6.6.2 THE ROLE OF RESIDUAL STRESS DURING PERIODIC TENSILE UNDERLOADING

It was important to investigate whether or not the effect of underloading would be affected by the presence of tensile residual stress because such stresses exist in actual welded structures. Comparing with the endurance under CA loading (Table 5.3.1), it was found that under application of the SBL2 spectrum, whilst the reduction in fatigue life for the aluminium alloy specimens compared with the plain material was modest, the reduction for steel was significantly greater. In other words, in the presence of welding tensile residual stresses acceleration was higher than that due to the underload alone, Tables 5.3.3 and 5.3.7; however, as noted in Section 5.3.4 for acceleration factors, had comparisons been made with welded CA specimens, the difference in β may have been less. The SBL1.5 spectrum had similar effects, with the greatest reduction in life due to the presence of the welds being observed for the steel, with little or no effect for the aluminium alloy, Tables 5.3.5 and 5.3.9.

As mentioned in Section 6.3.2 the level of tensile residual stress for the 6082 T651 aluminium alloy was low, with a maximum stress in the relevant longitudinal direction of 31N/mm². Typically it is expected that yield magnitude residual stresses are generated by welding (as in the case of the steel, see Section 6.3.2). However, in some aluminium alloys, including 6082, a zone of HAZ softening is created which has the effect of reducing residual stresses, typically by a factor of around two for 6082 aluminium alloy (BSI, 1991). In view of the contrasting results obtained from the present

steel and aluminium specimens, it is clear that this must have had a significant effect on both endurance and γ .

As the effect of stress ratio or residual tensile stress at the crack tip (i.e. mean stress effect) is to result in higher acceleration factors at the more sensitive low ΔK region, it would seem reasonable that on the basis of the results, the application of welding introduces tensile residual stresses (of various magnitudes) distributed across the plate width, which are magnified at the crack tip. The increase in crack opening, U (Figures 6.2.3 and 6.2.6), then serves to increase the effective stress intensity factor.

According to Fleck and Gurney (Figure 6.6.1), γ is at a maximum when the magnitude of underload is twice that of the minor stress range, γ reducing either side of this. No explanation for this was given by either of the researchers, but is presumably related to changes in crack closure from the CA level and the proportion of the reversed plastic zone to the monotonic zone. In the current investigation, the variations in local strain ahead of the crack tip (Figures 6.4.4 and 6.4.8) produce strain accumulation which increases with increasing underload ratio, with the result that γ would not drop off at underloads above SBL2.

In addition to the effects on crack growth acceleration of changes in the crack tip mean stress and the magnification brought on by the presence of high tensile residual stresses through welding, the role of crack closure, in particular the corresponding ΔK_{eff} , can also be considered. The different forms of crack closure have already been discussed in Chapter 2. As the application of welding would serve to effectively open up the crack (over the region of tensile residual stress), the degree of crack closure under tensile unloading would be expected to be less, and hence ΔK_{eff} would be equal to that of the applied stress.

This was supported by fatigue crack growth tests on stainless steel (CA6NM) at $R=0.1$ and 0.7 , whereby the presence of tensile residual stresses at the crack tip was found to maintain a fully open crack resulting in an applied ΔK being equal to the ΔK_{eff} and hence a faster FCGR (Trudel *et al.*, 2013). Similarly, the same effect was observed in tests of five different steels whereby the effective stress ratio was higher than that applied due to the tensile residual stress at the tip, leading to faster

growth rates due to the increased crack opening (Ohta *et al.*, 1997). Measured levels of crack closure in Section 6.2 showed that in the case of the steel, the addition of welding residual stresses increased the effective proportion of the applied stress range, particularly at low ΔK where γ values were highest. However, for the aluminium alloy, no significant increase in the effective stress range was found, presumably due to the low level of tensile residual stress in these specimens

The addition of tensile welding residual stresses would therefore result in a higher crack tip mean stress than in the plain material case resulting in a more damaging stress cycle. Ultimately, acceleration effects are highest in the cases where the crack is fully open and the upper limit stress (due to the applied stress plus welding residual stress) is high, suggesting a higher tensile mean stress (or strain) being the most significant reason for acceleration. The fact that the aluminium alloy gave same the acceleration factors for relatively lower residual stress, is consistent with the general finding that aluminium is more sensitive to applied mean stress than steel (see Chapter 4).

6.6.3 ACCELERATED GROWTH OBSERVATIONS FROM STRIATION SPACINGS

It only proved possible to obtain clear evidence from measurements of striation spacing in the aluminium alloy and therefore the following observations from work performed in Section 5.3.6 are confined to that material.

The evidence confirmed that fatigue crack growth acceleration occurred under both loading spectra. However, in contrast to the expected behaviour, as given in the literature for similar sequences cycling down from a constant maximum stress (McMillan and Pelloux, 1967; Fleck, 1985), this was not confined to the period following the application of the underload but included the effect of the underload itself.

The author is unaware of any published evidence to indicate that acceleration also occurs under the underload. Therefore, the measurement of striations has been very valuable for identifying the growth due to the minor stress and the underload itself.

Comparisons of γ values deduced from striations with those obtained from the crack growth data (Figures 5.3.16 and 5.3.17) show reasonable agreement for the plain material under SBL2 loading but not for SBL1.5 or in the case of the welded material. Here γ increases rather than decreases with increase in crack length. Although as noted earlier, in view of potential measurement errors, the crack growth data should provide the more reliable γ values than the striations, the similarity between γ and β at the shorter crack length end of the range considered, seen for both steel and aluminium (Tables 5.3.3 to 5.3.6), throws doubt on the indication from the crack growth-based analysis that γ and β are in closer agreement at the longer crack lengths. The same can also be said for the welded aluminium alloy specimens (Tables 5.3.7 to 5.3.10).

From the findings presented, it can be surmised that accelerated growth rates as observed from striation spacings are due to load sequence effects such as the crack tip mean stress remaining more tensile than under CA loading alone due to the presence of the underload. The inclusion of tensile residual stresses through welding the 6082 aluminium alloy has a negligible effect on generating any further increase in growth rate. Again this is presumably due to the magnitude of tensile residual stress being far lower than the expected yield magnitude, due to the presence of the HAZ softened zone (Section 6.3.2).

6.6.4 POSSIBLE MECHANISMS ASSOCIATED WITH CRACK GROWTH RATE ACCELERATION

The phenomenon of crack closure is a mechanism that has been used extensively to account for changes in fatigue crack growth due to VA loading, especially crack growth retardation (Fleck *et al.*, 1983; Shin and Fleck, 1987; Aguilar Espinosa *et al.*, 2013). As the crack closure findings indicate for plain specimens (Figures 6.2.2 and 6.2.5) with crack lengths above 20mm, the effective part of the minor stress range (U) following an underload was very similar for both materials. For the SBL2 spectrum, U values of 0.76 for the steel and 0.81 for the aluminium alloy were recorded. For SBL1.5 $U=1.0$ for both materials meaning that the entire stress range was effective. Consequently very similar differences between crack growth under spectrum loading compared with that from CA loading would be expected.

For welded aluminium alloy (Figure 6.2.6) U values of 1.0 for SBL1.5 were observed. Under SBL2, $U=0.87$ for all crack lengths investigated. Whereas for welded steel (Figure 6.2.3), at crack lengths below 20mm the range was fully effective under both SBL2 and SBL1.5 loading reducing to $U=0.86$ beyond 20mm for SBL2. Again as the minor stress range produced a fully open crack in each case, similar results would be expected for both spectrum and CA loading.

A comparison between crack closure findings and measured acceleration values under the same spectra demonstrated that crack closure does not reflect the changes in acceleration found in simple load sequence testing with two magnitudes of stress range. Thus, the occurrence of acceleration and differences in its values cannot be explained on the basis of crack closure characteristics.

Previous work performed on this form of load sequence (Fleck, 1985) used an applied underload at a stress ratio of $R=0.50$, well above that investigated here, which would suggest that crack closure effects would be more dominant and lower acceleration factors would be derived in the present case. However, as discussed in Section 6.6.1.1, the acceleration factors observed here were in fact in line with those reported by Fleck, again suggesting that a crack closure argument, or at least that based on the possibility of an increased ΔK_{eff} , is not supported.

A possible mechanism responsible for accelerated fatigue growth following an underload is strain hardening ahead of the crack tip caused by the major (underload) cycles (Fleck, 1985). Schijve investigated this for 2024-T3 aluminium alloy and found that with just one underload application, fatigue cracks grew up to twice as fast as in the as-received material (Schijve, 1976). It was thought that half of the acceleration effect was a result of the reduced ductility whilst the other half was related to crack closure effects.

Fleck postulated that a strain hardening argument would suggest faster growth accompanying the minor cycles after an underload. This was supported in a study on 2024-T3 aluminium alloy which, following careful measurement of striation spacing, showed that faster growth accompanied the minor stress range cycles (McMillan and Pelloux, 1967). However, a strain hardening argument, whereby a percentage of the materials useable ductility is reduced, generally occurs by modification of the material yield strength following application of a load well above that of the

applied maximum or indeed the yield stress. In the present case, and that of Fleck's investigation, a constant maximum stress was used with no excursion above that level.

Another possible mechanism is modification of the crack tip mean stress. Under CA loading, mean stress relaxation occurs in the reversed plastic zone at the crack tip (Saxena and Hudak, 1979). Work performed using high-low overloads (Table 2.10.1) established the effect of mean stress relaxation under both CA and VA loading (Arcari and Dowling, 2012). The findings of their work showed that under CA loading the mean stress relaxes to a compressive state, whereas under VA loading it stabilizes at a tensile value. The same argument was postulated by Fleck (1985) who established that observations in the subsequent crack advance of his minor cycles agreed with the trend described resulting in faster growth due to the maintained tensile mean stress (Figure 6.6.5), although the exact control condition at the crack tip was not known.

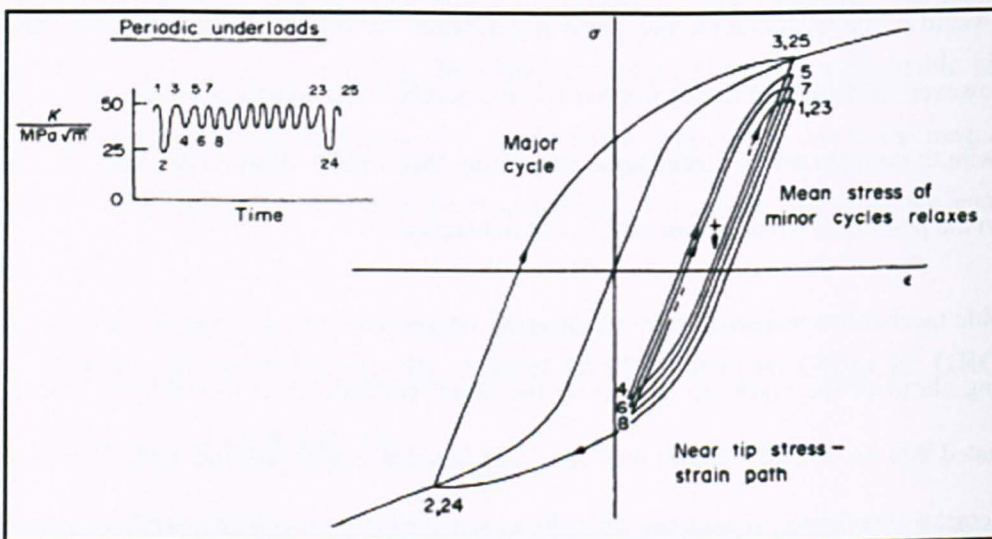


Figure 6.6.5 Assumed effect of tensile underloads on crack tip mean stress (Fleck, 1985).

The results of FE predictions for plain specimens in Section 6.4.2 show that close to the crack tip, the presence of the underload never allows the minor CA cycles to reduce to a compressive state agreeing with that found in the literature (Arcari and Dowling, 2012). Even when the underload was found not to increase the mean stress of subsequent minor cycles, the resulting effect on the CA cycles showed them to stabilize at a tensile stress. Thus, the results of the present FEA indicate that the presence of the underload maintains a higher mean stress than under CA loading alone,

which in turn results in faster crack growth, agreeing with observations of accelerated growth under spectrum loading in Section 5.3.2.

The addition of residual stress through welding has also been discussed. Whilst it is not thought to be the primary mechanism for generating crack growth acceleration (due to acceleration already being present in plain material, Tables 5.3.11 and 5.3.12), it is thought to be a contributing factor as acceleration is due to local changes at the crack tip, the effect of which is enhanced if the applied stress including any residual stress through welding is highly tensile, see Section 6.6.2.

In other words, the presence of a tensile residual stress enhances the accelerating effect, but it is the magnitude of the change in the local tensile mean stress at the crack tip which causes it.

As noted in Section 6.6.1.1, some test results indicate that acceleration effects increase with increasing K_{max} (Zitounis and Irving, 2007). However, this does not explain the present results (for plain material) since all the tests were performed with the same S_{max} and hence K_{max} at a given crack length was the same for both spectra. However, with the addition of welding residual stresses, an increased K_{max} would be generated over that for the plain material, which did result in an increase in acceleration.

Finally in Section 6.5 other possible mechanisms were discussed which may be considered to lead to accelerated crack growth. These metallurgical mechanisms (eg sharpening, branching, softening etc.), were not supported by the investigation performed here and are therefore not considered as suitable explanations leading to acceleration.

6.7 CONCLUSIONS

- Fatigue crack growth acceleration was observed in S355 structural steel and 6082 T651 aluminium alloy subjected to periodic underloads. The introduction of tensile residual stress by the addition of weld beads on the plate surfaces further increased the extent of acceleration.
- The measurement of crack growth from specimen fracture surfaces also confirmed that fatigue acceleration occurred under both loading spectra. Furthermore, acceleration was not

confined to the period following the application of the underload but also during the underload itself. This was also observed in the finite element models.

- The addition of residual stress through welding is a contributing factor leading to the enhancement of levels of acceleration.
- A comparison between crack closure measurements and acceleration factors for the same spectrum demonstrated that a change in effective stress range due to a change in the crack closure level did not reflect the changes in acceleration found in simple load sequence testing with two magnitudes of stress range. Thus, the occurrence of acceleration and differences in its values cannot be explained on the basis of crack closure characteristics.
- The area adjacent to the crack tip being constantly under tension, as determined from theoretical plastic zone size calculations, contributes towards the onset of accelerated growth. It is, however, not the mechanism responsible for generating acceleration.
- In contrast to behaviour under CA loading, the finite element analysis demonstrated that, in the region close to the crack tip, the presence of the underload does not allow the local strain range due to the minor stress cycles to reduce to a compressive state. Even when the effect of the underload has diminished, it still slowly stabilizes at a tensile level. These findings are consistent with the occurrence of increased crack growth rate, or acceleration, following an underload
- A change in mean stress at the crack tip due to the presence of tensile underloads is the primary cause of acceleration.
- Other potential mechanisms examined, including crack tip sharpening, branching, and work hardening or softening, were not considered to provide explanations for the occurrence of crack growth acceleration.
- For welded specimens, the acceleration (γ) factors observed are typically in the order of 2.0. In fatigue design, loading spectra cycling down from a constant maximum stress results in fatigue lives significantly shorter than predicted by Miners rule, typically by half i.e. $\sum n/N = 0.5$. Therefore, the level of acceleration is comparable with the reduction in life found.

Chapter 7

ENDURANCE TESTING OF WELDED JOINTS

7.1 INTRODUCTION

This Chapter presents details of work performed, using methods described in Chapter 3, on establishing the VA fatigue endurance of CCT and fillet welded specimens. CA loading tests were also performed in order to provide a bench mark *S-N* curve against which the VA tests could be compared.

The work under VA loading was conducted using spectra designed to promote fatigue crack growth acceleration. Each individual stress range in the spectrum was described in terms of the proportion p of the maximum, giving p_i , where $i = 1, 2, 3$. The value of p_i was varied to modify the ratio of minor to major stress range in the spectrum.

The load sequence effects discussed in Chapters 5 and 6 are also evaluated with respect to that observed under random loading spectra. The effects of variations in crack closure characteristics as well as a comparison of the measured and calculated crack growth rates under spectrum loading are also presented in this Chapter.

The results are expressed both in terms of Miner's damage summation values and acceleration factors, γ , based on increased crack growth rate or reduction in endurance. Fatigue life calculations based on fracture mechanics are also evaluated.

7.2 FATIGUE TESTING

7.2.1 OUTLINE OF TESTS

CA and VA fatigue tests were performed using CCT specimens in both the structural steel and aluminium alloy, as described in Section 3.4.1.1. To investigate the effect of tensile residual stress on fatigue behaviour some specimens included back-to-back weld beads on the plate surfaces.

Tests were also performed on specimens incorporating longitudinal fillet welded attachments as described in Section 3.4.1.2. Such weld details are widely used in industry for a range of structural applications. Therefore, understanding their performance under VA loading and determining the rate at which fatigue cracks grow is highly relevant to the fatigue design of welded joints.

Full details of the material properties are given in Section 4.3.

7.2.2 CONSTANT AMPLITUDE LOADING

7.2.2.1 CENTRE CRACK TENSION SPECIMENS

Reference CA tests were performed on all types of specimen at various stress ranges to establish their basic $S-N$ curves. In each case the applied loading cycled down from a constant maximum tensile stress, S_{max} , 280N/mm^2 in the steel specimens and 90N/mm^2 in the aluminium (approx. $0.60 \times$ yield strength and $0.28 \times$ yield strength respectively), as in the case of the VA tests. Tests were continued until complete failure of the specimen occurred, although, as noted in Section 3.3.3, the number of cycles needed to produce 1mm of crack growth was neglected when defining the endurance.

7.2.2.2 LONGITUDINAL FILLET WELDED SPECIMENS

Baseline CA tests were also performed on fillet welded specimens to establish their $S-N$ curves. The fatigue loading was as described for the CCT specimens with the same S_{max} for the steel specimens, but the higher S_{max} of 120N/mm^2 (Approx. $0.37 \times$ yield strength) for the aluminium. The need for this increase in S_{max} stemmed from the VA test results on CCT specimens (Section 7.5.2), where it was decided to increase the number of damaging cycles in the spectrum by

increasing S_{max} , and in turn S_r , without compromising the limiting direct stress in the softened weld HAZ, given as 150N/mm^2 (BSI, 1991).

Testing was again continued until complete failure of the specimen.

7.2.3 VARIABLE AMPLITUDE LOADING

7.2.3.1 VARIABLE AMPLITUDE LOADING SPECTRUM

To investigate whether accelerated crack growth occurred, a loading spectrum that has been shown to produce shorter lives from welded steel than those expected on the basis of Miner's rule (Gurney, 2000; Zhang and Maddox, 2009) was adopted. This involved nine stress range levels, each expressed in terms of the relative stress range p_i as in Eq. [7.2.1].

$$p_i = \frac{\text{Applied stress range}}{\text{Maximum stress range in spectrum}} \quad [7.2.1]$$

where $i = 1$ to 9 . The spectrum comprised 1,042 cycles (2,084 turning points), which constituted one block. A computer-controlled testing machine applied the stress cycles in a random order by selecting p_i values using a random number generator. Once the first block had been applied, subsequent blocks were applied in the same randomly generated order as the first.

7.2.3.2 CENTRE CRACK TENSION SPECIMENS

VA tests were performed on all types of CCT specimen. Details of the stress ranges and the corresponding number of cycles in a block are shown in Table 7.2.1. Following initial testing of plain material under CA loading, the stress range for the aluminium alloy was increased to 90N/mm^2 , Table 7.2.2. The stress time history for the revised spectrum is shown in Figure 7.2.1.

Table 7.2.1 Details of loading spectrum used for VA loading tests of CCT specimens, Spectrum name VA-AL-70-0.25; VA-ST-210-0.25

Relative stress range, pi	6082 T651	S355	Cycles	Exceedence
	Stress range, N/mm^2	Stress range, N/mm^2		
1.00	70.0	210.0	1	1
0.90	63.0	189.0	3	4
0.80	56.0	168.0	6	10
0.70	49.0	147.0	12	22
0.60	42.0	126.0	23	45
0.50	35.0	105.0	48	93
0.40	28.0	84.0	109	202
0.30	21.0	63.0	296	498
0.25	17.5	52.5	544	1,042

Table 7.2.2 Details of the revised loading spectrum used for VA loading tests of CCT and fillet welded specimens, spectrums name VA-AL-90-0.25; VA-ST-210-0.25

Relative stress range, pi	6082 T651	S355	Cycles	Exceedence
	Stress range, N/mm^2	Stress range, N/mm^2		
1.00	90.0	210.0	1	1
0.90	81.0	189.0	3	4
0.80	72.0	168.0	6	10
0.70	63.0	147.0	12	22
0.60	54.0	126.0	23	45
0.50	45.0	105.0	48	93
0.40	36.0	84.0	109	202
0.30	27.0	63.0	296	498
0.25	22.5	52.5	544	1,042

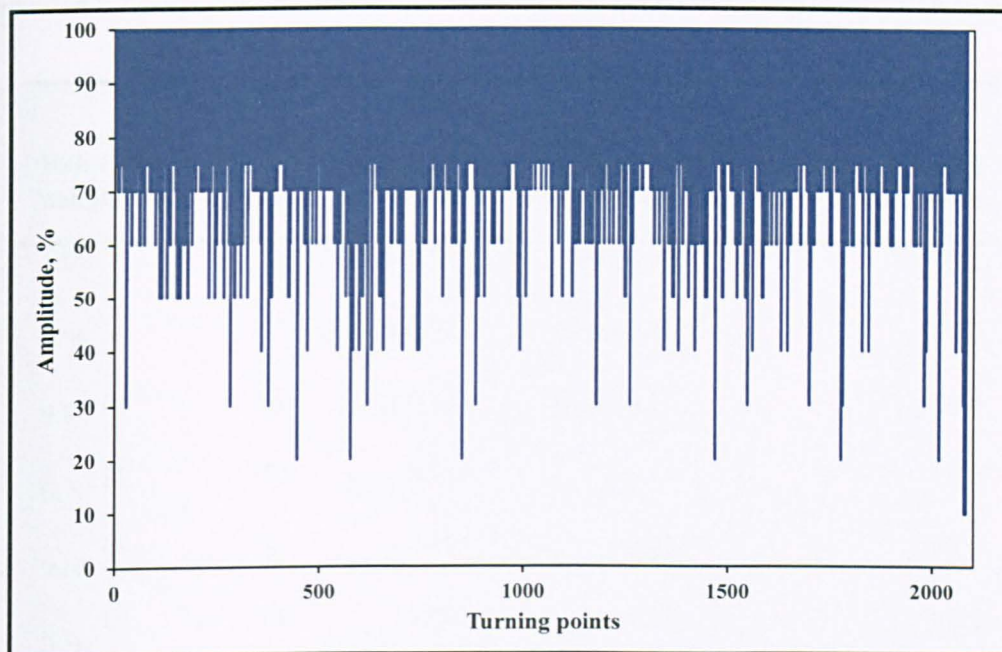


Figure 7.2.1 Variable amplitude loading spectrum cycling down from a constant maximum stress, Spectrum name VA-AL-90-0.25; VA-ST-210-0.25.

7.2.3.3 LONGITUDINAL FILLET WELDED SPECIMENS

The same form of loading was applied to the fillet welded specimens as that used for the CCT specimens above. However, to investigate the influence of small stress cycles on fatigue life (see Section 7.5.2.), three versions of the spectrum were used with minimum p_i values of 0.25, 0.20 and 0.40. Details of the stress ranges and number of cycles are shown in Tables 7.2.2 to 7.2.4, with the corresponding stress histories given in Figures 7.2.1 to 7.2.3.

For each of the applied spectra, the values of S_{max} and the maximum applied stress range for steel and aluminium specimens remained unchanged (see Section 7.2.2.2).

Table 7.2.3 Details of loading spectrum used for VA loading tests of fillet welded specimens, spectrum name VA-AL-90-0.20; VA-ST-210-0.20

Relative stress range, pi	6082 T651	S355	Cycles	Exceedence
	Stress range, N/mm^2	Stress range, N/mm^2		
1.00	90.0	210.0	1	1
0.90	81.0	189.0	3	4
0.80	72.0	168.0	6	10
0.70	63.0	147.0	12	22
0.60	54.0	126.0	23	45
0.50	45.0	105.0	48	93
0.40	36.0	84.0	109	202
0.30	27.0	63.0	296	498
0.25	22.5	52.5	544	1,042
0.20	18.0	42.0	1,125	2,167

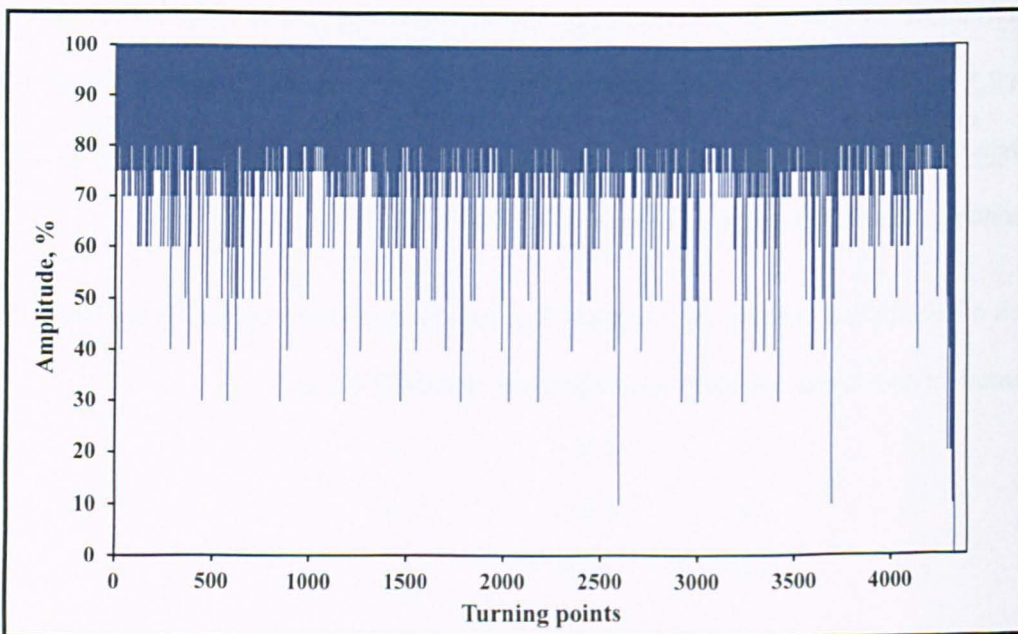


Figure 7.2.2 Variable amplitude loading spectrum cycling down from a constant maximum stress, spectrum name VA-AL-90-0.20; VA-ST-210-0.20.

Table 7.2.4 Details of loading spectrum used for VA loading tests of fillet welded specimens, spectrum name VA-AL-90-0.40; VA-ST-210-0.40

Relative stress range, pi	6082 T651	S355	Cycles	Exceedence
	Stress range, N/mm^2	Stress range, N/mm^2		
1.00	90.0	210.0	1	1
0.90	81.0	189.0	3	4
0.80	72.0	168.0	6	10
0.70	63.0	147.0	12	22
0.60	54.0	126.0	23	45
0.50	45.0	105.0	48	93
0.40	36.0	84.0	109	202

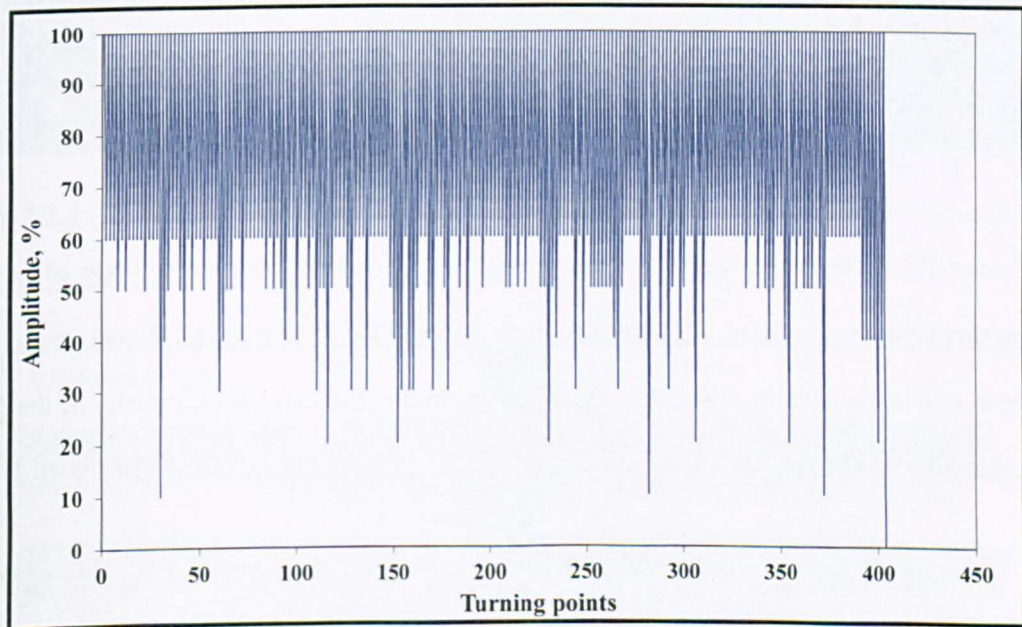


Figure 7.2.3 Variable amplitude loading spectrum cycling down from a constant maximum stress, spectrum name VA-AL-90-0.40; VA-ST-210-0.40.

7.2.4 EQUIVALENT CONSTANT AMPLITUDE STRESS RANGE

In order to compare fatigue test results obtained under both CA and VA loading it is useful to define the CA stress that is equivalent in terms of fatigue damage to the applied VA stress spectrum. For an applied stress spectrum consisting of n_i cycles at stress range s_i , and assuming that Miner's rule is correct, this is given by:

$$S_{eq} = \left[\frac{(\sum \Delta S_i^m \cdot n_i)}{\sum n_i} \right]^{1/m} \quad [7.2.2]$$

where m is the slope of the constant amplitude $S-N$ curve for the detail concerned expressed in the form given in Eq. [2.2.2], and ΔS_i is the stress range that is applied n_i times in a spectrum. Note that $\sum n_i$ is the spectrum block length N_b .

It is useful to express this equation in terms of the maximum applied stress range in the spectrum, Sr_{max} , and individual stress levels s_i included as proportions p_i of the maximum (i.e. $p = s/Sr_{max}$) as follows:

$$S_{eq} = Sr_{max} \left[\frac{(\sum p_i^m \cdot n_i)}{\sum n_i} \right]^{1/m} \quad [7.2.3]$$

The relevant BS 7608 design curve for the present fillet welded detail has a slope of $m=3$ and therefore this value is used here. This has also been assumed for the welded CCT specimens, which is considered to be reasonable since, in both cases, the fatigue life consists essentially of the growth of a crack.

It should be noted that the above definition of the equivalent stress is based on the assumption that the CA $S-N$ curve with a slope of $m=3$ extends to the lowest stress ranges in the spectrum. Making such an assumption increases S_{eq} slightly, if, in fact, some of them are below the constant amplitude fatigue limit (CAFL).

Good agreement between constant and variable amplitude test results with the latter expressed in terms of the equivalent stress range would indicate that Miner's rule was correct for the weld

details and stress spectrum considered, whereas disagreement would indicate that Miner's rule was not accurate.

7.2.5 METHODS OF FATIGUE CRACK DETECTION AND MEASUREMENT

Soap solution was used as an aid to visual inspection by travelling microscope in the region of expected fatigue cracking for both types of welded specimen. Apart from aiding inspection, soap solution stains the fatigue fracture surface and produces beachmarks corresponding to the crack front at that time, as seen in a CCT specimen in Figure 7.2.4. Weld toe fatigue cracks, such as those in the present fillet welded specimens, adopt a semi-elliptical shape, Figure 7.2.5. The application of this technique, which is used routinely by TWI, allowed the detection of small surface breaking fatigue cracks of this type (~2mm surface length). It is reported to have no influence on the fatigue lives of welded joints (Hinnant, 2007).

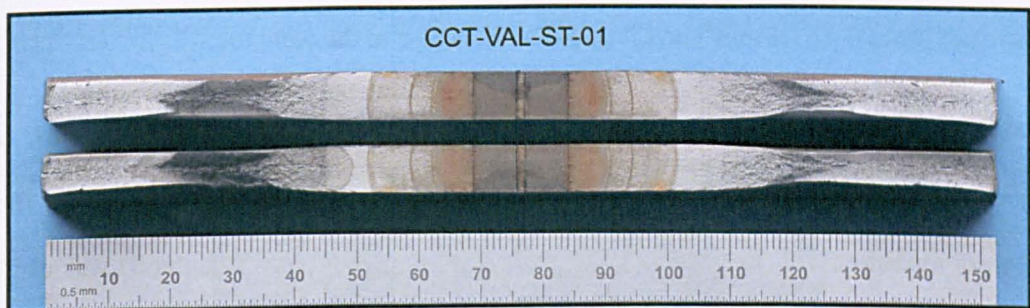


Figure 7.2.4 CCT specimen fracture surface showing curved-front beachmarks. An 8mm thick steel specimen is shown.

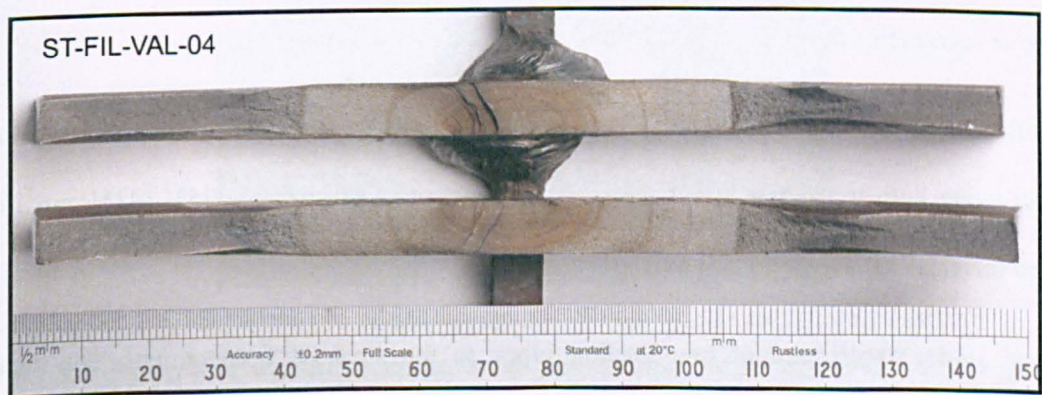


Figure 7.2.5 Fillet welded specimen fracture surface showing semi-elliptical beachmarks. An 8mm thick steel specimen is shown.

In some of the tests on fillet welded specimens, once a crack was detected visual inspection was supplemented by ACPD (see Section 3.5.2.2) crack depth measurements.

A record was kept of detected crack length and depth, with the corresponding number of cycles endured. This, together with macro examinations of failed specimen fracture surfaces and striation analysis using a SEM, allowed the generation of fatigue crack propagation data.

7.3 RESIDUAL STRESS MEASUREMENT

Negligence of the need to consider applied mean stress in fatigue design codes is based on the assumption that high tensile residual stresses will always be present in welded structures. As demonstrated in Chapter 6, yield magnitude residual stresses were indeed present in the steel CCT specimens. However, this was not the case in the aluminium alloy specimens, due to HAZ softening. Allowing for HAZ softening the residual stress in the region of the notch was about 19% (31N/mm^2) of proof ($\sim 161\text{N/mm}^2$) or 15% (24N/mm^2) close to the weld toe.

To establish the magnitude of residual stress in the present fillet welded specimens, and to investigate any change of residual stresses during cyclic loading, residual stresses close to the plate surface were measured in both materials. The hole drilling method (see Chapter 3) was used, with the holes located 2mm from the weld toe at the end of the attachment and extending across the plate width, Figure 7.3.1. In the case of the steel fillet welded specimen, measurements were also made using neutron diffraction (see Chapter 3), Figure 7.3.2. This was applied in the same region but also at increments through the plate thickness to establish any variation.

As in the case of the CCT specimens, yield magnitude residual stress were shown to be present in the steel using both techniques, with those in aluminium alloy measuring 25% (41N/mm^2) of the softened material's 0.2% proof strength ($\sim 161\text{N/mm}^2$).

However, under application of one loading block to the steel CCT specimens, the measured residual stress in the region of the notch decreased by 84% to 77N/mm^2 , but increased after 100 blocks to 168N/mm^2 . The aluminium alloy relaxed by 39% to 19N/mm^2 after one block, with a further decrease to 12N/mm^2 after ten blocks.

The relaxation of fillet welded specimens was also measured where on application of one loading cycle representing 40% yield for the steel and 75% of the softened 0.2% proof stress for the aluminium, the measured stress reduced by 72% to 142N/mm^2 for the steel and 125% to -40N/mm^2 for the aluminium alloy, therefore becoming slightly compressive in that case.

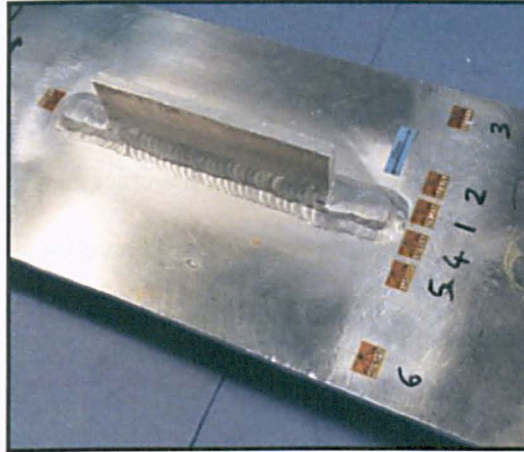


Figure 7.3.1 Fillet welded specimen with centre hole measurements performed across the plate width close to the end of the welded attachment.

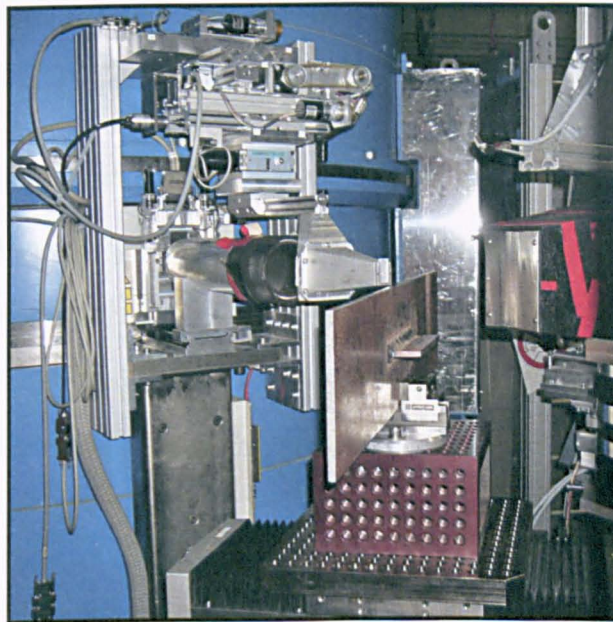


Figure 7.3.2 Steel Fillet welded specimen setup for residual stress measurement using neutron diffraction at FRMII, Munich.

7.4 CRACK CLOSURE MEASUREMENTS

Crack closure under the applied VA spectrum (*VA-AL-90-0.25*; *VA-ST-210-0.25*) was determined by use of uniaxial strain gauges bonded to the surface of CCT specimens (1.5mm behind the crack tip) as detailed in Chapter 3 (Section 3.6) and used previously for CCT specimens under simple loading spectra (Chapter 6, Section 6.2).

Figure 7.4.1 shows the response of the steel CCT specimen following application of the VA spectrum. As the crack propagates, the level at which the crack closes is un-changed at 91N/mm^2 such that $U = (280-91)/(280-70) = 0.90$. Between 20 and 30mm there is a transition, such that by the time the crack length is 30mm it is fully open. The findings therefore suggest that for $a = 12$ to 20mm, the proportion of the applied stress range that is effective, U , when the crack is open is 0.90, rising to $U = 1.0$ at and beyond 30mm.

For the aluminium (Figure 7.4.2), it will be seen that the closure stress remains constant at 27N/mm^2 for the three crack lengths considered, giving $U = ((90-27)/(90-20)) = 0.90$. In other words, as in the case of the steel, 90% of the applied stress range is effective in propagating the crack, but in aluminium this applies over the full range of crack lengths considered.

Welded CCT specimens were not included in this closure study but it can be inferred from results under simple loading spectra (Chapter 6, Section 6.2) that the introduction of tensile residual stresses would serve to increase the effective stress range for steel specimens by holding the crack open, even with the reduced level after cyclic redistribution (see Section 7.3), but would not change that for the aluminium alloy due to the low level of residual stress observed in these specimens (see Section 6.3).

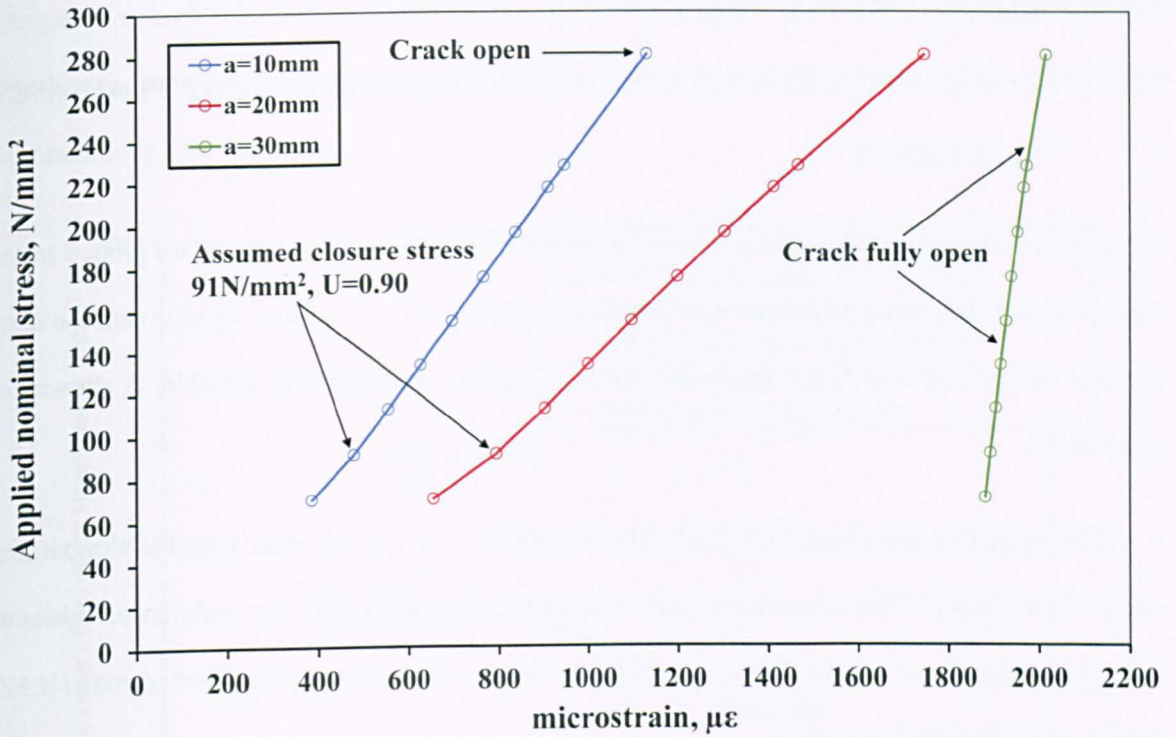


Figure 7.4.1 Recorded crack closure levels in plain S355 steel, upon application of an applied stress from 280N/mm² to 70N/mm².

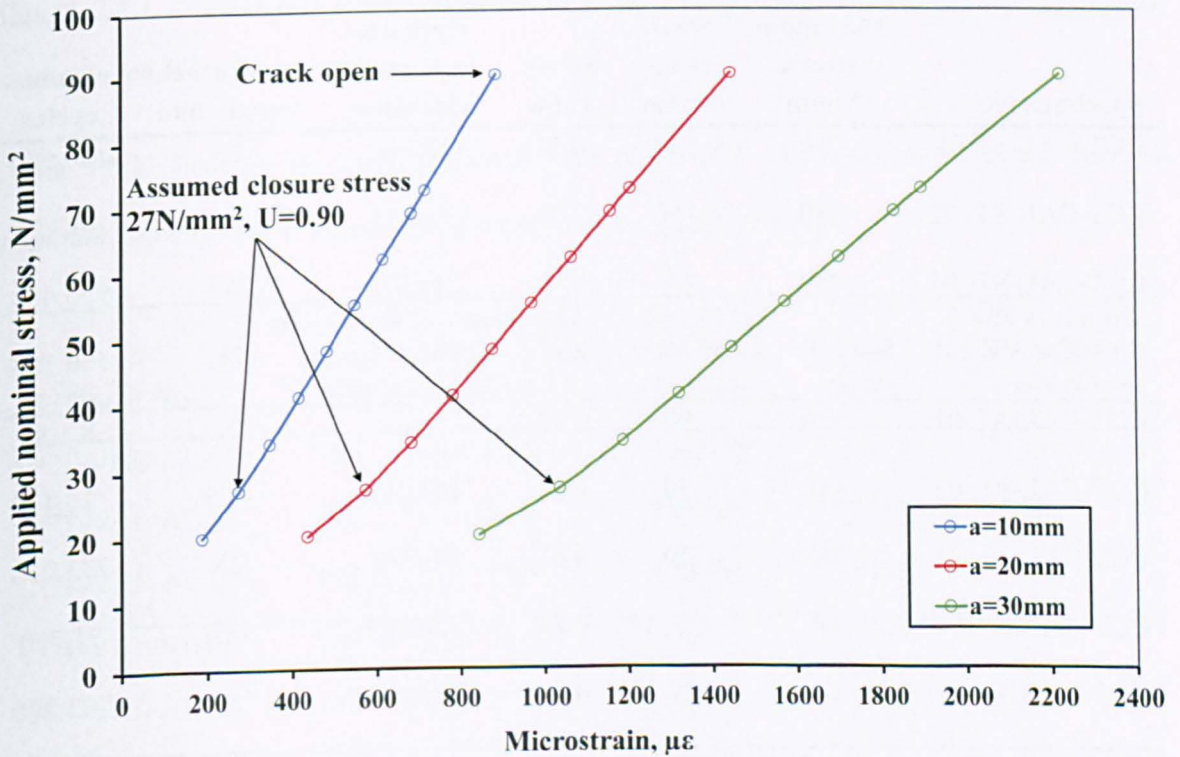


Figure 7.4.2 Recorded crack closure levels in plain 6082 aluminium alloy, upon application of an applied stress from 90N/mm² to 20N/mm².

7.5 EXPERIMENTAL RESULTS

7.5.1 CONSTANT AND VARIABLE AMPLITUDE TESTING OF PLAIN CCT SPECIMENS

Table 7.5.1 summarises the results of the CA reference tests. The endurance data are plotted in the form of an $S-N$ diagram with double logarithmic axes in Figure 7.5.1. A mean line through the data, estimate by least squares linear regression treating $\log N$ as the dependent variable, is shown for comparison.

It will be noted that specimens CCT-CAL-AL-01 and CCT-CAL-AL-02 were tested at a maximum stress of 160N/mm^2 . This was subsequently reduced because of the very low endurance achieved and the fact that it exceeds the limiting stress (BSI, 1991) of the softened heat affected zone (HAZ) for the planned welded specimens.

Table 7.5.1 Summary of results obtained from plain CCT specimens tested under constant amplitude loading

Specimen No.	Maximum stress, N/mm^2	Stress range, N/mm^2	Stress ratio	Cycles to 1mm crack extension	Final crack length, mm	Valid cycles
CCT-CAL-ST-01	280	120	0.57	35,148	26	100,580
CCT-CAL-ST-02	280	150	0.46	12,953	29	46,919
CCT-CAL-ST-04	280	60	0.79	215,398	26.5	936,460
CCT-CAL-ST-05	280	75	0.73	102,657	28	530,158
CCT-CAL-AL-01	160	90	0.44	-	15.5	8,100
CCT-CAL-AL-02	160	30	0.81	107,200	17.5	116,420
CCT-CAL-AL-03	90	30	0.67	80,770	25	233,030
CCT-CAL-AL-04	90	50	0.44	126,480	32.5	51,750
CCT-CAL-AL-05	90	20	0.78	248,750	31	792,290

The fatigue test results obtained under the VA loading spectrum presented in Table 7.2.2 are summarised in Table 7.5.2 and presented in Figure 7.5.1 in terms of their equivalent CA stress

ranges. For both materials the lives of the triplicate VA tests show good agreement with one another indicating that scatter on endurance was low. The table also includes the Miner's rule summation, $\sum n/N$, values.

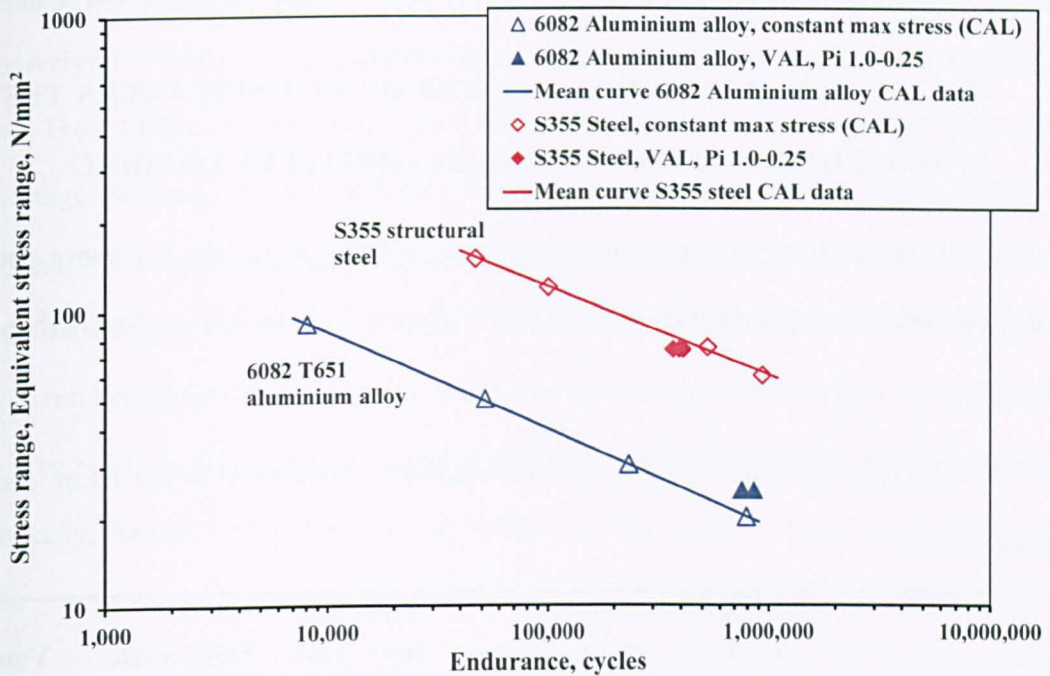


Figure 7.5.1 Fatigue test results obtained from plain CCT specimens tested under constant maximum tensile stress conditions.

Table 7.5.2 Summary of results obtained from plain CCT specimens tested under variable amplitude loading (spectrum names VA-AL-90-0.20 or VA-ST-210-0.25)

Specimen No.	Maximum stress, N/mm ²	Equivalent stress range, N/mm ²	Cycles to 1mm crack extension	Valid cycles	$\sum n/N$ at failure based on mean CA S-N curve
CCT-VAL-AL-01	120	24.5	165,040	855,412	1.98
CCT-VAL-AL-02	120	24.5	189,841	754,112	1.74
CCT-VAL-AL-03	120	24.5	170,491	759,782	1.76
CCT-VAL-ST-01	280	73.6	49,912	409,962	0.79
CCT-VAL-ST-02	280	73.6	50,197	394,663	0.76
CCT-VAL-ST-03	280	73.6	88,998	370,471	0.71

Comparing the VA results with the mean CA data in Figure 7.5.1, it can be seen that the lives for the steel specimens were slightly below the CA mean, whereas those for the aluminium specimens

exceeded the mean (discussed further in Section 7.7.1). According to Miner's rule, if an experimental result lies on or above the CA mean curve (i.e. $\sum n/N > 1$) then, for this type of detail and loading spectrum, use of the rule to estimate the fatigue life would be accurate or safe. Conversely, if the result is below the CA mean curve (i.e. $\sum n/N < 1$), then the rule would be unsafe.

7.5.2 THE EFFECT OF RESIDUAL STRESS ON CCT SPECIMENS TESTED UNDER CONSTANT AND VARIABLE AMPLITUDE LOADING

Table 7.5.3 summarises the results of the welded CA reference tests. The endurance data are plotted in the form of an $S-N$ diagram in Figure 7.5.2. A mean line through the data is shown for comparison.

Table 7.5.3 Summary of results obtained from welded CCT specimens tested under constant amplitude loading

Specimen No.	Maximum stress, N/mm ²	Stress range, N/mm ²	Stress ratio	Cycles to 1mm crack extension	Final crack length, mm	Valid cycles
CCT-CAL-ST-01R	280	120	0.57	21,429	32	73,046
CCT-CAL-ST-02R	280	150	0.46	7,931	33	42,866
CCT-CAL-ST-03R	280	90	0.68	42,797	32	210,363
CCT-CAL-ST-04R	280	60	0.79	166,595	30	801,711
CCT-CAL-ST-05R	280	75	0.73	79,981	31	387,953
CCT-CAL-ST-06R	280	50	0.82	355,733	31	1,224,827
CCT-CAL-AL-01R	120	30	0.67	232,270	33	330,970
CCT-CAL-AL-02R	120	50	0.44	14,590	33	55,940
CCT-CAL-AL-03R	120	20	0.78	69,380	32	548,650
CCT-CAL-AL-04R	120	40	0.56	27,940	33	85,030
CCT-CAL-AL-05R	120	25	0.72	91,000	29	231,820

Specimen CCT-CAL-AL-01R was excluded from the regression analysis as it was accidentally overloaded during installation, resulting in an increase in the number of cycles needed to propagate the crack from the notch tip.

The effect of welding residual stresses on the fatigue lives of the specimens under CA loading can be calculated by comparing the *S-N* curves for the plain and welded specimens. The mean curves given in Figures 7.5.1 and 7.5.2 are based on the ‘free slope’ of the data ($m=3.32$ and 3.04 for the plain steel and aluminium respectively; $m=3.17$ and 2.42 for the welded steel and aluminium respectively). For ease of comparison, the regression analysis was repeated with the slope (m) fixed at $m=3$. The difference in fatigue endurance between the fitted mean curves is then independent of stress range. However, for convenience it has been made at stress ranges corresponding to the equivalent stress ranges for the *VA-AL-90-0.25* and *VA-ST-210-0.25* spectra. The results of the comparison are given in Table 7.5.4, where it will be seen that the introduction of welding residual stresses resulted in similar reductions in mean life, 19% for the steel and 21% for the aluminium alloy. The result for the aluminium suggests that the residual stresses were larger than measured and actually, perhaps local to the crack tip, sufficiently high to justify the stress range concept for design.

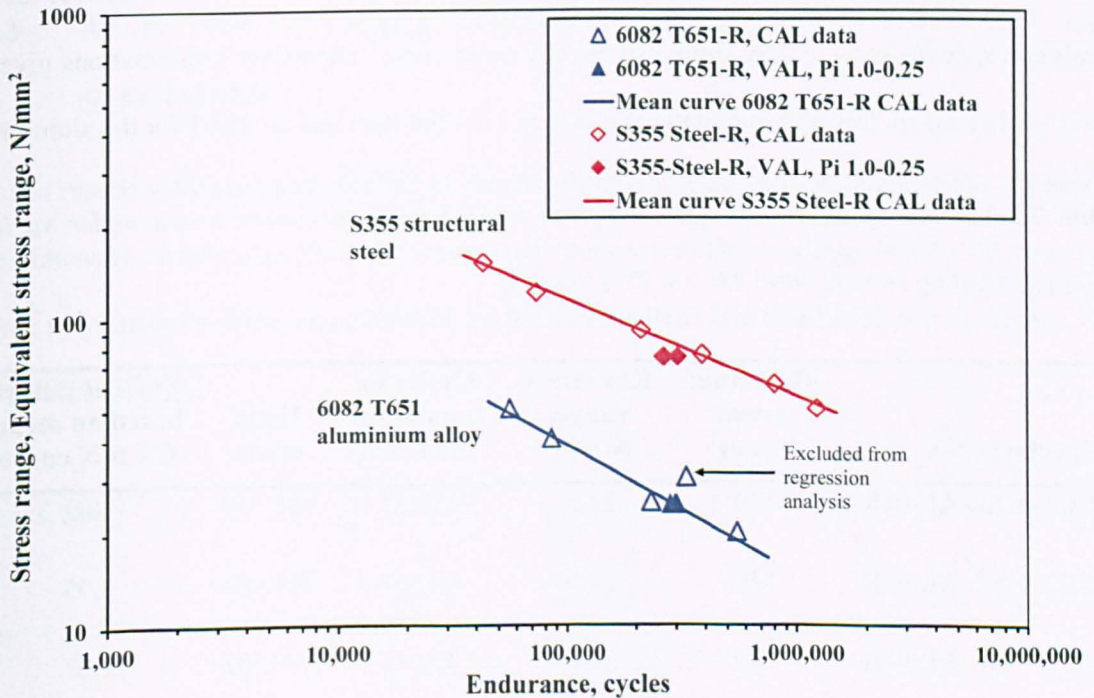


Figure 7.5.2 Fatigue test results obtained from welded CCT specimens tested under constant maximum tensile stress conditions.

Table 7.5.4 Comparison between endurance for plain and welded CCT specimens under CA loading based on CA S-N curves with slope of $m=3$

Material	Stress range, N/mm ²	Mean life, cycles		Reduction in endurance due to presence of weld, %
		Plain	Welded	
Steel	73.6	471,546	381,250	19
Aluminium alloy	24.5	424,993	337,274	21

The fatigue test results obtained under VA loading using the same spectrum as for the plain material (Section 7.5.1) are summarised in Table 7.5.5 and presented in Figure 7.5.2 in terms of the equivalent CA stress range.

Comparing with the mean CA data in Figure 7.5.2, it can again be seen that the lives of the steel specimens were slightly below the mean. However, for the plain material, the lives of the aluminium specimens were very similar to the CA mean curve. The Miner's summations given in Table 7.5.4 re-affirm this with summations less than 1 for the steel and around 1 for the aluminium.

Table 7.5.5 Summary of results obtained from welded CCT specimens tested under variable amplitude loading (VA-AL-90-0.25; VA-ST-210-0.25)

Specimen No.	Maximum stress, N/mm ²	Eqv stress range, N/mm ²	Cycles to 1mm crack extension	Valid cycles	$\sum n/N$ at failure based on mean CA S-N curve
CCT-VAL-AL-01R	120	24.5	45,831	296,139	1.03
CCT-VAL-AL-02R	120	24.5	49,567	281,984	0.95
CCT-VAL-AL-03R	120	24.5	42,612	300,582	1.07
CCT-VAL-ST-01R	280	73.6	59,245	304,359	0.77
CCT-VAL-ST-02R	280	73.6	79,173	265,802	0.67
CCT-VAL-ST-03R	280	73.6	89,507	261,649	0.66

Working as before, the effect of welding residual stresses on mean life under VA loading, again related to the equivalent CA stress range, is shown in Table 7.5.6. Under VA loading the introduction of welding residual stresses had a more significant effect on the aluminium alloy than the steel, with a reduction in mean life by 63% as compared with 29% for the steel. Both reductions were greater than those seen for CA loading.

Table 7.5.6 Comparison between mean endurance for plain and welded CCT specimens under VAL at the equivalent CA stress range

Material	Eqv CA stress range, N/mm ²	Mean life, cycles		Mean $\sum n/N$ at failure		Reduction in endurance due to welding, %
		Plain	Welded	Plain	Welded	
Steel	73.6	391,699	277,270	0.75	0.70	29
Aluminium alloy	24.5	789,769	292,902	1.83	1.02	63

7.5.3 A FATIGUE CRACK GROWTH RATE ANALYSIS OF CCT SPECIMENS

The test results were analysed in terms of the rate of fatigue crack growth da/dN versus the applied stress intensity factor range ΔK at the crack length concerned. The resulting da/dN v ΔK were then plotted in logarithmic terms and curves of the form of the Paris law fitted as shown in Figures 7.5.3 and 7.5.4, using:

$$\frac{da}{dN} = C(\Delta K)^m \quad [7.5.1]$$

where A and m are material constants.

The results were used to compare VA and CA crack growth rates at a given stress intensity factor range, ΔK , or, ΔK_{eq} for the VA loading tests. ΔK was calculated using the relevant (BSI, 2013) solution:

$$\Delta K = \Delta S \sqrt{\pi a} \left(\text{Sec} \frac{\pi a}{2.W} \right)^{\frac{1}{2}} \quad [7.5.2]$$

ΔK_{eq} was therefore derived by substituting ΔS with ΔS_{eq} , as established in Eq. 7.2.2.

For the plain material (Figure 7.5.3), it was found that for steel da/dN was initially higher under VA than CA loading, by a factor corresponding to an acceleration factor of $\gamma = 1.6$ at low ΔK ($400\text{Nmm}^{-3/2}$), with the results eventually converging at around $\Delta K = 1000\text{Nmm}^{-3/2}$. In contrast, da/dN in the aluminium alloy was lower under VA loading initially by a factor of 1.5 at low ΔK ($120\text{Nmm}^{-3/2}$), that is $\gamma = 0.7$, indicating crack growth retardation rather than acceleration. The difference between the VA loading and CA loading curves increased with increasing ΔK to a factor of 4.9 at high ΔK ($450\text{Nmm}^{-3/2}$), corresponding to $\gamma = 0.2$.

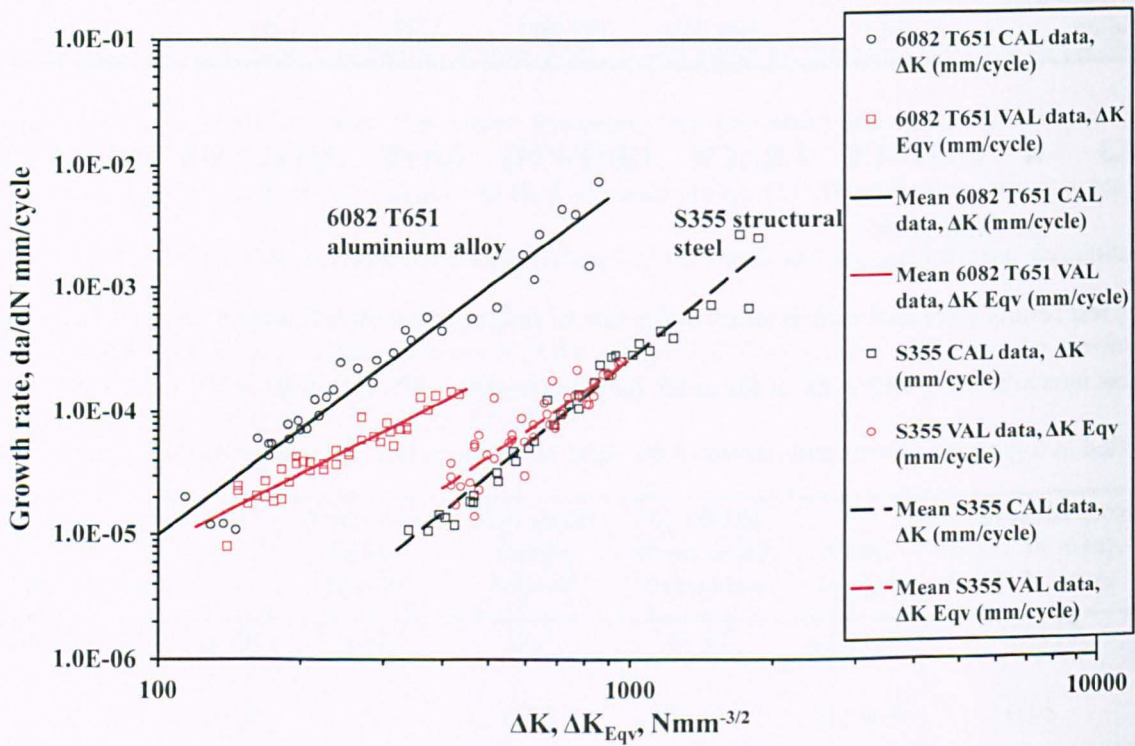


Figure 7.5.3 Comparison of fatigue crack growth rates for plain CCT specimens tested under constant and variable amplitude loading.

The above findings are consistent with the Miner's rule summations in Table 7.5.2, in that the lives of the steel specimens were reduced in comparison with the CA lives, while those of the aluminium alloy specimens were increased.

Recalling the acceleration factors obtained in Chapter 5 for specimens subjected to simple periodic underloading sequences (Table 5.3.11), the greatest acceleration occurred at low ΔK where sensitivity to mean stress effects is higher. For the steel, values of γ were in the range of 1.28 to 1.56 at $400\text{Nmm}^{-3/2}$, reducing to around 1.0 at $1000\text{Nmm}^{-3/2}$ consistent with the results in Figure 7.5.3. However, for the aluminium the result was very different. The trend in Figure 7.5.3 appears to be the same as that in Table 5.3.11, in that any accelerating effect would decrease as ΔK increased. In Table 5.3.11 only slight crack retardation appeared to be present (combined γ value of 0.89) but as shown in Figure 7.5.3, significant crack retardation was present. A possible reason for this is that the magnitudes of stresses in the load spectrum (Table 7.2.1) were too low to cause crack growth acceleration. This is discussed further in Section 7.7.1.

The corresponding results for the welded specimens are presented in Figure 7.5.4. For steel, da/dN was initially higher under VA than CA loading, by a factor corresponding to $\gamma = 1.9$ at low ΔK ($400\text{Nmm}^{-3/2}$), with the results eventually converging at around $\Delta K = 800\text{Nmm}^{-3/2}$. For the aluminium, in contrast to the behaviour of the plain specimens, da/dN under VA loading was slightly higher than that under CA loading, by the constant factor of $\gamma = 1.2$.

Based on the results for the simpler periodic underloading sequence tests (Chapter 5), the observed greater acceleration at low ΔK than at high in the steel was as expected. However, it was also expected that there would be a slight acceleration at high ΔK ; this was almost the case for the plain specimens tested under VA loading (Figure 7.5.3), but for the welded specimens, Figure 7.5.4 indicates there was none. For the aluminium, the general trend expected from the periodic underloading sequence tests was for acceleration to increase with increasing ΔK . This, however, has not been observed under VA loading.

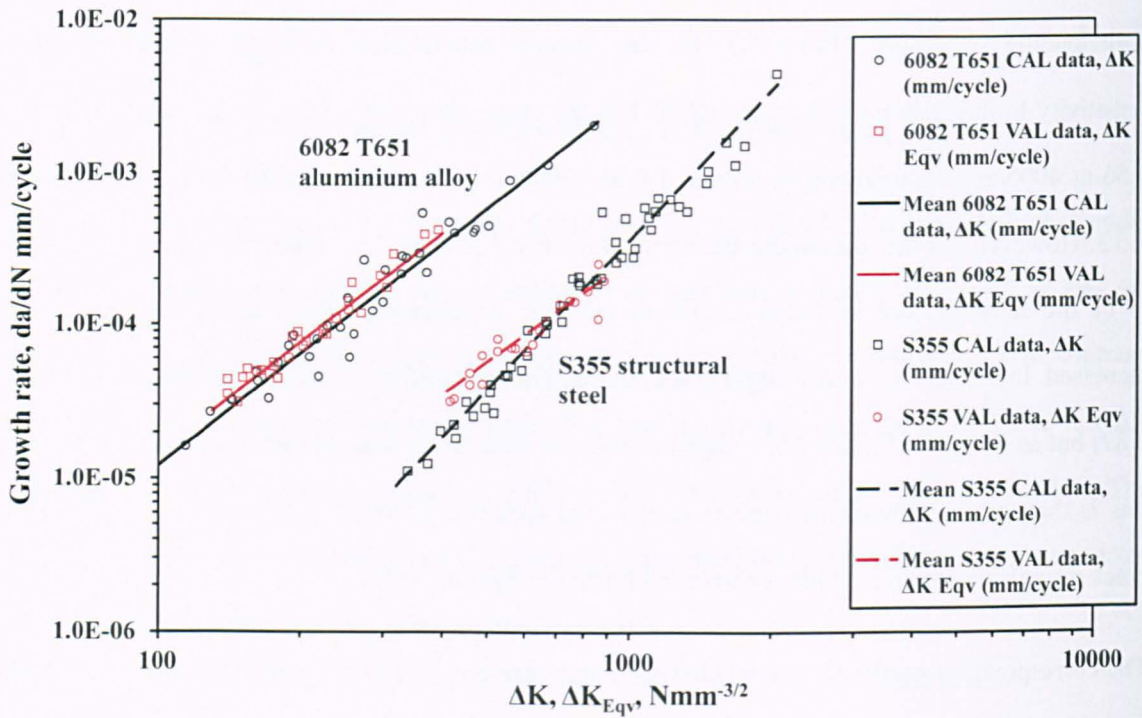


Figure 7.5.4 Comparison of fatigue crack growth rates for welded CCT specimens tested under constant and variable amplitude loading.

It should be borne-in-mind that the load sequence tests in Chapter 5 only involved two different magnitudes of underload. The VA spectra used here contain nine different stress ranges. Therefore, the load sequence effects generated may well be very different and more complex than investigated earlier, as discussed in the following section.

7.5.4 THE EFFECT OF LOAD SEQUENCES ON FATIGUE CRACK GROWTH

In Chapter 5 the effect of different magnitudes of underload and their subsequent effect on crack growth acceleration were discussed. It was generally found (Chapter 6) that the SBL1.5 spectrum gave rise to higher acceleration factors than SBL2 at high ΔK due to the increase in ΔK_{eff} . However, the FE models in Chapter 6 suggest that if there was no crack closure, the mean strain at the crack tip should increase with increasing underload magnitude resulting in a higher crack growth rate.

One block of the stress-time history for the VA-ST-210-0.25 spectrum is shown in Figure 7.5.5. The equivalent CA stress range is indicated along with x2 and x1.5 magnitudes of this value for the steel specimens. The same information for the aluminium alloy (spectrum VA-AL-90-0.25) is

presented in Figure 7.5.6. The approximate values, rounded to the closest p_i increment, with corresponding cycle exceedance are included in Table 7.5.7.

Based on the work performed in Chapter 5, combined acceleration factors for welded CCT specimens of 1.86 and 1.92 were determined for the steel (at low ΔK), and 1.92 and 1.19 for the aluminium (also at low ΔK) under SBL2 and SBL1.5 loading respectively. With 90% of the VA loading spectrum stress range being effective in propagating a crack (Section 7.4), both the SBL2 and SBL1.5 magnitudes in Figure 7.5.5 would be above the respective closure levels. Therefore, based on a Sr_{eff} argument, it would be expected that the observed acceleration factors would also apply under the VA loading spectrum for both materials.

Referring to Figure 7.5.4, the greatest difference between the CA and VA results in steel was at low ΔK , with a value of 1.90 agreeing well with that observed under periodic loading. However, acceleration decreased with increase in ΔK until the CA and VA results merged at high ΔK . In contrast, under periodic loading acceleration was still prevalent at high ΔK .

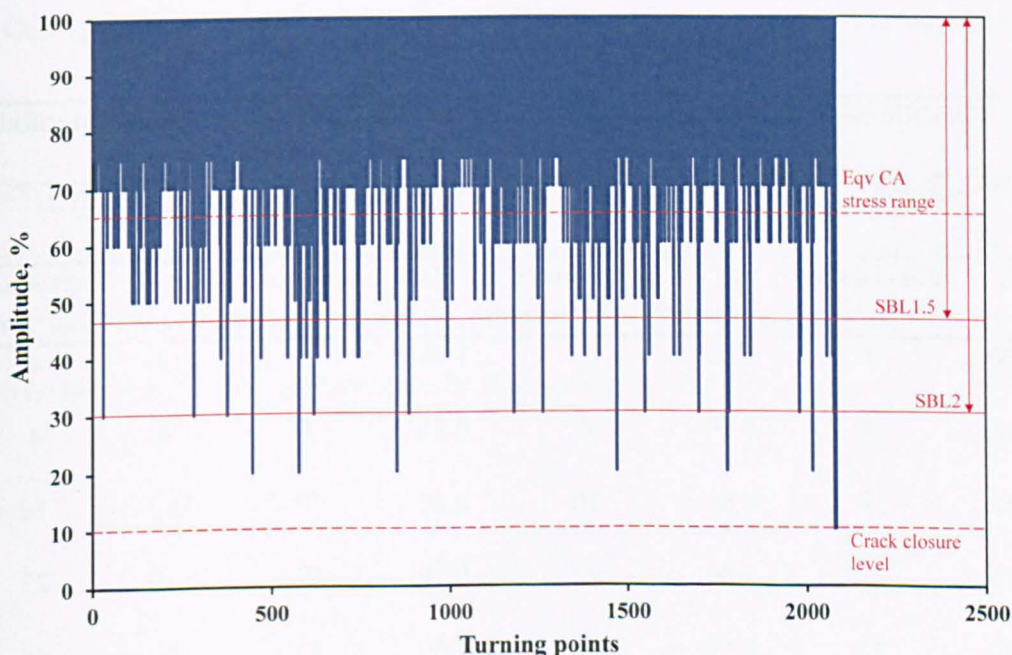


Figure 7.5.5 Variable amplitude loading spectrum cycling down from a constant maximum stress, showing the proportion of the spectrum which relates to the periodic underload sequences for steel specimens.

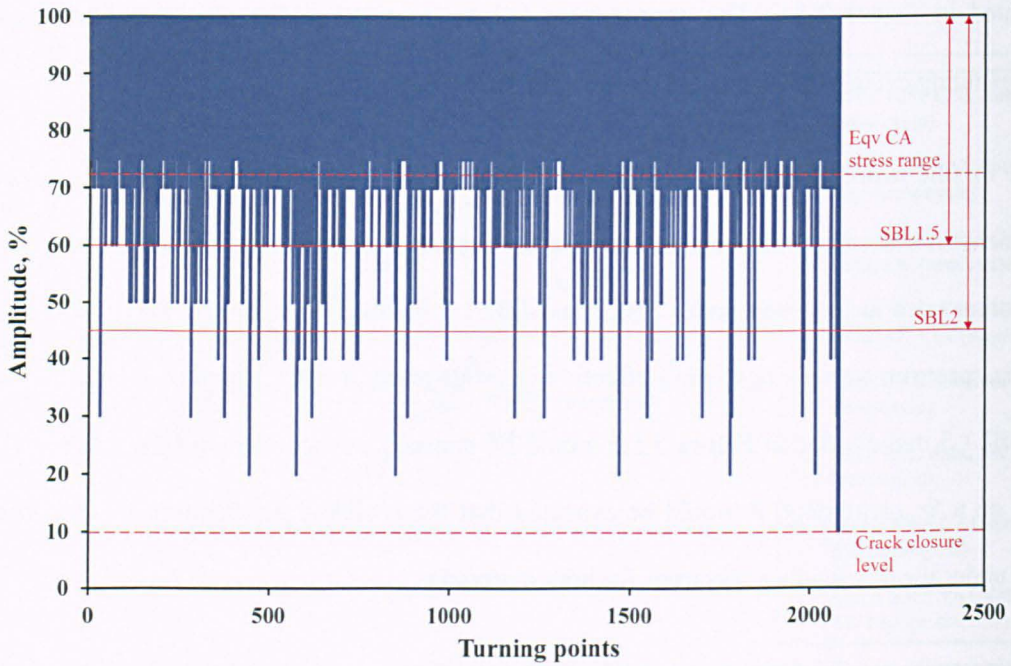


Figure 7.5.6 Variable amplitude loading spectrum cycling down from a constant maximum stress, showing the proportion of the spectrum which relates to the periodic underload sequences for aluminium alloy specimens.

Table 7.5.7 Details of the proportion of the VA loading spectrum used in relation to periodic underload sequence

Periodic underload sequence, steel				Periodic underload sequence, aluminium			
SBL1.5		SBL2		SBL1.5		SBL2	
P_i	Exceedance	P_i	Exceedance	P_i	Exceedance	P_i	Exceedance
1.00	1	1.00	1	1.00	1	1.00	1
0.90	4	0.90	4	0.90	4	0.90	4
0.80	10	0.80	10	0.80	10	0.80	10
0.70	22	0.70	22	0.70	22	0.70	22
0.60	45	0.60	45	0.60	45	0.60	45
0.50	93	0.50	93			0.50	93
		0.40	202				
		0.30	498				

For the aluminium alloy, a constant acceleration factor of 1.20 was found (Figure 7.5.4), which is below the observed value of 1.48 in the SBL2 tests but in agreement with the 1.19 found in the SBL1.5 tests.

It is considered that the variability in acceleration under VA loading, as compared to the simple load sequence tests, is due to the varying magnitude of stresses following underload cycles. The simple loading sequences in Chapter 5 contained only two stress ranges, of contrasting magnitude. In contrast, the sequence of loading in the present multi-level VA spectra was randomly generated. Therefore, there was no guarantee that a large underload would always be followed by a stress range of sufficient difference to produce crack growth acceleration.

7.5.5 VARIABLE AMPLITUDE TESTING OF FILLET WELDED SPECIMENS

Table 7.5.8 summarises the results of the CA reference tests. Due to the inherent defects found at weld toes, such as the typically 0.105mm x 0.030mm undercut found in the present steel specimens (see Chapter 4), no account was taken of the time to produce a fatigue crack, as previously required for the CCT specimens.

The endurance data are again plotted in the form of an *S-N* diagram in Figure 7.5.7. For steel, regression analysis indicated the slope *m* of the mean *S-N* curve to be 2.86, compared with the value of 3 adopted for the relevant Class F design curve (BSI, 2014). However, using Eq. [7.5.3] to determine the 95% confidence limits on the estimate of *m* (Schneider and Maddox, 2003), it is found to lie between 2.55 and 3.17, making the choice of $m=3$ valid.

Table 7.5.8 Summary of results obtained from fillet welded specimens tested under constant amplitude loading

Specimen No.	Maximum stress, N/mm ²	Stress range, N/mm ²	Stress ratio	Cycles to failure
FIL-CAL-ST- 01	280	120	0.57	516,249
FIL-CAL-ST- 02	280	150	0.46	269,426
FIL-CAL-ST- 03	280	90	0.68	1,328,870
FIL-CAL-ST- 04	280	75	0.73	2,000,418
FIL-CAL-ST- 05	280	175	0.38	145,168
FIL-CAL-ST- 06	280	105	0.63	676,569
FIL-CAL-ST- 07	280	50	0.82	5,266,198
FIL-CAL-AL- 01	120	50	0.58	325,958
FIL-CAL-AL- 02	120	40	0.67	651,233
FIL-CAL-AL- 03	120	30	0.75	1,340,919
FIL-CAL-AL- 04	120	65	0.46	90,836
FIL-CAL-AL- 05	120	20	0.83	8,414,641
FIL-CAL-AL- 06	120	25	0.79	3,899,339

$$m_{test, P\%}^{\pm} = m_{test} \pm t \hat{\sigma} \sqrt{\frac{1}{\sum_{i=1}^n (\log S_i - \overline{\log S})^2}} \quad [7.5.3]$$

In this equation each test result is expressed as $(\log S_i, \log N_i)$, where n is the number of test results, $i=1, \dots, n$, $\overline{\log S}$ is the mean of the n values of $\log S_i$, t is the two-sided $P\%$ percentage point (where $P=100-\alpha$) of Student's t distribution, within $n-2$ degrees of freedom, and $\hat{\sigma}^2$ is the best estimate of the variance of the data about the regression line. The resulting mean $S-N$ curve, for which $C = 8.28E+11$, is included in Figure 7.5.7. This curve was used in the evaluation of the results under VA loading.

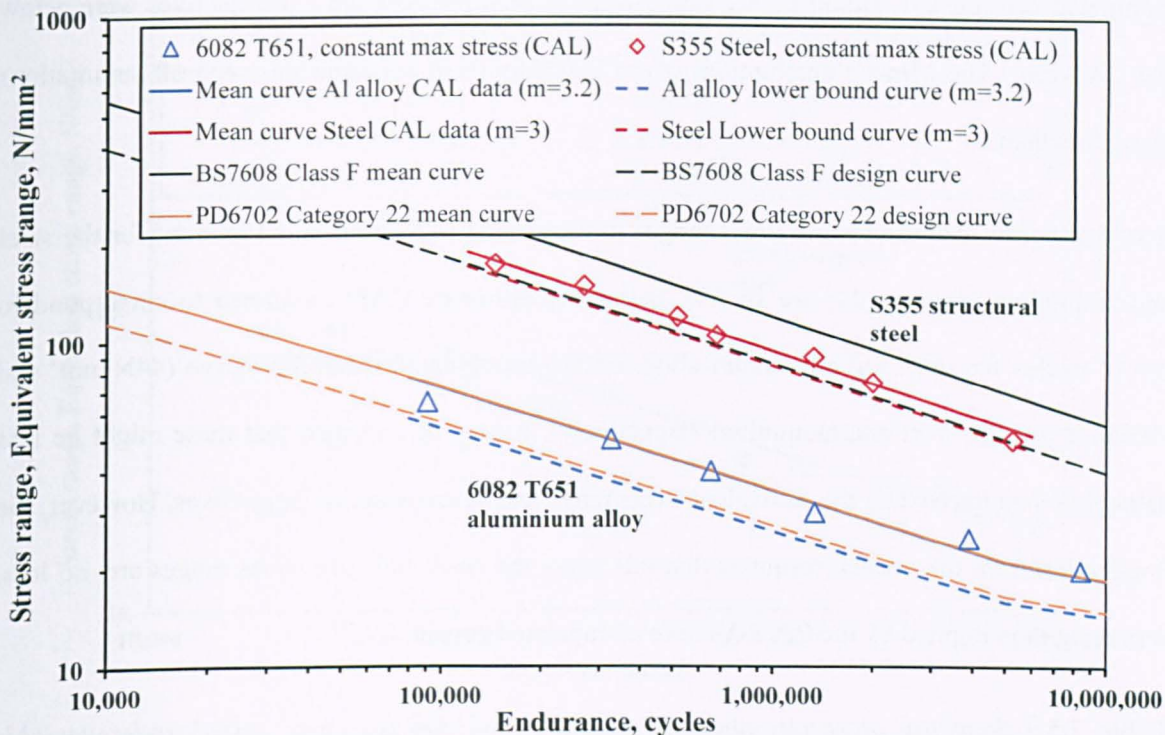


Figure 7.5.7 Constant amplitude fatigue test results obtained from fillet welded specimens tested under constant maximum tensile stress conditions.

Figure 7.5.7 shows that for both materials, the specimens behaved in a manner which was consistent with the relevant design classification.

For the aluminium alloy data, the slope m of the mean $S-N$ curve was estimated to be 3.72, compared with the value of 3.2 adopted for the PD 6702 Category 22 design curve (BSI, 2009). Again using Eq. [7.5.2], the 95% confidence limits on the estimate of m indicated that it could lie between 3.18 and 4.26, making the choice of $m=3.2$ valid. The resulting mean $S-N$ curve, for which $C = 8.77E+10$, is included in Figure 7.5.7.

The fatigue test results obtained under VA loading using the spectra presented in Tables 7.2.2 to 7.2.4 are summarised in Table 7.5.9 and presented in comparison with the CA results in Figure 7.5.8 in terms of their equivalent CA stress range. The maximum stress range was 210N/mm^2 for the steel and 90N/mm^2 for the aluminium alloy. Where possible, duplicate tests were performed in order to ensure the results were consistent. They gave good agreement, indicating that scatter on endurance was low.

Compared with the CA data in Figure 7.5.8, it can be seen that for both materials lives were below the CA mean. The Miner's summations given in Table 7.5.9, re-affirm this with all summations being less than 1.

It is noteworthy that the lowest stress ranges in the spectra (42N/mm^2 and 18N/mm^2 for the steel and aluminium respectively) are slightly below the estimated CAFL, assumed to correspond to $N=10^7$ cycles for steel and aluminium alloy, on the extrapolated mean $S-N$ curve (44N/mm^2 and 19N/mm^2 for the steel and aluminium respectively). It may be expected that these might be less damaging than implied by the equivalent stress range and hence result in longer lives. However, the implication from the present results is that this is not the case, and such stress ranges are, no less, damaging than implied by the CA $S-N$ curve extrapolated beyond CAFL.

Table 7.5.9 Summary of results obtained from fillet welded specimens tested under variable amplitude loading

Specimen No.	Minimum, P_i value	Maximum stress, N/mm^2	Equivalent stress range, N/mm^2	Cycles to failure	$\sum n/N$ at failure based on mean CA S-N curve	$\sum n/N$ at failure based on Class F/Cat. 22 mean curve
FIL-VAL-ST-01	0.25	280	73.6	1,232,362	0.59	0.28
FIL-VAL-ST-02	0.25	280	73.6	1,280,883	0.62	0.30
FIL-VAL-ST-03	0.40	280	109.1	437,080	0.69	0.33
FIL-VAL-ST-04	0.40	280	109.1	423,191	0.66	0.32
FIL-VAL-ST-05	0.20	280	61.3	2,130,304	0.59	0.28
FIL-VAL-AL-01	0.25	120	31.5	884,498	0.64	0.77
FIL-VAL-AL-02	0.25	120	31.5	898,953	0.65	0.78
FIL-VAL-AL-03	0.20	120	26.3	1,242,579	0.53	0.63
FIL-VAL-AL-04	0.20	120	26.3	1,082,632	0.46	0.55
FIL-VAL-AL-05	0.40	120	46.8	181,528	0.43	0.52
FIL-VAL-AL-06	0.40	120	46.8	214,401	0.51	0.61

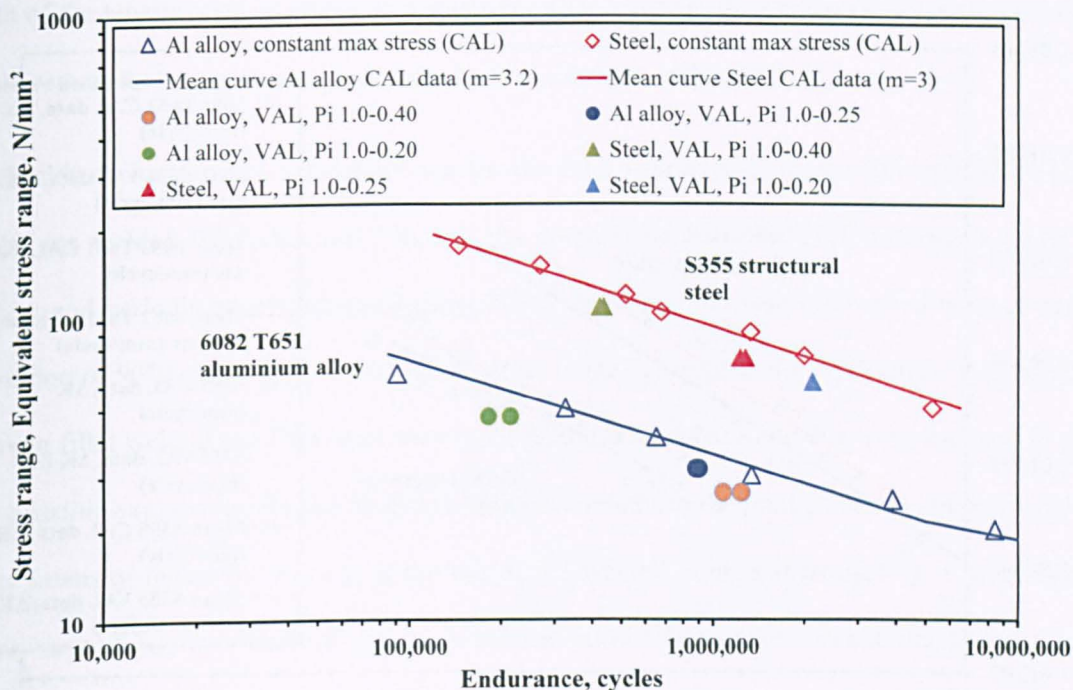


Figure 7.5.8 Variable amplitude fatigue test results obtained from fillet welded specimens tested under constant maximum tensile stress conditions.

7.5.6 FATIGUE CRACK GROWTH IN FILLET WELDED SPECIMENS

As in the case of the CCT specimens (Section 7.5.3), further analysis was performed by comparing VA and CA crack growth rates in the fillet welded specimens, Figure 7.5.9. ΔK and ΔK_{Eqv} values were again calculated using Eq. [7.5.2]. In these specimens, fatigue cracking starts at the weld toe and propagates through the plate thickness, after which it continues to grow across the plate width as a through-thickness crack. The results here mainly refer to this second stage. For the steel, da/dN was higher under VA loading than CA loading, by $\gamma = 1.8$ at low ΔK ($450\text{Nmm}^{-3/2}$), reducing to $\gamma = 1.5$ at high ΔK ($1000\text{Nmm}^{-3/2}$). For the aluminium alloy, da/dN was higher under VA loading initially by $\gamma = 1.6$ at low ΔK ($150\text{Nmm}^{-3/2}$), but increased to $\gamma = 2.2$ at high ΔK ($900\text{Nmm}^{-3/2}$).

Looking at as a whole, these acceleration factors are consistent with the calculated Miner's rule summations given in Table 7.5.9, suggesting that crack growth acceleration was the main reason for those low values for both materials.

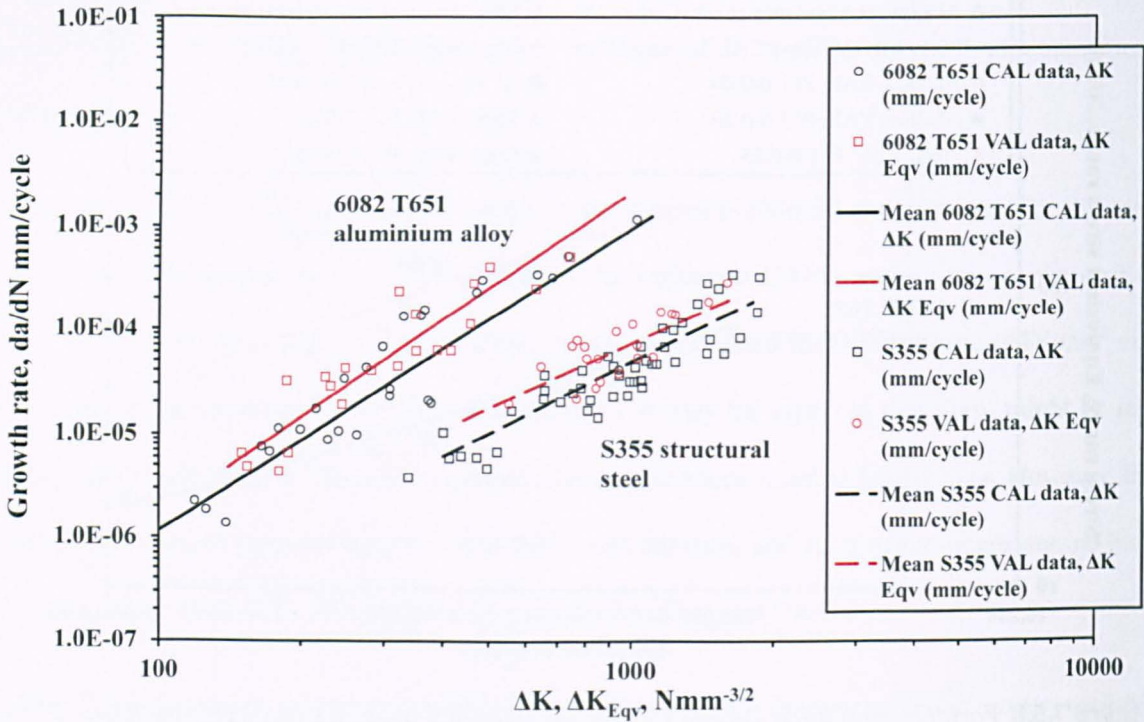


Figure 7.5.9 Comparison of fatigue crack growth rates for through-thickness cracks propagating across the plate width in longitudinal fillet welded specimens tested under constant and variable amplitude loading.

Compared with the results from the welded steel CCT specimens in Section 7.5.3, it can be seen that over the range of ΔK considered, acceleration was greatest in the fillet welded specimens, particularly at low ΔK . Unlike the welded CCT specimen results, which converged at $\sim 800 Nmm^{-3/2}$ (Figure 7.5.9), the fillet welded specimens still exhibited acceleration well above this value. In the case of the aluminium alloy specimens, the fillet welded specimens also exhibited greater acceleration than the welded CCT specimens, increasing slightly as ΔK increased.

For the steel specimens, yield magnitude tensile residual stresses were present in both the fillet welded and welded CCT specimens (Chapter 6). Therefore, the difference between their crack growth behaviour is not due to a residual stress difference. The distance at which residual stress had fallen to zero was also identical and therefore again not a reason for the observed crack growth differences. For the aluminium alloy, residual stresses were slightly higher in the fillet welded specimens which may have contributed towards the increase in acceleration factor. However, the

width of the tensile residual stress field was somewhat narrower than in the CCT specimens, which would reduce their significance at longer crack lengths and higher ΔK .

Crack closure levels were not determined for the fillet welded specimens, although based on the results for welded CCT (Section 7.4) and the comparison between CCT specimens under VA loading and periodic underloading (Section 7.5.4), the levels of closure observed were already in the region of 90% of the applied maximum stress range. Therefore, the differences in acceleration between fillet welded and CCT specimen types would not appear to be due to an increase in ΔK_{eff} . One possible explanation for the observed difference relates to the joint geometry. In particular, the stress intensity factor for a crack at the toe of the welded joint is increased by a magnification factor, termed M_k , as a result of the stress concentration effect of the welded attachment. For the present longitudinal welded attachment detail, M_k would be effective while the surface crack length of the toe crack is less than the total weld width (including the attachment itself). Beyond this, its effect would diminish with increasing crack length, reducing crack growth rate to that of a CCT specimen. To investigate this issue, a more detailed analysis which included crack growth from the weld toe through the plate thickness was performed, as described in Section 7.6.

7.6 FRACTURE MECHANICS ANALYSIS OF FATIGUE CRACK GROWTH IN FILLET WELDED SPECIMENS

7.6.1 OUTLINE

In order to examine more closely the extent of fatigue crack growth acceleration and its effect on fatigue life, fatigue crack growth data obtained from the fillet welded specimens were analysed in fracture mechanics terms. This entailed calculation of the applied stress intensity factor range ΔK , or ΔK_{Eqv} in the case of the VA data, for the semi-elliptical crack that grows from the weld toe (see Figure 7.6.1) and the through-thickness crack that later grows across the plate width. The CA data, presented in Appendix D in terms of crack size versus number of cycles, were used to determine crack growth laws relating crack growth rate da/dN and ΔK , which were then used to calculate the fatigue crack growth behaviour of the same specimens under VA loading for comparison with the measured data. The CA crack growth laws were finally used to calculate the total fatigue

endurances of the fillet welded specimens, based on crack growth from an assumed weld toe flaw through the plate thickness and then across the specimen width, in the two materials for comparison with the actual endurance data.



Figure 7.6.1 Steel specimen showing typical fatigue crack path at the end of the weld toe.

7.6.2 CRACK GROWTH MEASUREMENTS

The crack growth measurements obtained using the techniques described in Section 7.2.5 are presented in Appendix D. For their graphical presentation in the form of crack size versus number of cycles (N), N referred to the number of load cycles applied after the first recorded crack size measurement. It will be seen that the crack growth data generally exhibit smooth curves. Based on findings in the literature (Zhang and Maddox, 2007) it was envisaged that the crack growth would not produce smooth curves due to the anticipated change from initial growth, mainly through the plate thickness, within the influence of the stress concentrating effect of the weld and attachment, to growth across the plate width outside that influence. However, this transition was not evident as a discontinuity in the present data.

7.6.3 STRESS INTENSITY FACTORS

As noted previously, fatigue failure in the fillet-welded specimens starts with the growth of a crack from the weld toe through the plate thickness. The crack front for such cracks generally adopts a semi-elliptical shape (see Figure 2.5.1). ΔK for such a weld toe crack can be expressed as:

$$\Delta K = M_k Y \Delta S \sqrt{\pi a} \quad [7.6.1]$$

where M_k is a function of the stress concentration effect of the weld detail, Y is the plate width correction and a is the crack depth.

The width correction Y is a function of the crack depth to plate thickness (B) ratio a/B , the crack front aspect ratio $a/2c$, where $2c$ is the surface crack length, and the crack length to plate width ratio $2c/W$, W being the specimen width.

Based on examinations of the present fracture surfaces it was found that, in the early stages of crack growth, the crack aspect ratio was ~ 0.20 . This was slightly below other observations (0.25) in a similar type of specimen (Zhang and Maddox, 2009). The crack aspect ratio gradually increased with increasing crack size and was about 0.3 when the crack had just propagated through the plate thickness.

The solution for Y for semi-elliptical weld toe surface cracks in BS 7910 (BSI, 2013) was used in the present analysis. Once the through-thickness crack was outside the stress concentration influence of the weld, ΔK was calculated using Equation 7.5.2.

The stress intensity factor for a weld toe crack is increased by a magnification factor, M_k , due to the stress concentration effect of the joint geometry. It is defined as (Maddox, 1991):

$$M_k = k_{\text{in plate with weld}} / k_{\text{in plate without weld}} \quad [7.6.2]$$

M_k quantifies the change in stress intensity factor as a result of the surface discontinuity at the weld toe. M_k decreases sharply with increasing distance from the weld toe in the thickness direction and usually reaches unity at crack depths of typically 30% of plate thickness.

The M_k solution derived by Dahle (1993) on the basis of 3D finite element analysis of the same type of weld detail as the present welded specimen, using a model with a weld toe radius of 0.16mm, was adopted. This gave:

$$M_k = 0.845(a/B)^{-0.316} \quad \text{for } a/B \leq 0.1 \quad [7.6.3]$$

$$M_k = 0.853(a/B)^{-0.312} \quad \text{for } a/B > 0.1$$

These expressions provide M_k only at the deepest point of the crack. Crack growth in this direction also depends on the crack front aspect ratio $a/2c$, where $2c$ is the surface length of the semi-elliptical crack. In the present calculations of crack growth, the M_k value at the tips of the crack at the plate surface, M_{kc} , was assumed to be identical to the M_k value in depth, M_{ka} , at $a = 0.1\text{mm}$ since this represents a good approximation (Smith and Hurworth, 1984).

As described before, crack growth on the surface varied, depending on the crack tip locations relative to the weld. To reflect this observation, the M_{kc} values were varied, decreasing from an initial value corresponding to M_{ka} at $a = 0.1\text{mm}$ (about 3.4 for steel, 3.1 for aluminium) to $M_{kc} = 1.0$ when the crack had just grown beyond the weld (about 25mm long for steel and 30mm for aluminium) in front of the attachment. At and beyond this crack length it was assumed that the effect of the weld on surface crack growth could be neglected. The derived M_k parameters are presented in Tables D1 and D2 in Appendix D.

7.6.4 CRACK GROWTH CALCULATION

7.6.4.1 CRACK GROWTH UNDER CONSTANT AMPLITUDE LOADING FOR A FILLET WELDED SPECIMEN

Crack growth was monitored in all CA specimens. As discussed in Chapter 2, the fatigue crack growth relationship between da/dN and ΔK can be integrated in the way indicated in Eq. [2.5.2] to calculate the fatigue life of a specified crack. This approach was used to calculate the progress of the first detected fatigue crack in each fillet welded specimen. The resulting calculated crack size versus number of cycles curves were then compared with the measured crack growth data. The calculations were performed using the material specific simplified single slope fatigue crack growth relationships for welded specimens given in Tables 4.4.2 and 4.4.4, independently of the mean stress:

For steel specimens,

$$da/dN = 0, \text{ when } \Delta K < \Delta K_{th} = 63\text{N/mm}^{3/2} \quad [7.6.4]$$

$$da/dN = 2.78 \times 10^{-13} \Delta K^3, \text{ when } \Delta K \geq 63\text{N/mm}^{3/2}$$

For aluminium alloy specimens,

$$da/dN = 0, \text{ when } \Delta K < \Delta K_{th} = 21\text{N/mm}^{3/2} \quad [7.6.5]$$

$$da/dN = 6.87 \times 10^{-12} \Delta K^3, \text{ when } \Delta K \geq 21\text{N/mm}^{3/2}$$

The threshold stress intensity factor range, ΔK_{th} , for steel was the lower bound value recommended by BS 7910 (2013), that is $63\text{N/mm}^{3/2}$. This was corrected for aluminium alloy based on the difference in Young's modulus, using Eq. [7.6.6].

$$\Delta K_{th, \text{aluminium}} = \Delta K_{th, \text{steel}} \left(\frac{E_{\text{aluminium}}}{E_{\text{steel}}} \right) \quad [7.6.6]$$

E_{steel} was taken as 207kN/mm^2 and $E_{\text{aluminium}}$ was taken as 70kN/mm^2 .

The growth rate used for steel was slightly lower than that corresponding to the simplified mean growth rate given in BS 7910 for $R > 0.5$.

The resulting calculated crack growth curves for the fillet welded CA specimens are compared with the measurement crack sizes in Figures D1 and D2 in Appendix D. In the case of steel, it will be seen that both the calculated surface length and crack depth results agree well with the experimental data. For the aluminium, the calculated surface length results are reasonable but not as close as those for the steel. However, it is the calculated crack depth results which are the most important, as these are more applicable to failure in this type of joint as defined as the attainment of through thickness cracking (BSI, 2014). Referring to these, it can be seen that the results agree well with the experimental data.

7.6.4.2 CRACK GROWTH UNDER VARIABLE AMPLITUDE LOADING FOR A FILLET WELDED SPECIMEN

Similar calculations were performed for the fillet welded specimens subjected to VA loading by successively applying Eq. [2.5.2] with the crack growth relationship in Eq. [7.6.4] or [7.6.5] for each of the separate stress ranges in the spectrum. In this case it was found that crack growth under spectrum loading could not be calculated satisfactorily using the crack growth rate relationship that

had been suitable for CA loading. This significantly under-estimated crack growth, see Figures D3 and D4. It was generally found that the initial stages of crack growth ($2c = <10\text{mm}$) showed reasonable agreement, but beyond this the actual crack growth rate was much faster than calculated on the basis of CA data, suggesting that crack growth acceleration had occurred. This implies that the effect of stress interaction leading to crack growth acceleration was negligible in the early stages of crack growth but increasingly effective as the crack grew, but then its effect was not evident in the calculated behaviour because it took no account of possible load interaction effects.

Noting that da/dN is directly proportional to the crack growth constant C , the ratio of the C value for CA to the average C value for the VA sequence is equivalent to the Miner's rule summation. Following a linear regression analysis of the crack growth rates for the CA and VA tests and using a fixed slope of $m=3$, this was $5.11 \times 10^{-14} / 8.34 \times 10^{-14} = 0.61$ for steel and $1.05 \times 10^{-12} / 1.82 \times 10^{-12} = 0.58$ for aluminium alloy, values that agree well with the Miner's rule summations given in Table 7.5.9.

7.6.5 CALCULATION OF FATIGUE ENDURANCE

The fracture mechanics model (including K solution and M_k factor) used in Section 7.6.3 was also used to calculate the total fatigue endurance of the fillet welded specimens. The crack growth laws used were again the material specific curves for welded specimens used in Eq. [7.6.4] and [7.6.5].

In Section 4.5, the typical surface flaw found at the weld toe of the present fillet-welded steel specimens was 0.030mm (30 μm) deep. It is generally considered that the planar flaw depth needs to be $\geq 0.15\text{mm}$ (BSI, 2013) for a valid linear elastic fracture mechanics assessment of welded joints. Therefore, assuming a flaw depth of 0.15mm (Gurney and Johnston, 1979), as also assumed by Zhang and Maddox (2009), a crack length $2c = 0.75\text{mm}$ ($a/2c = 0.20$), and that fatigue endurance was controlled by fatigue crack propagation only, the predicted fatigue endurance $S-N$ curves are shown in Figure 7.6.2.

It will be seen that they agreed very well with the CA experimental data. This supported the fracture mechanics model and also implied that a crack propagation process, not crack initiation, predominantly controlled the fatigue endurance of this type of specimen.

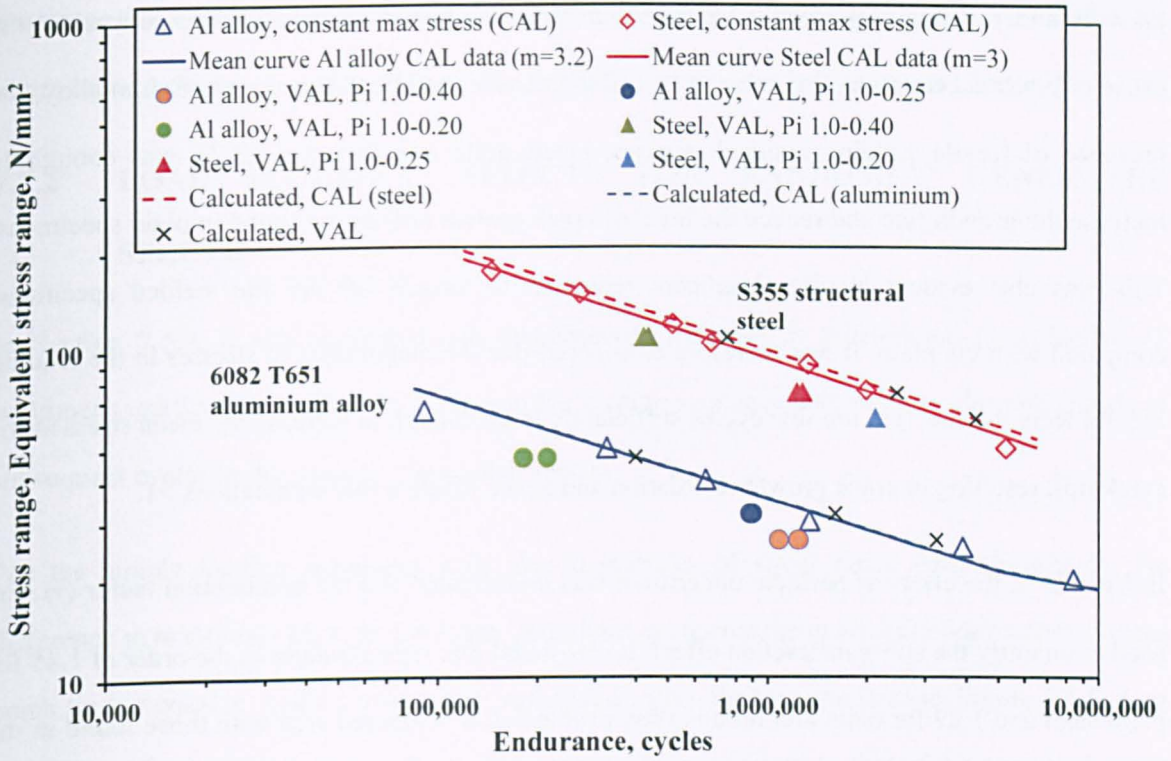


Figure 7.6.2 Variable amplitude fatigue test results obtained from fillet welded specimens tested under constant maximum tensile stress conditions, compared with the calculated response using fracture mechanics.

Figure 7.6.2 also presents the results of the calculated fatigue lives for the VA tests. It can be seen that without making any allowance for stress interaction, the calculated lives are coincident with those expected under CA loading, that is, they over-estimated the actual lives in this case. Therefore, as was found using Miner’s rule, under this form of spectrum loading unsafe life estimates would be derived by use of this approach.

7.7 DISCUSSION

7.7.1 THE EFFECT OF VARIABLE AMPLITUDE LOADING ON CRACK GROWTH RATE FOR CCT SPECIMENS

The Miner’s rule summation values of less than 1 for steel in both the plain and welded conditions (Tables 7.5.2 and 7.5.5) are indicative of stress interactions generating accelerated fatigue growth and hence lives less than those expected on the basis of the CA data. The presence of welding residual stresses in the steel specimens decreased the mean endurance, but had only a marginal effect on further reducing the Miner’s rule summation value. Therefore, as in the case of the simple

periodic underloading sequences (Chapter 5), the presence of tensile residual stresses was not the cause of crack acceleration, but rather it served to enhance the effect. For the aluminium alloy, the presence of tensile welding residual stresses, albeit quite low (Section 6.3.2), was enough to increase the growth rate and reduce the level of crack growth retardation found in plain specimens. This was also evident by the significant reduction in fatigue life for the welded specimens compared with the plain. It was therefore considered that the magnitudes of stresses in the loading spectra were too low (i.e. too few cycles sufficiently large enough to increase the mean stress at the crack tip), resulting in crack growth retardation and hence Miner's rule summations >1 .

In Chapter 5, the effect of periodic underloads was investigated and the acceleration factor (γ) was used to quantify the stress interaction effect. It was found that typical values in the order of 1.45 for plain steel and 1.29 for plain aluminium alloy (Table 5.3.4) compared well with those found in the literature for tests performed with the stress cycling down from a constant maximum stress (Fleck, 1985, Zitounis and Irving, 2007). The introduction of welding residual stresses increased them further (Table 5.3.8), to 1.86 for steel and 1.85 for the aluminium.

In this Chapter, under VA spectrum loading γ at low ΔK was generally found to either remain similar to that found in Chapter 5 for simple periodic underloading or decrease (as in the case of plain aluminium). However, at high ΔK , γ was always lower than for simple periodic underloading for both materials and in both conditions (plain or welded).

The results of crack closure measurements for both plain steel and aluminium specimens suggest that the proportion of applied stress range for which the crack is open corresponds to $U = 0.90$, compared with up to $U = 0.76$ for steel and $U = 0.80$ for aluminium alloy under simple periodic loading (Chapter 6). For welded specimens under simple periodic loading the effective stress range rose to $U = 1.0$, suggesting that the same would also hold true for the welded specimens considered in this Chapter. Therefore, it is unlikely that the differences in observed γ levels were related to crack closure.

The differences in γ were attributed to the varying magnitude of stresses following underload cycles. In particular, under the randomly generated spectra used in this Chapter, there was no

guarantee that a large underload would always be followed by a stress range of sufficient difference to produce crack growth acceleration, unlike that in the simple loading spectra in Chapter 5.

7.7.2 LOAD SEQUENCE EFFECTS FOR RANDOMLY GENERATED SPECTRA

In Section 7.5.4, it was suggested that the observed decrease in acceleration in welded CCT specimens, particularly at high ΔK , is due to the loading sequence and, in particular, magnitude of subsequent cycles in the randomly generated spectra.

For the simple loading sequences with two magnitudes of stress range (see Chapter 5), the difference in magnitude between the major and minor cycles results in a tensile region ahead of the crack tip (reversed or cyclic plastic zone), embedded within the monotonic zone, Figure 2.4.5. As a result, regardless of crack length, the reversed plastic zone is around $1/5$ that of the monotonic zone under SBL2 and $1/9$ under SBL1.5; hence the area of the crack fracture surface that is constantly under tension is reasonably large (see Chapter 6).

Whilst magnitudes similar to SBL2 or SBL1.5 may well occur in the random spectra considered in this Chapter, their occurrence will be more infrequent than that in the simple loading spectra. In addition, many of the subsequent loading cycles will be smaller or larger than SBL1.5 and SBL2, which may reduce the zone of tension within the monotonic plastic zone, thus reducing the tensile effect and crack growth rate. It is this effect on plastic zone sizes at the crack tip under the applied VA loading spectra that is thought to explain why the levels of acceleration for CCT specimens differ between the simple loading spectra and the more complex randomly generated spectra.

7.7.3 THE EFFECT OF VARIABLE AMPLITUDE LOADING ON THE FATIGUE PERFORMANCE OF THE FILLET WELDED SPECIMENS

The fatigue test results obtained under CA loading showed that the lower bound *S-N* curves for the test data met the desired classifications for this type of welded detail, Class F according to BS 7608 for steel and Category 22 according to PD 6702 (BSI, 2009) for aluminium alloy.

Considering the VA test results in terms of the equivalent CA stress range (Figure 7.5.8), their lives were less than those obtained under CA loading for each of the different minimum p_i levels considered. This suggests that crack growth acceleration occurred under VA loading. The corresponding Miner's rule summation values were all less than 1, being in the range 0.59 to 0.69 for steel and 0.43 to 0.65 for the aluminium alloy, in both cases depending (but not consistently) on the minimum p_i level in the spectrum. On the basis of the equivalent CA stress range, the $\sum n/N$ values imply that all stress ranges, including those below the CAFL (in the case of $p_i=0.20$), are more damaging than the CA $S-N$ curve implies.

In contrast to the behaviour of the fillet-welded aluminium alloy, there was no evidence of crack growth acceleration under the same spectra in the plain CCT specimens (see Figure 7.5.3). However, as seen in Figure 7.5.4, the presence of tensile residual stresses in welded CCT specimens served to generate accelerated growth. In this case, S_{max} and the stress ranges were increased compared with the spectra used to test the plain specimens, by 33 and 29% respectively. This suggests that a possible explanation for the lack of crack growth acceleration and Miner's rule summations > 1 in the plain CCT specimens is that the stresses in the loading spectra were too low.

These results could partly explain why higher γ values were obtained from the tests on the fillet-welded specimens than those from the tests on CCT specimens. However, the presence of the longitudinal attachment, and hence the stress magnification factor (M_k) at the weld toe, might also be an influencing factor during the initial stages of crack growth. At the surface of the specimen, M_k was estimated to be ~three times greater at the weld toe region than beyond this zone of influence (see Section 7.6.3). As the notch length of the welded CCT specimens was equal to the width of the weld bead on the plate surface, there was no effect of M_k . Thus, for short crack lengths (low ΔK) M_k has a big effect on crack growth rate in the fillet welded specimens.

The effect of crack closure and hence differences in ΔK_{eff} were dismissed as possible explanations for the observed increase in γ , since the cracks were open for 90% of their applied stress range in the welded CCT specimens. With regard to residual stress distributions, both the steel and aluminium CCT specimens showed a slight increase in the length of zones of residual tension over

that found for the fillet welded specimens (Section 6.3). Whilst for aluminium alloy specimens the peak tensile residual stress was slightly higher for the fillet welded specimen, it is considered that the effect of M_k is more significant in relation to the increase in γ .

Further to the observed rates of acceleration, Zhang and Maddox (2009) presented results of an investigation under VA loading with a constant maximum stress using the same weld detail as considered here. The ratio of the maximum crack growth rate under what they termed Sequence A, to the mean crack growth rate under CA was 2.6, greater than that measured in Chapter 5 for CCT specimens. Using the same methodology of the ratio of crack growth rates in this Chapter, values of $1.10 \times 10^{-13} / 5.11 \times 10^{-14} = 2.2$ for steel and $2.84 \times 10^{-12} / 1.05 \times 10^{-12} = 2.7$ for aluminium alloy are derived. Focusing on the steel, this is reasonably similar to that observed by Zhang and Maddox, for what is essentially a similar material grade, the same spectrum and the same applied constant maximum stress. It is considered that the slightly reduced acceleration may be due to differences in weld heat input, resulting in a difference in residual stress distribution, or simply scatter in fatigue performance particularly as both data sets considered are quite small. However, the same trend is seen in both cases, that cycling down from a constant maximum tensile stress results in accelerated crack growth and lives less than those calculated by Miners rule.

7.7.4 CALCULATED RESPONSE UNDER SPECTRUM LOADING

Unlike the calculations of crack growth response under CA loading, those for VA spectrum loading were found to significantly underestimate the actual measured performance. This indicated that due to the presence of load sequence effects, accelerated crack growth occurred under the VA loading.

The ratio of average C values for the mean $S-N$ curves fitted to the CA and VA test results agreed well with Miner's summations presented based on the mean CA $S-N$ curve performance. Similar measurements by Zhang and Maddox (2009) also presented good agreement with summations from their endurance data, therefore supporting the presence of crack growth acceleration under this form of spectrum loading.

Published literature suggests that the effect of stress interaction is related to crack initiation (James and Patterson, 1997; Niemi, 1997). The disparity in predictions at crack lengths $>10\text{mm}$ and the

agreement between resulting damage summations (discussed above), implies that the effect of stress interaction was mainly related to earlier crack growth.

Similar to the findings on crack growth, the calculated CA fatigue lives based on fracture mechanics agreed well with the experimental values, but lives under VA loading were over-estimated and thus unsafe. This was because, as in the case of the application of Miner's linear cumulative damage rule, the fracture mechanics approach makes no allowance for load sequence effects, merely summing the CA crack growth for each applied stress cycle in the spectrum until through-thickness cracking is achieved. In other words, the analysis process is exactly equivalent to the application of Miner's rule.

7.7.5 VALIDITY OF MINERS RULE

The results of VA tests on fillet welded specimens presented in Table 7.5.9 showed that when expressed in terms of the equivalent constant amplitude stress range, calculated using Miner's rule, the test lives generated were not in agreement with the CA data. This disagreement indicates that Miner's rule was inaccurate for the applied loading spectrum.

As discussed in Section 7.7.3, the derived Miner's summation was less than 1 for each of the different minimum p_i levels considered, resulting in lives less than those under CA loading and therefore suggesting accelerated crack growth.

One factor that can limit the accuracy of Miner's rule is the method of accounting for very low stresses in the spectrum, specifically those below the constant amplitude fatigue limit (CAFL). The CAFL was not established for the present specimens but is likely to be close the stress range corresponding to an endurance of 10^7 cycles for the steel and aluminium alloy, which from the extrapolated mean $S-N$ curves in Figure 7.5.7, is 19N/mm^2 for the aluminium and 44N/mm^2 for the steel. As shown in Tables 7.2.2 and 7.2.4, the applied stress spectra did not contain stress ranges below these levels, but at 18N/mm^2 and 42N/mm^2 the values for aluminium and steel respectively in Table 7.2.3 (*VA-AL-90-0.20*; *VA-ST-210-0.20*) were marginally lower. Under VA loading lower stresses can be damaging because the effective fatigue limit decreases as a fatigue crack develops under higher stresses in the spectrum. The most commonly used way to account for low stress

ranges, such as in BS 7608, is to assume that their damage contribution is represented by the $S-N$ curve extrapolated beyond the fatigue limit at a slope of $m = 5$ instead of 3. Whilst the difference in stress range is negligible, the fatigue damage contribution for stresses below 44N/mm^2 and 19N/mm^2 for that spectrum is 52%. Therefore, the resulting equivalent CA stress range decreases slightly to 57.6N/mm^2 for the steel and 24.7N/mm^2 for the aluminium alloy, resulting in a further increase in discrepancy with Miners rule, with a damage summation of 0.30 reducing to 0.25 for the steel, and an average summation of 0.5 for the aluminium alloy reducing to 0.41.

In Section 2.9.3, it was discussed that a limitation with Miners rule was that it does not allow for any stress interaction related to the prior stress history. In other words, it is assumed that the damage due to a given applied stress range is the same regardless of whether the loading is CA and VA. Thus, the average value of $\sum n/N$ for each sequence would be around 1.0. However, the present results have shown that this is not the case.

A second assumption is that the fatigue strength of welded joints is dependent only on stress range, such that the effect of mean stress can be ignored (Maddox, 1991). As observed in Chapter 6 this is based on the fact that (for the steel at least) high tensile residual stresses of yield magnitude are bound to be present in real welded structures. The applied stress is considered to be superimposed onto the residual stress resulting in an effective stress of the same range but cycling down from tensile yield, regardless of the applied mean stress.

To allow for the possibility that the above may not apply to the present relatively small-scale test specimens, all the CA and VA loading cycled down from a high tensile stress, thus reproducing the situation assumed to apply in the presence of high tensile residual stress. Thus, any effect of mean stress on the relative fatigue performance obtained under CA and VA loading was ruled out.

Based on the above, the test results suggest that stress interaction was the major factor contributing to the difference in Miner's summations.

7.8 CONCLUSIONS

Based on fatigue endurance tests on CCT and fillet welded specimens made from S355 steel and 6082 T651 aluminium alloy, subjected to VA loading, the following conclusions were drawn:

- Residual stress measurements confirmed the presence of high tensile residual stresses in regions of crack initiation in the fillet welded steel specimens. For the aluminium alloy fillet welded specimens, peak residual stress values were similar to those found for welded CCT specimens in Chapter 6.
- For both the fillet welded aluminium alloy and steel, residual stresses were reduced significantly under application of one loading cycle, which represented 75% of the softened 0.2% proof stress and 40% yield stress respectively. For the CCT specimens, one loading block represented a reduction in residual stress by 84% for the steel and 39% for the aluminium alloy. In spite of this, the welded specimens all gave a shorter life than the plain, suggesting that tensile residual stresses affected the majority of the fatigue life.
- Crack closure measurements on welded CCT specimens showed that a significant proportion of the maximum stress range under VA loading ($U = 0.9$) was effective in crack propagation.
- Tests under the VA loading spectrum (cycling down from a constant tensile maximum stress) generated Miner's rule summation values of $\sum n/N < 1$ at failure. For steel values were as low as 0.59, whereas for aluminium they went down to 0.43. Thus, Miner's rule gave unsafe life estimates for the spectrum used.
- For the equivalent CA stress range, the $\sum n/N$ values generated under VA loading imply that all stress ranges, including those below the CAFL, are more damaging than the CA $S-N$ curve implies.
- The above findings agreed very well with results from crack growth measurements. Crack growth under spectrum loading could not be calculated accurately by simply summing the CA response from each applied stress range due to the presence of accelerated crack growth in both materials.

- Comparison of the results of tests on fillet welded joints and welded CCT specimens under VA loading showed that the presence of the welded attachment, and hence high M_k values in the weld toe region, had a large effect on the rate of crack growth acceleration at low ΔK .
- Crack growth acceleration for fillet welded steel specimens subjected to VA loading resulted in crack growth rates 2.2 times faster than expected on the basis of crack growth under CA loading. For aluminium alloy, the rate was 2.7 times faster.
- The present acceleration factor for steel, $\gamma = 2.2$, is slightly below that reported in the literature ($\gamma = 2.6$) for the same type of specimen and loading. Scatter in fatigue test results owing to the small data sets considered and differences in residual stress distribution between these investigations are considered to be plausible explanations for this difference. However, in both cases, cycling down from a constant maximum tensile stress resulted in accelerated crack growth and lives less than those calculated by Miners rule.
- For the form of spectrum loading used in the present study, the major factor contributing to unsafe life estimates was accelerated fatigue crack growth due to stress interaction at cyclic stress changes. Such interaction effects in the VA spectra were different for fillet welded and CCT specimens. Such that, although it is easier to study crack growth in CCT specimens, they do not necessarily reflect what will happen in a welded joint.

Chapter 8

DISCUSSION

8.1 INTRODUCTION

The main aim of this project was to address a practical design problem associated with the calculation of the fatigue life of a welded structure or component subjected to VA loading. In particular, under spectra cycling down from a constant maximum stress, the widely used simple linear damage accumulation method (Miner's rule) proves to be unsafe, in that the actual life derived by endurance testing is less than that estimated. Some form of stress interaction, which is not taken into account in Miner's rule, is considered to be responsible for causing fatigue crack growth acceleration and hence a shorter life than calculated. To this end, the main aim of the project was to identify the mechanism(s) involved through fatigue crack propagation studies of relevant loading spectra, with a view to deriving improved design guidance that will enable more accurate fatigue life estimations to be made for spectrum loading conditions that produce crack growth acceleration.

The objectives of the project, as outlined in Chapter 1, have been addressed on the basis of an extensive investigation involving two materials, S355 structural steel and 6082 aluminium alloy. Through use of simple two-level loading sequences and a more complex VA loading spectrum, the occurrence of accelerated growth has been observed and different mechanisms for its occurrence evaluated, resulting in the establishment of a primary mechanism. The cause of crack growth acceleration and its implications on fatigue design are discussed in this Chapter.

8.2 CAUSE OF CRACK GROWTH ACCELERATION

Although stress interaction under VA loading has been well recognised, much of the work in this area has focused on factors that reduce crack growth rates (crack growth retardation), as opposed to what would be considered more concerning with respect to safety in fatigue design, crack growth acceleration. That said, the limited research undertaken to-date on acceleration effects (e.g. Fleck, 1985; Zitounis, 2003; Zitounis and Irving, 2007; Zhang and Maddox, 2009), has advanced understanding of this complex subject and challenged existing recommendations on fatigue life calculation for VA loading spectra.

The phenomenon of crack closure (Elber, 1971) has been used extensively to account for load sequence effects, the argument being that cyclic load changes can change the level at which a fatigue crack closes and hence the effective magnitude of the stress cycles following it. Although most research has focused on loading conditions that produce crack growth retardation (e.g. James, 1997; Suresh, 1998), acceleration has also been considered (e.g. Zitounis and Irving, 2007). A study of the effect of simple underloading spectra on two aluminium alloys reported enhanced crack propagation rates, of 30% in one aluminium alloy but up to 1200% in another (Zitounis and Irving, 2007). The level of acceleration was dependent on the number of smaller cycles interspersed between tensile underloads, as also observed by Fleck (1985), with the exceptionally high level being attributable to metallurgical features peculiar to the particular alloy studied. Both plasticity- and microstructurally-induced crack closure due to the underload cycles were said to be responsible. Increasing the stress ratio of the underload cycle increased the level of acceleration. Fleck (1985) found the same for steel and aluminium alloy, although the underload stress ratio ($R=0.5$) in this case was such that the crack was always fully open, suggesting that crack closure did not account for the observed acceleration.

Whilst it may be considered that the greater the effective proportion of the applied underload stress range, the greater the acceleration effect will be due to the crack being open, work here has found that when the crack is fully open, it does not necessarily mean acceleration will be higher. Indeed, underload stress ratios lower than applied by Fleck ($R=0.10$ in the case of SBL2 loading) still resulted in similar levels of acceleration to those found in his study. Elber postulated that just as

some loading sequences can increase the crack closure stress and hence reduce the effective magnitude of stresses following, causing crack growth retardation, the opposite is also possible (Elber, 1971). However, of the findings presented here and, as stated above, in the majority of cases from the literature, the crack was found to be near or completely open. On the occasions where closure did occur, the closure stress was similar to the minimum stress of the minor cycles. Therefore closure would be the same under CA loading or the applied sequence loading, again throwing doubt on the crack closure argument.

Another suggested explanation for crack growth acceleration in the case of welded joints is the presence of tensile welding residual stresses. Experimental results for welded 2024 aluminium alloy CCT specimens from (Liljedahl *et al.*, 2010) were in reasonable agreement with fracture mechanics crack growth calculations which included the original residual stress distribution. (Liljedahl *et al.*, 2010) hypothesized that accelerated growth would arise as a result of an increase in effective mean stress due to the introduction of tensile welding residual stresses. However, in light of the work performed here, whilst accelerated growth rates occurred for welded specimens (see Chapter 5), they were only slightly higher than those for plain material tested under the same loading spectra (Tables 5.3.11 and 5.3.12). The maximum acceleration factors were 1.45 and 1.40 for plain steel and aluminium respectively and 1.92 and 1.85 for welded steel and aluminium respectively. Therefore, welding tensile residual stresses are not responsible for generating acceleration, but rather appear to enhance it.

It has been suggested (Ranganathan, 1995 and 2002) that under periodic underload spectra, such as that considered here, the acceleration level increases with increase in the proportion of flat fracture (e.g. plane strain tensile growth), with growth rates reducing (Edwards *et al.*, 1984) at the transition to shear mode (plane stress tensile growth). This increase in acceleration during the flat growth mode has been attributed to a reduction in crack closure stress (Zitounis and Irving, 2007).

The work here has found that there are four modes of through-thickness crack growth in aluminium alloy specimens, Figure 5.3.19. In the flat growth mode, acceleration was already present and does not necessarily increase as ΔK (crack length) increases (Tables 5.3.11 and 5.3.12). Furthermore,

close to the transition from flat to shear, the growth rate was found to increase before reducing slightly during the shear growth mode prior to re-accelerating during the double shear mode as the specimen net cross-section reduces. However, this transition from plane strain to plane stress is not significant in the most important weld details where surface growth of semi-elliptical cracks is relevant, such that plane strain occurs for most of the fatigue life. In addition to observations on fracture mode, it has also been demonstrated (Figures 6.2.5 and 6.2.6) that depending on the magnitude of the underload cycle, the crack is either fully open throughout the flat growth mode or the closure stress does not alter. Furthermore, as discussed above, even when the crack is fully open it does not necessarily mean acceleration will be higher.

Instead, the primary mechanism for crack growth acceleration identified in this investigation is a change in the mean stress at the crack tip, resulting from a tensile local stress cycling about a tensile mean stress. Through use of validated FE models (Chapter 6 and Appendix B), the effect of underloads on the local stresses and strain in the vicinity of the crack tip has demonstrated, that whilst CA loading tends to stabilize at a mean stress of zero or just below, the presence of tensile underloads increases the mean stress back into high tension, meaning that the minor cycles are more damaging than under CA loading. In some cases, this local effect at a distance of 0.01mm ahead of the crack tip also occurred up to 0.05mm ahead of the crack tip. Such findings are supported by the work performed on aluminium alloys under VA loading (Arcari and Dowling, 2012). Here hysteresis loops generated under CA and four different VA loading spectra, showed that whilst under CA loading the mean stress relaxed to a compressive value, under VA loading only one of the sequences investigated (step change of S_{mean} , see Table 2.10.1) resulted in the loops stabilizing at a tensile value. A full explanation for this effect was not given but was considered to be due to load sequence effects.

Based on the current investigation, the introduction by welding of tensile residual stresses into the models (Chapter 6) was found to show a very distinct effect of increasing the mean stress near the crack tip following an underload, at a distance of 0.05mm for steel and 0.01mm for the aluminium, Figures B8 and B16 respectively. Beyond these distances, both models tend to revert to the same effect as observed in the plain materials, with the mean stress at a higher tensile value than at

0.01mm. This is presumably a reflection of the increase in tensile stress outside of the reversed cyclic plastic zone (see Section 6.2.3). For the steel, the fact that at 0.1mm the plain model showed no effect of an increase in mean stress from the underload, but the welded model does still show a slight increase (Figure B9), would suggest that the presence of tensile residual stresses tends to delay the relaxation effect, keeping the tip in a region of tension for a longer period and over a greater distance than under both CA loading and the plain material condition. Of course this effect would be less at longer crack lengths than considered here (10mm from the notch tip), where the residual stress would be lower. This would certainly account for the higher acceleration factors observed at low ΔK in Tables 5.3.11 and 5.3.12.

The fracture process itself was determined as strain ratchetting, seen by a progressive increase in strain at the crack tip (Appendix B), the level of which increased with increasing magnitudes of underload, Figures 6.4.3 and 6.4.7. The present findings agreed well with similar observations at approximately the same distances ahead of the crack tip, as determined by the examination of displacement fields in the region of the crack tip (Tong *et al.*, 2015).

It should be noted that the development of the models in Chapter 6 and their validation in Appendix B is not trivial. To correctly capture the behaviour of the crack tip it is important to ensure that the correct hardening laws are implemented; in the research performed here, a combined isotropic and kinematic behaviour was modelled (see Section 3.8). For elastoplastic materials, such combined hardening models are important in capturing Bauschinger-type effects (Toribio and Kharin, 2013), such as the accumulation of dislocations. In addition to this, is the detection of the ‘real’ behaviour at the crack tip, as it is affected by the stress peak due to the singularity. If elastic-plastic behaviour is assumed then the concern can be minimised. This behaviour was considered during the validation of the models (Appendix B) by applying the Irwin elastic-plastic offset from the LEFM curve. Using the von Mises equivalent stress and assuming LEFM and plane strain conditions, the modelled response agreed well with the calculated, providing validation of the accuracy and robustness of the FE representation of the conditions at the crack tip under the applied loads.

Mesh sensitivity should also be considered. In the case of the work performed here (see Section 3.8), the mesh was very refined (0.01mm) and was approximately to the order of the typical grain size of the structural materials considered (Lehto *et al.*, 2014; Bouquerel *et al.*, 2015).

A number of investigators have performed FE modelling crack tip plasticity. The effect of stress distribution ahead of the crack tip on fatigue crack growth rate using combined FE calculations and X-ray diffraction measurements was performed by Busch and Lebrun (1988). The stress profile ahead of the crack tip was estimated from 2D plane strain and plane stress FEA, assuming isotropic plastic behaviour. Whilst their work considered crack retardation, it did include the effect of residual stresses under VA loading. Other areas of focus have considered the effect of plasticity on fatigue crack propagation and plasticity induced crack closure (Singh and Khan, 2015), de-bonding of elements ahead of a crack under CA loading to determine plastic zones ahead of the crack tip and their effect on closure (Matsunaga *et al.*, 2013), and the effect on stress intensity factor due to residual stress distribution on fatigue crack propagation (Ilijedahl *et al.*, 2010), to name but a few.

A finding in the research performed is that the observed levels of acceleration for the materials considered were very similar. In addition to this, for both materials, the primary mechanism responsible for accelerated growth was the same.

The use of the CCT specimen for the study of load interaction effects during periodic load sequences has been very valuable in establishing the primary mechanism for fatigue crack growth acceleration. Other fracture mechanics specimens involving through-thickness cracks such as the CT specimen would probably be just as effective. However, a direct benefit from the use of the CCT specimen has been the possibility to apply weld beads to the plate surfaces for the introduction of tensile residual stresses. The specimen geometry has also favoured the examination of fracture surfaces under SEM for the analysis of accelerated crack growth by means of the direct measurement of striation spacing, for both plain and welded specimens, against accurate crack growth data. This in itself has been very important in establishing that during the periodic underload sequences considered here, accelerated crack growth was not confined just to the minor cycles following application of the underload, as is generally considered (McMillan and Pelloux,

1967; Fleck, 1985), but during the underload itself. However, although use of SEM was very beneficial, there is room for improvement in the reduction of the associated errors resulting from its use for identifying and measuring striations.

It is noted, however, that under VA loading such as the form of spectrum loading used in the present study, the major factor contributing to unsafe life estimates was accelerated fatigue crack growth due to stress interaction at cyclic stress changes. Such interaction effects in the VA spectra were reasonably similar for fillet welded and CCT specimens. However, whilst it is easier to study crack growth in CCT specimens, they may not necessarily reflect what will happen in a welded joint, due to the presence of the attachment and hence the stress magnification factor, M_k , at the weld toe during the early stages of fatigue crack growth. The variation in fracture mode from plane strain to plane stress in CCT specimens is also a practical problem. As discussed, crack growth in welded joints occurs in the plane strain fracture mode for most of the fatigue life, whereas, the use of fracture mechanics specimens also include this transition to plane stress growth which is not relevant for joints failing from a weld toe.

8.3 IMPLICATIONS OF THE CURRENT WORK TO FATIGUE DESIGN

The work performed under simple loading spectra cycling down from a constant maximum tensile stress (Chapters 5 and 6) found acceleration factors for welded specimens in the order of 1.9 – 2.0. Fatigue endurance testing of welded joints under similar forms of loading considered here (cycling-down from a constant maximum stress (Webber and Gurney, 1992; Gurney, 2000; Zhang and Maddox, 2009)) have resulted in fatigue lives significantly shorter than predicted by Miners rule, typically by half i.e. $\sum n/N = 0.5$. Therefore, the level of acceleration from crack propagation studies is comparable with the reduction in life found through endurance testing. These findings confirm that the fatigue endurance of welded joints is dominated by crack propagation.

The present work therefore suggests that Miner's rule is un-conservative under spectrum loading where cycling-down from a constant maximum stress is predominant. Indeed, considering the findings of work performed in Chapter 7, on fillet welded specimens of a geometry type well used within industry, a comparison of FCGRs also found acceleration factors of a similar order. Zhang

and Maddox (2009) reported acceleration factors in a structural steel of up to 2.6 for the same spectrum type and similar specimen geometry. A re-analysis of the data here and calculating acceleration in the same manner as performed in that study, found acceleration here to be up to 2.2 for the steel and 2.7 for aluminium alloy. The subsequent effect on the Miner's summation was $\sum n/N$ at failure <1 , with values of 0.59 for the steel and 0.43 for the aluminium alloy, based on an equivalent stress range comparison with the mean CA performance.

Although the results obtained from both materials considered agree that Miner's rule was unconservative, the differences in Miner's summation values are reflective of the faster crack growth rate for welded aluminium (Figure 4.4.12) as compared with welded steel (Figure 4.4.6), due to the lower Young's modulus of aluminium alloy. As the fatigue lives of welded joints are dominated by propagation, the faster rates associated with the aluminium alloy should be born-in-mind when considering fatigue design under the forms of loading spectra considered here.

The use of VA loading spectra that cycled down from constant high tensile stress levels in this investigation was primarily chosen to simulate the severe conditions that are thought to exist in welded joints containing high tensile residual stresses. It does also represent the actual service loading for some engineering structures, where periodic underloading can also arise, as reported by Fleck (1985):

- Gas storage vessels (e.g. accumulators) can be subjected to a daily cycle which consists of loading to a constant maximum pressure and discharging to various pressures depending on the demand.
- Gas turbine blades experience CA high frequency stress cycles due to vibrations; superimposed on these small cycles is a much larger run-down/start-up load cycle.
- Railway lines suffer random loading at constant maximum stress, each time a train passes.
- Aircraft wings experience gust loading at high mean stress during flight, and a large underload each time the aeroplane lands and takes off again.

Another example, that was behind an investigation on the effect of underloads on different metallic alloys (Zitounis, 2003), is helicopter loading. In this case many components experience loading at

high R ratios with excursions (underloads) below this, typically to R values of between 0.4 and 0.7, but also occasionally to zero load.

In much the same manner as accumulators discharge to various pressures depending on demand, the same can also be said of gas pipelines which are at a constant high pressure (for storage) which drops depending on demand.

Furthermore, some loading spectra that do not involve cycling down from a constant high tensile stress may also exhibit underloading behaviour. One such example is the wide band spectrum used by Gurney (2000), as shown in Figure 2.9.3.

On the basis of the implications of this investigation to fatigue design, and the identification of real engineering components or structures which experience these forms of underloading spectra, consideration needs to be given to fatigue design guidance.

8.4 DESIGN GUIDANCE

Current guidance on fatigue design under VA loading (BS 7608, 2014; BS EN 1999-1-3, 2007; Hobaccher, 2008) suggests that under certain loading conditions, Miner's rule should be applied assuming summation values of $\sum n/N < 1$. BS 7608 draws attention to the fact that under some stress spectra, e.g. fully-tensile stress cycling about a high mean stress or when there is little variation in the maximum applied tensile stress, fatigue testing has shown that failure can occur when $\sum n/N < 1$ and recommends that if there is any uncertainty about the service stress spectrum then $\sum n/N$ should be limited to 0.5.

A reduction in the value of $\sum n/N$ is also recommended by the IIW (Hobaccher, 2008). Here it is stated that the value should be ≤ 0.5 . The LBF Fraunhofer Institute (Sonsino *et al.*, 2009) also suggests that under constant mean stress conditions it should be assumed that $\sum n/N \leq 0.5$, whilst for varying mean stress such as wide band loading (Figure 2.9.3) e.g. underloading behaviour, the value should be reduced further to $\sum n/N \leq 0.2$.

Under constant maximum stress spectra, Maddox (2005) reported un-conservative fatigue life estimates based on Miner's rule during an investigation of girth welds. In this study, the CA *S-N*

curve was first established under the same constant maximum tensile stress used in the VA tests. The minimum $\sum n/N$ value obtained at failure was about 0.6 for steel and 0.5 for aluminium. The investigation by Zhang and Maddox (2009), also using constant maximum stress spectra, led to the conclusion that Miner's rule should be applied assuming $\sum n/N = <0.4$. This lower recommendation than that currently given in BS 7608 is primarily due to results on specimens incorporating longitudinal attachments to the plate edges (Class G detail). Based on their findings for longitudinal attachments to the plate surfaces (Class F detail), only one result from their test programme gave $\sum n/N < 0.4$, with the majority of data indicating that $\sum n/N \leq 0.5$ would be representative.

For the work performed here, the resulting Miner's rule summations would suggest that the current guidance for steel specimens given in BS 7608, a damage sum ≤ 0.5 , would be suitable, with a minimum damage sum of 0.59 being observed from tests incorporating longitudinal attachments (Chapter 7). This would therefore give support to the current recommendations in BS 7608. Considering the work by Zhang and Maddox, as the material grade and applied spectrum was similar to that used, and as both investigations are based on fairly small populations of results, it may be prudent at this stage to give recommendations for a damage sum of ≤ 0.5 for Class F details, but consider a lower value for Class G details such as ≤ 0.4 .

For aluminium alloy, BS EN 1999-1-3 suggests that fatigue assessments under VA loading should be based on partial safety factors or by defining a limit value (termed D_{Lim} , where $D = \sum n/N$). In such a case attention should be drawn to guidance in the National Annex, in this case, PD 6702-1:2009. Here D_{Lim} has retained a value of 1, but in critical cases where there are high numbers of low stress cycles, the uncertainty in D_{Lim} is covered by ignoring the normal cut-off limit at 5×10^6 cycles (16.5 N/mm^2 for Cat. 22) in the S-N curve and continuing it beyond 10^8 cycles.

In addition to the findings by Maddox (2005) for girth welded aluminium specimens, Webber and Gurney (1992) investigated the effect on 10mm thick 7019 aluminium alloy under VA loading cycling down from a constant maximum stress, reporting Miner's summation values of $\sum n/N = 0.47$. Findings of low Miner's rule summations ($\sum n/N < 1$) are not only confined to such VA loading spectra. Fatigue testing of 5454 and 5083 aluminium alloy, 5mm thickness specimens

containing butt welded joints, subjected to VA loading spectra with high mean stress fluctuations (Sonsino *et al.*, 2013), also generated low Miner's rule damage summations (0.76 and 0.41 respectively).

Referring to the present results in Tables 7.2.2 to 7.2.4, based on the continuation of the slope beyond the cut-off limit, the lowest stress in each case was 36%, 9% and 118% respectively above the Category 22 CAFL of 16.5N/mm^2 . Thus, on the basis of the above design recommendations, the lives obtained under the present spectra should have corresponded to $D_{Lim} \geq 1$, when in fact it was 0.43. In other words, D_{Lim} values below 1 are not simply due to stresses below the CAFL being more damaging than implied by the CA $S-N$ curve. Therefore, it is advised that, if the service loading spectrum is similar to that applied in this research project, or one which predominantly involves cycling down from a fixed level with a short spectrum length, consideration should be given to a reduction to the D_{Lim} value of 1, with the suggestion that $\sum n/N \leq 0.5$, based on the value of 0.43 found in this study. A higher value could be adopted if proved through specific testing or other relevant literature. The findings by Webber and Gurney (1992), Maddox (2005) and Sonsino *et al.* (2013) would also give support to this lower recommendation based on the observed Miner's rule damage summations of ≤ 0.5 . Clearly this recommendation needs further investigation as it is based on a limited dataset.

In short, for steel and aluminium alloy, due consideration of the type of VA loading spectrum and weld detail involved is required when Miner's rule is used in fatigue design. Design guidance for components under such loading conditions is urgently required from those code-writing organisations by incorporating the findings of the present investigation.

It is acknowledged that Miner's rule offers a simple approach to estimating fatigue life under VA loading. However, the work here has demonstrated that there is a need to improve these estimates in order to provide safer designs for components that experience the form of spectrum loading investigated here. Whilst it may be possible to apply a factor to Miner's rule to enable it to provide better life estimates for real structures, the lack of accurate loading spectra at the design stage would make it unrealistic to assume that one rule can be applied to all cases. It may be that several

factors are required for a range of weld details to provide more accurate assessments of fatigue damage.

To this end, although Miner's rule may continue to be suitable as the default simplistic approach, a range of correction factors to be applied to particular stress ranges (such as where the load sequence effects related to underloads considered here occur), during the cycle counting process, or as a constant to the Miner's rule summation, is a long term need.

Chapter 9

CONCLUSIONS AND RECOMMENDATIONS

9.1 RESEARCH AIM

The aim of this research project was to investigate fatigue crack growth acceleration, identifying the mechanism involved through fatigue crack propagation studies of simple loading spectra with different magnitudes of stress range, with a view to deriving improved design guidance that will enable more accurate fatigue life estimations to be made for spectrum loading conditions that produce crack growth acceleration.

9.2 CONCLUSIONS DRAWN

The principal conclusions drawn from this work are as follows:

1. Specific FCGR data for S355J2+N structural steel and 6082 T651 aluminium alloy were derived for both plain and welded CCT specimens, at stress ratios of $R=0.1$ and 0.5 . The data generated showed good agreement with the relevant curves given in BS 7910, with multiple stage crack growth observed in the aluminium alloy.
2. Tests performed under simple loading spectra with two magnitudes of stress range termed SBL2 and SBL1.5, resulted in fatigue crack growth acceleration being observed for both the steel and aluminium alloy.
3. Under SBL2 acceleration factors (γ) of up to 1.56 for steel and 1.35 for the aluminium were obtained. Reducing the magnitude of underload in SBL1.5 resulted in the same maximum γ

value for steel as under SBL2, but an increase in γ for aluminium to 1.55, comparable with the steel.

4. The addition of tensile residual stresses through the application of back-to-back weld beads on the plate surfaces further increased the extent of acceleration. Here γ increased to 1.88 for steel and 2.12 for the aluminium under SBL2. For the steel γ increased under SBL1.5 to 2.13 but for the aluminium it was reduced to 1.47.
5. As accelerated growth rates occurred for both plain and welded material under the same loading spectra, the addition of welding residual stresses is not responsible for generating acceleration but rather appears to enhance it.
6. An analysis of striation spacings on the fracture surfaces of plain and welded CCT aluminium specimens confirmed the presence of accelerated growth. Furthermore, it revealed that acceleration was not confined to the load cycles following the application of the underload but also to the underload itself.
7. Crack closure measurements in both plain and welded CCT specimens provided no support for the theory that crack growth acceleration is due to a reduction in the crack closure stress, and hence increase in effective stress range, following an underload. The crack never closed under the minor stress cycle, with or without an underload, while although the effective magnitude of the underload itself could be higher than under CA loading, this did not coincide with the period when the crack growth acceleration was most significant.
8. The application of one loading block (10 minor cycles and 1 major (underload) cycle), was found to reduce measured tensile residual stresses in welded CCT specimens by 84% in the steel and 39% for the aluminium. In spite of this, the welded specimens all gave a shorter life than the plain, suggesting that tensile residual stresses affected the majority of the fatigue life.
9. The application of a single load cycle representing 40% (steel) of the measured yield stress and 75% (aluminium) of the softened measured proof stress for fillet welded specimens, was found to significantly reduce the magnitude of tensile residual stresses by 72% for the steel

- and 197% for the aluminium. Again, in spite of this, the remaining tensile residual stresses were still thought to affect the majority of the fatigue life.
10. Other potential mechanisms to explain crack growth acceleration including sharpening, branching and softening/hardening, were examined but were not found to be plausible explanations.
 11. Finite element stress analysis of the CCT specimen was used to determine the changes in stress and strain that take place local to the crack tip as a result of the application of the periodic underload sequences. The models demonstrated that although under CA loading at the minor stress the local stress cycles from tension to compression with the mean stress approaching zero, application of the underload maintains a tensile local mean stress and/or stress range. Even as the effect of the underload diminishes, in some instances, the local cyclic stress range stabilizes at a tensile level.
 12. On the basis that tensile stresses are more damaging than compressive ones, it is concluded that the primary explanation for the observed crack growth acceleration under spectra containing periodic underloads is the production of a tensile local stress cycling about a tensile mean stress in the region of the fatigue crack tip.
 13. Whilst the above (conclusion 12) identifies the primary mechanism for crack growth acceleration, the actual fracture process at the crack tip is considered to be due to ratchetting strain, the effect of which was found to increase with increasing underload magnitude.
 14. The work performed has demonstrated that the observed levels of acceleration for the materials considered were very similar. In addition the same primary mechanism was responsible for accelerated growth in both materials.
 15. A limitation of the FE models produced was that the change in crack length due to propagation was not taken into account, as it was not compatible with the crack tip mesh employed. Therefore, in all models the crack was assumed to have only propagated by 10mm from the initial notch tip. The addition of crack propagation is not thought to affect findings for the

current crack length considered, but may result in a more pronounced effect of tensile mean stress ahead of a propagating crack for increasing crack lengths. This is discussed further in Section 9.4.

16. Tests performed on fillet welded specimens under VA loading generated endurance less than those expected on the basis of their CA performance. Depending on the spectrum applied, Miner's summations as low as 0.59 for steel and 0.43 for the aluminium were obtained, indicating that Miner's rule provided unsafe life estimates under this form of loading.
17. Although the present study was confined to the particular case of fatigue loading that cycled down from a high constant tensile level, partly to simulate the effect of welding residual stresses, such loading conditions are actually experienced by components and structures in many industry sectors, from power generation (pressure vessel, gas piping) to aerospace (aircraft, helicopters). Thus, the results of the project and the highlighted need for an improved cumulative damage calculation method are of widespread industrial significance.
18. An analysis of the rate of fatigue crack growth (da/dN) for fillet welded specimens, versus the applied stress intensity factor range (ΔK) for a given value of ΔK , resulted in acceleration factors (γ) of 1.8 for steel and 2.2 for aluminium. The ratio of the maximum growth rate under VA loading for fillet welded specimens compared with the mean crack growth rate under CA loading resulted in γ values of 2.2 for steel and 2.7 for the aluminium.

9.3 DESIGN RECOMMENDATIONS

1. The inaccuracy of Miner's rule, due to its inability to allow for stress interaction, highlights the need for modification to the existing rule, taking into consideration the levels of crack growth acceleration found here for different magnitudes of underload and the presence of welding residual stresses.
2. The Miner's rule summations for fillet welded steel specimens found here (see conclusion 16 in Section 9.2); and other relevant literature for the same Class F detail, support the BS 7608

recommendation that design based on $\sum n/N \leq 0.5$ is suitable for the VA spectrum considered here.

3. However, other findings in the literature suggest further caution is needed Class G details since the test data have indicated $\sum n/N = < 0.4$, at failure.
4. In the case of welded aluminium, the present results and published literature indicate that the current assumption implicit in BS EN 1999-1-3 (2007) that Miner's rule based on $\sum n/N \leq 1$ is safe as long as due account is taken of the damage due to stress ranges below the fatigue limit is false. In addition to attention to low stresses it is also necessary to allow for stress interaction that causes crack growth acceleration. Existing, admittedly rather limited, experimental data would suggest that design based on $\sum n/N \leq 0.5$ should be adopted until a higher value can be justified on the basis of further testing and research.

9.4 RECOMMENDATIONS FOR FUTURE WORK

1. Investigate the effect of mean stress at the crack tip by modelling crack propagation under the loading spectra used here. This will provide information on any changes to the local stress/strain pattern during crack growth. The simplest method for performing this would be by means of de-bonding elements along the crack plane following a pre-determined number of cycles, as defined by the experimental test data.

Typical contour plots showing crack propagation in a SENB specimen using the mesh type in Figure 9.4.1 is shown for reference in Figure 9.4.2. It can be seen that, as the crack length increases the stress distribution varies slightly, resulting in a slightly larger region of high tensile stress at the crack tip. The stress magnitude does not increase due to the stress level being limited by yielding.

As an alternative to the mesh in Figure 9.4.1, collapsed elements could be used to model crack propagation. However, this would require re-meshing at the crack tip for each desired crack length which would be extremely time consuming

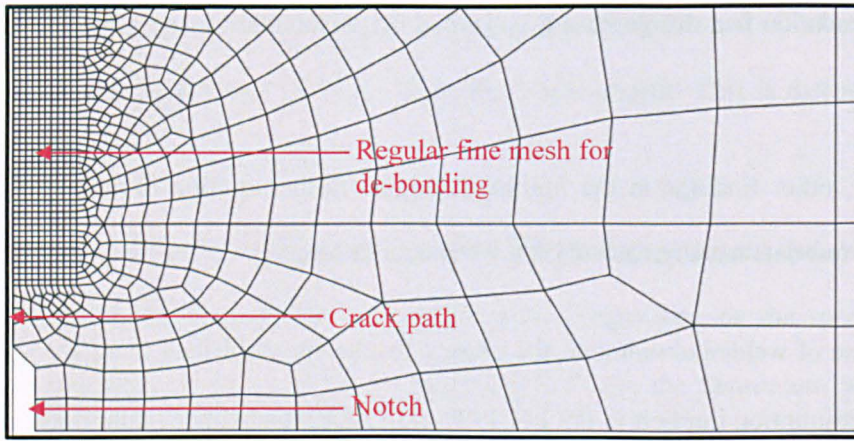


Figure 9.4.1 A finite element SENB specimen model showing regular mesh used for crack propagation (courtesy of TWI).

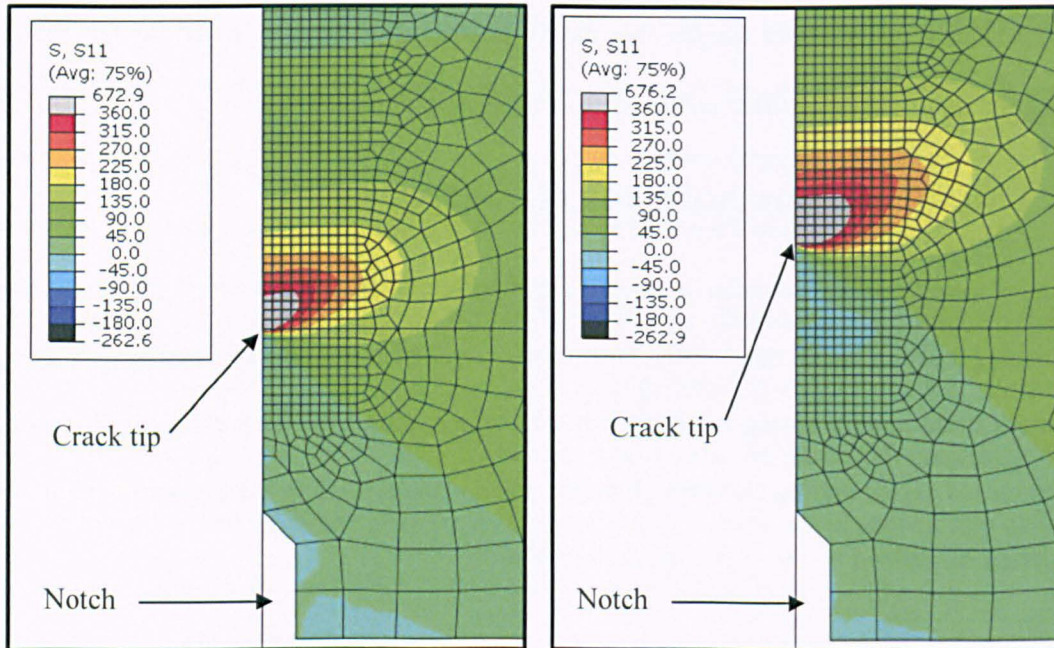


Figure 9.4.2 Contour plots of a finite element SENB specimen model showing crack propagation (courtesy of TWI).

2. The lack of accurate loading spectra at the design stage would make it unrealistic to assume that one rule, be it Miner’s rule or a completely new original rule, can be applied to different loading spectra, materials and weld geometries, providing an accurate estimate on fatigue life.

It is recommended that use is still made of the existing approach due its simplistic form and widespread acceptance. Therefore, to provide safer estimates under the form of VA loading considered, it is suggested that the data derived here and any additional data considered

necessary, be used to apply a factor to similar magnitudes of stress range as that under SBL2 and SBL1.5 loading, during the cycle counting stage. It may be that several rule variants are required for a range of weld details to provide a better assessment of fatigue damage.

3. To provide further support to point 4 in Section 9.3, additional VA data for welded aluminium alloy is required to correct the mistaken view that Miner's rule is safe when the low stresses alone are accounted for. Should a larger dataset provide similar results as presented in this research project, then it is recommended that the findings be submitted to the Standards body for consideration and implementation. In the short term, the recommendations given for the steel results (points 2 and 3 in Section 9.3) should be assumed.
4. The identification of other service loading spectra, be that actual or devised, that are likely to cause crack growth acceleration should be investigated, in order to provide evidence of the necessary changes to Miner's rule under their application.

Chapter 10

REFERENCES

- AASHTO, 2010: American Association of State Highway and Transportation Officials, "*AASHTO LRFD Bridge Design Specifications*," Fifth Edition, Washington, D.C., 2010.
- Abaqus Standard 6.14, Analysis user' manual, Dassault Systèmes, 2013.
- Abdel Mageed A M and Pandey R K, 1992: 'Studies on cyclic crack path and the mixed-mode crack closure behaviour in Al alloy', *International Journal of Fatigue*, 14, pp 21-29
- Arcari A and Dowling N E, 2012: 'Modelling mean stress relaxation in variable amplitude loading for 7075-T6511 and 7249-T76511 high strength aluminium alloys', *International Journal of Fatigue*, Volume 42, pp 238-247.
- Aguilar Espinosa A A, Fellows N A and Durodola, 2013: 'Experimental measurement of crack opening and closure loads for 6082-T6 aluminium alloy subjected to periodic single and block overloads and underloads', *International Journal of Fatigue*, 47, pp 71-82.
- ASM, 1996: 'Speciality handbook – Carbon and alloy steels', Edited by J R Davis, *ASM International*, p 111, ISBN: 978-0-87170-557-0.
- ASTM E 647-13a, 2013a: 'Standard test method for measurement of fatigue crack growth rates', *In: Annual Book of ASTM Standards*, Volume 03.01, Metals – Mechanical testing; elevated and low temperature tests; metallography, ISBN 978 1 6220 4305 7.

- ASTM E 837-13a, 2013b: 'Standard test method for determining residual stresses by the hole drilling strain gage method', In: *Annual Book of ASTM Standards*, Volume 03.01, Metals – Mechanical testing; elevated and low temperature tests; metallography, ISBN 978 1 6220 4305 7.
- Banerjee S, 1984: 'A review of crack closure', Report AFWAL-TR-84-403 1 , Air Force Materials Laboratory, Wright-Patterson Air Force Base, Dayton, OH, April, pp 3-14.
- Bao R, Zhang X and Yahama N A, 2010: 'Evaluating stress intensity factors due to weld residual stresses by the weight function and finite element methods', *Engineering Fracture Mechanics*, 77, pp 2550-2566.
- Barnby J T, 1972: '*Fatigue*', Mills & Boon Ltd, London.
- Beaney E and Procter E, 1974: 'A critical evaluation of the centre-hole technique for measurement of residual stress', *Strain*, July, pp 7-14.
- Beaney E M, 1976: 'Accurate measurement of residual stress on any steel using the centre hole method', *Strain*, July, pp 99-106.
- Berger C, Eulitz K-G, Heuler P, Kotte K-L, Naundorf H, Schuetz W, Sonsino C M, Wimmer A and Zenner H, 2002: 'Betriebsfestigkeit in Germany - an overview', *International Journal of Fatigue*, Volume 24, No. 6, pp 603-625.
- Bernard P J, Lindley T C and Richards C E, 1976: 'Mechanisms of overload retardation during fatigue crack propagation', *ASTM STP 595*, pp 78-97.
- Bettaieb M B, Lemoine X, Bouaziz O, Habraken A M and Duchene L, 2011: 'Numerical modelling of damage evolution of DP steels on the basis of X-ray tomography measurements', *Mechanics of Materials*, 43, pp 139-156.
- Blom A F and Holm D K, 1985: 'An experimental and numerical study of crack closure', *Engineering Fracture Mechanics*, Volume 22, pp 997-1011.
- Blom A F, 1989: 'Overload retardation during fatigue crack propagation in steels of different strengths', *Scan. J. Metal*, Volume 18, pp 197-202.

- Blom A F, 1995: 'Spectrum fatigue behaviour of welded joints', *International Journal of Fatigue*, Vol. 17, No. 7, pp 485-491.
- Bouquerel J, Diawara B, Dubois A, Dubar M, Vogt J-B and Najjar D, 2015: 'Investigations of the microstructural response to a cold forging process of the 6082-T6 alloy', *Materials and Design*, Vol. 68, March 2015, pp 245-258.
- BS 7270, 2006: 'Metallic materials. Constant amplitude strain controlled axial fatigue. Method of test', *British Standards Institute*, London, ISBN 0 580 49023 8.
- BS 7448-4, 1997: 'Fracture mechanics toughness tests, Part 4: Method for determination of fracture resistance curves and initiation values for stable crack extension in metallic materials ', *British Standards Institute*, London.
- BS 7608, 2014: 'Guide to fatigue design and assessment of steel products', *British Standards Institute*, London, ISBN 978 0 580 54090 5.
- BS 7910, 2013: 'Guide to methods for assessing the acceptability of flaws in metallic structures', *British Standards Institute*, London, ISBN 978 0 580 74334 4.
- BS 8118, 1991: 'Structural use of aluminium, Part 1: Code of practice for design', *British Standards Institute*, London, ISBN 0 580 19209 1.
- BS EN 485-2, 2008: 'Aluminium and aluminium alloys. Sheet, strip and plate. Mechanical properties. *British Standards Institute*, London.
- BS EN 1993-1-9, 2005: 'Eurocode 3: Design of steel structures', *British Standards Institute*, London.
- BS EN 1999-1-3, 2007: 'Eurocode 9: Design of aluminium structures', *British Standards Institute*, London.
- BS EN 10002-1, 2001: 'Tensile testing of metallic materials - Method of test at ambient temperature', *British Standards Institute*, London.

BS EN 10025-2:2004: 'Hot rolled products of structural steels – Part 2 technical delivery conditions for non-alloy structural steels', *British Standards Institute*, London.

BS EN ISO 6507-1, 1998: 'Metallic material, Vickers hardness test - Test method', *British Standards Institute*, London.

BS EN ISO 6892-1, 2009: 'Tensile testing of metallic materials - Method of test at ambient temperature', *British Standards Institute*, London.

BS ISO 12108, 2012: 'Metallic materials - Fatigue testing - Fatigue crack growth method', *British Standards Institute*, London, ISBN 978 0 580 66453 3.

BS, 2009: 'PD 6702-1: Structural use of aluminium, Part 1~: Recommendations for the design of aluminium structures to BS EN 1999', Published document, *British Standards Institute*, London, ISBN 978 0 580 63065 1.

Busch M L and Lebrun J L, 1988: 'X-ray diffraction study of stress distributions following a single tensile overload'. *Fatigue crack growth under variable amplitude loading*, Kluwer Academic Pub; 1988. p. 76–86.

Bush A J and Kromer F J, 1973: 'Simplification of hole drilling method of residual stress measurement', *ISA Trans*, 112, (3), pp 249-260.

Chand S, 1992: 'Crack closure and propagation studies to determine the effects of simple load interaction', *J. Eng. Mat. Tech.*, July, p 229.

Chand S and Garg S B L, 1984: 'Variation of effective stress range ratio under simple variable amplitude loading', *Proc. ICF6*, p 1711.

Codrington J, 2008: Non-linear individual and interaction phenomena with fatigue crack growth', *PhD thesis*, University of Adelaide, Australia, November.

Codrington J and Kotousov A, 2009: 'A crack closure model of fatigue crack growth in plates of finite thickness under small scale yielding conditions', *Mechanics and Materials*, Volume 41, pp 165-173.

- Coffin L F, 1954: 'A study of the effects of cyclic thermal stresses on a ductile metal', *Transactions of the American Society of Mechanical Engineers*, 76, pp 931-950.
- Costa J D M and Ferreira J A M, 1998: 'Effect of stress ratio and specimen thickness on fatigue crack growth of CL45 steel', *Theoretical and Applied Fracture Mechanics*, Volume 30, pp 65-73.
- Cottrell A H and Hull D, 1957: 'Extrusion and intrusion by cyclic slip in copper', *Proceedings of the Royal Society, London A242*, pp 211-213.
- Dahle T, 1993: 'Spectrum fatigue life of welded specimens in relation to the linear damage rule', - Proceedings of the Conference '*Fatigue under spectrum loading and in corrosive environments*', edited by Blom A F, EMAS, p 133.
- Davies C M, O'Dowd N P, Nikbin K M, Webster G A and Biglari F, 2005: 'Comparison of methods for obtaining crack-tip stress distributions in an elastic-plastic material', *Journal of Strain Analysis*, Vol. 40, No. 5, pp 431-450.
- Dhar S, 1989: 'Influence of multiple overload on fatigue crack retardation in high strength low alloy structural steel', *Proc. ICF7*, Houston, p 1395.
- DNV, 2012: Recommended practice DNV-RP-C203, 'Fatigue design of offshore steel structures', *Det Norske Veritas*, October.
- Drubay B, Marie S, Chapuliot S, Lacire M H, Michel B and Deschanel H, 2003: 'A16: guide for defect assessment at elevated temperature', *International Journal of Pressure Vessels and Piping*, 80 (2003), pp 499-516.
- Druce S G, Beevers C J and Walker E F, 1979: 'Fatigue crack growth retardation following load reductions in a plain C.Mn steel', *Eng. Frac. Mech.*, Vol. 11, pp 385-395.
- Dugdale D S, 1960: 'Yielding of steel sheets containing slits', *Journal of Mechanical Physical Solids*, Volume 8, pp 100-104.
- DuQuesnay D L, Pompetzki M A and Topper T H, 1993: 'Fatigue life predictions for variable amplitude strain histories', *SAE Transcripts*, Volume 5.

- Edwards R A H, Jong E M and Zuidema J, 1984: 'The fracture mode transition and its effect on crack growth retardation', *Proceedings, Fatigue 84*, University of Birmingham, UK, pp 463-478.
- Elber W, 1971: 'The significance of crack closure', *Damage Tolerance in Aircraft Structures, ASTM STP 486*, American Society for Testing and Materials, pp 230-242.
- Fleck N A, 1982: 'The use of compliance and electrical resistance techniques to characterise fatigue crack closure', Report CUED/C-MATS/TR. 89, Engineering department, Cambridge University.
- Fleck N A, Smith I F C and Smith R A, 1983: 'Closure behaviour of surface cracks', *Fatigue of Engineering Materials and Structures*, Vol. 6, No. 3, pp 225-239.
- Fleck N A, 1984: 'An investigation of fatigue crack closure', Report CUED/C-MATS/TR. 104, Engineering department, Cambridge University, May.
- Fleck N A and Smith R A, 1984: 'Fatigue life prediction of a structural steel under service loading', *International Journal of Fatigue*, Vol. 6, No. 4, pp 203-210.
- Fleck N A, 1985: 'Fatigue crack growth due to periodic underloads and overloads', *Acta metal.* Vol. 33, No. 7, pp 1339-1354.
- Forrest P G, 1962: '*Fatigue of Metals*', Pergamon press.
- Forsyth P J E, 1953: 'Exudation of material from slip bands at the surface of fatigued crystals of an aluminium-copper alloy, *Nature* 171, pp 172-173.
- Forsyth P J E, 1962: 'A two stage process of fatigue crack growth. In *Crack propagation: Proceedings of Cranfield Symposium*, pp 76-94. London: Her Majesty's Stationery Office.
- Forsyth P J E and Stubbington A, 1955: 'The influence of substructure on the slip observed in pure aluminium and some aluminium alloys when subjected to fatigue stresses', *Journal of the Institute of Metals* 84, pp 173-175.
- Frost N E, Marsh K J and Pook L P, 1974: '*Metal Fatigue*', Clarendon Press, Oxford.

- Gamboa E, Giuliani M and Lavigne O, 2014: 'X-ray microtomography observation of subsurface stress corrosion crack interactions in a pipeline low carbon steel', *Scripta Materialia*, 81, pp 1-3.
- Ganguly S, 2004: 'Non-destructive measurement of residual stresses in welded aluminium 2024 airframe alloy, Ph.D thesis, Material engineering, The Open University, Milton Keynes.
- Ganguly S, Stelmukh V, Edwards L and Fitzpatrick M E, 2008: Measurement of residual stresses in Mig-welded AL-2024 using neutron and synchrotron X-ray diffraction, *Materials Science and Engineering*, 491(1-2), pp 248-257.
- Garwood S J, 1978: 'Cumulative damage to welded steel structures', *TWI Report 3477/11/1978*, *ECSC Report 6210.KD/8/801*.
- Granjon H, 1967: Notes on Carbon Equivalent, IIW Doc IX-555-67 (*International Institute of Welding, AWS, Miami, FL*).
- Guo W, Wang C H and Rose L R F, 1999: 'The influence of cross-sectional thickness on fatigue crack growth', *Fatigue and Fracture of Engineering Materials and Structures*, Volume 22, pp 437-444.
- Gurney T R, 1976: 'Finite element analysis of some joints with welds transverse to the direction of stress', *Welding Research International*, Volume 6, No.4, pp 40-72.
- Gurney T R, 1977: 'Residual stresses in welded construction and their effects', *WI Conference Proceedings*, 15-17 November, London, Paper 23, pp 151 - 163.
- Gurney T R, 1978: 'A comparison of three stress counting methods using simulated stress spectra', *TWI Member Report 60/1978/E*, March.
- Gurney T R and Johnston G O, 1979: 'A revised analysis of the influence of toe defects on the fatigue strength of transverse non-load carrying fillet welds', *Welding Research International*, Vol 9, No. 3, Paper 23, pp 43 - 80.
- Gurney T R, 1981: 'Some fatigue tests on fillet welded joints under simple variable amplitude loading', *TWI Member Report 144/1981*, May.

- Gurney T R, 1983: 'Fatigue tests on fillet welded joints to assess the validity of Miner's cumulative damage rule, *Proceedings Royal Society*, A386, P 393.
- Gurney T R, 1985: 'Fatigue tests on fillet welded joints under variable amplitude loading', *TWI Report 7816.02/85/462.3*, November.
- Gurney T R, 1992: 'The influence of mean and residual stresses on the fatigue strength of welded joints under variable amplitude loading – some exploratory tests', *TWI Report 7065.01/92/725.03*, December.
- Gurney T R, 1993: 'Comparative fatigue tests on fillet welded joints under variable amplitude loading in air', OMAE – volume III-B, *Materials Engineering ASME*, pp 537–542.
- Gurney T R, 2000: 'Exploratory investigation of the significance of the low stresses in a fatigue loading spectrum', TWI Member Report 718/2000, December.
- Gurney T R, 2006: '*Cumulative damage of welded joints*', Woodhead Publishing, Cambridge, ISBN 13-978-1-85573-983-3.
- Haibach E, Ostermann H and Ruckert H, 1980: 'The operational strength of structural steel weld joints under a fortuitous sequence of load conditions', *Schw. Und Schn.*, volume 32, No.3, pp 93-98.
- Hinnant C, 2007: 'Fatigue testing of welded pressure vessel joints', *Proceedings of 2007 ASME Pressure Vessels and Piping Division Conference*, July, San Antonio, Texas, USA, pp 1-15
- Hobbacher A, 2008: 'Recommendations for Fatigue design of welded joints and components', *IIW Doc 1823-07/XIII-2151r4-07/XV-1254r4-07*, *The International Institute of Welding*.
- Holden T M, Suzuki H, Carr D G, Ripley M I and Clause B, 2006: 'Stress measurements in welds - Problem areas', *Material Science Engineering A2006*; 437(1), pp 33-37.
- Holtam C, 2010: 'Structural integrity assessment of C-Mn pipeline steels exposed to sour environments', *EngD thesis*, Loughborough University, April.

- Holzapfel H, Schulze V, Vöhringer O and Macherauch E, 1998: 'Residual stress relaxation in an AISI 4140 steel due to quasistatic and cyclic loading at higher temperatures, *Materials Science and Engineering*, A248 (1998) pp 9-18.
- Horner D A, Connolly B J, Zhou S, Crocker L and Turnbull A, 2011: 'Novel images of the evolution of stress corrosion cracks from corrosion pits', *Corrosion Science*, 53, pp 3466-3485.
- Huang Y, 2004: 'Alternating current potential drop and eddy current methods for non-destructive evaluation of case depth', *PhD Thesis*, Iowa State University.
- Hutchings M T, Withers P J, Holden T M and Lorentzen T, 2005: '*Introduction to the Characterization of Residual Stress by Neutron Diffraction*', Taylor and Francis (CRC Press).
- Iida K, Yamamoto S and Takanashi M, 1996: 'Residual stress relaxation by reversed loading', IIW, Doc. XIII-1628-96.
- Iida K and Takanashi M, 1997: 'Relaxation of welding stresses by cyclic zero-to-tension loading', IIW, Doc. XIII-1685-97.
- Irwin G R, 1957: 'Analysis of stresses and strains near the end of a crack traversing a plate', *Transcripts ASME Journal of Applied Mechanics*.
- Irwin G R, 1958: '*Fracture in Handbuch der Physik*', 6, Springer-Verlag, Heiddberg, Berlin, pp 551-590.
- Irwin G R, 1960: 'Plastic zones near a crack and fracture toughness', Proc, 7th *Sagamore Ord, Materials, Res, Conference*, p63.
- Jack A R and Price A T, 1972: 'Effects of thickness on fatigue crack initiation and growth in notched mild steel specimens', *Acta Metallurgica*, Volume 20, pp 857-866.
- Jacoby G H, Nowack H and van Lipzig H T M, 1976: 'Experimental results and a hypothesis for fatigue crack propagation under variable amplitude loading', *Fatigue crack growth under spectrum loads, ASTM STP 595*, American Society for Testing and Materials, pp 172-183.

James M N, 1997: 'Some unresolved issues with fatigue crack closure -measurement, mechanism and interpretation problems', in: *Advances in Fracture Research (ICF9)*, B L Karihaloo, Y W Mai, M I Ripley and R O Ritchie (Eds.), Elsevier Science, Amsterdam, Vol.5, 1997, pp.2403-2414.

James M N and Paterson A E, 1997: 'Fatigue performance of 6261-T6 aluminium alloy – constant and variable amplitude loading of parent plate and welded specimens', *International Journal of Fatigue*, Volume 19, Supp. No. 1, p S109.

Johnson H H, 1965: Calibrating the electric potential method for studying slow crack growth, *Materials Research and Standards*, Vol 5, No. 9, September, pp 442-445.

Kapoor A, 1994: 'A re-evaluation of the life to rupture of ductile metals by cyclic plastic strain', *Fatigue and Fracture of Engineering Materials and Structures*, 17, pp 201-219.

Kim E S and Kim I S, 1998: 'Effect of specimen thickness in the near threshold fatigue crack propagation of nuclear structural materials'. In: Proceedings of 'Workshop on the Integrity of Nuclear Power Plant Equipment' Taejon, Korea, pp 143-158.

King R, 1998: 'A review of fatigue crack growth rates in air and seawater' – HSE Report OTH 511, London, Health & Safety Executive books, ISBN 0-7176-2143-7.

Knott J F and Pickard A C, 1977: 'Effects of overloads on fatigue crack propagation in aluminium alloys', *Metal Science*, Vol. 11, pp 399-404.

Korsunsky A M, Song X, Belnoue J, Jun T, Hofmann F, De Matos P, Nowell D, Dini D, Aparicio-Blanco O and Walsh M J, 2009: 'Crack tip deformation fields and fatigue crack growth rates in Ti-6AL-4V', *International Journal of Fatigue* 31, pp 1771-1779.

Kudryastev Y F, 2008: 'Residual stress – Part B', Springer Handbook of *Experimental Solid Mechanics*, pp 374-376.

Kumar R, 1991: 'Effect of variable single cycle peak overload on fatigue life', *Int. J. Pres. Ves. and Piping*, Vol. 48, pp 293-303.

- Kumar J, Abulrub A-H G, Attridge A and Williams M, 2011: 'Effect of X-ray computed tomography scanning parameters on the estimated porosity of foam specimens', *2nd International Conference on Mechanical, Industrial and Manufacturing Technologies MIMT 2011*).
- Landis E N and Keane D T, 2010: 'X-ray microtomography', *Materials Characterization* (2010) pp 1305-1316.
- Lassen T, Recho N, 2006: '*Fatigue Life Analyses of Welded Structures*', ISTE Ltd.
- Lee C S, Park C G and Chang Y W, 1996: 'Precise determination of fatigue crack closure in Al alloys', *Materials Science and Engineering, A216 (1996)*, pp 131-138.
- Lee S Y, 2009: 'Effects of overloads and underloads on internal strains/stresses and crack closure during fatigue crack propagation', *PhD thesis*, University of Tennessee.
- Lehto P, Remes H, Saukkonen T, Hannien H and Romanoff J, 2014: 'Influence of grain size distribution on the Hall-Petch relationship of welded structural steel', *Material Science and Engineering: A*, Vol. 592, pp 28-39.
- Leity G P, 1988: '*Residual stresses and fatigue crack propagation*', PhD thesis, St. Johns College, Cambridge University, September.
- Lemaitre J and Chaboche J-L, 1990: '*Mechanics of solid materials*', Cambridge University Press, ISBN 0-521-32853-5.
- Lewis S J and Truman C E 2010: 'Diffraction measurements for evaluating plastic strain in A533B ferritic steel – A feasibility study', *J. Phys. D: Appl. Phys.* **43** 265501.
- Liljedahl C D M, Zanellato O, Fitzpatrick M E, Lin J and Edwards L, 2010: 'The effect of weld residual stresses and their redistribution with crack growth during fatigue under constant amplitude loading', *International Journal of Fatigue*, 32(2010), pp 735-743.
- Ling and Schjive J, 1990. In: *Fatigue and Fracture of Engineering Materials and Structures*, Vol. 13, pp 443-456.

Lu Y and Li K, 1993: 'A new model for fatigue crack growth after a single overload', *Eng. Frac. Mech.*, Vol. 46, No. 5, pp 849-856.

Maddox S J, 1970: 'Calculating the fatigue strength of a welded joint using fracture mechanics', *Metal Construction*, Vol. 2, No. 8, August, p 327.

Maddox S J, 1971: 'Fracture mechanics applied to fatigue of welded structures', *Proceedings Conference on 'Fatigue of Welded Structures'*, The Welding Institute, 1970.

Maddox S J, 1972: 'A fracture mechanics analysis of the fatigue strength of welded joints', *PhD Thesis*, University of London, July.

Maddox S J, 1974: 'A fracture mechanics approach to service load fatigue in welded structures', *Welding Research International*, Vol. 4, No. 2, pp 1-30.

Maddox S J, Gurney T R, Mummery A M and Booth G S, 1978: 'An investigation of the influence of applied stress ratio on fatigue crack propagation in structural steels', TWI Members Report, 72/1978/E, September.

Maddox S J, 1982: 'Influence of tensile residual stresses on the fatigue behaviour of welded joints in steel', *Residual Stress Effects in Fatigue*, ASTM STP 776, pp 63-96.

Maddox S J, 1985: 'Aspects of the improvement in fatigue strength of fillet welds by peening', TWI Members Report No. 261, February.

Maddox S J and Booth G S, 1986: 'Correlation of fatigue crack growth data obtained at different stress ratios' in '*Mechanics of Fatigue Crack Closure*', ASTM STP 982, pp.516-527

Maddox S J, 1991: '*Fatigue strength of welded structures*', Second Edition, Woodhead Publishing, Cambridge, pp 15-18, 27-29, 117, 175-180.

Maddox S J, 2005: 'Fatigue evaluation of steel riser girth welds', TWI Report 15216/1/05 (to be published).

- Makabe C, McEvily A J, Purnowidodo A and Yamauchi A, 2003: 'Effects of negative stress ratios on crack propagation behaviour after an overload', *International Journal of Modern Physics B*, Volume 17, No. 8/9, pp 1580-1586.
- Makabe C, Purnowidodo A, and McEvily A J, 2004: 'Effects of surface deformation and crack closure on fatigue crack propagation after overloading and underloading'. *International Journal of Fatigue*, Volume 26, pp 1341-1348.
- Makabe C, Purnowidodo A, Miyazaki T, and McEvily A J, 2005: 'Deceleration and acceleration of crack propagation after an overload under negative baseline stress ratio', *Journal of Testing and Evaluation*, Volume 33, No. 3, pp 181-187.
- Manson S S, 1954: 'Behaviour of materials under conditions of thermal stress', *National Advisory Commission on Aeronautics: Report 1170*, Cleveland, Lewis Flight Propulsion Laboratory.
- Manson S S and Halford G R, 2006: 'Fatigue and durability of structural materials', *ASM International*, March, p 181.
- Marrow T J, Mostafavi M, Hashimoto T and Thompson G E, 2014: 'A quantitative three-dimensional in situ study of a short fatigue crack in a magnesium alloy', *International Journal of Fatigue*, 66, pp 183-193.
- Martin B A, 2000: 'Measuring residual stress – yesterday and today', *TWI Bulletin*, May/June, pp 35-38.
- Mathar J, 1934: Determination of initial stresses by measuring the deformation around a drilled hole', *American Society of Mechanical Engineers*, 56, pp 249-254.
- Matsunaga H, Makizaki M and Yanase K, 2013: 'Finite element modelling of plasticity induced crack closure due to occasional mode II loading on mode I fatigue crack growth', *Engineering Fracture Mechanics*, Volume 111, pp38-49
- Matsuoka S, Tanaka K and Kawahara M, 1976: 'The retardation phenomenon of fatigue crack growth in HT80 steel', *Engineering Fracture Mechanics*, Volume 8, pp 507-523.

- McClung R C, 1991: 'Crack closure and plastic zone sizes in fatigue', *Fatigue and Fracture of Engineering Materials and Structures*, Volume 14, No. 4, pp 455-468.
- McClung R C, 2007: 'A literature survey on the stability and significance of residual stresses during fatigue', In: *Fatigue and Fracture of Engineering Materials and Structures*, Volume 30, No. 3, March, pp 173-205.
- McEvily A J, Yang Z, 1990: 'The nature of the two opening levels following an overload in fatigue crack growth', *Metallurgical Transactions*, 21A, pp 2717-2727.
- McMillan J C and Pelloux R M N, 1967: 'Fatigue crack propagation under program and random loads', *Fatigue Crack Propagation, ASTM STP 415*, American Society for Testing and Materials, p 505.
- Meguid S A, 1989: '*Engineering Fracture Mechanics*', Elsevier Science Publishers Limited.
- Miner M A, 1945: 'Cumulative damage in fatigue', *Trans ASM Journal Applied Mechanics*, Volume 12, pp A159-A164.
- Missori S and Sili S, 2000: 'Mechanical behaviour of 6082-T6 aluminium alloy welds', *Metallurgical Science & Technology*, Vol 18 (1).
- Mrówka-Nowotnik G, 2008: 'The effect of intermetallics on the fracture mechanism in AlSi1MgMn alloy', *Journal of Achievements in Materials and Manufacturing Engineering*, Vol 30, Issue 1, September, pp 35-42.
- Newman J C Jr, 1981: 'A crack closure model for predicting fatigue crack growth under aircraft spectrum loading' *Methods and Models for Predicting Fatigue Crack Growth under Random Loading, ASTM STP 748*, pp 53-84.
- Newman J C Jr, 1995: 'Fatigue life prediction methodology using a crack closure model', *Journal of Engineering Materials and Technology*, Volume 117, pp 433-439.
- Neuber H, 1961: 'Theory of stress concentration for shear-strained prismatical bodies with arbitrary nonlinear stress-strain law', *J. Appl. Mech.*, 28 (1961), pp. 544-550.

- Niemi E, 1997: 'Random loading behaviour of welded components', *Proc IIW Conf on: 'Performance of dynamically loaded welded structures'*, Welding Research Council, New York, p 339.
- Nowack H, Trautmann K H, Schulte K and Lutjering G, 1979: 'Sequence effects on fatigue crack propagation; Mechanical and microstructural contributions', *Fracture Mechanics, ASTM STP 677*, Editor Smith C W, American Society for Testing and Materials, pp 36-53.
- Paris P C, 1962: '*The growth of cracks due to variations in load*', PhD Thesis, Lehigh University.
- Park H B and Lee B W, 2000: 'Effect of specimen thickness on fatigue crack growth rate', *Nuclear Engineering and Design*, pp 197-203.
- Pedersen T N and Agersov H, 1991: 'Fatigue life prediction of offshore steel structures under stochastic loading', *Technical University of Denmark, Report R274*.
- Peterson R E, 1959: 'Notch sensitivity', In *Metal Fatigue*, Editors: Sines G and Waismann J L, New York, pp 293-306.
- Peterson R E, 1974: '*Stress Concentration Factors*', John Wiley & Sons Inc, p 150.
- Pook L P, 2007: '*Metal fatigue - what it is, why it matters*', Springer, ISBN 978-1-4020-5596-6.
- Rahgozar R, Saffari H and Tabatabaei R, 2007: 'Finite element analysis of plasticity-induced fatigue crack closure with singular element', *American Journal of Applied Sciences*, Volume 4, No. 6, pp 357-361.
- Ranganathan N, Petit J and de Fouquet J, 1984: 'On the influence of the initial ΔK level on the post overload crack propagation behaviour', *Proc. ICF6*, Delhi, p 1767.
- Ranganathan N, Adiwijayayanto F, Petit J and Baillon J P, 1995: 'Fatigue crack propagation mechanisms in an aluminium-lithium alloy', *Acta Metall Mater*, 43, pp 1029-1035.
- Ranganathan N, 2002: 'Certain aspects of variable amplitude fatigue', In: *Proceedings 8th International Conference on Fatigue*, Stockholm, pp 613-623..

- Rendler N J and Vigness I, 1966: 'Hole drilling strain gauge method of measuring residual stress', *Experimental Stress Analysis*, 23, (2), pp 577-586.
- Rice J R, 1965: 'Plastic yielding at a crack tip', *Proceedings First International Conference on Fracture*, Sendai, Japan, p 283.
- Rice J R, 1967: 'Mechanics of crack tip deformation by fatigue', In: '*Fatigue crack propagation*', *ASTM STP 415*, American Society for Testing and Materials, Philadelphia, PA, pp 247-311.
- Rossini N S, Dassisti M, Benyounis K Y and Olabi A G, 2012: 'Methods of measuring residual stresses in components', *Materials and design*, 35, pp 572-588.
- Russ S, Rosenberger A, Larsen J and Johnson W, 2001: Paper 21 In.. *Proc of the NATO RTO (AVT) Symposium on Monitoring and Management of Gas Turbine Fleets for Extended Life and Reduced Costs*, Manchester, UK, Oct 8-11.
- Russ S M and Johnson D A, 2002: 'Load-interaction effects in simple mission spectra for Ti-17: Understanding the deformation before and after an underload', *Proceedings of 8th International Fatigue Congress*, Vol 2, Stockholm, Sweden, June, pp 1037-1044.
- Sarkani S, 1990: 'A sequence dependent damage model for stochastic fatigue damage calculations, *Localised Damage: Computer Aided Assessment and Control*', *Proceedings First International Conference*, Portsmouth, June.
- Saxena A and Hudak S J Jr, 1979: 'Role of crack-tip stress relaxation in fatigue crack growth', *Fracture Mechanics*, *ASTM STP 677*, Editor. Smith C W, American Society for Testing and Materials, pp 215-232.
- Scaramangas A A, Porter Goff R F D and Leggatt R H, 1982: 'On the correction of residual stress measurements obtained using the centre hole method', '*Strain*', August.
- Schijve J, 1974: 'Fatigue damage accumulation and incompatible crack front orientation', *Engineering Fracture Mechanics*, Volume 6, pp 245-252.

- Schijve J, 1976: 'The effect of pre-strain on fatigue crack growth and crack closure', *Engineering Fracture Mechanics*, Volume 8, pp 575-581.
- Schijve J, 1986: 'Fatigue crack closure, observations and technical significance', *Report LR-485*, Department of Aerospace Engineering, Delft University of Technology, April.
- Schijve, J, 1988: 'Fatigue crack closure: observations and technical significance', *ASTM STP 982*, Editors: Newman J C Jr and Elber W, American Society for Testing and Materials, Philadelphia,
- Schijve J, Skorupa M, Skorupa A, Machniewicz T and Gruszczynski P, 2004: Fatigue crack growth in the aluminium alloy D16 under constant amplitude loading', *International journal of fatigue*, 26, pp 1-15.
- Schneider C R and Maddox S J, 2003: 'Best practice guide on statistical analysis of fatigue data', IIW-XIII-WG1-114-03, International Institute of Welding, February.
- Shahinian P, 1972: 'Influence of section thickness on fatigue crack growth in type 304 stainless steel', *Nuclear Technology*, Volume 30, pp 390-397.
- Shercliff and Fleck, 1990: 'Effect of specimen geometry on fatigue crack growth in plain strain-I. Constant amplitude response', *Fatigue and Fracture of Engineering Materials and Structures*, Vol. 13, No. 6, pp. 287-296.
- Shin C S and Fleck N A, 1987: 'Overload retardation in a structural steel', *Fatigue and Fracture of Engineering Materials and Structures*, Vol. 9, No. 5, pp 379-393.
- Signes E G, Baker R G, Harrison J D and Burdekin F M, 1967: 'Factors affecting the fatigue strength of welded high strength steels', *British Welding Journal*, Vol. 14, No. 3, p 108.
- Singh K D and Khan I A, 2015: 'Numerical models of plane strain plasticity induced crack closure effect for biomaterial interfacial cracks', *International Journal of Fatigue*, 77(2015), pp 28-40.
- Skorupa M, 1998: 'Load interaction effects during fatigue crack growth under variable amplitude loading – A literature review. Part 1: Empirical trends', *Fatigue and Fracture Engineering Materials and Structures*, 21, pp 987-1006.

- Skorupa M, Skorupa A, 2005: Experimental results and predictions on fatigue crack growth in structural steel, *International Journal of Fatigue*, 27(2005), pp 1016-1028.
- Smith I F C and Smith R A, 1982: 'Defects and crack shape development in fillet welded joints', *Fatigue of Engineering Materials and Structures*, Vol. 5, No. 2, pp 151-165.
- Smith I J and Hurworth S J, 1984: 'The effect of geometry changes upon the predicted fatigue strength of welded joints', TWI Members Report 244/1984.
- Sonsino C M, Guminor P and Hanselka A, 2009: 'Cumulative damage behaviour of magnesium welded joints under service loadings', In. Sonsino C.M, McKeighan P.C: '*Material and component performance under variable amplitude loading*', Second International Conference, Proceedings Volume II, Darmstadt, Germany, pp 1013-1020.
- Sonsino C M, Morgenstern C, Streicher M, Opermann H and Schmid A M, 2013: 'Corrosion fatigue of welded aluminium vehicle structures under constant and variable amplitude loadings', Doc. IIW-2316, *Rivista Italiana della Saldatura*, N. 3, pp 403-411.
- Stephens R I, Fatemi A, Stephens R R and Fuchs H O, 2001: 'Metal Fatigue in Engineering, 2nd edition, Wiley Interscience, New York.
- Suresh S, 1998: '*Fatigue of Materials*', Second Edition, Cambridge University Press, ISBN 13 978 0 521 57847 9.
- Tada H, Paris P C and Irwin G R, 2000: '*The Stress Analysis of Cracks Handbook*', 3rd edition, New York, The American Society of Mechanical Engineers.
- Taylor J R, 1982, 'An Introduction to Error Analysis', Oxford University Press.
- Tilly G P, 1985: 'Fatigue of land-based structures', *International Journal of Fatigue*, Volume 7, No. 2, pp 67-78.
- Tong J, Zhao L G and Lin B, 2013: 'Ratchetting strain as a driving force for fatigue crack growth', *International Journal of Fatigue*, 46, pp 49-57.

- Tong J, Lin B, Lu Y-W, Madi K, Tai Y-H, Yates J R and Doquet V, 2015: 'Near-tip strain evolution under cyclic loading: In situ experimental observation and numerical modelling', *International Journal of Fatigue*, 71, pp 45-52.
- Topper T H and DuQuesnay D L, 2001: 'The effects of overloads in service load histories on crack closure and fatigue damage', Society of Automotive Engineers Inc, *International Conference on Fatigue*, Brazil, pp 43-54.
- Toribio J and Kharin V, 2013: 'Plastic zone evolution near a crack tip and its role in environmentally assisted cracking', *Frattura ed Integrità Strutturale*, 25 (2013), pp 124-129
- Tubby P J, Razmjoo G R, Gurney T R and Priddle E K, 1996: 'Fatigue of welded joints under variable amplitude loading', *OTO 94 804*, HSE books, Sudbury.
- Trudel A, Brochu M and Lévesque M, 2013: 'Residual stress effects on the propagation of fatigue cracks in the weld of a CA6NM stainless steel', *13th Int'l Conference on Fracture*, June 16-21, Beijing, China.
- Von Mises, R, 1913: 'Mechanik der festen Körper im plastisch deformablen Zustand'. *Göttin. Nachr. Math. Phys.*, vol. 1, pp. 582-592.
- Voormald M and Seeger T, 1991: 'The consequences of short crack closure on fatigue crack growth under variable amplitude loading', *Fatigue and Fracture of Engineering Materials and Structures*, Volume 14, No, 2/3, pp 205-225.
- Voorwald H J C, Torres M A S and Pinto Júnior C C E, 1991: 'Modelling of fatigue crack growth following overloads', *International Journal of Fatigue* 13(5), pp 423-427
- Wallace W P and Frankel J P, 1949: 'Relief of residual stresses by single fatigue cycle', *Welding Journal*, 38:565s.
- Ward-close C M, Blom A F and Ritchie R O, 1989: 'Mechanisms associated with transient fatigue crack growth under V.A. loading: an experimental and numerical study', *Eng. Frac. Mech.*, Vol. 32, No. 4, pp 613-638.

- Webber D and Gurney T R, 1992: 'The effect of some programme variables on fillet weld cumulative fatigue damaged test results', *Proceedings, 5th INALCO Conference on Aluminium Weldments*, Aluminium Zentrale/Technical University of Munich.
- Westergaard H M, 1939: 'Bearing pressures and cracks', *Journal of Applied Mechanics*, 61, A49-53.
- Wevers M, 2012: 'X-ray computed tomography for non-destructive testing', *Proceedings iCT 2012, International Conference on Industrial Computed Tomography*, 19th – 21st September.
- Williams M L, 1957: 'On the stress distribution at the base of a stationary crack', *Transcripts ASME Journal of Applied Mechanics*.
- Withers P J, Bhadeshia H K D H, 2001a: 'Residual stress: Part I – Measurement techniques', *Materials Science and Technology*, Volume 17, April, pp 359-362.
- Withers P J, Turski M, Edwards L, Bouchard P J and Buttle D J, 2008: 'Recent advances in residual stress measurement', *International Journal of Pressure Vessels and Piping*, 85, pp 118-127.
- Wohler A, 1870: 'Über die festigkeitsversuche mit eisen and stahl, Zeitschrift für bauwesen.
- Wood W A, 1958: 'Formation of fatigue cracks', *Philosophical Magazine* 3, pp 692-699.
- Xiong Y, Katsuta J, Kawano K, Sakiyama T, 2006: 'Characteristics of fatigue crack propagation behaviour as identified by hysteresis loop at the crack tip', *Fatigue and Fracture of Engineering Materials and Structures* (2006), Volume 29, Issue 6, pp 454-463.
- Xiong Y, Hu X X, Katsuta J, Sakiyama T and Kawano K, 2006: 'Influence of compressive plastic zone at the crack tip upon fatigue crack propagation', *International Journal of Fatigue*, Volume 30 (2008), pp 67-73.
- Yieshieng W and Schijve J, 1995: 'Fatigue crack closure measurements on 2024-T3 sheet specimens', *Fatigue Fracture Engineering Materials Structures*, Vol. 18, No. 9, pp 917-921.

- Yigeng X, Gegson P J and Sinclair I, 2000: 'Systematic assessment and validation of compliance based crack closure measurements in fatigue', *Material Science and Engineering*, A284, pp 114-125.
- Zhang Y, Maddox S J, 2007: 'Investigation of fatigue damage to welded joints under variable amplitude loading spectra', *TWI Members Report No. 889/2007*, December.
- Zhang Y, Maddox S J, 2009: 'Investigation of fatigue damage to welded joints under variable amplitude loading spectra', *International Journal of Fatigue*, Volume 31, Issue 1, pp 138-152.
- Zhao L G, Tong J and Byrne J, 2003: 'The evolution of the stress-strain fields near a fatigue crack tip and plasticity-induced crack closure revisited', *Fatigue and Fracture of Engineering Materials and Structures*, 27, pp 19-29.
- Zhao T, Zhang J and Jiang Y, 2008: 'A study of fatigue crack growth of 7075-T651 aluminium alloy', *International Journal of Fatigue*, Volume 30, pp 1169-1180.
- Zheng X, Cui H, Engler-Pinto Jr CC, Su X and Wen W, 2014: 'Numerical modelling of fatigue crack propagation based on the theory of critical distances: effects of overloads and underloads', *Engineering Fracture Mechanics*, 128, pp 91-102.
- Zhou F G and Cai Q G, 1980: 'A fracture mechanics analysis of low cycle fatigue in a superalloy', *Fatigue of Engineering Materials and Structures*, Vol. 2, pp 419-422.
- Zhuang W Z and Halford G R, 2001: 'Investigation of residual stress relaxation under cyclic load', *International Journal of Fatigue* Volume, 23 pp S31-S37.
- Zitounis V and Irving P E, 2002: 'Crack acceleration, underloads and crack closure in fatigue life prediction', *Fatigue 2002*, Proceedings of the eighth international fatigue congress 3-7 June, Stockholm, Sweden.
- Zitounis V, 2003: 'Fatigue crack growth rates under variable amplitude load spectra containing tensile underloads', *PhD thesis*, Cranfield University.

Zitounis V, Irving P.E, 2007: 'Fatigue crack acceleration effects during tensile underloads in 7010 and 8090 aluminium alloys', *International Journal of Fatigue*, Volume, 29 (2007), pp 108-118.

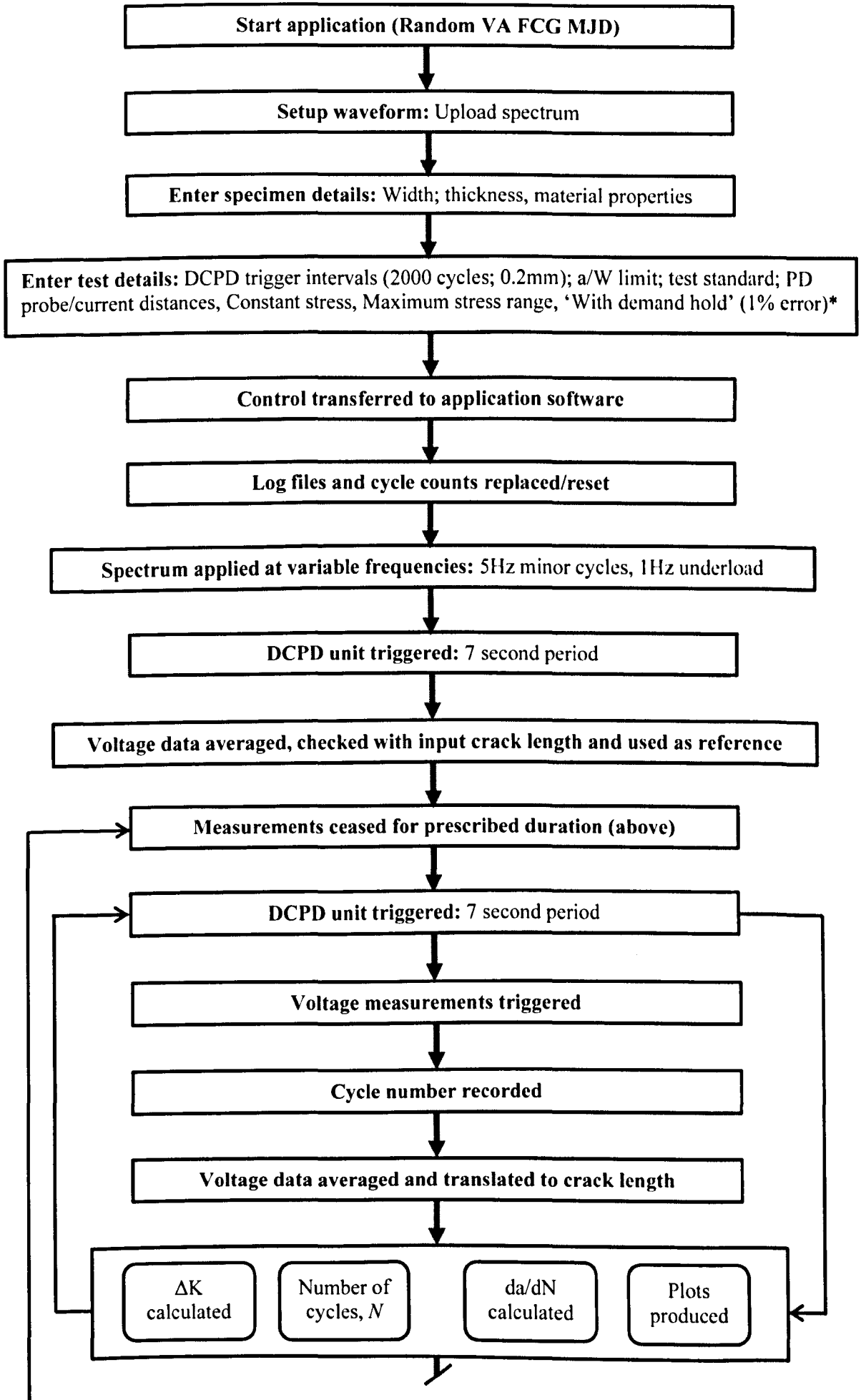
Zuidema J and Mannesse M, 1991: 'Interaction of fatigue crack growth properties and crack surface geometry in Al 2024', *Engineering Fracture Mechanics*, Vol. 40, Issue 1, pp 105-117.

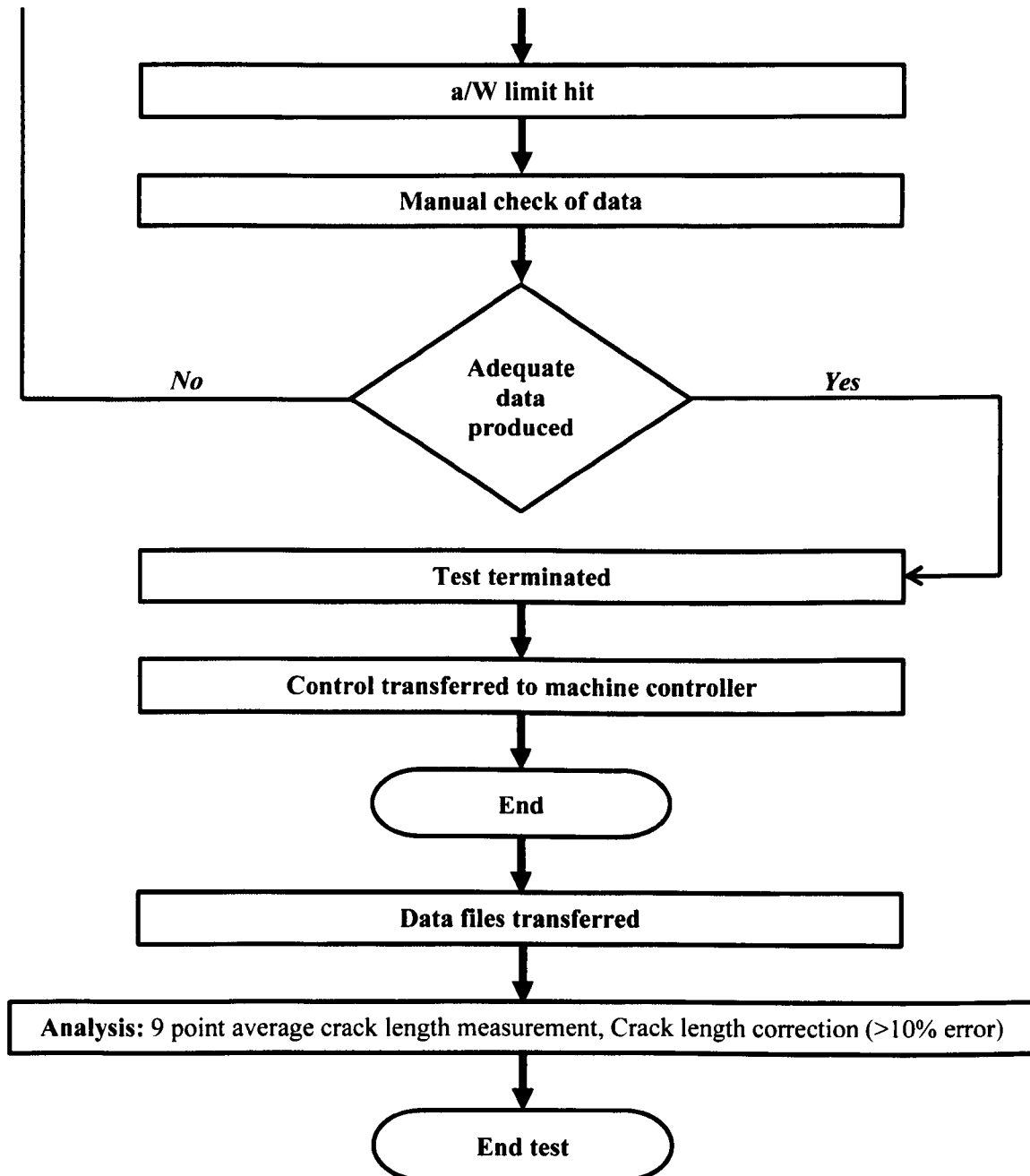
Appendix A

SOFTWARE AND PROCESS FLOWCHARTS

CONTENTS

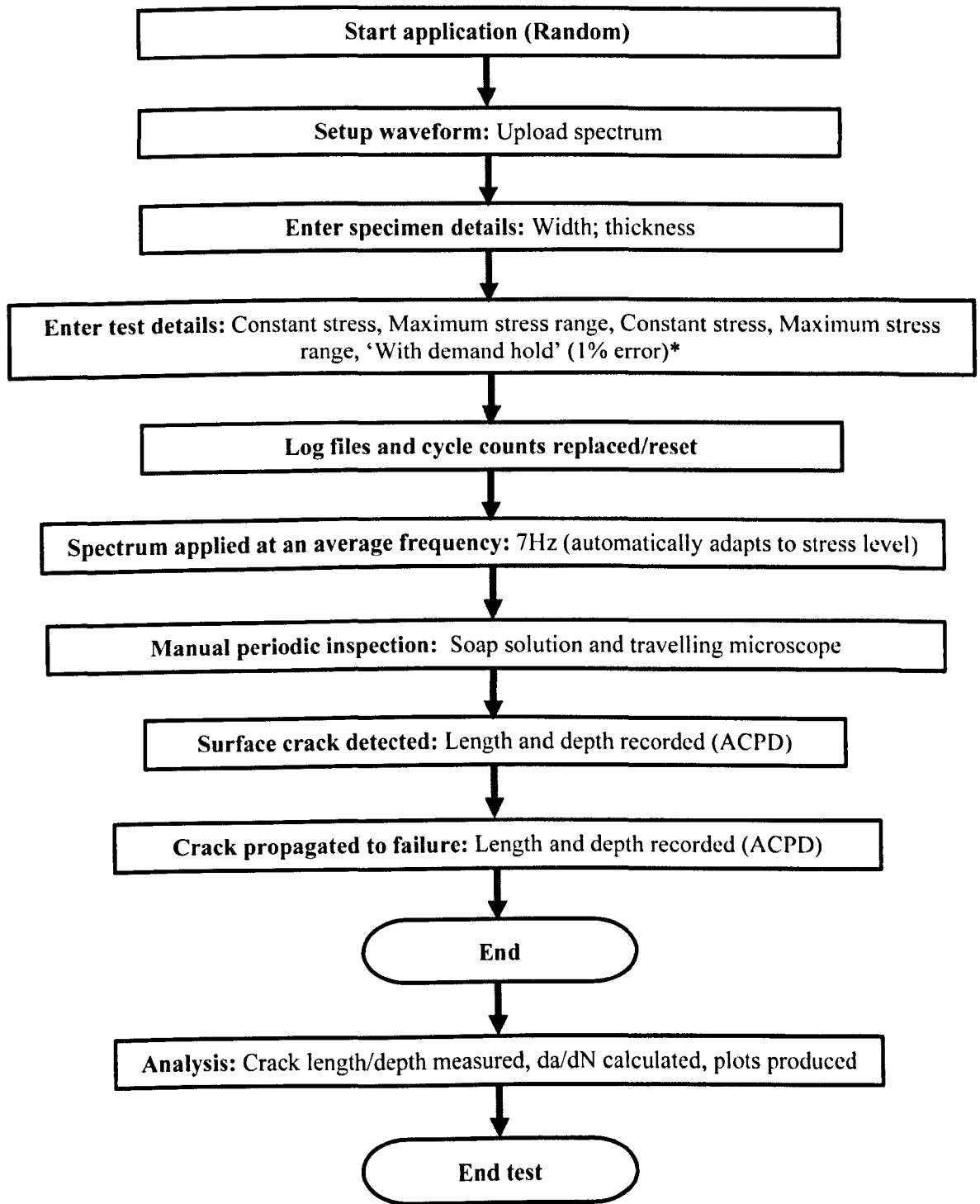
- Figure A1 Periodic underload software and process flowchart
- Figure A2 Variable amplitude loading software and process flowchart





Note. *With demand hold (1% error), this means that the next load cycle is not applied until the load is within 1% of the desired level. If not achievable at set frequency, the software adjusts the frequency to suit.

Figure A1 Periodic underload software flowchart.



Note. *With demand hold (1% error), this means that the next load cycle is not applied until the load is within 1% of the desired level. If not achievable at set frequency, the software adjusts the frequency to suit.

Figure A2 Variable amplitude loading process flowchart.

Appendix B

FINITE ELEMENT ANALYSIS MODEL PLOTS AND VALIDATION

CONTENTS

B1 Finite element analysis plots

- Figure B1 Variation of stress and strain 0.01mm from the crack tip in S355 structural steel, obtained at the maximum and minimum applied loads (minor cycles) under constant amplitude loading.
- Figure B2 to B6 Variation of stress in S355 steel at 0.01mm from crack tip under SBL1.5 and SBL2.2 loading, and at 0.01, 0.05 and 0.1mm under SBL2 loading.
- Figure B7 to B9 Variation of stress in welded S355 steel at 0.01, 0.05 and 0.1mm from crack tip under SBL2 loading.
- Figure B10 Variation of strain 0.01mm from crack tip in S355 steel for different underload ratios. The SBL2.2 underload corresponds to zero minimum stress.
- Figure B11 Variation of stress and strain 0.01mm from the crack tip in 6082 al alloy, obtained at the maximum and minimum applied loads (minor cycles) under constant amplitude loading.
- Figure B12 to B15 Variation of stress in 6082 al alloy at 0.01mm from crack tip under SBL1.5, SBL2 and SBL2.3 loading.
- Figure B16 to B17 Variation of stress in welded 6082 al alloy at 0.01 and 0.05mm from crack tip under SBL2 loading.
- Figure B18 Variation of strain 0.01mm from crack tip in 6082 al alloy for different underload ratios. The SBL2.3 underload corresponds to zero minimum stress.
-

B2 Finite element analysis model validation

- Figure B19 Validation of FE model showing comparison of the stress profile near the crack tip due to the loading portion of the minor stress cycle with the stress profile derived using LEFM.
- Figure B20 Validation of FE model showing the variation of stress near the crack tip between the loading and unloading portions of the minor stress cycle and that derived using LEFM.
- Figure B21 Irwin's corrected crack tip stress fields allowing for the plastic zone.
- Figure B22 Validation of FE model showing the stress profile near the crack tip during application of the maximum nominal stress and that derived using plane strain LEFM considering the elastic-plastic offset.
- Figure B23 Validation of FE model showing the stress profile near the crack tip at the minimum nominal stress, and that derived using plane strain LEFM considering the elastic-plastic offset.

B3 Comparison between collapsed and quadrilateral elements

- Figure B24 Comparison of the strain profile in S355 structural steel, obtained at the maximum and minimum applied loads (minor cycles) under constant amplitude loading.
- Figure B25 Comparison of the stress profile in S355 structural steel, obtained at the maximum and minimum applied loads (minor cycles) under constant amplitude loading.
- Figure B26 Contour plots using quadrilateral elements for S355 structural steel, obtained at the maximum applied load for the minor cycle, showing a) Stress σ_{22} and b) strain ϵ_{22} .
- Figure B27 Contour plots using collapsed elements for S355 structural steel, obtained at the maximum applied load for the minor cycle, showing a) Stress σ_{22} and b) strain ϵ_{22} .
-

B.1 FINITE ELEMNT ANALYSIS PLOTS

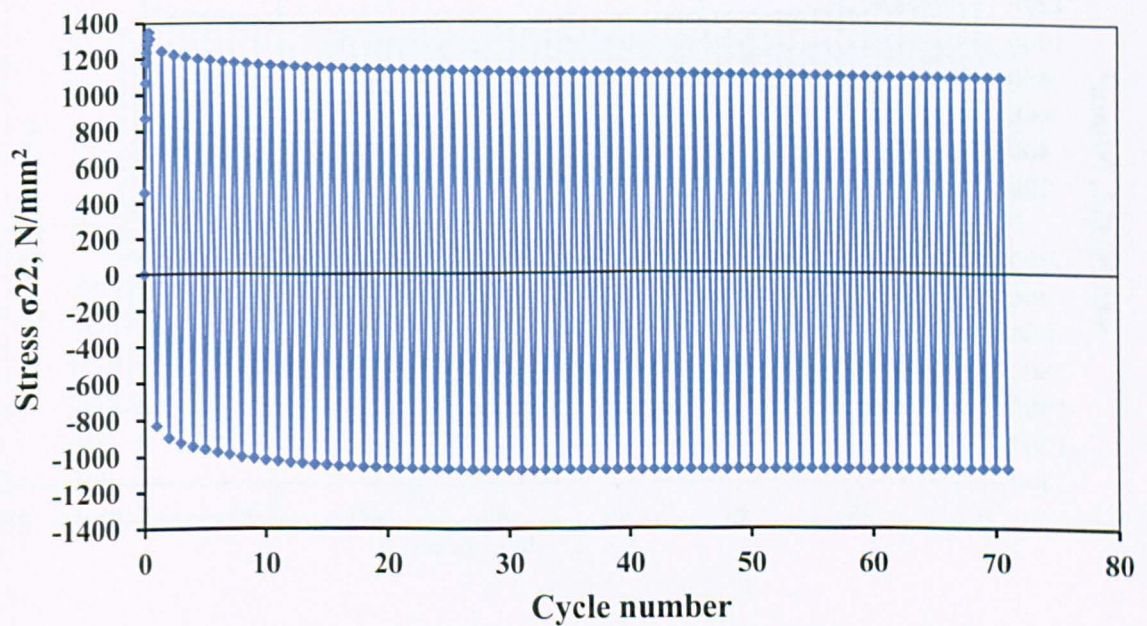
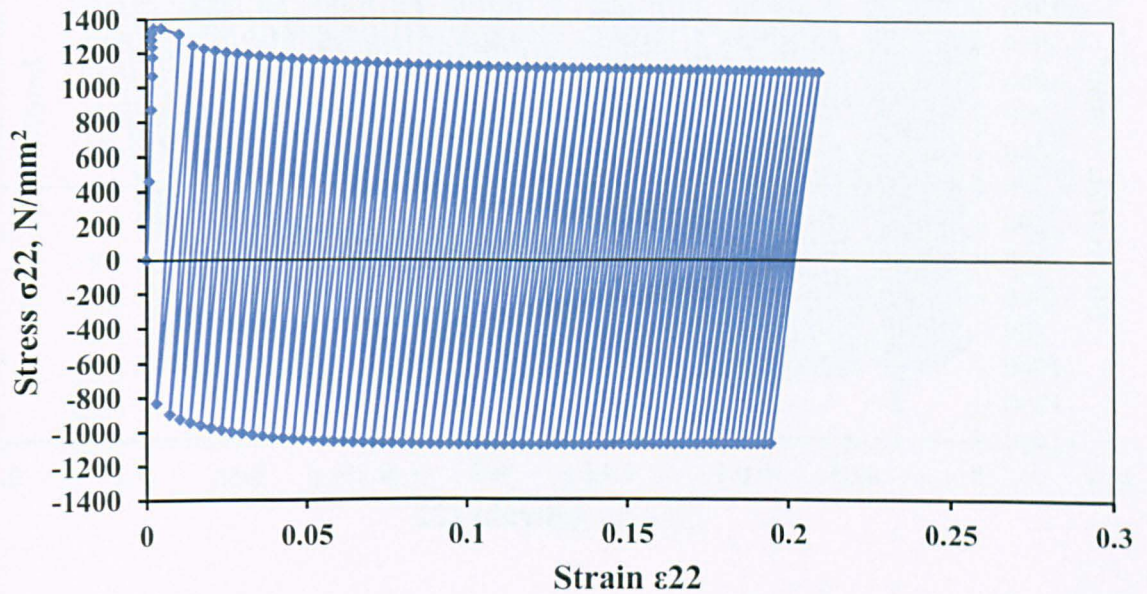


Figure B1 Variation of stress and strain 0.01mm from the crack tip in S355 structural steel, obtained at the maximum and minimum applied loads (minor cycles) under constant amplitude loading.

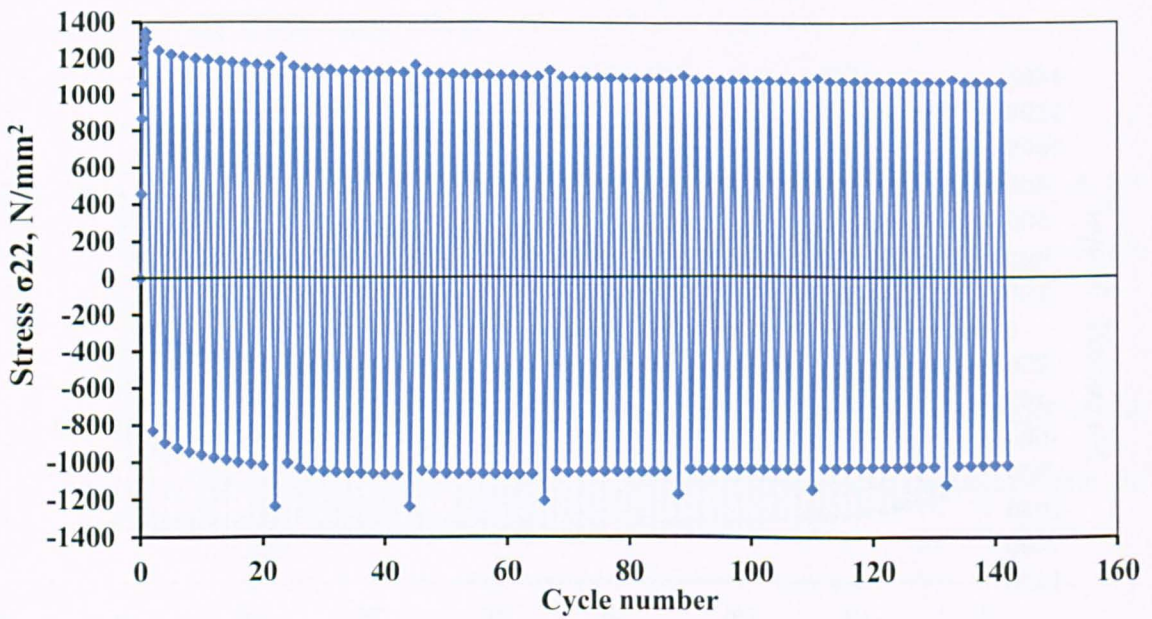
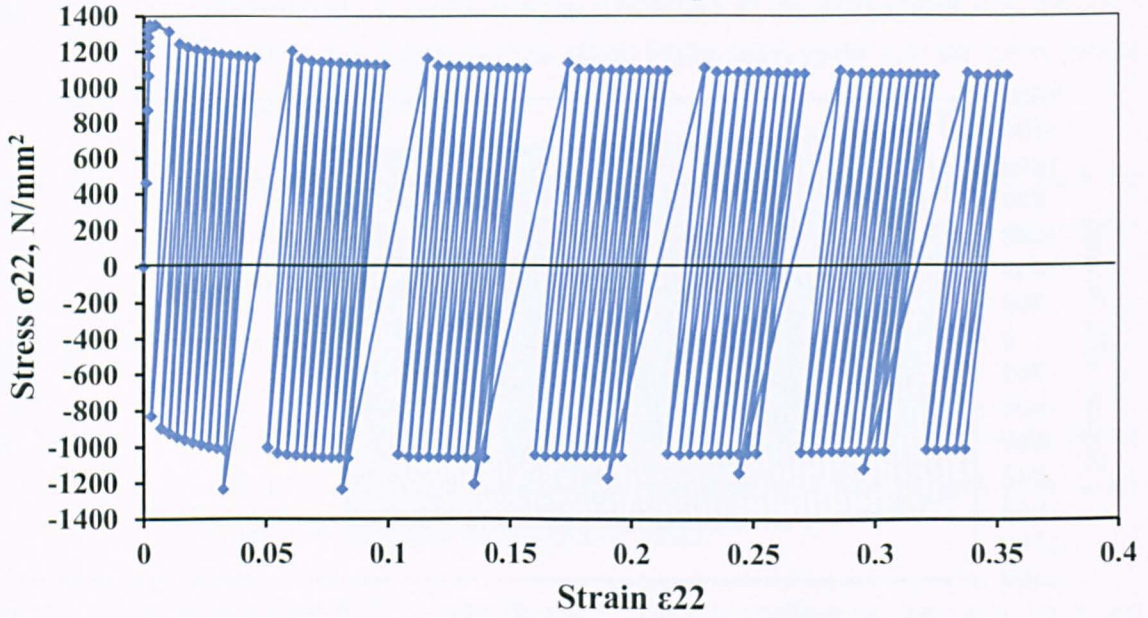


Figure B2 Variation of stress 0.01mm from crack tip in S355 steel obtained at maximum and minimum applied loads for the first six blocks of cycles under SBL1.5 loading.

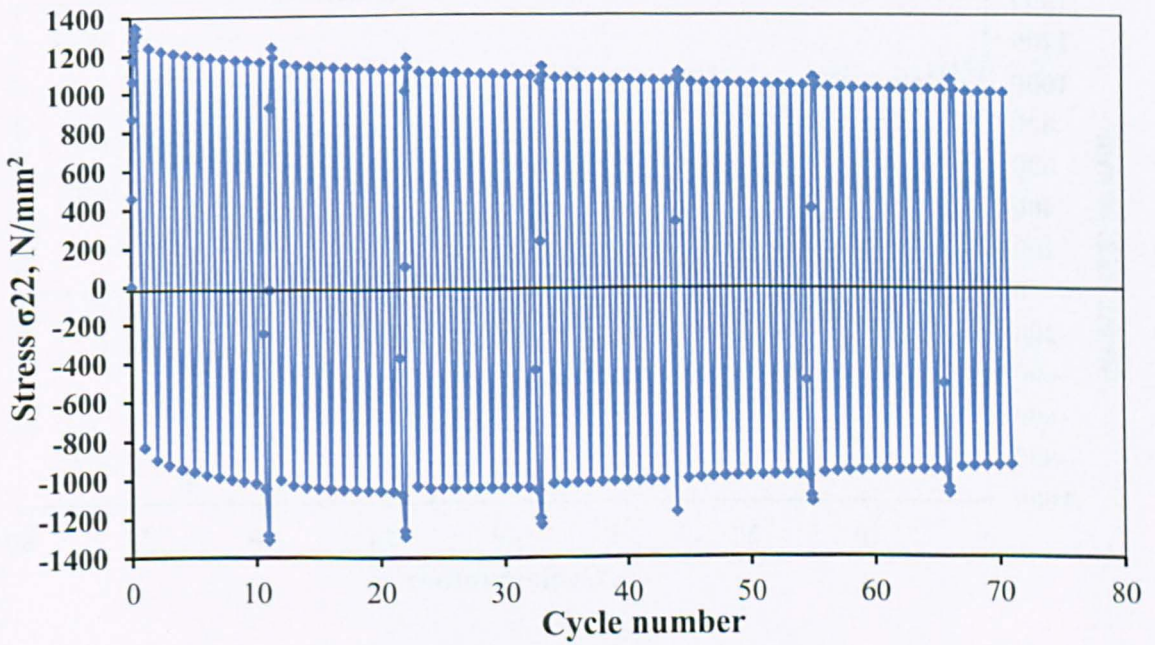
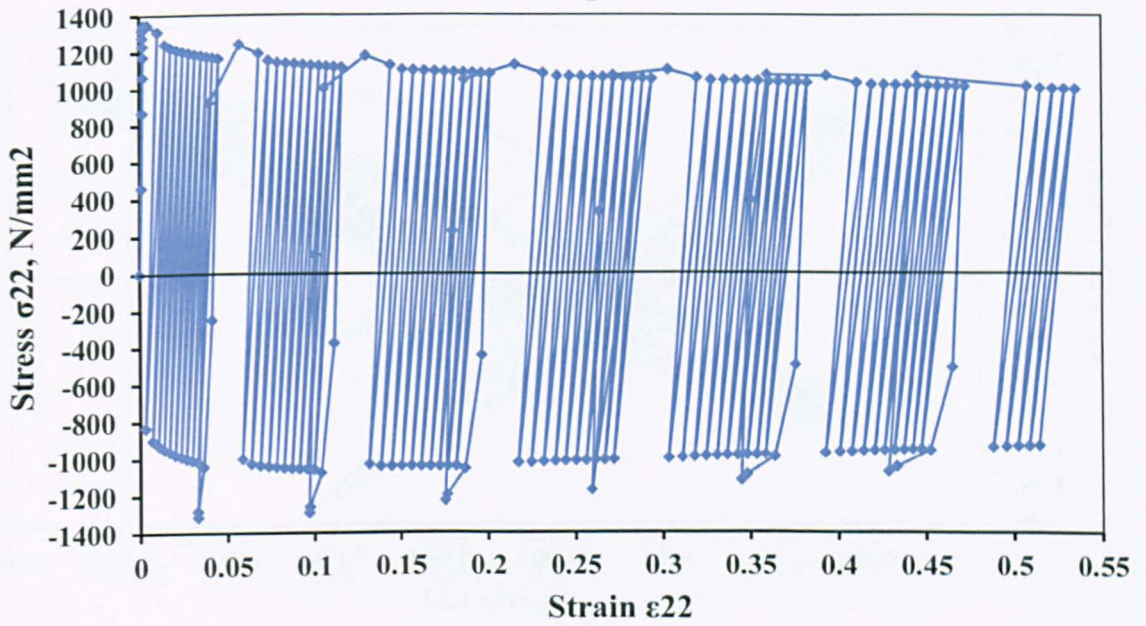


Figure B3 Variation of stress 0.01mm from crack tip in S355 steel obtained at maximum and minimum applied loads for the first six blocks of cycles under SBL2 loading.

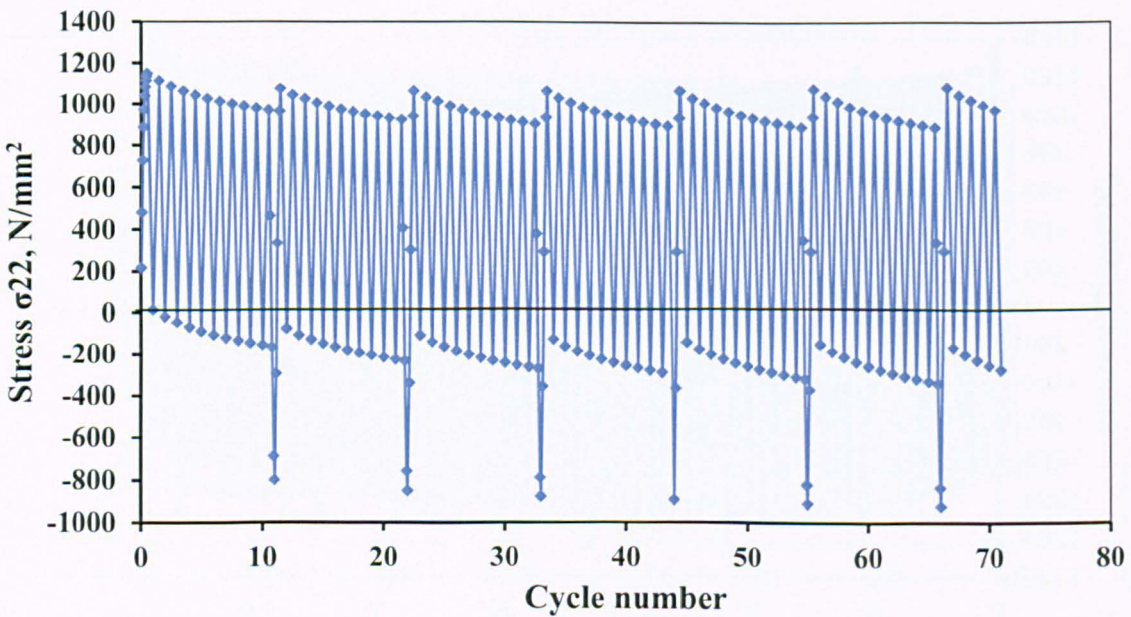
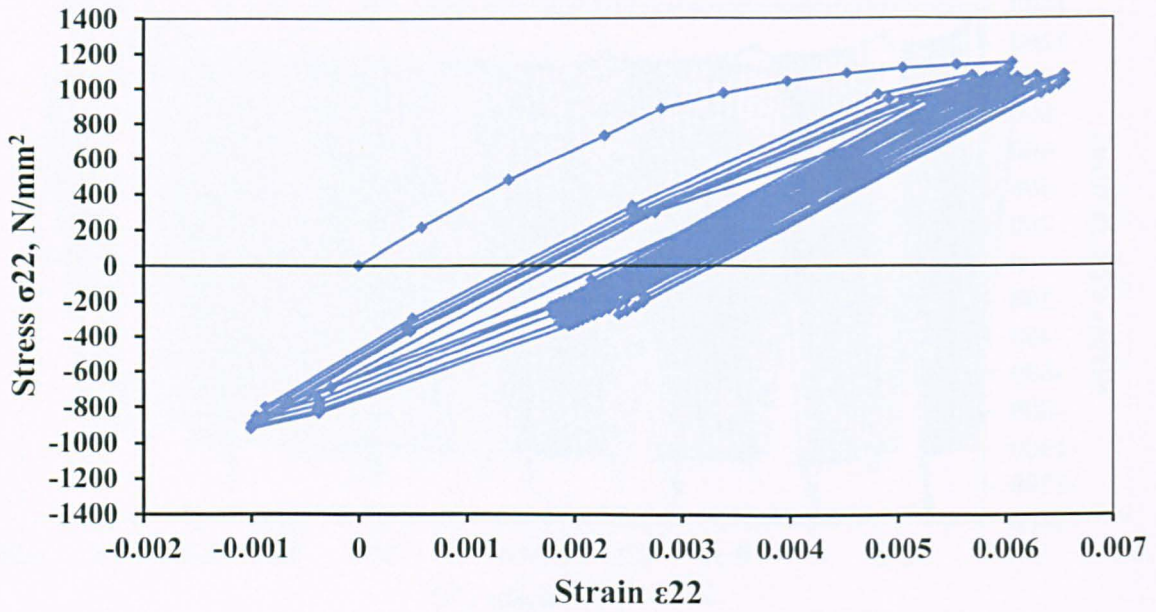


Figure B4 Variation of stress 0.05mm from crack tip in S355 steel obtained at maximum and minimum applied loads for the first six blocks of cycles under SBL2 loading.

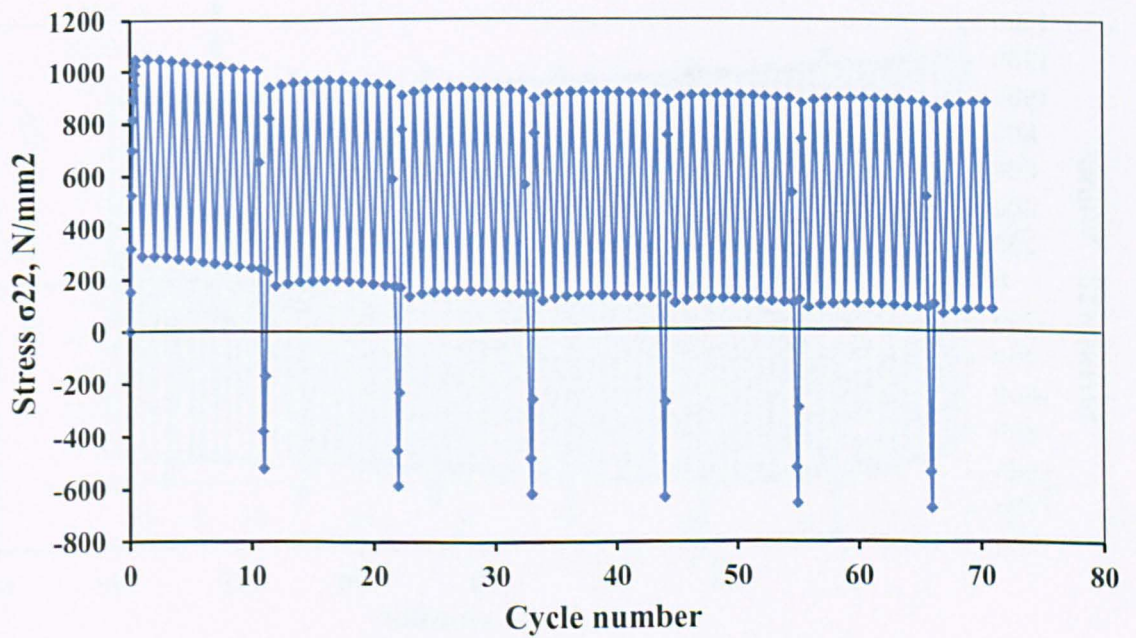
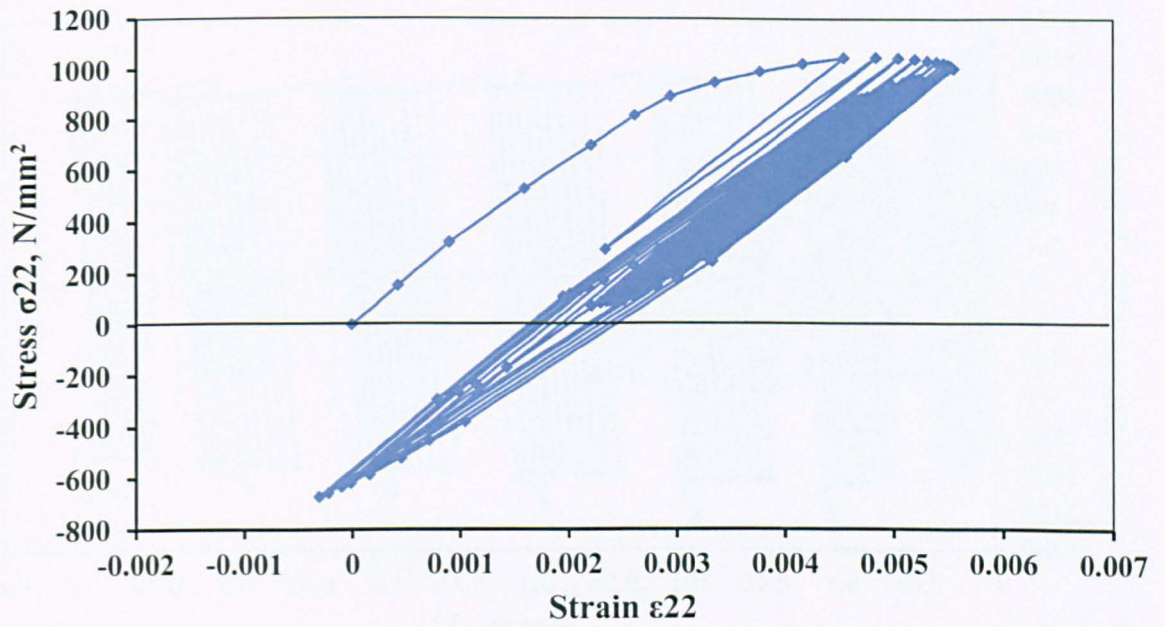


Figure B5 Variation of stress 0.1mm from crack tip in S355 steel obtained at maximum and minimum applied loads for the first six blocks of cycles under SBL2 loading.

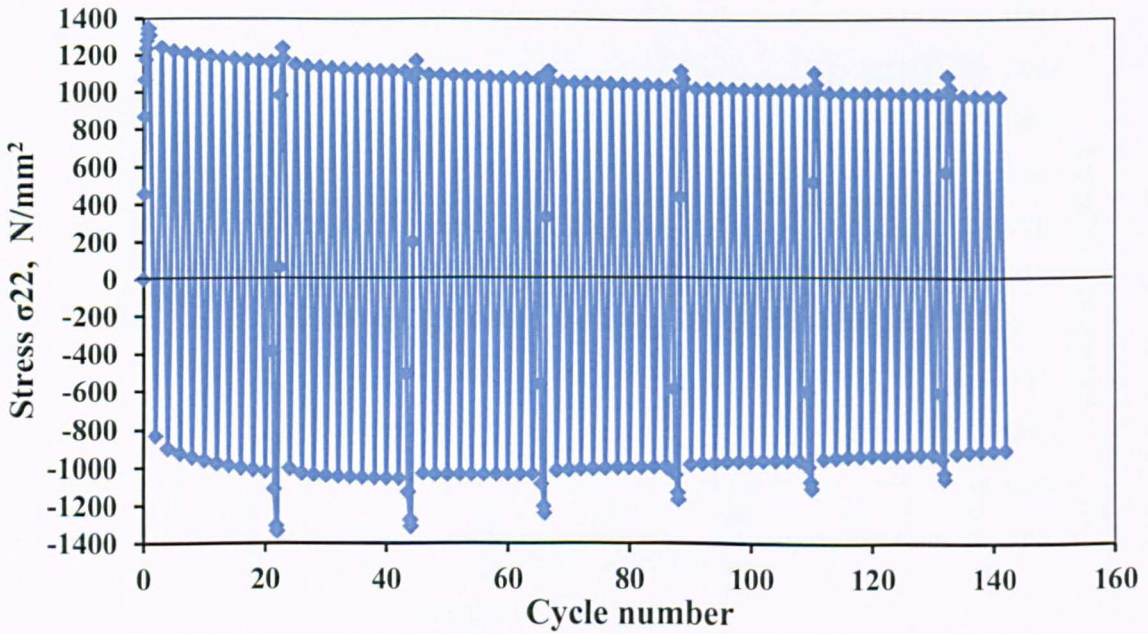
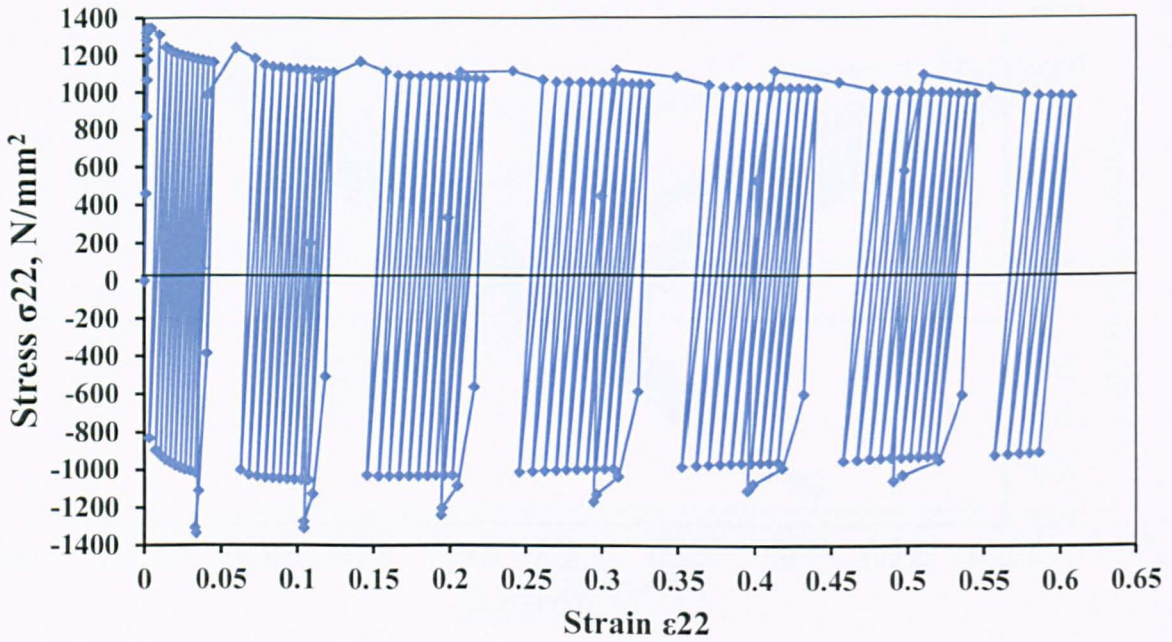


Figure B6 Variation of stress 0.01mm from crack tip in S355 steel obtained at maximum and minimum applied loads for the first six blocks of cycles under SBL2.2 loading.

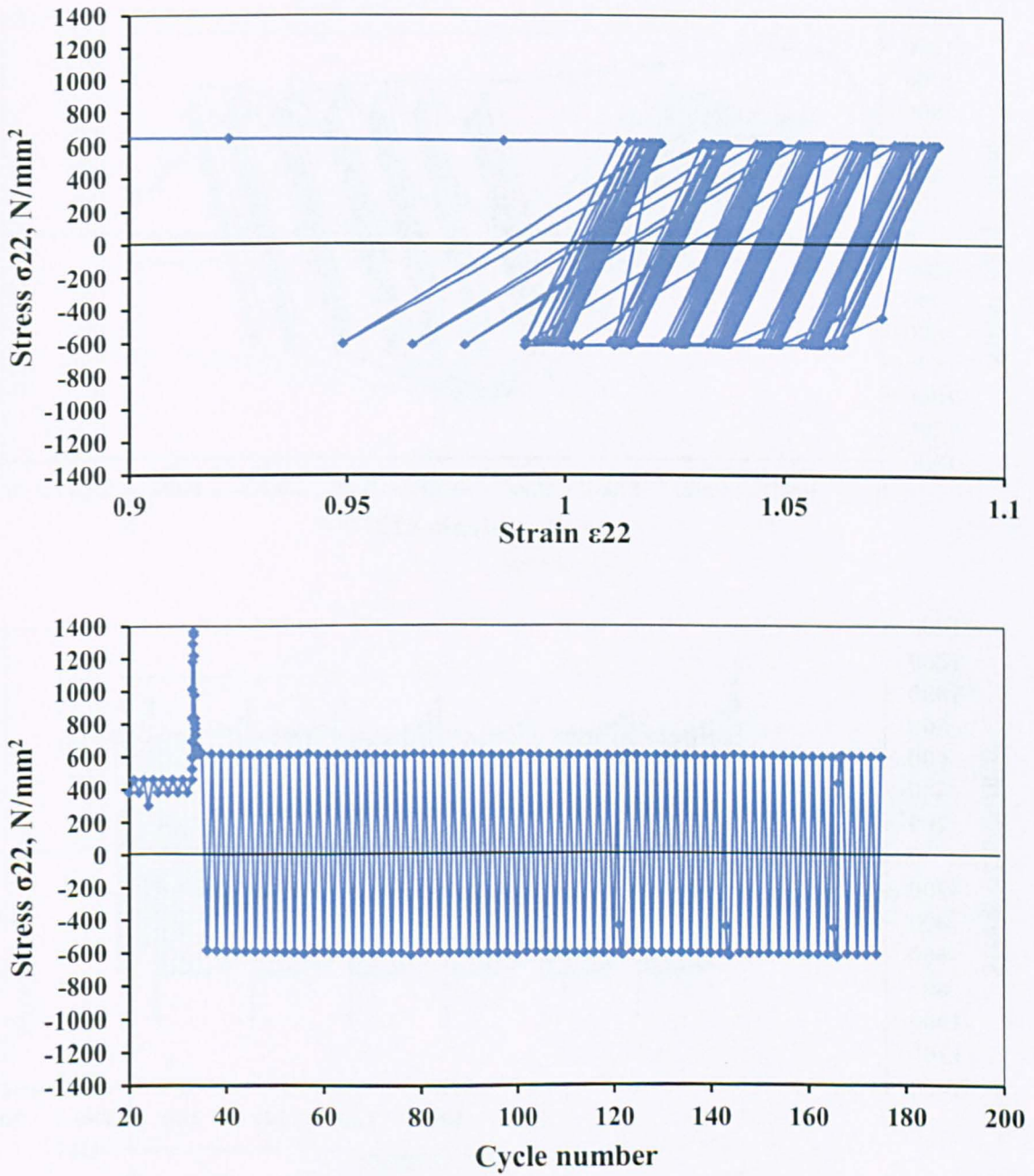


Figure B7 Variation of stress 0.01mm from crack tip in welded S355 steel obtained at maximum and minimum applied loads for the first six blocks of cycles under SBL2 loading.

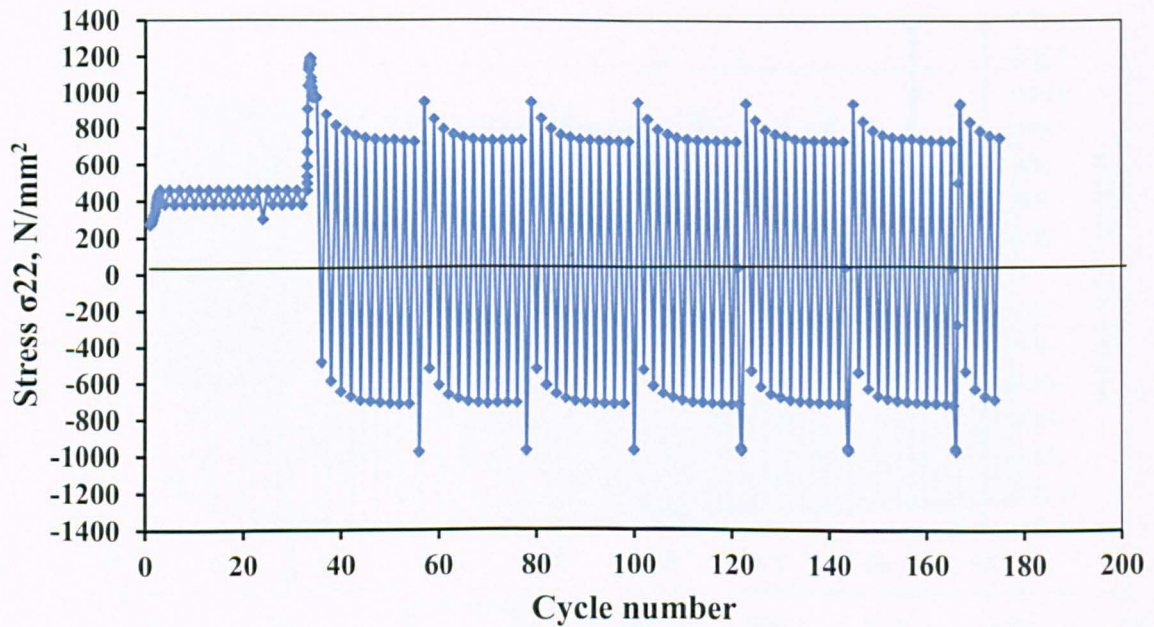
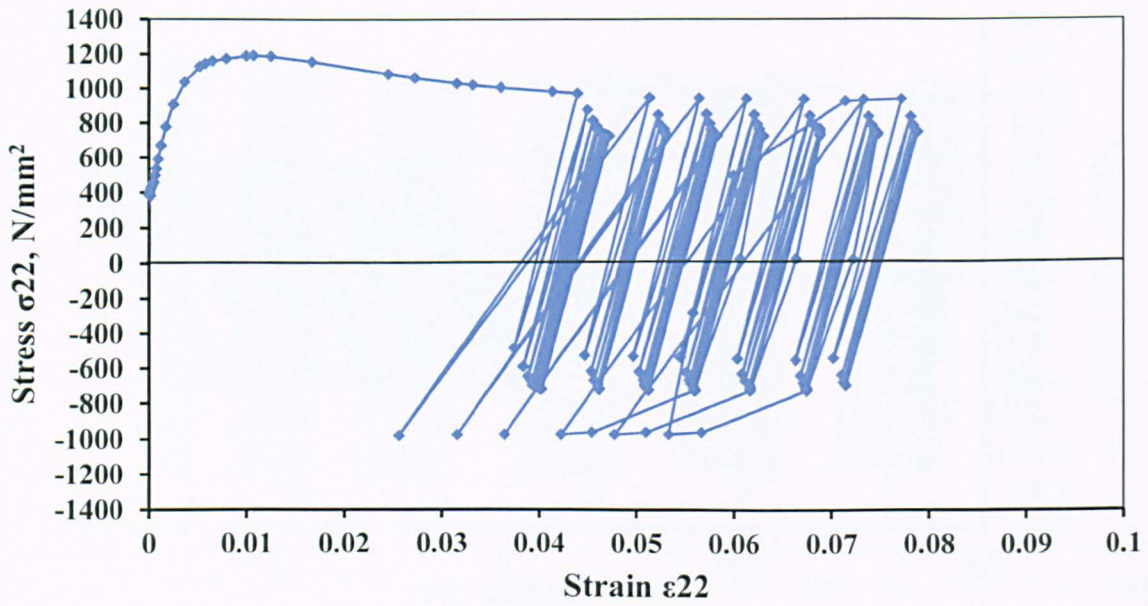


Figure B8 Variation of stress 0.05mm from crack tip in welded S355 steel obtained at maximum and minimum applied loads for the first six blocks of cycles under SBL2 loading.

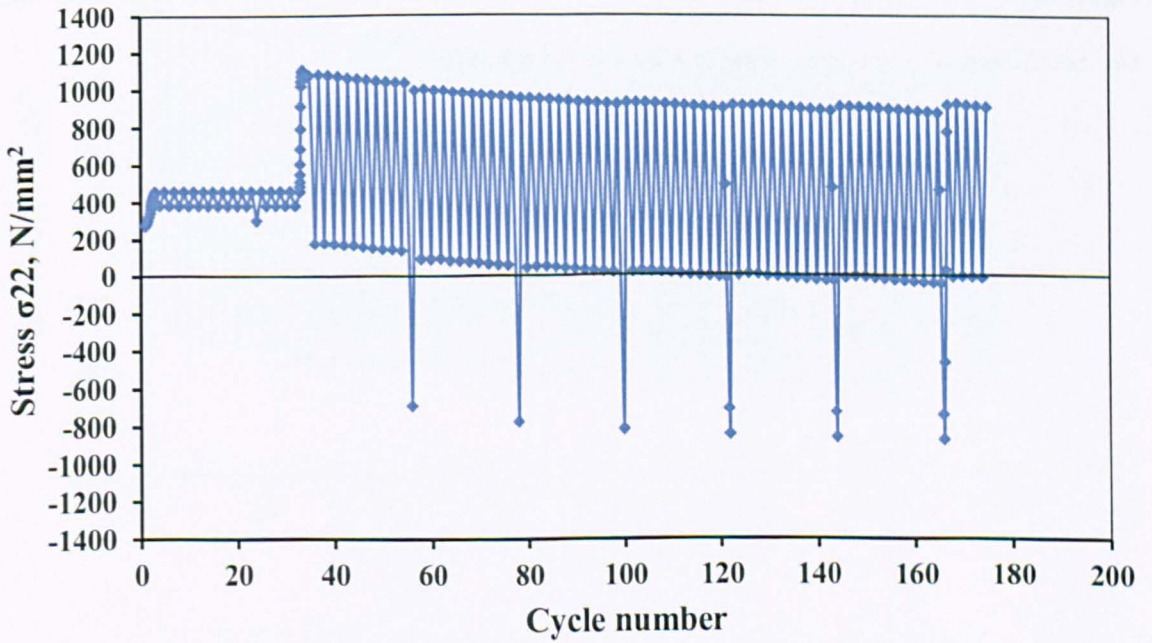
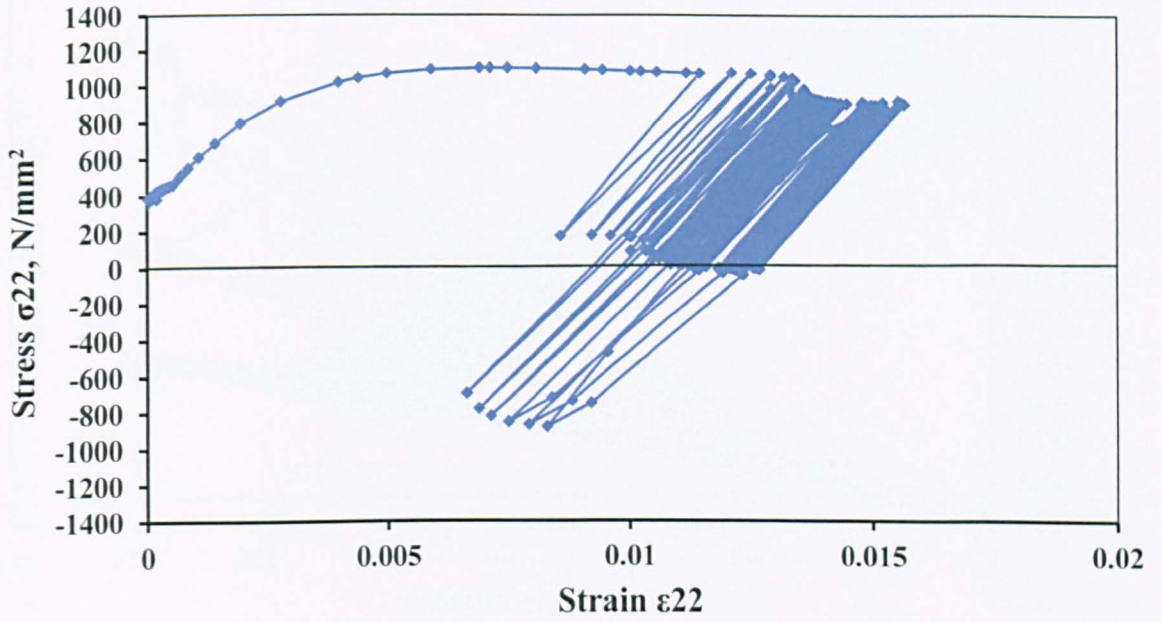


Figure B9 Variation of stress 0.1mm from crack tip in welded S355 steel obtained at maximum and minimum applied loads for the first six blocks of cycles under SBL2 loading.

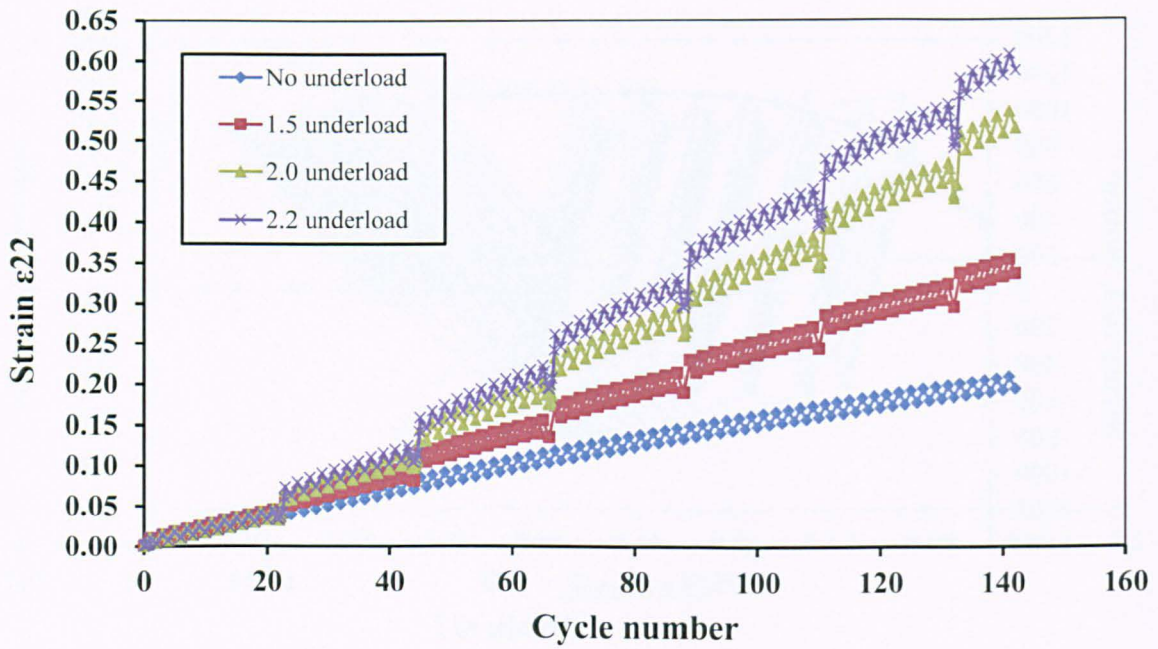


Figure B10 Variation of strain 0.01mm from crack tip in S355 steel for different underload ratios.

The SBL2.2 underload corresponds to zero minimum stress.

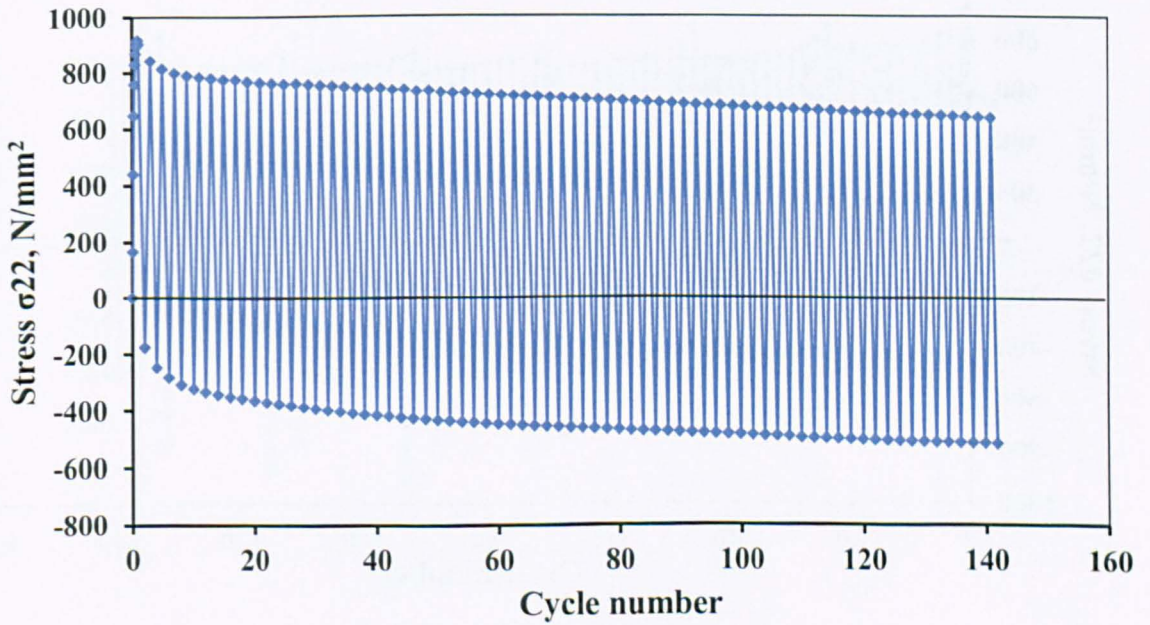
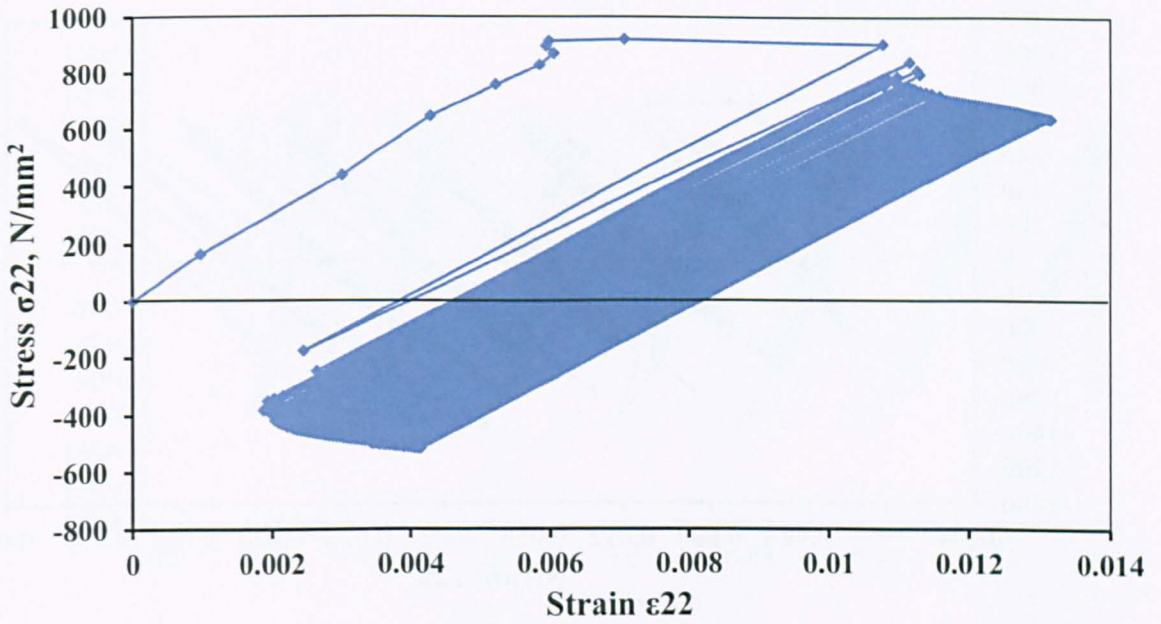


Figure B11 Variation of stress and strain 0.01mm from the crack tip in 6082 al alloy, obtained at the maximum and minimum applied loads (minor cycles) under constant amplitude loading.

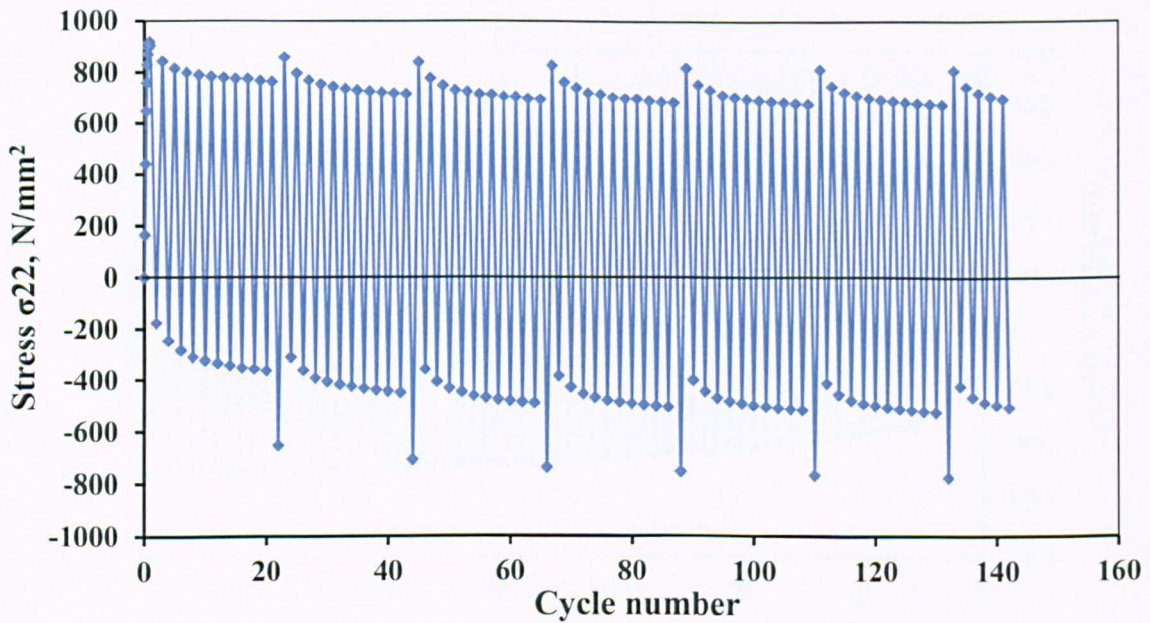
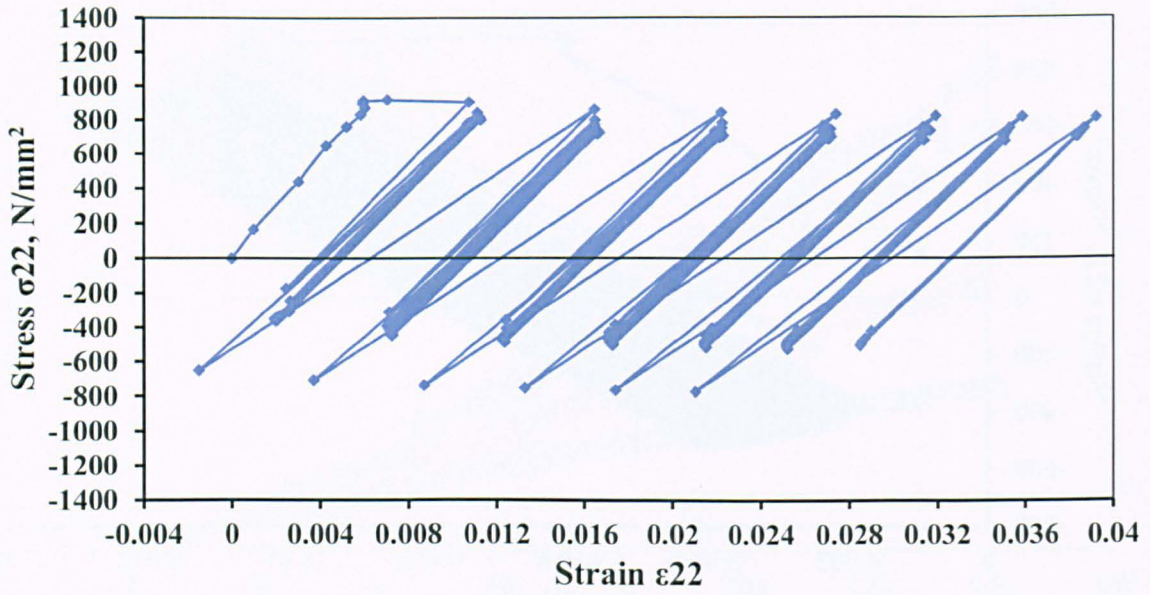


Figure B12 Variation of stress 0.01mm from crack tip in 6082 al alloy obtained at maximum and minimum applied loads for the first six blocks of cycles under SBL1.5 loading.

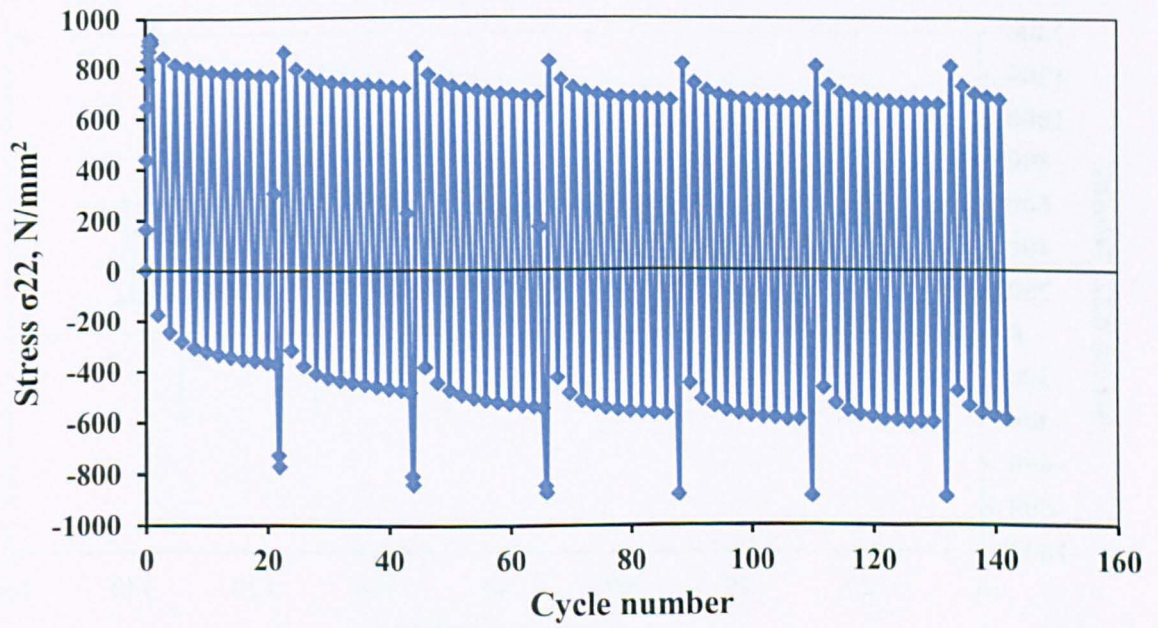
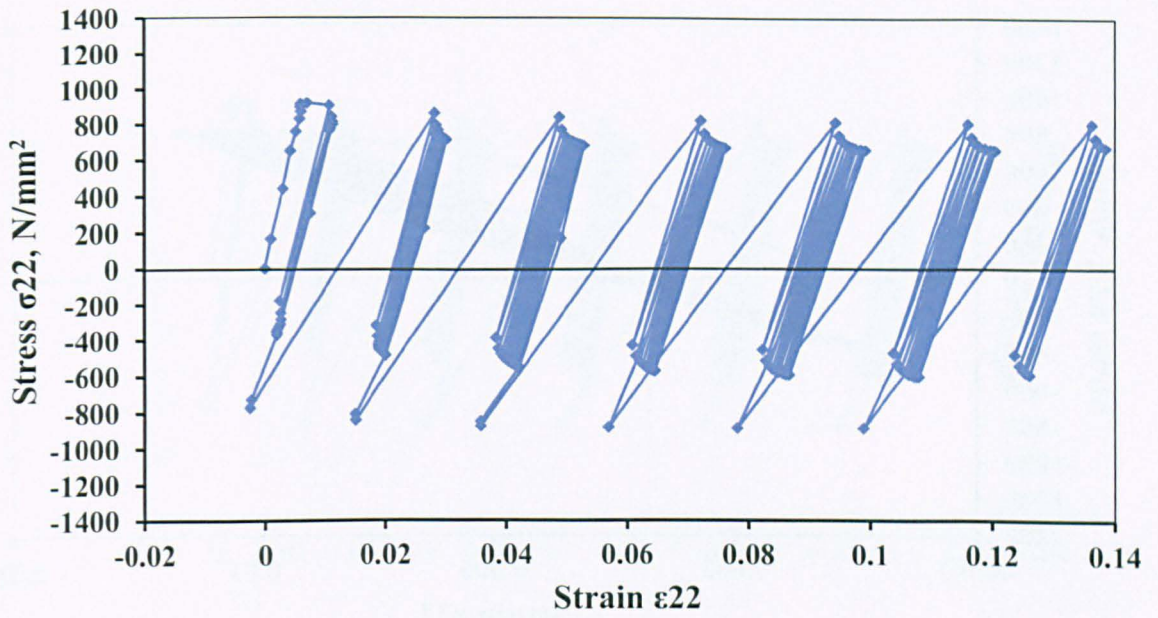


Figure B13 Variation of stress 0.01mm from crack tip in 6082 al alloy obtained at maximum and minimum applied loads for the first six blocks of cycles under SBL2 loading.

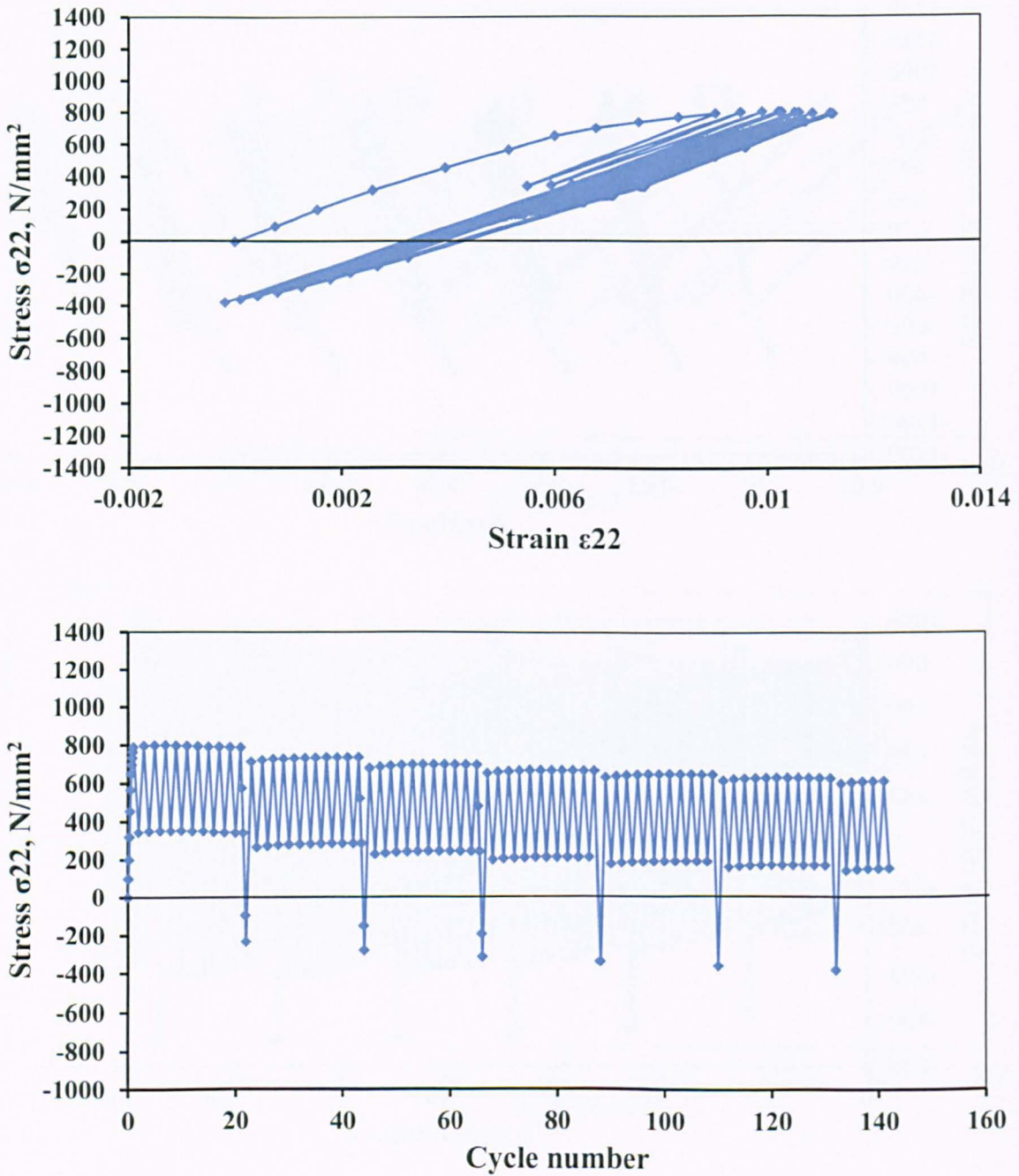


Figure B14 Variation of stress 0.05mm from crack tip in 6082 al alloy obtained at maximum and minimum applied loads for the first six blocks of cycles under SBL2 loading.

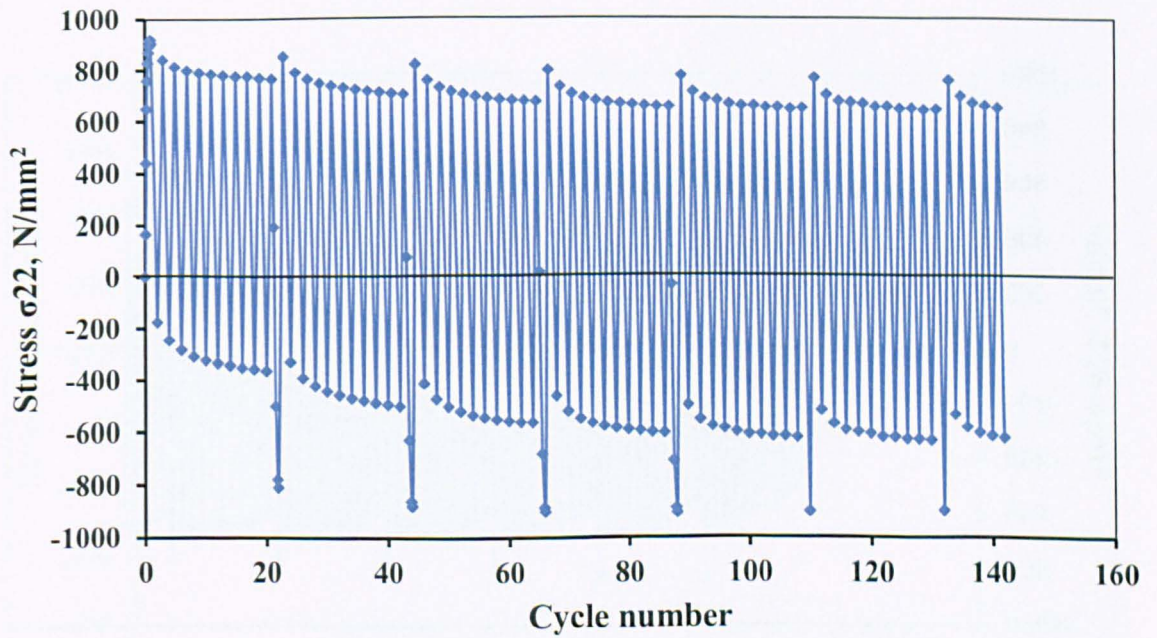
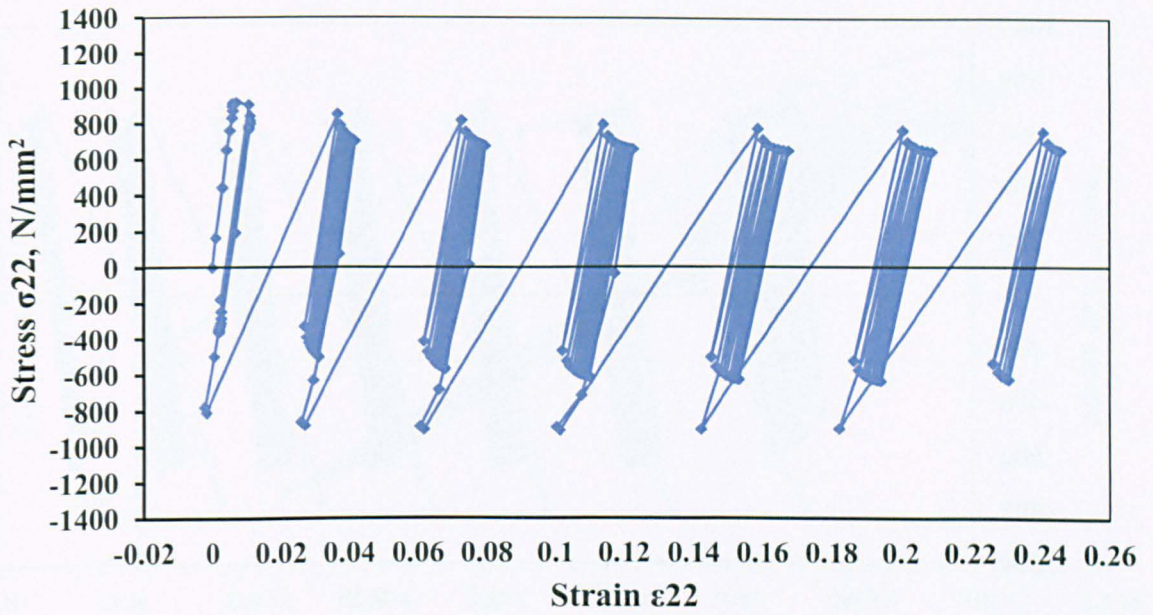


Figure B15 Variation of stress 0.01mm from crack tip in 6082 al alloy obtained at maximum and minimum applied loads for the first six blocks of cycles under SBL2.3 loading.

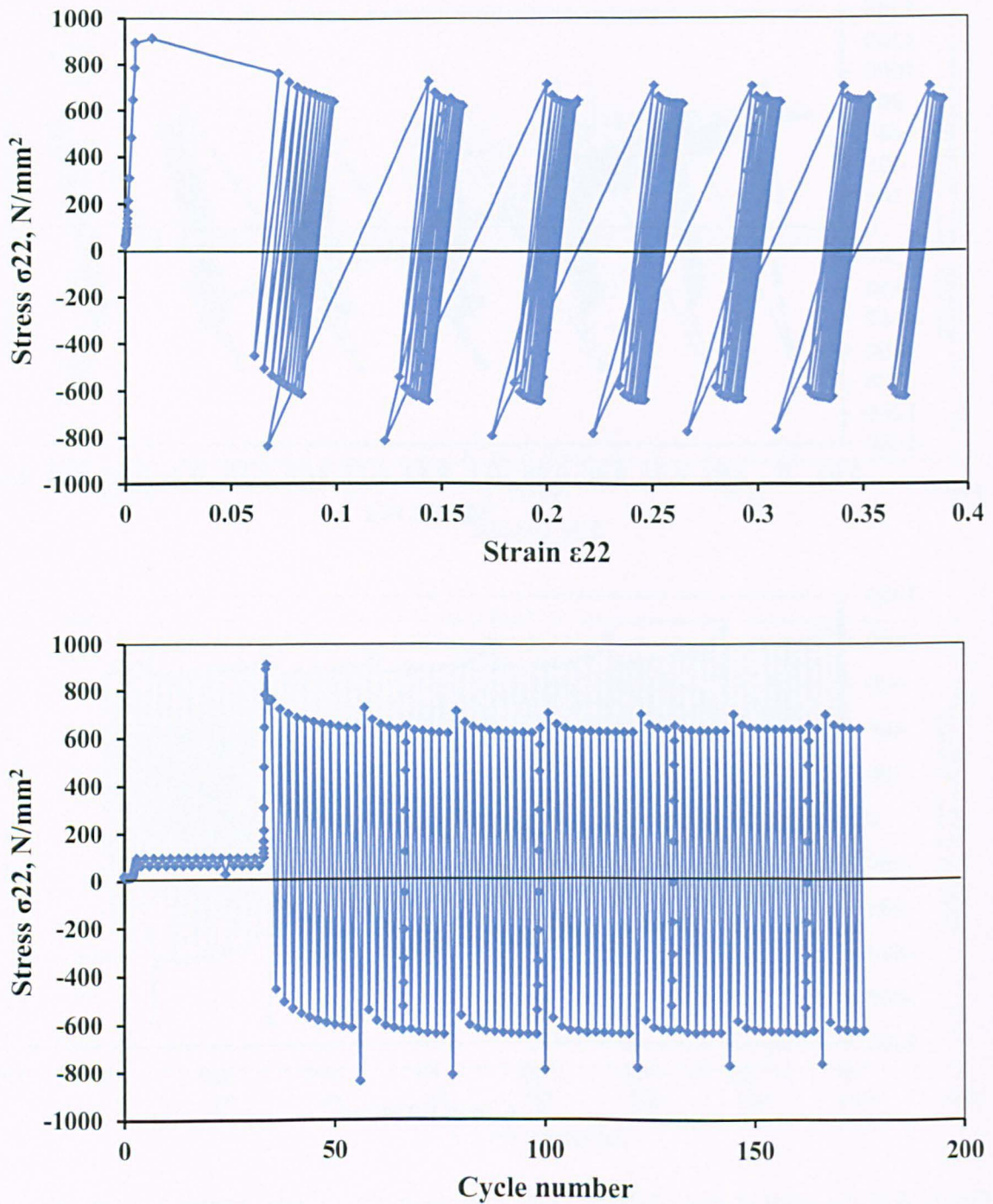


Figure B16 Variation of stress 0.01mm from crack tip in welded 6082 al alloy obtained at maximum and minimum applied loads for the first six blocks of cycles under SBL2 loading.

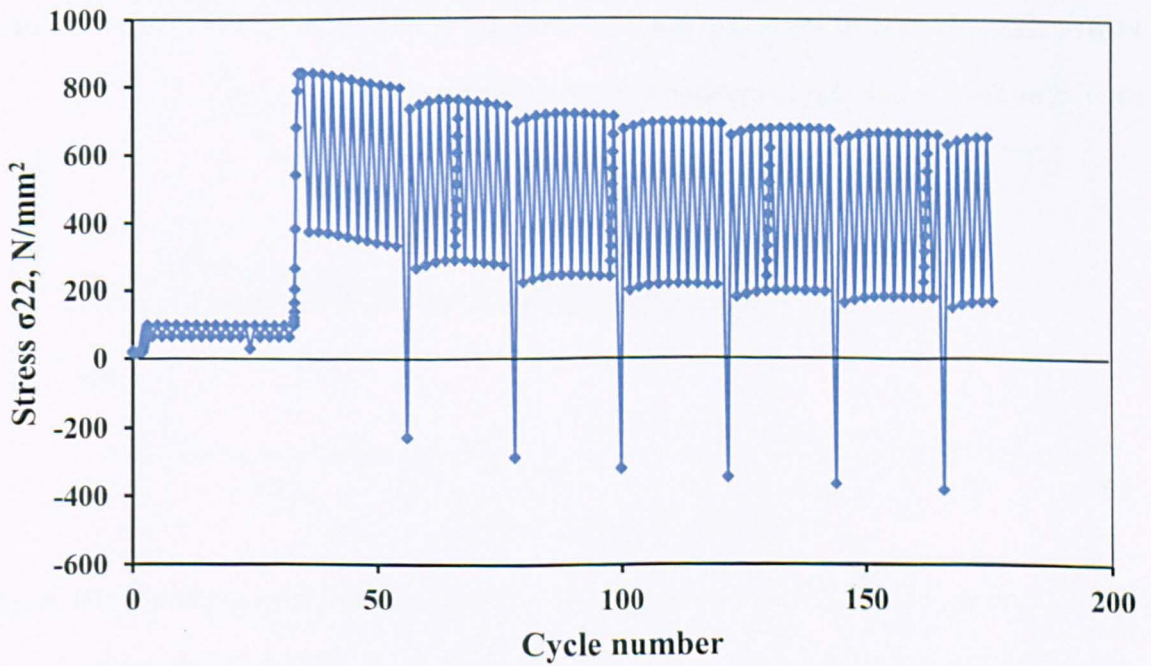
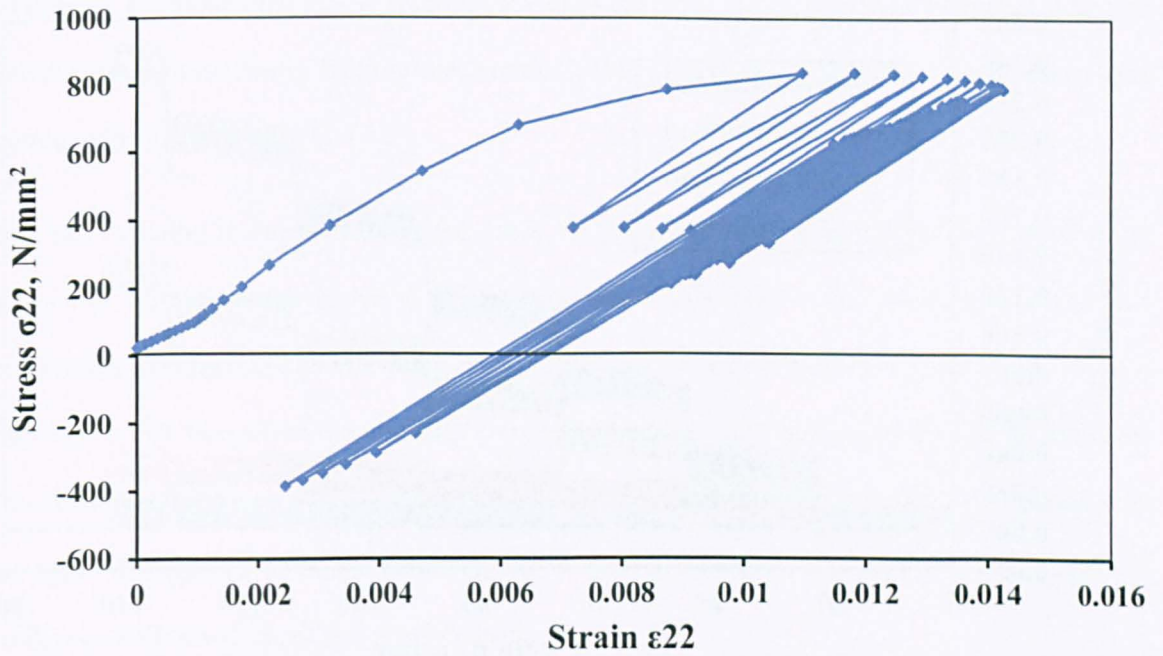


Figure B17 Variation of stress 0.05mm from crack tip in welded 6082 al alloy obtained at maximum and minimum applied loads for the first six blocks of cycles under SBL2 loading.

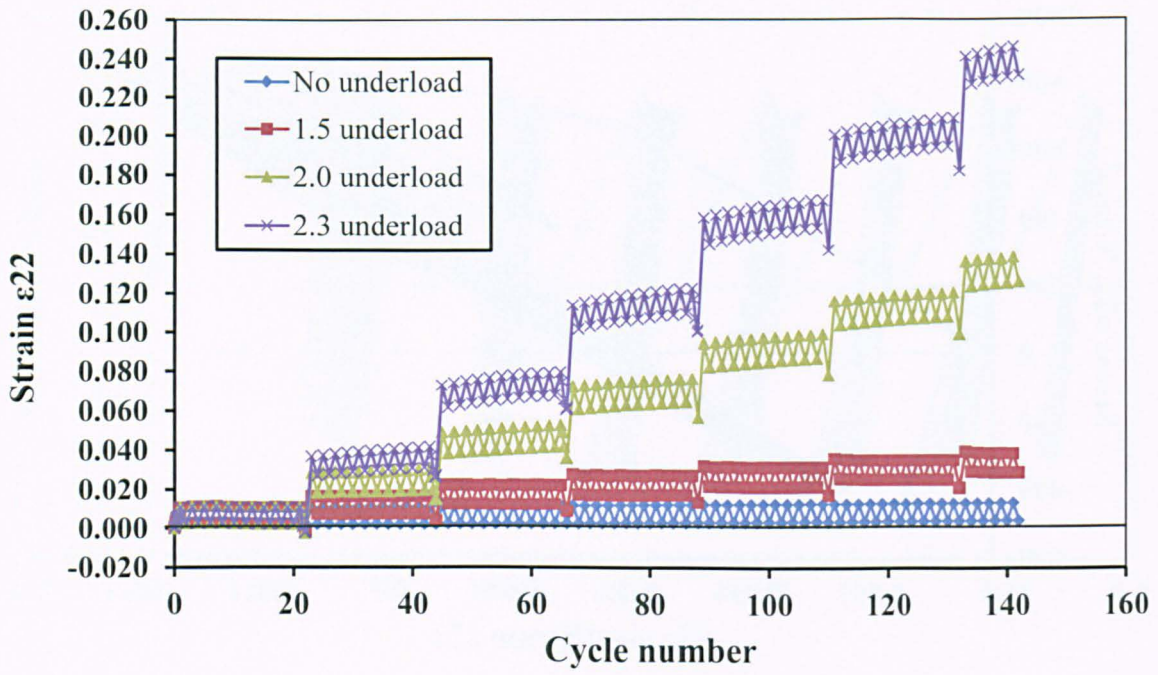


Figure B18 Variation of strain 0.01mm from crack tip in 6082 al alloy for different underload ratios. The SBL2.3 underload corresponds to zero minimum stress

B.2 MODEL VALIDATION

To validate FE model, the elastic response ahead of the crack tip in steel was compared with that derived using linear elastic fracture mechanics (LEFM) using the cylindrical co-ordinate system centred at the crack tip, Eq. [2.4.1].

First, the variation in stress close to the crack tip under the loading portion of the minor stress cycles was determined, as shown in Figure B19. The results refer to the application of the first minor stress loading cycle and the tenth one (i.e. the start and end of the minor cycle block). Here it can be seen that away from the crack tip ($>0.2\text{mm}$) the FE results agree with the LEFM response. However, close to the crack tip, where large plastic deformation would exist, the two solutions do not agree. However, this is not surprising since the FEA models allowed for yielding and the validation (LEFM response) was purely elastic.

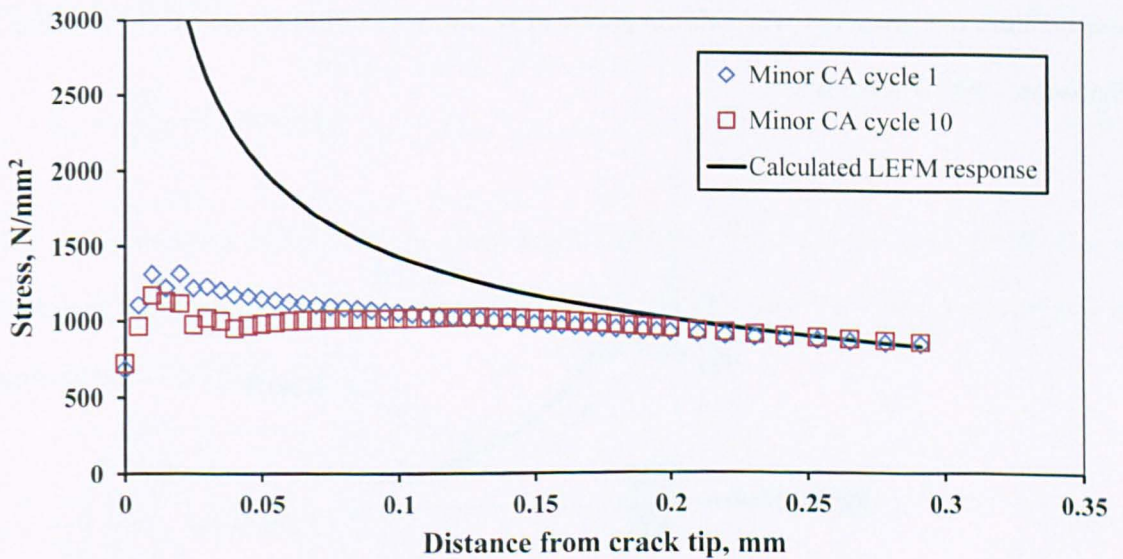


Figure B19 Validation of FE model showing comparison of the stress profile near the crack tip due to the loading portion of the minor stress cycle with the stress profile derived using LEFM.

The process was repeated this time using the variation in crack tip stress between the loading and unloading portions of the minor cycle, again for the first and tenth cycles, Figure B20. As this response is totally elastic, it can be seen that good correlation is achieved.

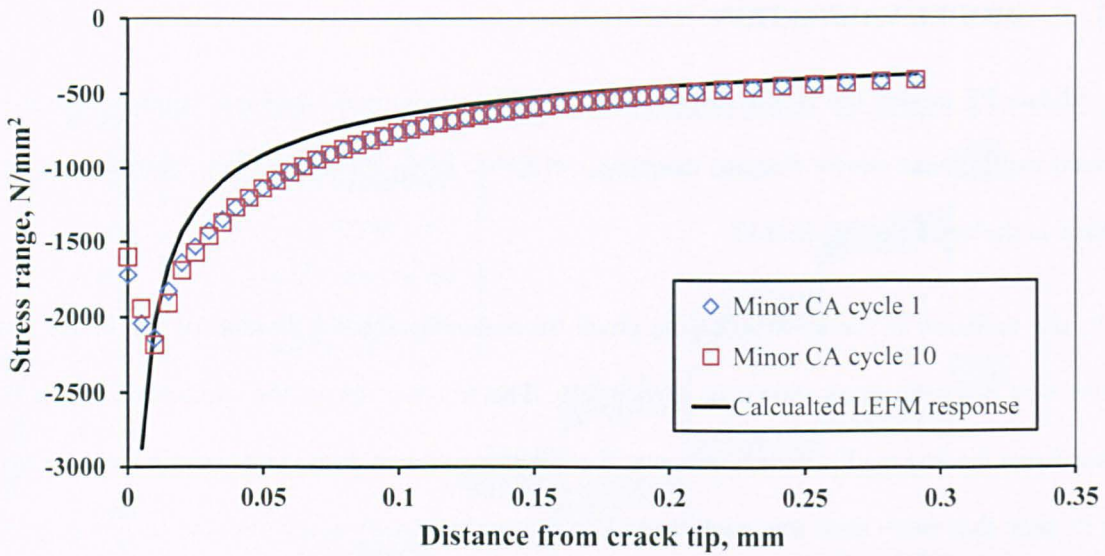


Figure B20 Validation of FE model showing the variation of stress near the crack tip between the loading and unloading portions of the minor stress cycle and that derived using LEFM.

To ensure the model was robust, validation was repeated using an alternative approach. Here consideration was given to Irwin’s elastic-plastic offset from the LEFM elastic curve (Lemaitre and Chaboche, 1990), Figure B21.

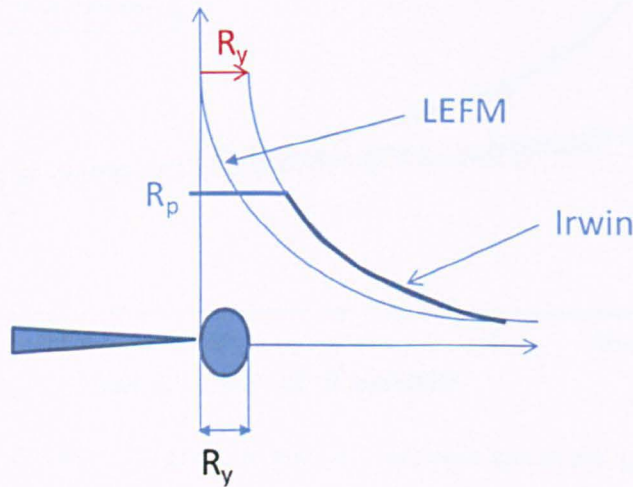


Figure B21 Irwin’s corrected crack tip stress fields allowing for the plastic zone.

Irwin suggested that the stress at the crack tip is limited by the value R_p over the distance $2 \times R_y$ (offset distance). Considering again the steel, where the maximum applied stress = 155N/mm^2 and $\sigma_{YS} = 455\text{N/mm}^2$, R_p was determined using the von Mises equivalent stress. Assuming LEFM and plane strain conditions:

$$\sigma_{xx} = \sigma_{yy} = \frac{K_I}{\sqrt{2\pi r}} \quad [B1]$$

$$\sigma_{zz} = \nu(\sigma_{xx} + \sigma_{yy}) \quad [B2]$$

$$K_I = \sigma_{nom} \sqrt{\pi a} \sqrt{\cos\left(\frac{\pi a}{W}\right)} \quad [B3]$$

Based on a plate width of $W = 160\text{mm}$ and a crack length $2a=36\text{mm}$, the Von Mises stress ($\bar{\sigma}$) is given by Eq. [B4].

$$\bar{\sigma} = \sqrt{\frac{1}{2}[(\sigma_{xx} - \sigma_{yy})^2 + (\sigma_{yy} - \sigma_{zz})^2 + (\sigma_{zz} - \sigma_{xx})^2]} = 0.4\sigma_{yy} \quad [B4]$$

Assuming the von Mises stress is limited to the material yield strength, the value of R_p can be determined as follows:

$$\sigma_{yy} = R_p = \frac{455}{0.4} = 1138\text{N/mm}^2 \quad [B5]$$

Based on a plate width of $W = 160\text{mm}$, crack length $2a=36\text{mm}$ and the maximum applied stress of 155N/mm^2 , the stress intensity factor K_I in Eq. [B3] = $1129\text{MPa}\sqrt{\text{mm}}$. The offset R_y could then be calculated from Eq. [B6]:

$$R_y = \frac{1}{2\pi} \left(\frac{K_I}{R_p} \right)^2 = 0.157\text{mm} \quad [B6]$$

The LEFM curve was then truncated so that for R_y below 0.157mm , the stress = 1138N/mm^2 . The resulting responses are compared with the FEA results for the minor stress cycles in Figures B22 and B23. In Figure B22 it will be seen that at the maximum nominal stress 155N/mm^2 the truncated response agrees reasonably well with the CA cycles.

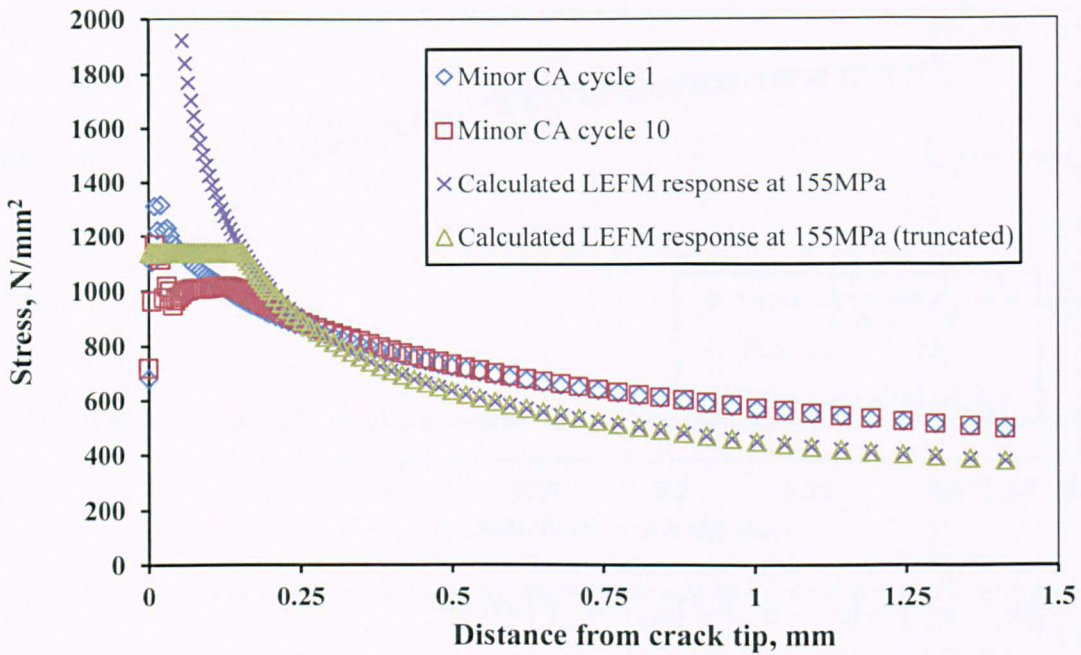


Figure B22 Validation of FE model showing the stress profile near the crack tip during application of the maximum nominal stress and that derived using plane strain LEFM considering the elastic-plastic offset.

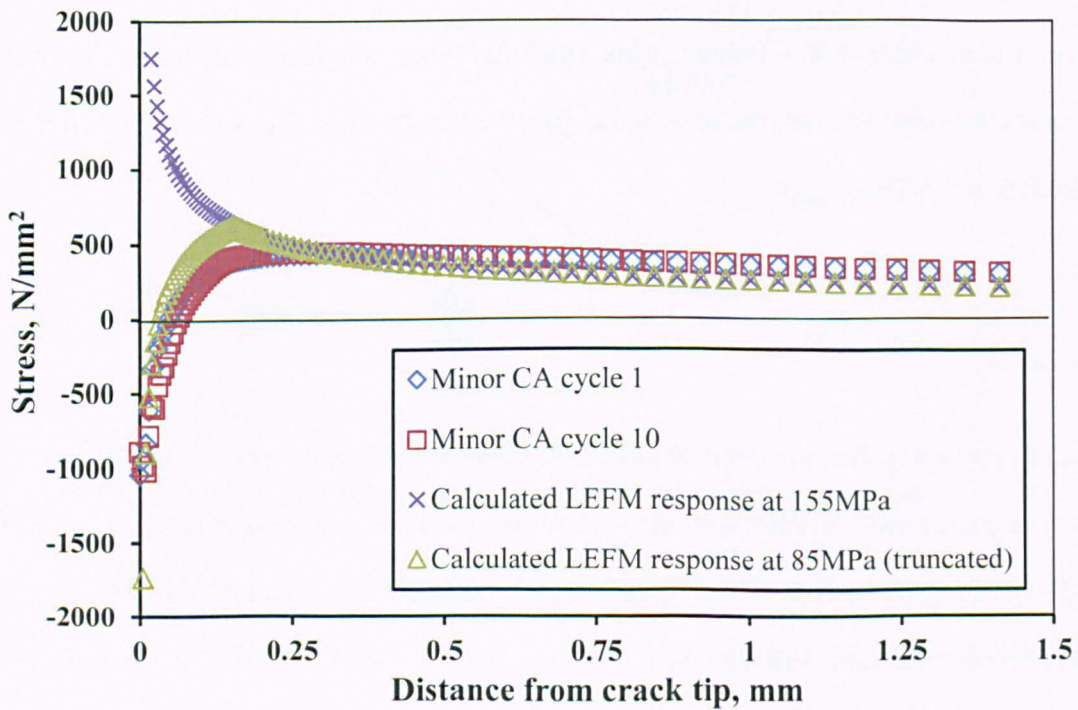


Figure B23 Validation of FE model showing the stress profile near the crack tip at the minimum nominal stress, and that derived using plane strain LEFM considering the elastic-plastic offset.

In Figure B23, the LEFM solutions are compared with the FEA results for application of the minimum nominal stress (85N/mm^2) by deducting the CA stress range (70N/mm^2) from the LEFM truncated maximum stress of 155N/mm^2 . As will be seen, the truncated LEFM response agrees well with the FEA results, providing further validation of the accuracy and robustness of the FE representation of the conditions at the crack tip under the applied loads.

B3 COMPARISON BETWEEN COLLAPSED AND QUADRILATERAL ELEMENTS

As discussed in Section 3.8, due to the uncertainty in whether crack growth would be modelled within this project, the more traditional method of meshing at the crack tip using collapsed elements was not performed; instead quadrilateral elements were used, Figure 3.8.6. It was considered that quadrilateral elements would be sufficiently fine to capture the crack tip stress field in the same way that collapsed elements would.

To investigate this, a second model of the plain steel CCT specimen was prepared and meshed using collapsed elements at the crack tip in order to compare the stress and strain plots obtained from this model with those obtained with the initial model meshed with quadrilateral elements.

Plots of stress and strain were obtained at the first loading (155N/mm^2 nominal stress) and first unloading (85N/mm^2 nominal stress) i.e. minor cycle, are presented in Figures B24 and B25, and show good similarity between the models. However, the stress at the first loading is predicted to be slightly larger with collapsed elements. It is worth noting that in both cases, the stress and strain profiles seem to be near-identical, but slightly offset. Because the offset is the same at loading and unloading, the difference in strain and stress between the profile at loading and unloading indicates good agreement between the models.

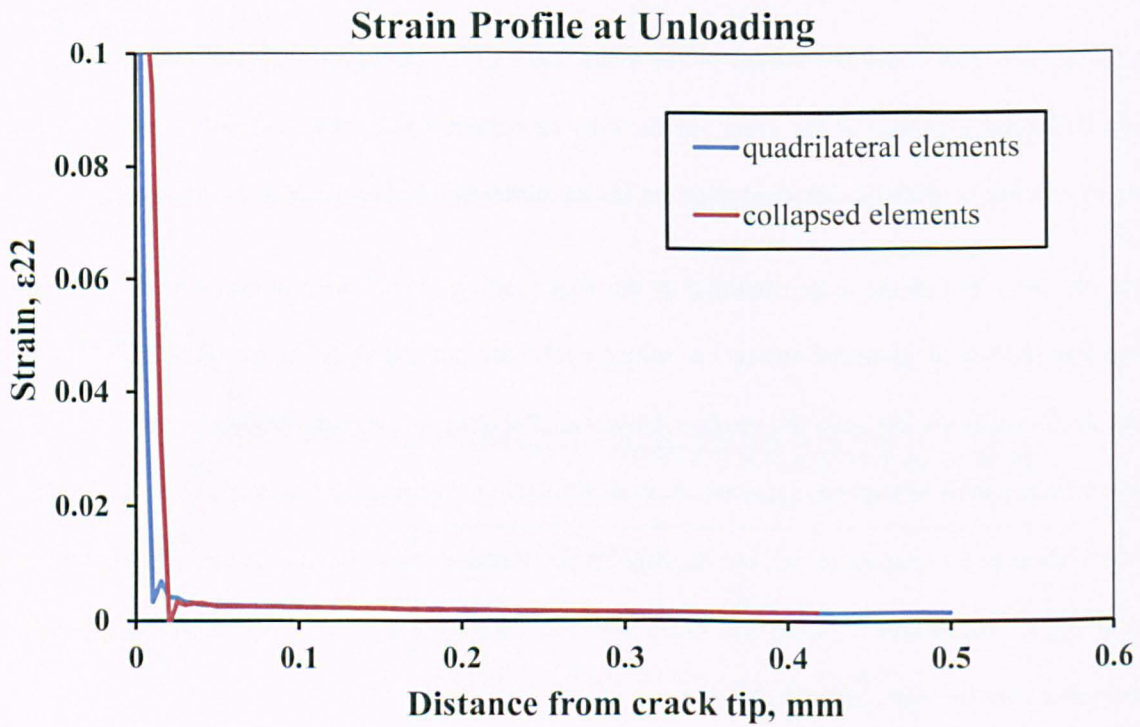
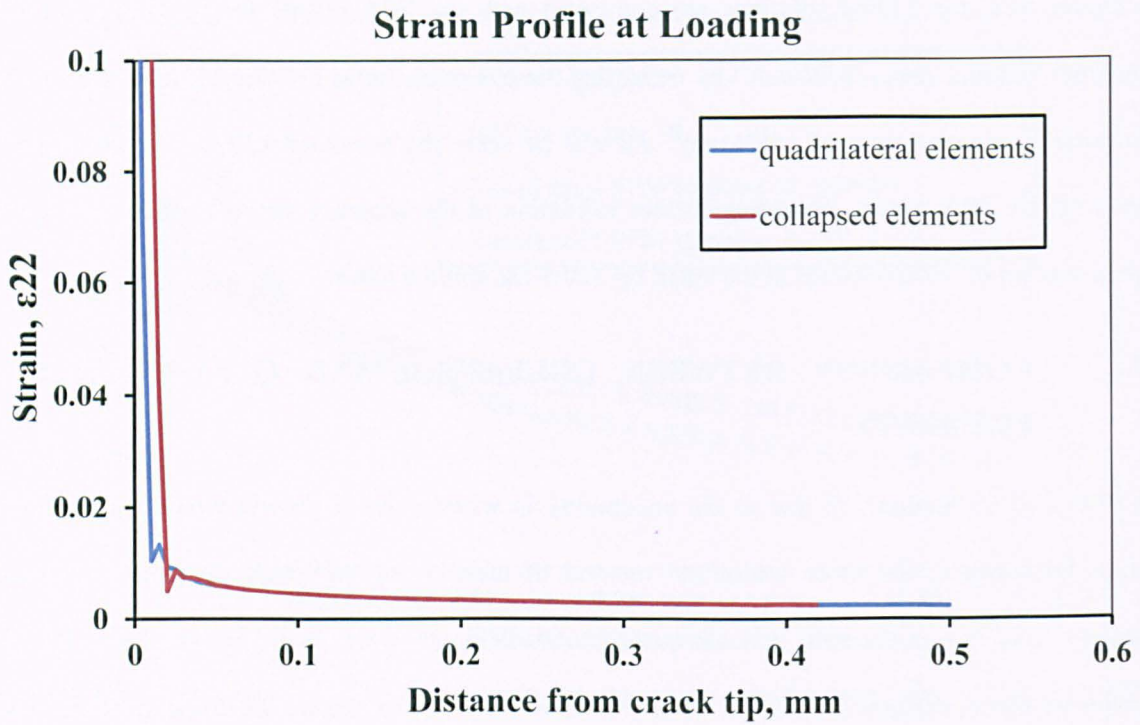


Figure B24 Comparison of the strain profile in S355 structural steel, obtained at the maximum and minimum applied loads (minor cycles) under constant amplitude loading.

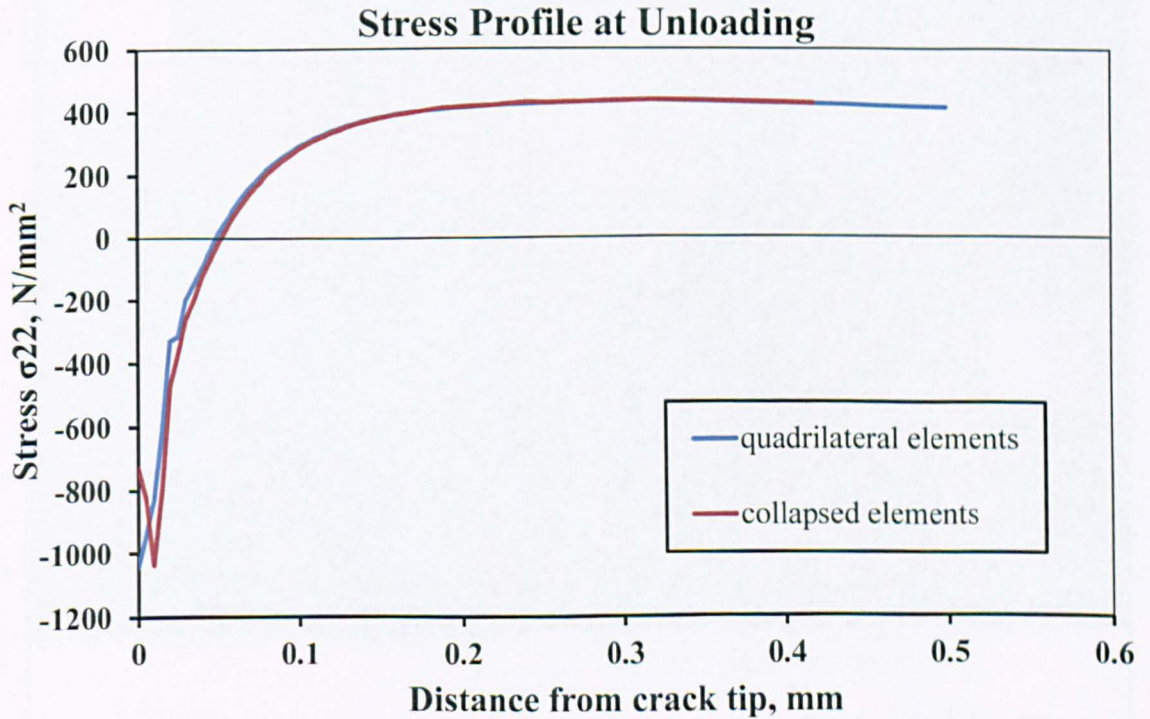
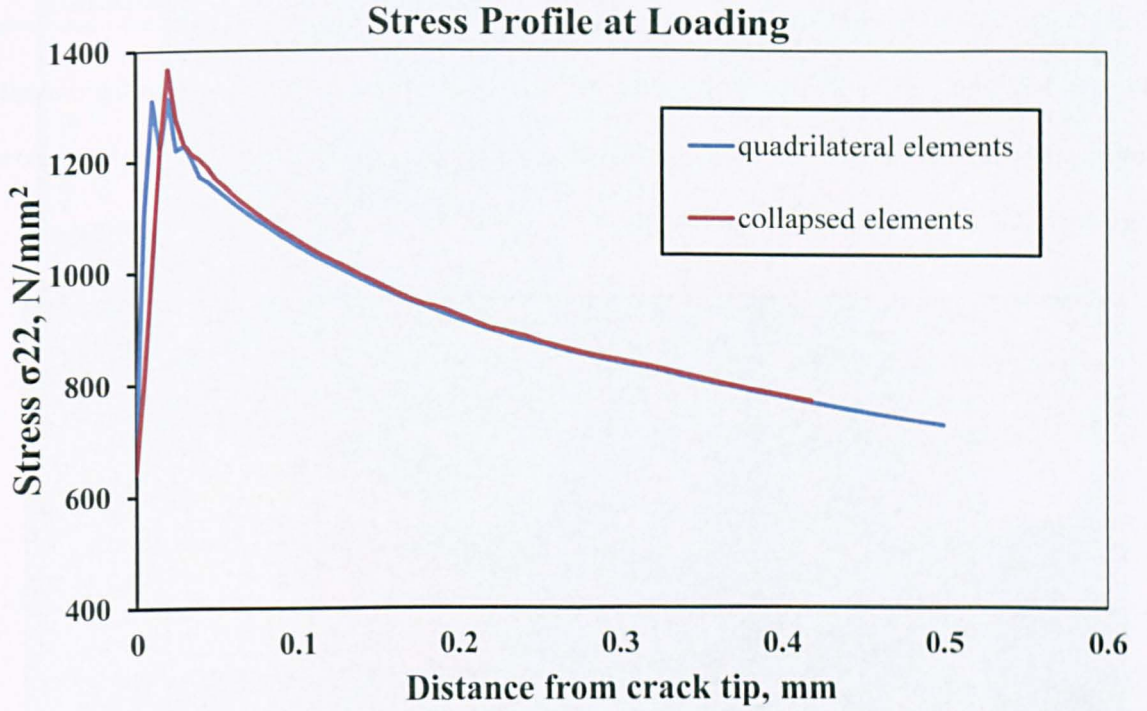
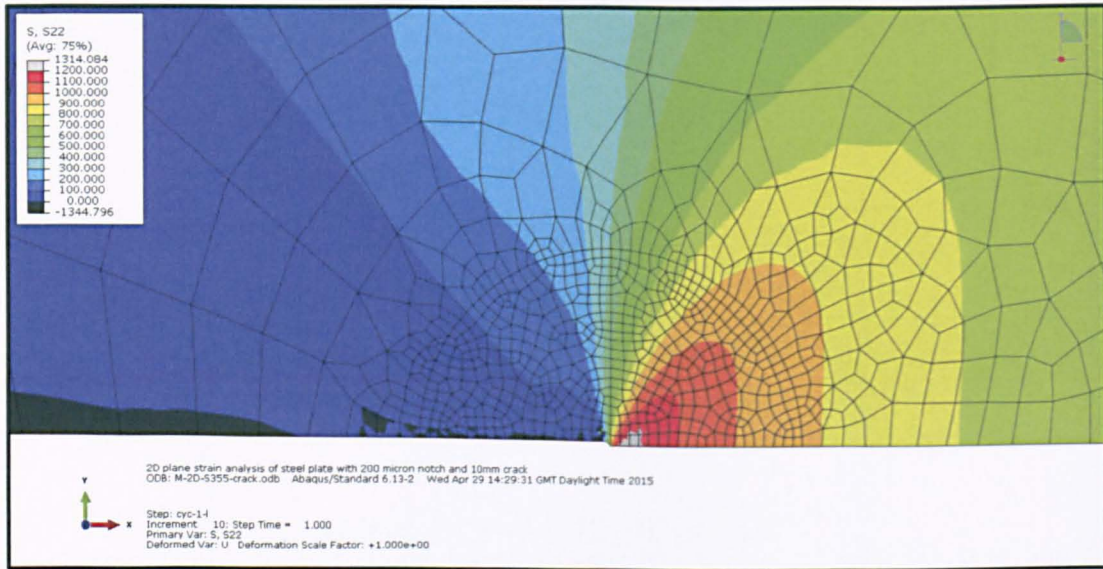
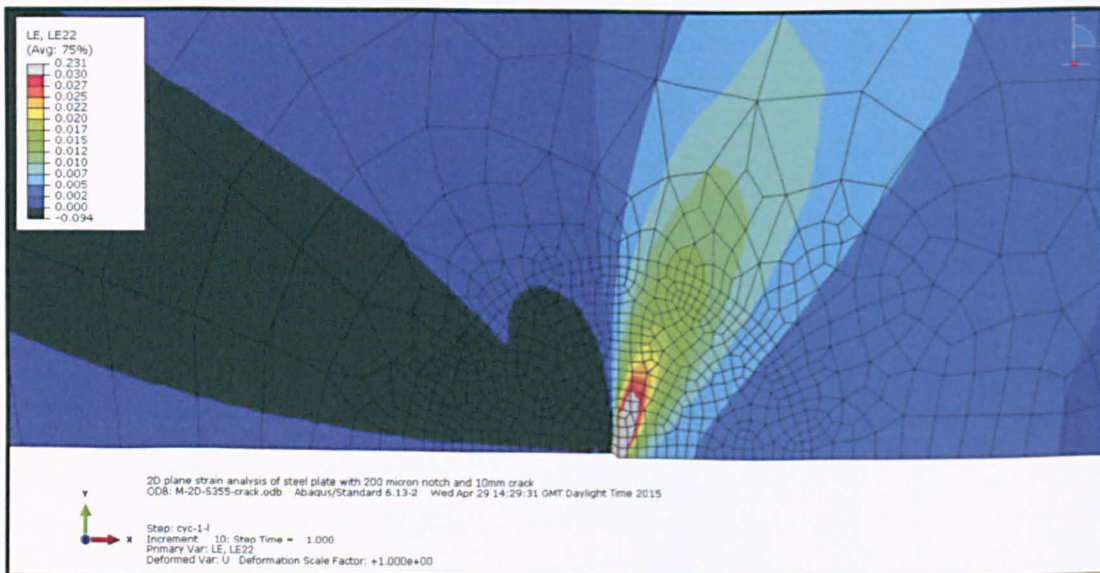


Figure B25 Comparison of the stress profile in S355 structural steel, obtained at the maximum and minimum applied loads (minor cycles) under constant amplitude loading.

Contour plots of stress and strain for the maximum load in the minor cycle were also produced (Figures B26 and B27) and also show good agreement between the models, although the multiple untied crack tip nodes used for the collapsed elements (Figure B27) allow for a more rounded blunting of the crack tip after the first loading due to low constraint.

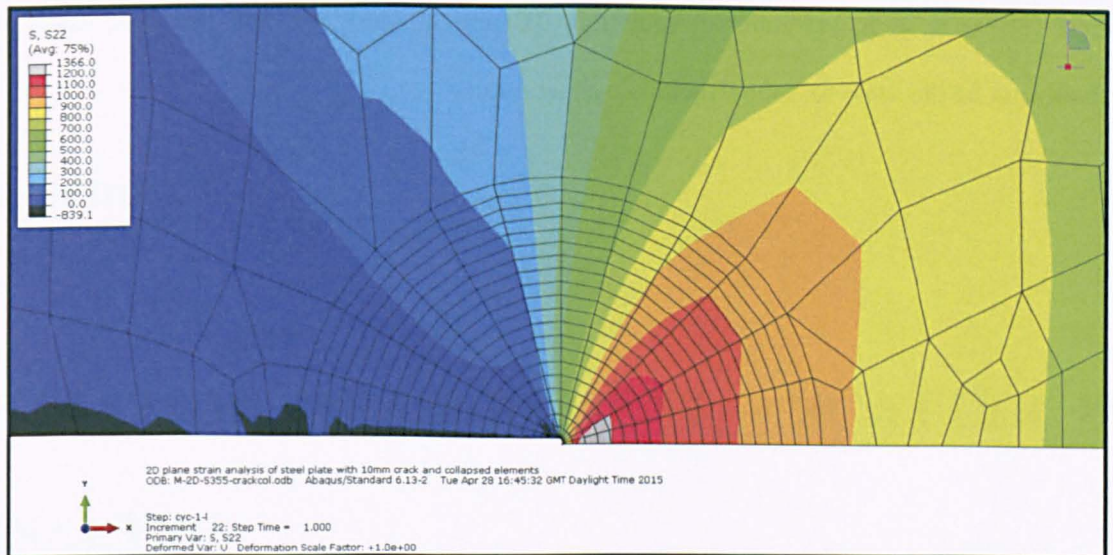


a)

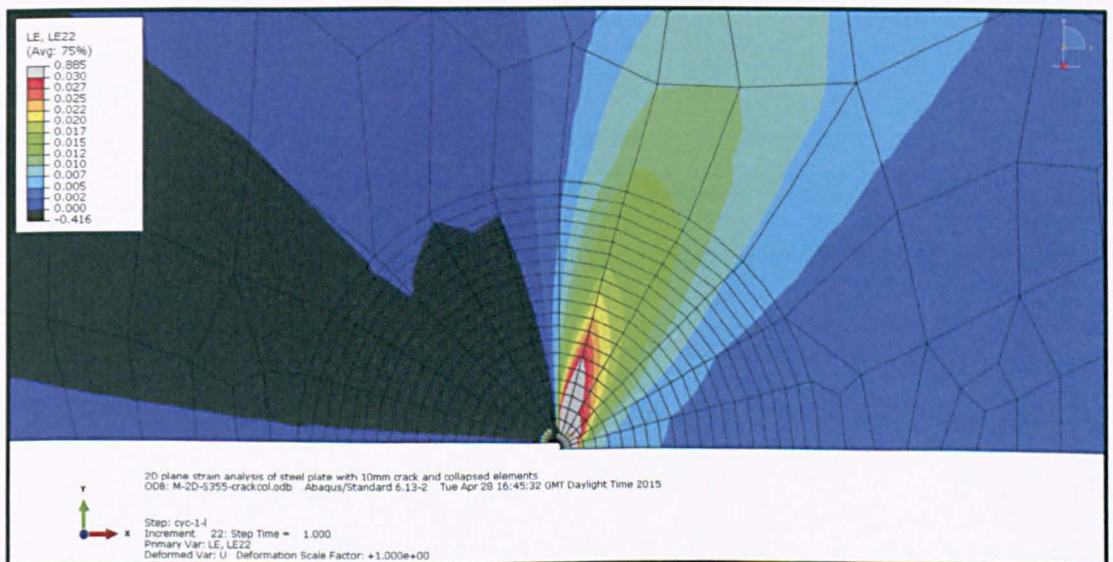


b)

Figure B26 Contour plots using quadrilateral elements for S355 structural steel, obtained at the maximum applied load for the minor cycle, showing a) Stress σ_{22} and b) strain ϵ_{22} .



a)



b)

Figure B27 Contour plots using collapsed elements for S355 structural steel, obtained at the maximum applied load for the minor cycle, showing a) Stress σ_{22} and b) strain ϵ_{22} .

This comparative study shows that, if quadrilateral elements are chosen for the crack tip in order to obtain a regular mesh that would allow for crack growth modelling (which was not analysed in this study), the stress and strain near the crack tip would not be significantly different to those obtained using collapsed elements, although the latter are designed for better capture of the crack tip singularity. However, it must be highlighted that in both models, the crack tip mesh was very

refined (elements with quadratic interpolation, 0.01mm in size), and that this conclusion may probably not be the same for models with a coarser mesh.

Appendix C

STRIATION MEASUREMENT – SCATTER IN ANALYSIS

CONTENTS

Table C1	Paris law constants derived from crack growth increment striation analysis on CCT-CAL-AL-12 (R=0.57), including upper and lower bound (mean $\pm 2SD$).
Table C2	Paris law constants derived from crack growth increment striation analysis on aluminium alloy major stress range SBL2 (R=0.14), including upper and lower bound (mean $\pm 2SD$).
Table C3	Paris law constants derived from crack growth increment striation analysis on aluminium alloy major stress range SBL1.5 (R=0.35), including upper and lower bound (mean $\pm 2SD$).
Figure C1	Comparison of mean $\pm 2SD$ of striation measurement data with FCGR data.
Figure C2	Comparison of mean $\pm 2SD$ of striation measurement data with FCGR data.
Figure C3	Comparison of mean $\pm 2SD$ and mean $-3SD$ of striation measurement data with FCGR data.

Table C1 Paris law constants derived from crack growth increment striation analysis on CCT-CAL-AL-12 ($R=0.57$), including upper and lower bound (mean $\pm 2SD$)

		$\Delta K,$ $N/mm^{3/2}$	$da/dN,$ $mm/cycle$	Upper bound	Lower bound
m	2.07	205	9.68E-05	1.56E-04	6.01E-05
C-mean	1.55E-09	390	3.68E-04	5.92E-04	2.28E-04
SD	0.10				
C-Upper Bound	2.49E-09				
C-Lower Bound	9.61E-10				

Table C2 Paris law constants derived from crack growth increment striation analysis on aluminium alloy major stress range SBL2 ($R=0.14$), including upper and lower bound (mean $\pm 2SD$)

		$\Delta K,$ $N/mm^{3/2}$	$da/dN,$ $mm/cycle$	Upper bound	Lower bound
m	2.02	400	3.02E-04	5.31E-04	1.72E-04
C-mean	1.68E-09	770	1.13E-03	1.99E-03	6.44E-04
SD	0.12				
C-Upper Bound	2.96E-09				
C-Lower Bound	9.57E-10				

Table C3 Paris law constants derived from crack growth increment striation analysis on aluminium alloy major stress range SBL1.5 (R=0.35), including upper and lower bound (mean $\pm 2SD$)

		ΔK , $N/mm^{3/2}$	da/dN , $mm/cycle$	Upper bound	Lower bound
M	2.88	305	2.53E-04	3.81E-04	1.68E-04
C-mean	1.76E-11	570	1.53E-03	2.31E-03	1.02E-03
SD	0.09				1.37E-04 ⁽¹⁾
C-Upper Bound	2.65E-11				8.32E-04 ⁽²⁾
C-Lower Bound	1.17E-11				
C-Lower Bound⁽¹⁾	9.55E-12				

Note. ⁽¹⁾ Constant C for mean -3SD; ⁽²⁾ crack growth law for mean -3SD.

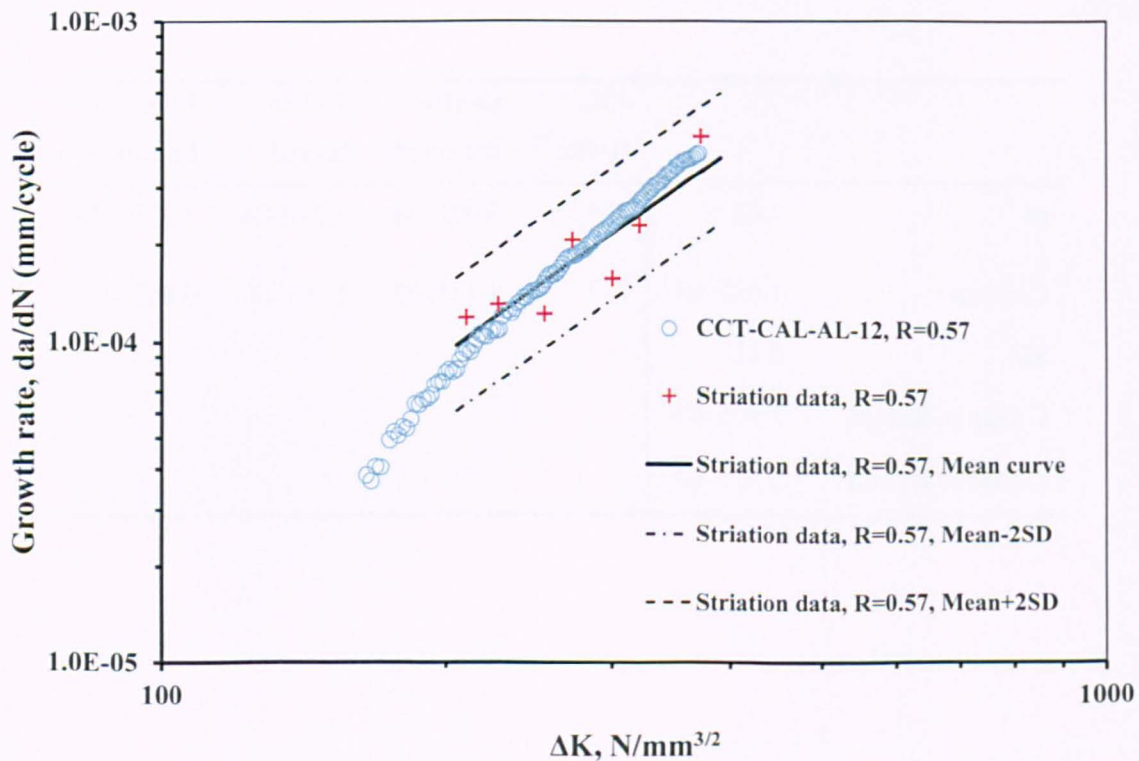


Figure C1 Comparison of mean $\pm 2SD$ of striation measurement data with FCGR data.

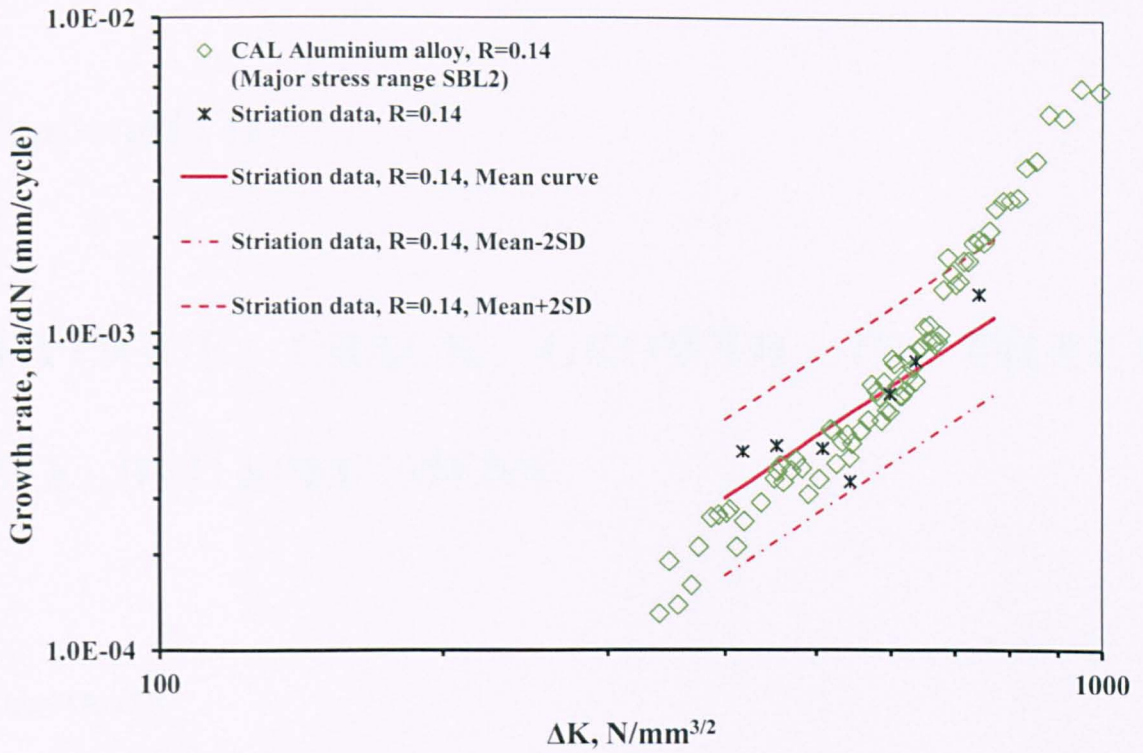


Figure C2 Comparison of mean $\pm 2SD$ of striation measurement data with FCGR data.

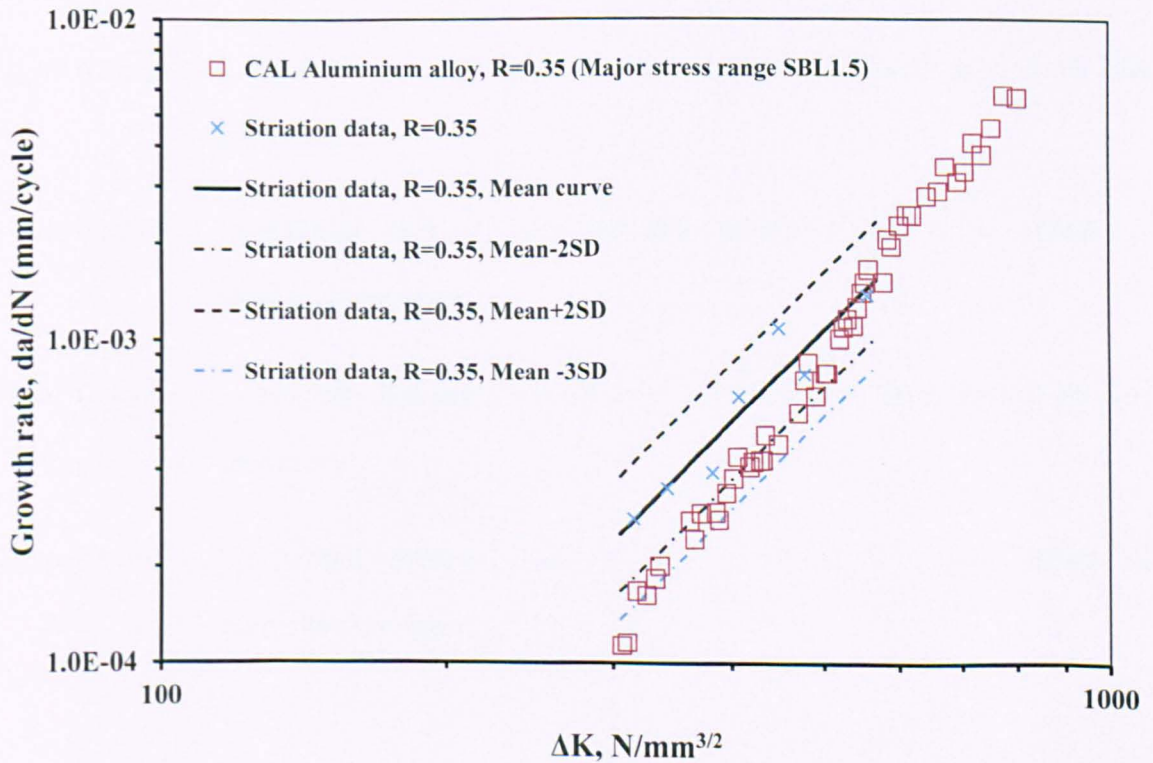


Figure C3 Comparison of mean $\pm 2SD$ and mean $-3SD$ of striation measurement data with FCGR data.

Appendix D

FATIGUE CRACK GROWTH IN FILLET WELDED SPECIMENS

CONTENTS

Table D1	Mk parameters for steel specimens.
Table D2	Mk parameters for aluminium alloy specimens.
Figure D1a)-g)	Comparison between measured and calculated CA crack growth for steel specimens.
Figure D2a)-f)	Comparison between measured and calculated CA crack growth for aluminium specimens.
Figure D3a)-e)	Comparison between measured and calculated VA crack growth for steel specimens.
Figure D4a)-f)	Comparison between measured and calculated VA crack growth for aluminium specimens.

Table D1 *Mk* parameters derived for steel crack growth predictions

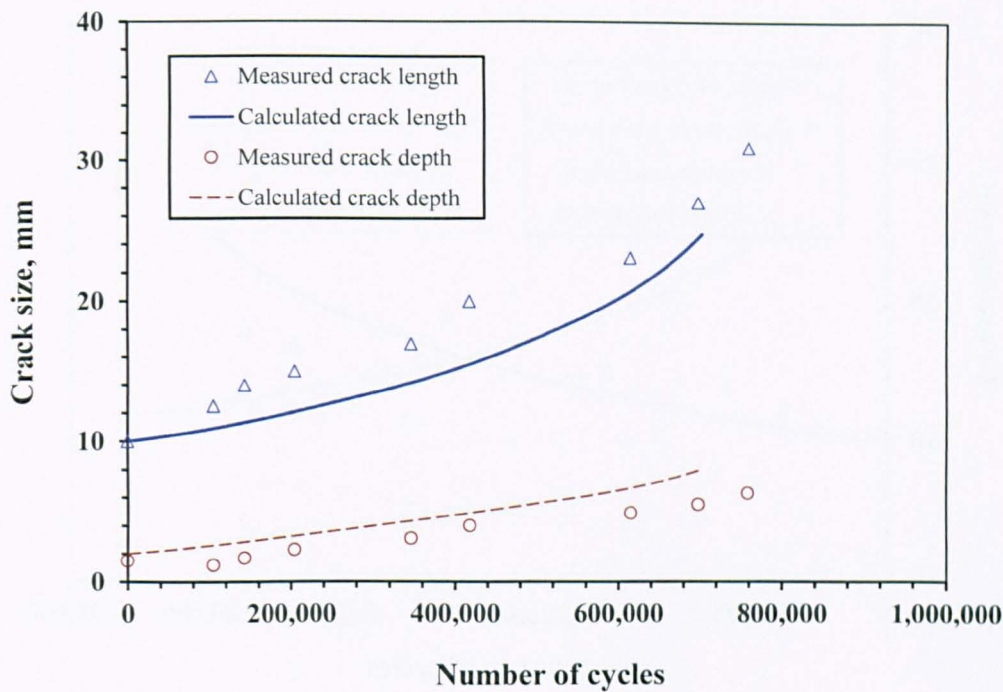
Crack length, $2c$	Crack depth, a	Ratio crack depth and specimen thickness, $a/B^{(1)}$		
		M_{ka}	M_{kc}	
0	0	0.003	4.7	3.4
0.25	0.05	0.006	4.2	3.4
0.5	0.1	0.013	3.4	3.4
0.75	0.15	0.019	3.0	3.4
1.5	0.3	0.038	2.4	3.2
2.5	0.5	0.063	2.0	2.8
3.75	0.75	0.094	1.8	2.4
6.5	1.3	0.163	1.5	2.0
10	2	0.250	1.3	1.6
20	4	0.500	1.1	1.2
30	6	0.750	1.0	1.0
40	8	1.000	1.0	1.0

Note. ⁽¹⁾ Steel specimens were 8mm in thickness.

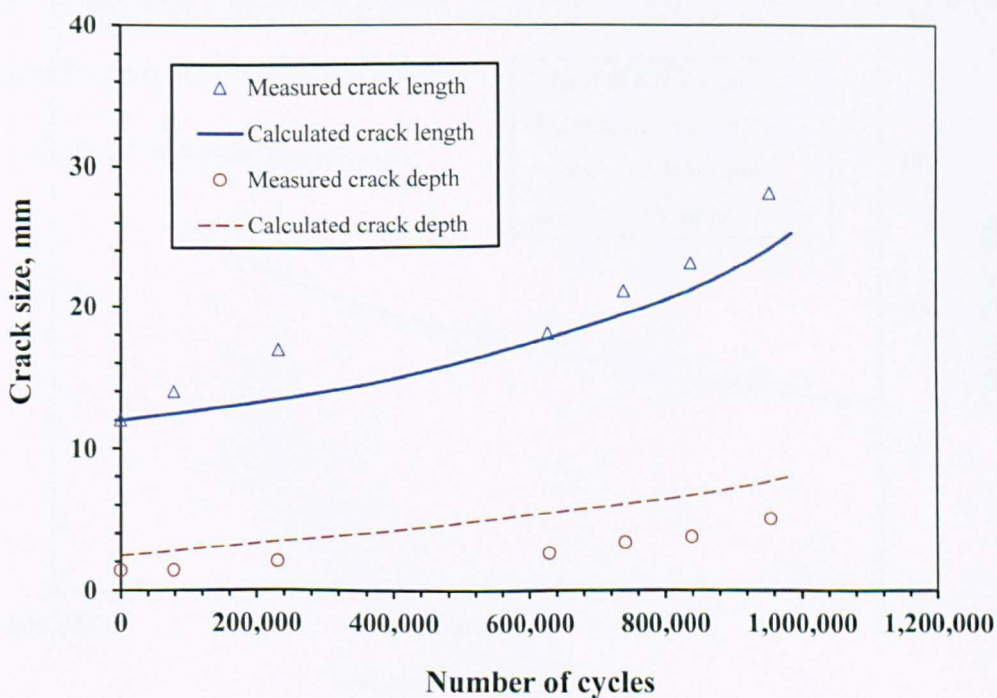
Table D2 *Mk* parameters derived for aluminium alloy crack growth predictions

Crack length, $2c$	Crack depth, a	Ratio crack depth and specimen thickness, $a/B^{(1)}$		
		M_{ka}	M_{kc}	
0	0	0.002	4.5	3.1
0.25	0.05	0.008	3.8	3.1
0.5	0.1	0.017	3.1	3.1
0.75	0.15	0.025	2.7	3.0
1.5	0.3	0.050	2.2	2.8
2.5	0.5	0.083	1.9	2.5
3.75	0.75	0.125	1.6	2.2
5	1	0.167	1.5	1.9
10	2	0.333	1.2	1.6
15	3	0.500	1.1	1.3
20	4	0.667	1.0	1.2
25	5	0.833	1.0	1.1
30	6	1.000	1.0	1.0

Note. ⁽¹⁾ Aluminium specimens were 6mm in thickness.



c)

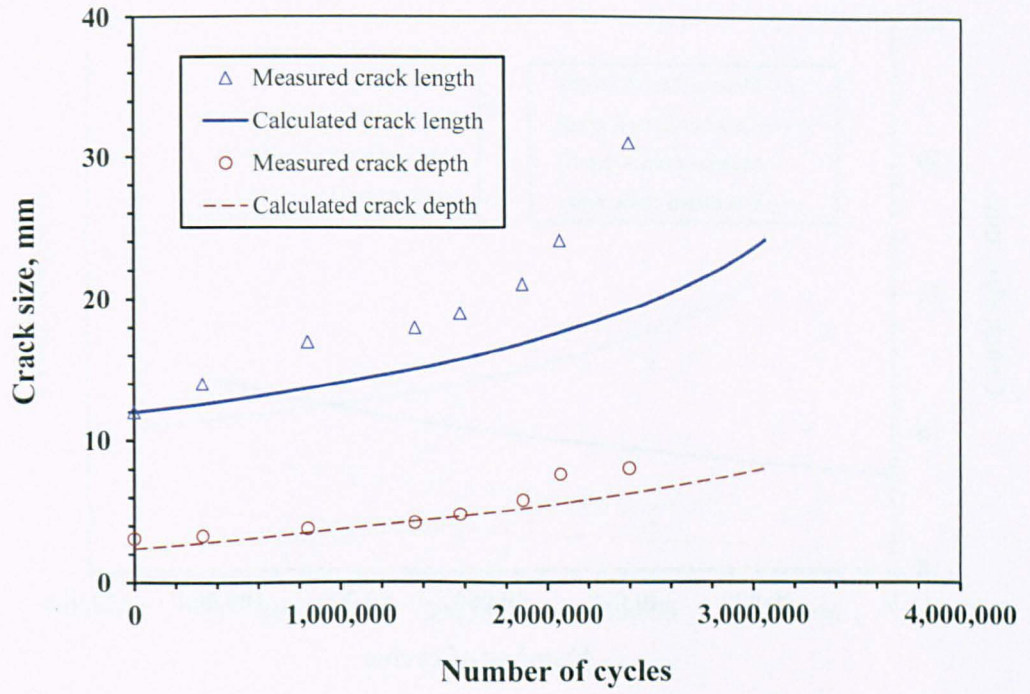


d)

Figure D1 (Continued) Comparison between the measured and calculated fatigue crack growth in steel specimens under CA loading at a maximum stress of 280N/mm^2 :

c) FIL-CAL-ST-03, 90N/mm^2 stress range;

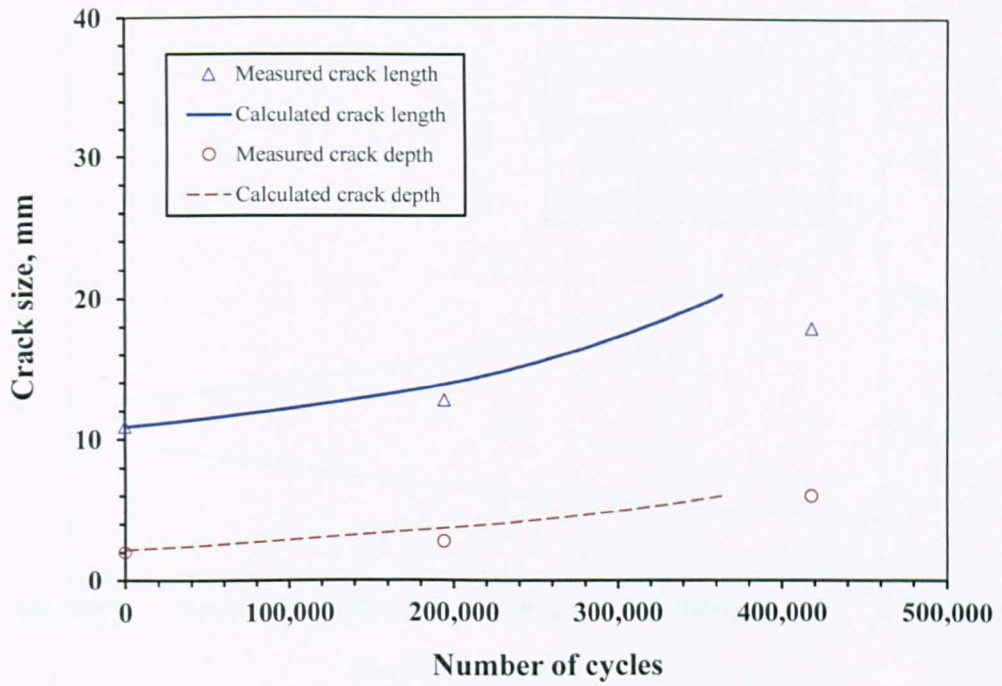
d) FIL-CAL-ST-04, 75N/mm^2 stress range;



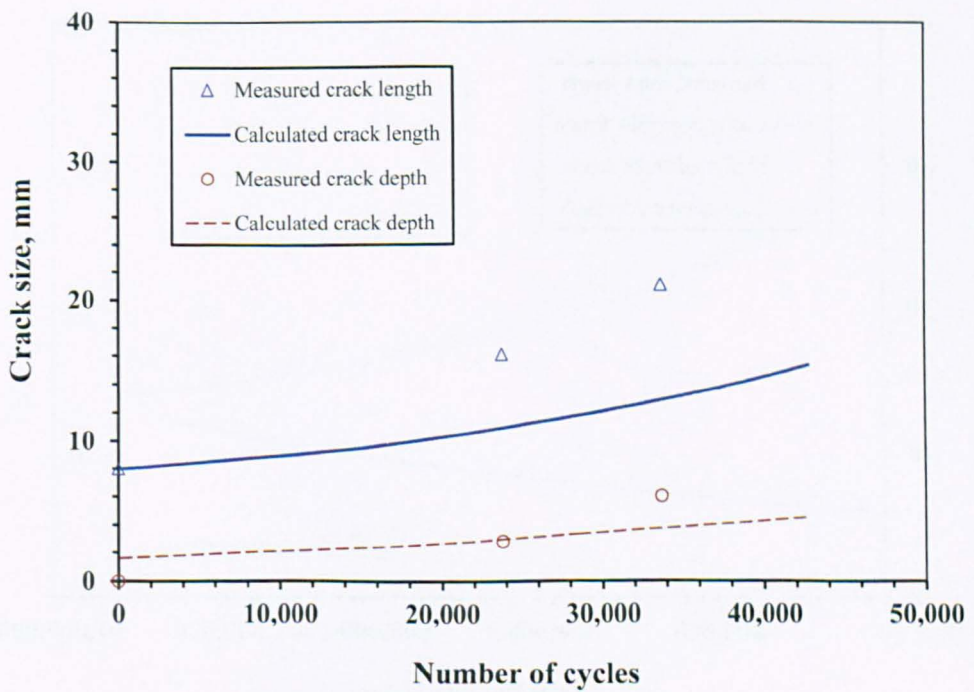
g)

Figure D1 (Continued) Comparison between the measured and calculated fatigue crack growth in steel specimens under CA loading at a maximum stress of 280N/mm^2 :

g) FIL-CAL-ST-07, 50N/mm^2 stress range.



c)

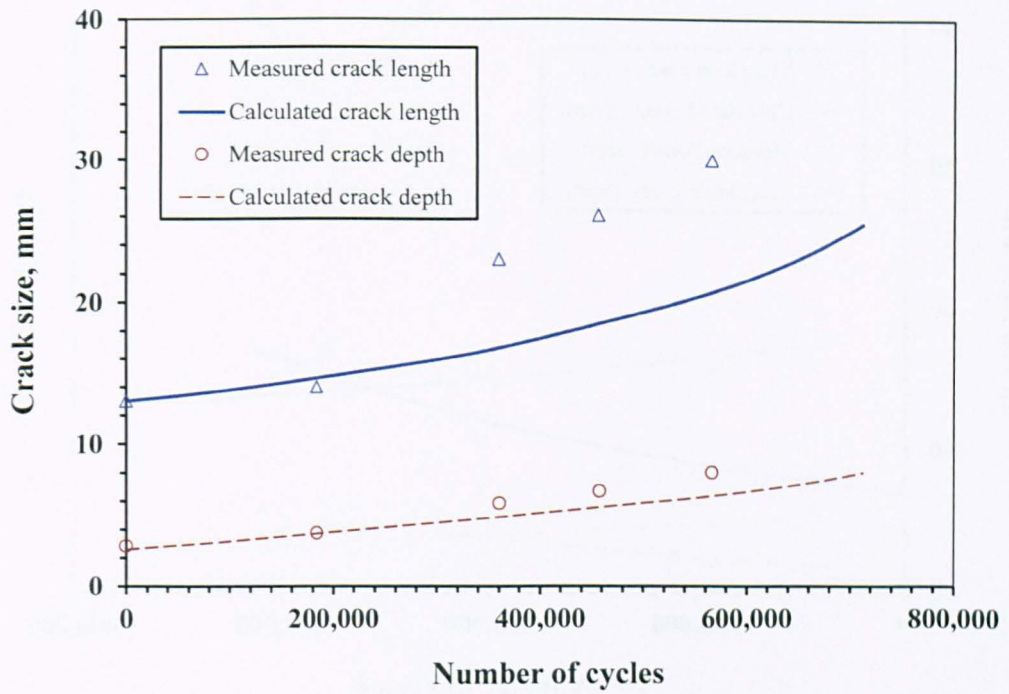


d)

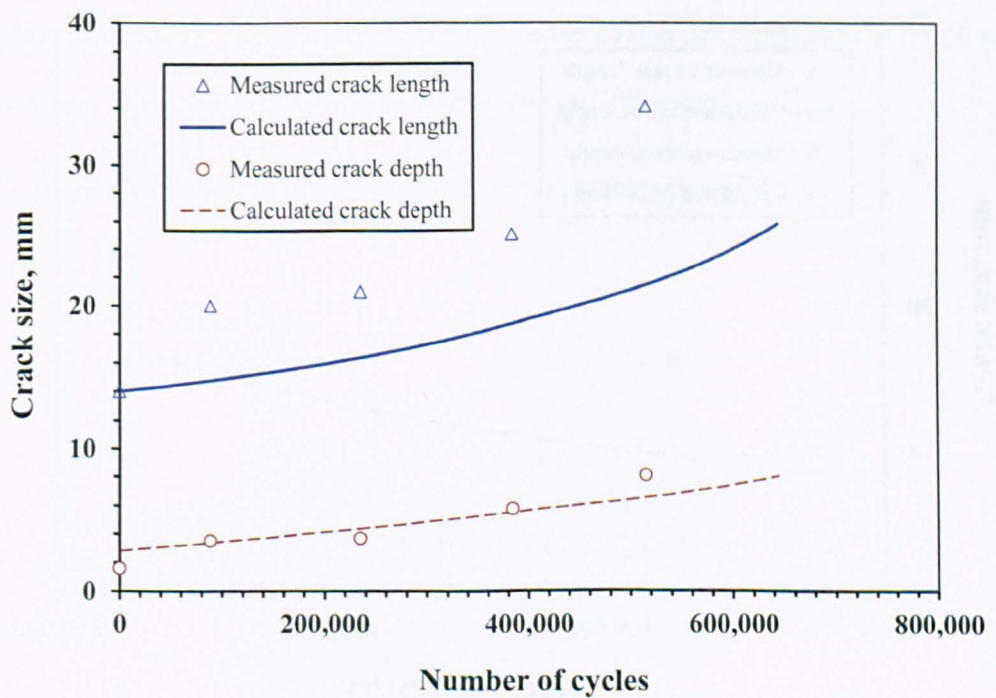
Figure D2 (Continued) Comparison between the measured and calculated fatigue crack growth in aluminium specimens under CA loading at a maximum stress of 120N/mm²:

c) FIL-CAL-AL-03, 30N/mm² stress range;

d) FIL-CAL-AL-04, 65N/mm² stress range;



a)

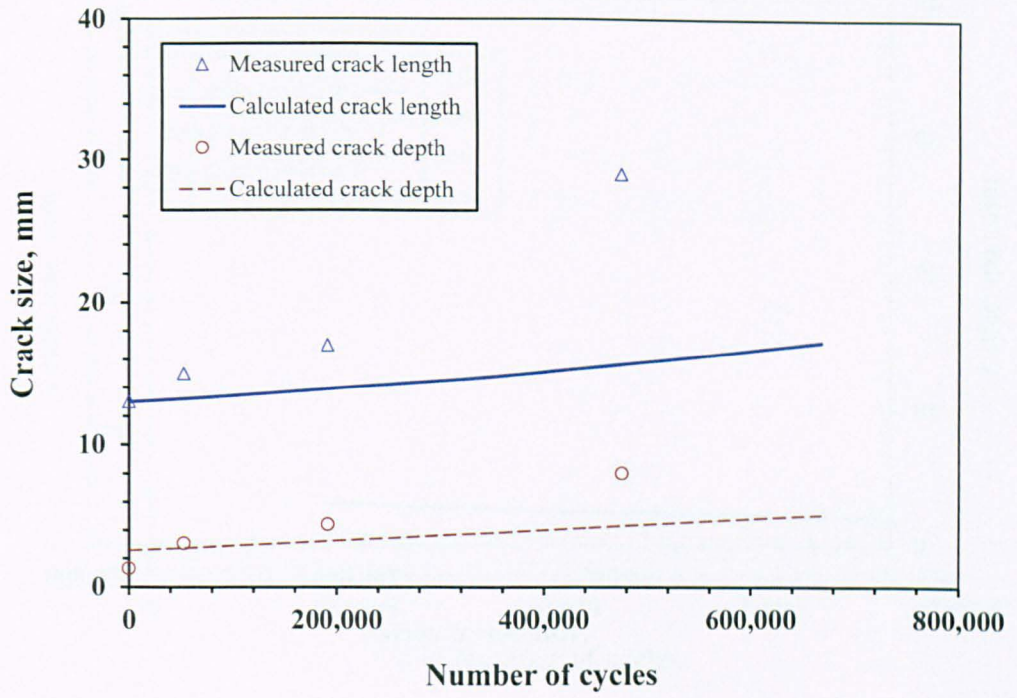


b)

Figure D3 Comparison between the measured and calculated fatigue crack growth in steel specimens under VA loading at a maximum stress of 280N/mm^2 :

a) FIL-VAL-ST-01, 73.6N/mm^2 equivalent stress range, minimum p_i 0.25;

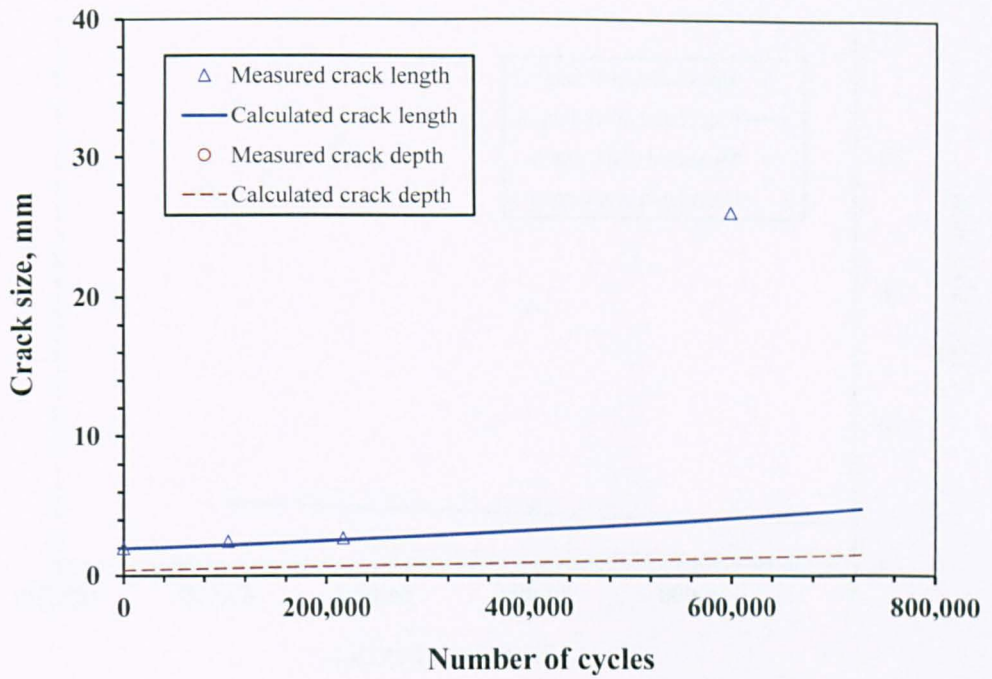
b) FIL-VAL-ST-02, 73.6N/mm^2 equivalent stress range, minimum p_i 0.25;



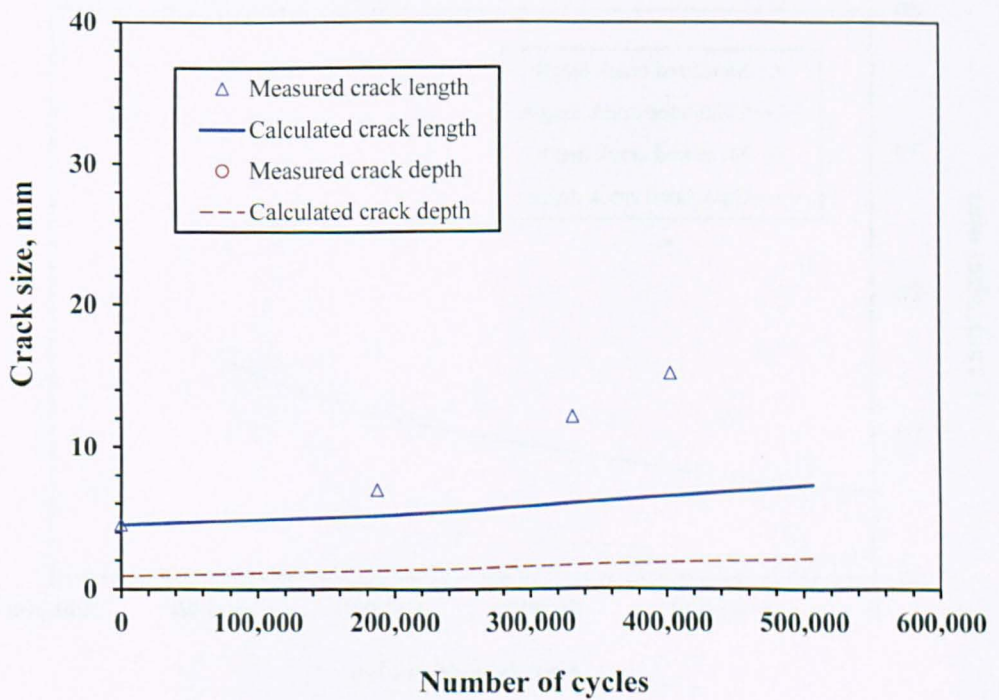
e)

Figure D3 (Continued) Comparison between the measured and calculated fatigue crack growth in steel specimens under VA loading at a maximum stress of 280N/mm^2 :

e) FIL-VAL-ST-05, 61.3N/mm^2 equivalent stress range, minimum p_i 0.20.



c)



d)

Figure D4 Comparison between the measured and calculated fatigue crack growth in aluminium specimens under VA loading at a maximum stress of 120N/mm^2 :

c) FIL-VAL-AL-03, 26.3N/mm^2 equivalent stress range, minimum p_i 0.20;

d) FIL-VAL-AL-04, 26.3N/mm^2 equivalent stress range, minimum p_i 0.20;